Scaled Boundary Finite Element Method for 2D and 3D Acoustic-Structure Interaction Analyses Considering Structural Elastoplasticity

by

Lei Liu

A thesis submitted in fulfilment
of the requirements for the degree of
Doctor of Philosophy

School of Civil and Environmental Engineering
The University of New South Wales
Sydney, Australia

August 2018

Thesis/Dissertation Sheet

Surname/Family Name	:	**Liu**
Given Name/s	:	**Lei**
Abbreviation for degree as give in the University calendar	:	**PhD**
Faculty	:	**Faculty of Engineering**
School	:	**School of Civil and Environmental Engineering**
Thesis Title	:	**Scaled Boundary Finite Element Method for 2D and 3D Acoustic-Structure Interaction Analyses Considering Structural Elastoplasticity**

Abstract 350 words maximum: (PLEASE TYPE)

The acoustic-structure interaction commonly exists in numerous civil and mechanical engineering applications, such as dam-reservoir interaction system, air-coupled ultrasonic testing and the design of underwater structures. In all these applications, the acoustic domains are usually infinitely large. Moreover, the distinct physical properties of acoustic and structural domains lead to the preference of using different mesh sizes for each domain in numerical modelling. Due to the intrinsic nature of scaled boundary finite element method in modelling unbounded domain and its versatility in mesh generation. This thesis presents the developments of this method for simulating 2D and 3D acoustic-structure interaction systems by considering the infinite acoustic domain and structural elastoplasticity, which frequently appears under strong excitations.

The high-order doubly-asymptotic open boundary is developed to simulate the wave propagation in 2D and 3D exterior acoustics accurately and efficiently. This is accomplished by solving the scale boundary finite element equation for unbounded acoustic domain in the frequency domain using doubly-asymptotic continued fractions. Via introducing the auxiliary variables, this open boundary can be formulated into a system of time-domain equations and thus suitable for non-linear analysis.

For the elastoplastic analysis of structures, the efficient scaled boundary formulation for elastoplasticity with stabilization is extended to 3D analysis. In this formulation, the computationally expensive return-mapping algorithm is only required to be performed at scaling centres as the elastoplastic constitutive matrices and internal stresses are assumed to be constants within each subdomain. Stabilisation matrices are introduces to control spurious modes. Additionally, Newmark's scheme is employed for dynamic elastoplastic analysis.

Mesh generation from the STL models of the whole system and mesh transition on the acoustic-structure interface, especially for 3D models with complex geometry, can be easily addressed with automatic mesh generation techniques, which benefit from the boundary discretization in scaled boundary finite element method. Both 2D and 3D numerical examples are presented in this thesis to highlight the accuracy, efficiency and robustness of the proposed techniques for the numerical simulations of acoustics, elastoplastic structures and acoustic-structure interaction problems.

FOR OFFICE USE ONLY Date of completion of requirements for Award:

ORIGINALITY STATEMENT

'I hereby declare that this submission is my own work and to the best of my knowledge it contains no materials previously published or written by another person, or substantial proportions of material which have been accepted for the award of any other degree or diploma at UNSW or any other educational institution, except where due acknowledgement is made in the thesis. Any contribution made to the research by others, with whom I have worked at UNSW or elsewhere, is explicitly acknowledged in the thesis. I also declare that the intellectual content of this thesis is the product of my own work, except to the extent that assistance from others in the project's design and conception or in style, presentation and linguistic expression is acknowledged.'

Signed …….....

Date …….....

COPYRIGHT STATEMENT

Signed …….....

Date …….....

AUTHENTICITY STATEMENT

‘I certify that the Library deposit digital copy is a direct equivalent of the final officially approved version of my thesis. No emendation of content has occurred and if there are any minor variations in formatting, they are the result of the conversion to digital format.’

Signed …….....

Date …….....

Abstract

The acoustic-structure interaction commonly exists in numerous civil and mechanical engineering applications, such as dam-reservoir interaction system, air-coupled ultrasonic testing and the design of underwater structures. In all these applications, the acoustic domains are usually infinitely large. Moreover, the distinct physical properties of acoustic and structural domains lead to the preference of using different mesh sizes for each domain in numerical modelling. Due to the intrinsic nature of scaled boundary finite element method in modelling unbounded domain and its versatility in mesh generation. This thesis presents the developments of this method for simulating 2D and 3D acoustic-structure interaction systems by considering the infinite acoustic domain and structural elastoplasticity, which frequently appears under strong excitations.

The high-order doubly-asymptotic open boundary is developed to simulate the wave propagation in 2D and 3D exterior acoustics accurately and efficiently. This is accomplished by solving the scale boundary finite element equation for unbounded acoustic domain in the frequency domain using doubly-asymptotic continued fractions. Via introducing the auxiliary variables, this open boundary can be formulated into a system of time-domain equations and thus suitable for non-linear analysis.

For the elastoplastic analysis of structures, the efficient scaled boundary formulation for elastoplasticity with stabilization is extended to 3D analysis. In this formulation, the computationally expensive return-mapping algorithm is only required to be performed at scaling centres as the elastoplastic constitutive matrices and

internal stresses are assumed to be constants within each subdomain. Stabilisation matrices are introduces to control spurious modes. Additionally, Newmark's scheme is employed for dynamic elastoplastic analysis.

Mesh generation from the STL models of the whole system and mesh transition on the acoustic-structure interface, especially for 3D models with complex geometry, can be easily addressed with automatic mesh generation techniques, which benefit from the boundary discretization in scaled boundary finite element method. Both 2D and 3D numerical examples are presented in this thesis to highlight the accuracy, efficiency and robustness of the proposed techniques for the numerical simulations of acoustics, elastoplastic structures and acoustic-structure interaction problems.

"*Success is not final, failure is not fatal. It is the courage to continue that counts.*"

Winston Churchill $(1874 - 1965)$

Acknowledgements

I would like to express my deepest gratitude and appreciation to my supervisor, Prof. Chongmin Song for his patient guidance and continuous support during my whole PhD study. His countless help and suggestions, as well as his vision to future developments in pertinent research areas, lead me to the correct path of academic research. Most importantly, his preciseness and well organized logic on research have greatly enlightened me on overcoming further obstacles in my life. Without his invaluable guidance and encouragement, this thesis would hardly have been completed.

I would also like to express my sincere thanks to my co-supervisor, Prof. Wei Gao for his advice on not only my studies but also my life since I was an undergraduate student. I am also grateful to Prof. Carolin Birk for her patient guidance and inspiring discussions during the past three and half years. Her consolation and assistance provide me with great courage to tackle numerous problems during my research. Many thanks go to Dr. Albert Saputra, Dr. Ke He and Mr. Junqi Zhang for their discussions on exchanging research ideas and collaborations. I would like to thank Dr. Di Wu and all my friends in office 602 and office 713 for our friendship.

I wish to express my heartfelt appreciation to my parents, Mr. Yi Liu and Mrs. Yuyan Ge, for supporting and encouraging me unconditionally with their selfless love. No word can describe how grateful I am to the sacrifices they have made on raising and teaching me. A special thank goes to my girlfriend, Miss. Baodai Liu, for her love and understanding during the completion of my degree.

Finally, I hope this thesis will not be the end of the explorations in my life.

Publications

Journal papers:

1. Birk, C., Liu, L., and Song, C. (2016). Coupled acoustic response of two-dimensional bounded and unbounded domains using doubly-asymptotic open boundaries. *Journal of Computational Physics*, 310:252-284.

2. Li, J., Shi, Z. and Liu, L. (2018). A unified scaled boundary finite element method for transient two-dimensional vibro-acoustic analysis of plate-like structures. *Computers & Structures*, 202:105-128.

3. Shi, Z., Li, J. and Liu, L. (2018). Vibro-acoustic analysis of two-directional functionally graded plates with infinite width using the scaled boundary finite element method. *Composite Structures*, under review.

4. Liu, L., Zhang, J., Song, C., Birk, C. and Gao, W. (2018). An automatic approach for the acoustic analysis of three-dimensional bounded and unbounded domains by scaled boundary finite element method. *International Journal of Mechanical Sciences*, under review

5. Liu, L., Song, C., Birk, C. and Gao, W. (2018). Automatic scaled boundary finite element method for three-dimensional acoustic-structure interaction analysis. *Computer Methods in Applied Mechanics and Engineering*, to be submitted

6. Liu, L., Song, C. He, K., Saputra, A. A. and Gao, W. (2018). Scaled boundary finite element method for three-dimensional elastoplastic analysis. *Composite Structures*, to be submitted

Conference paper:

1. Liu, L., Song, C., Gao, W. and Birk, C., 2016, November. Scaled boundary finite element method for exterior acoustic-structure interaction analyses. In *Mechanics of Structures and Materials XXIV : Proceedings of the* 24*th Australian Conference on the Mechanics of Structures and Materials* (*ACMSM*24, *Perth*, *Australia*, 6 – 9 *December* 2016) (p. 299). CRC Press.

Nomenclature

$\boldsymbol{\epsilon}$	Structural strain
$\boldsymbol{\Lambda}$	Diagonal matrix of eigenvalues for unbounded acoustic domain
$\boldsymbol{\Phi}$	Scaled boundary shape function for polyhedral subdomain
$\boldsymbol{\psi}^{(i_H)}$, $\boldsymbol{\psi}_L^{(0)}$	Additional coefficient matrices for unbounded acoustic domain
$\boldsymbol{\Psi}_\epsilon$	Scaled boundary strain modes for polyhedral subdomain
$\boldsymbol{\Psi}_\epsilon^{(c)}$, $\boldsymbol{\Psi}_\epsilon^{(n)}$	Constant and non-constant parts of scaled boundary strain modes for polyhedral subdomain
$\boldsymbol{\Psi}_\infty$	Matrix of eigenvectors for unbounded acoustic domain
$\boldsymbol{\Psi}_{q_n}$	Modal force for bounded structural domain in static analysis
$\boldsymbol{\Psi}_{q_p}$	Modal force for unbounded structural domain in static analysis
$\boldsymbol{\Psi}_{u_n}$	Modal displacement for bounded structural domain in static analysis
$\boldsymbol{\Psi}_{u_n}^{(c)}$, $\boldsymbol{\Psi}_{u_n}^{(n)}$	Constant and non-constant parts of modal displacement for bounded structural domain in static analysis
$\boldsymbol{\Psi}_{u_p}$	Modal displacement for unbounded structural domain in static analysis
$\boldsymbol{\sigma}$	Structural stress

$\boldsymbol{\sigma}^{(c)}$, $\boldsymbol{\sigma}^{(n)}$	Constant and non-constant stress parts for polyhedral subdomain
$\boldsymbol{\theta}$, $\boldsymbol{\varphi}$	Nodal angles on the boundary in polar coordinates
χ	Relative norm of residual force
χ_{tol}	Predefined convergence tolerance value
$\Delta\boldsymbol{\epsilon}$	Total incremental strain
$\Delta\boldsymbol{\epsilon}_e$	Elastic incremental strain
$\Delta\boldsymbol{\epsilon}_p$	Plastic incremental strain
$\Delta\boldsymbol{\sigma}$	Incremental stress
$\Delta\lambda$	Plastic multiplier
γ, β	Coefficients in Newmark's method
λ_j	Square root of eigenvalues for unbounded acoustic domain
(ξ, η, ζ)	Scaled boundary coordinates
ν	Poisson ratio
ω	Excitation frequency
ω_{max}	Maximum relevant excitation frequency
ρ_a	Acoustic density
ρ_s	Structural density
σ_y	Uniaxial yield stress
θ, φ	Angles in polar coordinates

$\bar{\mathbf{F}}_G$	Right-hand-side of symmetric time-domain equations for coupled system of infinite acoustic and structural domains
$\bar{\mathbf{F}}_G^{ep}$	Right-hand-side of symmetric time-domain equations for coupled system of infinite acoustic and elastoplastic structural domains
$\bar{\mathbf{M}}_G$, $\bar{\mathbf{C}}_G$, $\bar{\mathbf{K}}_G$	Global mass, damping and stiffness matrices in symmetric formulation for coupled system of infinite acoustic and structural domains
$\bar{\mathbf{M}}_G^{ep}$, $\bar{\mathbf{C}}_G^{ep}$, $\bar{\mathbf{K}}_G^{ep}$	Global mass, damping and stiffness matrices in symmetric formulation for coupled system of infinite acoustic and elastoplastic structural domains
$\bar{\mathbf{Z}}_G$	Global vector of unknowns in symmetric formulation for coupled system of infinite acoustic and structural domains
$\bar{\mathbf{Z}}_G^{ep}$	Global vector of unknowns in symmetric formulation for coupled system of infinite acoustic and elastoplastic structural domains
Δt	Time step
$\Delta\mathbf{u}_b$	Incremenal nodal displacement for bounded structural subdomain
$\hat{\mathbf{F}}$	Vector of nodal force amplitude
$\hat{\mathbf{p}}$	Vector of nodal pressure amplitude
$\hat{\mathbf{p}}_e$	Vector of nodal pressure amplitude on open boundary
$\hat{\mathbf{Q}}$	Vector of internal nodal flux amplitude
$\hat{\mathbf{q}}$	Vector of internal nodal force amplitude
$\hat{\mathbf{R}}$	Vector of nodal flux amplitude

$\hat{\mathbf{R}}_e$	Vector of nodal flux amplitude on the open boundary
$\hat{\mathbf{T}}$	Vector of surface traction amplitude
$\hat{\mathbf{u}}$	Vector of nodal displacement amplitude for structural domain
$(\hat{x},\, \hat{y},\, \hat{z})$	Cartesian coordinates
$(\mathbf{x}_b,\, \mathbf{y}_b,\, \mathbf{z}_b)$	Vectors of nodal coordinates on the boundary
$(x,\, y,\, z)$	Cartesian coordinates on the boundary
$\mathbf{B}$	Scaled boundary strain-displacement matrix for polyhedral subdomain
$\mathbf{B}^{(c)},\, \mathbf{B}^{(n)}$	Constant and non-constant parts of scaled boundary strain-displacement matrix for polyhedral subdomain
$\mathbf{B}_1^a,\, \mathbf{B}_2^a$	B matrices for acoustic domain
$\mathbf{b}_1^a,\, \mathbf{b}_2^a,\, \mathbf{b}_3^a$	Small b matrices for acoustic domain
$\mathbf{B}_1^s,\, \mathbf{B}_2^s$	B matrices for structural domain
$\mathbf{b}_1^s,\, \mathbf{b}_2^s,\, \mathbf{b}_3^s$	Small b matrices for structural domain
$\mathbf{c}_n$	Integration constant for bounded structural domain in static analysis
$\mathbf{D}$	Elasticity matrix
$\mathbf{D}_{ep}$	Elastoplastic constitutive matrix
$\mathbf{E}_0^a,\, \mathbf{E}_1^a,\, \mathbf{E}_2^a,\, \mathbf{M}_0^a$	Element coefficient matrices for acoustic domain
$\mathbf{E}_0^s,\, \mathbf{E}_1^s,\, \mathbf{E}_2^s,\, \mathbf{M}_0^s$	Element coefficient matrices for structural domain
$\mathbf{F}$	Vector of nodal force

$\mathbf{F}_{as}$	Vector of nodal force on acoustic-structure interface
$\mathbf{F}_{ext}$	External load vector for bounded structural subdomain
$\mathbf{F}_G$	Right-hand-side of time-domain equations for coupled system of infinite acoustic and structural domains
$\mathbf{f}_G$	Right-hand-side of time-domain equations for structural domains
$\mathbf{F}_G^{ep}$	Right-hand-side of time-domain equations for coupled system of infinite acoustic and elastoplastic structural domains
$\mathbf{F}_{int}$	Internal load vector for bounded structural subdomain
$\mathbf{F}_{int}^{(c)}$, $\mathbf{F}_{int}^{(n)}$	Constant and non-constant stress parts of internal load vector for bounded structural subdomain
$\mathbf{H}_{as}$	Coupling matrix in acoustic-structure interaction
$\mathbf{I}$	Identity matrix
$\mathbf{J}$	Jacobian matrix on the boundary
$\mathbf{K}_{ep}$	Elastoplastic stiffness matrix for bounded structural subdomain
$\mathbf{K}_{ep}^{(c)}$, $\mathbf{K}_{ep}^{(n)}$	Constant and non-constant stress parts of elastoplastic stiffness matrix for bounded structural subdomain
$\mathbf{K}_e$	Elastic stiffness matrix for bounded structural subdomain
$\mathbf{K}_e^a$, $\mathbf{C}_e^a$	Stiffness and damping matrices for unbounded acoustic domain
$\mathbf{L}$	Strain-displacement relationship for structural domain
$\mathbf{M}$	Mass matrix for bounded structural subdomain
$\mathbf{M}_a$, $\mathbf{K}_a$	Mass and stiffness matrices from low-frequency expansions of acoustic impedance for bounded acoustic domain

$\mathbf{M}_G$, $\mathbf{C}_G$, $\mathbf{K}_G$	Global mass, damping and stiffness matrices for coupled system of infinite acoustic and structural domains
$\mathbf{M}_G^a$, $\mathbf{C}_G^a$, $\mathbf{K}_G^a$	Global mass, damping and stiffness matrices for coupled system of bounded and unbounded acoustic domains
$\mathbf{M}_G^{ep}$, $\mathbf{C}_G^{ep}$, $\mathbf{K}_G^{ep}$	Global mass, damping and stiffness matrices for coupled system of infinite acoustic and elastoplastic structural domains
$\mathbf{M}_G^s$, $\mathbf{K}_G^s$	Global mass and stiffness matrices for structural domains
$\mathbf{M}_h^a$, $\mathbf{K}_h^a$	Mass and stiffness matrices for bounded acoustic domain
$\mathbf{M}_s$, $\mathbf{K}_s$	Mass and stiffness matrices from low-frequency expansions of dynamic stiffness for structural domain
$\mathbf{N}$	Mapping function for geometry or shape function for acoustic domain
$\mathbf{N}_s$	Shape function for structural domain
$\mathbf{p}$	Vector of nodal pressure
$\mathbf{p}^{(i)}$	Auxiliary variables for bounded acoustic domain
$\mathbf{p}_e$	Vector of nodal pressure on open boundary
$\mathbf{r}$	Right-hand-side of time-domain equations for bounded acoustic domain
$\mathbf{R}^{ext}$	Vector of external nodal flux
$\mathbf{R}_{as}$	Vector of nodal flux on acoustic-structure interface
$\mathbf{R}_e$	Vector of nodal flux on open boundary
$\mathbf{r}_e$	Right-hand-side of time-domain equations for unbounded acoustic domain

$\mathbf{r}_G$	Right-hand-side of time-domain equations for coupled system of bounded and unbounded acoustic domains
$\mathbf{S}^a$	Impedance matrix for bounded acoustic domain
$\mathbf{S}^s$	Dynamic-stiffness matrix for structural domain
$\mathbf{S}_{a0}^{(i)}$, $\mathbf{S}_{a1}^{(i)}$	High-order continued-fraction coefficient matrices for bounded acoustic domain
$\mathbf{S}_n$	Eigenvalues with negative real part for bounded structural domain in static analysis
$\mathbf{S}_p$	Eigenvalues with positive real part for unbounded structural domain in static analysis
$\mathbf{S}_{s0}^{(i)}$, $\mathbf{S}_{s1}^{(i)}$	High-order continued-fraction coefficient matrices for structural domain
$\mathbf{T}_{as}$	Normal traction on acoustic-structure interface
$\mathbf{u}$	Vector of nodal displacement for structural domain
$\mathbf{u}^{(i)}$	Auxiliary variables for structural domain
$\mathbf{u}_G$	Global vector of unknowns for structural domain
$\mathbf{X}_a^{(i)}$	Additional coefficient matrices for bounded acoustic domain
$\mathbf{X}_s^{(i)}$	Additional coefficient matrices for structural domain
$\mathbf{y}$	Vector of unknowns for bounded acoustic domain
$\mathbf{Y}_{L0}^{(i_H)}$, $\mathbf{Y}_{L0}^{(i_H)}$	Doubly-asymptotic continued-fraction coefficient matrices from high-frequency expansions for unbounded acoustic domain
$\mathbf{Y}_{L0}^{(i_L)}$, $\mathbf{Y}_{L0}^{(i_L)}$	Doubly-asymptotic continued-fraction coefficient matrices from low-frequency expansions for unbounded acoustic domain

$\mathbf{Z}$	Hamiltonian coefficient matrix
$\mathbf{z}$	Vector of unknowns for unbounded acoustic domain
$\mathbf{Z}_G$	Global vector of unknowns for coupled system of infinite acoustic and structural domains
$\mathbf{z}_G$	Global vector of unknowns for coupled system of bounded and unbounded acoustic domains
$\mathbf{Z}_G^{ep}$	Global vector of unknowns for coupled system of infinite acoustic and elastoplastic structural domains
$\tilde{\mathbf{P}}$	Modal pressure vector for unbounded acoustic domain
$\tilde{\mathbf{p}}^{(i_H)}$, $\tilde{\mathbf{p}}_L^{(i_L)}$	Auxiliary variables for unbounded acoustic domain
$\tilde{\mathbf{R}}$	Modal flux vector for unbounded acoustic domain
$\vec{\mathbf{n}}$	Unit normal vector
a	Dimensionless frequency
a_0	Dimensionless frequency on the boundary
c	Sound speed
c_p	Pressure wave speed in structure
c_s	Shear wave speed in structure
E	Elastic modulus
H	Hardening modulus
M	Order of continued fractions for bounded domain
M_H, M_L	Orders of doubly-asymptotic continued fractions for unbounded acoustic domain

p	Acoustic pressure
p_{as}	Acoustic pressure on the acoustic-structure interface
r_0	Radius of open boundary
S_j	Modal impedance coefficient for unbounded acoustic domain

Contents

List of Tables

List of Figures

Chapter 1

Introduction

1.1 Background

In numerous engineering and physical systems, the dynamic interactions between man-made structures and acoustic media are inevitable due to the ubiquity of acoustic media, such as water and air. The modelling of these dynamic interactions are of great significance in various of practical problems including the sound propagation into ears, radiation of sound from bells, dam-reservoir interaction, noise control in high-speed rail way and the designs of microphones and speakers. In some of these problems, the sound radiated into the acoustic field is caused by the vibration of structures or the structural vibration is induced by the incident sound wave. This type of acoustic-structure interaction problems, which is also known as the vibroacoustics, is studied in this thesis. The acoustic media investigated in this research are assumed to be compressible but irrotational and inviscid and undergo small perturbations from the equilibrium hydrostatic state. In addition, the acoustic media can be infinite or semi-infinite for representing the environment, such as the atmosphere, ocean, lake or reservoir, surrounding the structure. In another type of acoustic-structure interaction problems, which is commonly known as the aeroacoustics, the generation of acoustic waves is caused by the interactions between

unsteady fluid flows and structures. Typical examples of aeroacoustics include the noise from the rotation of propeller and voice generated from human vocal cord. The considerations of aeroacoustics are out of the scope of present work. In the following part of this section, some of the early works on acoustic-structure interactions are introduced.

In a broader sense, the problems on the interaction between fluids, including acoustics, and structures are old and relevant studies can be traced back to eighteenth century. In 1779, Pierre Louis Gabriel Du Buat (Du Buat et al., 1779) observed the vibrations of submerged spherical pendulums made of glass, lead and wood in water. According to the results from observations, He concluded that the effect of surrounding fluid on the vibrating solid is approximately equal to the increase of its mass by one-half the mass of fluid, which is displaced by the submerged solid. Since then, a variety of experiments and analyses were performed to investigate the influence of fluid media on the responses of submerged structures (Stelson, 1955). Later, similar results were also published by Stokes in 1843 when he was studying the uniform acceleration of an infinitely long cylinder in infinite fluid medium (Lamb, 1932). Although these early formulas proposed by Du Buat and Stokes for evaluating the added mass on structure are limited to the geometry and boundary conditions of the structures, these formulas for describing the interactions between fluids and structures are simple and efficient.

The concept of added mess has been used to solve engineering problems and one of the early studies is commenced on the dam-reservoir interaction analysis by Westergaard in 1933 for the design of Hoover dam located in Arizona, the United States (Westergaard, 1933). In this study, Westergaard proposed a pioneering method to estimate the response of a rigid rectangular dam subjected to the harmonic seismic excitation and the reservoir in this coupled system is considered to be semi-infinite with constant depth. The fluid of reservoir in the dynamic analysis is represented by an added mass term and the inertial forces exerted by the added mess is assumed to

be identical to the hydrodynamic pressure on the dam body. The conclusion states that the distribution of hydrodynamic pressure applied on the dam wall is parabolic and the applicability of the solution is limited to low excitation frequency.

Following Westergaard's study mentioned above, a discussion about the hydrodynamic pressures on dams was published by von Karman et al. with the considerations of flexibility of dam and length of reservoir (von Karman et al., 1933). In terms of the reservoir length, it was found that the hydrodynamic pressure on the dam is overestimated if the finite reservoir is assumed to be infinite. However, when the length of reservoir approaches twice of its height, this overestimation is negligible. As for the flexibility of dam, the conclusion implies that the consideration of flexible dams makes no significant difference from the consideration of rigid dams in the analysis of dam-reservoir interaction system. Despite the fact that these conclusions are incorrect, the discussion by von Karman et al. was the first attempt to investigate the flexibility of dam in the dam-reservoir system.

Hydrodynamic pressure in water tank under seismic loads was experimentally and numerically studied by Hoskins and Jacobsen (Hoskins and Jacobsen, 1934). Later, Jacobsen extended the above work to model fluid in cylindrical tank and piers surrounded by fluid (Jacobsen, 1949). In order to calculate the hydrodynamic pressure and height of free surface wave in fluid tank subjected to the horizontal ground motion, Housner developed simplified formulas for containers with twofold symmetry, dams with sloping faces and flexible retaining walls (Housner, 1957). In this simplified approach, the fluid and structure are evaluated independently. First of all, the hydrodynamic pressure of fluid is calculated via assuming the structure is rigid. Next, the response of structure subjected to the hydrodynamic pressure evaluated previously is obtained. Because it was widely believed during that period of time that the hydrodynamic pressure calculated based on the assumption of rigid structure is greater than the actual hydrodynamic pressure acting on the flexible structure, the hydrodynamic pressures evaluated by this simplified approach should

be conservative and lead to safe designs. As a result, this approach was widely accepted and applied in the designs. However, the faultiness of those assumptions and the inadequacy of this approach were evidenced by a number of structural failures during earthquakes. For example, in the United States, the Alaska earthquake in 1964 caused failures of petrochemical tanks and catastrophic damages (Steinbrugge, 1970). In 1971, the buckling of tanks and lift-off of anchored tanks from foundations were observed after the earthquake happened in San Fernando, California. These evidences indicate that the aforementioned approach which considers the uncoupled motions of fluid and structure leads to unsafe designs. Therefore, coupled approaches were widely used in the designs of fluid-structure or acoustic-structure interaction systems during recent decades (Belytschko, 1980; Liu and Chang, 1984; Kulak, 1985; Hamdan, 1999).

1.2 Statement of problem

As mentioned at the end of last section that the uncoupling of acoustics and structural motions in the design may yield unsafe structures. This is especially true with the occurrence of resonance between acoustic media and structures. Consequently, coupling approaches are used in modern analysis of acoustic-structure interaction systems. An illustration of a typical acoustic structure interaction system is given in Figure 1.1. Except for the coupling of acoustic and structural domains, other factors may also influence the accuracy of the modelling of acoustic-structure interaction problems and should thus be considered in the pertinent researches. Among them, one of the most important and challenging factors is the modelling of unbounded acoustic media.

Accurate and efficient representation of the unbounded domain, or the far field, is significant in modelling the wave propagation in the infinite extent of media. When the waves, which could be elastic or acoustic, travel from the near field to the far field,

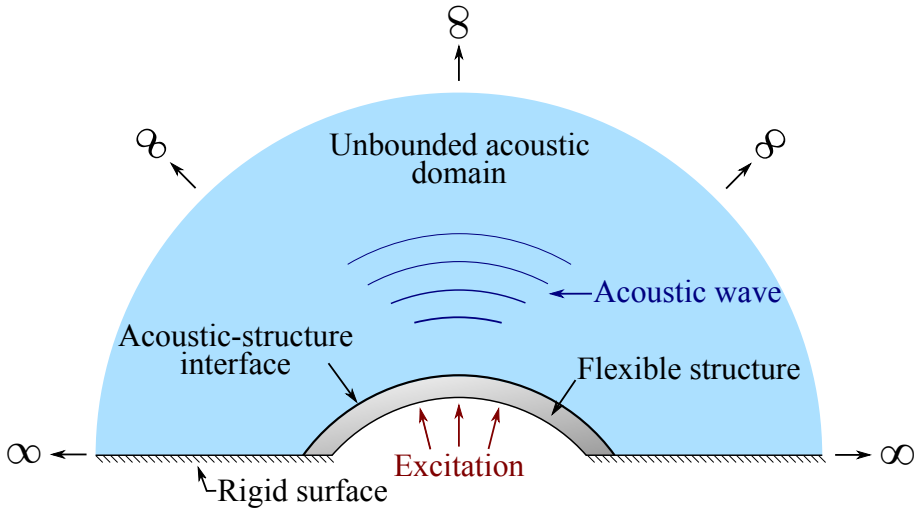

Figure 1.1. Acoustic-structure interaction problems.

they will not be reflected back. This irreversible withdrawal of the energy carried by waves from the near field to the far field causes damping effect on the wave amplitude and are known as the radiation damping. The boundary condition at infinity in the numerical modelling is also called the radiation condition. For modelling the unbounded domain, the radiation condition indicates that the unbounded domain should behave like an energy sink and the energy from the source must scatter to infinity but must not radiate from infinity back to the near field. Therefore, the radiation condition guarantees the uniqueness of the solutions to the boundary-value problems. Arnold Sommerfeld defined the radiation condition for the propagation of scalar wave governed by Helmholtz equation in 1949 (Sommerfeld, 1949). For the acoustic wave governed by the Helmholtz equation, it can be written as

$$\nabla^2 p + k^2 p = 0 \tag{1.1}$$

where the ∇^2 denotes the Laplace operator, k represents wavenumber and p is the amplitude of acoustic wave. The Sommerfeld radiation condition for the solution of p can be expressed by:

$$\lim_{r\to\infty} r^{\frac{s-1}{2}} \left(\frac{\partial p(r)}{\partial r} + \mathrm{i}kp(r) \right) = 0 \tag{1.2}$$

where s is the spacial dimension with $s = 2$ for 2D and $s = 3$ for 3D, r is the

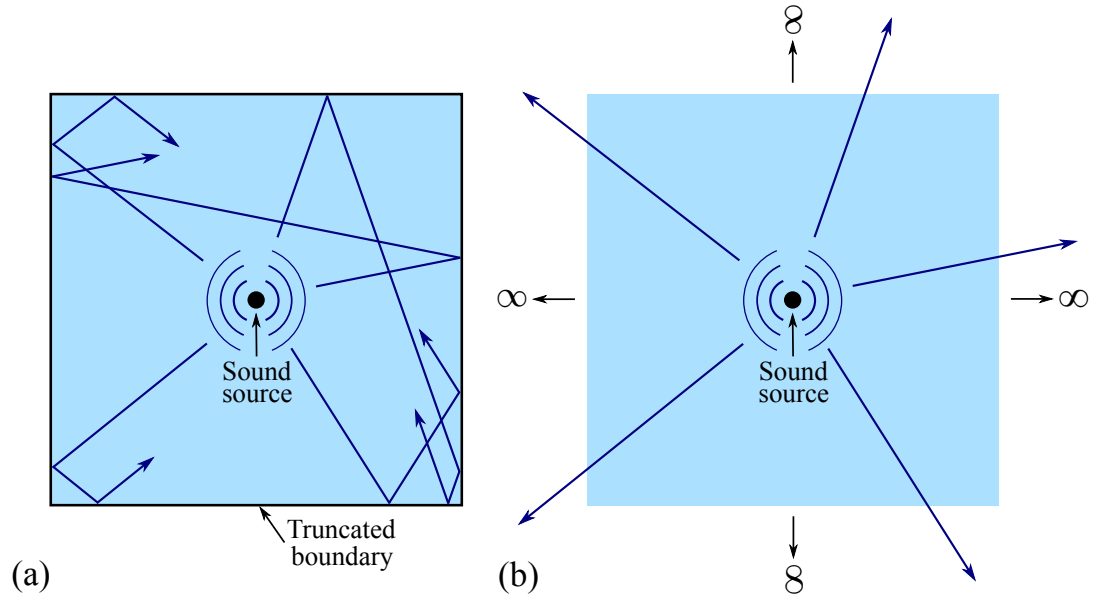

Figure 1.2. Acoustic wave (a) reflection on the truncated boundary and (b) propagation into infinity.

radial coordinate and i is the imaginary unit. Only the outgoing waves can satisfy Equation (1.2).

For the numerical modelling of unbounded domains with discretization schemes, such as the finite element method, the finite mesh should be truncated at certain distance. Simple boundary conditions, such as fixed boundaries in elastic analysis, on the truncated boundary might be sufficient for static analysis. However, for the dynamic analysis, the waves generated from the source of excitation or scatterer will be reflected back on the truncated boundary and this does not satisfy the radiation condition. This is shown in the two-dimensional acoustic problem in Figure 1.2. In Figure 1.2(a), the infinite acoustic domain is truncated at certain distance to the sound source. The acoustic wave propagates outwardly at first. When it impinges the truncated boundary, it is reflected back and trapped inside the bounded acoustic domain. However, for the acoustic wave propagation in real unbounded domain in Figure 1.2(b), the wave should propagate outwardly without any reflection. Eventually, the energy carried by the acoustic wave should travel to infinity. Therefore, two different strategies are proposed to analyse the coupled systems of unbounded

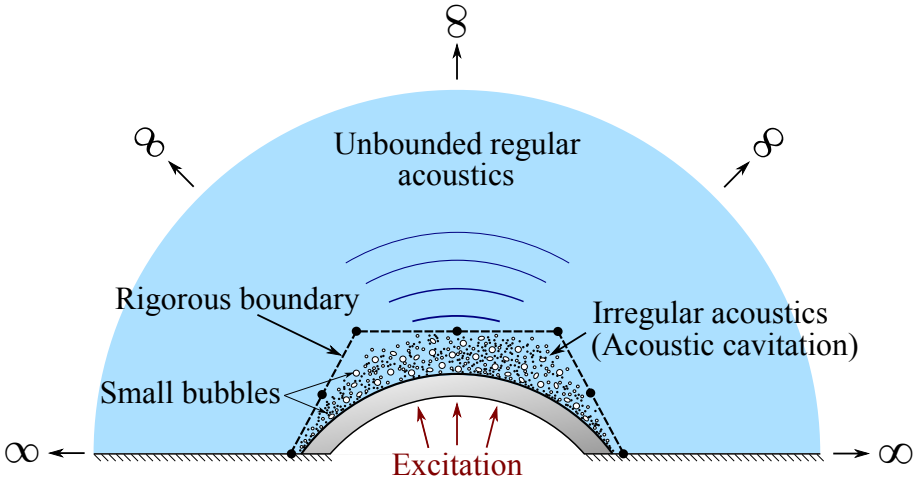

Figure 1.3. Substructure method.

and bounded domains: the substructure method and direct method.

The basic concept of substructure method is to divide the acoustic-structure interaction system into substructures of bounded and unbounded domains as shown in Figure 1.3. The bounded domain includes the finite structure. Part of the acoustic domain adjacent to the acoustic-structure interface could also be included if it is irregular, such as the nonlinearity caused by acoustic cavitation, which commonly exists in the part of liquid where the pressure drops below the vapor pressure and generates many small bubbles (liquid-free zones). Whereas the unbounded domain represents the infinite extent of the acoustic domain with linear and regular properties. Then, the unbounded domain can be modeled separately and the radiation condition is rigorously satisfied in the substructure method. The corresponding impedance properties of unbounded acoustic domain are adopted later in the evaluation of the bounded domain (Wolf and Song, 1996; Vaish and Chopra, 1974). To this end, the discretization of both bounded and unbounded domains are compatible on the common interface in numerical analysis. In acoustics, the dynamic relationship between the acoustic flux $\mathbf{R}$ and pressure $\mathbf{p}$ on the common interface are used to represent the unbounded domain. This relationship can be expressed in frequency

domain for an excitation frequency ω as:

$$\mathbf{R}(\omega) = \mathbf{S}^{\infty}(\omega)\mathbf{p}(\omega) \tag{1.3}$$

where $\mathbf{S}^{\infty}(\omega)$ is the impedance matrix for the unbounded acoustic domain. The relationship in Equation (1.3) is later used as the boundary condition in the analysis of the bounded domain. In case of the existence of nonlinear behaviors in the bounded domain, the time-domain formulation for the flux-pressure relationship in the unbounded domain can also be derived via applying the inverse Fourier transform to Equation (1.3):

$$\mathbf{R}(t) = \int_0^t \mathbf{S}^{\infty}(t-\tau)\mathbf{p}(\tau)d\tau \tag{1.4}$$

In Equation (1.4), the interacting flux at time t on the common interface $\mathbf{R}(t)$ is equal to the convolution integral of the unit-impulse response matrix of the unbounded acoustic domain $\mathbf{S}^{\infty}(t)$ and the corresponding pressure vector $\mathbf{p}(t)$. This convolution integral is similar to the Duhamel's integral in structural dynamics. In the substructure method, the boundary condition in Equation (1.3) or (1.4) is generally global. This indicates that the response at a specific location and time is dependent of the responses at all other locations, i.e. spatially global, and all previous times, i.e. temporally global. However, the spatially global boundary conditions may lead to fully populated impedance matrix $\mathbf{S}^{\infty}$ and the computationally expensive convolution integral is involved in the transient analysis. Literature review on several global procedures for modelling unbounded domain is presented in Section 2.2.1.

In terms of the direct method, a finite part of the unbounded acoustic domain is included in the bounded domain along with the finite structure. The interface between bounded and unbounded domains are thus placed with a certain distance away from the vibrating structure or other sources of excitation as presented in Figure 1.4. For the representation of unbounded domain, simple and approximate

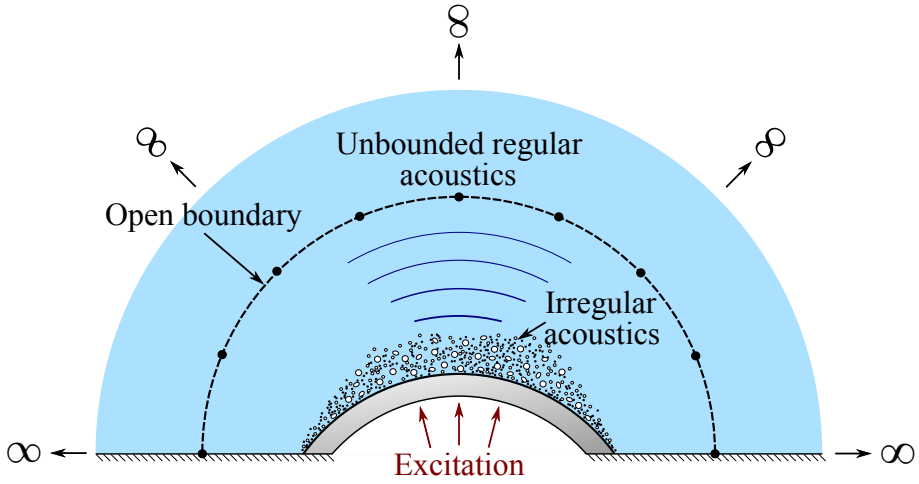

Figure 1.4. Direct method.

boundary conditions are usually applied on the discretized interface. These approximate boundary conditions are usually local, which means that the response at a specific location and time only depends on the responses at its neighboring locations, i.e. spatially local, and a few previous times, i.e. temporally local. These properties of local boundary conditions guarantee the sparsity of impedance matrix and the use of standard time-step integration schemes for transient analysis. Therefore, the local boundary conditions are numerically cheaper than global boundary conditions. This type of boundary conditions on the discretized boundary is known by several different terms such as: artificial boundary, absorbing boundary, transmitting boundary, open boundary, non-reflection boundary, one-way boundary, anechoic boundary, radiation boundary etc. The term open boundary is adopted in this thesis. A summary of commonly used local boundary conditions is stated in Section 2.2.2.

Although the local boundaries are efficient and simple in numerical modelling, they are approximations and the spurious reflections may occur on the truncated interface. As a result, the performances of local boundaries deteriorate when they are placed near the excitations (Givoli, 1991). However, increasing the distance between the local boundary and excitation results in a large bounded domain and increased computational efforts. Hence, local boundary conditions with high accuracy are

demanded in the numerical modelling of unbounded domain.

Except for the limitations in the modelling of unbounded domain using substructure or direct method, there are other factors worth considering in the numerical analysis of acoustic-structure interaction system. Because the wave speeds in acoustic fluids and structures might be very different and yield distinct wave lengths in these two separate domains, different mesh sizes should be used in acoustic and structural domains respectively for efficiently representing these different wave lengths. Efficient mesh transition between non-matching meshes from acoustic and structural domains on the acoustic-structure interface are required.

In addition, nonlinear behaviors, such as elastoplasticity, may occur in the structures under strong excitations. Material nonlinearity should be considered in the corresponding structural models. The numerical modelling of nonlinear problems is usually time-consuming as the incremental formulations and iterative procedures are normally involved. Therefore, For the dynamic analysis of nonlinear problems, efficient time-domain equations for the structural domain in the coupled acoustic-structure system are required. Apart from that, defects and cracks may also exist in structures and vary the corresponding responses.

Moreover, due to the dramatic increases in the complexities and scales in modern engineering designs, the efficient and automatic techniques to generate meshes from geometrical models are also necessary to reduce the human efforts in the numerical simulations of acoustic-structure interaction problems in practice and highly demanded.

1.3 Objectives and significance of study

As discussed in the last section, a number of factors in modelling of acoustic-structure interaction problems are discussed and certain limitations in the currently existing numerical methods are given. In order to overcome these limitations, This

thesis provides new techniques to accurately and efficiently model the acoustic-structure interaction problems with arbitrary and complex geometries based on the scaled boundary finite element method. The scaled boundary finite element method excels in modelling unbounded domain as it only requires boundary discretization and provides analytical solutions in the radial direction. The boundary discretization of the scaled boundary finite element method also gives unique advantages on efficient mesh transition on acoustic-structure interface and automatic mesh generations. The aforementioned elastoplastic behavior of structures is also considered in the acoustic-structure interactions within this study. The main objectives of this thesis are listed as follows:

1. Extend the scaled boundary finite element method to two- and three- dimensional acoustic analyses by utilizing the high-order doubly-asymptotic open boundary for the unbounded domain. This includes developing accurate, efficient and robust approach for modelling two-dimensional acoustics and extending the existing high-order doubly-asymptotic open boundary to three-dimensional acoustics.

2. Extend the scaled boundary finite element method to model both two- and three-dimensional acoustic-structure interaction problems with efficient mesh transition on the acoustic-structure interface.

3. Extend the scaled boundary finite element method to efficiently model both static and dynamic elastoplastic structures in three-dimensions.

4. Extend the scaled boundary finite element method to model both two- and three-dimensional acoustic-structure interaction problems with elastoplastic structures.

5. Apply automatic scaled boundary finite element mesh generation technique to generate scaled boundary meshes from standard tessellation language (STL)

models in three-dimensional analysis leading to high efficiency in mesh generation and reduced human efforts.

Via completing these objectives mentioned above, the scaled boundary finite element method is further developed in several major research areas including acoustic analysis, elastoplastic analysis and acoustic-structure interaction analysis. Outcomes from this research can also contribute to the numerical analysis of relevant engineering problems. In addition, because the commonly used STL file format in computer-aided design (CAD) industry is directly used here as the input files of three-dimensional models, presented techniques can be conveniently applied to practical engineering analysis.

1.4 Outline of the thesis

The outline of this thesis is listed below:

Chapter 2 presents the literature review on topics related to this research. Firstly, numerical methods for modelling the wave propagation in unbounded domains are firstly reviewed and categorized into the global procedures and local procedures. Brief introductions and discussions on several techniques in both categories are stated. Next, fundamentals on the theories for elastoplastic analysis are summarized. This is followed by an introduction to the numerical implementation in the finite element scheme. Reviews on several reduced integration methods with hourglass control for improving the efficiency of elastoplastic analysis are also presented.

In Chapter 3, the scaled boundary finite element method is developed to model two-dimensional acoustic problems. The unbounded domain is modeled based on the high-order doubly-asymptotic open boundary with circular geometry proposed in (Prempramote, 2011). Additional factor coefficients for eliminating singularities in continued-fraction expansions and rules for using singly-asymptotic continued fractions for low-frequency modes are given to improve the stability and efficiency

of doubly-asymptotic open boundary. The bounded domain, which includes cavities with arbitrary geometry is modeled using scaled boundary finite element method with continued fractions for efficiently solving the impedance matrices. Bounded and unbounded acoustic domains are then coupled via the nodal flux on the common interface. The resulting global equations of motion can be directly adopted in transient analysis.

In Chapter 4, three-dimensional acoustic analysis is performed using the scaled boundary finite element method. To this end, the high-order doubly-asymptotic open boundary is extended to model acoustic wave propagation in three-dimensional unbounded domain with a spherical boundary. The bounded acoustic domain including any complex geometry is again modeled by scaled boundary finite element method with continued-fraction expansions for impedance matrices. For the efficient modelling of acoustic problems with complex geometry and reducing the corresponding human efforts, octree mesh technique is adopted to automatically generate meshes for three-dimensional models provided in STL files. In scaled boundary finite element method, each octree cell can be treated as a polyhedral subdomain with arbitrary number of faces. Displacement incompatibility between cells with different sizes can be easily addressed by subdivisions of surface elements.

Chapter 5 develops the scaled boundary finite element method for acoustic-structure interaction analyses in both two and three dimensions. The linearly elastic behaviors of structures are assumed in this chapter. The infinite acoustic domains in these coupled systems are modeled using the approaches provided in Chapters 3 and 4 for two- and three-dimensional cases respectively. As for the modelling of structures, the scaled boundary finite element method is applied. The continued fractions are again involved to evaluate dynamic stiffness matrices in structural domain accurately and efficiently. Then, the time-domain formulations for acoustic and structural domains are coupled together by enforcing the boundary conditions on the acoustic-structure interface. Different mesh sizes can be used in structural

and acoustic domains. The mesh transition on the acoustic-structure interface is efficiently handled in scaled boundary finite element method due to its boundary discretization.

In Chapter 6, the scaled boundary finite element formulation for two-dimensional elastoplasticity with stabilization in (He, 2017) is extended to three-dimensional static and dynamic analyses. In this formulation, the varying elastoplastic constitutive matrix and stresses are assumed to be constants within each scaled boundary subdomain. Comparing with the original formulation in (Ooi et al., 2014), this leads to higher efficiency in elastoplastic analysis as the number of locations for performing the computationally expensive return mapping algorithm in each subdomain is significantly reduced. Meanwhile, stabilisation matrix is introduced to control the hourglass modes of each subdomain. Standard time-stepping scheme is adopted to perform the dynamic elastoplastic analysis with iterative procedure in each time step to enforce the force equilibrium. Octree mesh is again applied for automatic mesh generation.

Chapter 7 extends the scaled boundary finite element method to model acoustic-structure interaction problems with elastoplastic behavior in the structural domain. The approaches developed in Chapters 3 and 4 are again used here to model the two- and three-dimensional infinite acoustic domains, respectively. Additionally, the scaled boundary finite elements formulations with stabilisation for two- and three-dimensional elastoplasticity from (He, 2017) and Chapter 6 are utilized here for modelling the structural domains. Formulations for acoustics and structures can be coupled via the same way presented in Chapter 5. Dynamic analysis of this nonlinear coupled system is achieved by applying standard implicit time-stepping scheme with iterative procedure in each time step to enforce both force equilibrium in structural part and flux equilibrium in acoustic part.

Finally, conclusions of this thesis, along with recommendations for future research, are drawn in Chapter 8.

Chapter 2

Literature review

2.1 Introduction

Numerical modelling of acoustic-structure interaction systems has been studied for decades as discussed in Chapter 1. Many factors in modelling such a coupled system will affect the accuracy of results in both acoustic and structural fields. According to the scope of this research, the emphases of the literature review presented in this chapter are placed on two aspects: the numerical methods for modelling wave propagation in unbounded domain and elastoplastic analysis for structures. For the latter one, the reduced integration methods with stabilization are also reviewed as these approaches can be used to improve the efficiency of computational elastoplasticity and are related to the research in this thesis.

This chapter is organized as the following sections: Section 2.2 presents the literature review on some well-known procedures for modelling the unbounded domains. These procedures can be categorized into two groups: global and local procedures. Both of the global and local procedures are reviewed in Sections 2.2.1 and 2.2.2, respectively. The developments as well as the strengths and drawbacks of these approaches are summarized and discussed in these sections. For the review on structural elastoplasticity in Section 2.3, the fundamentals of plastic theory are

briefly summarized in Section 2.3.1. Then, a brief introduction of finite element implementation for elastoplastic analysis is given at the beginning of Section 2.3.2. Reduced integration methods with stabilization are reviewed in the same section. Finally, conclusions are stated in Section 2.4.

2.2 Wave propagation in infinite domain

In modelling wave propagation in infinite media, the infinite domain is normally truncated into a bounded near field and an unbounded far field. Boundary conditions are assigned on the near-far field interface to prevent the wave reflections and thus represent the unbounded domain. Various approached have been proposed to represent the unbounded domain during the last years and can basically be divided into two types: the global procedures and local procedures (Tsynkov, 1998).

The global procedures usually give accurate representations of unbounded domain and show robustness in the computational analysis, However, the global procedures are also computationally expensive as they are spatially and temporally global. This is even more so for simulating large-scale problems during long-time analysis as the computational costs rapidly increase with the number of degrees of freedom in the system and the number of time steps used in convolution integrals. Commonly used global procedures, including boundary element method, exact non-reflecting boundaries and scaled boundary finite element method, are reviewed in the following Section 2.2.1.

Alternatively, the local procedures are attractive in terms of computational efficiency and simplicity in implementations as they are spatially and temporally local. Hence, this type of methods are practical in modelling large-scale problems and for transient analysis as the computationally expensive convolution integral is not required. Nevertheless, because the formulations in local procedures are not rigorous but approximate, they are normally found to be lack of accuracy and should therefore

be placed at certain distance away from the near field excitations for minimizing the effects of spurious reflections. Some frequently used local procedures are discussed in Section 2.2.2.

2.2.1 Global procedures for modelling unbounded domains

2.2.1.1 Boundary element method

The boundary element method (BEM) has been developed and widely applied to unbounded-domain problems for more than 40 years. It is usually known as the numerical approach for solving the boundary integral equations (BIEs) based on Green's formula. Some of the early attempts for solving BIEs were performed by Jaswon, et al. in 1963 for potential problems (Jaswon, 1963; Symm, 1963; Jaswon and Ponter, 1963). Later on, numerous studies have been performed on the BIE formulations and their numerical solutions for two and three-dimensional elastic problems in both statics and dynamics (Rizzo, 1967; Rizzo and Shippy, 1968; Cruse and Rizzo, 1968; Cruse, 1968, 1969; Rizzo and Shippy, 1970a; Cruse, 1974; Lachat and Watson, 1976; Stippes and Rizzo, 1977; Wilson and Cruse, 1978) during 1960s and 1970s. Among them, an efficient numerical approach for solving BIEs of three-dimensional elastostatics by subdividing the elastic body into subdomains and discretizing all surfaces by triangular and quadrilateral elements, which are similar to those used in FEM, was introduced by Lachat and Watson (Lachat and Watson, 1976). During the same period of time, BIEs for heat conduction (Rizzo and Shippy, 1970b), thermalelasticity (Rizzo and Shippy, 1977), linear viscoelasticity (Rizzo and Shippy, 1971) and fracture mechanics (Cruse and Vanburen, 1971) have also been investigated and the name 'boundary element method' appeared in several literatures (Banerjee and Butterfield, 1976; Brebbia and Dominguez, 1977; Brebbia, 1978). A detailed review of the history and developments of BEM and BIEs can be found in (Cheng and Cheng, 2005).

As a result of the development during the past decades, BEM has become a

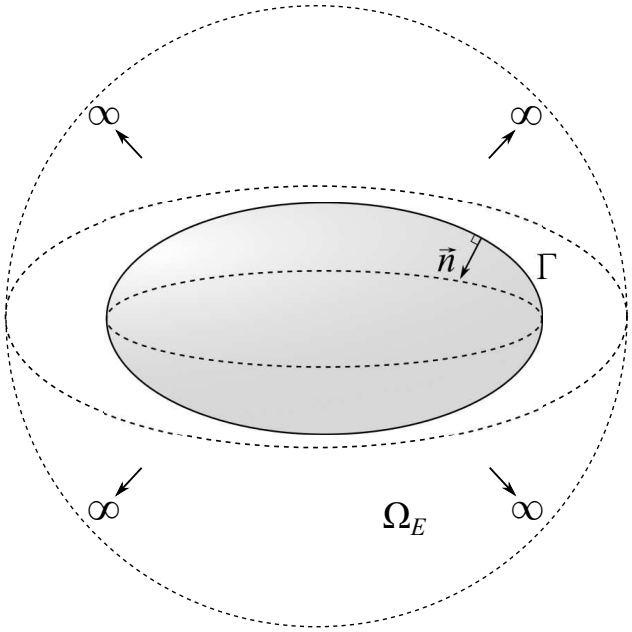

Figure 2.1. A typical 3D exterior domain Ω_E in BEM with the boundary Γ.

powerful method in modelling exterior acoustic problems due to its intrinsic advantages in simulating unbounded domains. Considering the steady-state linear acoustic problems in three-dimensional unbounded domain Ω_E (the infinite space outside the surface Γ) in Figure 2.1, the acoustic pressure $p(\mathbf{x})$ is governed by the following Helmholtz equation:

$$\nabla^2 p(\mathbf{x}) + k^2 p(\mathbf{x}) = 0 \tag{2.1}$$

with the a wavenumber k and any source point $\mathbf{x}$ in the unbounded domain Ω_E.

The Sommerfeld radiation condition should also be satisfied on the boundary Γ for modelling the unbounded domain. Utilizing the Green's second identity, Equation (2.1) can be transformed into the following conventional boundary integral equation (CBIE) as (Schenck, 1968; Seybert et al., 1985):

$$c(\mathbf{x})p(\mathbf{x}) = \int_{\Gamma} \left[G(\mathbf{x},\mathbf{y},k)\frac{\partial p(\mathbf{y})}{\partial \vec{n}_{\mathbf{y}}} - \frac{\partial G(\mathbf{x},\mathbf{y},k)}{\partial \vec{n}_{\mathbf{y}}} p(\mathbf{y}) \right] d\Gamma(\mathbf{y}) + p^I(\mathbf{x}) \tag{2.2}$$

where $\vec{n}$ is the unit vector normal to the boundary Γ shown in Figure 2.1 pointing away from Ω_E. $\mathbf{y}$ is any point on the boundary Γ (field point) and $p^I(\mathbf{x})$ describes any incident acoustic wave. $c(\mathbf{x}) = 0.5$ if Γ is smooth around $\mathbf{x}$. The Green's function

$G(\mathbf{x}, \mathbf{y}, k)$ in Equation (2.2), which is a fundamental solution for three-dimensional acoustic problems, can be expressed as:

$$G(\mathbf{x}, \mathbf{y}, k) = \frac{1}{4\pi r} e^{\mathrm{i}kr} \tag{2.3}$$

In Equation (2.3), r is the distance between source point $\mathbf{x}$ and field point $\mathbf{y}$. $\mathrm{i} = \sqrt{-1}$ is the imaginary unit.

For exterior problems, the CBIE in Equation (2.2) has one major defect. At the so-called fictitious eigenfrequencies, the solution is not unique (Burton and Miller, 1971). This difficulty can be addressed by using the linear combination of CBIE and hypersingular boundary integral equation (HBIE). The latter can be derived via taking the normal derivative of the representation integral of the solution p at point $\mathbf{x}$ and let this point approaching the boundary Γ. This combined formulation is also known as the Burton-Miller formulation and can provide unique solutions at all frequencies (Burton and Miller, 1971; Kress, 1985).

Compared with other domain based numerical methods, such as the finite element method (FEM) and finite difference method (FDM), one of the salient advantages of BEM is the boundary discretization. In BEM, a three-dimensional domain should only be discretized by two-dimensional surface elements on the boundary and a two-dimensional domain is discretized using one-dimensional line elements on its boundary. This reduces the problem dimension by one, and alleviates the difficulties in mesh generations for complicated geometries. Additionally, due to the use of the so-called fundamental solution in its formulations, the BEM can yield accurate solutions. For the same reason, BEM is able to model unbounded domains (such as the three-dimensional unbounded domain in Figure 2.1) accurately as the boundary condition at infinity is rigorously satisfied in Equation (2.2).

In the conventional BEM formulations, the discretization of BIEs, such as Equation (2.2), yields a global system of algebraic equations with unsymmetrical and fully-populated coefficient matrices. The numerical solution of such a system requi-

res a large amount of memory and is usually computationally expensive. To obtain a time-domain solution, an inverse of Fourier transform and a convolution integral in time can be employed. Due to the high computation costs of conventional BEM, it is often not used for solving transient problems and also limited to small-scale problems.

For improving the efficiency of BEM, several fast solution methods, such as the fast multiple method (FMM) and pre-corrected fast Fourier transformation (pFFT) method have been developed. The FMM used for accelerating the solution of BEM is firstly studied by Rokhlin and Greengard (Rokhlin, 1985; Greengard and Rokhlin, 1987). This is later extended to solve Helmholtz equation for acoustic problems. A detailed review can be found in (Nishimura, 2002). The basic approach of the fast multiple accelerated BEM is to solve the global system of algebraic equations with iterative solver, such as GMRES (Saad and Schultz, 1986). Within each iteration, the FMM is utilized to accelerate the matrix-vector multiplication. The great reduction of computation efforts achieved by using the fast multiple accelerated BEM leads to the application of BEM to large-scale and practical problems with some of the examples given in (Liu, 2009). Compared with the fast multiple accelerated BEM, the pFFT accelerated technique developed by Philips and White shows unique advantages on its kernel independent nature and simplicity of implementation (Phillips and White, 1997). This method has been applied in BEM for solving large-scale problems in recent years. Some examples are shown in (Ding and Ye, 2004; Masters and Ye, 2004; Ding and Ye, 2006; Fata, 2008; Yan et al., 2010a,b).

2.2.1.2 DtN finite element method

An alternative global procedure for modelling the wave propagation in infinite domains is the Dirichlet-to-Neumann (DtN) finite element method (Givoli, 1999). The DtN finite element method was developed by Keller and Givoli in 1989 (Keller and Givoli, 1989; Givoli and Keller, 1989). A typical setup of this method for a 2D

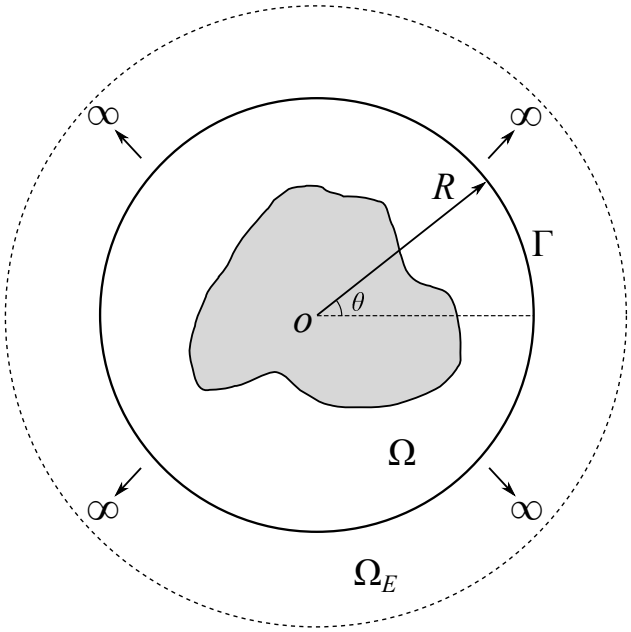

Figure 2.2. A typical setup for DtN finite element method.

problem is illustrated in Figure 2.2. For modelling the exterior problem, the infinite domain is firstly truncated by an artificial boundary Γ outside the irregular obstacle in grey color. Ω is the surrounding near-field medium and Ω_E is the unbounded domain. As the name DtN finite element method implies, this method combines the finite element scheme for modelling the bounded domain Ω with a DtN boundary condition on the artificial boundary Γ for representing the unbounded domain. The DtN boundary condition is an exact spatially non-local solution of the unbounded domain in the frequency domain.

Because the analytical expressions of the DtN boundary conditions are required, the problem in unbounded domain Ω_E, as well as the geometry of the boundary Γ, are normally simple for obtaining such an analytical solution. Some early works for using exact boundary conditions to represent the unbounded domain and finite element method for the bounded domain are collected in References (Fix and Marin, 1978; Maccamy and Marin, 1980; Marin, 1982; Goldstein, 1982; Bayliss et al., 1985; Canuto et al., 1985; Feng, 1983, 1984; Masmoudi, 1987; Lenoir and Tounsi, 1988). Comparing with these methods, the DtN finite element method proposed by Keller

and Givoli is well-known as a practical method for modelling wave propagation in infinite domain as the exact boundary condition is expressed explicitly in terms of known functions. In (Keller and Givoli, 1989), the boundary Γ is chosen to be a circle for two-dimensional problems, which is also plotted in Figure 2.2 denoted by the circular artificial boundary Γ with the radius R, or a sphere for three-dimensional problems. The DtN boundary condition can be generally described by the following equation:

$$u_\nu = -Mu \tag{2.4}$$

In Equation (2.4), u is the unknown scattered field (or sound pressure for acoustics) and u_ν is its outward normal derivative. The non-local operator M is also known as the DtN map, which relates the Dirichlet datum u to the Neumann datum u_ν on Γ. For two-dimensional wave propagation problems governed by the Helmholtz equation (Equation (2.1)), Equation (2.4) can be expressed as:

$$u_\nu(R,\theta) = -{\sum_{n=0}^{\infty}}' \int_0^{2\pi} m_n(\theta-\theta')u(R,\theta')d\theta' \tag{2.5}$$

with the prime after the sum indicating that the term with $n = 0$ is multiplied by a factor of $\frac{1}{2}$. The DtN kernels $m_n(\theta - \theta')$ in Equation (2.5) is

$$m_n(\theta-\theta') = -\frac{k}{\pi}\frac{H_n^{(1)'}(kR)}{H_n^{(1)}(kR)}\cos(n(\theta-\theta')) \tag{2.6}$$

where $H_n^{(1)}$ is the Hankel function of the the first kind, k is the wavenumber in Helmholtz equation.

As for the three-dimensional problems, the DtN boundary condition in Equation (2.4) can be derived for the spherical boundary with radius R as:

$$u_\nu(R,\theta,\varphi) = -\sum_{n=0}^{\infty}\int_0^{\pi}\int_0^{2\pi} m_n(\theta,\varphi\theta',\varphi')u(R,\theta',\varphi')R^2\sin\varphi' d\theta' d\varphi' \tag{2.7}$$

with the DtN kernels $m_n(\theta,\varphi,\theta',\varphi')$ given by

$$m_n(\theta,\varphi,\theta',\varphi') = {\sum_{j=0}^{\infty}}'\beta_{jn}P_n^j(\cos\varphi)P_n^j(\cos\varphi')\cos(j(\theta-\theta')) \tag{2.8a}$$

$$\beta_{jn} = -\frac{(2n+1)(n-j)!\gamma_n}{2\pi R^2(n+j)!} \tag{2.8b}$$

$$\gamma_n = \frac{1}{R^{-0.5}H^{(1)}_{n+0.5}(kR)} \frac{\partial\left(R^{-0.5}H^{(1)}_{n+0.5}(kR)\right)}{\partial R} \tag{2.8c}$$

In Equation (2.8), P_n^j is the associated Legendre function of the first kind. The DtN boundary condition can be implemented as the boundary condition for finite element formulations for u on the artificial boundary Γ. The DtN boundary condition is non-local as the integration over the whole boundary Γ exists in Equations (2.5) and (2.7). DtN maps have been derived and combined with finite element method for analyzing various problems and structures. In 1990, Givoli modeled the long elastic beam and cylinder, as well as the elastic wave propagation with DtN maps (Givoli, 1990b,a; Givoli and Keller, 1990). Later, the modelling of wave propagation governed by Helmholtz equation in semi-infinite plane is published in (Givoli and Vigdergauz, 1993). Derivations of the DtN boundary conditions for simulating acoustic waves in three-dimensional problems and wave guides are given in (Patlashenko and Givoli, 1997) and (Harari et al., 1998) respectively. In (Grote and Keller, 1995), the DtN boundary conditions were developed for boundary of elliptical shape via utilizing the trigonometric functions. The DtN finite element method was also used to model microwaves, which are governed by Maxwell's equations, in two dimensions (Ayappa et al., 1992).

The DtN boundary conditions, such as those given in Equations (2.5) and (2.7), contains infinite series. From a practical point of view, these infinite series have to be truncated with the first N terms involved in the calculations. However, this leads to non-unique solutions for certain wavenumber k, which is very similar to the uniqueness problem in the solutions of CBIE in BEM as discussed in Section 2.2.1.1. The uniqueness problem for DtN finite element method is also studied in (Harari and Hughes, 1992, 1994; Harari et al., 1996). The conclusion for Helmholtz problem states that if the (exact) DtN boundary condition with infinite series is used, the solution is unique for all wavenumbers k. However, if the truncated DtN

boundary condition is used, the uniqueness of solution is only guaranteed when $N \geq kR$. This problem can be addressed by the modified DtN method (Grote and Keller, 1995). In this method, the truncated DtN condition is combined with the Sommerfeld boundary condition for those modes higher than N. The resulting DtN condition provides unique solutions for all wavenumbers k regardless of the number of terms N retained in the truncated series. Further reviews of the DtN boundary conditions can be found in (Givoli, 1999; Thompson and Pinsky, 2004).

2.2.1.3 Scaled boundary finite element method

The scaled boundary finite element method (SBFEM) is a semi-analytically computational method, which combines the major advantages of the finite element method and boundary element method. Similar to the boundary element method, this method only requires the boundary discretization with interpolation functions used in standard finite elements. Thus, the spatial dimension is reduced by one. When modelling an unbounded domain, the SBFEM can rigorously satisfy the radiation condition at infinity. In addition, the stress singularities around the tips of cracks and notches can be expressed semi-analytically in the radial direction, which leads to direct and accurate calculations of stress intensity factors. The boundary discretization also leads to the reduction of computational difficulties and human efforts on automatic mesh generation since the meshing process should only be performed on the two-dimensional surfaces for three-dimensional problems and one-dimensional lines for two-dimensional problems. Unlike the boundary element method, the SBFEM doesn't require fundamental solutions and evaluation of singular integrals. This feature allows the SBFEM to handle anisotropic materials with no additional computational effort. The SBFEM was firstly developed by Song and Wolf in 1995 for modelling unbounded domains in two-dimensional dynamic soil-structure interaction analysis (Song and Wolf, 1995; Wolf and Song, 1995). The name "Consistent infinitesimal finite-element-cell method" was used at that time

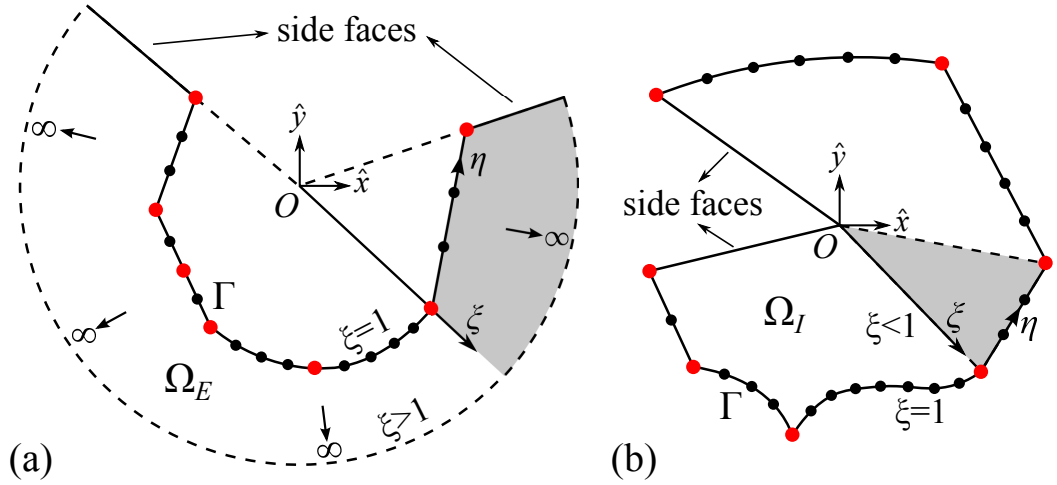

Figure 2.3. The scaled boundary finite element method for modelling two-dimensional: (a) unbounded domain and (b) bounded domain.

since the original derivation of this method was based on the assemblage of infinitesimal finite-element cell and the similarity between exterior and interior boundary. This infinitesimal finite-element cell is introduced in the radial direction adjacent to the soil-structure interface. Using the relationship of the similar exterior and interior cell boundaries and performing the limit of infinitesimal cell width approaching zero yield the consistent infinitesimal finite-element cell equation in the frequency domain. This equation is transformed into the time domain via an inverse Fourier transform. This method was extended to three-dimensional vector waves in the following year (Song and Wolf, 1996). Later, a new derivation of this method for elastodynamics is published in (Song and Wolf, 1997). The new derivation is based on the Galerkin's weighted residual method and is more consistent with the derivation of finite element formulation. This method is named as the "scaled boundary finite element method".

For explaining the basic concept of SBFEM, typical two-dimensional unbounded and bounded domains with arbitrary geometry are plotted in Figure 2.3(a) and 2.3(b) respectively. For modelling an unbounded or a bounded domain in SBFEM, a scaling centre is chosen from where the whole boundary Γ of the domain can be visible. For a bounded domain with complex geometry, this requirement can always

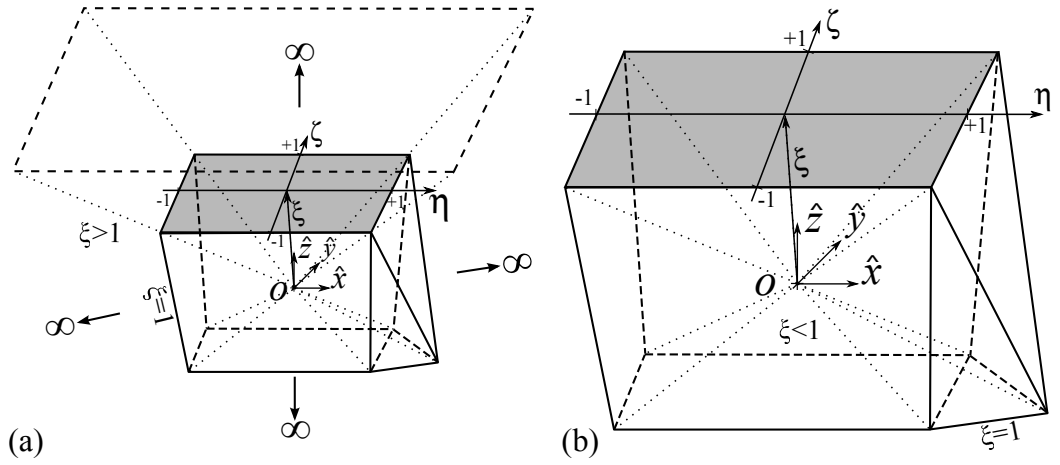

Figure 2.4. The scaled boundary finite element method for modelling three-dimensional: (a) unbounded domain and (b) bounded domain.

be satisfied by subdividing the original domain into smaller subdomains. Only the boundaries Γ of the domains are discretized. For a two-dimensional domain, line elements of any arbitrary orders can be used. Their shape functions are the same as those of one-dimensional finite elements. In the isoparametric formulation, the shape functions are formulated in their local coordinate η. In Figure 2.3, the end points of elements are marked by the larger red dots, while other nodes of elements are denoted by smaller black dots. The radial coordinate ξ starting from the scaling centre O and pointing at any node on the boundary Γ is introduced for describing the whole domain by scaling the boundary. The radial coordinate is set to be $\xi > 1$ for modelling the unbounded domain Ω_E, whereas $\xi < 1$ for describing the bounded domain Ω_I. On the boundary Γ and scaling centre O, the radial coordinate ξ is equal to one and zero separately.

The shaded grey areas in Figure 2.3(a) and (b) indicate parts of the unbounded and bounded domains formed by scaling the corresponding line elements respectively. The side faces, which are the straight lines passing through the scaling centre and boundary, are not discretized as they are generated by scaling the corresponding points on the boundary. The transformation of coordinate system from the Cartesian coordinate $(\hat{x}, \hat{y})$ to the scaled boundary coordinate (ξ, η) is known as the

scaled boundary transformation. For three-dimensional problems shown in Figure 2.4, two local circumferential coordinates η and ζ are introduce to describe the surface element of the boundary. One of the quadrilateral elements on the boundary of SBFEM unbounded and bounded subdomains is shown as the shaded area in Figure 2.4(a) and (b) respectively. The same radial coordinate ξ is used to describe the whole three-dimensional domain (unbounded or bounded) via scaling the corresponding surface elements.

After the scaled boundary transformation, the nodal displacement functions (or nodal pressure functions for acoustics) are introduced along radial direction ξ and discretized in the circumferential direction η for two-dimensional case (or in the circumferential direction η and ζ for three-dimensional case) with corresponding shape functions. After expressing the governing equation in the scaled boundary coordinates, the Galerkin's weighted residual method can be applied to the governing equation in the circumferential direction. A system of ordinary differential equations for displacement with the independent variable ξ are obtained. This system of differential equations is also known as the scaled boundary finite element equation. The coefficient matrices of the differential equations are calculated on an element-by-element basis and assembled in the same way as the assemblage of stiffness and mass matrices in finite element method (Song and Wolf, 1997). The modelling of body load is developed in SBFEM by Song and Wolf in (Song and Wolf, 1999a). The derivation of the scaled boundary finite element equation for elastostatics using principle of virtual work is published by Deek and Wolf (Deeks and Wolf, 2002b). A technique allowing the displacement to be prescribed using power series on side faces is also developed in (Deeks, 2004).

In elastostatic analysis, the scaled boundary finite element equation can be transformed into a system of linear first-order differential equations. The system of equations can be decoupled by an eigenvalue decomposition (Song and Wolf, 1997). The solution is obtained as a series of power functions. However, the eigenvalue method

for solving the scaled boundary finite element equation breaks down when multiple eigenvalues with parallel eigenvectors exist. This situation corresponds to the existence of logarithmic functions in the solution. It occurs in the solutions of two-dimensional unbounded domains and of a multi-material wedge at certain opening angles. This problem of the eigenvalue method is addressed in (Deeks and Wolf, 2002a) by including additional logarithmic terms in the solution. Based on the matrix function solution and real Schur decomposition, a new solution procedure is proposed by Song (Song, 2004a). This new approach is numerically more stable. Power and logarithmic functions in the solution, as well as their transition, can be semi-analytically represented by this procedure.

For modelling wave propagation in unbounded domains using SBFEM, the integration of the scaled boundary finite element equation in dynamic stiffness is performed in the frequency domain. This leads to the dynamic stiffness matrix of the unbounded domain. To perform a time-domain analysis, a unit-impulse response matrix can be obtained (Wolf, 2003). The original formulation of SBFEM are spatially and temporally global. Many efforts have been made to reduce the computational costs of SBFEM in dynamic analysis of unbounded domains (Paronesso and Wolf, 1995, 1998; Zhang et al., 1999; Wegner et al., 2005; Lehmann, 2005; Lehmann and Rüberg, 2006; Song, 2006). Among them, a reduced set of base functions are employed in (Song, 2006). Utilizing the Schur decomposition in elastostatics (Song, 2004a), modes with the small real parts of eigenvalues are selected as the reduced set of base functions in this approach. Reformulating the scaled boundary finite element equation with the reduced set of base functions leads to reduced size of system equations. The formulation is still temporally global. Therefore, an approximation of the dynamic stiffness matrix of the unbounded domain using Padé series constructed from the high-frequency expansion of the scaled boundary finite element equation is developed by Song and Bazyar (Song and Bazyar, 2007). The solution in Padé series has a larger convergence range and faster convergence rate

than a solution in power series.

This solution procedure using Padé series is further improved by a continued-fraction expansion at high-frequency limit (Bazyar and Song, 2008), which is also closely related to Padé series in terms of convergence rate and range (Baker and Graves-Morris, 1996). By introducing the auxiliary variables, the continued-fraction expansions can be transformed into a temporally local open boundary condition, which can be directly applied for transient analysis. The continued-fraction expansions has also been applied to evaluate the dynamic stiffness matrices of bounded domains by Song (Song, 2009). It does no require an internal mesh to capture short wave lengths at high frequencies. The dynamic stiffness matrix converges rapidly with increasing order of continued fraction.

Extending the singly-asymptotic continued-fraction expansion at low-frequency limit, a doubly-asymptotic continued-fraction expansion is proposed by Prempramote et al. to evaluate the dynamic stiffness matrix. Since this formulation is exact in both high- and low-frequency limits, it shows high convergence rate for high-order modes (Prempramote et al., 2009). In literatures (Prempramote, 2011; Birk et al., 2012), the numerical studies prove that the continued-fraction expansion used in both (Bazyar and Song, 2008) and (Prempramote et al., 2009) may break down when the mode number λ is equal to $\lambda = i + 0.5$ (i is an integer). Hence, improved approaches are proposed in (Prempramote, 2011; Birk et al., 2012) by introducing additional factor coefficients in the continued-fraction expansion.

The SBFEM has been applied to model the acoustic (Lehmann et al., 2006) and acoustic-structure interaction problems (Fan et al., 2005; Li, 2006). Additionally, the SBFEM has been applied to other research areas, such as ultrasonics (Gravenkamp et al., 2012, 2013, 2014, 2015, 2017), dam-reservoir interaction systems (Lin et al., 2007; Wang et al., 2011; Fan and Li, 2008), fracture mechanics (Song, 2004b, 2005; Yang, 2006; Song and Vrcelj, 2008; Ooi and Yang, 2009; Song et al., 2010; Ooi and Yang, 2011; Ooi et al., 2012; Li et al., 2013, 2014; Sun et al., 2015; Ooi et al.,

2016; Song et al., 2017; Ooi et al., 2017; Zhong et al., 2018) due to its superiorities in modelling the unbounded domain and stress singularities. The SBFEM has also been developed for elastoplastic analysis in references (Ooi et al., 2014; Chen et al., 2017a,b,c). In these approaches, multiple fitting points are required within each subdomain for accurately interpolating the stresses and elastoplastic constitutive matrices. The computationally expensive return mapping algorithm should be performed on each fitting point for updating the stresses. For improving the efficiency of the scaled boundary formulation in elastoplastic analysis, a novel approach is proposed in (He, 2017) with only one fitting point required in each subdomain. Comparing with the original formulation, the new approach is more computationally efficient and suitable for image-based automatic analysis.

Recently, automatic mesh generation techniques have been proposed for SBFEM. In SBFEM, the shapes of subdomains are more flexible than finite elements. Formulations of polygonal or polyhedral subdomains are derived with boundary discretization only. This allows the use of simple and efficient mesh generation algorithm. Quadtree and octree algorithms have been developed for the generation of scaled boundary finite element meshes. Automatic image-based stress analysis are performed (Saputra et al., 2017a). Automatic octree mesh generation from standard tessellation language (STL) models are developed in (Liu et al., 2017) by trimming the octree grid with the facets in STL models. These automatic meshing approaches reduce the human burdens on generating appropriate meshes for modelling realistic and complicated engineering problems using SBFEM (Talebi et al., 2016; Saputra et al., 2017b; Zou et al., 2017).

2.2.2 Local procedures for modelling unbounded domains

2.2.2.1 Absorbing boundary conditions

As mentioned at the beginning of Section 2.2, local approaches, such as absorbing boundary conditions (ABCs), are more popular than global approaches in the simu-

lation of wave propagation in unbounded domains for large-scale problems. Nevertheless, these local approaches have certain limitations on accuracy because they are approximations in general. Many ABCs have been proposed during the last decades to address this issue.

The first local open boundary applied in finite element analysis of unbounded domains is probably the standard viscous boundary developed by Lysmer and Kuhlemeyer in 1969 (Lysmer and Kuhlemeyer, 1969). The viscous boundary is proposed for elastodynamics and can be interpreted as dash-pots applied on the normal and tangential directions of the boundary in physics. The relationships between the stresses and velocities in both normal and tangential directions are quite empirical. The viscous boundary can be expressed by the following first-order differential equations:

$$\sigma = a\rho c_p \dot{u} \tag{2.9a}$$

$$\tau = b\rho c_s \dot{v} \tag{2.9b}$$

In Equation (2.9), σ and τ are the normal and shear stresses respectively. ρ is the density of the medium. c_p and c_s are the longitudinal and shear velocities separately. The minimizing of the reflected wave energy from the boundary is achieved by the introduction of the dimensionless parameters a and b. In (Lysmer and Kuhlemeyer, 1969), good absorption of wave energy is achieved by setting $a = b = 1$. It is also applied in the modelling of anisotropic media in (White et al., 1977) and is called the unified boundary condition. The viscous boundary is simple, frequency independent and suitable for any geometry of the boundary. Thus, it is commonly implemented in commercial finite element software packages. However, severe spurious reflections may occur at certain cases, such as sharp incident angle between impinging waves and boundary or close distance between the scattering source and viscous boundary. This is even more so for absorbing waves in the low-frequency range due to the lack of stiffness. Later, the viscous-spring boundary is developed in (Deeks and Randolph,

1994) via adding spring coefficients to improve its behavior in low-frequency limit.

The viscous boundary can be considered as a low-order absorbing boundary condition due to its order of approximation. For improving the accuracy of absorbing boundary conditions, high-order absorbing boundary conditions were proposed and can yield more accurate results with the increase of their orders of approximations. In 1975, the "free-space" boundary conditions for time-dependent wave equation were constructed by Lindman via using the projection operators (Lindman, 1975). Past data on the boundary, which are processed in the form of updating three to six wave equations, are used by the projection operators. Reflection coefficients less than one percent are obtained for a wide range of incident angles for both propagating and evanescent waves.

The paraxial boundary condition proposed by Engquist and Majda (Engquist and Majda, 1977) is possibly one of the most cited works on absorbing boundary conditions. A hierarchy of local high-order boundary conditions are used to approximate the non-local boundary conditions for the acoustic wave equations. The approximation is accomplished by utilizing Padé series, which is a rational function. This is also the first time that a rational approximation is used to construct the local formulations for absorbing boundary conditions. High-order derivatives are included in these formulations and the first three paraxial boundary conditions for scalar waves are:

$$\text{A1}: \frac{\partial p}{\partial x} + \frac{1}{c}\frac{\partial p}{\partial t} = 0 \tag{2.10a}$$

$$\text{A2}: \frac{\partial^2 p}{\partial x \partial t} + \frac{1}{c}\frac{\partial^2 p}{\partial t^2} - \frac{c}{2}\frac{\partial^2 p}{\partial y^2} = 0 \tag{2.10b}$$

$$\text{A3}: \frac{\partial^3 p}{\partial x \partial t^2} - \frac{c^2}{4}\frac{\partial^3 p}{\partial x \partial y^2} + \frac{1}{c}\frac{\partial^3 p}{\partial t^3} - \frac{3c}{4}\frac{\partial^3 p}{\partial t \partial y^2} = 0 \tag{2.10c}$$

with the speed of acoustic wave c, the solution of wave equation p. The first-order boundary condition in Equation (2.10a) is identical to the viscous boundary of Lysmer and Kuhlemeyer's.

Then, the paraxial boundary condition is developed for scalar and elastic waves

in (Clayton and Engquist, 1977). Many of the theoretical and practical aspects of this method are developed in (Engquist and Majda, 1979). Although the accuracy will be improved by increasing the orders of approximation, instability issues may arise for high-order formulations and inclined body waves (Wolf and Hall, 1988).

The Bayliss-Turkel boundary condition is a sequence of absorbing boundary conditions for three-dimensional wave-like equations in polar coordinates (Bayliss and Turkel, 1980). This boundary conditions are constructed based on the asymptotic expansion in $\frac{1}{r}$ of the radiating solution p to the wave equation. r is the distance from a fixed point. Based on the method of separation of variables, the asymptotic expansion of p can be of the form:

$$p(t, r, \theta, \phi) = \sum_{j=1}^{\infty} \frac{f_j(t - r, \theta, \phi)}{r^j} \tag{2.11}$$

Where r, θ and ϕ are the spherical coordinates centered at a fixed origin in space. The series in Equation (2.11) is convergent providing that the f_j is an analytical function of θ and ϕ. This boundary condition forms a sequence of differential operators B_m to annihilate the first m terms in the asymptotic expansion in Equation (2.11). The mth Bayliss-Turkel boundary condition has the form:

$$B_m p = 0 \tag{2.12}$$

with the differential operators B_m formulated as:

$$B_m = \prod_{j=1}^{m} \left(\frac{\partial}{\partial t} + \frac{\partial}{\partial r} + \frac{2j - 1}{r} \right) \tag{2.13}$$

Accuracy of this open boundary is able to be improved by increasing its order. However, for the mth-order absorbing condition, a product of m first-order derivatives is included in Equation (2.13). The discrete representation of the high-order derivatives might be impractical (Givoli, 2004). This sequence of absorbing boundary conditions is further developed to model the nonlinear compressible Navier-Stokes and Euler equations (Bayliss and Turkel, 1982). The performance of the above ab-

sorbing boundary conditions deteriorates once the boundary is close to the domain of interest.

An alternative approach to construct the absorbing boundary conditions without deriving the analytical boundary conditions was proposed by Higdon in 1986 (Higdon, 1986). This absorbing boundary condition is developed for multi-dimensional wave equations. The finite difference method is firstly employed in this approach to approximate the scalar wave equation in both space and time. The Resulting boundary condition is consistent with the analytical boundary condition and can be expressed as:

$$H_m p = \left(\prod_{j=1}^{m} \left((\cos \alpha_j) \frac{\partial}{\partial t} - \frac{\partial}{\partial x} \right) \right) p = 0 \tag{2.14}$$

Equation (2.14) is the Higdon boundary condition. α_j is the angle of incidence with $|\alpha_j| < \frac{\pi}{2}$ for all j. p is the solution of the scalar wave equation. Because the Higdon boundary condition is exact for wave propagation in those angles of incidence $\pm\alpha_j$, it can be considered as the general form of the viscous boundary and paraxial boundary condition. According to (Higdon, 1986), the numerical studies indicate that this absorbing boundary performs well for absorbing waves with a wide range of incidence angles. This absorbing boundary condition is practically and theoretically advantageous as it can be increased to arbitrary order of m. It was later developed to model the acoustic and elastic waves in stratified media (Higdon, 1992) and also the dispersive waves (Higdon, 1994). However, stability issues appear for these absorbing boundary conditions with the order higher than two. Analogous to the paraxial boundary condition (Engquist and Majda, 1977) and Bayliss-Turkel boundary condition (Bayliss and Turkel, 1980), the high-order derivatives in these formulations provide difficulties in the implementations of these absorbing boundary conditions beyond certain orders.

In order to avoid the existence of high-order derivatives and instabilities in some classical absorbing boundary conditions mentioned above, local high-order absor-

bing boundary conditions without high-order derivatives are constructed. This is achieved by introducing auxiliary variables to eliminate those high-order terms. The boundary condition proposed by Collino (Collino et al., 1993) in 1993 is the pioneer of this kind and the formulations are derived based on the paraxial boundary. The resulting formulations involve no high-order derivatives beyond second-order and thus benefits to the implementation of this absorbing boundary condition to arbitrarily high order. For two-dimensional scalar wave equation of the solution p, the high-order absorbing boundary condition of Collino's with the order J is formulated as:

$$\frac{\partial p}{\partial x} + \frac{1}{c}\frac{\partial p}{\partial t} - \frac{1}{c}\sum_{j=1}^{J} \beta_j \frac{\partial \phi_j}{\partial t} = 0 \tag{2.15a}$$

$$\frac{1}{c^2}\frac{\partial^2 \phi_j}{\partial t^2} - \alpha_j \frac{\partial^2 \phi_j}{\partial y^2} - \frac{\partial^2 p}{\partial y^2} = 0 \tag{2.15b}$$

with $j = 1, 2, \cdots, J$.

In Equation (2.15), ϕ_j are the auxiliary variables, c is the speed of scalar wave. The coefficients α_j and β_j can be expressed as:

$$\alpha_j = \cos^2\left(\frac{j\pi}{2J+1}\right) \tag{2.16a}$$

$$\beta_j = \frac{2}{2J+1}\sin^2\left(\frac{j\pi}{2J+1}\right) \tag{2.16b}$$

It should be noticed that Equation (2.15a) is similar to a modified Sommerfeld-like boundary condition and Equation (2.15b) is a one-dimensional wave equation for ϕ_j on the boundary. This implies that special corner conditions have to be proposed for Equation (2.15b) if the boundary has corners, such as rectangle. These corner conditions are also demonstrated in (Collino et al., 1993).

Hagstrom and Hariharan presented asymptotic boundary conditions for isotropic wave equations in both two-dimensional and three dimensional cases (Hagstrom and Hariharan, 1998). These boundary conditions are formulated based on the Bayliss-Turkel boundary condition (Bayliss and Turkel, 1980). For avoiding the

high-order derivatives in Bayliss-Turkel boundary condition, the boundary condition of arbitrary order is expressed recursively using auxiliary variables. The Hagstrom-Hariharan boundary condition with the order of J for two-dimensional wave equation can be written as the following sequence of equations:

$$\frac{1}{c}\frac{\partial p}{\partial t} + \frac{\partial p}{\partial r} + \frac{1}{2r}p = \omega_1 \tag{2.17a}$$

$$\frac{1}{c}\frac{\partial \omega_j}{\partial t} + \frac{j}{r}\omega_j = \frac{\left(j-\frac{1}{2}\right)^2}{4r^2}\omega_{j-1} + \frac{1}{4r^2}\frac{\partial^2 \omega_{j-1}}{\partial \theta^2} + \omega_{j+1} \tag{2.17b}$$

where, c and r are scalar wave speed and radius of the circle. ω_j are the auxiliary variables with $j = 1, 2, \cdots, J$. The ω_0 is set to be,

$$\omega_0 = 2p \tag{2.18}$$

For three-dimensional wave equation, the boundary condition is obtained as:

$$\frac{1}{c}\frac{\partial p}{\partial t} + \frac{\partial p}{\partial r} + \frac{1}{r}p = \omega_1 \tag{2.19a}$$

$$\frac{1}{c}\frac{\partial \omega_j}{\partial t} + \frac{j}{r}\omega_j = \frac{1}{4r^2}\left(\nabla_s^2 + j(j-1)\right)\omega_{j-1} + \omega_{j+1} \tag{2.19b}$$

with the radius of the sphere r and $j = 2, 3, \cdots, J$. ∇_s^2 is the Laplacian in spherical coordinates. For the absorbing boundary conditions in Equations (2.17) and (2.19) with the order of J, setting $\omega_{j+1} = 0$ is involved. This leads to the accuracy of $O(r^{-2J-2})$. However, for the special three-dimensional case when the solution p is a finite sum of spherical harmonics, the Hagstrom-Hariharan boundary condition can be exact.

The Givoli-Neta absorbing boundary condition was developed by Givoli and Neta in 2003 (Givoli and Neta, 2003; Givoli et al., 2003) and the derivations are based on the reformulation of Higdon boundary condition (Higdon, 1986). This boundary condition is developed for semi-infinite layers, such as wave-guide, with dispersive media. The dispersive media is governed by the Klein-Gordon equation:

$$\partial_t^2 u - C_0 \nabla^2 u + f^2 u = s \tag{2.20}$$

with the unknown wave field u, given dispersion parameter f and the reference wave speed C_0. s represents the given wave source function. Again, no high-order derivative beyond second order exists in the formulations as the result of including special auxiliary variables. The auxiliary variables in Givoli-Neta absorbing boundary condition can be calculated using simpler recursive formulations than those in Hagstrom-Hariharan boundary condition (Hagstrom and Hariharan, 1998). In Cartesian coordinates, the Givoli-Neta absorbing boundary condition with the order of J can be summarized as:

$$\beta_0 u_{,t} + u_{,t} = \phi_1 \tag{2.21a}$$

$$\beta_j \phi_{j,t} - \alpha_j \phi_{j-1,tt} - \phi_{j-1,yy} + \lambda \phi_{j-1} = \phi_{j+1} \tag{2.21b}$$

with $j = 1, 3, \cdots, J-1$, and $\phi_0 \equiv u$, $\phi_J \equiv 0$. Comma in the subscript represents partial derivative. The coefficients in Equation (2.21) are:

$$\alpha_j = \frac{1}{C_j^2} - \frac{1}{C_0^2},\ \beta_j = \frac{1}{C_j} - \frac{1}{C_{j+1}},\ \beta_0 = \frac{1}{C_1},\ \lambda = \frac{f^2}{C_0^2} \tag{2.22}$$

where C_j is the phase speed of propagating wave and should be selected either manually via "educated guess" based on exact solution or by computer codes. Different approaches for selecting C_j are also discussed in (Givoli and Neta, 2003). These absorbing boundary conditions are coupled with finite difference discretization and finite element discretization in (Givoli and Neta, 2003) and (Givoli et al., 2003) respectively.

Comparing with the Givoli-Neta absorbing boundary condition (Givoli and Neta, 2003), the Hagstrom-Warburton absorbing boundary condition (Hagstrom and Warburton, 2004) leads to balanced and symmetrizable system of equations on the boundary for the scalar wave problems. The recursive relations for J-order Hagstrom-Warburton absorbing boundary condition in (Hagstrom and Warburton, 2004) can be expressed as:

$$(a_0 \partial_t + c\partial_x) u \;=\; a_0 \partial_t \phi_1 \tag{2.23a}$$

$$l_{j,j-1}\partial_t^2\phi_{j-1} + l_{j,j}\partial_t^2\phi_j + l_{j,j+1}\partial_t^2\phi_{j+1} = c^2(m_{j,j-1}\partial_y^2\phi_{j-1} + m_{j,j}\partial_y^2\phi_j + m_{j,j+1}\partial_y^2\phi_{j+1}) \tag{2.23b}$$

In Equation (2.23), c is the speed of scalar wave. ∂_a^i is the shorthand for the ith order partial derivative with respect to a. ϕ_j with $j = 1, 2, \cdots J$ represent auxiliary variables, which are functions of location on the boundary. For the absorbing boundary conditions truncated at Jth order, ϕ_{J+1} is setting to be zero and $\phi_0 = u$. For $j = 1$, the coefficients $l_{j,k}$ and $m_{j,k}$ $(k = j-1, j, j+1)$ are listed as:

$$\begin{aligned} l_{1,0} &= 2a_1(1-a_0^2), & m_{1,0} &= 2a_1, \\ l_{1,1} &= a_0(1+2a_0a_1+a_1^2), & m_{1,1} &= a_0, \\ l_{1,2} &= a_0(1-a_1^2), & m_{1,2} &= a_0. \end{aligned} \tag{2.24}$$

For $j = 2, 3, \cdots, J$, coefficients $l_{i,j}$ and $m_{i,j}$ are:

$$\begin{aligned} l_{j,j-1} &= a_j(1-a_{j-1}^2), & m_{j,j-1} &= a_j, \\ l_{j,j} &= (a_{j-1}+a_j)(1+a_{j-1}a_j), & m_{j,j} &= a_{j-1}+a_j, \\ l_{j,j+1} &= a_{j-1}(1-a_j^2), & m_{j,j+1} &= a_{j-1}. \end{aligned} \tag{2.25}$$

In Equations (2.24) and (2.25), the computational parameters $a_j \in (0, 1]$ for $j = 0, 1, \cdots, J$ have to be chosen. A study of the selection of parameters a_j is performed in (Hagstrom et al., 2007) and suggests that the simplest choice for $a_j = 1$ is reasonable in general. These absorbing boundary conditions are also implemented in finite element scheme (Givoli et al., 2006). Further extensions and improvements are also made in (Hagstrom et al., 2008). The performance of Hagstrom-Warburton absorbing boundary condition in frequency domain is investigated and compared with perfectly matched layer in (Rabinovich et al., 2010).

Besides the aforementioned absorbing boundary conditions, the wave propagation in infinite medium can be approximated by the doubly asymptotic approximations (DAAs). As the name implies, the DAAs are approximations that approach the exact boundary integral representation of unbounded domain asymptotically at both high-frequency and low-frequency limits. This approach was firstly employed

in the acoustic-structure interaction analysis by Geers in the 1970's (Geers, 1971, 1974, 1978). In DAAs, the integral-equation solution of the governing equation of acoustics is written in the form of Kirchhoff's integral equation (KIE). The early time approximations (ETAs), which are related to the high-frequency responses, are then constructed based on the KIE. A hierarchical family of ETAs for transient acoustic-structure interaction was published by Felippa in 1980 (Felippa, 1980) and then extended to a third-order ETA which can be applied to the crude plane-wave approximation (Geers, 1991). The low-frequency responses are then approximated by the late time approximations (LTAs) constructed from the Laplace transform of KIE and are spatially non-local due to the spacial integral included. Via matching the early-time and late-time approximations, the DAAs can be formulated as:

$$\text{DAA}_1: \quad \dot{p}(R,t) + c\beta^{-1}\gamma p(R,t) = \rho c\dot{v}(R,t) \tag{2.26a}$$

$$\text{DAA}_2: \quad \ddot{p}(R,t) + c(\chi+\kappa)\dot{p}(R,t) + c^2\chi\beta^{-1}\gamma p(R,t) = \rho c[\ddot{v}(R,t) + c\chi\dot{v}(R,t)] \tag{2.26b}$$

$$\begin{aligned}\text{DAA}_3: \quad & \dddot{p}(R,t) + c(\lambda\beta^{-1}\alpha + \zeta + \kappa)\ddot{p}(R,t) \\ & + c^2\zeta\beta^{-1}\gamma\dot{p}(R,t) + c^3\lambda\beta^{-1}\gamma p(R,t) = \rho c[\dddot{v}(R,t) \\ & + c(\lambda\beta^{-1}\alpha + \zeta)\ddot{v}(R,t) + c^2\lambda\dot{v}(R,t)]\end{aligned} \tag{2.26c}$$

In Equation (2.26), p is the acoustic pressure, R is any point on the boundary and v is the normal fluid velocity at the boundary. The sound speed is c and the fluid density is ρ. κ is the mean curvature. All the other Greek alphabets in Equation (2.26) denote spatial integration operators. The first-order doubly asymptotic approximation (DAA_1) was heuristically formulated in (Geers, 1971). Then, DAA_1 was further developed for elastodynamics (Underwood and Geers, 1981) and nonlinear ground shock analysis (Mathews and Geers, 1987). Both DAA_1 and DAA_2 have been used for acoustic-structure interaction analysis in (Geers, 1978; Geers and Felippa, 1983). Promising results have been obtained via employing DAA_2. DAAs were also extended to electromagnetic scattering problems (Geers and Zhang, 1988)

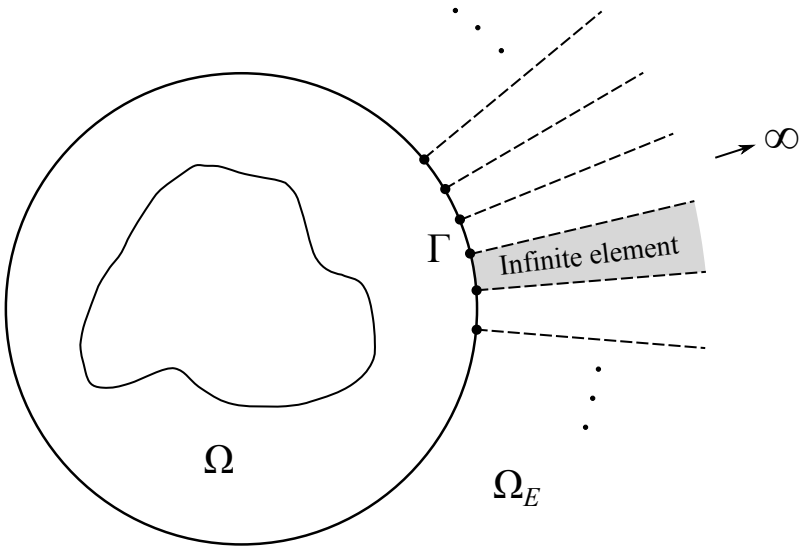

Figure 2.5. An illustration of infinite element.

and poroelastodynamics (Qi and Geers, 1997). The geometrical versatility is the major advantage of DAA boundaries. The major limitation is the difficulty of implementing DAA boundaries with order higher than two as the improving accuracy requires increasing DAA orders (Geers and Sprague, 2010). To the author's knowledge, the highest order of DAAs reported in literature is three (Geers and Toothaker, 2000).

2.2.2.2 Infinite elements

The infinite elements can replace the open boundary conditions by a layer of elements on the boundary. In this method, the infinite domain is entirely represented by elements with infinite extent. The concept of infinite elements is analogous to finite elements in FEM for modelling bounded domains but with appropriate shape functions that can extend elements to the unbounded domain. Therefore, the infinite elements are spatially and temporally local. An illustration of infinite elements on the boundary Γ of the bounded domain Ω for representing the unbounded domain Ω_E is plotted in Figure 2.5.

The work on infinite element was firstly performed by Zienkiewicz and Bettess in 1976 (Zienkiewicz and Bettess, 1976). In this original approach, the elements can be

extended to infinity via multiplying the corresponding shape functions with suitable decay functions. Then, exponential decay functions are chosen in this approach for the Laplace problems in (Bettess, 1977). This shape function of infinite elements for one-dimensional problems can be formulated as:

$$N_j(r) = e^{\frac{(r_j - r)}{L}} l_j(r) \tag{2.27}$$

with the Lagrange polynomial $l_j(r)$ and the nodal coordinates r_j. L is an arbitrary distance parameter, which measures the severity of the exponential decay. Via discretizing the unbounded domain into infinite elements, this approach can be implemented into existing finite element programs easily as an additional element library. As an alternative choice, the reciprocal decay functions can also be applied. The above infinite elements were also extended to model wave propagation problems governed by the Helmholtz equation (Bettess and Zienkiewicz, 1977). In order to model the decay of waves to infinity due to energy dissipation, a harmonic function of type $e^{\mathrm{i}kr}$ is multiplied to Equation (2.27) as:

$$N_j(r) = e^{\mathrm{i}kr} e^{\frac{(r_j - r)}{L}} l_j(r) \tag{2.28}$$

with the wavenumber k.

Except decay-function infinite elements, the mapped infinite elements developed by Zienkiewicz et al. show simplicity in the generation of one-, two- and three-dimensional infinite elements (Zienkiewicz et al., 1983). For one-dimensional problems, the introduced mapping function in this approach can transform the finite parent element with the interval of $\xi \in [-1, 1]$ to an infinite element with the interval $x \in [x_2 - x_1, \infty)$. This transformation can be formulated in the form of:

$$x(\xi) = (2x_1 - x_2)\tilde{N}_0(\xi) + x_2\tilde{N}_2(\xi) \tag{2.29}$$

where x_1 and x_2 are nodal coordinates and the expressions for $\tilde{N}_0(\xi)$ and $\tilde{N}_2(\xi)$ are

give by:

$$\tilde{N}_0(\xi) = \frac{-\xi}{1-\xi}, \quad \tilde{N}_2(\xi) = 1 + \frac{\xi}{1-\xi} \tag{2.30}$$

This mapped formulation also imposes the correct asymptotic decay behavior, such as $r^{-0.5}$ for two-dimensional problems, in the radial direction. In contrast, the infinite elements with exponential decay functions (Bettess, 1977) are not able to correctly represent that. The mapped infinite elements are also applied to two-dimensional surface wave and three-dimensional acoustics in (Moyer, 1992) and (Goransson and Davidsson, 1987) respectively.

A third type of infinite elements called wave envelope elements was firstly developed by Astley and Eversman for acoustics (Astley, 1983; Astley and Eversman, 1983). In this approach, the complex conjugates of shape functions are employed as the weighting functions in the Galerkin weight-residual approach. This leads to correct asymptotic behavior of the infinite elements and great simplification to the integration of elements as the oscillatory terms are removed in the integrands of weighting functions. However, this also makes the discrete problem unsymmetrical. The weighting function can be expressed as:

$$W_i = N_i(r,\theta)\frac{r_i}{r}e^{+\mathrm{i}k(r-r_i)} \tag{2.31}$$

with the global shape function in polar coordinates $N_i(r,\theta)$ for any node i. This scheme also shows capability of predicting accurate behaviors of unbounded domains with sparse meshes. Then, the wave envelope elements were tested by a simple one-dimensional problem for revealing their significance and hidden snags (Bettess, 1987). Later, Astley et al. extended the wave envelope idea by including element mapping from infinite elements methodology (Astley et al., 1994). The complex conjugate weighting functions in this approach are scaled by a geometric weight factor. This approach is also known as the conjugated Astley-Leis formulation as it fits within the variational framework of Leis (Leis, 2013). The wave envelop

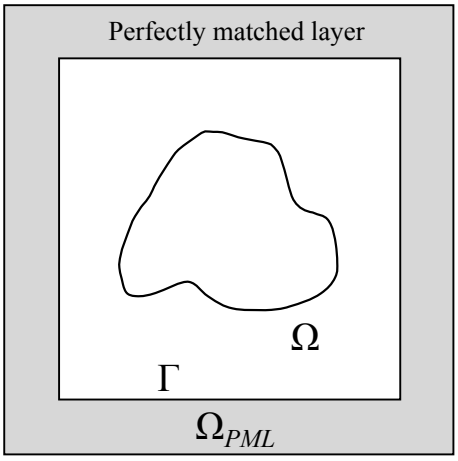

Figure 2.6. An illustration of perfectly matched layer.

formulation in the frequency domain is also developed for transient analysis via incorporating the inverse Fourier transform (Astley, 1996). However, ill-conditioning problems might be caused by increasing the order of element or at large wavenumber (Astley, 2000; Astley and Coyette, 2001). Additionally, a study in (Astley and Hamilton, 2006) reveals that the stability of infinite elements for transient wave problems depends on the inner surface of the infinite element domain.

2.2.2.3 Perfectly matched layer

An alternative type of procedure for modelling wave propagation in unbounded domains is the absorbing layers. Several absorbing layers, such as the sponge layers (Israeli and Orszag, 1981), have been developed in the past decades. The perfectly matched layer (PML) is one of the most widely developed absorbing layers. The PML is a hypothetical layer surrounding the bounded domain with finite thickness and artificial medium. This layer is capable of eliminating the reflected waves back to the computational domain and thus replacing the unbounded domain. As illustrated in Figure 2.6, the computational domain Ω is surrounded by the PML (Ω_{PML}) along its boundary Γ.

The PML was firstly constructed in time domain based on the finite-difference method by Berenger for the unbounded electromagnetic problems governed by Max-

well's equations (Berenger, 1994). Then, the same author extended the PML to three-dimensional electromagnetic problems (Berenger, 1996). Later, the original approach developed by Berenger is proved to be weakly will-posed and may lead to instabilities (Abarbanel and Gottlieb, 1997). As a result, strong well-posted formulations based on Lorentz-material model and mathematical construct are proposed in (Abarbanel and Gottlieb, 1998). The PML has been applied to various problems such as linearized Euler equations (Hu, 1996), poroelastic media (Zeng et al., 2001) and elastodynamics (Chew and Liu, 1996). Surveys of PML can be found in publications (Gedney, 1998; Hagstrom, 1999). The wave propagation in unbounded acoustic media has also be modeled by PML in literatures (Qi and Geers, 1998; Harari et al., 2000; Tsynkov and Turkel, 2001; Singer and Turkel, 2004; Bécache et al., 2004; Bermúdez et al., 2007). For two-dimensional acoustic problems governed by Helmholtz equation in Equation (2.1), the governing equation in PML (Ω_{PML}) is the modified Helmholtz (PML-Helmholtz) equation with complex-valued anisotropic material properties suitable for standard finite-element scheme and can be expressed as:

$$\frac{\partial}{\partial x}\left(\frac{S_y}{S_x}\frac{\partial p}{\partial x}\right)+\frac{\partial}{\partial y}\left(\frac{S_x}{S_y}\frac{\partial p}{\partial y}\right)+k^2 S_x S_y p=0 \tag{2.32}$$

with the acoustic pressure p and wavenumber k. S_x and S_y are functions responsible for the decay within the layer Ω_{PML} and can be written in a general form of:

$$S_x=1+\frac{\sigma_x}{\mathrm{i}k},\quad S_y=1+\frac{\sigma_y}{\mathrm{i}k} \tag{2.33}$$

In Equation (2.33), σ_x and σ_y, which are corresponding to the rate of decay, are functions with respect to x and y. When $\sigma_x=\sigma_y=0$ and $S_x=S_y=1$, Equation (2.32) will be reduced to the original Helmholtz equation in Equation (2.1) for the computational domain Ω. For the absorbing layer Ω_{PML}, σ_x or σ_y is zero in the part of layer normal to y or x direction respectively. Therefore, both σ_x and σ_y are not zeros in those corner regions only. In the PML formulations developed by Tsynkov

and Turkel (Tsynkov and Turkel, 2001), constant decaying functions in Ω_{PML} are adopted for the convenience of analysis. For obtaining high-accuracy approximation to Helmholtz equation, Singer and Turkel employed polynomial decay functions (Singer and Turkel, 2004). Then, the PML based on an unbounded decay function, which only depends on the sound speed of acoustics, is proposed by Bermúdez et al (Bermúdez et al., 2007). It is also called the optimal or exact PML as it shows significantly smaller errors than the classical ones.

Via utilizing the insights obtained with PML for electromagnetics, Basu and Chopre also developed a novel PML for time-harmonic elastodynamics. This novel PML can be implemented into a displacement-based finite element formulation (Basu and Chopra, 2003). In the next year, it was extended to transient elastodynamics for homogeneous and isotropic media (Basu and Chopra, 2004). Recently, a new absorbing layer was constructed by Harari and Albocher based on PML concept with the layer viewed as an anisotropic material with continuously varying complex material properties (Harari and Albocher, 2006). This absorbing layer can also be easily implemented in finite element software. The PML has been employed in the transient analysis of dam-reservoir interaction system in (Khazaee and Lotfi, 2014) and nonlinear analysis of soil-structure interaction in (Lee et al., 2014). Optimal placement of the interface, thickness of layer, number of elements, types of decay functions and implementation in the time domain is still debatable (Collino and Monk, 1998).

2.3 Structural elastoplasticity

In the elastoplastic analysis preformed in this thesis, only small strain problems without large rigid body rotations are considered. The problems of large deformations are out of the scope of this research. Therefore, literature reviews on the former type of problems are presented in the following sections.

Studies on microplasticity have already revealed some physical mechanisms of plastic deformations, such as the crystal slip in metal (Hull and Bacon, 2001) or microcracks in rocks and concrete (Vermeer, 1998). However, microplasticity modelling of plastic behaviors is not feasible in the engineering level due to the demands of efficient analyses and minimum costs from industries. Therefore, classical continuum plasticity with mathematical descriptions, such as the yield criteria, plastic flow and hardening rules, is widely used in the engineering analysis of plastic deformations.

As an introduction to the classical plasticity theories, some well-known yield criteria, hardening rules and constitutive relationships between stresses and strains are discussed in Section 2.3.1. Next, a brief description of finite element implementations for elastoplastic analysis are given at the beginning of Section 2.3.2. This is then followed by a review of the reduced integration methods with stabilizations. The reduced integration methods were commonly used to improve the efficiency of computational elastoplasticity and eliminate the locking phenomena in finite element analysis.

2.3.1 Fundamentals of plasticity theory

The origin of plasticity theory can be traced back to the pioneer work done by Tresca in 1864 (Tresca, 1864). Later, other important theories on plasticity were also developed by Saint-Venant (St Venant, 1870), Mohr (Mohr, 1906), Mises (Mises, 1913), Drucker and Prager (Drucker and Prager, 1952) et al. Detailed descriptions and discussions can be found in many books on plastic theory (Hill, 1998; Chen and Han, 2007; de Souza Neto et al., 2011). In the plasticity theory, the limit that the material shows plastic behavior is defined as the yield criterion. After the yielding happens, the stress-strain relationship of material is determined by the flow rule. In the following sections, brief descriptions of the plasticity theory and key formulations are demonstrated.

2.3.1.1 Yield criteria

In a simple uniaxial tension test, the elastic limit of material before the exist of any plastic deformation is easily defined by the uniaxial yield stress σ_0. However, the definition of this limit in multiaxial stress test is less straightforward as the stress components in several directions are included. In general, the yield condition can be expressed as a function of the state of stress $\boldsymbol{\sigma}$ as:

$$F(\boldsymbol{\sigma}, k) = f(\boldsymbol{\sigma}) - k^2 = 0 \tag{2.34}$$

with f representing some function and k representing material parameter which can be determined experimentally. The k can also be a function of the hardening parameter κ if the work hardening is considered. In the stress space, the yield function given by Equation (2.34) describes the yield surface. For any stress point in this space, $F < 0$ indicates it inside the surface and corresponding to the elastic stress state. Points on the surface define the elastic limit with $F = 0$ and points outside the yield surface with $F > 0$ is considered to be plastically inadmissible. Two classical yield criteria for defining the yield surface of metallic materials, the Tresca yield criterion and von Mises yield criterion, are briefly summarized here.

In 1864, the first yield criterion for a combined state of stresses in metal was proposed by Tresca (Tresca, 1864). The Tresca yield criterion suggests that the plastic yielding begins when the maximum shear stress reaches a critical value. This can be formulated using principle stresses $(\sigma_1, \sigma_2, \sigma_3)$ as:

$$\tau_{max} = \max\left(\frac{1}{2}|\sigma_1 - \sigma_2|, \frac{1}{2}|\sigma_1 - \sigma_2|, \frac{1}{2}|\sigma_1 - \sigma_2|\right) = k \tag{2.35}$$

where the material parameter k can be determined by the simple tension test as:

$$k = \frac{\sigma_0}{2} \tag{2.36}$$

The Tresca yield criterion in Equation (2.35) defines an infinitely long regular hexagonal cylinder in the principle stress space. The axis of this hexagonal cylinder

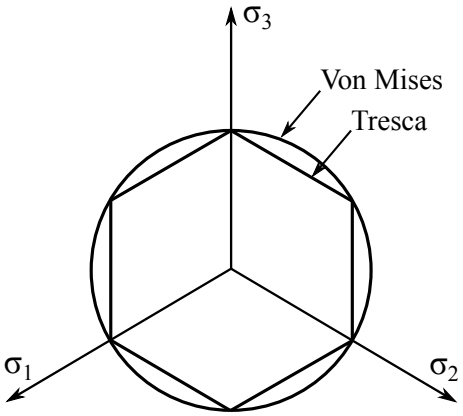

Figure 2.7. π plane representation of Tresca and von Mises yield criteria.

coincides with the space diagonal. Because each normal section of this cylinder is identical, the geometrical representation of this yield surface can make use of its projection on the π plane (or deviatoric plane), which is a plane passing through the origin of principle stress space and perpendicular to the space diagonal with $\sigma_1 + \sigma_2 + \sigma_3 = 0$. The π plane representation of Tresca yield criterion is plotted as the regular hexagon in Figure 2.7.

Although Tresca yield criterion is simple, no influence of the intermediate principle stress is reflected in this criterion. In 1913, von Mises suggested that the plastic yielding begins when the second deviatoric stress invariant reaches a critical value. The mathematical expression of von Mises yield criterion is:

$$\sqrt{J_2} = k \tag{2.37}$$

with the second deviatoric stress invariant J_2 defined as:

$$J_2 = \frac{1}{6}\left[(\sigma_1 - \sigma_2)^2 + (\sigma_2 - \sigma_3)^2 + (\sigma_3 - \sigma_1)^2\right] \tag{2.38}$$

In Equation (2.37), k is a material parameter that can be determined by experiments. Consider the yielding occurred in uniaxial tension test when $\sigma_1 = \sigma_0$ and $\sigma_2 = \sigma_3 = 0$, utilizing Equations (2.37) and (2.38) yields:

$$k = \frac{\sigma_0}{\sqrt{3}} \tag{2.39}$$

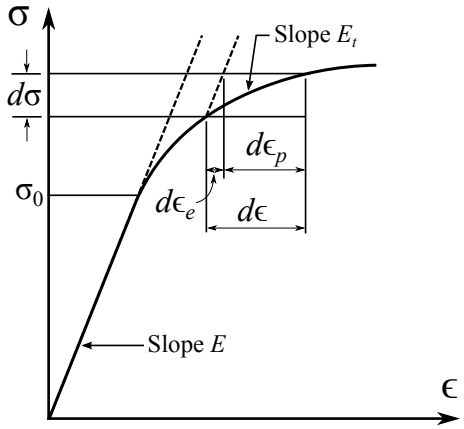

Figure 2.8. Stress-strain curve of uniaxial tension test with hardening.

The von Mises yield surface is an infinitely long cylinder in the principle stress space with its axis coincides with the space diagonal. π plane representation of von Mises yield criteria is also given in Figure 2.7. In this figure, the von Mises circle is set to intersect the vertices of Tresca hexagon under uniaxial stress. For many metallic materials, the experimental yield surfaces fall between the von Mises and Tresca yield surfaces.

2.3.1.2 Hardening rules

The hardening phenomenon in a typical uniaxial test is shown in Figure 2.8. Generally, hardening means that the yield stress level after the initial yielding is dependent on the history of plastic straining. In the uniaxial test, hardening is described by allowing the uniaxial yield stress σ_0 to vary with respect to the accumulated plastic strain. For describing the nonlinear stress-strain relationship of elastoplastic materials, the incremental procedure is adopted. The strain increment $d\epsilon$ is assumed to consist two parts: the elastic strain increment $d\epsilon_e$ and the plastic strain increment $d\epsilon_p$ as:

$$d\epsilon = d\epsilon_e + d\epsilon_p \tag{2.40}$$

In Figure 2.8, the stress increment $d\sigma$ is related to the strain increment $d\epsilon$ by:

$$d\sigma = E_t d\epsilon \tag{2.41}$$

with the tangent modulus E_t, which is varying during the plastic deformation. Utilizing Hook's law for elastic strain increment $d\epsilon_e$ and substituting Equation (2.40) into (2.41) yields:

$$d\sigma = E_t \left(\frac{d\sigma}{E} + d\epsilon_p \right) \tag{2.42}$$

where E is the Elastic modulus. Rearranging Equation (2.42) yields the relationship between stress increment $d\sigma$ and plastic strain increment $d\epsilon_p$:

$$d\sigma = H d\epsilon_p \tag{2.43}$$

with the hardening parameter H (or plastic modulus) defined as:

$$\frac{1}{H} = \frac{1}{E_t} - \frac{1}{E} \tag{2.44}$$

For the two- or three-dimensional cases, the hardening is introduced by changing the material parameter k in the yield function $F(\boldsymbol{\sigma}, k)$ in Equation (2.34). This may lead to the change of size, shape and orientation of the yield surface. First of all, the material is perfectly plastic if there is no hardening exist. In this scenario, the yield stress level does not depend on the degree of plastic deformation and the yield surface is fixed regardless of any deformation process. The k in Equation (2.34) is then a constant in this situation. Figure 2.9 shows the π plane representation of a perfectly plastic von Mises model on the left-hand-side. The corresponding uniaxial cyclic test with loading (tension), unloading and reloading (compression) process is also plotted on the right-hand-side in Figure 2.9 for explanation. The perfectly plastic model is normally used for stability analysis of structures and calculating limit loads and safety factors in engineering practices.

If the subsequent yield surface is corresponding to the uniform (isotropic) expansion of the initial yield surface at any state of hardening, this plastic model

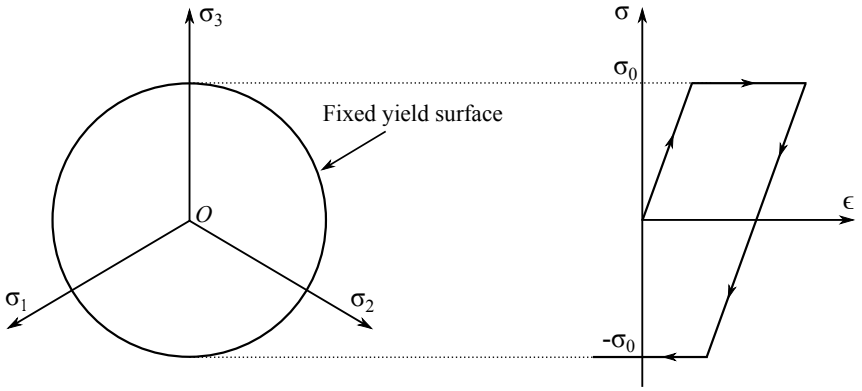

Figure 2.9. Perfect plasticity: π plane representation of von Mises yield surface and uniaxial test.

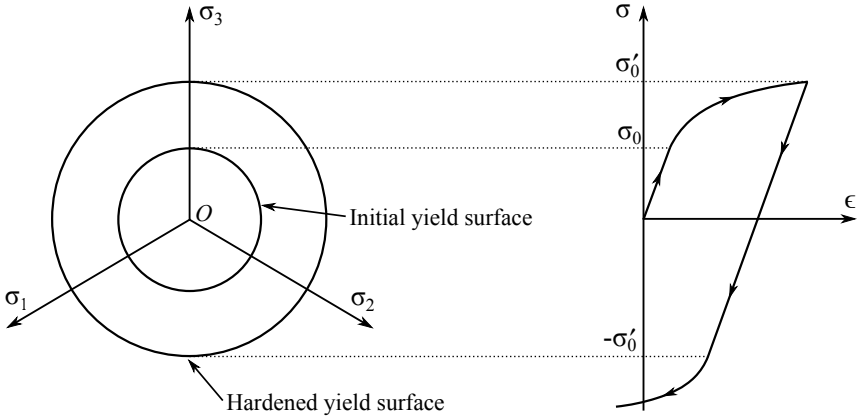

Figure 2.10. Isotropic hardening: π plane representation of von Mises yield surface and uniaxial test.

is considered to be isotropic hardening. The size of the yield surface in the isotropic hardening depends on the material parameter $k(\bar{\epsilon}_p)$, which is a function of the plastic strain history now. The effective plastic strain $\bar{\epsilon}_p$ can be determined as a scalar function of the work done by plastic deformation or as the accumulated plastic strain. The graphical interpretation of isotropic hardening is illustrated in Figure 2.10 with the π plane representation of von Mises yield surface and a typical stress-stain curve of uniaxial cyclic test.

After being loaded and hardened in one direction, it is frequently observed in the experiments that some material show less resistance to the plastic yielding in the opposite direction. This type of phenomenon is known as the Bauschinger effect, which is not included in the isotropic hardening. Therefore, the kinematic hardening

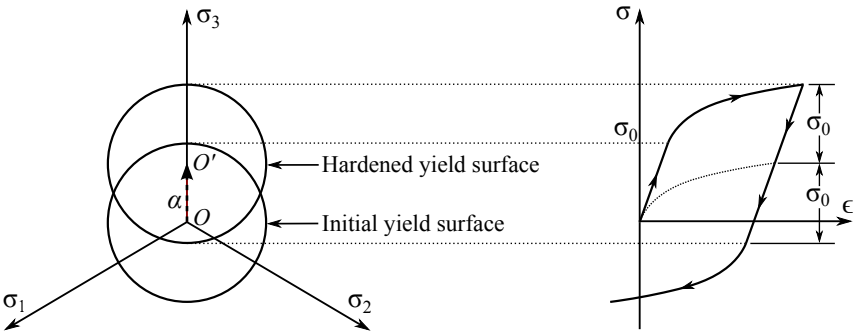

Figure 2.11. Kinematic hardening: π plane representation of von Mises yield surface and uniaxial test.

is developed to included the Bauschinger effect. In the kinematic hardening, the shape and size of the yield surface are preserved but the yield surface translates in the stress space. Again, the kinematic hardening of von Mises yield surface is plotted in Figure 2.11 along with the stress-strain curve of uniaxial cyclic test. The yield function of kinematic hardening can be written in the general form of:

$$f(\boldsymbol{\sigma} - \boldsymbol{\alpha}) - k = 0 \tag{2.45}$$

where the material parameter k is a constant and $\boldsymbol{\alpha}$ is known as the back stress or shift stress, which defines the shifting ($\overline{OO'}$) of the yield surface and varies with the plastic deformation.

2.3.1.3 Elastoplastic constitutive relationship

For deriving the stress-strain relationship after the yielding, the loading criterion is firstly addressed here. As discussed in Section 2.3.1.1, the elastic stress states are located inside the yield surface and the plastic deformation occurs when the stress point is on the yield surface. Therefore, during the plastic loading, the stress point stays on the yield surface and the additional loading or the incremental stress $d\boldsymbol{\sigma}$ should point outwardly from the current elastic region. In order to precisely express the above statement, the criterion for loading can be written as:

$$F = 0, \text{ and } \frac{\partial F}{\partial \boldsymbol{\sigma}} d\boldsymbol{\sigma} > 0 \tag{2.46}$$

For the loading condition described in Equation (2.46), $\frac{\partial F}{\partial \boldsymbol{\sigma}}$ is normal to the yield surface. Since the incremental stress $d\boldsymbol{\sigma}$ is pointing outwardly from elastic region during loading, the angles between $d\boldsymbol{\sigma}$ and $\frac{\partial F}{\partial \boldsymbol{\sigma}}$ is less than 90° and the product of them should be larger than zero. In contrast, unloading occurs when the stress point moves back from yield surface to the current elastic region inside. The angles between $d\boldsymbol{\sigma}$ and $\frac{\partial F}{\partial \boldsymbol{\sigma}}$ is larger than 90°. Hence, the unloading will occur when:

$$F = 0, \text{ and } \frac{\partial F}{\partial \boldsymbol{\sigma}} d\boldsymbol{\sigma} < 0 \tag{2.47}$$

In the neutral loading case, the incremental stress $d\boldsymbol{\sigma}$ is tangential to the yield surface and perpendicular to $\frac{\partial F}{\partial \boldsymbol{\sigma}}$. No additional plastic deformation will occur. Thus, the criterion for neutral loading is:

$$F = 0, \text{ and } \frac{\partial F}{\partial \boldsymbol{\sigma}} d\boldsymbol{\sigma} = 0 \tag{2.48}$$

After the initial yielding, part of the material will be plastic. Any increment in stress $d\boldsymbol{\sigma}$ is corresponding to the changes in strain. Following Equation (2.40), the incremental strain for multidimensional case $d\boldsymbol{\epsilon}$ can be decomposed in to elastic and plastic parts as:

$$d\boldsymbol{\epsilon} = d\boldsymbol{\epsilon}_e + d\boldsymbol{\epsilon}_p \tag{2.49}$$

A further assumption is made for deriving the relationship between plastic strain increment $d\boldsymbol{\epsilon}_p$ and the stress increment $d\boldsymbol{\sigma}$ for the multidimensional case. Because the relationship between elastic strain increment $d\boldsymbol{\epsilon}_e$ and the stress increment $d\boldsymbol{\sigma}$ is governed by the Hook's law, the plastic strain increment is assumed to be proportional to the stress gradient of plastic potential G as:

$$d\boldsymbol{\epsilon}_p = d\lambda \frac{\partial G}{\partial \boldsymbol{\sigma}} \tag{2.50}$$

where the scalar of proportionality $d\lambda$ is the plastic multiplier, Equation (2.50) is the flow rule, which governs the plastic flow after yielding. Generally, the expression for G should be determined by experiments. As the simplest guess, it is reasonable

to assume $G = F$ and yields:

$$d\boldsymbol{\epsilon}_p = d\lambda \frac{\partial F}{\partial \boldsymbol{\sigma}} \tag{2.51}$$

Equation (2.51) is known as the associate flow rule as the plastic flow is associate or connected to the yield criterion. In contrast, Equation (2.50) is also known as the nonassociate flow rule. The relationship between incremental stress and strain is defined as the constitutive relation below:

$$d\boldsymbol{\sigma} = \mathbf{D}_{ep} d\boldsymbol{\epsilon} \tag{2.52}$$

where $\mathbf{D}_{ep}$ is the elastoplastic constitutive matrix. Here, only the detailed derivation of $\mathbf{D}_{ep}$ for perfectly plastic material is given for conciseness. Derivations for stress-strain relationship under other yielding criteria and hardening rules can be found in books for plastic theory (Hill, 1998; Chen and Han, 2007). Utilizing Hook's law and Equation (2.49), the stress increment $d\boldsymbol{\sigma}$ can be expressed as:

$$d\boldsymbol{\sigma} = \mathbf{D} d\boldsymbol{\epsilon}_e = \mathbf{D} \left(d\boldsymbol{\epsilon} - d\boldsymbol{\epsilon}_p \right) \tag{2.53}$$

with $\mathbf{D}$ the elastic matrix. Substituting Equation (2.50) into (2.53) yields:

$$d\boldsymbol{\sigma} = \mathbf{D} \left(d\boldsymbol{\epsilon} - d\lambda \frac{\partial G}{\partial \boldsymbol{\sigma}} \right) \tag{2.54}$$

Because the stress state $(\boldsymbol{\sigma} + d\boldsymbol{\sigma})$ after the incremental change $d\boldsymbol{\sigma}$ should still satisfy the yield criterion $F = 0$, the following relationship must exist for perfectly plastic material:

$$F(\boldsymbol{\sigma} + d\boldsymbol{\sigma}) = F(\boldsymbol{\sigma}) + dF = 0 = F(\boldsymbol{\sigma}) \tag{2.55}$$

Then, the consistency condition can be derived from Equation (2.55) as:

$$dF = \left(\frac{\partial F}{\partial \boldsymbol{\sigma}} \right)^T d\boldsymbol{\sigma} = 0 \tag{2.56}$$

Substituting the expression for $d\boldsymbol{\sigma}$ in Equation (2.54) into Equation (2.56):

$$\left(\frac{\partial F}{\partial \boldsymbol{\sigma}}\right)^T \left(\mathbf{D}d\boldsymbol{\epsilon} - d\lambda \mathbf{D}\frac{\partial G}{\partial \boldsymbol{\sigma}}\right) = 0 \tag{2.57}$$

Solving the plastic multiplier $d\lambda$ from Equation (2.57):

$$d\lambda = \frac{\left(\frac{\partial F}{\partial \boldsymbol{\sigma}}\right)^T \mathbf{D}d\boldsymbol{\epsilon}}{\left(\frac{\partial F}{\partial \boldsymbol{\sigma}}\right)^T \mathbf{D}\frac{\partial G}{\partial \boldsymbol{\sigma}}} \tag{2.58}$$

Substituting Equation (2.58) into (2.54) and rearranging the resulting formula into the form of Equation (2.52) yields the expression for the elastoplastic constitutive matrix:

$$\mathbf{D}_{ep} = \mathbf{D} - \frac{\mathbf{D}\frac{\partial G}{\partial \boldsymbol{\sigma}}\left(\frac{\partial F}{\partial \boldsymbol{\sigma}}\right)^T \mathbf{D}}{\left(\frac{\partial F}{\partial \boldsymbol{\sigma}}\right)^T \mathbf{D}\frac{\partial G}{\partial \boldsymbol{\sigma}}} \tag{2.59}$$

According to Equations (2.52) and (2.59), the stress and strain relationship in finite element formulations is nonlinear as the evaluation of current stress is influenced by the magnitude of the stress increment. Therefore, the iterative procedure must be applied in each incremental step. The finite element implementation of elastoplastic analysis is briefly summarized at the beginning of next section.

2.3.2 Improving efficiency of computational elastoplasticity

For the purpose of discussing the use of reduced integration methods in improving the efficiency of computational elastoplasticity, the computational procedures for the finite element analysis of elastoplasticity are briefly summarized at first. Some early implementations of plastic theory into finite element scheme can be traced back to mid-1960s (Marcal and King, 1967; Yamada et al., 1968; Zienkiewicz et al., 1969). Detailed descriptions, including computer codes, for the finite element analysis of elastoplastic problems are available in various books (Owen and Hinton, 1980; de Souza Neto et al., 2011; Kim, 2014). Performing the finite element analysis for normal static problems yields the following global system of equations:

$$\mathbf{KU} = \mathbf{F}_{ext} \tag{2.60}$$

with the nodal displacement vector $\mathbf{U}$, external nodal force vector $\mathbf{F}_{ext}$ and the stiffness matrix $\mathbf{K}$ for elastoplastic analysis given by:

$$\mathbf{K} = \int_{\Omega} \mathbf{B}^T \mathbf{D}_{ep} \mathbf{B} d\Omega \tag{2.61}$$

where $\mathbf{B}$ is the strain-displacement matrix. According to Equation (2.59), the evaluation of $\mathbf{D}_{ep}$ in Equation (2.61) requires the current state of stress. Additionally, the response of elastoplastic system also depends on the deformation history. Therefore, the incremental form of Equation (2.60) is adopted:

$$\mathbf{K}_t \Delta \mathbf{U} = \Delta \mathbf{F}_{ext} \tag{2.62}$$

The tangent stiffness matrix $\mathbf{K}_t$ in Equation (2.62) is a linearization of the exact nonlinear stiffness matrix $\mathbf{K}$ within this incremental step and is calculated based on the stress state at the end of last step. Consequently, the incremental displacement and strain can be evaluated. Then, the incremental stresses can be calculated using the nonlinear relation defined in Equation (2.59). The evaluation of incremental stresses also requires the elastic predictor/plastic corrector algorithm, which is also known as the return mapping algorithm. As the name suggests, this algorithm involves two steps: the elastic trial step and the plastic corrector step. In the elastic trial step, the elastic trial state is solved by assuming that the material is purely elastic. If the elastic trial state lies within the elastic domain or on the yield surface defined by the yield criterion in Equation (2.34), this solution is accepted. However, if the elastic trial state violates plastic admissibility, the plastic corrector step is required to enforce the plastic admissibility and bring the stress state back to the updated yield surface (in case of the exist of hardening). Once the stresses of this current step $\boldsymbol{\sigma}$ are calculated, the internal nodal force vector $\mathbf{F}_{int}$ can be calculated as:

$$\mathbf{F}_{int} = \int_{\Omega} \mathbf{B}^T \boldsymbol{\sigma} d\Omega \tag{2.63}$$

Then, the global force equilibrium has to be satisfied by examining the difference of internal and external nodal forces. The difference, which is known as the residual force $\mathbf{R}$, is:

$$\mathbf{R} = \mathbf{F}_{ext} - \mathbf{F}_{int} \tag{2.64}$$

The residual force $\mathbf{R}$ should be smaller than a tolerance value for accuracy. If $\mathbf{R}$ is larger than the tolerance, it is then used as a new applied external force for evaluating the new strain and stress increments via the aforementioned procedure to update the results. In each of these iterations, a new residual force will be calculated at the end and this iteration procedure will stop until the residual is smaller than the predefined tolerance. Common iterative procedures, such as Newton-Raphson or modified Newton-Raphson method, could be employed.

As discussed earlier, the update of stresses within each incremental load step requires the return mapping algorithm and should be performed at each integration point (Gauss point) of an element independently. Due to the nonlinearity of the elastoplastic constitutive equations, the return mapping algorithm should include a stepping or iterative procedure and thus is computationally expensive. For improving the efficiency of elastoplastic analysis via finite element method, developments have been made on constructing stable iterative procedures with accelerated convergence rate, such as line search techniques (Matthies and Strang, 1979; Crisfield, 1983, 1984), arc length methods (Wempner, 1971; Riks, 1972, 1979; Crisfield et al., 2012) and consistence tangent operators (Simo and Taylor, 1985). Alternatively, the efficiency of the elastoplastic analysis can be increased by reducing the number of integration points required in each element, such as the quadrilateral element with a single quadrature point introduced by Hughes et al. in (Hughes et al., 1978). However, reducing the integration points leads to rank-deficient elements. This means that the sum of the rank of element stiffness matrix and the number of rigid body modes is less than the total number of degree of freedom. This may cause singulari-

ties of the assembled global stiffness matrix under certain boundary conditions and meshes. Although the singularity is absent in the transient system matrix, spatial oscillations may exist in the solutions. These spatial oscillations are physically uninterpretable and similar to the hourglass patterns in finite difference computations (Maenchen and Sack, 1964). In order to reduce the rank deficiency, numerous reduced integration methods with hourglass control have been developed during the last decades. In these methods, the spurious modes, which is also known as the hourglass modes, of the underintegrated elements are often controlled by introducing an additional stabilization matrix. The stabilization matrix should be used to ensure the element passes the patch test via preserving the conditions of invariance and consistency. Moreover, deformation modes other than the hourglass modes should not be effected by the stabilization matrix.

During the past decades, a number of literatures have been contributed to develop stable underintegrated elements for finite element analysis and a good review on those techniques for controlling the hourglass modes are discussed in the paper by Belytschko et al. (Belytschko et al., 1984). The hourglass control scheme published by Kosloff and Frazier (Kosloff and Frazier, 1978) is considered to be seminal. In their work, the stabilization matrix is constructed to be orthogonal to all linear displacement field and its magnitude is determined by a stabilization parameter. However, the solution of equation is required in the derivation of the element stiffness. Then, a scheme with simple expression for the projection in stabilization matrix are established by Flanagan and Belytschko (Flanagan and Belytschko, 1981) without the solution of any equation. This projection is also known as the γ-projection operator. Based on the approach developed by Flanagan and Belytschko (Flanagan and Belytschko, 1981), quadrilateral elements with one-point integration for plates (Belytschko and Tsay, 1983) and heat conduction (Liu and Belytschko, 1984) are developed. The stabilization parameter in (Liu and Belytschko, 1984) is determined by solving an eigenvalue problem. The numerical results imply that the

accuracy of underintegrated element for Laplace equation is slightly decreased but the rate of convergence is not influenced by the hourglass control. In (Belytschko et al., 1984), the γ-projection is used to construct the optimal bending element with the magnitude of stabilization parameter obtained by the Hu-Washizu variational principle. The stability and convergence of the 4-nodes quadrilateral element with one-point integration are also examined by Jacquotte and Oden (Jacquotte and Oden, 1984). The conclusion of the examination states that the convergence rate of the 4-nodes quadrilateral element with one-point integration is nearly the same as the fully integrated element. The γ-projection operator was also used to develop two flexural-superconvergent elements and two elements that avoid volumetric locking in (Belytschko and Bachrach, 1986). The corresponding numerical examples show that the hourglass control may improve the accuracy of underintegrated elements for certain types of problems such as the beam bending and incompressible materials.

The stabilization matrix can also be derived by approaches which do not require stabilization parameters. An assumed strain stabilization of the 4-nodes quadrilateral element and 8-nodes hexahedral element with one-point integration was constructed in (Belytschko and Bindeman, 1991) and (Belytschko and Bindeman, 1993) respectively by Belytschko and Bindeman. Based on the material properties and element geometry, this stabilization procedure is developed via the assumed strain method. This type of element is accurate in coarse mesh as the symmetric displacement gradient is projected to the assumed strain field. This strain field is chosen in a similar way as it developed in (Belytschko and Bachrach, 1986). Alternatively, Liu et al. suggested that the strain field used in stabilization can be constructed by Taylor series (Liu et al., 1985). This approach is a unification of the stabilization-matrix concept as it is applicable to all two-dimensional and three-dimensional elements. However, shear-related locking phenomenon are not considered. Another hourglass control approach was also published by Schulz via expanding the stress field using Taylor series about the centre of element (Schulz, 1985). Based on the procedure

proposed by Liu et al. (Liu et al., 1985), the directional reduced integration is developed by Koh and Kikuchi (Koh and Kikuchi, 1987). In the directional reduced integration, the full integration is still used along on of the referential directions for stabilization. The computational effort is thus smaller than full integration but greater than one-point quadrature. The approach proposed by Koh and Kikuchi works well for two-dimensional problems. Nevertheless, hourglass modes have been found for three-dimensional plate and shell elements. In order to overcome the locking problems in (Liu et al., 1985), new two-dimensional and three-dimensional underintegrated elements are constructed in (Liu et al., 1994) for solving beam, plate and shell problems. The approaches proposed by Liu et al. in (Liu et al., 1985, 1994) are based on the Taylor expansion of stain-displacement matrix, while approaches based on the Taylor expansion of the derivatives of shape function with respect to physical coordinates are proposed by Hueck and Wriggers for linear elasticity (Hueck and Wriggers, 1995) and large deformation (Wriggers and Hueck, 1996). Later, Korelc and Wriggers published a more efficient element. This element utilizes the Taylor expansion of the derivatives with respect to reference coordinates rather than physical coordinates (Korelc and Wriggers, 1997). Elements with reduced integration and hourglass control have been successfully implemented in several software packages such as LS-DYNA3D (Hallquist, 1983, 1994), MSC Nastran (Lahey et al., 1994), ANSYS (ANSYS, 2002) and ABAQUS (Systèmes, 2007). Recently, reduced integration has also been applied to isogeometric analysis (IGA) (Schillinger et al., 2014; Adam et al., 2015; Hiemstra et al., 2017; Fahrendorf et al., 2018; Leonetti et al., 2018).

2.4 Conclusions

Reviews on the numerical simulations of both wave propagation in unbounded domains and structural elastoplasticity are performed in this chapter. For modelling the

unbounded domains, the developments on global and local approaches are stated and the corresponding advantages and disadvantages are discussed. Considering the intrinsic nature of SBFEM in modelling unbounded domains and several local high-order open boundaries developed for improving its computational efficiency, this method is extended to model both two- and three- dimensional unbounded acoustic domains as well as the acoustic-structure interaction problems in this thesis. Not to mention the inherent advantages of SBFEM in automatic meshing of complex geometry and efficient mesh transitions on acoustic-structure or material interface.

The fundamentals for structural elastoplasticity, along with the implementations in finite element scheme, are briefly summarized in this chapter as well. The developments and discussions of reduced integration methods with hourglass control are reviewed. As an approach to reduce the number of locations for performing the computationally expensive return mapping algorithm in elastoplastic analysis, the scaled boundary formulation with stabilization is developed for three-dimensional elastoplasticity in this thesis for efficient and automatic analysis.

Chapter 3

2D acoustic analysis using SBFEM

3.1 Introduction

The propagation of acoustic waves in unbounded domains, including sound wave radiation and scattering by obstacles, is of importance in many practical applications such as sonar, crack detection, acoustic optimization of vehicles and the seismic design of dam-reservoir systems. The numerical modelling of these types of problems is challenging due to the requirement to satisfy the radiation condition at infinity. Moreover, the modelling of waves in bounded domains poses its own problems with regards to fine mesh requirements when high wavenumbers are involved.

With respect to accurately and efficiently representing unbounded domains, different numerical approaches have been proposed, some of the most popular methods used in modelling exterior acoustics are reviewed and compared in Chapter 2. Local absorbing boundary conditions are particularly attractive in terms of efficiency and ease of implementation. Most of the proposed local absorbing boundaries are only singly asymptotic at the high-frequency limit. That is, they are suitable for radiative fields where all of the field energy propagates to infinity. This is not the case in a layered system, where evanescent modes exist. Even if all modes are propagating, the rate of convergence of high-order singly-asymptotic open boundaries may be

low. For a circular cavity embedded in a full plane, the modal stiffness coefficient approaches that of a horizontal layer with increasing mode number λ (Prempramote et al., 2009). The slow convergence can be overcome by using a doubly-asymptotic approximation (DAA), which is accurate not only at the high-frequency limit, but also at statics. The development of the DAA is documented in Section 2.2.2.1. The highest order of the DAA reported in the literature is three (Geers and Toothaker, 2000).

As discussed in Section 2.2.1.3, a high-order doubly-asymptotic open boundary was proposed specifically for the modal equations of scalar waves (Prempramote et al., 2009). This formulation has been shown to accurately model evanescent waves and long-time responses. Compared to singly-asymptotic open boundaries, it leads to a significant gain in accuracy at no additional cost. However, this algorithm can become ill-conditioned for mode number λ close to $i + 0.5$, where i is an integer. Therefore, an improvement is proposed in (Prempramote, 2011) to increase the numerical robustness of the solution procedure. This is achieved by introducing additional factor coefficients in the derivation of the doubly-asymptotic continued-fraction solution. As a result, the denominators of certain continued-fraction coefficients turn into only sign functions, whereby singularities are avoided. In addition, it is also proposed to use singly-asymptotic approximations for the low-order modes only and to combine these with doubly-asymptotic approximations of all other modes. This contributes to improving robustness and reducing the computational cost.

The approach presented in References (Prempramote et al., 2009; Prempramote, 2011) for modal equations is extended to the two-dimensional case in this chapter. To this end, it is combined with a scaled boundary finite element approach. The SBFEM is a semi-analytical technique that is particularly suitable for modelling waves in unbounded domains and for representing singularities. It has also been used in the context of dynamic dam-reservoir interaction (Lin et al., 2012). The

development of this method is documented in References (Song and Wolf, 1995; Wolf and Song, 1995; Song and Wolf, 1996; Wolf and Song, 1996; Song and Wolf, 1997; Wolf, 2003).

A two-dimensional acoustic domain of arbitrary shape can be divided into a near field region containing any irregular geometrical features and a far field region by introducing a circular boundary as will be illustrated in Figure 3.1 later in Section 3.2. The near field can be further divided into bounded scaled boundary finite element subdomains, which can be regarded as superelements. The far field region is represented by the proposed high-order doubly-asymptotic open boundary. The scaled boundary finite element equations of the unbounded domain with circular boundary are decoupled in this approach. The resulting modal scaled boundary finite element equations can be cast in terms of a frequency-dependent modal impedance coefficient and the solutions can be sought recursively by expanding this coefficient into a series of continued fractions and satisfying the scaled boundary finite element equation at both high and low frequency limits. Via introducing auxiliary variables and superimposing the contributions of individual modes, the continued-fraction expansion is transformed into a temporally local open boundary condition in the time-domain (Prempramote et al., 2009). The resulting system of first-order differential equations to represent the unbounded domain is easily coupled to the standard equations of motions representing the interior via the nodal flux vector on the circular boundary. The main materials of this chapter have been published as a research paper in Journal of Computational Physics (Birk et al., 2016).

This chapter is organized as follows. The scaled boundary finite element approach for two-dimensional linear acoustics is outlined in Section 3.2. The improved doubly-asymptotic open boundary for 2D exterior acoustics is derived in Section 3.3. The coupling of the scaled boundary finite element model of the bounded domain and the high-order doubly-asymptotic open boundary is addressed in Section 3.4. Numerical examples are presented in Section 3.5 to illustrate the improved numerical

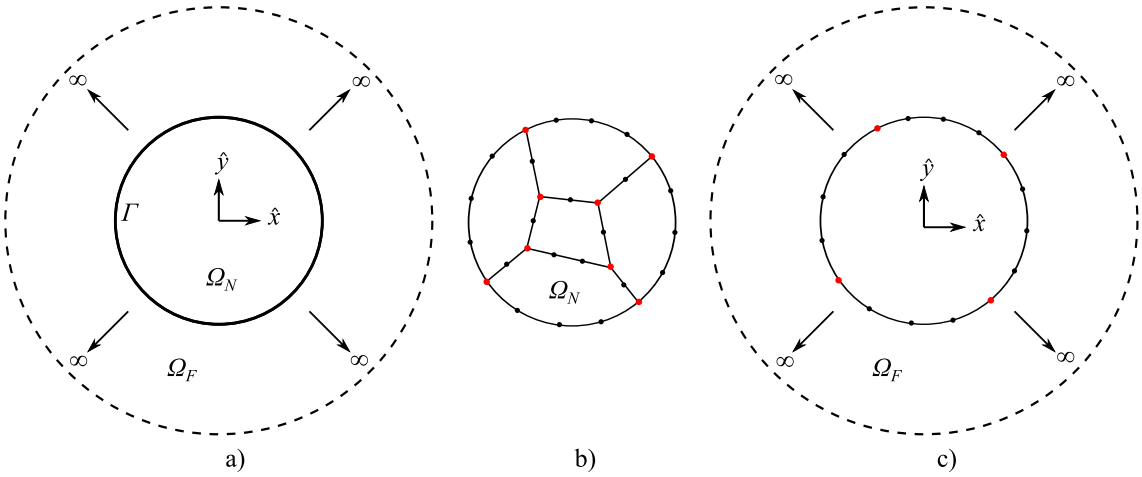

Figure 3.1. Modeling 2D infinite acoustic domain: (a) the 2D acoustic domain, (b) bounded near field and (c) unbounded far field

robustness, accuracy and efficiency of the proposed approach.

3.2 Scaled boundary finite element formulations for 2D linear acoustics

Wave propagation in a linear acoustic medium is governed by the scalar wave equation,

$$\nabla^2 p - \frac{1}{c^2}\frac{\partial^2 p}{\partial t^2} = 0. \tag{3.1}$$

In Equation (3.1), the symbols p and c denote the acoustic pressure and the speed of sound, respectively. The gradient operator ∇ is formulated in Cartesian coordinates $\hat{x}$, $\hat{y}$ as $\nabla = \left[\frac{\partial}{\partial \hat{x}}, \frac{\partial}{\partial \hat{y}}\right]^T$.

Consider a two-dimensional domain, which is split into a near field region Ω_N and a far field region Ω_F by a circular boundary Γ as shown in Figure 3.1.

Both the bounded and unbounded parts of the system can be efficiently modeled using the SBFEM, as will be demonstrated in this chapter. To this end, the near field region is split into a number of bounded subdomains to capture the essential geometric features. The SBFEM is applied to each of these subdomains. The far field

is treated as one unbounded subdomain with a circular surface. Near field and far field are coupled via the nodal flux on the circular boundary Γ. The computational implementation of the coupling of the scaled boundary finite element models of bounded and unbounded substructures is straightforward, provided that compatible meshes are used to discretize the circular boundaries. The scaled boundary finite element formulations for the bounded and unbounded domains are summarized in Sections 3.2.1 and 3.2.2, respectively.

3.2.1 2D bounded acoustic domain

Figure 3.2 shows a scaled boundary finite element model of a typical polygon-shaped bounded domain. Only the boundary is discretized using line finite elements. Here, higher-order elements can be employed (Vu and Deeks, 2006). Individual sections of the boundary can be modeled using different numbers of elements and varying element orders. In Figure 3.2, the bigger red dots indicate nodes that coincide with the endpoints of elements, whereas the smaller black dots indicate internal nodes. For each element, the geometry of the boundary is described by interpolating local nodal coordinates $\mathbf{x}_b$ and $\mathbf{y}_b$ using 1D mapping functions $\mathbf{N}(\eta)$ in terms of the local coordinate η,

$$x(\eta) = \mathbf{N}(\eta)\mathbf{x}_b, \qquad y(\eta) = \mathbf{N}(\eta)\mathbf{y}_b. \tag{3.2}$$

with the 1D mapping functions

$$\mathbf{N}(\eta) = [N_1(\eta),\ N_2(\eta),\ \cdots N_m(\eta)] \tag{3.3}$$

where m is the number of nodes in this element. The total bounded domain is described by scaling the geometry of the boundary using the radial coordinate ξ,

$$\hat{x} = \xi \cdot x = \xi \mathbf{N}(\eta)\mathbf{x}_b \tag{3.4a}$$

$$\hat{y} = \xi \cdot y = \xi \mathbf{N}(\eta)\mathbf{y}_b \tag{3.4b}$$

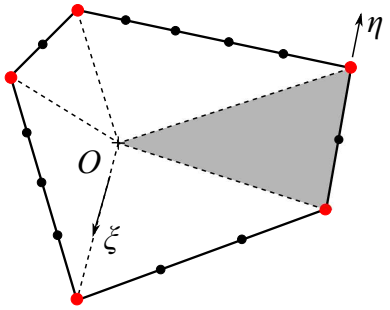

Figure 3.2. A Typical 2D polygon-shaped bounded subdomain in SBFEM coordinates

The radial coordinate ξ is equal to one at the boundary and zero at the scaling centre O. In Figure 3.2, the grey shaded triangle indicates the part of the bounded polygon that is obtained by scaling the corresponding line element.

Equation (3.4) is referred to as the scaled boundary transformation. It is used to express the differential operator in a governing equation in terms of the scaled boundary coordinates η and ξ. Following the general concept of the SBFEM (Wolf, 2003; Wolf and Song, 2000), the gradient operator in Equation (3.1) for 2D acoustics is formulated as

$$\nabla = [\mathbf{J}(\eta)]^{-1} \begin{bmatrix} 1 & \\ & \xi \end{bmatrix} \begin{Bmatrix} \frac{\partial}{\partial \xi} \\ \frac{\partial}{\partial \eta} \end{Bmatrix} = \{\mathbf{b}_1^a(\eta)\} \frac{\partial}{\partial \xi} + \frac{1}{\xi} \mathbf{b}_2^a(\eta) \frac{\partial}{\partial \eta}, \tag{3.5}$$

with

$$\mathbf{J}(\eta) = \begin{bmatrix} x(\eta) & y(\eta) \\ x(\eta)_{,\eta} & y(\eta)_{,\eta} \end{bmatrix}. \tag{3.6}$$

The superscript 'a' in vectors $\mathbf{b}_1^a$ and $\mathbf{b}_2^a$ in Equation (3.5) denotes the acoustic domain. Using Equation (3.2), $\mathbf{b}_1^a$ and $\mathbf{b}_2^a$ can be expressed as

$$\mathbf{b}_1^a = \frac{1}{|\mathbf{J}|} \begin{Bmatrix} y_{,\eta} \\ -x_{,\eta} \end{Bmatrix}, \quad \mathbf{b}_2^a = \frac{1}{|\mathbf{J}|} \begin{Bmatrix} -y \\ x \end{Bmatrix}, \quad |\mathbf{J}| = x y_{,\eta} - y x_{,\eta}. \tag{3.7}$$

Discretizing the pressure field $p(x, y, t)$ using the same mapping functions as for the

geometry,

$$p(x,y,t) = \mathbf{N}(\eta)\hat{\mathbf{p}}(\xi)\mathrm{e}^{\mathrm{i}\omega t}, \tag{3.8}$$

$\hat{\mathbf{p}}(\xi)$ is the radial pressure amplitude. Applying the method of weighted residuals to Equation (3.1) in the circumferential direction, a differential equation for the nodal pressure amplitude $\hat{\mathbf{p}}(\xi)$ in two-dimensional acoustics is obtained. In this equation, the absence of prescribed flux along side-face (boundary with constant circumferential coordinates η) in a subdomain is also considered:

$$\mathbf{E}_0^a\xi^2\hat{\mathbf{p}}(\xi)_{,\xi\xi} + \left(\mathbf{E}_0^a - \mathbf{E}_1^a + [\mathbf{E}_1^a]^T\right)\xi\hat{\mathbf{p}}(\xi)_{,\xi} - \mathbf{E}_2^a\hat{\mathbf{p}}(\xi) + \omega^2\mathbf{M}_0^a\xi^2\hat{\mathbf{p}}(\xi) = 0 \tag{3.9}$$

In Equation (3.9), the symbols $\mathbf{E}_0^a$, $\mathbf{E}_1^a$, $\mathbf{E}_2^a$ and $\mathbf{M}_0^a$ denote coefficient matrices that are calculated on an element-by-element basis and assembled using standard finite element techniques. For two-dimensional acoustics, these matrices calculated for each boundary element are defined as

$$\mathbf{E}_0^a = \int_{-1}^{+1} [\mathbf{B}_1^a(\eta)]^T \mathbf{B}_1^a(\eta)\,|\mathbf{J}(\eta)|\,d\eta \tag{3.10a}$$

$$\mathbf{E}_1^a = \int_{-1}^{+1} [\mathbf{B}_2^a(\eta)]^T \mathbf{B}_1^a(\eta)\,|\mathbf{J}(\eta)|\,d\eta \tag{3.10b}$$

$$\mathbf{E}_2^a = \int_{-1}^{+1} [\mathbf{B}_2^a(\eta)]^T \mathbf{B}_2^a(\eta)\,|\mathbf{J}(\eta)|\,d\eta \tag{3.10c}$$

$$\mathbf{M}_0^a = \int_{-1}^{+1} \mathbf{N}^T(\eta)\frac{1}{c^2}\mathbf{N}(\eta)\,|\mathbf{J}(\eta)|\,d\eta \tag{3.10d}$$

with

$$\mathbf{B}_1^a(\eta) = \mathbf{b}_1^a\mathbf{N}(\eta), \qquad \mathbf{B}_2^a = \mathbf{b}_2^a\mathbf{N}(\eta)_{,\eta}. \tag{3.11}$$

The second-order differential equation (3.9) in nodal pressure can be transformed in an equivalent nonlinear first-order differential equation in impedance $\mathbf{S}^a(\omega)$,

$$(\mathbf{S}^a(\omega) - \mathbf{E}_1^a)\,[\mathbf{E}_0^a]^{-1}\left(\mathbf{S}^a(\omega) - [\mathbf{E}_1^a]^T\right) - \mathbf{E}_2^a + \omega\mathbf{S}^a(\omega)_{,\omega} + \omega^2\mathbf{M}_0^a = 0 \tag{3.12}$$

where the frequency-dependent impedance matrix $\mathbf{S}^a(\omega)$ relates the amplitudes of

the nodal flux $\hat{\mathbf{R}}$ to those of the nodal pressure $\hat{\mathbf{p}}$ at the boundary $\xi = 1$,

$$\hat{\mathbf{R}} = \mathbf{S}^a(\omega)\hat{\mathbf{p}} \tag{3.13}$$

In a 2D bounded domain, the nodal flux $\hat{\mathbf{R}}(\xi)$ is equal to the internal nodal flux $\hat{\mathbf{Q}}(\xi)$, which is related to the nodal pressure as (Wolf and Song, 2000; Wolf, 2003)

$$\hat{\mathbf{Q}}(\xi) = \mathbf{E}_0^a \xi \hat{\mathbf{p}}(\xi)_{,\xi} + [\mathbf{E}_1^a]^T \hat{\mathbf{p}}(\xi) \tag{3.14}$$

At $\xi = 1$, the nodal flux vector $\hat{\mathbf{R}}$ is defined as

$$\hat{\mathbf{R}} = \int_{\Gamma_\xi} \mathbf{N}^T \frac{\partial \hat{p}}{\partial \vec{\mathbf{n}}} d\Gamma \tag{3.15}$$

In Equation (3.15), the integration is over the boundary Γ_ξ with $\xi = 1$ and $d\Gamma$ is the infinitesimal line. $\vec{\mathbf{n}}$ is the unit normal vector to the boundary curve and $\frac{\partial \bar{p}}{\partial \vec{\mathbf{n}}}$ denotes the prescribed normal derivative of the pressure at the boundary. Equation (3.12) can be solved by expanding the impedance matrix into a series of continued fractions, as has been proposed for structural dynamics in Reference (Song, 2009). Later, the coefficient matrix $\mathbf{X}_a^{(i)}$ is added in the continued fractions and lead to better conditioned mass and stiffness matrices in the time-domain equations (Chen et al., 2014). The continued-fraction solution for $\mathbf{S}^a(\omega)$ is summarized in the following section.

3.2.1.1 Continued-fraction solution for 2D bounded acoustics

In this section, the improved continued-fraction solution for solving the impedance of 2D bounded acoustic domain is summarized. Readers are referred to (Song, 2009; Chen et al., 2014) for more details. Equation (3.12) can be rewritten as

$$(\mathbf{S}^a(\bar{\omega}) - \mathbf{E}_1^a)\,[\mathbf{E}_0^a]^{-1}\left(\mathbf{S}^a(\bar{\omega}) - [\mathbf{E}_1^a]^T\right) + 2\bar{\omega}\mathbf{S}^a(\bar{\omega})_{,\bar{\omega}} - \mathbf{E}_2^a - \bar{\omega}\mathbf{M}_0^a = 0 \tag{3.16}$$

with $\bar{\omega} = -\omega^2$. The impedance matrix $\mathbf{S}^a(\bar{\omega})$ can be expressed as the sum of constant term $\mathbf{K}_a$, linear term $\bar{\omega}\mathbf{M}_a$ and a high-order residual term $-\bar{\omega}^2\left(\mathbf{R}_a^{(1)}(\bar{\omega})\right)$ as

$$\mathbf{S}^a(\bar{\omega}) = \mathbf{K}_a + \bar{\omega}\mathbf{M}_a - \bar{\omega}^2\left(\mathbf{R}_a^{(1)}(\bar{\omega})\right) \tag{3.17}$$

In Equation (3.17), $\mathbf{K}_a$ and $\mathbf{M}_a$ are the static stiffness and mass matrix of bounded acoustic domain. $\mathbf{R}_a^{(1)}(\bar{\omega})$ represents the high-frequency response of this bounded domain. Substituting Equation (3.17) into (3.16) gives

$$\begin{aligned}\left(\mathbf{K}_a - \mathbf{E}_1^a + \bar{\omega}\mathbf{M}_a - \bar{\omega}^2\left(\mathbf{R}_a^{(1)}(\bar{\omega})\right)\right)\left[\mathbf{E}_0^a\right]^{-1}&\left(\mathbf{K}_a - \left[\mathbf{E}_1^a\right]^T + \bar{\omega}\mathbf{M}_a\right.\\ &\left. - \bar{\omega}^2\left(\mathbf{R}_a^{(1)}(\bar{\omega})\right)\right) + 2\bar{\omega}\left(\mathbf{M}_a - 2\bar{\omega}\left(\mathbf{R}_a^{(1)}(\bar{\omega})\right) - \bar{\omega}^2\left(\mathbf{R}_a^{(1)}(\bar{\omega})\right)_{,\bar{\omega}}\right)\\ &- \mathbf{E}_2^a - \bar{\omega}\mathbf{M}_0^a = 0\end{aligned} \tag{3.18}$$

Next, Equation (3.18) can be rearranged in ascending orders of the power of $\bar{\omega}$. By setting all constant terms to zero yields

$$\left(\mathbf{K}_a - \mathbf{E}_1^a\right)\left[\mathbf{E}_0^a\right]^{-1}\left(\mathbf{K}_a - \left[\mathbf{E}_1^a\right]^T\right) - \mathbf{E}_2^a = 0 \tag{3.19}$$

The solution of the algebraic Riccati equation in Equation (3.19) for $\mathbf{K}_a$ is described in (Song, 2004a). Setting all linear terms in Equation (3.18) to zero leads to

$$\left(\mathbf{K}_a - \mathbf{E}_1^a\right)\left[\mathbf{E}_0^a\right]^{-1}\mathbf{M}_a + \mathbf{M}_a\left[\mathbf{E}_0^a\right]^{-1}\left(\mathbf{K}_a - \left[\mathbf{E}_1^a\right]^T\right) + 2\mathbf{M}_a - \mathbf{M}_0^a = 0 \tag{3.20}$$

Equation (3.20) is the Lyapunov equation for the mass matrix $\mathbf{M}_a$. Setting the remaining terms in Equation (3.18) to zero yields the following equation for $\mathbf{R}_a^{(1)}(\bar{\omega})$:

$$\begin{aligned}\mathbf{M}_a\left[\mathbf{E}_0^a\right]^{-1}\mathbf{M}_a - \left(\mathbf{K}_a - \mathbf{E}_1^a\right)&\left[\mathbf{E}_0^a\right]^{-1}\left(\mathbf{R}_a^{(1)}(\bar{\omega})\right) - \left(\mathbf{R}_a^{(1)}(\bar{\omega})\right)\left[\mathbf{E}_0^a\right]^{-1}\\ &\cdot\left(\mathbf{K}_a - \left[\mathbf{E}_1^a\right]^T\right) - 4\left(\mathbf{R}_a^{(1)}(\bar{\omega})\right) - \bar{\omega}\mathbf{M}_0^a\left[\mathbf{E}_0^a\right]^{-1}\left(\mathbf{R}_a^{(1)}(\bar{\omega})\right)\\ &- \bar{\omega}\left(\mathbf{R}_a^{(1)}(\bar{\omega})\right)\left[\mathbf{E}_0^a\right]^{-1}\mathbf{M}_a - 2\bar{\omega}\left(\mathbf{R}_a^{(1)}(\bar{\omega})\right)_{,\bar{\omega}}\\ &+ \bar{\omega}^2\left(\mathbf{R}_a^{(1)}(\bar{\omega})\right)\left[\mathbf{E}_0^a\right]^{-1}\left(\mathbf{R}_a^{(1)}(\bar{\omega})\right) = 0\end{aligned} \tag{3.21}$$

In this improved continued-fraction solution, the unknown residual term $\mathbf{R}_a^{(i)}(\bar{\omega})$ is decomposed by the yet undetermined scaling factor $\mathbf{X}_a^{(i)}$ with $i = 1, 2, \ldots M$ (M

is the number of terms in continued fraction).

$$\mathbf{R}_a^{(i)}(\bar{\omega}) = \mathbf{X}_a^{(i)} \left(\mathbf{S}_a^{(i)}(\bar{\omega})\right)^{-1} \left(\mathbf{X}_a^{(i)}\right)^T \tag{3.22}$$

The term $\mathbf{S}_a^{(i)}(\bar{\omega})$ in Equation (3.22) corresponds to the denominator of the continued-fraction term. Similar to the expression for $\mathbf{S}^a(\bar{\omega})$ in Equation (3.17), $\mathbf{S}_a^{(i)}(\bar{\omega})$ can be expressed as the sum of a constant term $\mathbf{S}_{a0}^{(i)}$, a linear term $\bar{\omega}\mathbf{S}_{a1}^{(1)}$ and a high-order residual term $-\bar{\omega}^2 \left(\mathbf{R}_a^{(i+1)}(\bar{\omega})\right)$ as

$$\mathbf{S}_a^{(i)}(\bar{\omega}) = \mathbf{S}_{a0}^{(i)} + \bar{\omega}\mathbf{S}_{a1}^{(1)} - \bar{\omega}^2 \left(\mathbf{R}_a^{(i+1)}(\bar{\omega})\right) \tag{3.23}$$

The derivative of $\left(\mathbf{R}_a^{(i)}(\bar{\omega})\right)_{,\bar{\omega}}$ can be obtained as

$$\left(\mathbf{R}_a^{(i)}(\bar{\omega})\right)_{,\bar{\omega}} = -\mathbf{X}_a^{(i)} \left(\mathbf{S}_a^{(i)}(\bar{\omega})\right)^{-1} \left(\mathbf{S}_a^{(i)}(\bar{\omega})\right)_{,\bar{\omega}} \left(\mathbf{S}_a^{(i)}(\bar{\omega})\right)^{-1} \left(\mathbf{X}_a^{(i)}\right)^T \tag{3.24}$$

Substituting Equation (3.22) into (3.21) and pre- and post-multiplying the resulting expression by $\left(\mathbf{S}_a^{(i)}(\bar{\omega})\right)\left(\mathbf{X}_a^{(i)}\right)^{-1}$ and $\left(\mathbf{X}_a^{(i)}\right)^{-T}\left(\mathbf{S}_a^{(i)}(\bar{\omega})\right)$, respectively, leads to the expression for $\mathbf{S}_a^{(1)}(\bar{\omega})$ (with $i = 1$) as:

$$\begin{aligned}
&\left(\mathbf{S}_a^{(1)}(\bar{\omega})\right)\mathbf{c}^{(1)}\left(\mathbf{S}_a^{(1)}(\bar{\omega})\right) - \left(\mathbf{S}_a^{(1)}(\bar{\omega})\right)\left(\mathbf{b}_0^{(1)}\right)^T - \left(\mathbf{b}_0^{(1)}\right)\left(\mathbf{S}_a^{(1)}(\bar{\omega})\right) \\
&- \bar{\omega}\left(\mathbf{S}_a^{(1)}(\bar{\omega})\right)\left(\mathbf{b}_1^{(1)}\right)^T - \bar{\omega}\left(\mathbf{b}_1^{(1)}\right)\left(\mathbf{S}_a^{(1)}(\bar{\omega})\right) + 2\bar{\omega}\left(\mathbf{S}_a^{(1)}(\bar{\omega})\right)_{,\bar{\omega}} + \bar{\omega}^2\mathbf{a}^{(1)} = 0
\end{aligned} \tag{3.25}$$

with:

$$\mathbf{a}^{(1)} = \left(\mathbf{X}_a^{(1)}\right)^T [\mathbf{E}_0^a]^{-1} \mathbf{X}_a^{(1)} \tag{3.26a}$$

$$\mathbf{b}_0^{(1)} = \left(\mathbf{X}_a^{(1)}\right)^T [\mathbf{E}_0^a]^{-1} \left(\mathbf{K}_a - [\mathbf{E}_1^a]^T\right) \left(\mathbf{X}_a^{(1)}\right)^{-T} - 2\mathbf{I} \tag{3.26b}$$

$$\mathbf{b}_1^{(1)} = \left(\mathbf{X}_a^{(1)}\right)^T [\mathbf{E}_0^a]^{-1} \mathbf{M}_a \left(\mathbf{X}_a^{(1)}\right)^{-T} \tag{3.26c}$$

$$\mathbf{c}^{(1)} = \left(\mathbf{X}_a^{(1)}\right)^T \mathbf{M}_a [\mathbf{E}_0^a]^{-1} \mathbf{M}_a \left(\mathbf{X}_a^{(1)}\right)^{-T} \tag{3.26d}$$

Equation (3.25) can be expanded by utilizing (3.23). Rewriting the resulting expression in ascending order of powers of $\bar{\omega}$, the following equation can be obtained by setting the constant term to zero

$$-\mathbf{b}_0^{(i)}\mathbf{S}_{a0}^{(i)} - \mathbf{S}_{a0}^{(i)}\left(\mathbf{b}_0^{(i)}\right)^T + \mathbf{S}_{a0}^{(i)}\mathbf{c}^{(1)}\mathbf{S}_{a0}^{(i)} = 0 \tag{3.27}$$

Equation (3.27) can be transformed into a Lyapunov equation for solving $\mathbf{S}_{a0}^{(i)}$ via pre- and post-multiplying with $\left(\mathbf{S}_{a0}^{(i)}\right)^{-1}$

$$\left(\mathbf{S}_{a0}^{(i)}\right)^{-1}\mathbf{b}_0^{(i)} + \left(\mathbf{b}_0^{(i)}\right)^T\left(\mathbf{S}_{a0}^{(i)}\right)^{-1} = \mathbf{c}^{(1)} \tag{3.28}$$

Equating all linear terms to zero yields

$$\begin{aligned}\left(-\mathbf{b}_0^{(i)} + \mathbf{S}_{a0}^{(i)}\mathbf{c}^{(1)}\right)\mathbf{S}_{a1}^{(i)} + \mathbf{S}_{a1}^{(i)}\left(-\left(\mathbf{b}_0^{(i)}\right)^T + \mathbf{c}^{(1)}\mathbf{S}_{a0}^{(i)}\right) + 2\mathbf{S}_{a1}^{(i)} \\ = \mathbf{b}_1^{(i)}\mathbf{S}_{a0}^{(i)} + \mathbf{S}_{a0}^{(i)}\left(\mathbf{b}_1^{(i)}\right)^T\end{aligned} \tag{3.29}$$

which is again a Lyapunov equation for $\mathbf{S}_{a1}^{(i)}$. Equating the remaining terms to zero, substituting Equation (3.22) and (3.24) into resulting equation and pre- and post-multiplying it by $\left(\mathbf{S}_a^{(i+1)}(\bar{\omega})\right)\left(\mathbf{X}_a^{(i+1)}\right)^{-1}$ and $\left(\mathbf{X}_a^{(i+1)}\right)^{-T}\left(\mathbf{S}_a^{(i+1)}(\bar{\omega})\right)$, respectively, yields an equation for the residual term $\mathbf{R}_a^{(i+1)}(\bar{\omega})$:

$$\begin{aligned}&\left(\mathbf{S}_a^{(i+1)}(\bar{\omega})\right)\mathbf{c}^{(i+1)}\left(\mathbf{S}_a^{(i+1)}(\bar{\omega})\right) - \left(\mathbf{S}_a^{(i+1)}(\bar{\omega})\right)\left(\mathbf{b}_0^{(i+1)}\right)^T \\ &\quad - \left(\mathbf{b}_0^{(i+1)}\right)\left(\mathbf{S}_a^{(i+1)}(\bar{\omega})\right) - \bar{\omega}\left(\mathbf{S}_a^{(i+1)}(\bar{\omega})\right)\left(\mathbf{b}_1^{(i+1)}\right)^T \\ &\quad - \bar{\omega}\left(\mathbf{b}_1^{(i+1)}\right)\left(\mathbf{S}_a^{(i+1)}(\bar{\omega})\right) + 2\bar{\omega}\left(\mathbf{S}_a^{(i+1)}(\bar{\omega})\right)_{,\bar{\omega}} + \bar{\omega}^2\mathbf{a}^{(i+1)} = 0\end{aligned} \tag{3.30}$$

with:

$$\mathbf{a}^{(i+1)} = \left(\mathbf{X}_a^{(i+1)}\right)^T\mathbf{c}^{(i+1)}\mathbf{X}_a^{(i+1)} \tag{3.31a}$$

$$\mathbf{b}_0^{(i+1)} = \left(\mathbf{X}_a^{(i+1)}\right)^T\left(2\mathbf{I} - \left(\mathbf{b}_0^{(i)}\right)^T + \mathbf{c}^{(i)}\mathbf{S}_{a0}^{(i)}\right)\left(\mathbf{X}_a^{(i+1)}\right)^{-T} \tag{3.31b}$$

$$\mathbf{b}_1^{(i+1)} = \left(\mathbf{X}_a^{(i+1)}\right)^T\left(-\left(\mathbf{b}_1^{(i)}\right)^T + \mathbf{c}^{(i)}\mathbf{S}_{a1}^{(i)}\right)\left(\mathbf{X}_a^{(i+1)}\right)^{-T} \tag{3.31c}$$

$$\mathbf{c}^{(i+1)} = \left(\mathbf{X}_a^{(i+1)}\right)^T\left(\mathbf{a}^{(i)} - \mathbf{b}_1^{(i)}\mathbf{S}_{a1}^{(i)} - \mathbf{S}_{a1}^{(i)}\left(\mathbf{b}_1^{(i)}\right)^T + \mathbf{S}_{a1}^{(i)}\mathbf{c}^{(i)}\mathbf{S}_{a1}^{(i)}\right)\left(\mathbf{X}_a^{(i+1)}\right)^{-T} \tag{3.31d}$$

The continued fraction is terminated when $i = M$ and the residual of order $M+1$ is neglected. In the expressions of continued-fraction solution for bounded domain in this section, if the coefficient matrix $\mathbf{X}_a^{(i)}$ is chosen to be identical, this improved continued fraction will be reduced to the original one in (Song, 2009). In the improved continued fraction, the coefficient matrix $\mathbf{X}_a^{(i)}$ is chosen in a way

that can lead to numerically better conditioned coefficient matrices in the continued fraction. According to (Chen et al., 2014), the evaluation of $\mathbf{X}_a^{(i)}$ is given by:

$$\mathbf{c}^{(i)} = \left(\mathbf{X}_a^{(i)}\right)^{-1} \tilde{\mathbf{c}}^{(i)} \left(\mathbf{X}_a^{(i)}\right)^{-T} \tag{3.32}$$

The coefficient matrix $\mathbf{X}_a^{(i)}$ can be determined using LDL^T decomposition.

3.2.1.2 Time-domain formulation for 2D bounded acoustics

The continued fraction for impedance matrix in Section 3.2.1.1 can be transformed to a series of linear equations in $\bar{\omega} = (i\omega)^2$. Detailed derivations can be referred to (Song, 2009). In this section, key equations are stated. Firstly, utilizing Equation (3.17), Equation (3.13) can be expressed as

$$\hat{\mathbf{R}} = \left(\mathbf{K}_a + \bar{\omega}\mathbf{M}_a\right)\left(\hat{\mathbf{p}}(\omega)\right) - \bar{\omega}\mathbf{X}_a^{(1)}\left(\hat{\mathbf{p}}^{(1)}(\omega)\right) \tag{3.33}$$

with the introduction of the first auxiliary variable $\hat{\mathbf{p}}^{(1)}(\omega)$:

$$\bar{\omega}\left(\mathbf{X}_a^{(1)}\right)^T\left(\hat{\mathbf{p}}(\omega)\right) = \left(\mathbf{S}_a^{(1)}(\bar{\omega})\right)\left(\hat{\mathbf{p}}^{(1)}(\omega)\right) \tag{3.34}$$

Equation (3.34) can be generalized as:

$$\bar{\omega}\left(\mathbf{X}_a^{(i)}\right)^T\left(\hat{\mathbf{p}}^{(i-1)}(\omega)\right) = \left(\mathbf{S}_a^{(i)}(\bar{\omega})\right)\left(\hat{\mathbf{p}}^{(i)}(\omega)\right) \tag{3.35}$$

with $\hat{\mathbf{p}}^{(0)}(\omega) = \hat{\mathbf{p}}(\omega)$. Using Equation (3.23) and new auxiliary variable $\hat{\mathbf{p}}^{(i+1)}(\omega)$, the following equation for i-th continued fraction can be obtained

$$\begin{aligned} -\bar{\omega}\left(\mathbf{X}_a^{(i)}\right)^T\left(\hat{\mathbf{p}}^{(i-1)}(\omega)\right) + \left(\mathbf{S}_{a0}^{(i)} + \bar{\omega}\mathbf{S}_{a1}^{(i)}\right)\left(\hat{\mathbf{p}}^{(i)}(\omega)\right) \\ -\bar{\omega}\left(\mathbf{X}_a^{(i+1)}\right)^T\left(\hat{\mathbf{p}}^{(i+1)}(\omega)\right) = 0 \end{aligned} \tag{3.36}$$

Finally, the continued fraction terminates at order M and $\hat{\mathbf{p}}^{(M+1)}(\omega)$ should be zero. Equations (3.33) and (3.36) can be formulated into matrix form. Its time-domain expression with frequency-independent coefficient matrices for bounded acoustic dom-

ain is:

$$\mathbf{M}_h^a \ddot{\mathbf{y}}(t) + \mathbf{K}_h^a \mathbf{y}(t) = \mathbf{r}(t) \tag{3.37}$$

The superscript and subscript 'a' indicate the acoustic domain in this chapter. For a continued-fraction expansion with the order of M, the high order mass and stiffness matrices $\mathbf{M}_h^a$ and $\mathbf{K}_h^a$ are expressed as:

$$\mathbf{M}_h^a = \begin{bmatrix} \mathbf{M}_a & -\mathbf{X}_a^{(1)} & 0 & \cdots & 0 \\ -\left[\mathbf{X}_a^{(1)}\right]^T & \mathbf{S}_{a1}^{(1)} & -\mathbf{X}_a^{(2)} & \cdots & 0 \\ 0 & -\left[\mathbf{X}_a^{(2)}\right]^T & \mathbf{S}_{a1}^{(2)} & \ddots & 0 \\ \vdots & \vdots & \ddots & \ddots & -\mathbf{X}_a^{(M)} \\ 0 & 0 & 0 & -\left[\mathbf{X}_a^{(M)}\right]^T & \mathbf{S}_{a1}^{(M)} \end{bmatrix} \tag{3.38a}$$

$$\mathbf{K}_h^a = \text{diag}\left(\mathbf{K}_a \; \mathbf{S}_{a0}^{(1)} \; \mathbf{S}_{a0}^{(2)} \; \cdots \; \mathbf{S}_{a0}^{(M)}\right) \tag{3.38b}$$

In Equation (3.38), $\mathbf{S}_{a0}^{(i)}$ and $\mathbf{S}_{a1}^{(i)}$ with $i = 1, 2, 3, \cdots, M$ are those coefficient matrices calculated recursively in the continued-fraction expansion for impedance matrices $\mathbf{S}^a(\omega)$ of all subdomains and assembled using standard finite element techniques. $\mathbf{M}_a$ and $\mathbf{K}_a$ are corresponding to the low-frequency expansion of impedance matrix with the order of continued-fraction expansion $M = 0$. The vector of unknowns $\mathbf{y}(t)$ includes both the nodal pressure $\mathbf{p}(t)$ and auxiliary variables $\mathbf{p}^{(i)}(t)$. The vector of unknowns can be expressed below:

$$\mathbf{y}(t) = \left\{ \mathbf{p}(t) \quad \mathbf{p}^{(1)}(t) \quad \mathbf{p}^{(2)}(t) \quad \cdots \quad \mathbf{p}^{(M)}(t) \right\}^T \tag{3.39}$$

The right-hand-side of Equation (3.37) $\mathbf{r}(t)$ only contains the time-dependent nodal flux vector $\mathbf{R}^{ext}(t)$ from any external sources as:

$$\mathbf{r}(t) = \left\{ \mathbf{R}^{ext}(t) \quad 0 \quad 0 \quad \cdots \quad 0 \right\}^T \tag{3.40}$$

The bounded and unbounded substructures shown in Figure 3.1 are coupled via the nodal flux vector on the interface Γ. The numerical modelling of the unbounded domain is addressed in the following section.

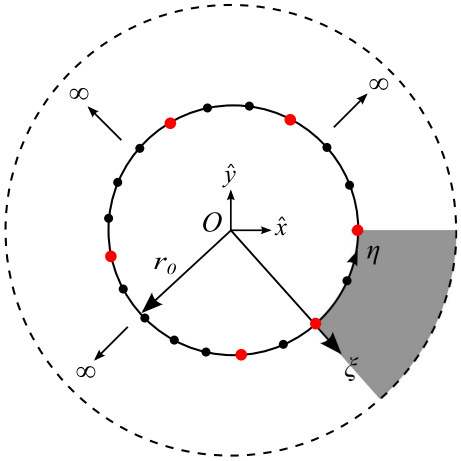

Figure 3.3. Scaled boundary finite element model of a 2D unbounded domain with circular interface

3.2.2 2D unbounded acoustic domain

A scaled boundary finite element model of an unbounded domain with a circular interface of radius r_0 is shown in Figure 3.3.

The scaling centre O is located at the centre of the circle. The circular boundary is discretized with line elements, analogously to the bounded domain. The unbounded domain is described by scaling the geometry of the circular interface using the scaling factor $\xi \geq 1$,

$$\hat{x} = \xi \cdot x(\eta) \tag{3.41a}$$

$$\hat{y} = \xi \cdot y(\eta) \tag{3.41b}$$

In order to accurately represent the circular geometry of the boundary, $x(\eta)$ and $y(\eta)$ are expressed in terms of polar coordinates, the constant radius r_0 and the angle θ, where θ is measured anti-clockwise from the positive x-axis.

$$x(\eta) = r_0 \cos(\theta(\eta)) \tag{3.42a}$$

$$y(\eta) = r_0 \sin(\theta(\eta)) \tag{3.42b}$$

Only the angular coordinate $\theta(\eta)$ is approximated by using the mapping functions

$\mathbf{N}(\eta)$ to interpolate nodal values $\boldsymbol{\theta}$,

$$\theta(\eta) = \mathbf{N}(\eta)\boldsymbol{\theta}. \tag{3.43}$$

Substituting the coordinate transformation defined by Equations (3.42) and (3.43) into Equation (3.5) yields for the unbounded domain

$$\mathbf{b}_1^a = \frac{1}{r_0}\left\{\begin{array}{c}\cos(\theta(\eta))\\ \sin(\theta(\eta))\end{array}\right\}, \quad \mathbf{b}_2^a = \frac{r_0}{|J(\eta)|}\left\{\begin{array}{c}-\sin(\theta(\eta))\\ \cos(\theta(\eta))\end{array}\right\}, \tag{3.44}$$

with

$$|\mathbf{J}| = r_0^2\theta(\eta)_{,\eta} = r_0^2\mathbf{N}(\eta)_{,\eta}\boldsymbol{\theta}.$$

Note that $\mathbf{b}_1^a$ and $\mathbf{b}_2^a$ are orthogonal. The further procedure is analogous to the steps described for the bounded domain in Section 3.2.1. For the unbounded medium with a circular boundary, the scaled boundary finite element equation in nodal pressure amplitude is obtained from Equation (3.9) (Wolf and Song, 2000),

$$\mathbf{E}_0^a\xi^2\hat{\mathbf{p}}_e(\xi)_{,\xi\xi} + \mathbf{E}_0^a\xi\hat{\mathbf{p}}_e(\xi)_{,\xi} - \mathbf{E}_2^a\hat{\mathbf{p}}_e(\xi) + \omega^2\mathbf{M}_0^a\xi^2\hat{\mathbf{p}}_e(\xi) = 0. \tag{3.45}$$

In Equation (3.45), the subscript 'e' indicates the exterior domain. The matrices $\mathbf{E}_0^a$, $\mathbf{E}_2^a$ and $\mathbf{M}_0^a$ are calculated using Equations (3.10) and (3.11) with $\mathbf{b}_1^a$ and $\mathbf{b}_2^a$ defined in Equation (3.44). The coefficient matrix $\mathbf{E}_1^a$ vanishes for orthogonal $\mathbf{b}_1^a$ and $\mathbf{b}_2^a$. Thus, the internal nodal flux defined in Equation (3.14) is simplified as

$$\hat{\mathbf{Q}}(\xi) = \mathbf{E}_0^a\xi\hat{\mathbf{p}}_e(\xi)_{,\xi} \tag{3.46}$$

Substituting Equation (3.11) in Equation (3.10a) and using Equation (3.44), the coefficient $\mathbf{E}_0^a$ can be expressed as

$$\mathbf{E}_0^a = \frac{1}{r_0^2}\int_{-1}^{+1}\mathbf{N}^T(\eta)\mathbf{N}(\eta)\,|\mathbf{J}(\eta)|\,d\eta \tag{3.47}$$

which is diagonal when using Gauss-Labotto quadrature. Comparing Equations

(3.10d) and (3.47), $\mathbf{E}_0^a$ is proportional to $\mathbf{M}_0^a$,

$$\mathbf{M}_0^a = \left(\frac{r_0}{c}\right)^2 \mathbf{E}_0^a. \tag{3.48}$$

Substituting Equation (3.48) into (3.45), the scaled boundary finite element equation in nodal pressure can be written for an unbounded domain with a circular boundary as

$$\mathbf{E}_0^a \xi^2 \hat{\mathbf{p}}_e(\xi)_{,\xi\xi} + \mathbf{E}_0^a \xi \hat{\mathbf{p}}_e(\xi)_{,\xi} - \mathbf{E}_2^a \hat{\mathbf{p}}_e(\xi) + a^2 \mathbf{M}_0^a \xi^2 \hat{\mathbf{p}}_e(\xi) = 0 \tag{3.49}$$

where the dimensionless frequency a is defined as

$$a = \frac{\omega r_0 \xi}{c}. \tag{3.50}$$

Equation (3.46) and (3.49) provide the basis of constructing an open boundary condition to represent the unbounded domain. This is explained in detail in the following section.

3.3 Doubly-asymptotic open boundary for 2D unbounded acoustics

A novel doubly-asymptotic open boundary for scalar wave propagation in an elastic full plane with a circular cavity has been proposed by Prempramote in Reference (Prempramote, 2011). It is transferred to the acoustic case in the following. Here, only the key equations are presented, while the detailed derivation can be found in Reference (Prempramote, 2011).

The proposed approach is based on decoupling the differential equations in nodal pressure (3.49) to derive scalar equations for the modal impedance coefficients of the circular cavity. These equations can be solved by means of continued-fraction expansions. The final high-order doubly-asymptotic open boundary condition is obtained by introducing internal variables and combining the modal flux-pressure

relationships in a global matrix formulation.

3.3.1 Modal impedance coefficients of a full plane with a circular cavity

The scaled boundary finite element equation (3.49) can be decoupled by using the following eigenvalue problem,

$$\mathbf{E}_2^a \boldsymbol{\Psi}_\infty = \mathbf{E}_0^a \boldsymbol{\Psi}_\infty \boldsymbol{\Lambda} \tag{3.51}$$

$\boldsymbol{\Lambda}$ is the diagonal matrix with eigenvalues λ_j^2 on its diagonal terms. $\boldsymbol{\Psi}_\infty$ is the corresponding eigenvector matrix. The eigenvectors are normalized as

$$\boldsymbol{\Psi}_\infty^T \mathbf{E}_0^a \boldsymbol{\Psi}_\infty = \mathbf{I} \tag{3.52a}$$

$$\boldsymbol{\Psi}_\infty^T \mathbf{E}_2^a \boldsymbol{\Psi}_\infty = \boldsymbol{\Lambda} \tag{3.52b}$$

Pre- and post-multiplying Equation (3.49) by $\boldsymbol{\Psi}_\infty^T$ and $\boldsymbol{\Psi}_\infty$, respectively, and using Equation (3.52) results in

$$\xi^2 \tilde{\mathbf{P}}(\xi)_{,\xi\xi} + \xi \tilde{\mathbf{P}}(\xi)_{,\xi} - \boldsymbol{\Lambda} \tilde{\mathbf{P}}(\xi) + a^2 \tilde{\mathbf{P}}(\xi) = 0 \tag{3.53}$$

with

$$\tilde{\mathbf{P}}(\xi) = \boldsymbol{\Psi}_\infty^{-1} \hat{\mathbf{p}}_e(\xi) \tag{3.54}$$

Here and in the following, $\tilde{\mathbf{P}}(\xi)$ is referred to as the modal pressure vector. For a 2D unbounded domain with N_e nodes on the circular boundary, $j = 1, 2, 3, \cdots, N_e$. Equation (3.53) is a series of N_e independent modal equations,

$$\xi^2 \tilde{P}_{j,\xi\xi} + \xi \tilde{P}_{j,\xi} + (a^2 - \lambda_j^2) \tilde{P}_j = 0 \qquad (j = 1, 2, \cdots, N_e) \tag{3.55}$$

for the components $\tilde{P}_j$ of $\tilde{\mathbf{P}}(\xi)$. In an unbounded domain, the radial flux $\hat{\mathbf{R}}_e(\xi)$ is related to the internal radial flux $\hat{\mathbf{Q}}(\xi)$ as follow,

$$\hat{\mathbf{R}}_e(\xi) = -\hat{\mathbf{Q}}(\xi) \tag{3.56}$$

As before, the subscript 'e' denotes the exterior domain. Substituting Equation (3.46) in Equation (3.56), pre-multiplying by $\mathbf{\Psi}_{\infty}^{T}$ and using Equations (3.52a) and (3.54) yields

$$\tilde{\mathbf{R}}(\xi) = -\xi\tilde{\mathbf{P}}(\xi)_{,\xi} \tag{3.57}$$

with

$$\tilde{\mathbf{R}}(\xi) = \mathbf{\Psi}_{\infty}^{T}\hat{\mathbf{R}}_{e}(\xi) \tag{3.58}$$

Equation (3.57) is a series of scalar equations for the modal flux $\tilde{R}_j$,

$$\tilde{R}_j(\xi) = -\xi\tilde{P}_j(\xi)_{,\xi} \qquad (j = 1, 2, \cdots, N_e). \tag{3.59}$$

The modal flux-pressure relationship is defined as

$$\tilde{R}_j(\xi) = S_j(a)\tilde{P}_j(\xi) \qquad (j = 1, 2, \cdots, N_e), \tag{3.60}$$

where $S_j(a)$ is referred to as the modal impedance coefficient. An equation for $S_j(a)$ is obtained by eliminating $\tilde{R}_j(\xi)$ from Equations (3.59) and (3.60), differentiating the resulting formulation with respect to ξ and substituting in Equation (3.55) (Prempramote et al., 2009; Prempramote, 2011). On the circular boundary ($\xi = 1$), it is expressed as

$$S_j^2(a_0) - a_0 S_j(a_0)_{,a_0} + a_0^2 - \lambda_j^2 = 0, \qquad (j = 1, 2, \cdots, N_e), \tag{3.61}$$

with

$$a_0 = \frac{\omega r_0}{c}. \tag{3.62}$$

Equation (3.61) is solved by expanding $S_j(a_0)$ into continued fractions as outlined in (Prempramote, 2011).

3.3.2 Doubly-asymptotic continued-fraction solution for modal impedance coefficient

Constructing a doubly-asymptotic solution of Equation (3.61) involves two steps: a recursive continued-fraction solution at the high-frequency limit and a recursive continued-fraction solution of the residual equation of the high-frequency expansion at the low-frequency limit. The same strategy has been used in Reference (Prempramote et al., 2009) to construct high-order doubly-asymptotic open boundaries. In (Prempramote, 2011) it was shown that the approach presented in Reference (Prempramote et al., 2009) fails for certain parameters λ_j and an improved derivation containing scaling factors has been proposed.

3.3.2.1 Continued-fraction solution at high frequency

The continued-fraction solution

$$S_j(a_0) = K_\infty + \mathrm{i}a_0 C_\infty - \left(\psi^{(1)}\right)^2 \left(Y^{(1)}(a_0)\right)^{-1} \tag{3.63}$$

is assumed. Here, the coefficients K_∞ and C_∞ correspond to the constant and linear terms of the asymptotic solution, while the third term in Equation (3.63) corresponds to the yet undetermined residual of the high-frequency expansion. $\psi^{(1)}$ is a scaling factor that will subsequently be determined to guarantee the numerical stability of the solution procedure. The superscript '(1)' indicates the first step of a recursive technique. In subsequent steps of this recursive algorithm, the residual $Y^{(i)}$ will be expanded into a constant term, a linear term and a residual term, analogously to Equation (3.63),

$$Y^{(i_H)} = Y_0^{(i_H)} + \mathrm{i}a_0 Y_1^{(i_H)} - \left(\psi^{(i_H+1)}\right)^2 \left(Y^{(i_H+1)}(a_0)\right)^{-1} \tag{3.64}$$

with $i_H = 1, 2, \cdots, M_H$ indicating the steps of recursive iterations and M_H is the order of the continued-fraction solution at high-frequency limit. Equations for C_∞ and K_∞ are obtained by substituting Equation (3.63) in Equation (3.61) and setting

terms in $(\mathrm{i}a_0)^2$ and $\mathrm{i}a_0$, respectively, to zero.

$$C_\infty = 1, \tag{3.65a}$$

$$K_\infty = 0.5. \tag{3.65b}$$

The remaining terms yield an equation for $Y^{(1)}(a_0)$,

$$K_\infty^2 - \lambda_j^2 - 2\left(\mathrm{i}a_0 C_\infty + K_\infty\right)(\psi^{(1)})^2 \left(Y^{(1)}(a_0)\right)^{-1} + (\psi^{(1)})^4 \left(Y^{(1)}(a_0)\right)^{-2} - a_0(\psi^{(1)})^2 \left(Y^{(1)}(a_0)\right)^{-2} \left(Y^{(1)}(a_0)\right)_{,a_0} = 0. \tag{3.66}$$

After multiplication by $\left(Y^{(1)}(a_0)\right)^2 \left(\psi^{(1)}\right)^{-2}$, Equation (3.66) can be formulated as the case $i_H = 1$ of

$$a^{(i_H)} - 2\left(b_0^{(i_H)} + \mathrm{i}a_0\right) Y^{(i_H)}(a_0) + c^{(i_H)} \left(Y^{(i_H)}(a_0)\right)^2 - a_0 \left(Y^{(i_H)}(a_0)\right)_{,a_0} = 0, \tag{3.67}$$

with

$$a^{(1)} = \left(\psi^{(1)}\right)^2 = \left|0.25 - \lambda_j^2\right|, \tag{3.68a}$$

$$b_0^{(1)} = 0.5, \tag{3.68b}$$

$$c^{(1)} = \left(0.25 - \lambda_j^2\right) / \left(\psi^{(1)}\right)^2 = \begin{cases} +1 & \text{when } 0.25 - \lambda_j^2 \geq 0, \\ -1 & \text{when } 0.25 - \lambda_j^2 < 0. \end{cases} . \tag{3.68c}$$

In Equation (3.68a) the factor $\psi^{(1)}$ has been selected to avoid the occurrence of $c^{(1)} = 0$ in Equation (3.68c). To solve Equation (3.67), Equation (3.64) is used. Setting the quadratic term and the linear term in the resulting equation to zero leads to equations for $Y_1^{(i_H)}$

$$Y_1^{(i_H)} = \frac{2}{c^{(i_H)}} = 2 \cdot \mathrm{sgn}^{(i_H)}. \tag{3.69}$$

and $Y_0^{(i_H)}$, respectively.

$$Y_0^{(i_H)} = \frac{2b_0^{(i_H)} + 1}{c^{(i_H)}} = \left(2b_0^{(i_H)} + 1\right) \mathrm{sgn}^{(i_H)}. \tag{3.70}$$

Note that the coefficients $Y_1^{(i_H)}$ and $Y_0^{(i_H)}$ as defined in Equations (3.69) and (3.70), respectively, become singular when the parameter $c^{(i_H)}$ appearing in the denomi-

nators is equal to zero. This situation occurs in the original continued-fraction procedure (Prempramote et al., 2009) when $\lambda_j = k + 0.5$ ($k = 0, 1, 2, \cdots$). If λ_j approaches these values, $Y_1^{(i_H)}$ and $Y_0^{(i_H)}$ tend to infinity and the continued-fraction expansion becomes ill-conditioned. Choosing the factor $\psi^{(i_H)}$ according to Equation (3.68a) guarantees that the coefficients $Y_1^{(i_H)}$ and $Y_0^{(i_H)}$ remain finite, since $c^{(i_H)}$ can only be equal to either $+1$ or -1. This improves the numerical accuracy and stability of the continued-fraction solution.

In subsequent steps of the recursive procedure Equation (3.67) is expressed as

$$a^{(i_H+1)} - 2\left(b_0^{(i_H+1)} + \mathrm{i}a_0\right) Y^{(i_H+1)}(a_0) + c^{(i_H+1)} \left(Y^{(i_H+1)}(a_0)\right)^2 - a_0 \left(Y^{(i_H+1)}(a_0)\right)_{,a_0} = 0, \quad (3.71)$$

with

$$a^{(i_H+1)} = c^{(i_H)} \left(\psi^{(i_H+1)}\right)^2, \quad (3.72a)$$

$$b_0^{(i_H+1)} = b_0^{(i_H)} + 1 = i_H + 0.5, \quad (3.72b)$$

$$c^{(i_H+1)} = \left(a^{(i_H)} + Y_0^{(i_H)}\right) / \left(\psi^{(i_H+1)}\right)^2 = \mathrm{sgn}^{(i_H+1)}. \quad (3.72c)$$

In Equation (3.72c), the factor $\psi^{(i_H+1)}$ is selected as

$$\psi^{(i_H+1)} = \begin{cases} |a^{(i_H)} + Y_0^{(i_H)}|^{1/2}, & \text{when } i_H < M_H, \\ |(2\lambda_j - 1)(a^{(M_H)} + Y_0^{(M_H)})|^{1/2}, & \text{when } i_H = M_H. \end{cases} \quad (3.73)$$

For $i_H < M_H$, the choice of $\psi^{(i_H+1)}$ is analogous to Equation (3.68a). The slightly different choice of $\psi^{(i_H+1)}$ for $i_H = M_H$ will be explained later in the derivation.

Equation (3.71) for $Y^{(i_H+1)}(a_0)$ can be solved using the same steps as for solving Equation (3.67). The continued-fraction solution is thus determined recursively using Equations (3.70) and (3.69). The coefficients $a^{(i_H)}$, $b_0^{(i_H)}$ and $c^{(i_H)}$ are initialized in Equation (3.68) and updated in each step of the recursion using Equation (3.72). After M_H steps of the expansion at the high-frequency limit, the residual satisfies Equation (3.71) with $i_H = M_H$. The modal impedance coefficient

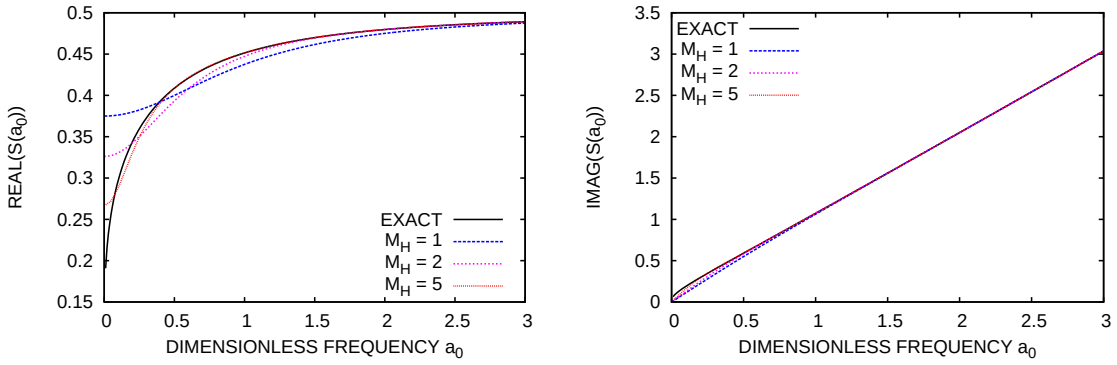

Figure 3.4. High-frequency continued-fraction solution for modal impedance coefficient of circular cavity ($\lambda_j = 0$)

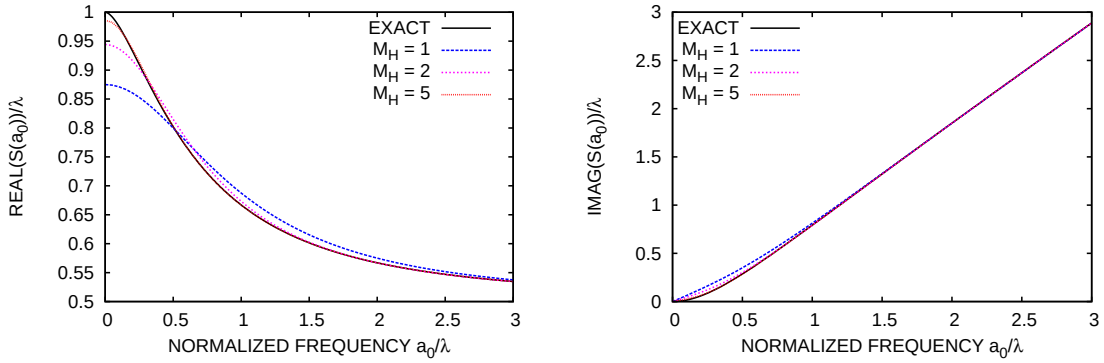

Figure 3.5. High-frequency continued-fraction solution for modal impedance coefficient of circular cavity ($\lambda_j = 1$)

of the mode $\lambda_j = 0$ and the normalized modal impedance coefficients of the modes $\lambda_j = 1, 1.5, 2, 2.5, 5, 30$ are determined using the above recursive procedure and shown in Figures 3.4-3.10, respectively.

Note that the original high-order asymptotic expansion proposed in Reference (Prempramote et al., 2009) fails for $\lambda_j = 1.5, 2.5$. It can be seen that the improved singly-asymptotic expansion converges with increasing M_H over the whole frequency range. Figures 3.4-3.10 also show, however, that the convergence decreases considerably as the modal eigenvalue λ_j increases. This has also been observed in Reference (Prempramote et al., 2009). Obviously, for lower modes up to $\lambda_j = 5$, the singly asymptotic solution of order $M_H = 5$ is highly accurate. For higher modes, and thus for problems with many degrees of freedom, high orders of expansion M_H are

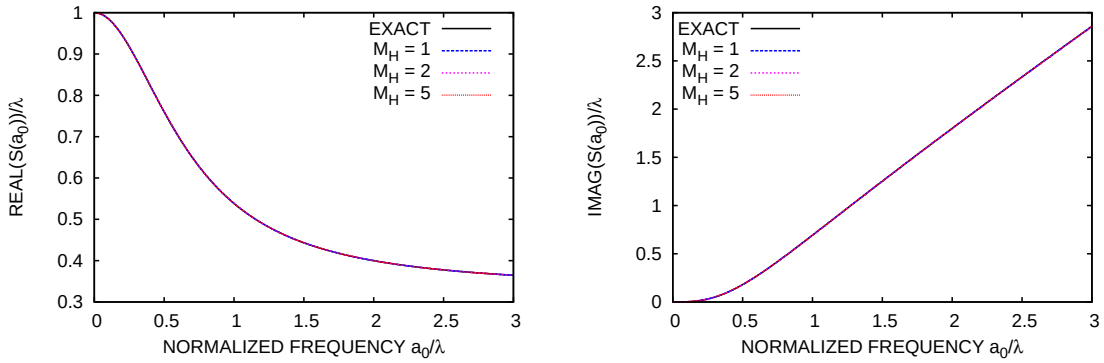

Figure 3.6. High-frequency continued-fraction solution for modal impedance coefficient of circular cavity ($\lambda_j = 1.5$)

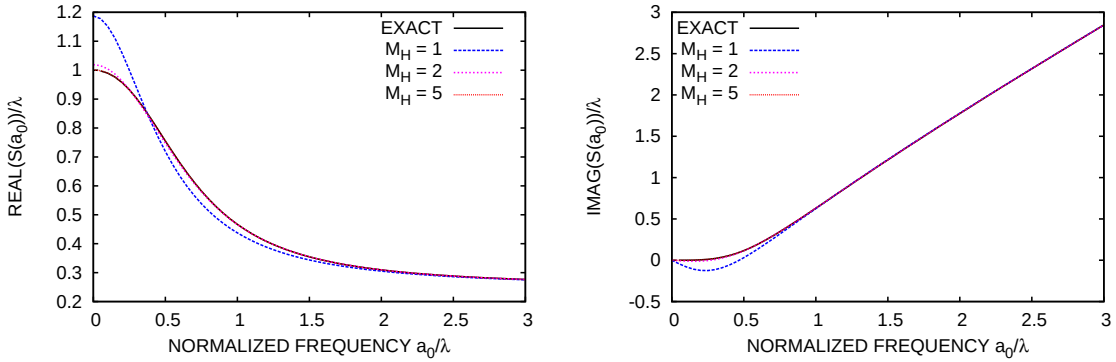

Figure 3.7. High-frequency continued-fraction solution for modal impedance coefficient of circular cavity ($\lambda_j = 2$)

required, if only the high-frequency solution is used. To overcome this problem, a doubly-asymptotic solution, which is exact for $\omega = 0$ is sought in the following for modes $\lambda_j > M_H + 1$. This is achieved by further expanding the residual of the high-frequency solution. For later use in the low-frequency limit, the following identity is derived from Equations (3.72), (3.70) and (3.68).

$$\left(b_0^{(i_H+1)}\right)^2 - a^{(i_H+1)}c^{(i_H+1)} = \left(b_0^{(i_H)} + 1\right)^2 - c^{(i_H)}a^{(i_H)} - c^{(i_H)}Y_0^{(i_H)} = \left(b_0^{(i_H)}\right)^2 - c^{(i_H)}a^{(i_H)} = \lambda_j^2. \quad (3.74)$$

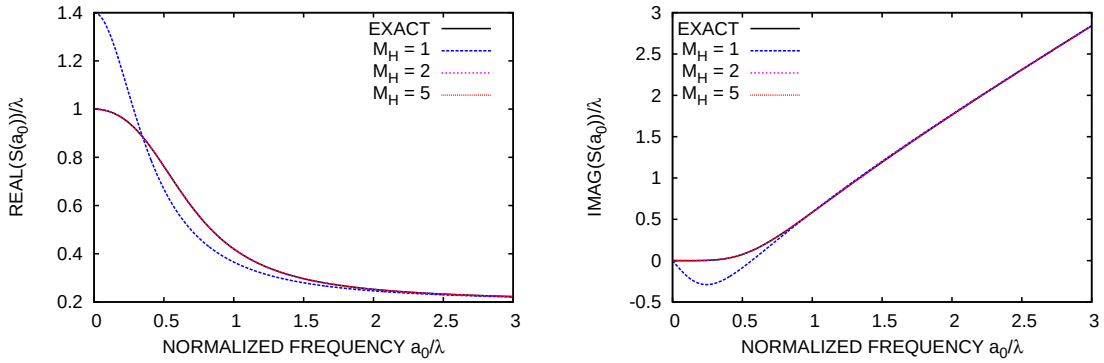

Figure 3.8. High-frequency continued-fraction solution for modal impedance coefficient of circular cavity ($\lambda_j = 2.5$)

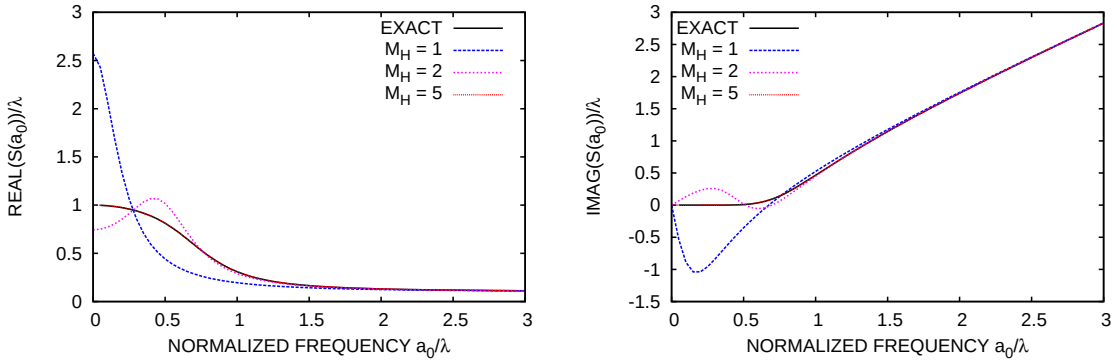

Figure 3.9. High-frequency continued-fraction solution for modal impedance coefficient of circular cavity ($\lambda_j = 5$)

3.3.2.2 Continued-fraction solution at low frequency

The residual of the high-frequency continued-fraction solution is denoted as

$$Y_L(a_0) = Y^{(M_H+1)}(a_0), \tag{3.75}$$

and the residual equation (3.71) is expressed as

$$a_L - 2\left(b_{L0} + \mathrm{i}a_0\right) Y_L(a_0) + c_L \left(Y_L(a_0)\right)^2 - a_0 \left(Y_L(a_0)\right)_{,a_0} = 0, \tag{3.76}$$

with

$$a_L = a^{(M_H+1)} = c^{(M_H)} \left(\psi_L^{(0)}\right)^2, \tag{3.77a}$$

$$b_{L0} = b_0^{(M_H+1)} = M_H + 0.5, \tag{3.77b}$$

$$c_L = c^{(M_H+1)} = \left(a^{(M_H)} + Y_0^{(M_H)}\right) / \left(\psi_L^{(0)}\right)^2 = \mathrm{sgn}_L^{(0)} / |2\lambda_j - 1|, \tag{3.77c}$$

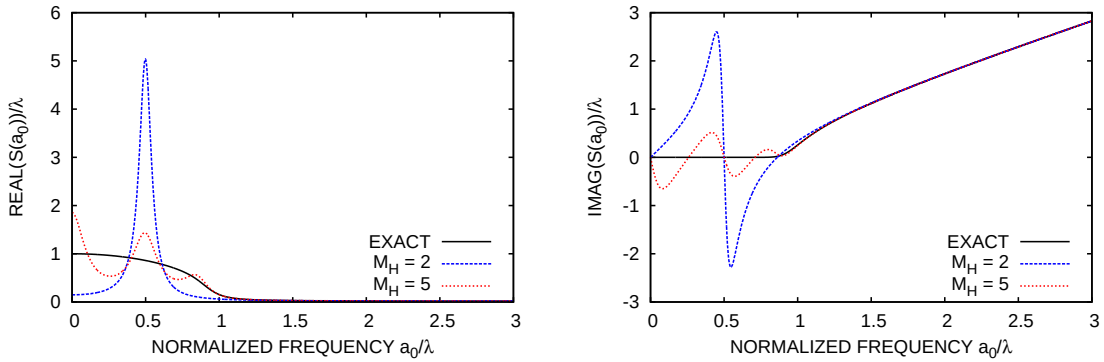

Figure 3.10. High-frequency continued-fraction solution for modal impedance coefficient of circular cavity ($\lambda_j = 30$)

where

$$\psi_L^{(0)} = \psi^{(M_H+1)}, \tag{3.78a}$$

$$\mathrm{sgn}_L^{(0)} = \mathrm{sgn}^{(M_H+1)}. \tag{3.78b}$$

The continued-fraction solution (3.79) is assumed at the low-frequency limit,

$$Y_L(a_0) = Y_{L0}^{(0)} + \mathrm{i}a_0 Y_{L1}^{(0)} - (\mathrm{i}a_0)^2 \left(Y_L^{(1)}(a_0)\right)^{-1} \tag{3.79a}$$

$$Y_L^{(i_L)}(a_0) = Y_{L0}^{(i_L)} + \mathrm{i}a_0 Y_{L1}^{(i_L)} - (\mathrm{i}a_0)^2 \left(Y_L^{(i_L+1)}(a_0)\right)^{-1} \tag{3.79b}$$

with $i_L = 1, 2, \cdots, M_L$ in Equation (3.79b) indicating the steps of recursive iterations and M_L is the order of the continued-fraction solution at low frequency limit. Note that Equation (3.79) approaches a constant value for $\omega \to 0$. The coefficients $Y_{L0}^{(i_L)}$, $Y_{L1}^{(i_L)}$ are determined recursively, analogously to the high-frequency expansion. Substituting Equation (3.79) into Equation (3.76) leads to a power series in terms of $\mathrm{i}a_0$, which is satisfied by setting individual terms corresponding to different powers of $\mathrm{i}a_0$ equal to zero in ascending order. The constant term yields

$$a_L - 2b_{L0} Y_{L0}^{(0)} + c_L \left(Y_{L0}^{(0)}\right)^2 = 0. \tag{3.80}$$

The two solutions of this quadratic equation are

$$Y_{L0}^{(0)} = \frac{1}{c_L}\left(b_{L0} \pm \sqrt{b_{L0}^2 - c_L a_L}\right) \tag{3.81}$$

Using Equation (3.74), the coefficient $Y_{L0}^{(0)}$ is determined as

$$Y_{L0}^{(0)} = (b_{L0} + \lambda_j) / c_L = (b_{L0} + \lambda_j) |2\lambda_j - 1| / \mathrm{sgn}_L^{(0)}. \tag{3.82}$$

Setting the linear term in $\mathrm{i}a_0$ to zero leads to the solution for $Y_{L1}^{(0)}$,

$$Y_{L1}^{(0)} = 2Y_{L0}^{(0)} / (2\lambda_j - 1). \tag{3.83}$$

Note that $Y_{L1}^{(0)}$ in Equation (3.83) becomes infinite if $\lambda_j = 0.5$. In order to avoid this, the factor $|2\lambda_j - 1|$ has been included in the definition of the coefficient $\psi^{(M_H+1)}$ in Equation (3.73). Using Equation (3.82), $Y_{L1}^{(0)}$ is expressed as

$$Y_{L1}^{(0)} = 2 (b_{L0} + \lambda_j) / \left(\mathrm{sgn}_L^{(0)} \mathrm{sgn}_{L0}^{(0)} \right), \tag{3.84}$$

with

$$\mathrm{sgn}_{L0}^{(0)} = \begin{cases} +1, & \text{when } 2\lambda_j - 1 \geq 0, \\ -1, & \text{when } 2\lambda_j - 1 < 0. \end{cases} \tag{3.85}$$

The remaining terms result in an equation for $Y_L^{(1)}$, which is expressed as the $i_L = 1$ case of

$$(\mathrm{i}a_0)^2 a_L^{(i_L)} - 2 \left(b_{L0}^{(i_L)} + \mathrm{i}a_0 b_{L1}^{(i_L)} \right) Y_L^{(i_L)}(a_0) + c_L^{(i_L)} \left(Y_L^{(i_L)}(a_0) \right)^2 - a_0 \left(Y_L^{(i_L)}(a_0) \right)_{,a_0} = 0, \tag{3.86}$$

with

$$a_L^{(1)} = c_L, \tag{3.87a}$$

$$b_{L0}^{(1)} = -1 - b_{L0} + c_L Y_{L0}^{(0)} = -1 + \lambda_j, \tag{3.87b}$$

$$b_{L1}^{(1)} = -1 + c_L Y_{L1}^{(0)} = 2(M_H + 1)/(2\lambda_j - 1), \tag{3.87c}$$

$$c_L^{(1)} = -2Y_{L1}^{(0)} + c_L \left(Y_{L1}^{(0)} \right)^2. \tag{3.87d}$$

Equation (3.86) is solved using the same strategy as for solving Equation (3.67). The recursive equation of the low-frequency limit (3.79b) is substituted into Equation (3.86). The resulting formulation is a power series of $\mathrm{i}a_0$, which is satisfied by

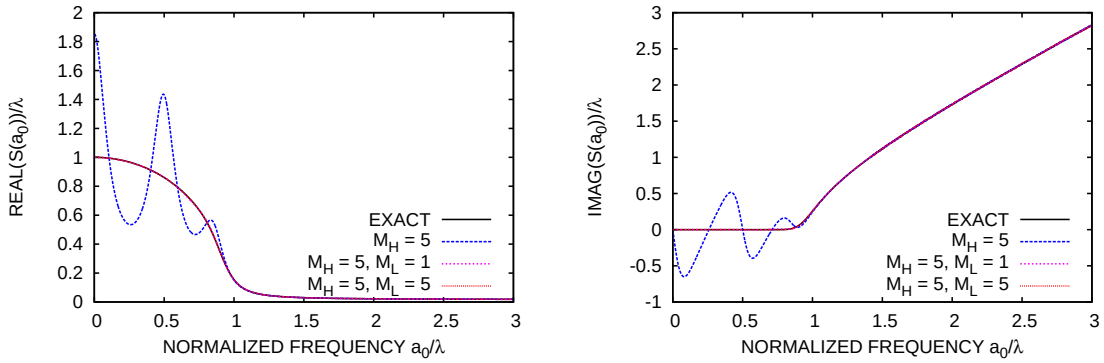

Figure 3.11. Doubly-asymptotic continued-fraction solution for modal impedance coefficient of circular cavity ($\lambda_j = 30$)

setting individual terms equal to zero. The constant term yields

$$Y_{L0}^{(i_L)} = 2b_{L0}^{(i_L)}/c_L^{(i_L)}. \tag{3.88}$$

Setting the linear term in $\mathrm{i}a_0$ to zero and using Equation (3.88) results in the solution for $Y_{L1}^{(i_L)}$,

$$Y_{L1}^{(i_L)} = 2b_{L1}^{(i_L)}Y_{L0}^{(i_L)}/(2b_{L0}^{(i_L)} - 1). \tag{3.89}$$

Setting the remaining terms equal to zero yields the residual equation

$$(\mathrm{i}a_0)^2 a_L^{(i_L+1)} - 2\left(b_{L0}^{(i_L+1)} + \mathrm{i}a_0 b_{L1}^{(i_L+1)}\right) Y_L^{(i_L+1)}(a_0) + c_L^{(i_L+1)}(Y_L^{(i_L+1)}(a_0))^2 - a_0(Y_L^{(i_L+1)}(a_0))_{,a_0} = 0, \tag{3.90}$$

with

$$a_L^{(i_L+1)} = c_L^{(i_L)}, \tag{3.91a}$$

$$b_{L0}^{(i_L+1)} = c_L^{(i_L)}Y_{L0}^{(i_L)} - b_{L0}^{(i_L)} - 1 = b_{L0}^{(i_L)} - 1, \tag{3.91b}$$

$$b_{L1}^{(i_L+1)} = c_L^{(i_L)}Y_{L1}^{(i_L)} - b_{L1}^{(i_L)}, \tag{3.91c}$$

$$c_L^{(i_L+1)} = a_L^{(i_L)} - 2b_{L1}^{(i_L)}Y_{L1}^{(i_L)} + c_L^{(i_L)}(Y_{L1}^{(i_L)})^2. \tag{3.91d}$$

Equation (3.90) for $Y_L^{(i_L+1)}$ is solved analogously to Equation (3.86) for $Y_L^{(i_L)}$. The continued-fraction solution at low frequency is thus evaluated using Equations (3.88) and (3.89), where the recursive constants are initialized using Equation (3.87)

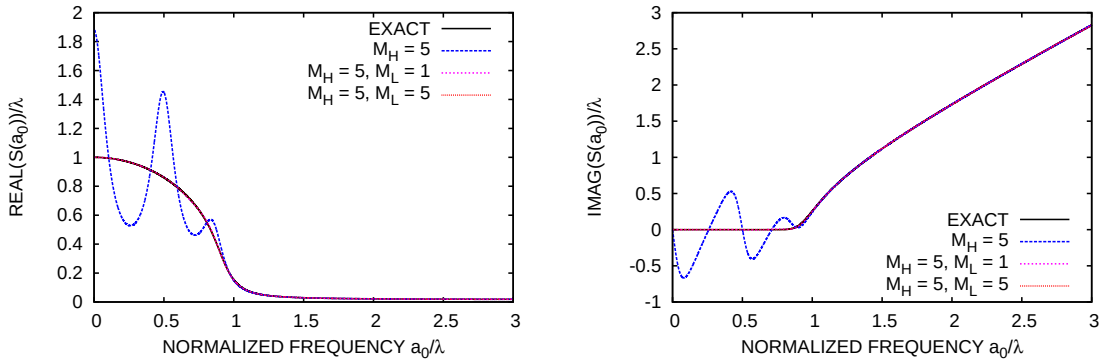

Figure 3.12. Doubly-asymptotic continued-fraction solution for modal impedance coefficient of circular cavity ($\lambda_j = 30.5$)

and updated using Equation (3.91). The expansion terminates with the assumption that the residual term $(\mathrm{i}a_0)^2/Y_L^{(M_L+1)}(a_0)$ is zero. The final doubly-asymptotic continued-fraction solution of Equation (3.61) is obtained by combining the high-frequency continued-fraction solution in Equations (3.63) and (3.64) with the low-frequency continued-fraction solution in Equation (3.79) using $Y^{(M_H+1)}(a_0) = Y_L(a_0)$. It is expressed as :

$$S_j(a_0) = K_\infty + \mathrm{i}a_0 C_\infty - \cfrac{\left(\psi^{(1)}\right)^2}{Y_0^{(1)} + \mathrm{i}a_0 Y_1^{(1)} - \cfrac{\left(\psi^{(2)}\right)^2}{\cdots - \cfrac{\left(\psi^{(M_H)}\right)^2}{Y_0^{(M_H)} + \mathrm{i}a_0 Y_1^{(M_H)} - \cfrac{\left(\psi_L^{(0)}\right)^2}{Y_{L0}^{(0)} + \mathrm{i}a_0 Y_{L1}^{(0)} \cfrac{(\mathrm{i}a_0)^2}{Y_{L0}^{(1)} + \mathrm{i}a_0 Y_{L1}^{(1)} - \cfrac{(\mathrm{i}a_0)^2}{\cdots - \cfrac{(\mathrm{i}a_0)^2}{Y_{L0}^{(M_L)} + \mathrm{i}a_0 Y_{L1}^{(M_L)}}}}}}} \tag{3.92}$$

Figures 3.11 - 3.13 show the normalized impedance coefficients for $\lambda_j = 30$, 30.5 and 200, respectively. The agreement of the doubly-asymptotic approximations of order $M_H = 5$, $M_L = 5$ with the exact solutions is excellent, even for high-order modes. Moreover, for relatively low λ_j, there is actually no need to use high values of the order of continued-fraction expansion at low frequency M_L. Only two terms ($M_L = 1$) can provide very accurate solutions for modal impedance coefficients of intermediate order. For high-order modes λ_j, more terms of continued-fraction at low frequency are required. The singly-asymptotic expansions of order $M_H = 5$ are

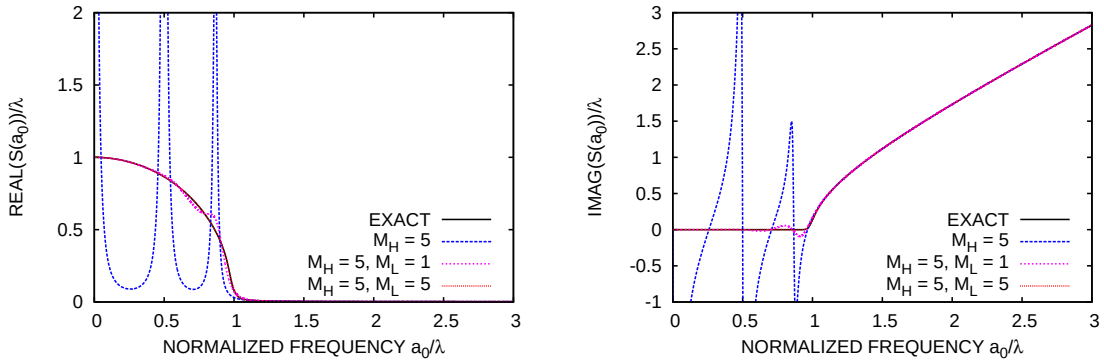

Figure 3.13. Doubly-asymptotic continued-fraction solution for modal impedance coefficient of circular cavity ($\lambda_j = 200$)

also shown for comparison. It can be clearly seen that the high-order expansions oscillate in the low frequency range for high λ_j. Based on these observations the following procedure will be used:

- choose orders M_H and M_L of continued-fraction expansion,
- approximate all modes corresponding to $\lambda_j \leq M_H + 1$ by singly-asymptotic expansions of order M_H,
- approximate all modes corresponding to $\lambda_j > M_H + 1$ by doubly-asymptotic expansions of orders M_H, M_L.

3.3.3 Time-domain formulation for 2D exterior acoustics

The procedure of transforming the continued-fraction expansion into the time domain is based on the technique described in Reference (Prempramote et al., 2009; Prempramote, 2011). It begins with the modal flux-pressure relationship in the frequency domain as expressed in Equation (3.60). Substituting the first equation of the continued-fraction solution at the high-frequency limit (3.63) in Equation (3.60) yields,

$$\tilde{R}_j = S_j(a_0)\tilde{P}_j = K_\infty \tilde{P}_j + \mathrm{i}a_0 C_\infty \tilde{P}_j - \left(\psi_j^{(i)}\right)^2 (Y_j^{(1)}(a_0))^{-1}\tilde{P}_j. \tag{3.93}$$

Equations (3.65a) and (3.65b) are substituted in Equation (3.93). Furthermore, the first auxiliary variable $\tilde{P}_j^{(1)}$ is introduced, which leads to

$$\tilde{R}_j = 0.5\tilde{P}_j + \mathrm{i}a_0\tilde{P}_j - \psi_j^{(1)}\tilde{P}_j^{(1)}, \tag{3.94}$$

with

$$\psi_j^{(1)}\tilde{P}_j = Y_j^{(1)}(a_0)\tilde{P}_j^{(1)}. \tag{3.95}$$

Using Equations (3.58) and (3.94), the amplitude of the nodal flux vector is

$$\hat{\mathbf{R}}_e = 0.5\boldsymbol{\Psi}_\infty^{-T}\tilde{\mathbf{P}} + \mathrm{i}a_0\boldsymbol{\Psi}_\infty^{-T}\tilde{\mathbf{P}} - \boldsymbol{\Psi}_\infty^{-T}\boldsymbol{\psi}^{(1)}\tilde{\mathbf{p}}^{(1)}. \tag{3.96}$$

$\boldsymbol{\psi}^{(1)}$ is diagonal matrices with diagonal terms equal to continued-fraction coefficients $\psi_j^{(1)}$ for all modes.

Using $\tilde{\mathbf{P}} = \boldsymbol{\Psi}_\infty^{-1}\hat{\mathbf{p}}_e$ and $\mathbf{E}_0^a = \boldsymbol{\Psi}_\infty^{-T}\boldsymbol{\Psi}_\infty^{-1}$, Equation (3.96) is re-formulated in terms of the nodal pressure vector $\hat{\mathbf{p}}_e$,

$$\hat{\mathbf{R}}_e = 0.5\mathbf{E}_0^a\hat{\mathbf{p}}_e + \mathrm{i}a_0\mathbf{E}_0^a\hat{\mathbf{p}}_e - \boldsymbol{\Psi}_\infty^{-T}\boldsymbol{\psi}^{(1)}\tilde{\mathbf{p}}^{(1)}, \tag{3.97}$$

where $\hat{\mathbf{p}}_e$ and $\hat{\mathbf{R}}_e$ denote $\hat{\mathbf{p}}_e(\xi = 1)$ and $\hat{\mathbf{R}}_e(\xi = 1)$, respectively. Substituting Equation (3.64) in Equation (3.95) yields

$$\psi_j^{(1)}\tilde{P}_j = Y_{0,j}^{(1)}\tilde{P}_j^{(1)} + \mathrm{i}a_0 Y_{1,j}^{(1)}\tilde{P}_j^{(1)} - \psi_j^{(2)}\tilde{P}_j^{(2)}, \tag{3.98}$$

where the second auxiliary variable $\tilde{P}_j^{(2)}$ is defined as the $i_H = 1$ case of

$$\psi_j^{(i_H+1)}\tilde{P}_j^{(i_H)} = Y_j^{(i_H+1)}(a_0)\tilde{P}_j^{(i_H+1)}. \tag{3.99}$$

Equation (3.98) is formulated for all modes j. Using $\tilde{\mathbf{P}} = \boldsymbol{\Psi}_\infty^{-1}\hat{\mathbf{p}}_e$ yields

$$\boldsymbol{\psi}^{(1)}\boldsymbol{\Psi}_\infty^{-1}\hat{\mathbf{p}}_e = \mathbf{Y}_0^{(1)}\tilde{\mathbf{p}}^{(1)} + \mathrm{i}a_0\mathbf{Y}_1^{(1)}\tilde{\mathbf{p}}^{(1)} - \boldsymbol{\psi}^{(2)}\tilde{\mathbf{p}}^{(2)}. \tag{3.100}$$

$\mathbf{Y}_0^{(1)}$, $\mathbf{Y}_1^{(1)}$ and $\boldsymbol{\psi}^{(2)}$ are all diagonal matrices with diagonal terms equal to continued-fraction coefficients $Y_{0,j}^{(1)}$, $Y_{1,j}^{(1)}$ and $\psi_j^{(2)}$ for all modes separately. Substituting the remaining terms of the continued-fraction solution (3.64) in Equation

(3.99) results in

$$\psi_j^{(i_H)}\tilde{P}_j^{(i_H-1)} = Y_{0,j}^{(i_H)}\tilde{P}_j^{(i_H)} + \mathrm{i}a_0 Y_{1,j}^{(i_H)}\tilde{P}_j^{(i_H)} - \psi_j^{(i_H+1)}\tilde{P}_j^{(i_H+1)}. \tag{3.101}$$

For modes corresponding to $\lambda_j \leq M_H + 1$, the continued-fraction expansion terminates with Equation (3.101). For higher modes, however, the residual term of an order M_H high-frequency continued-fraction solution defined in Equation (3.99) with $i_H = M_H$ is the initial term of the low-frequency continued-fraction solution. It is expressed as

$$\psi_j^{(M_H+1)}\tilde{P}_j^{(M_H)} = Y_j^{(M_H+1)}(a_0)\tilde{P}_j^{(M_H+1)} = Y_{L,j}(a_0)\tilde{P}_{L,j}^{(0)}, \quad (j = N_H+1, \cdots, N_e) \tag{3.102}$$

with the auxiliary variable $\tilde{P}_{L,j}^{(0)} = \tilde{P}_j^{(M_H+1)}$. In Equation (3.102), N_H corresponds to the number of modes approximated by high-order expansions only with $\lambda_j \leq M_H+1$ and N_e is the total number of nodes on the circular boundary. Equations (3.78a) and (3.79a) are substituted in Equation (3.102),

$$\psi_{L,j}^{(0)}\tilde{P}_j^{(M_H)} = Y_{L0,j}^{(0)}\tilde{P}_{L,j}^{(0)} + \mathrm{i}a_0 Y_{L1,j}^{(0)}\tilde{P}_{L,j}^{(0)} - \mathrm{i}a_0\tilde{P}_{L,j}^{(1)}, \quad (j = N_H+1, \cdots, N_e). \tag{3.103}$$

In Equation (3.103), the auxiliary variable $\tilde{P}_{L,j}^{(1)}$ is defined as the $i_L = 1$ case of

$$\mathrm{i}a_0\tilde{P}_{L,j}^{(i_L-1)} = Y_{L,j}^{(i_L)}(a_0)\tilde{P}_{L,j}^{(i_L)}, \quad (j = N_H+1, \cdots, N_e). \tag{3.104}$$

Substituting Equation (3.79b) in Equation (3.104) yields

$$\mathrm{i}a_0\tilde{P}_{L,j}^{(i_L-1)} = Y_{L0,j}^{(i_L)}\tilde{P}_{L,j}^{(i_L)} + \mathrm{i}a_0 Y_{L1,j}^{(i_L)}\tilde{P}_{L,j}^{(i_L)} - \mathrm{i}a_0\tilde{P}_{L,j}^{(i_L+1)}, \quad (j = N_H+1, \cdots, N_e). \tag{3.105}$$

For a low-frequency continued-fraction expansion of order M_L, $\tilde{P}_{L,j}^{(M_L+1)} = 0$ is assumed. Equations (3.97), (3.100), (3.101), (3.103) and (3.105) are assembled in a system of linear equations,

$$\left(\mathbf{K}_e^a + \mathrm{i}\omega\mathbf{C}_e^a\right)\hat{\mathbf{z}} = \hat{\mathbf{r}}. \tag{3.106}$$

The vector of unknowns $\hat{\mathbf{z}}$ contains the nodal pressure amplitudes at the circular boundary and auxiliary variables,

$$\hat{\mathbf{z}} = \left\{ \begin{array}{ccccccccc} \hat{\mathbf{p}}_e & \tilde{\mathbf{p}}^{(1)} & \cdots & \tilde{\mathbf{p}}^{(M_H)} & \tilde{\mathbf{p}}_L^{(0)} & \tilde{\mathbf{p}}_L^{(1)} & \cdots & \tilde{\mathbf{p}}_L^{(M_L)} \end{array} \right\}^T . \tag{3.107}$$

Note that the auxiliary variables $\tilde{\mathbf{p}}^{(1)}$ to $\tilde{\mathbf{p}}^{(M_H)}$ are of size N_e, whereas the auxiliary variables $\tilde{\mathbf{p}}_L^{(0)}$ to $\tilde{\mathbf{p}}_L^{(M_L)}$ are of size $N_e - N_H$. The right-hand side vector $\hat{\mathbf{r}}$ contains the nodal flux amplitude applied on the circular boundary,

$$\hat{\mathbf{r}} = \left\{ \begin{array}{ccccccccc} \hat{\mathbf{R}}_e & 0 & \cdots & 0 & 0 & 0 & \cdots & 0 \end{array} \right\}^T \tag{3.108}$$

The symbols $\mathbf{K}_e^a$ and $\mathbf{C}_e^a$ in Equation (3.106) refer to the banded and symmetric high-order stiffness and damping matrices of the unbounded medium, respectively.

$$\mathbf{K}_e^a = \begin{bmatrix} 0.5\mathbf{E}_0^a & -\boldsymbol{\Psi}_\infty^{-T}\boldsymbol{\psi}^{(1)} & & & & & & \\ -\boldsymbol{\psi}^{(1)}\boldsymbol{\Psi}_\infty^{-1} & \mathbf{Y}_0^{(1)} & -\boldsymbol{\psi}^{(2)} & & & & & \\ & -\boldsymbol{\psi}^{(2)} & \ddots & \ddots & & & & \\ & & \ddots & \mathbf{Y}_0^{(M_H)} & -\boldsymbol{\psi}_L^* & & & \\ & & & -[\boldsymbol{\psi}_L^*]^T & \mathbf{Y}_{L0}^{(0)} & 0 & & \\ & & & & 0 & \mathbf{Y}_{L0}^{(1)} & \ddots & \\ & & & & & \ddots & \ddots & 0 \\ & & & & & & 0 & \mathbf{Y}_{L0}^{(M_L)} \end{bmatrix} \tag{3.109}$$

$$\mathbf{C}_e^a = \frac{r_0}{c}\begin{bmatrix} \mathbf{E}_0^a & 0 & & & & & & \\ 0 & \mathbf{Y}_1^{(1)} & 0 & & & & & \\ & 0 & \ddots & \ddots & & & & \\ & & \ddots & \mathbf{Y}_1^{(M_H)} & 0 & & & \\ & & & 0 & \mathbf{Y}_{L1}^{(0)} & -\mathbf{I} & & \\ & & & & -\mathbf{I} & \mathbf{Y}_{L1}^{(1)} & \ddots & \\ & & & & & \ddots & \ddots & -\mathbf{I} \\ & & & & & & -\mathbf{I} & \mathbf{Y}_{L1}^{(M_L)} \end{bmatrix} \tag{3.110}$$

where $\boldsymbol{\psi}^{(i_H)}$ are diagonal matrices and $\boldsymbol{\psi}_L^*$ is a rectangular matrix with N_e rows and $N_e - N_H$ columns defined as:

$$\boldsymbol{\psi}_L^* = \begin{bmatrix} \mathbf{0} \\ \boldsymbol{\psi}_L^{(0)} \end{bmatrix} \tag{3.111}$$

The matrix $\boldsymbol{\psi}_L^{(0)}$ in the lower partition in Equation(3.111) is also a diagonal matrix with diagonal terms $\psi_{L,j}^{(0)}$ for all modes with $\lambda_j > M_H + 1$ in 2D and therefore has the same size of $\mathbf{Y}_{L0}^{(i_L)}$. Equation (3.106) represents the high-order doubly-asymptotic open boundary condition in the frequency domain. In the time domain, it corresponds to a system of first-order differential equations,

$$\mathbf{K}_e^a \mathbf{z}(t) + \mathbf{C}_e^a \dot{\mathbf{z}}(t) = \mathbf{r}_e(t) \tag{3.112}$$

with the time-dependent vector of unknowns $\mathbf{z}(t)$ expressed as:

$$\mathbf{z}(t) = \begin{Bmatrix} \mathbf{p}_e(t) & \tilde{\mathbf{p}}^{(1)}(t) & \cdots & \tilde{\mathbf{p}}^{(M_H)}(t) & \tilde{\mathbf{p}}_L^{(0)}(t) & \tilde{\mathbf{p}}_L^{(1)}(t) & \cdots & \tilde{\mathbf{p}}_L^{(M_L)}(t) \end{Bmatrix}^T \tag{3.113}$$

The right-hand-side of Equation(3.112) $\mathbf{r}_e(t)$ includes any nodal flux $\mathbf{R}_e(t)$ applied on the circular boundary and written as,

$$\mathbf{r}_e(t) = \begin{Bmatrix} \mathbf{R}_e(t) & 0 & \cdots & 0 & 0 & 0 & \cdots & 0 \end{Bmatrix}^T \tag{3.114}$$

Equation (3.112) is a temporally local formulation of size $N_e \times (M_H + 1) + (N_e -$

$N_H) \times (M_L + 1)$ that can be coupled to the high-order equations of motion of the near field (3.37) straightforwardly. This is addressed in the following Section 3.4.

3.4 Coupling of bounded and unbounded domain models

In order to facilitate the coupling of Equations (3.37) and (3.112), that represent the bounded and unbounded domain respectively, the equations of motion of the near field are re-written as

$$\left[\begin{array}{cc|c} \mathbf{M}_{bb} & \mathbf{M}_{be} & \\ \mathbf{M}_{be}^T & \mathbf{M}_{ee} & * \\ \hline * & & \mathbf{M}_{ii} \end{array}\right] \left\{\begin{array}{c} \ddot{\mathbf{p}}_b(t) \\ \ddot{\mathbf{p}}_e(t) \\ \hline \ddot{\mathbf{p}}_i(t) \end{array}\right\} + \left[\begin{array}{cc|c} \mathbf{K}_{bb} & \mathbf{K}_{be} & \\ \mathbf{K}_{be}^T & \mathbf{K}_{ee} & 0 \\ \hline 0 & & \mathbf{K}_{ii} \end{array}\right] \left\{\begin{array}{c} \mathbf{p}_b(t) \\ \mathbf{p}_e(t) \\ \hline \mathbf{p}_i(t) \end{array}\right\}$$
$$= \left\{\begin{array}{c} \mathbf{R}_b^{ext}(t) \\ \mathbf{R}_e^{ext}(t) \\ \hline 0 \end{array}\right\} - \left\{\begin{array}{c} 0 \\ \mathbf{R}_e(t) \\ \hline 0 \end{array}\right\} \quad (3.115)$$

In Equation (3.115), the subscripts 'e' and 'b' refer to the nodes on the circular boundary and in the interior of the bounded domain, respectively, whereas the subscript 'i' refers to all auxiliary variables $\mathbf{p}^{(1)}(t)$ to $\mathbf{p}^{(M)}(t)$ of the bounded domain. Note that the right-hand side vector $\mathbf{r}(t)$ in Equation (3.37) has been split into two contributions. The terms $\mathbf{R}_b^{ext}(t)$ are due to any external sources acting on the bounded domain, whereas the term $\mathbf{R}_e(t)$ corresponds to the prescribed normal derivative of the pressure at the circular near field / far field boundary. This term is defined in the first block row of the system of first-order differential equations (3.112) to represent the exterior domain. Substituting the first block row of Equation (3.112) in Equation (3.115) leads to a global system of second-order differential equations in the time domain with global mass, damping and stiffness matrices,

$$\mathbf{M}_G^a \ddot{\mathbf{z}}_G(t) + \mathbf{C}_G^a \dot{\mathbf{z}}_G(t) + \mathbf{K}_G^a \mathbf{z}_G(t) = \mathbf{r}_G(t) \quad (3.116)$$

The global vector of unknowns $\mathbf{z}_G(t)$ contains the acoustic pressure $\mathbf{p}(t)$ at all nodes of the coupled model, the internal variables of the bounded domain $\mathbf{p}^{(i)}(t)$ in Equation (3.39) and the auxiliary variables of the exterior domain $\tilde{\mathbf{p}}^{(i_H)}(t)$ and $\tilde{\mathbf{p}}_L^{(i_L)}(t)$ from Equation (3.113),

$$\mathbf{z}_G(t) = \left\{ \mathbf{p}(t) \,\middle|\, \mathbf{p}^{(1)}(t) \;\cdots\; \mathbf{p}^{(M)}(t) \,\middle|\, \tilde{\mathbf{p}}^{(1)}(t) \;\cdots\; \tilde{\mathbf{p}}^{(M_H)}(t) \;\; \tilde{\mathbf{p}}_L^{(0)}(t) \;\cdots\; \tilde{\mathbf{p}}_L^{(M_L)}(t) \right\}^T \tag{3.117}$$

The total number of unknowns is $(M+1) \times N + M_H \times N_e + (M_L+1) \times (N_e - N_H)$, where N and N_e denote the total number of nodes and the number of nodes on the circular boundary, respectively. The global right-hand side vector $\mathbf{r}_G(t)$ in Equation (3.116) contains the nodal flux $\mathbf{R}^{ext}(t)$ due to any source in the bounded domain,

$$\mathbf{r}_G(t) = \left\{ \mathbf{R}^{ext}(t) \,\middle|\, 0 \;\cdots\; 0 \,\middle|\, 0 \;\cdots\; 0 \;\; 0 \cdots \;\; 0 \right\}^T \tag{3.118}$$

The global mass, damping and stiffness matrix in Equation (3.116) contains all the coefficient matrices from both bounded and unbounded acoustic domains in Equations (3.37) and (3.112). They are also partitioned in the same way as for the global vector of unknowns $\mathbf{z}_G(t)$ and global flux vector $\mathbf{r}_G(t)$ and listed below,

$$\mathbf{M}_G^a = \left[\begin{array}{c|ccc|c} \mathbf{M}_a & -\mathbf{X}_a^{(1)} & 0 & \cdots & 0 & 0 \\ \hline -\left[\mathbf{X}_a^{(1)}\right]^T & \mathbf{S}_{a1}^{(1)} & -\mathbf{X}_a^{(2)} & \cdots & 0 & 0 \\ 0 & -\left[\mathbf{X}_a^{(2)}\right]^T & \mathbf{S}_{a1}^{(2)} & \ddots & 0 & 0 \\ \vdots & \vdots & \ddots & \ddots & -\mathbf{X}_a^{(M)} & \vdots \\ 0 & 0 & 0 & -\left[\mathbf{X}_a^{(M)}\right]^T & \mathbf{S}_{a1}^{(M)} & 0 \\ \hline 0 & 0 & 0 & \cdots & 0 & 0 \end{array}\right] \tag{3.119}$$

$$\mathbf{C}_G^a = \frac{r_0}{c}\left[\begin{array}{cc|c|cccccccc} 0 & 0 & & & & & & & & \\ 0 & \mathbf{E}_0^a & 0 & & & & 0 & & & \\ \hline & 0 & 0 & & & & 0 & & & \\ \hline & & & \mathbf{Y}_1^{(1)} & 0 & & & & & \\ & & & 0 & \ddots & \ddots & & & & \\ & & & & \ddots & \mathbf{Y}_1^{(M_H)} & 0 & & & \\ & 0 & 0 & & & 0 & \mathbf{Y}_{L1}^{(0)} & -\mathbf{I} & \ddots & \\ & & & & & & -\mathbf{I} & \mathbf{Y}_{L1}^{(1)} & & \\ & & & & & & & \ddots & \ddots & -\mathbf{I} \\ & & & & & & & & -\mathbf{I} & \mathbf{Y}_{L1}^{(M_L)} \end{array}\right] \tag{3.120}$$

$$
\mathbf{K}_G^a = \left[\begin{array}{cc|ccc|ccccccc}
\mathbf{K}_{bb} & \mathbf{K}_{be} & 0 & \cdots & 0 & 0 & \cdots & 0 & 0 & 0 & \cdots & 0 \\
\mathbf{K}_{be}^T & \mathbf{K}_{ee}+0.5\mathbf{E}_0^a & 0 & \cdots & 0 & -\boldsymbol{\Psi}_\infty^{-T}\boldsymbol{\psi}^{(1)} & \cdots & 0 & 0 & 0 & \cdots & 0 \\
\hline
0 & 0 & \mathbf{S}_{a0}^{(1)} & \cdots & 0 & 0 & \cdots & 0 & 0 & 0 & \cdots & 0 \\
\vdots & \vdots & \vdots & \ddots & \vdots & \vdots & \ddots & \vdots & \vdots & \vdots & \ddots & \vdots \\
0 & 0 & 0 & \cdots & \mathbf{S}_{a0}^{(M)} & 0 & \cdots & 0 & 0 & 0 & \cdots & 0 \\
\hline
0 & -\boldsymbol{\psi}^{(1)}\boldsymbol{\Psi}_\infty^{-1} & 0 & \cdots & 0 & \mathbf{Y}_0^{(1)} & -\boldsymbol{\psi}^{(2)} & & & & & \\
\vdots & \vdots & \vdots & \ddots & \vdots & -\boldsymbol{\psi}^{(2)} & \ddots & \ddots & & & & \\
0 & 0 & 0 & \cdots & 0 & & \ddots & \mathbf{Y}_0^{(M_H)} & -\boldsymbol{\psi}_L^* & & & \\
0 & 0 & 0 & \cdots & 0 & & & -\left[\boldsymbol{\psi}_L^*\right]^T & \mathbf{Y}_{L0}^{(0)} & 0 & & \\
0 & 0 & 0 & \cdots & 0 & & & & 0 & \mathbf{Y}_{L0}^{(1)} & \ddots & \\
\vdots & \vdots & \vdots & \ddots & \vdots & & & & & \ddots & \ddots & 0 \\
0 & 0 & 0 & \cdots & 0 & & & & & & 0 & \mathbf{Y}_{L0}^{(M_L)}
\end{array}\right] \tag{3.121}
$$

Note that Equation (3.116) represents the coupled acoustic system in the time domain. The global mass matrix $\mathbf{M}_G^a$ is a result of the bounded domain only, whereas the global damping matrix $\mathbf{C}_G^a$ is entirely due to the unbounded domain. The global stiffness matrix $\mathbf{K}_G^a$ contains contributions from both near and far field. $\mathbf{M}_G^a$, $\mathbf{C}_G^a$ and $\mathbf{K}_G^a$ are symmetric and sparse. The coupled system of equations (3.116) can be solved for arbitrary time-variations of the source $\mathbf{r}_G(t)$ using standard time stepping algorithms, such as Newmark's method.

3.5 Numerical examples

In this section, five numerical examples are studied to demonstrate the accuracy, robustness and efficiency of the proposed method. In examples 3.5.1, 3.5.2, 3.5.4, and 3.5.5, the non-viscous fluid is assumed to have a sound velocity c and density ρ. In Section 3.5.1, a circular cavity embedded in a full plane is considered. Accuracy and efficiency of the proposed method are presented and compared with results obtained using the singly-asymptotic open boundary proposed in (Birk et al., 2012). Then, Section 3.5.2 presents an infinite wedge with circular arc subjected to a long-time flux to examine the performance of the present method for $\lambda = i + 0.5$ (i is a non-negative integer) and long-time excitation. Next, Section 3.5.3 addresses the out-of-plane wave propagation in a non-uniform half-plane with piecewise constant shear modulus G and mass density ρ to demonstrate the applicability of the coupled SBFEM model. In Section 3.5.4, a coupled system with elliptical cavity partially subjected to a flux with relatively high frequency is addressed to test the capacity of the present doubly-asymptotic open boundary in the high-frequency range. In the last example in Section 3.5.5, the wave radiation from a more complicated open structure is investigated to demonstrate the robustness of the proposed approach. Newmark's method with $\alpha = 0.5$ and $\beta = 0.25$ (average acceleration scheme) is applied to Equation (3.116) for all time-domain analyses. To provide reference

solutions, all numerical examples are modeled by the commercial software ANSYS using an extended mesh of finite elements. The boundary of each finite element model is sufficiently far away from the investigated bounded domain to avoid wave reflections.

3.5.1 Circular cavity subject to transient flux on entire boundary

A circular cavity of radius r_0 is modeled as a coupled system consisting of a ring of bounded domains and an unbounded subdomain (the open boundary). The radius of the open boundary is $r_1 = 2r_0$. The geometry of this model is illustrated in Figure 3.14. It is subject to a transient flux on the entire circular boundary Γ which is given as

$$\frac{\partial \bar{p}}{\partial \vec{\mathbf{n}}}(\theta, t) = h(\theta) f(t). \tag{3.122}$$

In Equation (3.122), $h(\theta)$ and $f(t)$ are functions of angle θ and time t describing the spatial and temporal variation of the prescribed flux, respectively. The flux varies spatially as a cosine function,

$$h(\theta) = \cos(m\theta), \tag{3.123}$$

where the factor m is selected as $m = 25$ in the following time-domain example. The time history $f(t)$ is plotted in Figure 3.15 as non-dimensional flux $f(t)/F_t$ (F_t is the maximum value of function $f(t)$) as a function of the dimensionless time tc/r_0.

Based on Figure 3.15(b), the maximum dimensionless frequency of interest is estimated at $a_{0,max} = 30$. In order to proceed with the time-domain analysis, the order of continued-fraction M in the bounded domain must be selected. A guideline for the choice of this parameter has been given in Reference (Song, 2009). According to (Song, 2009), 3 to 4 terms per wavelength are required. The wavelength λ of the sound pressure wave propagating outwards is related to the frequency content of the

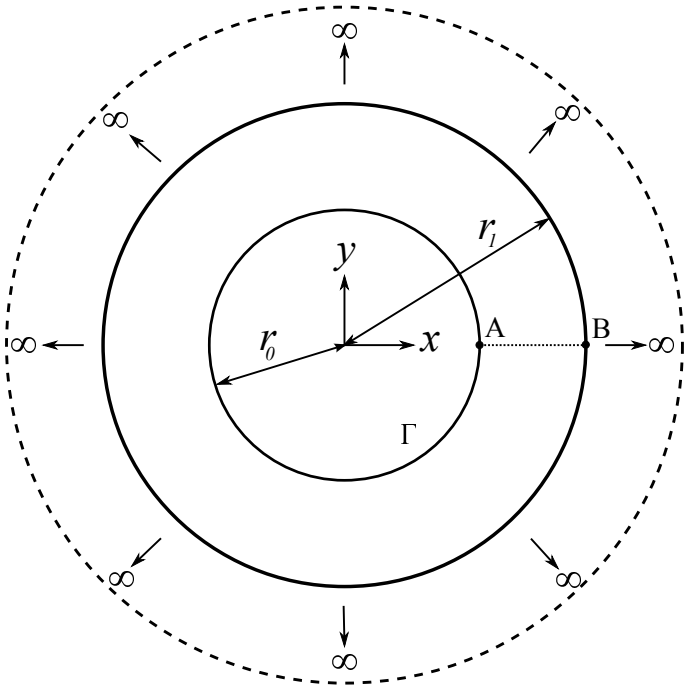

Figure 3.14. Geometry of circular cavity model

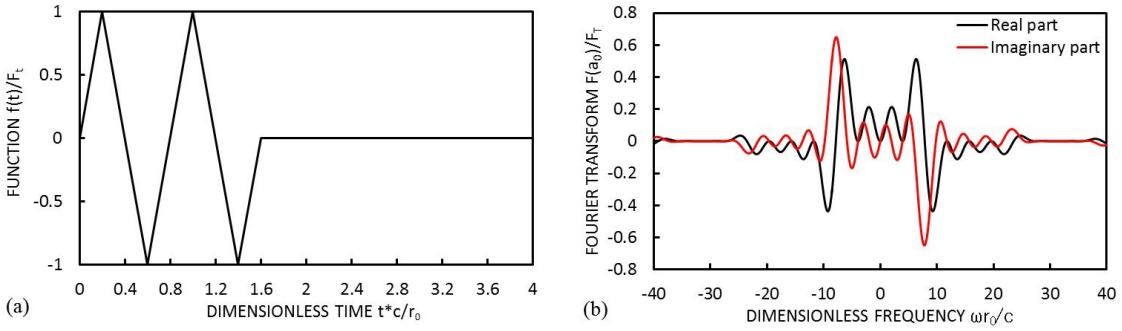

Figure 3.15. Time variation $f(t)$ of transient flux applied to entire circular boundary: (a) time history and (b) Fourier transform

prescribed flux as:

$$\lambda = \frac{2\pi}{a_0} r_0. \tag{3.124}$$

Therefore, the shortest wavelength is calculated as $\lambda_{min} = \frac{2\pi}{30} r_0 \approx 0.21 r_0$. In order to be able to use relatively small values of M, the total bounded domain is divided into 64 subdomains evenly in the circumferential direction and into 8 layers in the radial direction as illustrated in Figure 3.16(a). The scaling centre of the unbounded domain coincides with the origin of the Cartesian coordinate system. The scaling

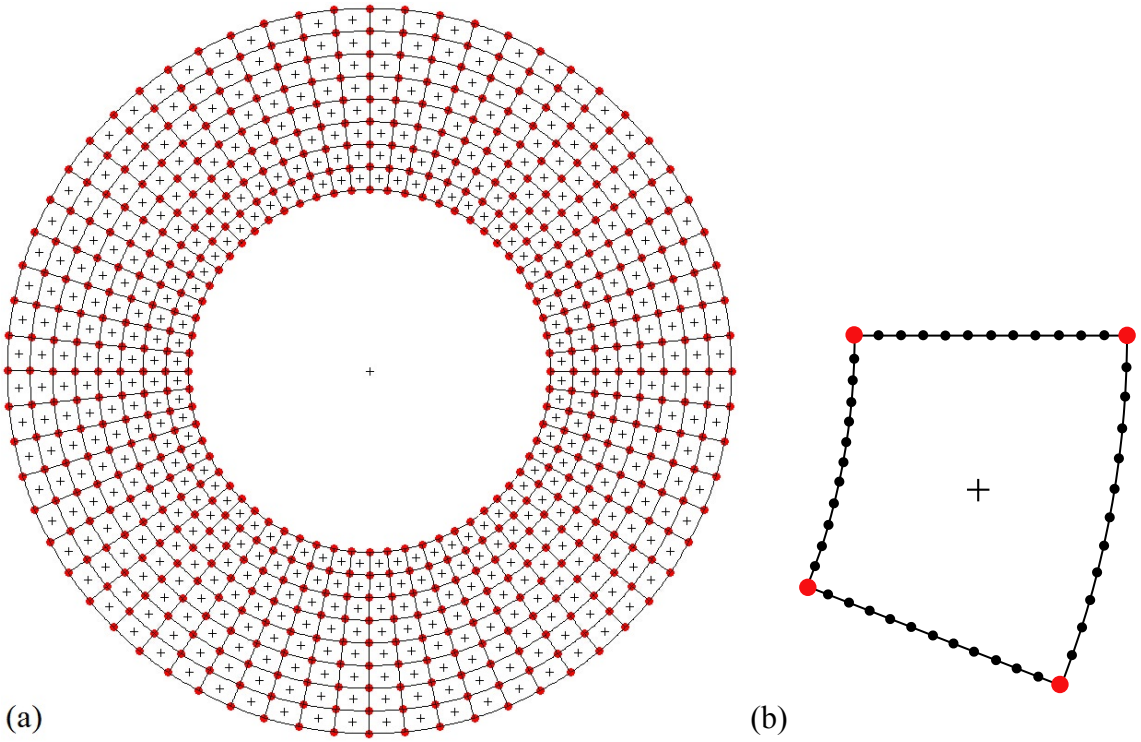

Figure 3.16. The coupled SBFE circular cavity model (a) mesh of near field and far field (b) mesh of one subdomain

centres of all $64 \times 8 = 512$ bounded subdomains are located at the respective centres of gravity of these subdomains and marked by $'+'$. The keypoints defining the individual subdomains are shown as red solid dots. To guarantee the accuracy of the results, six 3-node elements are used on each curved or straight edge of a subdomain, which gives about 13 nodes per shortest wavelength. It should be noticed that the nodes of the scaled boundary finite elements are not shown in Figure 3.16(a) for clarity. One arbitrary subdomain with all nodes shown is illustrated in Figure 3.16(b) as an example. The maximum radial distance in each subdomain is $d_{max} \approx 0.11 r_0$. Therefore, the order of continued-fraction expansion is chosen as $M = \frac{d_{max}}{\lambda_{min}} \times 4 \approx 2$ for all bounded subdomains.

The resulting pressure due to the applied flux is calculated by applying Newmark's method to Equation (3.116). A constant time step is set to $\Delta t = 0.01 r_0/c$ for accuracy as it gives about 21 time steps per period at the highest frequency of interest. The pressure response at point A in Figure 3.14 is illustrated in Figure 3.17,

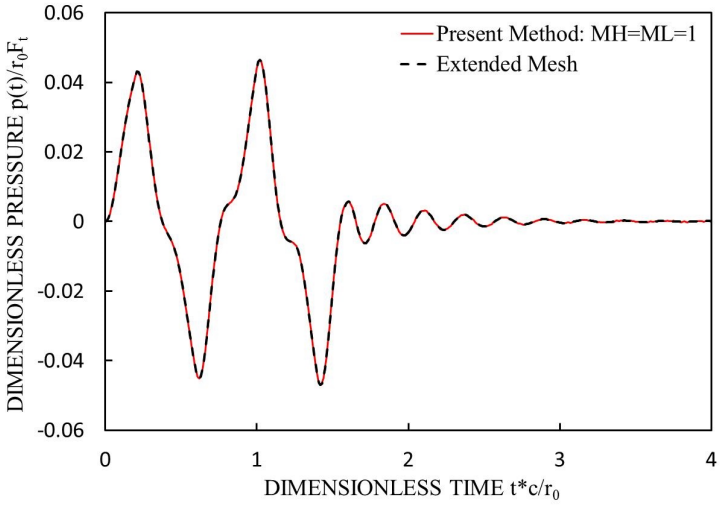

Figure 3.17. Dimensionless pressure response at point A of circular cavity

where the vertical axis is non-dimensionalized by r_0F_t and the horizontal axis represents the dimensionless time tc/r_0. The orders of high-frequency and low-frequency continued-fraction expansions of the open boundary are chosen as $M_H = M_L = 1$. A converged reference solution calculated using an extended mesh finite element model in ANSYS is plotted with a dashed line for comparison. The outer radius of this extended mesh is set to be $3.5r_0$ in order to prevent wave reflections. In Figure 3.17, the difference between the results of the present SBFEM approach and the reference solution is hardly appreciable. The accuracy of the proposed coupled SBFEM model is thus proven to be very high for transient flux on the entire cavity boundary. In addition, the pressure variations along the radial line AB shown in Figure 3.14 at the dimensionless times $t\frac{c}{r_0} = 0.9$ and 1.5 are plotted in Figure 3.18 and compared with the reference solution. The vertical axis is again non-dimensionalized by r_0F_t and the horizontal axis represents the distance to the centroid of the circular cavity. Very good agreement is observed in these two figures. The corresponding non-dimensionalized pressure contour plots calculated by using the proposed method on the mesh shown in Figure 3.16 and ANSYS are also shown in Figures 3.19 and 3.20 respectively, for illustration.

The proposed doubly-asymptotic open boundary can be placed very close to the

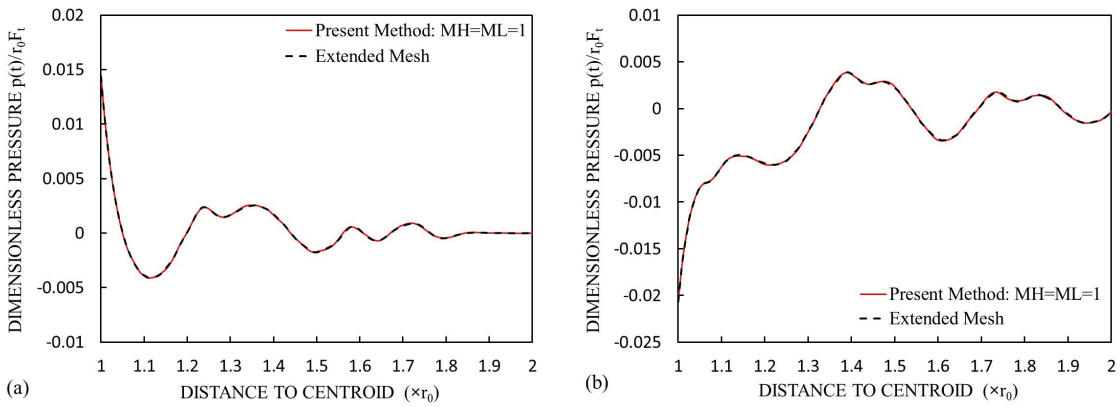

Figure 3.18. Pressure variation along line AB: (a) at $t\frac{c}{r_0} = 0.9$ and (b) at $t\frac{c}{r_0} = 1.5$

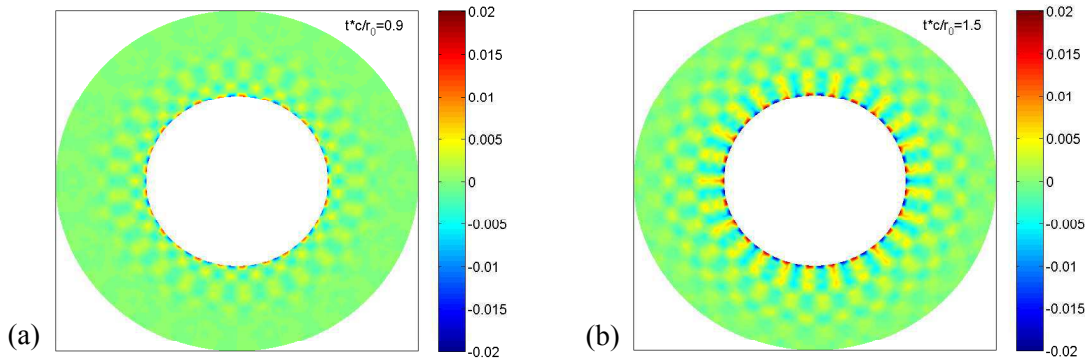

Figure 3.19. Circular cavity subject to transient flux (Eq. (3.122)) on entire boundary. Pressure contour obtained using the proposed method at: (a) $t\frac{c}{r_0} = 0.9$ and (b) $t\frac{c}{r_0} = 1.5$

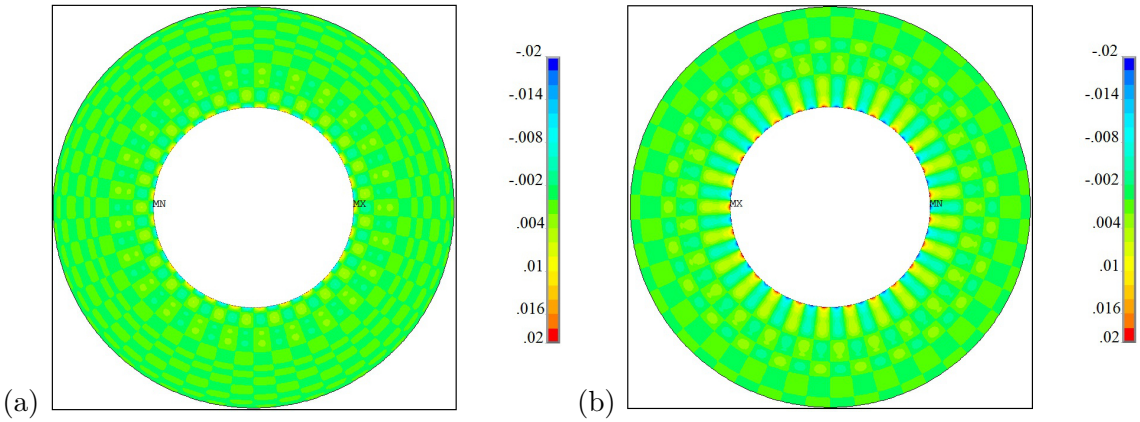

Figure 3.20. Circular cavity subject to transient flux (Eq. (3.122)) on entire boundary. Pressure contour obtained using ANSYS at: (a) $t\frac{c}{r_0} = 0.9$ and (b) $t\frac{c}{r_0} = 1.5$

radiator and accurate results can be obtained by using higher orders of expansion. This is demonstrated in the following. The previously developed singly-asymptotic open boundary (Birk et al., 2012) is also used here for comparison. The same circular cavity with radius r_0 is again subjected to the same transient flux described in Equations (3.122) and (3.123) with $m = 25$. Both singly-asymptotic and doubly-asymptotic open boundaries are used in this model. This time, the radius of the open boundary r_1 is chosen to be a slightly extreme value of $r_1 = 1.01r_0$ (which is about 1/20 of the shortest wavelength away from the circular cavity). The bounded ring is divided into 64 subdomains in the circumferential direction as shown in Figure 3.21(a) (mesh size in Figure 3.21 is not to scale for illustration). Three 3-node elements are used on each circumferential line and one 3-node element on each radial line (see 3.21(b)) to yield at least 15 nodes per minimum wavelength. According to Reference (Song, 2009), the degree of continued-fraction expansion M in the bounded domain is set to $M = 2$ as the maximum radial distance for each subdomain now is $d_{max} \approx 0.1r_0$ and the minimum wavelength is still $\lambda = \lambda_{min} \approx 0.21r_0$. The time step for Newmark's method is still $\Delta t = 0.01r_0/c$. The resulting pressure variation at point A in Figure 3.14 is shown in Figure 3.22 with the reference solution obtained from the extended mesh model described earlier. It should be noticed that M_H in Figure 3.22 represents the order of the high-frequency continued-fraction term in the doubly-asymptotic open boundary or the order of continued fraction in the singly-asymptotic open boundary.

From Figure 3.22, it can be seen that the doubly-asymptotic open boundary can achieve higher accuracy than the singly-asymptotic open boundary with less computational effort. For example, the present doubly-asymptotic open boundary with $M_H = M_L = 1$ leads to a high-order stiffness matrix $\mathbf{K}_e^a$ and to a damping matrix $\mathbf{C}_e^a$ of the unbounded domain of the same size as the previous singly-asymptotic open boundary with $M_H = 3$, however, the result calculated by the present method is much more accurate than the result calculated by the previous method. Moreo-

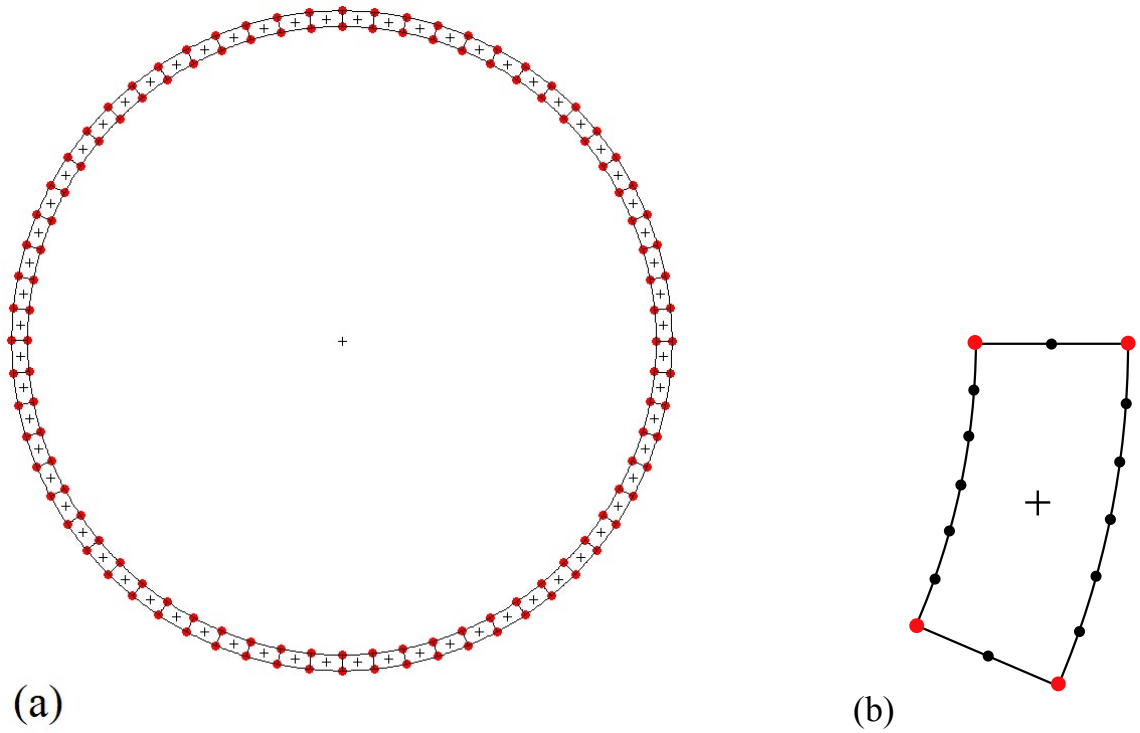

Figure 3.21. The coupled SBFE circular cavity model with $r_1 = 1.01r_0$ (a) mesh of near field and far field (b) mesh of one subdomain

ver, the agreement between the pressure response calculated by the present method with $M_H = M_L = 1$ and the reference solution is similar to the agreement between the reference solution and the results calculated using the singly-asymptotic open boundary with $M_H = 7$, which leads to more than twice the computational effort.

The accuracy of this doubly asymptotic open boundary can still be improved by increasing the number of M_H or M_L as shown in Figure 3.23. It can be seen that the present method with $M_H = M_L = 2$ matches the reference solution very well even with the open boundary located merely about 1/20 of the minimum wavelength away from the cavity.

3.5.2 Semi-infinite wedge with circular arc cavity

In order to demonstrate the capability of the present doubly-asymptotic open boundary to handle eigenvalues λ equal to $i + 0.5$ (where i is an arbitrary non-negative integer), a semi-infinite wedge with circular arc cavity and an opening angle of 120° is

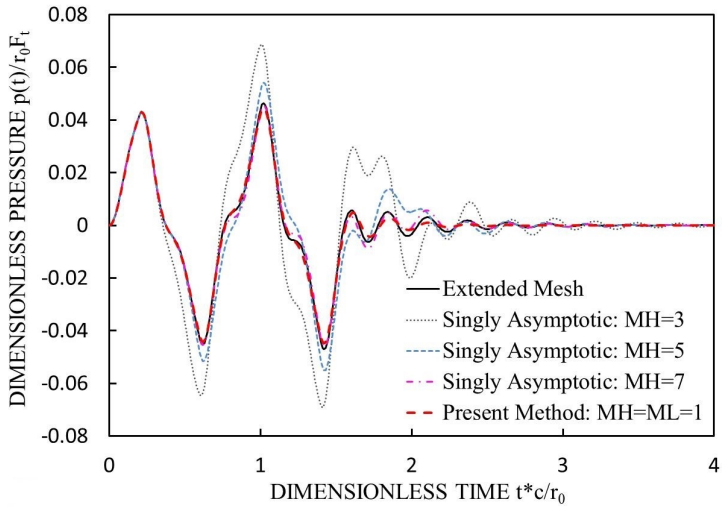

Figure 3.22. Dimensionless pressure response at point A of circular cavity due to transient flux on entire boundary: Comparison of time-domain solutions calculated by singly-asymptotic and doubly-asymptotic open boundary

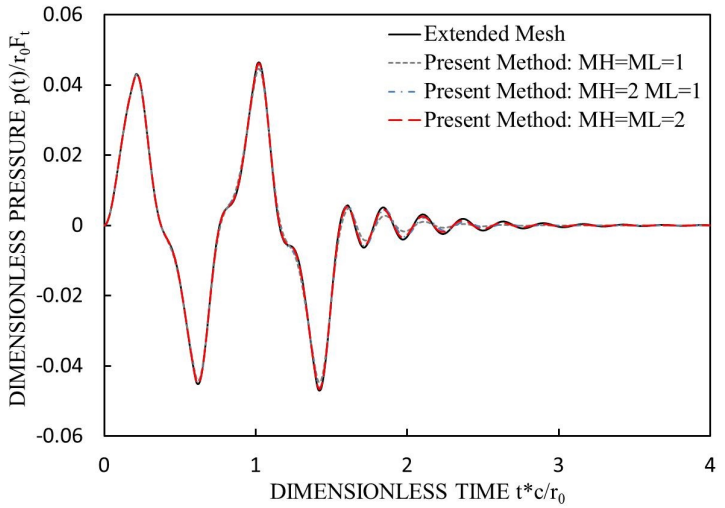

Figure 3.23. Dimensionless pressure response at point A of circular cavity due to transient flux on entire boundary: Results obtained using doubly-asymptotic open boundaries of various orders for $r_1 = 1.01r_0$

addressed in this example. The geometrical details are illustrated in Figure 3.24(a). The radius of the circular arc cavity is $r_1 = \frac{r_0}{2}$ and the doubly-asymptotic boundary is located at r_0. Additionally, a long-time flux is used in this example to investigate the long-time pressure response at certain points during $t = 0$ to $t = 30\frac{r_0}{c}$. The flux is assumed to be zero on the two side faces, i.e.:

$$\frac{\partial \bar{p}}{\partial \vec{\mathbf{n}}}(\theta = 0, t) = \frac{\partial \bar{p}}{\partial \vec{\mathbf{n}}}(\theta = \frac{2\pi}{3}, t) = 0, \tag{3.125}$$

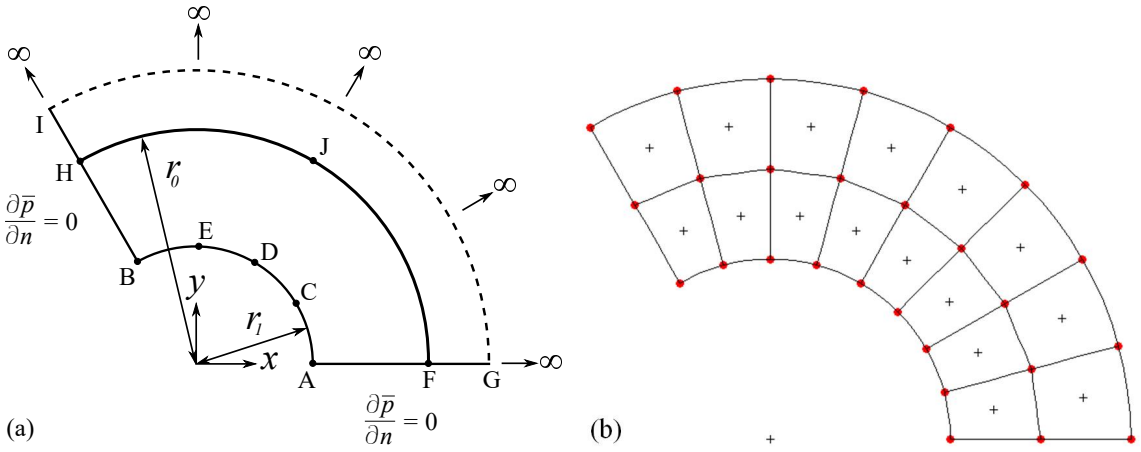

Figure 3.24. Semi-infinite wedge with circular arc cavity: (a) geometry, (b) mesh

where θ is the angle measured anti-clockwise from the positive x-axis.

An equation for the modal impedance coefficient of the semi-infinite wedge with a circular arc boundary and homogeneous boundary conditions on the side faces can be derived using the method of separation of variables. For details, the reader is referred to Reference (Song, 2009), Section 3.1. There, it is shown that the corresponding eigenvalues λ can be expressed as,

$$\lambda_j = \frac{\pi}{\alpha} j \qquad (j = 0, 1, 2, \cdots, n), \tag{3.126}$$

where, α is the opening angle of the wedge. Thus, the eigenvalues in the present example are: $\lambda = 0, 1.5, 3, \cdots, 1.5n$. Note that the previous doubly-asymptotic open boundary proposed in Reference (Prempramote et al., 2009) cannot handle this example as singularities will occur in the continued-fraction expansions for all modes with $\lambda = i + 0.5$. The flux applied on the circular arc $\widehat{AB}$ is defined by the following Equations (3.127) and (3.128),

$$\frac{\partial \bar{p}}{\partial \vec{\mathbf{n}}}(\theta, t) = h_w(\theta) f_w(t), \tag{3.127}$$

with

$$h_w(\theta) = \begin{cases} 1 & \text{when } \frac{\pi}{6} \leq \theta \leq \frac{\pi}{2} \\ 0 & \text{otherwise.} \end{cases} \tag{3.128}$$

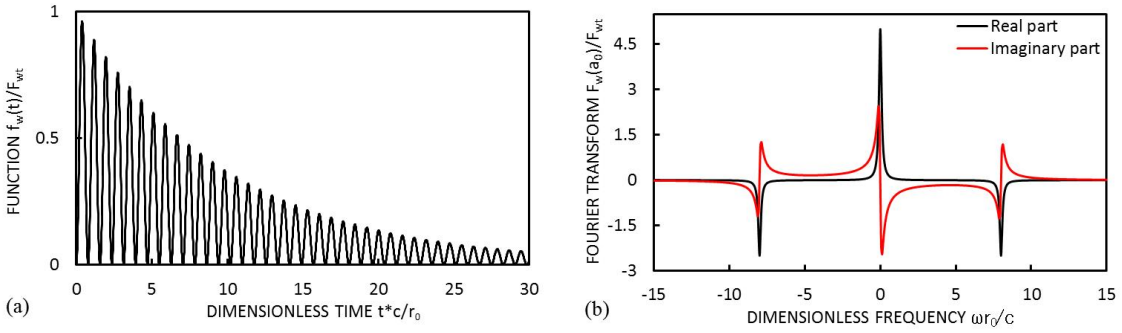

Figure 3.25. Time variation $f_w(t)$ of transient flux applied on circular arc: (a) time history and (b) Fourier transform

In other words, the flux is applied only on arc $\widehat{CDE}$ in Figure 3.24(a). The time-dependent function $f_w(t)$ is defined as

$$f_w(t) = F_{wt} \times \sin^2(4\frac{1}{\mathrm{s}}t) \cdot e^{-0.1\frac{1}{\mathrm{s}}t}, \tag{3.129}$$

and plotted in Figure 3.25(a) with its Fourier transform in Figure 3.25(b). Here, the applied flux $f_w(t)$ is non-dimensionalized by the peak value F_{wt} and the time t is also non-dimensionalized by r_0/c.

The SBFEM mesh is shown in Figure 3.24(b). The scaling centre of the unbounded subdomain is placed at the origin of the Cartesian coordinate system, and the scaling centres of the other $8 \times 2 = 16$ bounded subdomains are located at the respective centres of gravity. All red small solid dots mark keypoints of individual subdomains. The nodes of individual elements are not shown in Figure 3.24(b) for clarity.

According to Figure 3.25(b), the maximum dimensionless frequency of interest in this numerical example is estimated at $a_{0,max} = 10$. Therefore, the shortest wavelength can be calculated from Equation (3.124) as $\lambda_{min} = r_0\frac{2\pi}{10} \approx 0.63r_0$. A sufficient number of nodes are used on each curved or straight line. Generally, two 3-node elements are used on each edge of individual subdomains, which yields approximately 11 nodes per wavelength. The same guideline of selecting the order of continued-fraction expansion M of the bounded domain as in Section 3.5.1 is applied. In Figure 3.24(b), the maximum radial distance in each subdomain is $d_{max} \approx 0.18r_0$.

Thus, the order of continued-fraction expansion is selected as $M = \frac{d_{max}}{\lambda_{min}} \times 4 \approx 1$.

A long-duration time-domain solution of this problem is calculated by Newmark's method with a constant time step of $\Delta t = 0.03 r_0/c$ to demonstrate the accuracy and robustness of the proposed method. This selected value for Δt provides about 21 time steps per period at the highest frequency of interest. The pressure variations at the mid-points of the circular arc cavity and the open boundary (points D and J in Figure 3.24(a)) are illustrated in Figures 3.26(a) and 3.26(b), respectively, for the first $30\frac{r_0}{c}$ seconds. During this period, any 'fictitious reflections' would be reflected 60 times between the circular arc cavity $\widehat{AB}$ and the open boundary $\widehat{FH}$. Any errors during this time integration would also be accumulated. The vertical axes in Figure 3.26 are non-dimensionalized by $r_0 F_{wt}$ and the horizontal axes represent the dimensionless time tc/r_0.

In order to verify the accuracy of the coupled SBFEM model, an extended finite element mesh of an semi-infinite wedge with an opening angle of $\frac{2\pi}{3}$ is again built in ANSYS, where the outer circular boundary is located at $r = 16 r_0$ in order to avoid wave reflections. The converged pressure responses from the extended mesh model at points D and J are also plotted in Figures 3.26(a) and (b) as a reference solution. Different combinations of M_H and M_L have been studied, i.e. solutions obtained with continued-fraction expansions of order '$M_H = M_L = 1$', '$M_H = 3, M_L = 1$', '$M_H = 6, M_L = 1$' and '$M_H = 9, M_L = 1$' are presented in Figure 3.26.

Figure 3.26 shows that all results obtained using the proposed doubly-asymptotic open boundary agree very well with the reference solution during the first $5\frac{r_0}{c}$ seconds. After this, the results obtained with the doubly-asymptotic open boundary with '$M_H = M_L = 1$' differ significantly form the extended mesh solutions. However, by increasing the high-frequency continued-fraction term M_H, the results obtained using the doubly-asymptotic open boundary are approaching the extended mesh results. For both points D and J, the doubly-asymptotic open boundary with continued-fraction expansions of order '$M_H = 6, M_L = 1$' provides results

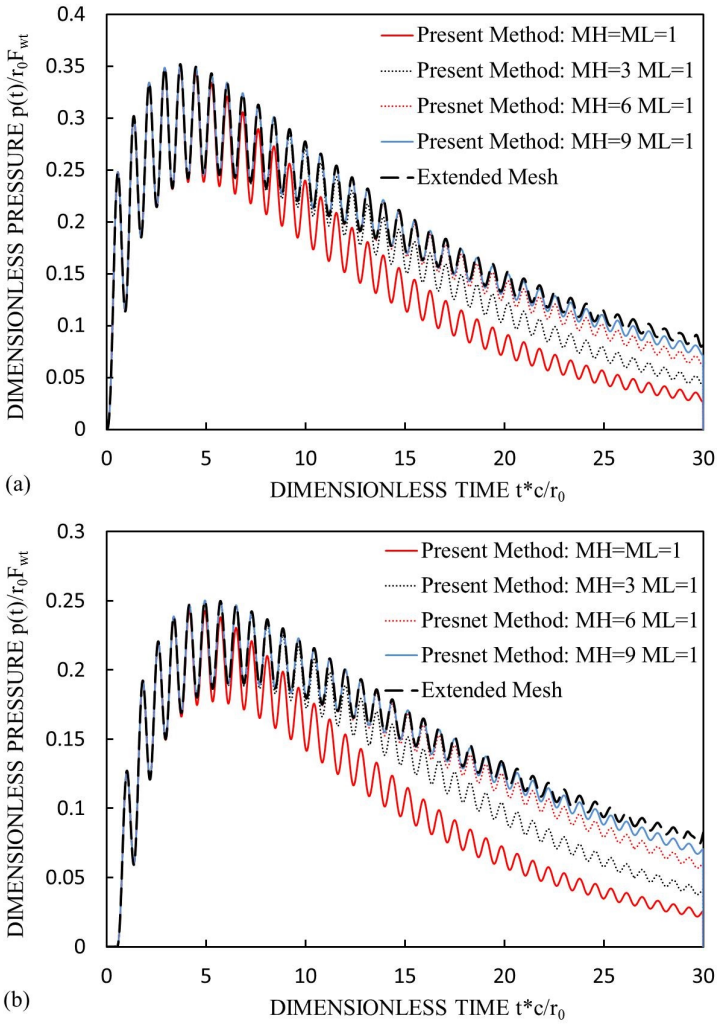

Figure 3.26. Dimensionless pressure response of semi-infinite wedge subject to long-time transient flux: (a) at point D and (b) at point J

with good agreement with the extended mesh results in the first $20\frac{r_0}{c}$ seconds, and, the doubly-asymptotic open boundary with continued-fraction expansions of order '$M_H = 9, M_L = 1$' yields results with good agreement with the extended mesh results in the first $30\frac{r_0}{c}$seconds. In summary, it can be said that convergence for late times is achieved by increasing the order of M_H. Obviously, the late time-response is governed by the low-order modes. Modes with $\lambda \leq M_H + 1$ are approximated by singly-asymptotic expansions of order M_H only in the proposed approach. Thus, the accuracy of these modes is affected by increasing M_H only.

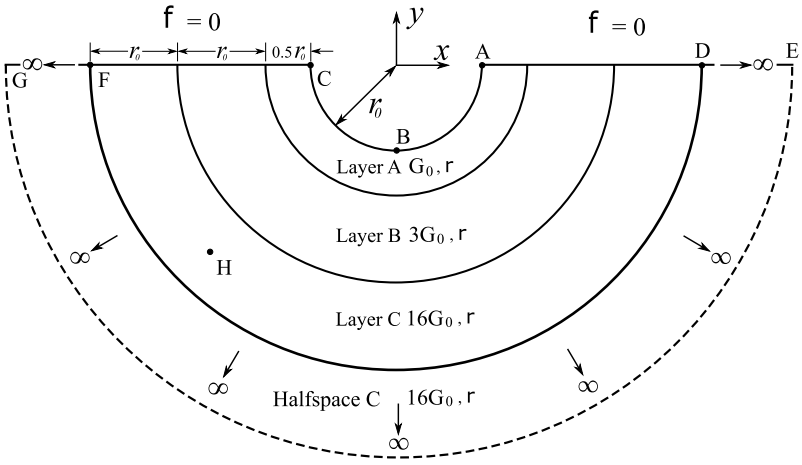

Figure 3.27. Geometry of non-uniform half-plane model

3.5.3 Non-uniform half-plane with semi-circular cavity

For illustrating the applicability of the proposed approach, the propagation of out-of-plane waves in an elastic half-plane with a non-uniform circular bounded domain is addressed in this section. This elastodynamic problem is governed by the scalar wave equation and can therefore be modeled using the proposed approach. Figure 3.27 shows the layout and dimensions of a circular canyon with radius r_0 enclosed by three different circular layers. All three types of material A, B and C are assumed to have the same density ρ but different shear moduli G_0, $3G_0$ and $16G_0$, respectively. The shear wave velocity in material A can be calculated as $c_A = \sqrt{\frac{G_0}{\rho}} = c_0$. Consequently, the shear wave velocities in layers B and C are $\sqrt{3}c_0$ and $4c_0$, respectively. The surface traction f on the canyon $\widehat{ABC}$ and ground surface $\overline{ADE}$ and $\overline{CFG}$ are assumed to be zero. Only a point load is applied at point H with coordinates $(x, y) = (-3r_0 \cos 45°, -3r_0 \cos 45°)$. The point load f_h varies as a Ricker wavelet with respect to time according to Equation (3.130). f_h is non-dimensionalized by its peak value F_{ht} and plotted in Figure 3.29(a). Its Fourier transform is shown in Figure 3.29(b).

$$f_h(t) = F_{ht} \times [1 - 20\frac{1}{\mathrm{s}^2}(t - 1.5\,\mathrm{s})^2]e^{-10\frac{1}{\mathrm{s}^2}(t-1.5\,\mathrm{s})^2}. \tag{3.130}$$

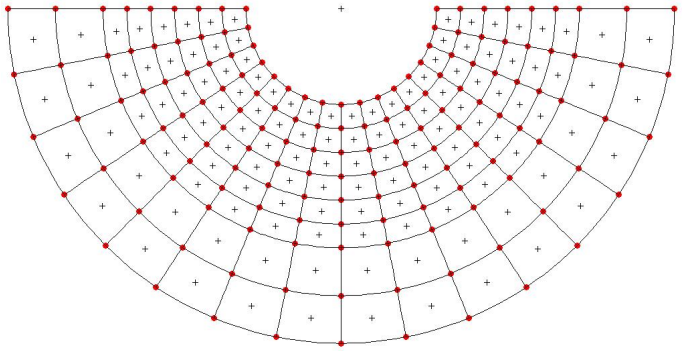

Figure 3.28. Mesh of non-uniform half-plane model

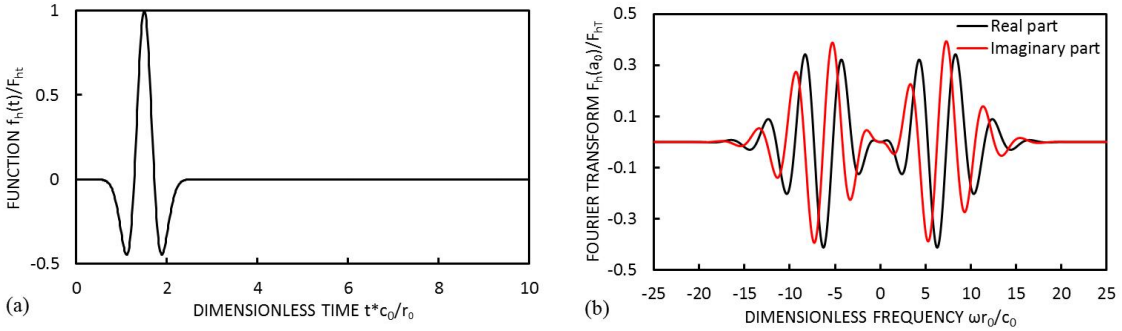

Figure 3.29. Time variation $f_h(t)$ of point load applied at non-uniform half-plane: (a) time history and (b) Fourier transform

The SBFE mesh of the half-plane is illustrated in Figure 3.28. The scaling centre of the unbounded subdomain is placed at the origin of the Cartesian coordinate system, and the scaling centres of the other $16 \times 8 = 128$ bounded subdomains are located at the respective centres of gravity. All red solid dots mark keypoints of individual subdomains but the nodes of individual line elements are not shown for clarity. From the Fourier transform of the applied load in Figure 3.29(b), the maximum dimensionless frequency of interest is estimated at $a_{0,max} = 20$. Since the shear wave velocity varies across the different layers, the shortest wavelengths $\lambda_{A,min}$, $\lambda_{B,min}$ and $\lambda_{C,min}$ in the three layers A, B and C can be calculated according to Equation (3.124) as:

$$\lambda_{A,min} = r_0 \frac{2\pi}{20c_0} \times c_A = r_0 \frac{2\pi}{20} \approx 0.314 r_0, \tag{3.131a}$$

$$\lambda_{B,min} = r_0 \frac{2\pi}{20c_0} \times c_B = r_0 \frac{2\pi}{20} \times \sqrt{3} \approx 0.544 r_0, \tag{3.131b}$$

$$\lambda_{C,min} = r_0 \frac{2\pi}{20c_0} \times c_C = r_0 \frac{2\pi}{20} \times 4 \approx 1.257 r_0. \tag{3.131c}$$

Therefore, the number of required elements and terms of continued-fraction expansion also vary across the different layers. In order to provide a sufficient number of nodes per wavelength during the analysis, six 3-node elements are used on each edge of individual subdomains in material A and material B, whereas layer C only requires three 3-node elements on each edge. Thus, the entire domain is modeled with at least 12 nodes per wavelength. The same guideline of selecting the order of continued-fraction expansion M of the bounded domain as in Section 3.5.1 is applied to the different material types. In Figure 3.27(b), the order of continued-fraction expansion for subdomains in layer A is selected as $M_A = 2$. The orders of continued-fraction expansions for subdomains in layers B and C are selected as $M_B = 2$ and $M_C = 1$, respectively, to satisfy the guideline.

The time-domain solutions are calculated by Newmark's method with a constant time step of $\Delta t = 0.02 r_0/c$ for the fist $t = 10 r_0/c$ seconds, which yields at least 15 time steps per period at the highest frequency of interest. The out-of-plane displacements at points B, C, D and F shown in Figure 3.27(a) are illustrated in Figure 3.30(a)-(d), respectively. The vertical axes are non-dimensionalized by $F_{ht}/G_0 r_0$ and the horizontal axes represent the dimensionless time tc_0/r_0.

For verification, an extended finite element mesh is built in ANSYS, where the outer circular boundary is located at $r = 24 r_0$ to avoid reflected waves entering the area of interest. The converged reference displacement responses from the extended mesh model at all corresponding points match the results from the SBFEM model very well in Figure 3.30. The dimensionless displacement contour plots calculated by the coupled SBFEM model at the dimensionless times $t\frac{c}{r_0} = 1.8, 2.2, 3.2$ and 3.6 are also shown in Figure 3.31 for illustration.

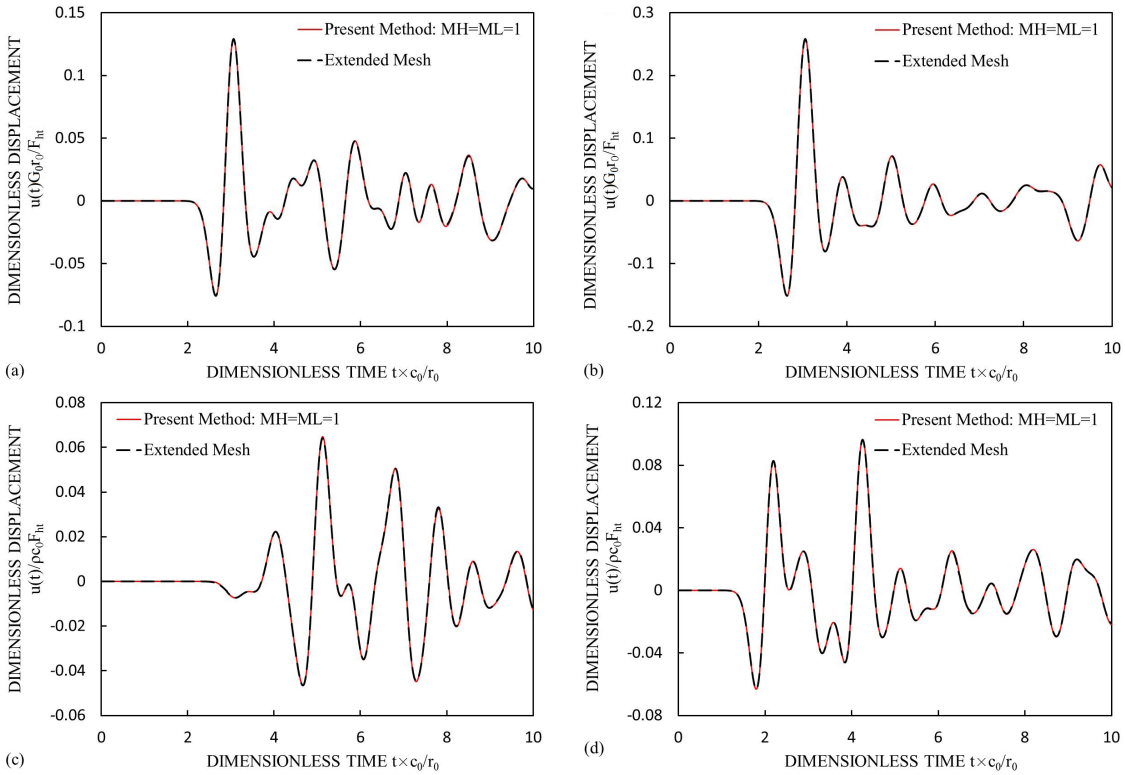

Figure 3.30. Dimensionless displacement response of non-uniform half-plane subjected to a point load: (a) at point B, (b) at point C, (c) at point D, (d) at point F

3.5.4 Elliptical cavity subject to transient flux on part of the boundary

In this section, an elliptical cavity with semi-major axis $a = 0.6r_0$ and semi-minor axis $b = 0.4r_0$ as shown in Figure 3.32(a) with an unbounded subdomain of radius r_0 is studied. The elliptical boundary is partially subjected to a transient flux which is defined by the following Equation (3.132):

$$\frac{\partial \bar{p}}{\partial \vec{\mathbf{n}}}(\theta, t) = h_e(\theta) f_e(t), \tag{3.132}$$

with the spacial variation described by:

$$h_e(\theta) = \begin{cases} 1 & \text{when } -\theta_1 \leq \theta \leq \theta_1, \\ 0 & \text{otherwise.} \end{cases} \tag{3.133}$$

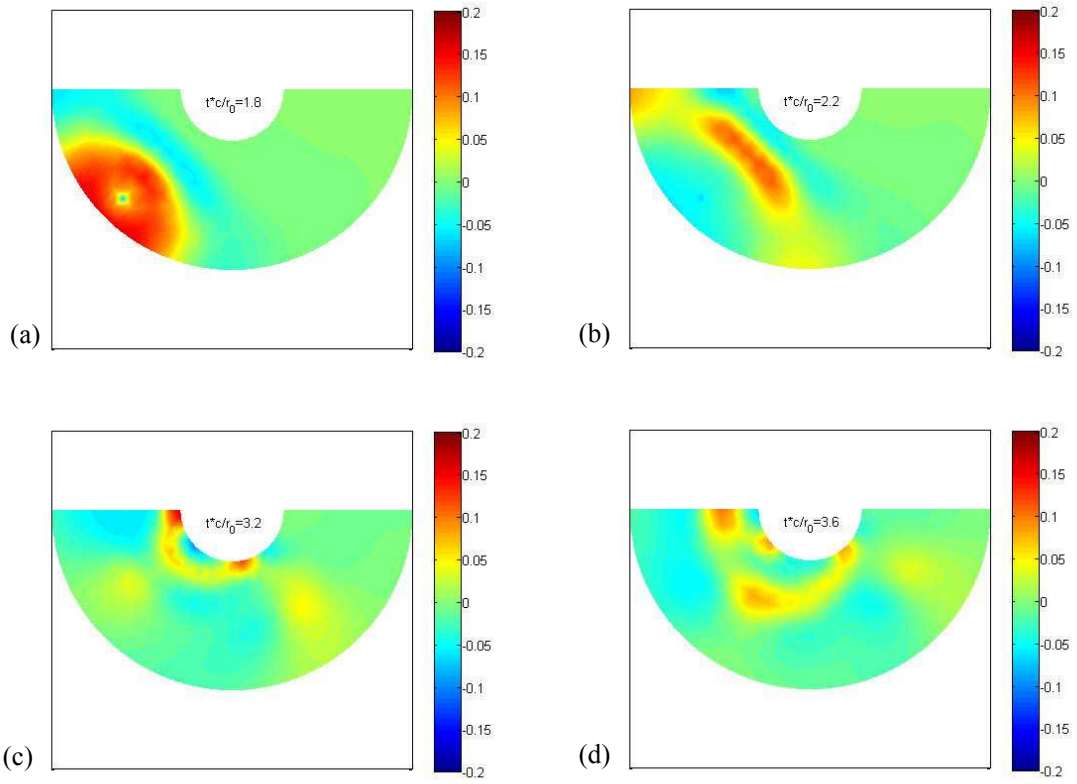

Figure 3.31. Displacement contour due to Ricker pulse applied at point H of half-plane model at: (a) $t\frac{c}{r_0} = 1.8$, (b) $t\frac{c}{r_0} = 2.2$, (c) $t\frac{c}{r_0} = 3.2$ and (d) $t\frac{c}{r_0} = 3.6$

In Equation (3.133), $\theta_1 = \arctan(\frac{2}{3}) \approx 33.69°$. In other words, the flux is applied only on arc $\widehat{BAC}$ in Figure 3.32. The time-dependent function $f_e(t)$ is plotted in Figure 3.33(a) with its Fourier transform in Figure 3.33(b). Similarly, the applied flux $f_e(t)$ is non-dimensionalized by F_{et}, which is the peak value, and the time t is also non-dimensionalized by r_0/c.

As shown in Figure 3.32(b), the scaling centre of the unbounded subdomain is placed at the origin of the Cartesian coordinate system, and the scaling centres of the other $64 \times 8 = 512$ bounded subdomains are located at the respective centres of gravity. All red small solid dots mark keypoints of individual subdomains but the nodes are not shown for conciseness.

In this numerical example, the maximum dimensionless frequency of interest is estimated at $a_{0,max} = 60$ from Figure 3.33(b). Therefore, the shortest wavelength

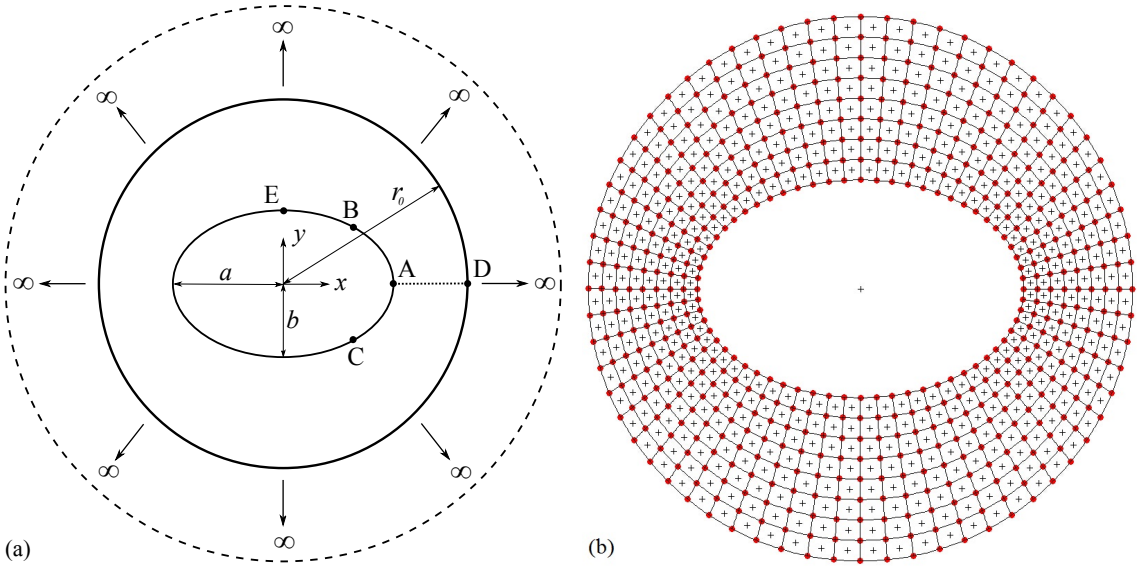

Figure 3.32. Elliptical cavity model: (a) geometry (b) mesh

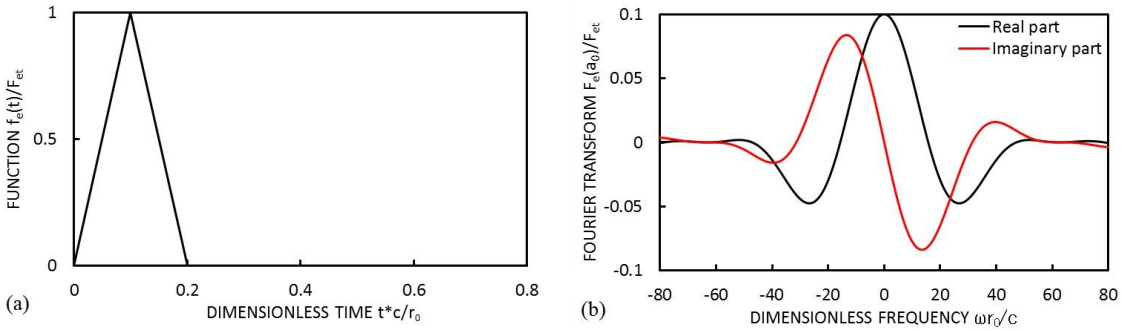

Figure 3.33. Time variation $f_e(t)$ of transient flux applied partially to elliptical boundary: (a) time history and (b) Fourier transform

can be calculated from Equation (3.124) as $\lambda_{min} = r_0 \frac{2\pi}{60} \approx 0.105 r_0$. The same guideline for selecting the order of continued-fraction expansion M of the bounded domain is applied. In Figure 3.32(b), the maximum radial distance in each subdomain is $d_{max} \approx 0.061 r_0$. Thus, the order of continued-fraction expansion is selected as $M = \frac{d_{max}}{\lambda_{min}} \times 4 \approx 2$. Additionally, a sufficient number of nodes are used on each curved or straight line. Generally, six 3-node elements are used on each line of individual subdomains which yield approximately 13 nodes per wavelength. The time-domain solutions of this problem are also calculated by Newmark's method with the constant time step of $\Delta t = 0.005 r_0/c$, which gives about 21 time steps per period at the highest frequency of interest for accuracy. The pressure variations at

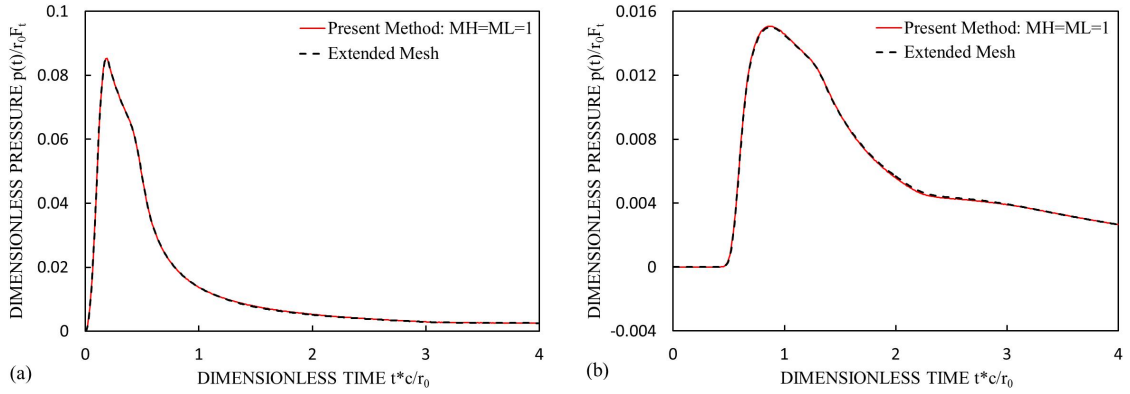

Figure 3.34. Dimensionless pressure response of elliptical cavity partially subject to transient flux: (a) at point A and (b) at point E

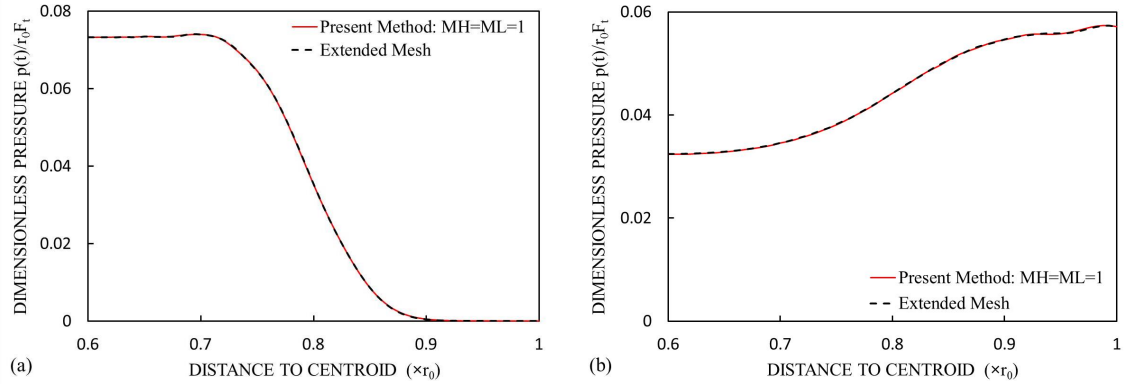

Figure 3.35. Pressure variation along radial line AD: (a) at $t\frac{c}{r_0} = 0.3$ and (b) at $t\frac{c}{r_0} = 0.6$

points A and E in Figure 3.32(a) are illustrated in Figure 3.34(a) and (b) respectively. The vertical axes are non-dimensionalized by $r_0 F_{et}$ and the horizontal axes represent the dimensionless time tc/r_0.

In order to verify the accuracy of the coupled SBFEM model, an extended finite element mesh is built in ANSYS, where the outer circular boundary is located at $r = 3r_0$ in order to avoid wave reflections. The converged reference pressure responses from the extended mesh model at points A and E match the results from the coupled SBFEM model very well in Figure 3.34. Therefore, the accuracy of the proposed coupled SBFEM model is proven to be very good when it is subjected to transient flux on part of the elliptical cavity boundary.

The dimensionless pressure variation along line AD in Figure 3.32 is also evalu-

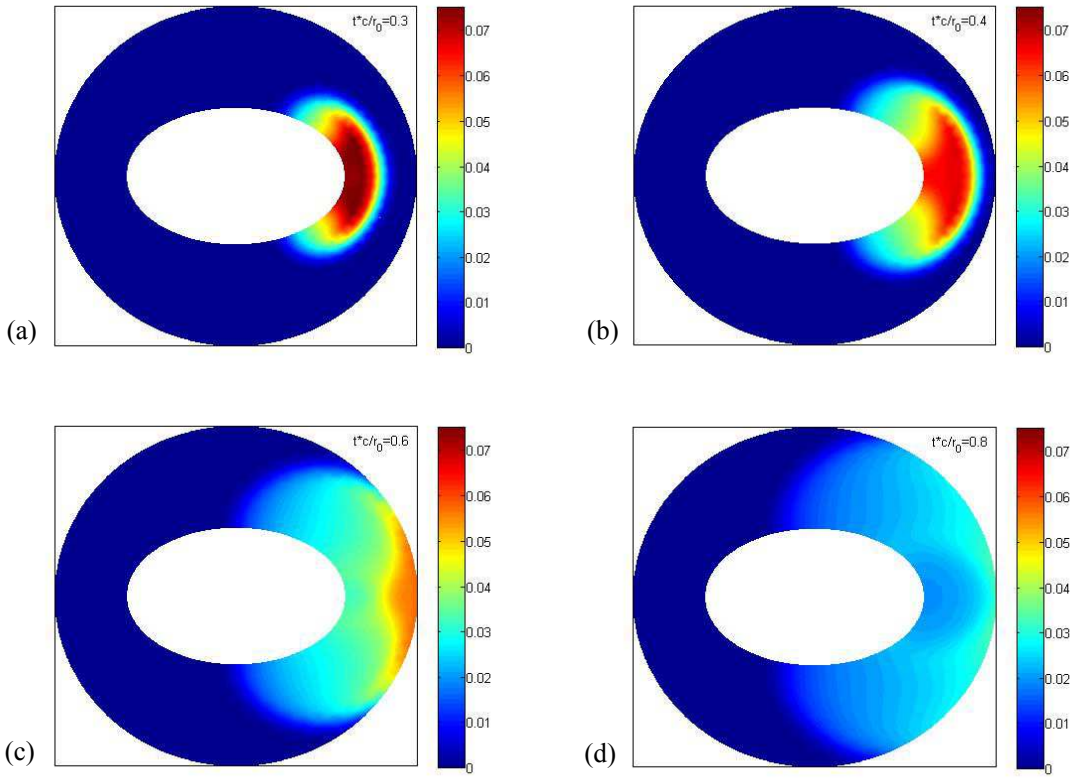

Figure 3.36. Elliptical cavity partially subject to transient flux. Pressure contour obtained using the proposed method at: (a) $t\frac{c}{r_0} = 0.3$, (b) $t\frac{c}{r_0} = 0.4$, (c) $t\frac{c}{r_0} = 0.6$ and (d) $t\frac{c}{r_0} = 0.8$

ated at times $t\frac{c}{r_0} = 0.3$ and 0.6 and shown in Figures 3.35(a) and (b) respectively. The vertical axes show the dimensionless pressure $p(t)/\rho cF_t$ and the horizontal axes represent the distance to the origin of the Cartesian coordinate system. Reference solutions from the same extended FEM model are also plotted. Very good agreement with the pressure responses obtained from the coupled SBFE model is observed. Additionally, the non-dimensionalized pressure contour plots calculated by the coupled SBFEM model and ANSYS at the dimensionless times $t\frac{c}{r_0} = 0.3, 0.4, 0.6$ and 0.8 are also shown in Figures 3.36 and 3.37, respectively, to illustrate how the pressure wave passes through the open boundary.

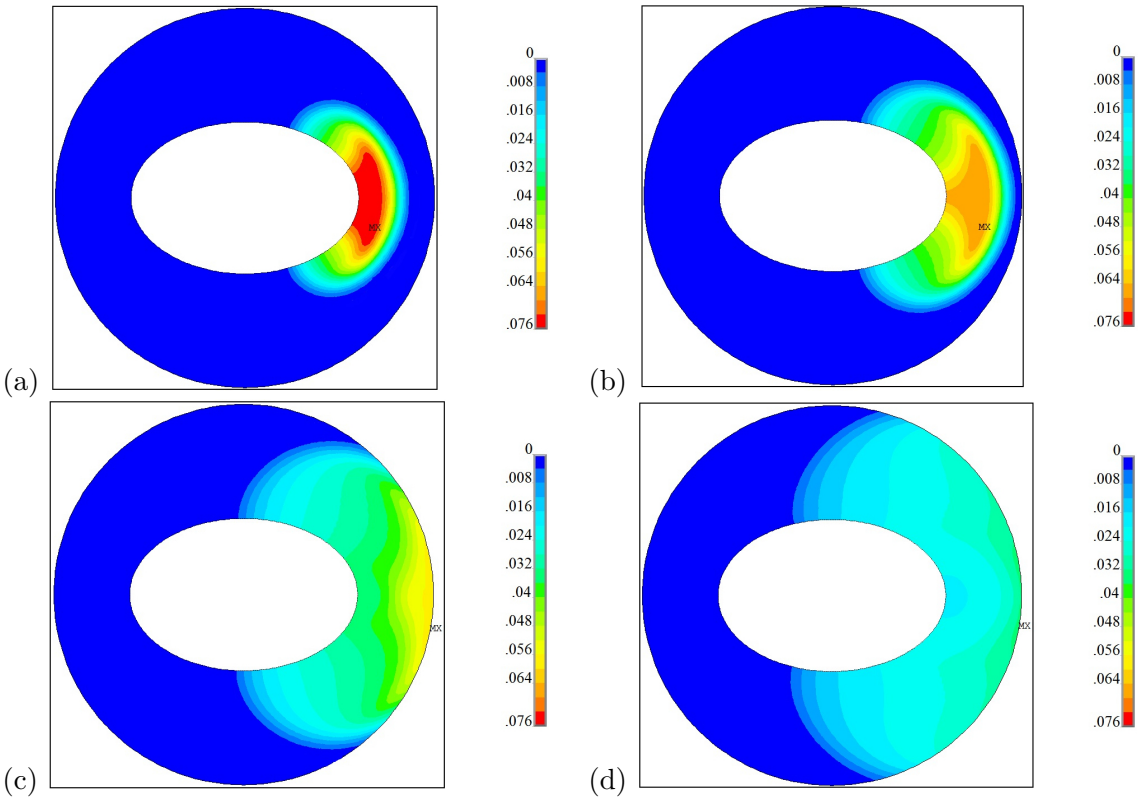

Figure 3.37. Elliptical cavity partially subject to transient flux. Pressure contour obtained using ANSYS at: (a) $t\frac{c}{r_0} = 0.3$, (b) $t\frac{c}{r_0} = 0.4$, (c) $t\frac{c}{r_0} = 0.6$ and (d) $t\frac{c}{r_0} = 0.8$

3.5.5 Wave radiation from an open structure

A more complex structure which is considered to be submerged into a non-viscous fluid is studied in this section. The structure is a 2D hollow square box with an outlet at the right bottom. The exact shape and dimensions of the structure are illustrated in Figure 3.38(a). The coupled system consisting of the bounded domain and unbounded domain around this box is also shown in Figure 3.38(b). The radius of the open boundary is r_0. A transient flux is applied on line AB, where A and B are located at the coordinates $(-0.45r_0, 0.225r_0)$ and $(-0.45r_0, -0.225r_0)$, respectively. The time variation of the flux on line AB in Figure 3.38(b) is the same as $f(t)$ used in the first numerical example described by Figure 3.15 in Section 3.5.1.

The mesh of this model is plotted in Figure 3.39 with keypoints marked as red solid dots and scaling centres marked by '+'. The domain inside the box is divided

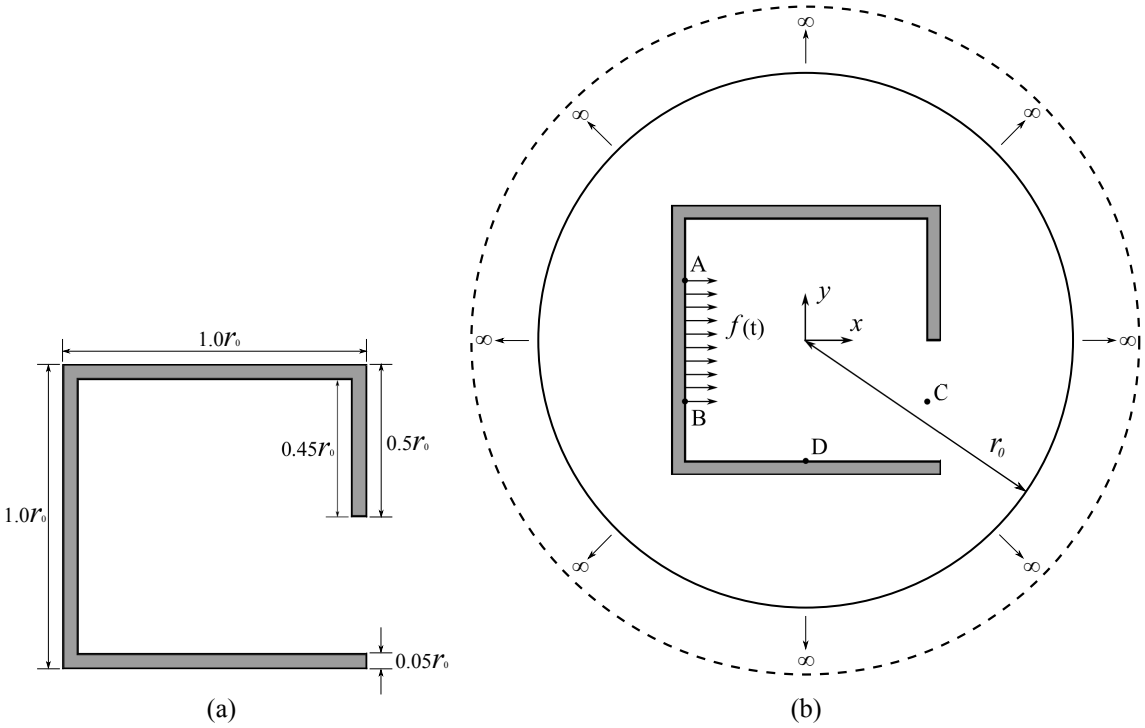

Figure 3.38. 2D open box structure: (a) layout of open box and (b) coupled SBFE model

into $16 \times 16 = 256$ subdomains, and the domain outside the box is divided into 65 subdomains in the circumferential direction and 8 layers in the radial direction. The outlet region (a small strip) is also discretized into 8 subdomains in the vertical direction.

According to Figure 3.15(b), the maximum dimensionless frequency of interest is about $a_{0,max} = 30$. From Equation (3.124), the shortest wavelength is thus $\lambda_{min} = r_0 \frac{2\pi}{30} \approx 0.21 r_0$. For accurately modelling the variation of flux and resulting response, all curved and straight lines in Figure 3.39 are discretized by three 3-node elements, which yields approximately 13 nodes per wavelength. The order of continued-fraction expansion M for the bounded domains can be chosen by using the same guideline as applied in the previous examples. The maximum radial distance of each subdomain in Figure 3.39 is $d_{max} \approx 0.058 r_0$. Therefore, the degree of continued-fraction expansion in this first case is chosen as $M = \frac{d_{max}}{\lambda_{min}} \times 4 \approx 1$. Newmark's method is also applied here to obtain the time-domain solution with

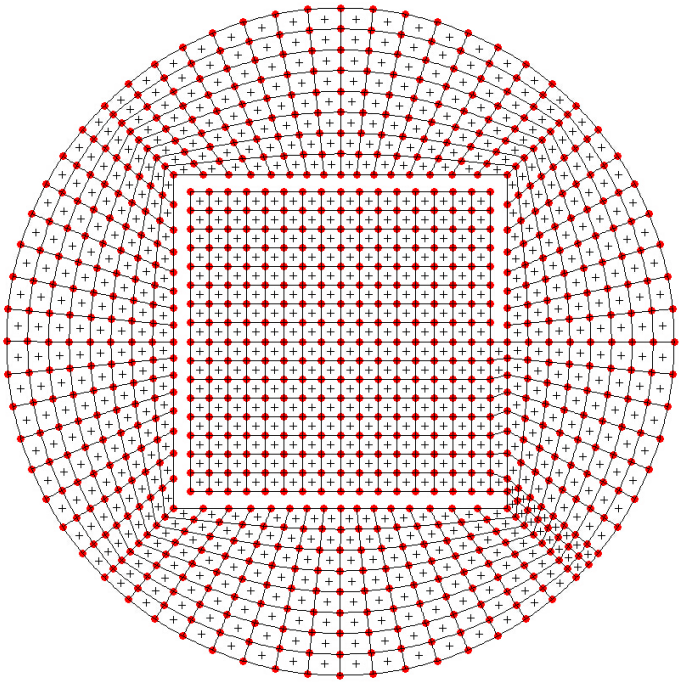

Figure 3.39. Mesh of the coupled SBFE open structure model

constant time step of $\Delta t = 0.01 r_0/c$ for accuracy.

Points C and D with coordinates $(0.45r_0,\ -0.225r_0)$ and $(0,\ -0.45r_0)$ are indicated in Figure 3.38(b). The dimensionless pressure response $p(t)/r_0F_{bt}$ at points C and D is plotted in Figure 3.40 versus the dimensionless time $t \times c/r_0$. For verification, an extended mesh of finite elements is built in ANSYS with the outer boundary located at $6r_0$ to avoid reflected waves approaching the bounded domain during the considered time range. The converged reference solutions are also plotted in Figure 3.40 for both points. It can be seen that the results from the SBFEM model match the reference solutions very well. This demonstrates that the proposed coupled SBFEM model is able to deal with complex geometrical shapes with very high accuracy.

In addition, the dimensionless pressure contour plots calculated by the coupled SBFEM model and ANSYS at times $t\frac{c}{r_0} = 0.95, 1.55, 3.0$ and 6.0 are shown in Figures 3.41 and 3.42, respectively, for illustration. It can be seen that at $t = 0.95r_0/c$, the pressure wave just meets the outlet and part of the outgoing wave propagates through the outlet of the open box and the open boundary while the other part

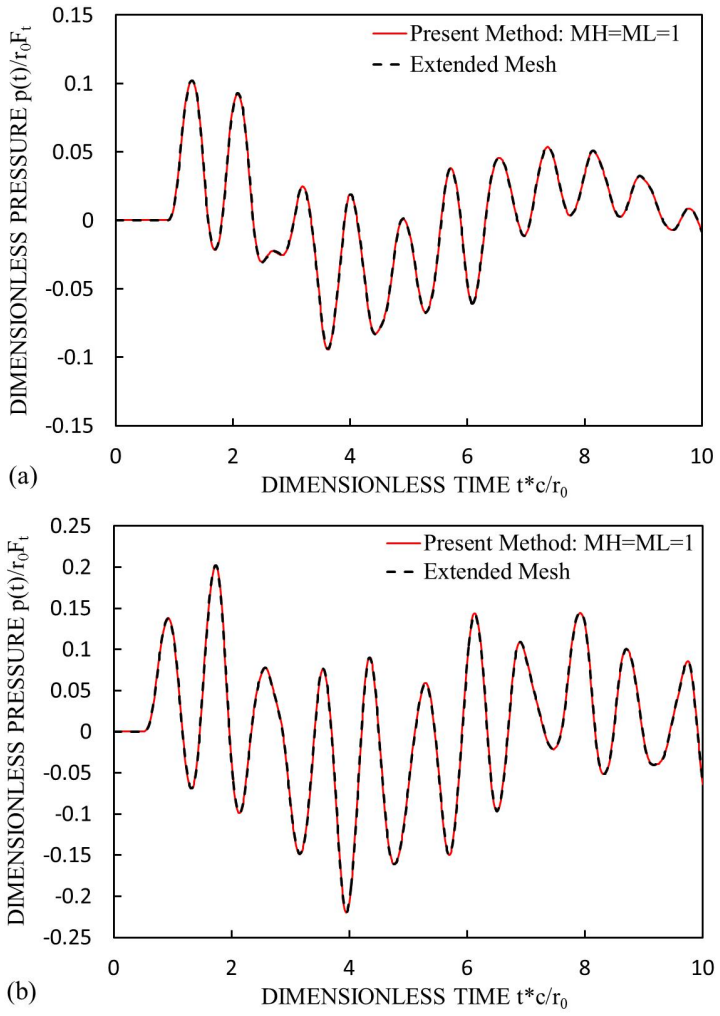

Figure 3.40. Dimensionless pressure response of open box structure at: (a) point C and (b) point D

is trapped and reflected inside the box. When $t = 1.55r_0/c$, the outgoing wave is passing through the open boundary and spreading into the whole unbounded domain.

3.6 Conclusions

A doubly-asymptotic open boundary for modelling acoustic wave propagation in two-dimensional unbounded domains of arbitrary geometry is proposed in this chapter. It is based on the previous approach in Reference (Prempramote et al., 2009) for modal equations. In order to solve two-dimensional acoustic problems of arbi-

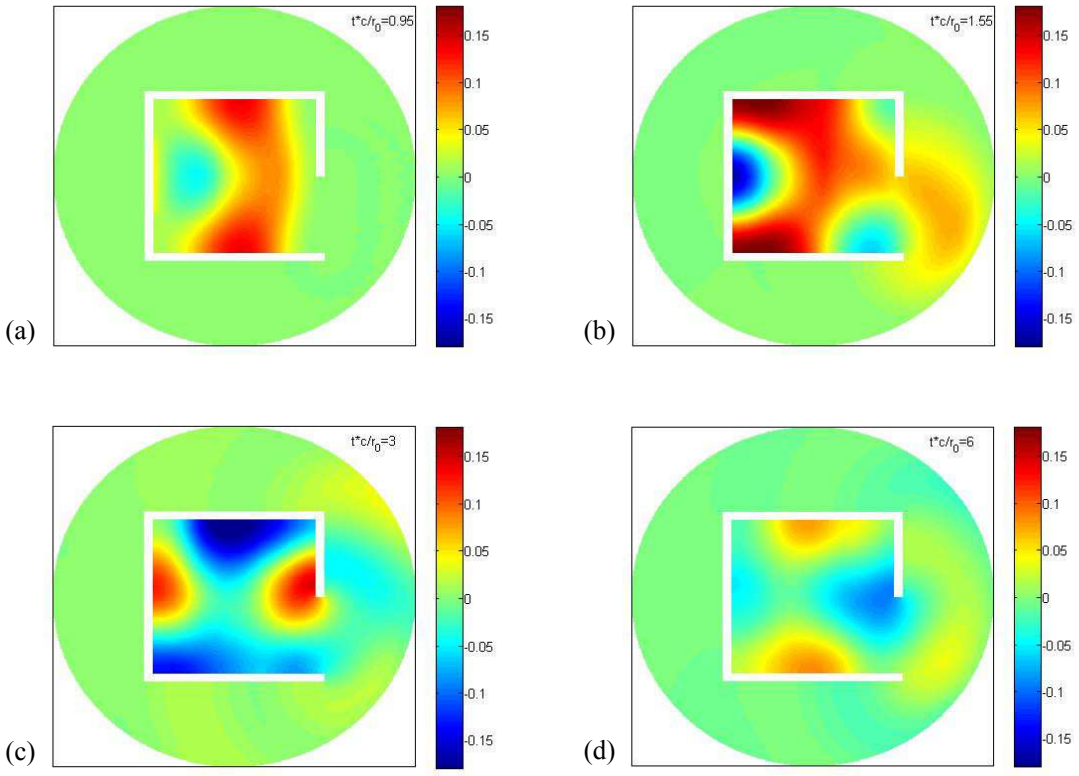

Figure 3.41. Open box model. Pressure contour obtained using the proposed coupled SBFE method at: (a) $t\frac{c}{r_0} = 0.95$, (b) $t\frac{c}{r_0} = 1.55$, (c) $t\frac{c}{r_0} = 3$ and (d) $t\frac{c}{r_0} = 6$

trary geometry, the whole region is divided into a near field (bounded domain) and a far field (unbounded domain). In the bounded domain, the scaled boundary finite element method in the time domain is applied. In the unbounded domain, modal expansion is used. The modal impedance coefficients are expressed as series of continued fractions. Here, singularities are avoided by introducing additional factors into certain continued-fraction coefficients. Rules for using singly-asymptotic continued fractions for low-frequency modes are stated to further improve the efficiency and stability of doubly-asymptotic open boundary. As a result, the present method is more robust than the previous approach.

Auxiliary variables are introduced to transform the continued-fraction expansion into the time-domain. In this way, the computationally expensive numerical integration of the stiffness and damping coefficient matrices is avoided. The proposed

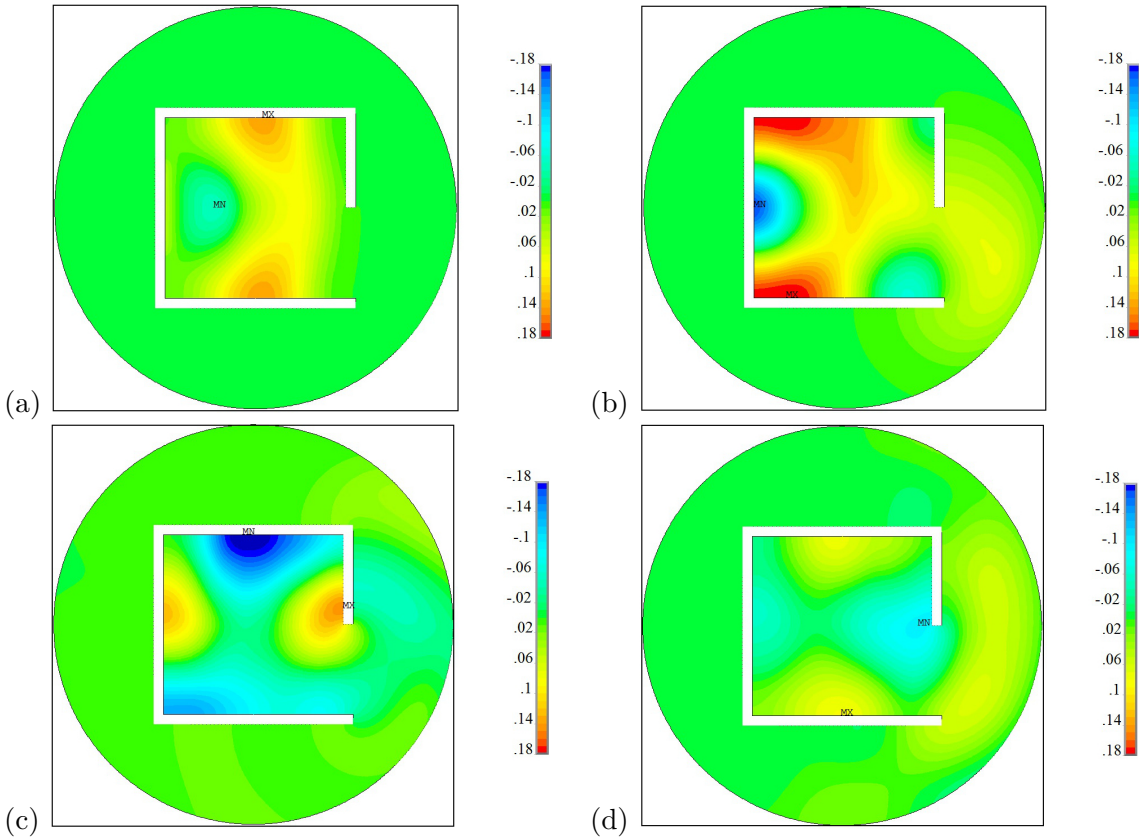

Figure 3.42. Open box model. Pressure contour obtained using ANSYS at: (a) $t\frac{c}{r_0} = 0.95$, (b) $t\frac{c}{r_0} = 1.55$, (c) $t\frac{c}{r_0} = 3$ and (d) $t\frac{c}{r_0} = 6$

unbounded domain model can easily be coupled with the equations of motion of the near field. A global system of second-order differential equations in the time domain is obtained, which can be solved using standard time stepping algorithms such as Newmark's method. Five numerical examples related to two-dimensional exterior acoustics are presented in this paper to demonstrate the accuracy and efficiency of this coupled approach, as well as its ability to handle complex problem. Generally, highly accurate solutions have been obtained with low orders of continued-fraction expansion. Compared to the singly-asymptotic open boundary, the high-order doubly-asymptotic formulation leads to a significant gain in accuracy at no additional cost. Moreover, the proposed doubly-asymptotic boundary can be placed very close to the radiating field.

Chapter 4

Automatic 3D acoustic analysis using octree mesh and SBFEM

4.1 Introduction

As it has been implemented into most of the commercial software packages, the finite element method (FEM) is one of the most popular and versatile computational tools for solving practical engineering problems. Similar to most of the computational methods, the analysis based on FEM starts from the mesh generation of the input model, that is, the discretization of the problem domain into numbers of finite elements with simple geometries, such as triangular or quadrilateral elements in 2D and tetrahedral or hexahedral elements in 3D. With the increasing use of computer-aided design (CAD) in solving engineering problems and manufacturing processes, automatic mesh generation techniques are highly desirable in finite element analysis to reduce the human efforts on mesh generation from CAD models, especially for problems with complex geometry.

For three-dimensional problems, two popular techniques can be used to generate tetrahedral elements from arbitrary domains automatically. They are advancing front technique (AFT) (Löhner and Parikh, 1988) and Delaunay triangulation (Du

and Wang, 2006). The major advantage of these techniques is the simplicity of implementation. However, the quality of the produced mesh is not always guaranteed and highly depend on the surface triangulation of the model. Moreover, it is preferred to use hexahedral elements in finite element analysis rather than tetrahedral elements due to the consideration of accuracy of the results (Blacker, 2001). Therefore, a large number of meshing methods have been proposed for generating hexahedral mesh, such as general sweeping (Staten et al., 1999), whisker weaving (Tautges et al., 1996), plastering (Blacker and Meyers, 1993) and octree-based approach (Yerry and Shephard, 1984). Nevertheless, these techniques for hexahedral mesh generation are reported to be less robust than those for tetrahedral mesh generation (Young et al., 2008). Furthermore, the hexahedral meshing from CAD model with arbitrary geometry remains to be a challenge in automatic mesh generation (Liu et al., 2017).

The development of other numerical methods provides alternative approaches for applying the automatic mesh generation techniques and thus circumvent the difficulties encountered in traditional FEM, such as extended finite element method (XFEM) (Moës et al., 1999) and finite cell method (FCM) (Parvizian et al., 2007). The mesh generation burden is greatly reduced in these methods because the mesh conforming to the geometrical boundary is not required. Quadtree in 2D and octree in 3D have been applied to XFEM for image-based analysis (Legrain et al., 2011). Quadtree and octree are hierarchical meshing structures, which allow efficient transition between different cell sizes (Legrain et al., 2011; Young et al., 2008; Huang and Li, 2013). The mesh is generated by subdividing a larger cell into four equal sized square cells in quadtree or eight equal sized cubic cells in octree recursively until a customized stopping condition is satisfied. Additionally, the efficiency of quadtree and octree approach is further improved as they only generate limited number of cell patterns and the corresponding element solutions for these cell patterns can be precomputed for later use (He, 2017; Saputra et al., 2017a; Liu et al., 2017). Ho-

wever, the direct implementation of quadtree or octree mesh in traditional FEM or XFEM may lead to hanging nodes between two adjacent cells with different sizes due to the displacement incompatibility. Numerous techniques have been presented to overcome the hanging-node problem and a few are listed in References (Fries et al., 2011; Legrain et al., 2011; Lo et al., 2010; Krysl et al., 2003; Tabarraei and Sukumar, 2007).

The SBFEM is a semi-analytical computational tool developed by Song and Wolf (Wolf and Song, 2000; Song and Wolf, 2000; Wolf, 2003). This method only requires boundary discretization and can describe the whole domain by scaling the boundary using a dimensionless radial coordinate. The SBFEM excels in modeling unbounded domain and stress singularities as it can provide analytical solutions in the radial direction. This method has been applied to numerous engineering problems including elastostatics (Song and Wolf, 1997, 1999a; Song, 2004a), elastodynamics (Song and Wolf, 1997; Song, 2009), wave propagation (Bazyar and Song, 2008; Birk et al., 2012; Bazyar and Song, 2017), diffusion (Song and Wolf, 1999b; Birk and Song, 2010), soil-structure interaction (Birk and Behnke, 2012), fluid-structure interaction (Fan et al., 2005; Lin et al., 2007; Xu et al., 2018), ultrasonics (Gravenkamp et al., 2015, 2017), electromagnetics (Liu and Lin, 2012), isogeometric analysis (Natarajan et al., 2015), piezoelectric materials (Saputra et al., 2017b), et al. SBFEM has also been applied to acoustics in some researches (Lehmann et al., 2006; Birk et al., 2016; Li et al., 2018). In most of these references, SBFEM is only used to simulate unbounded domain in one or two dimensions, that is, an infinite layer or 2D infinite plane. In this study, 3D bounded and unbounded acoustic domains are modeled via SBFEM.

The boundary discretization in SBFEM provides extra advantages in automatic mesh generation as demonstrated in recent researches (Saputra et al., 2017a; Talebi et al., 2016; Liu et al., 2017; Natarajan et al., 2017; Zou et al., 2017). The quadtree and octree based techniques have been applied in SBFEM for solving engineering

problems and some of them are listed in References (Gravenkamp et al., 2017; Bazyar and Song, 2017; Chen et al., 2018). The displacement incompatibility between neighboring cells with different sizes usually leads to hanging-node problem in standard FEM. In SBFEM, the hanging-node problem doesn't exist in quadtree mesh as the number of edges in a polygonal subdomain can be an arbitrary number. For the octree mesh, the hanging-node problem can be addressed by simple subdivisions of the common surfaces connecting cells with different sizes. Furthermore, only a limit number of cell patterns are generated in quadtree or octree approach. The element solutions for geometrically similar cells are identical or proportional to each other. Therefore, these element solutions can be precomputed and stored for later use (Saputra et al., 2017a). The automatic mesh generation process reduces the burdens on analysts for creating quality meshes from a the input of geometric models, especially when the geometry and material distributions are complex. The octree algorithm is able to handle not only conventional computer-aided design (CAD) models (Talebi et al., 2016) but also digital images (Saputra et al., 2017a) and models in the Standard Tessellation Language (STL) file format widely used in 3D printing industry (Liu et al., 2017).

This chapter extends the SBFEM to model wave propagation in 3D infinite acoustic domain with arbitrary geometry of cavity inside. The modeling of infinite acoustic domain can be addressed by dividing the whole infinite domain into acoustic near field and far field via a spherical boundary. The improved high-order doubly asymptotic open boundary in Chapter 3 for 2D problems is further developed to model 3D unbounded acoustic far field in this Chapter. The modeling of acoustic far field in 3D is based on decoupling the scaled boundary finite element equation for spherical unbounded domain into a series of modal equations with frequency-dependent modal impedances. These modal impedances can then be expanded into continued fractions and solved recursively by satisfying those modal equations at both high and low frequency limits. The improved doubly-asymptotic continued-

fraction expansion in Chapter 3 are used to solve modal impedances as the mode number $\lambda = i + 0.5$, with the integer i, for 3D spherical unbounded domain. Auxiliary variables are again introduced here to transform the continued fraction solutions into the nodal flux-pressure relationship in the time domain. The acoustic near field containing irregular complex geometries is also modeled by SBFEM. The automatic mesh generation technique presented in (Liu et al., 2017) is adopted in this chapter for 3D acoustic analysis from any STL model. Therefore, very complex geometrical features embedded in the acoustic medium can be meshed and then modeled automatically by this presented approach. The acoustic near field and far field are coupled via the nodal flux on the spherical boundary at the end to form the global system of equations representing the whole infinite acoustic domain.

This chapter is organized as follows: The scaled boundary finite element equations for 3D acoustic near field and far field are expressed in Section 4.2. Next, the continued-fraction solutions for the spherical doubly-asymptotic open boundary are derived in Section 4.3. Section 4.4 describes the derivations of time-domain equations for unbounded domains and the whole 3D acoustic system. Several numerical examples are presented in Section 4.5 to demonstrate the accuracy, efficiency and ability of the proposed approach to handle practical acoustic problems with complex geometries. Finally, conclusions are stated in Section 4.6.

4.2 Scaled boundary finite element formulations for 3D linear acoustics

The acoustic fluid in this chapter is assumed to be linear, inviscid and isentropic with small perturbations. The scalar wave propagation in such a linear acoustic domain is described by the governing equation in Equation (3.1). The symbol ∇ represents the gradient operator in 3D as $\nabla = \left[\frac{\partial}{\partial \hat{x}}, \frac{\partial}{\partial \hat{y}}, \frac{\partial}{\partial \hat{z}}\right]^T$. $\hat{x}$, $\hat{y}$ and $\hat{z}$ are the Cartesian coordinates shown in Figure 4.1.

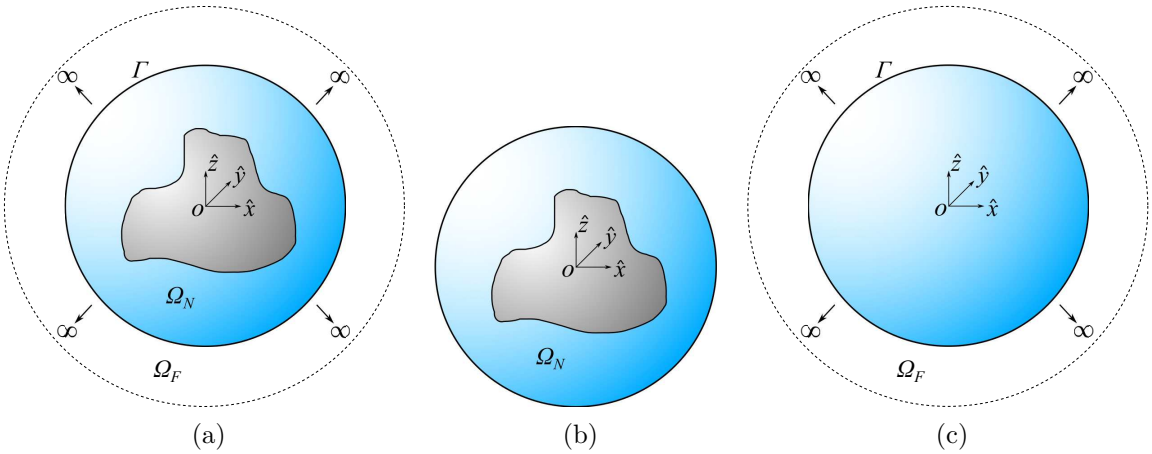

Figure 4.1. Modeling 3D infinite acoustic domain: (a) the 3D acoustic domain, (b) bounded near field and (c) unbounded far field

In the proposed approach, the idea of modeling acoustic wave propagation in an infinite 3D domain is similar to the approach used for 2D acoustics in Chapter 3 but a spherical surface is used to truncate the infinite 3D domain instead of the circular boundary for truncating 2D infinite domain described in Section 3.2. An illustration for such an idea in 3D case is shown in Figure 4.1. The whole infinite 3D domain with gray region of cavity is illustrated in Figure 4.1(a). A spherical boundaryΓ is then chosen to truncate the infinite 3D domain into an acoustic near field Ω_N in Figure 4.1(b) and an acoustic far field Ω_F in Figure 4.1(c). The near field Ω_N is a bounded domain and can include cavities with arbitrary geometries. The far field Ω_F is an unbounded domain with a spherical interior boundary.

The modeling of 3D acoustic near field by SBFEM is summarized in the following Section 4.2.1. In this chapter, the hierarchical octree structure is utilized to discretize the 3D near field and any geometrical features in the near field are able to be captured efficiently and automatically. The acoustic far field Ω_F in Figure 4.1(c) is modeled by one unbounded subdomain in SBFEM with spherical boundary Γ for 3D case. The derivation of the scaled boundary finite element equation for 3D unbounded domain is summarized in Section 4.2.2. The meshes of the bounded and unbounded domains are compatible at the interface. The solutions for bounded and

unbounded domains are coupled together straightforwardly via the nodal flux on the interface Γ.

4.2.1 3D bounded acoustic domain

After the meshing process, SBFEM polyhedral subdomains with arbitrary number of faces are generated. These subdomains are described by the so called scaled boundary coordinates (Wolf, 2003). In this section, the derivation for 3D acoustic analysis is addressed. Figure 4.2 illustrates a bounded polyhedral subdomain with scaled boundary coordinates (ξ, η, ζ) and Cartesian coordinates $(\hat{x}, \hat{y}, \hat{z})$. Only boundary discretization is required in SBFEM. For a 3D problem, standard 2D surface elements, such as triangular or quadrilateral elements used in the standard FEM, can be adopted and described by the local scaled boundary coordinates (η, ζ). The shaded area in Figure 4.2 shows an example of quadrilateral element on one of the faces of the 3D bounded subdomain. The scaling centre O is placed within the bounded domain and the whole boundary should be visible from this point. This is also known as the scaling requirement in SBFEM. For subdomains with complex geometry, this condition can be satisfied by subdivisions. Then, the entire boundary can be scaled inwardly by a dimensionless radial coordinate ξ to describe the polyhedral subdomain. Following the geometrical transformation described above, any surface element on the boundary of polyhedral subdomain with m nodes can be described by interpolating the local nodal coordinates $\mathbf{x}_b$,$\mathbf{y}_b$,$\mathbf{z}_b$ using the 2D mapping functions $\mathbf{N}(\eta, \zeta)$ as given in Equation (4.1).

$$x(\eta, \zeta) = \mathbf{N}(\eta, \zeta)\mathbf{x}_b \tag{4.1a}$$

$$y(\eta, \zeta) = \mathbf{N}(\eta, \zeta)\mathbf{y}_b \tag{4.1b}$$

$$z(\eta, \zeta) = \mathbf{N}(\eta, \zeta)\mathbf{z}_b \tag{4.1c}$$

$\mathbf{N}(\eta, \zeta) = [N_1(\eta, \zeta),\ N_2(\eta, \zeta),\ \cdots,\ N_m(\eta, \zeta)]$ is the 2D mapping functions for an m-nodes surface element. Subscript 'b' in the nodal coordinate vectors $\mathbf{x}_b$, $\mathbf{y}_b$ and

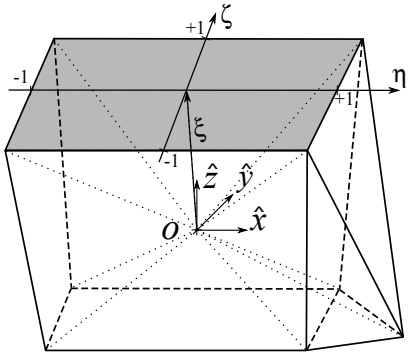

Figure 4.2. A typical 3D polyhedral bounded subdomain in SBFEM coordinates.

$\mathbf{z}_b$ indicates nodal Cartesian coordinates on the boundary. Any point inside the subdomain with coordinates $(\hat{x}, \hat{y}, \hat{z})$ is then described by scaling the boundary along the radial lines using the radial coordinate ξ. These radial lines connect any nodes on the boundary to the scaling centre O. This coordinate transformation can be expressed below:

$$\hat{x}(\xi, \eta, \zeta) = \xi \mathbf{N}(\eta, \zeta)\mathbf{x}_b \tag{4.2a}$$

$$\hat{y}(\xi, \eta, \zeta) = \xi \mathbf{N}(\eta, \zeta)\mathbf{y}_b \tag{4.2b}$$

$$\hat{z}(\xi, \eta, \zeta) = \xi \mathbf{N}(\eta, \zeta)\mathbf{z}_b \tag{4.2c}$$

For a bounded domain, $0 \leq \xi \leq 1$ with $\xi = 1$ on the boundary and $\xi = 0$ at the scaling centre O applies. Equation (4.2) is also known as the scaled boundary transformation in 3D. It relates the Cartesian coordinates $(\hat{x}, \hat{y}, \hat{z})$ to the scaled boundary coordinates (ξ, η, ζ). The Jacobian matrix on the boundary with $\xi = 1$ can be written as:

$$\mathbf{J}(\eta, \zeta) = \begin{bmatrix} x(\eta,\zeta) & y(\eta,\zeta) & z(\eta,\zeta) \\ x(\eta,\zeta)_{,\eta} & y(\eta,\zeta)_{,\eta} & z(\eta,\zeta)_{,\eta} \\ x(\eta,\zeta)_{,\zeta} & y(\eta,\zeta)_{,\zeta} & z(\eta,\zeta)_{,\zeta} \end{bmatrix} \tag{4.3}$$

with its determinant $|\mathbf{J}|$ expressed as:

$$|\mathbf{J}| = x\left(y_{,\eta}z_{,\zeta} - z_{,\eta}y_{,\zeta}\right) + y\left(z_{,\eta}x_{,\zeta} - x_{,\eta}z_{,\zeta}\right) + z\left(x_{,\eta}y_{,\zeta} - y_{,\eta}x_{,\zeta}\right) \tag{4.4}$$

The gradient operator in Equation (3.1) can also be written in the scaled boundary coordinates for 3D acoustics as:

$$\nabla = \mathbf{b}_1^a(\eta,\zeta)\frac{\partial}{\partial\xi} + \frac{1}{\xi}\left(\mathbf{b}_2^a(\eta,\zeta)\frac{\partial}{\partial\eta} + \mathbf{b}_3^a(\eta,\zeta)\frac{\partial}{\partial\zeta}\right) \tag{4.5}$$

with the vectors $\mathbf{b}_1^a$, $\mathbf{b}_2^a$ and $\mathbf{b}_3^a$ given as:

$$\mathbf{b}_1^a(\eta,\zeta) = \frac{1}{|\mathbf{J}|}\begin{Bmatrix} y_{,\eta}z_{,\zeta} - z_{,\eta}y_{,\zeta} \\ z_{,\eta}x_{,\zeta} - x_{,\eta}z_{,\zeta} \\ x_{,\eta}y_{,\zeta} - y_{,\eta}x_{,\zeta} \end{Bmatrix} \tag{4.6a}$$

$$\mathbf{b}_2^a(\eta,\zeta) = \frac{1}{|\mathbf{J}|}\begin{Bmatrix} zy_{,\zeta} - yz_{,\zeta} \\ xz_{,\zeta} - zx_{,\zeta} \\ yx_{,\zeta} - xy_{,\zeta} \end{Bmatrix} \tag{4.6b}$$

$$\mathbf{b}_3^a(\eta,\zeta) = \frac{1}{|\mathbf{J}|}\begin{Bmatrix} yz_{,\eta} - zy_{,\eta} \\ zx_{,\eta} - xz_{,\eta} \\ xy_{,\eta} - yx_{,\eta} \end{Bmatrix} \tag{4.6c}$$

The acoustic pressure $p(x,y,z,t)$ in a subdomain can also be interpolated by the same 2D mapping function $\mathbf{N}(\eta,\zeta)$ in Equation (4.2) for geometry as,

$$p(\xi,\eta,\zeta,t) = \hat{p}(\xi,\eta,\zeta)\mathrm{e}^{\mathrm{i}\omega t} = \mathbf{N}(\eta,\zeta)\hat{\mathbf{p}}(\xi)\mathrm{e}^{\mathrm{i}\omega t} \tag{4.7}$$

In Equation (4.7), $\hat{p}(\xi,\eta,\zeta)$ is the pressure amplitude in the subdomain and $\hat{\mathbf{p}}(\xi)$ is the pressure amplitude in the radial direction. Applying the method of weighted residual to the governing Equation (3.1) in the frequency domain for 3D in the circumferential directions (η,ζ) as in Reference(Song and Wolf, 1997) yields the following differential equation for the radial pressure amplitude $\hat{\mathbf{p}}(\xi)$ in 3D acoustics with the absence of prescribed flux along side-face (boundary with constant circumferential coordinates (η,ζ)) in a subdomain.

$$\mathbf{E}_0^a\xi^2\hat{\mathbf{p}}(\xi)_{,\xi\xi} + \left(2\mathbf{E}_0^a - \mathbf{E}_1^a + [\mathbf{E}_1^a]^T\right)\xi\hat{\mathbf{p}}(\xi)_{,\xi} + \left([\mathbf{E}_1^a]^T - \mathbf{E}_2^a\right)\hat{\mathbf{p}}(\xi) + \omega^2\mathbf{M}_0^a\xi^2\hat{\mathbf{p}}(\xi) = 0 \tag{4.8}$$

Equation (4.8) is also known as the scaled boundary finite element equation in pressure amplitude. $\mathbf{E}_0^a$, $\mathbf{E}_1^a$, $\mathbf{E}_2^a$ and $\mathbf{M}_0^a$ are coefficient matrices for acoustic domain. These coefficient matrices depend on the geometry and materials of the corresponding elements and can be expressed as:

$$\mathbf{E}_0^a = \int_{-1}^{+1}\int_{-1}^{+1} \left[\mathbf{B}_1^a(\eta,\zeta)\right]^T \mathbf{B}_1^a(\eta,\zeta)\,|\mathbf{J}(\eta,\zeta)|\,d\eta d\zeta \tag{4.9a}$$

$$\mathbf{E}_1^a = \int_{-1}^{+1}\int_{-1}^{+1} \left[\mathbf{B}_2^a(\eta,\zeta)\right]^T \mathbf{B}_1^a(\eta,\zeta)\,|\mathbf{J}(\eta,\zeta)|\,d\eta d\zeta \tag{4.9b}$$

$$\mathbf{E}_2^a = \int_{-1}^{+1}\int_{-1}^{+1} \left[\mathbf{B}_2^a(\eta,\zeta)\right]^T \mathbf{B}_2^a(\eta,\zeta)\,|\mathbf{J}(\eta,\zeta)|\,d\eta d\zeta \tag{4.9c}$$

$$\mathbf{M}_0^a = \int_{-1}^{+1}\int_{-1}^{+1} \mathbf{N}^T(\eta,\zeta)\frac{1}{c^2}\mathbf{N}(\eta,\zeta)\,|\mathbf{J}(\eta,\zeta)|\,d\eta d\zeta \tag{4.9d}$$

where c is the sound speed in Equation (3.1). The matrices $\mathbf{B}_1^a(\eta,\zeta)$ and $\mathbf{B}_2^a(\eta,\zeta)$ in Equation (4.9) are defined as:

$$\mathbf{B}_1^a(\eta,\zeta) = \mathbf{b}_1^a(\eta,\zeta)\mathbf{N}(\eta,\zeta) \tag{4.10a}$$

$$\mathbf{B}_2^a(\eta,\zeta) = \mathbf{b}_2^a(\eta,\zeta)\mathbf{N}(\eta,\zeta)_{,\eta} + \mathbf{b}_3^a(\eta,\zeta)\mathbf{N}(\eta,\zeta)_{,\zeta} \tag{4.10b}$$

The coefficient matrices in Equation (4.9) are calculated on an element-by-element basis and assembled as in finite element method for each polyhedral subdomain. The frequency-dependent impedance matrix $\mathbf{S}^a(\omega)$ is introduced in acoustics. The impedance matrix relates the nodal flux amplitude $\hat{\mathbf{R}}$ to nodal pressure amplitude $\hat{\mathbf{p}}$ on the boundary with $\xi = 1$ as shown in Equation (3.13). The nodal flux amplitude vector $\hat{\mathbf{R}}$ is also defined in Equation (3.15). For 3D acoustics, the integration in Equation (3.15) is over the boundary $\mathit{\Gamma}_\xi$ of a polyhedral subdomain with $\xi = 1$ and $d\Gamma$ is the infinitesimal area for 3D. $\vec{\mathbf{n}}$ is the unit normal vector to the boundary surface and $\frac{\partial \hat{p}}{\partial \vec{\mathbf{n}}}$ represents any prescribed normal derivative of pressure amplitude on the boundary of a polyhedral subdomain. For the 3D bounded domains, the radial flux $\hat{\mathbf{R}}(\xi)$ is equal to the internal radial flux $\hat{\mathbf{Q}}(\xi)$ on any surface with constant ξ. The internal radial flux $\hat{\mathbf{Q}}(\xi)$ is related to the radial pressure $\hat{\mathbf{p}}(\xi)$

as: (Song and Wolf, 1997; Wolf, 2003)

$$\hat{\mathbf{Q}}(\xi) = \mathbf{E}_0^a \xi^2 \hat{\mathbf{p}}(\xi)_{,\xi} + \left[\mathbf{E}_1^a\right]^T \xi \hat{\mathbf{p}}(\xi) \tag{4.11}$$

Substituting Equations (3.13) and (4.11) for 3D acoustics into Equation (4.8), this second-order differential equation can be transformed to a nonlinear first-order differential equation for impedance matrix $\mathbf{S}^a(\omega)$:

$$\left(\mathbf{S}^a(\omega) - \mathbf{E}_1^a\right)\left[\mathbf{E}_0^a\right]^{-1}\left(\mathbf{S}^a(\omega) - \left[\mathbf{E}_1^a\right]^T\right) - \mathbf{E}_2^a + \mathbf{S}^a(\omega) + \omega \mathbf{S}^a(\omega)_{,\omega} + \omega^2 \mathbf{M}_0^a = 0 \tag{4.12}$$

Equation (4.12) is solved in (Song, 2009) by expanding $\mathbf{S}^a(\omega)$ into a series of continued fractions similar to those summarized in Section 3.2.1.1 for 2D acoustics. Later, an improved procedure leading to better conditioned mass and stiffness matrices id developed in (Chen et al., 2014). After introducing the auxiliary variables, the continued-fraction expansions can again be transformed into the same time-domain equations of motion with frequency-independent coefficient matrices for 3D bounded acoustic domain:

$$\mathbf{M}_h^a \ddot{\mathbf{y}}(t) + \mathbf{K}_h^a \mathbf{y}(t) = \mathbf{r}(t) \tag{4.13}$$

$\mathbf{M}_h^a$, $\mathbf{K}_h^a$, $\mathbf{y}(t)$ and $\mathbf{r}(t)$ are the same as in Equations (3.38a) - (3.40) but with coefficients calculated in 3D case.

4.2.2 3D unbounded acoustic domain

This section presents the derivations of the scaled boundary finite element equation for 3D unbounded acoustic domain. The far field of a 3D acoustic problem is modeled by one spherical unbounded subdomain in SBFEM as shown in Figure 4.3 with a spherical boundary Γ. This spherical subdomain has a radius of r_0 with the scaling centre O at its centroid. The spherical surface is also discretized using standard 2D elements in FEM. One of the quadrilateral element on the surface with local

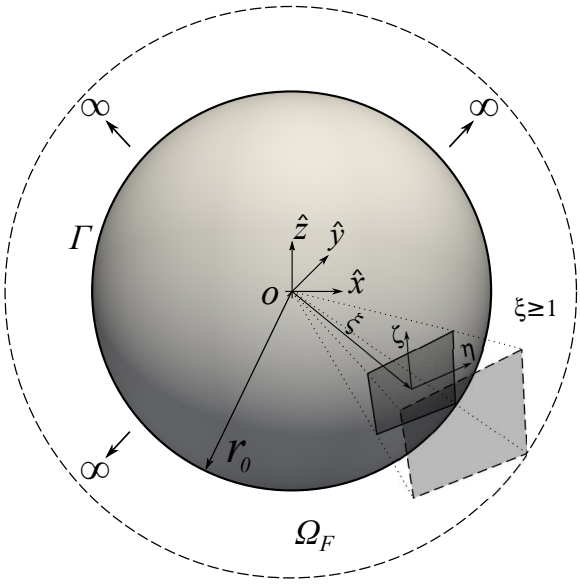

Figure 4.3. Scaled boundary finite element model of unbounded domain with spherical interface.

boundary coordinates (η, ζ) is shaded in Figure 4.3 as an example. Similar to the scaled boundary transformation for bounded domain in Section 4.2.1, the infinite acoustic medium is then described by scaling the spherical surface outwardly using the dimensionless radial coordinate ξ in scaled boundary coordinates with $\xi \geq 1$. Given the Cartesian coordinates of any point on the spherical boundary $x(\eta, \zeta)$, $y(\eta, \zeta)$ and $z(\eta, \zeta)$, the Cartesian coordinates of any point in the unbounded domain can be described by,

$$\hat{x}(\xi, \eta, \zeta) = \xi \cdot x(\eta, \zeta) \tag{4.14a}$$

$$\hat{y}(\xi, \eta, \zeta) = \xi \cdot y(\eta, \zeta) \tag{4.14b}$$

$$\hat{z}(\xi, \eta, \zeta) = \xi \cdot z(\eta, \zeta) \tag{4.14c}$$

Spherical coordinates are then introduced to describe any node on the spherical boundary with a constant radius r_0, polar angle $\theta(\eta, \zeta)$ and azimuthal angle $\varphi(\eta, \zeta)$. For any point on the sphere Γ, the azimuthal angle $\varphi(\eta, \zeta)$ is measured in the $\hat{x}$-$\hat{y}$ plane from positive $\hat{x}$ direction to the line segment connecting the coordinate origin to any point on the sphere. The polar angle $\theta(\eta, \zeta)$ represents the angle between the positive $\hat{z}$ direction and the same line segment connecting the coordinate origin to

the point on the sphere. The coordinates of nodes on spherical boundary written in spherical coordinate (r_0, θ, φ) is then given in the following Equation (4.15),

$$x(\eta,\zeta) = r_0 \sin\left(\theta(\eta,\zeta)\right) \cos\left(\varphi(\eta,\zeta)\right) \tag{4.15a}$$

$$y(\eta,\zeta) = r_0 \sin\left(\theta(\eta,\zeta)\right) \sin\left(\varphi(\eta,\zeta)\right) \tag{4.15b}$$

$$z(\eta,\zeta) = r_0 \cos\left(\theta(\eta,\zeta)\right) \tag{4.15c}$$

Then, the same 2D mapping function $\mathbf{N}(\eta,\zeta)$ used in Section 4.2.1 is adopted here for interpolating the two angles $\theta(\eta,\zeta)$ and $\varphi(\eta,\zeta)$ as,

$$\theta(\eta,\zeta) = \mathbf{N}(\eta,\zeta)\boldsymbol{\theta} \tag{4.16a}$$

$$\varphi(\eta,\zeta) = \mathbf{N}(\eta,\zeta)\boldsymbol{\varphi} \tag{4.16b}$$

where, $\boldsymbol{\theta}$ and $\boldsymbol{\varphi}$ are the vector of nodal angles on the boundary in spherical coordinates. Substituting Equation (4.15) into Equation (4.4) and (4.6) respectively yields the determinant of the Jacobian for the spherical subdomain:

$$|\mathbf{J}| = r_0^3 \sin\theta \cdot (\theta_{,\eta}\varphi_{,\zeta} - \theta_{,\zeta}\varphi_{,\eta}) \tag{4.17}$$

and the vectors $\mathbf{b}_1^a$, $\mathbf{b}_2^a$ and $\mathbf{b}_3^a$ are written as:

$$\mathbf{b}_1^a(\eta,\zeta) = \frac{1}{r_0} \begin{Bmatrix} \sin\theta\cos\varphi \\ \sin\theta\sin\varphi \\ \cos\varphi \end{Bmatrix} \tag{4.18a}$$

$$\mathbf{b}_2^a(\eta,\zeta) = \frac{r_0^2}{|\mathbf{J}|} \begin{Bmatrix} \varphi_{,\zeta}\sin\theta\cos\theta\cos\varphi + \theta_{,\zeta}\sin\varphi \\ \varphi_{,\zeta}\sin\theta\cos\theta\sin\varphi - \theta_{,\zeta}\cos\varphi \\ -\varphi_{,\zeta}\sin^2\varphi \end{Bmatrix} \tag{4.18b}$$

$$\mathbf{b}_3^a(\eta,\zeta) = -\frac{r_0^2}{|\mathbf{J}|} \begin{Bmatrix} \varphi_{,\eta}\sin\theta\cos\theta\cos\varphi + \theta_{,\eta}\sin\varphi \\ \varphi_{,\eta}\sin\theta\cos\theta\sin\varphi - \theta_{,\eta}\cos\varphi \\ -\varphi_{,\eta}\sin^2\theta \end{Bmatrix} \tag{4.18c}$$

The scaled boundary finite element equation in pressure amplitude presented in Equation (4.8) applies to both bounded and unbounded domains with the same

definition of all coefficient matrices $\mathbf{E}_0^a$, $\mathbf{E}_1^a$, $\mathbf{E}_2^a$ and $\mathbf{M}_0^a$. The only difference is the range of radial coordinates: $0 \leq \xi \leq 1$ for a bounded domain, while $\xi \geq 1$ for an unbounded domain. It should be noted that $\mathbf{b}_1^a$ is orthogonal to $\mathbf{b}_2^a$ and $\mathbf{b}_3^a$ respectively in Equation (4.18). Therefore, according to Equations (4.10) and (4.9b), $\mathbf{E}_1^a$ vanishes due to the orthogonality and the internal radial flux $\hat{\mathbf{Q}}(\xi)$ defined in Equation (4.11) for 3D acoustics can thus be simplified as:

$$\hat{\mathbf{Q}}(\xi) = \mathbf{E}_0^a \xi^2 \hat{\mathbf{p}}_e(\xi)_{,\xi} \tag{4.19}$$

The subscript 'e' in $\hat{\mathbf{p}}_e$ denotes the exterior acoustic domain. Substituting Equations (4.10a) and (4.18a) into Equation (4.9a) gives the expression of $\mathbf{E}_0^a$ for a spherical subdomain,

$$\mathbf{E}_0^a = \frac{1}{r_0^2} \int_{-1}^{+1} \int_{-1}^{+1} \mathbf{N}^T(\eta,\zeta)\mathbf{N}(\eta,\zeta)\, |\mathbf{J}(\eta,\zeta)|\, d\eta d\zeta \tag{4.20}$$

Comparing $\mathbf{E}_0^a$ and $\mathbf{M}_0^a$ defined in Equations (4.20) and (4.9d) yields the relationship between $\mathbf{E}_0^a$ and $\mathbf{M}_0^a$ in Equation (4.21)

$$\mathbf{M}_0^a = \left(\frac{r_0}{c}\right)^2 \mathbf{E}_0^a \tag{4.21}$$

The above Equations (4.14) - (4.21) are derived for the unbounded domain in 3D acoustic analysis in this section. The proportional relationships between $\mathbf{E}_0^a$ and $\mathbf{M}_0^a$ for 2D and 3D unbounded acoustic domains are the same by observing Equations (4.21) and (3.48). Now, for 3D unbounded acoustic domain, the scaled boundary finite element equation in pressure amplitude in Equation (4.8) can be simplified, using Equation (4.21) and vanishing $\mathbf{E}_1^a$ as

$$\mathbf{E}_0^a \xi^2 \hat{\mathbf{p}}_e(\xi)_{,\xi\xi} + 2\mathbf{E}_0^a \xi \hat{\mathbf{p}}_e(\xi)_{,\xi} - \mathbf{E}_2^a \hat{\mathbf{p}}_e(\xi) + a^2 \mathbf{M}_0^a \xi^2 \hat{\mathbf{p}}_e(\xi) = 0 \tag{4.22}$$

where$a$ is the same dimensionless frequency as defined in Equation (3.50).

4.3 Doubly-asymptotic open boundary for 3D unbounded acoustics

The derivations of high-order doubly asymptotic open boundary for 3D acoustics is discussed in this section. Analogous to the derivation of circular open boundary for 2D acoustics in Section 3.3. The scaled boundary finite element equation for unbounded acoustic domain in Equation (4.22) is firstly decoupled into a series of scalar equations for modal impedance coefficients of the 3D unbounded domain. These modal impedance coefficients can be solved via using doubly-asymptotic continued-fraction expansions (Prempramote et al., 2009). Comparing with singly-asymptotic continued-fraction expansion (Bazyar and Song, 2008), the doubly-asymptotic continued-fraction solution involves an extra continued-fraction approximation of the residual term at the low-frequency limit. This results in a more accurate and efficient estimation of the model impedance coefficients comparing with the singly-asymptotic one. In this section, the improved solutions in Section 3.3.2 from Chapter 3 is adopted for 3D problems via introducing the newly defined modal impedance and the shifted mode number. Comparing with the original doubly-asymptotic continued-fraction solution in (Prempramote et al., 2009), certain ill-conditions in the original solution is avoided in the improved solution. After obtaining the continued-fraction expansions for modal impedances, auxiliary variables and modal flux-pressure relationship are introduced to form global matrix formulation for time-domain analysis.

As described above, the scaled boundary finite element equation in pressure amplitude for an unbounded acoustic domain in Equation (4.22) is firstly decoupled using the same eigenvalue problem defined in Equations (3.51) - (3.52) from Section 3.3.1, but with the coefficient matrices $\mathbf{E}_0^a$ and $\mathbf{E}_2^a$ defined in Equations (4.20) and (4.9c) respectively. Pre- and post-multiplying Equation (4.22) by $\mathbf{\Psi}_\infty^T$ and $\mathbf{\Psi}_\infty$ respectively and utilizing Equation (3.52) yields the following partial differential

equations with the radial coordinate ξ and excitation frequency ω as independent variables. These partial differential equations for modal pressure amplitude $\tilde{\mathbf{P}}(\xi)$ can be defined the same as in Equation (3.54) with dimensionless excitation frequency a and the radial coordinate ξ as the independent variable,

$$\xi^2\tilde{\mathbf{P}}(\xi)_{,\xi\xi} + 2\xi\tilde{\mathbf{P}}(\xi)_{,\xi} - \mathbf{\Lambda}\tilde{\mathbf{P}}(\xi) + a^2\tilde{\mathbf{P}}(\xi) = 0 \tag{4.23}$$

Equation (4.23) can be written into a series of independent scalar equations in Equation (4.24) with $j = 1, 2, 3, \cdots, N_e$, N_e is the number of nodes on the spherical open boundary.

$$\xi^2\tilde{P}_j(\xi)_{,\xi\xi} + 2\xi\tilde{P}_j(\xi)_{,\xi} - \lambda_j^2\tilde{P}_j(\xi) + a^2\tilde{P}_j(\xi) = 0 \quad (j = 1, 2, \cdots, N_e) \tag{4.24}$$

Substituting Equation (4.19) for 3D unbounded domain into (3.56) yields,

$$\hat{\mathbf{R}}_e(\xi) = -\mathbf{E}_0^a\xi^2\hat{\mathbf{p}}_e(\xi)_{,\xi} \tag{4.25}$$

Pre-multiplying both sides of Equation (4.25) by $\mathbf{\Psi}_\infty^T$ and applying Equations (3.52a) and (3.54) results in,

$$\tilde{\mathbf{R}}(\xi) = -\xi^2\tilde{\mathbf{P}}(\xi)_{,\xi} \tag{4.26}$$

The modal flux $\tilde{\mathbf{R}}(\xi)$ in Equation (4.26) is defined in Equation (3.58). Again, Equation (4.26) can be written into a series of scalar equations as,

$$\tilde{R}_j(\xi) = -\xi^2\tilde{P}_j(\xi)_{,\xi} \tag{4.27}$$

with $j = 1, 2, 3, \cdots, N_e$ (the range of the subscript j is the same in the following equations of this section and not repeated). The relationship between modal flux $\tilde{R}_j(\xi)$ and modal pressure $\tilde{P}_j(\xi)$ can then be described by introducing the modal impedance coefficient $S_j(a)$ as in Equation (3.60). Substituting Equation (3.60) into (4.27) to eliminate model flux $\tilde{R}_j(\xi)$ yields,

$$-\xi^2\tilde{P}_j(\xi)_{,\xi} = S_j(a)\tilde{P}_j(\xi) \tag{4.28}$$

Differentiating Equation(4.28) with respect to ξ results in,

$$\xi^2 \tilde{P}_j(\xi)_{,\xi\xi} + 2\xi \tilde{P}_j(\xi)_{,\xi} + S_j(a)\tilde{P}_j(\xi)_{,\xi} + S_j(a)_{,\xi}\tilde{P}_j(\xi) = 0 \tag{4.29}$$

Replacing $\tilde{P}_j(\xi)_{,\xi}$ in the third term in Equation (4.29) with $\tilde{P}_j(\xi)$ using Equation (4.28) gives:

$$\xi^2 \tilde{P}_j(\xi)_{,\xi\xi} + 2\xi \tilde{P}_j(\xi)_{,\xi} - \frac{S_j^2(a)}{\xi^2}\tilde{P}_j(\xi) + S_j(a)_{,\xi}\tilde{P}_j(\xi) = 0 \tag{4.30}$$

Substituting Equation (4.30) into (4.24) and eliminating the modal pressure $\tilde{P}_j(\xi)$ yields,

$$\frac{S_j^2(a)}{\xi^2} - S_j(a)_{,\xi} + a^2 - \lambda_j^2 = 0 \tag{4.31}$$

Introducing the intermediate variable $\widetilde{S}_j(a) = \frac{S_j(a)}{\xi}$, Equation (4.31) can be written into,

$$\left(\widetilde{S}_j(a)\right)^2 - \left(\xi \widetilde{S}_j(a)\right)_{,\xi} + a^2 - \lambda_j^2 = 0 \tag{4.32}$$

Evaluating the partial differentiation term in Equation (4.32) and changing the independent variable ξ to a using its definition in Equation(3.50) yields,

$$\left(\widetilde{S}_j(a)\right)^2 - \widetilde{S}_j(a) - a\widetilde{S}_j(a)_{,a} + a^2 - \lambda_j^2 = 0 \tag{4.33}$$

On the spherical boundary with $\xi = 1$, the dimensionless frequency $a(\xi = 1) = a_0 = \frac{\omega r_0}{c}$ from Equation (3.62), and the intermediate variable $\widetilde{S}_j(a_0) = S_j(a_0)$. The following scaled boundary finite element equation for modal impedance on the boundary of unbounded acoustic domain can be obtained,

$$S_j^2(a_0) - S_j(a_0) - a_0 S_j(a_0)_{,a_0} + a_0^2 - \lambda_j^2 = 0 \tag{4.34}$$

In order to simplify the implementation of this doubly-asymptotic open boundary in 3D, $S_j(a_0)$ can be solved using the same continued-fraction expansions for 2D acoustics in Section 3.3.2. The ordinary differential equation (4.34) for 3D case is

transformed into the following form:

$$\left(\bar{S}_j(a_0)\right)^2 - a_0\bar{S}_j(a_0)_{,a_0} + a_0^2 - \left(\bar{\lambda}_j\right)^2 = 0 \tag{4.35}$$

with $\bar{S}_j(a_0)$ and $\bar{\lambda}_j$ defined as:

$$\bar{S}_j(a_0) = S_j(a_0) - 0.5 \tag{4.36a}$$

$$\left(\bar{\lambda}_j\right)^2 = \lambda_j^2 + 0.5^2 \tag{4.36b}$$

Equation (4.35) is mathematically identical to the differential equation expressed in Equation (3.61) in Section 3.3.1 for solving the modal impedance coefficient of a two-dimensional unbounded acoustic domain with a circular boundary. Then, the same strategy used in Section 3.3.2 for the improved doubly-asymptotic continued-fraction solution can be employed here to calculate $\bar{S}_j(a_0)$ from Equation (4.35). To this end, all λ_j and $S_j(a_0)$ in Equations (3.63)-(3.92) from Section 3.3.2 can be replaced by $\bar{\lambda}_j$ and $\bar{S}_j(a_0)$ respectively. The singly-asymptotic continued fraction can be expressed by:

$$\bar{S}_j(a_0) = K_\infty + \mathrm{i}a_0C_\infty - \cfrac{\left(\psi^{(1)}\right)^2}{Y_0^{(1)} + \mathrm{i}a_0Y_1^{(1)} - \cfrac{\left(\psi^{(2)}\right)^2}{\cdots - \cfrac{\left(\psi^{(M_H)}\right)^2}{Y_0^{(M_H)} + \mathrm{i}a_0Y_1^{(M_H)}}}} \tag{4.37}$$

while the doubly-asymptotic continued fraction is:

$$\begin{aligned}\bar{S}_j(a_0) &= K_\infty + \mathrm{i}a_0C_\infty \\ &- \cfrac{\left(\psi^{(1)}\right)^2}{Y_0^{(1)} + \mathrm{i}a_0Y_1^{(1)} - \cfrac{\left(\psi^{(2)}\right)^2}{\cdots - \cfrac{\left(\psi^{(M_H)}\right)^2}{Y_0^{(M_H)} + \mathrm{i}a_0Y_1^{(M_H)} - \cfrac{\left(\psi_L^{(0)}\right)^2}{Y_{L0}^{(0)} + \mathrm{i}a_0Y_{L1}^{(0)} \cfrac{(\mathrm{i}a_0)^2}{Y_{L0}^{(1)} + \mathrm{i}a_0Y_{L1}^{(1)} - \cfrac{(\mathrm{i}a_0)^2}{\cdots - \cfrac{(\mathrm{i}a_0)^2}{Y_{L0}^{(M_L)} + \mathrm{i}a_0Y_{L1}^{(M_L)}}}}}}}\end{aligned} \tag{4.38}$$

The procedures for applying singly- and doubly-asymptotic expansions at the end of Section 3.3.2 for 2D open boundary can be written for the 3D case by considering Equation (4.36b) as:

- choose orders M_H and M_L of continued-fraction expansion,
- approximate all modes corresponding to $\sqrt{\lambda_j^2 + 0.5^2} \leq M_H + 1$ by singly-asymptotic expansions of order M_H,
- approximate all modes corresponding to $\sqrt{\lambda_j^2 + 0.5^2} > M_H + 1$ by doubly-asymptotic expansions of orders M_H, M_L.

Once the continued-fraction expansion in Equation (4.37) or (4.38) for $\bar{S}_j(a_0)$ is obtained, the modal impedance coefficient $S_j(a_0)$ on the spherical boundary of 3D acoustic unbounded domain can be obtained by simply adding 0.5 to $\bar{S}_j(a_0)$ according to Equation (4.36a).

4.4 Time-domain formulation for 3D acoustics

Based on the same approach in Section 3.3.3, the modal flux-pressure relationship in the frequency domain in Equation (3.60) with the continued-fraction expansion of model impedance of unbounded domain $S_j(a_0)$ can be transformed to time domain equations. Substituting Equations (3.63) and (4.36a) into Equation (3.60) yields:

$$\begin{aligned}\tilde{R}_j = S_j(a_0)\tilde{P}_j &= \left(0.5 + \overline{S}_j(a_0)\right)\tilde{P}_j \\ &= \left(0.5 + K_\infty\right)\tilde{P}_j + \mathrm{i}a_0 C_\infty \tilde{P}_j - \left(\psi_j^{(i)}\right)^2 \left(Y_j^{(1)}(a_0)\right)^{-1}\tilde{P}_j. \quad (4.39)\end{aligned}$$

Values of constant coefficients K_∞ and C_∞ from Equations (3.65a) and (3.65b) respectively are substituted in Equation (4.39). Then, introducing the first auxiliary variable $\tilde{P}_j^{(1)}$ in Equation (3.95) yields,

$$\tilde{R}_j = \tilde{P}_j + \mathrm{i}a_0\tilde{P}_j - \psi_j^{(1)}\tilde{P}_j^{(1)}, \quad (4.40)$$

Utilizing the definition of $\tilde{\mathbf{R}}_j$ in Equation (3.58) and (4.40), the amplitude of the nodal flux vector is expressed as

$$\hat{\mathbf{R}}_e = \boldsymbol{\Psi}_\infty^{-T}\tilde{\mathbf{P}} + \mathrm{i}a_0\boldsymbol{\Psi}_\infty^{-T}\tilde{\mathbf{P}} - \boldsymbol{\Psi}_\infty^{-T}\boldsymbol{\psi}^{(1)}\tilde{\mathbf{p}}^{(1)}. \quad (4.41)$$

Substituting Equations (3.54) and (3.52a) into Equation (4.41), this equation can be reformulates as

$$\hat{\mathbf{R}}_e = \mathbf{E}_0^a \hat{\mathbf{p}}_e + \mathrm{i}a_0 \mathbf{E}_0^a \hat{\mathbf{p}}_e - \boldsymbol{\Psi}_\infty^{-T} \boldsymbol{\psi}^{(1)} \tilde{\mathbf{p}}^{(1)}, \tag{4.42}$$

Next, following exactly the same procedures described by Equations (3.98) - (3.112) in Section 3.3.3 for 2D doubly-asymptotic open boundary, the system of first-order equations for 3D doubly-asymptotic open boundary can also be formulated as follow:

$$\mathbf{K}_e^a \mathbf{z}(t) + \mathbf{C}_e^a \dot{\mathbf{z}}(t) = \mathbf{r}_e(t) \tag{4.43}$$

with the high-order damping matrix $\mathbf{C}_e^a$, vector of unknown $\mathbf{z}(t)$ and right-hand side vector $\mathbf{r}_e(t)$ expressed the same as in Equations (3.110), (3.113) and (3.114) respectively but with coefficients calculated in 3D case. The high-order stiffness matrix $\mathbf{K}_e^a$ in 3D is slightly different from its 2D expression in Equation (3.109) and given by

$$\mathbf{K}_e^a = \begin{bmatrix}
\mathbf{E}_0^a & -\boldsymbol{\Psi}_\infty^{-T}\boldsymbol{\psi}^{(1)} & & & & & & & \\
-\boldsymbol{\psi}^{(1)}\boldsymbol{\Psi}_\infty^{-1} & \mathbf{Y}_0^{(1)} & -\boldsymbol{\psi}^{(2)} & & & & & & \\
 & -\boldsymbol{\psi}^{(2)} & \ddots & \ddots & & & & & \\
 & & \ddots & \mathbf{Y}_0^{(M_H)} & -\boldsymbol{\psi}_L^* & & & & \\
 & & & -[\boldsymbol{\psi}_L^*]^T & \mathbf{Y}_{L0}^{(0)} & 0 & & & \\
 & & & & 0 & \mathbf{Y}_{L0}^{(1)} & \ddots & & \\
 & & & & & \ddots & \ddots & 0 & \\
 & & & & & & 0 & \mathbf{Y}_{L0}^{(M_L)}
\end{bmatrix} \tag{4.44}$$

with the diagonal matrices $\boldsymbol{\psi}^{(i_H)}$ and the rectangular matrix $\boldsymbol{\psi}_L^*$ given in Equation (3.111). For 3D expressions, the lower partition $\boldsymbol{\psi}_L^{(0)}$ in Equation (3.111) is a diagonal matrix with diagonal terms $\psi_{L,j}^{(0)}$ for all modes with $\sqrt{\lambda_j^2 + 0.5^2} > M_H + 1$.

The coupling of acoustic near field and far field is performed along the spherical

interface Γ in Figure 4.1(a). Therefore, Equation (4.13) is firstly divided into three parts corresponding to the nodes inside the spherical interface, nodes on the interface and auxiliary variables as in Equation (3.115). Substituting the first block row of Equation (4.43) into (3.115) and rearranging all terms related to acoustic pressures and auxiliary variables to the left-hand-side yields the following global second-order differential equations for the coupled bounded and unbounded 3D acoustic domains:

$$\mathbf{M}_G^a \ddot{\mathbf{z}}_G(t) + \mathbf{C}_G^a \dot{\mathbf{z}}_G(t) + \mathbf{K}_G^a \mathbf{z}_G(t) = \mathbf{r}_G(t) \tag{4.45}$$

with the global vector of unknowns $\mathbf{z}_G(t)$, global flux vector $\mathbf{r}_G(t)$, global mass $\mathbf{M}_G^a$ and global damping matrices $\mathbf{C}_G^a$ defined in Equations (3.117) - (3.120), respectively. The expression for the global stiffness matrix $\mathbf{K}_G^a$ in 3D is slightly different from its 2D form. This is due to the difference between Equations (3.109) and (4.44) for the high-order stiffness matrix of 2D and 3D unbounded domains $\mathbf{K}_e^a$. In 3D acoustic, $\mathbf{K}_G^a$ is thus given by:

$$
\mathbf{K}_G^a = \left[\begin{array}{cc|ccc|ccccccc}
\mathbf{K}_{bb} & \mathbf{K}_{be} & 0 & \cdots & 0 & 0 & \cdots & 0 & 0 & 0 & \cdots & 0 \\
\mathbf{K}_{be}^T & \mathbf{K}_{ee}+\mathbf{E}_0^a & 0 & \cdots & 0 & -\boldsymbol{\Psi}_\infty^{-T}\boldsymbol{\psi}^{(1)} & \cdots & 0 & 0 & 0 & \cdots & 0 \\
\hline
0 & 0 & \mathbf{S}_{a0}^{(1)} & \cdots & 0 & 0 & \cdots & 0 & 0 & 0 & \cdots & 0 \\
\vdots & \vdots & \vdots & \ddots & \vdots & \vdots & \ddots & \vdots & \vdots & \vdots & \ddots & \vdots \\
0 & 0 & 0 & \cdots & \mathbf{S}_{a0}^{(M)} & 0 & \cdots & 0 & 0 & 0 & \cdots & 0 \\
\hline
0 & -\boldsymbol{\psi}^{(1)}\boldsymbol{\Psi}_\infty^{-1} & 0 & \cdots & 0 & \mathbf{Y}_0^{(1)} & -\boldsymbol{\psi}^{(2)} & & & & & \\
\vdots & \vdots & \vdots & \ddots & \vdots & -\boldsymbol{\psi}^{(2)} & \ddots & \ddots & & & & \\
0 & 0 & 0 & \cdots & 0 & & \ddots & \mathbf{Y}_0^{(M_H)} & -\boldsymbol{\psi}_L^* & & & \\
0 & 0 & 0 & \cdots & 0 & & & -\left[\boldsymbol{\psi}_L^*\right]^T & \mathbf{Y}_{L0}^{(0)} & 0 & & \\
0 & 0 & 0 & \cdots & 0 & & & & 0 & \mathbf{Y}_{L0}^{(1)} & \ddots & \\
\vdots & \vdots & \vdots & \ddots & \vdots & & & & & \ddots & \ddots & 0 \\
0 & 0 & 0 & \cdots & 0 & & & & & & 0 & \mathbf{Y}_{L0}^{(M_L)}
\end{array}\right] \tag{4.46}
$$

Then, the global Equation (4.45) can be solved using standard time-stepping method. Newmark's method is employed in Section 4.5 to obtain the time-domain solutions.

4.5 Numerical examples

In this section, four numerical examples in 3D acoustics are studied to demonstrate the accuracy, robustness and efficiency of the proposed method. In all the numerical examples presented in this chapter, the non-viscous fluid is assumed to have a sound velocity c and density ρ. In Section 4.5.1, a spherical cavity inside an infinite acoustic space is studied for verifying the implementation of present method. Then, Section 4.5.2 presents a 3D open structure with the flux applied on the inner surface to test the accuracy of proposed SBFEM for modelling the wave reflections inside the cavity and radiation from the outlet. In the last two examples in Sections 4.5.3 and 4.5.4, the wave propagation around more complicated structures, including a 3D human external ear and an ancient Chinese bell in the air, are simulated using SBFEM to demonstrate the possible applications of this present approach to acoustic problems with complex geometries. All SBFEM meshes of these examples are generated automatically from the input STL models of the cavities. Newmark's method with $\alpha = 0.5$ and $\beta = 0.25$ (average acceleration scheme) is applied to Equation(4.45) for all time-domain analyses. To provide reference solutions, the first two numerical examples are also modeled by the commercial software ANSYS using an extended mesh of finite elements. The boundary of each finite element model in ANSYS is sufficiently far away from the investigated bounded domain to avoid reflected waves reaching the bounded domain.

4.5.1 Spherical cavity subject to transient flux on entire boundary

As an initial verification of the implementation of the proposed method, an infinite acoustic space with a spherical cavity as shown in Figure 4.4 is addressed. The surface of the spherical cavity Γ has a radius of r_0 shown as the smaller sphere in Figure 4.4, while the spherical open boundary is represented by a translucent spherical shell with the radius of $r_1 = 2r_0$. The acoustic medium between the cavity and open boundary is modeled as a bounded domain and the medium exterior to the open boundary is modeled as an unbounded domain. In this example, the transient flux applied to the spherical boundary Γ is given in the equation below:

$$\frac{\partial \bar{p}}{\partial \vec{\mathbf{n}}}(\theta, \varphi, t) = h_i(\theta, \varphi) f_s(t). \tag{4.47}$$

where $h_i(\theta, \varphi)$ describes the spatial variation of the applied flux with the polar angle θ and azimuthal angle φ as defined in Equation(4.15) Section 4.2.2. Three spatial variations of flux ($i = 1, 2, 3$) on the spherical cavity are considered:

$$h_1(\theta, \varphi) = 1 \tag{4.48a}$$

$$h_2(\theta, \varphi) = \cos\theta \tag{4.48b}$$

$$h_3(\theta, \varphi) = 3\cos^2\theta - 1 \tag{4.48c}$$

$f_s(t)$ is a time-dependent function non-dimensionalized by its peak value F_{st} and plotted in Figure 4.5(a) with the dimensionless time $t\frac{c}{r_0}$. Its corresponding Fourier transform is shown in Figure 4.5(b).

For a 3D acoustic analysis, the recently developed automatic mesh generation technique based on octree decomposition for SBFEM by Liu et al. (Liu et al., 2017) is integrated here for automatic and efficient mesh generation. The STL model containing the spherical cavity and the spherical open boundary is shown in Figure 4.4. This STL model is used as the geometrical input for mesh generation of SBFE mesh.

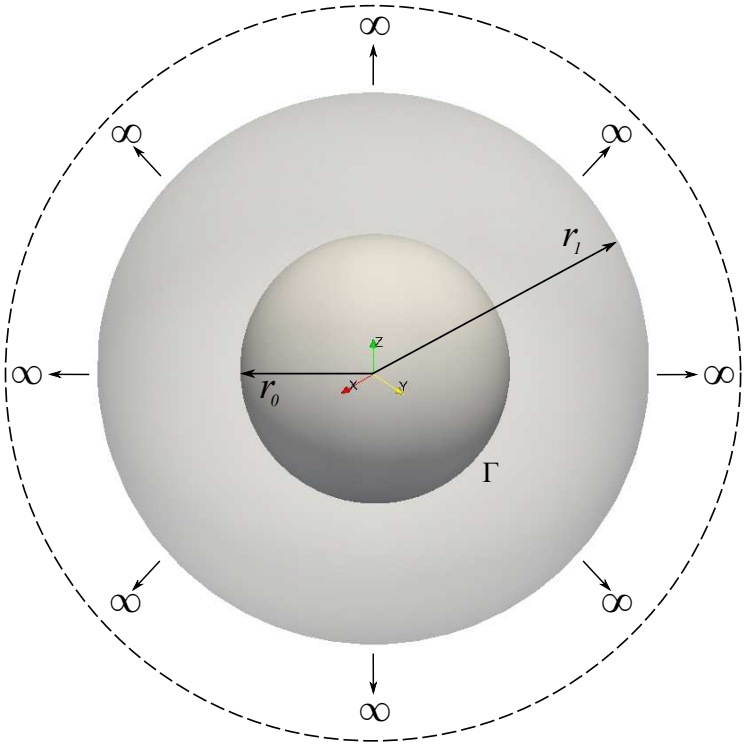

Figure 4.4. Geometry of spherical cavity model.

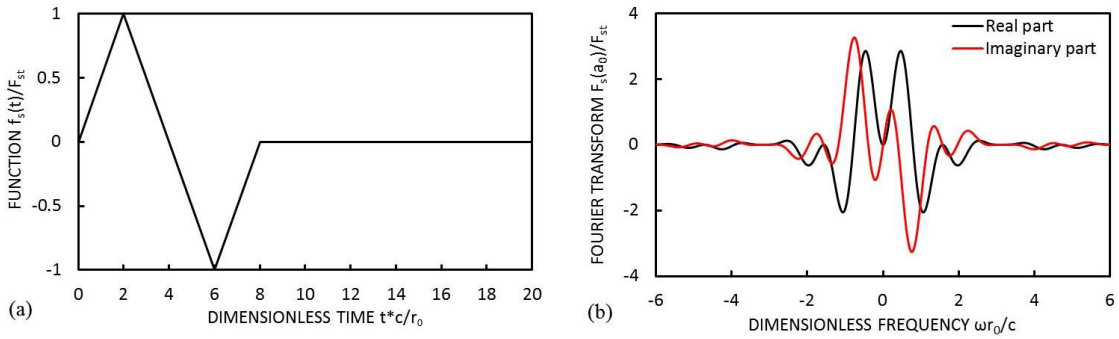

Figure 4.5. Time variation $f_s(t)$ of transient flux applied to entire spherical boundary: (a) time history and (b) Fourier transform.

According to Figure 4.5(b), the maximum dimensionless frequency of interest is approximately $a_{0,max} = 4$. Therefore, the shortest wave length can be calculated from Equation (3.124) as $\lambda_{min} = \frac{2\pi}{4} r_0 \approx 1.57 r_0$. In order to guarantee the accuracy of the time-domain analysis, the maximum cell size in the octree grid is set to be $0.156 r_0$, which provides at least 10 nodes per shortest wavelength. The automatically generated mesh is illustrated in Figure 4.6 with the outer view in Figure 4.6(a) showing the trimmed octree mesh of spherical surface. The mesh is also cut in half

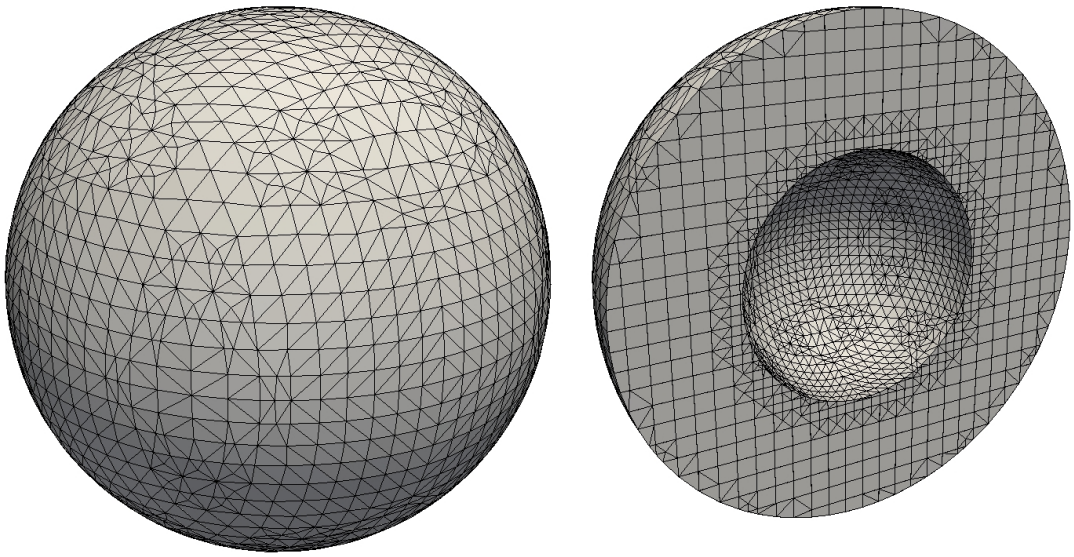

(a) (b)

Figure 4.6. The SBFEM mesh of spherical cavity model: (a) view of the outer surface of the mesh (b) view of half of the mesh with interior details.

in Figure 4.6(b) to show the interior of the mesh. The octree cells around the inner spherical cavity in Figure 4.6(b) is further divided into smaller cells automatically with the size of $0.078r_0$ to accurately represent the geometry of the smaller inner spherical surface. The spherical unbounded domain includes all surface elements on the outer spherical surface and its scaling centre is located at the centroid of the sphere.

Due to the use of 3-node triangular or 4-node quadrilateral elements as the surface elements for each octree cell in the bounded domain, the octree cells are relatively small and can thus sufficiently represent the shortest wavelength. As a result, the orders of continued-fraction expansion for cells in bounded domain are all set to be $M = 0$. In other words, only low-frequency expansion of impedance matrix for each bounded cell is adopted. The high order mass and stiffness matrices $\mathbf{M}_h^a$ and $\mathbf{K}_h^a$ for bounded domain in Equation (3.38) are reduced to:

$$\mathbf{M}_h^a = \mathbf{M}_a \tag{4.49a}$$

$$\mathbf{K}_h^a = \mathbf{K}_a \tag{4.49b}$$

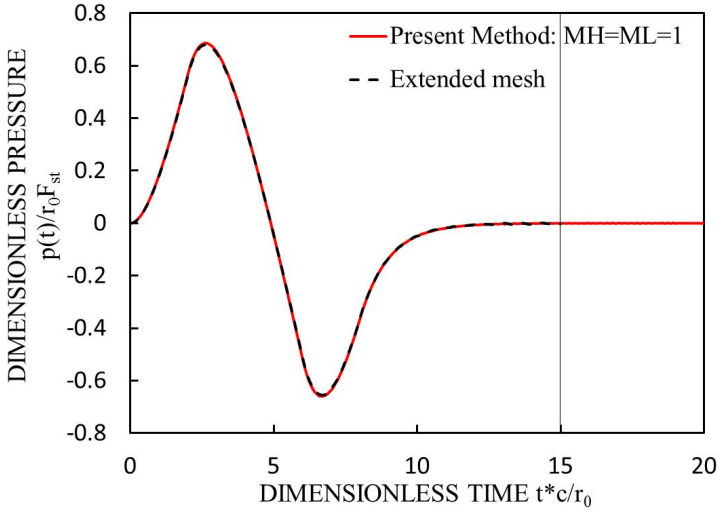

Figure 4.7. Dimensionless pressure response of spherical cavity subject to transient flux with spacial variation $h_1(\theta, \varphi)$.

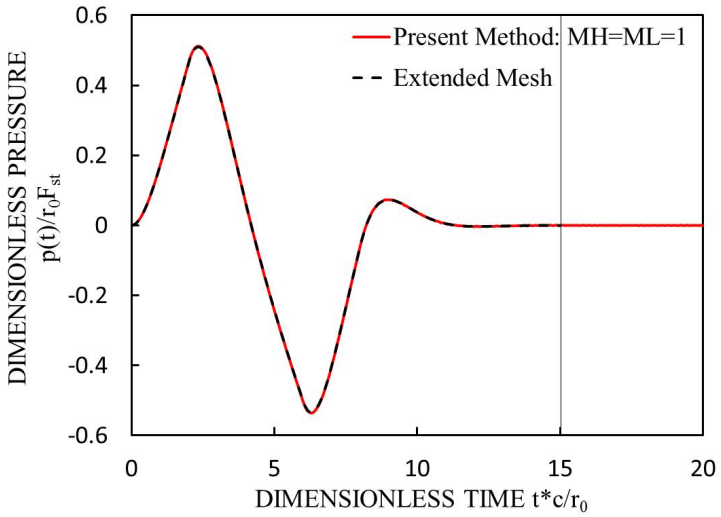

Figure 4.8. Dimensionless pressure response of spherical cavity subject to transient flux with spacial variation $h_2(\theta, \varphi)$.

The time-domain solutions of this problem are calculated by Newmark's method with a fixed time step of $\Delta t = 0.1\frac{r_0}{c}$ for all applied fluxes $\frac{\partial \bar{p}}{\partial \vec{\mathbf{n}}}$ defined in Equation (4.47) with the spacial variation $h_i(\theta, \varphi)$ with $i = 1, 2, 3$ in Equation (4.48). This choice of Δt provides at least 15 time steps per period at the highest frequency of interest. The pressure variations for all three types of flux during the first $t = 20r_0/c$ at the intersection point between spherical cavity and z-axis with the coordinate of $(0, 0, 1)$ are plotted in Figures 4.7-4.9 respectively in red solid lines.

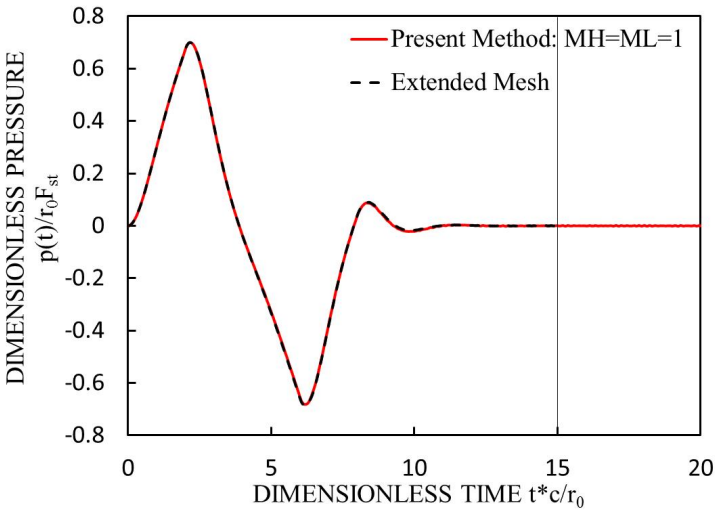

Figure 4.9. Dimensionless pressure response of spherical cavity subject to transient flux with spacial variation $h_3(\theta, \varphi)$.

The orders of high and low frequency continued-fraction expansions for the spherical open boundary is set as $M_H = M_L = 1$ in this analysis. Again, the vertical axes are non-dimensionalized by $r_0 F_{st}$ and the horizontal axes indicate the dimensionless time tc/r_0. The same problem with extended finite element mesh is built in ANSYS for verification. In the extended mesh in ANSYS, 4-nodes tetrahedral elements is employed with minimum edge length of $0.075r_0$ around cavity and maximum edge length of $0.15r_0$ for accuracy. The truncated spherical boundary in the extended mesh is located at $r = 9r_0$ to avoid any reflected waves polluting the interested region between $r_0 \leq r \leq r_1$ during the time t between 0 to $15r_0/c$. The converged reference solutions from the extended mesh model at the same points are illustrated in Figures 4.7 - 4.9 with black dash lines and match the results from the SBFEM model very well.

4.5.2 Wave radiation from a 3D open structure

For the further investigation of the accuracy of proposed SBFEM in 3D acoustic analysis, an open structure submerged in infinite acoustic space is studied in this section. The open structure is a rigid hollow sphere with one quarter missing as

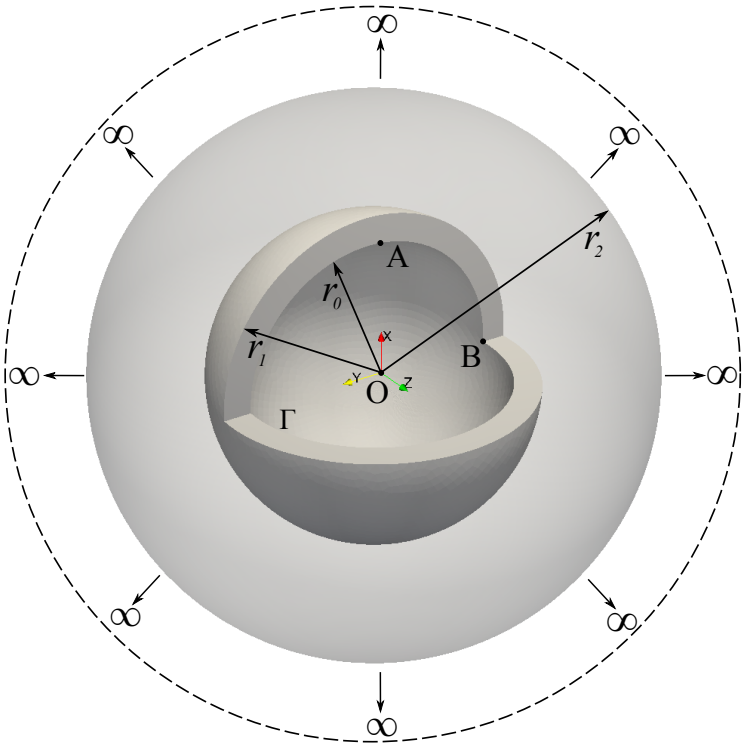

Figure 4.10. Geometry of 3D open sphere structure model.

shown in Figure 4.10. r_0 and r_1 are the inner and outer radii of the open hollow sphere with $r_1 = 1.2r_0$. The translucent spherical shell with the radius of $r_2 = 2r_0$ is the spherical open boundary for representing the unbounded domain. The entire inner surface of the open structure Γ is uniformly subjected to the same transient flux $f_s(t)$ defined by Figure 4.5(a) in Section 4.5.1.

The inner radius of the open structure and the radius of the open boundary in this numerical example are equal to the radii of spherical cavity and open boundary of the example in Section 4.5.1, respectively. Therefore, the maximum and minimum octree cell sizes for meshing this acoustic domain are chosen to be the same as those used in Section 4.5.1 and they are equal to $0.156r_0$ and $0.078r_0$ respectively. The SBFEM mesh is automatically generated and shown in Figures 4.11 and 4.12. Figure 4.11 illustrates the outer surface of the spherical open boundary and Figure 4.12 shows the details of the interior of the mesh by cutting the octree mesh in half along x-y and x-z planes respectively. Smaller cell size is used around the open structure to accurately represent the geometry. Similar to the SBFEM mesh in the previous

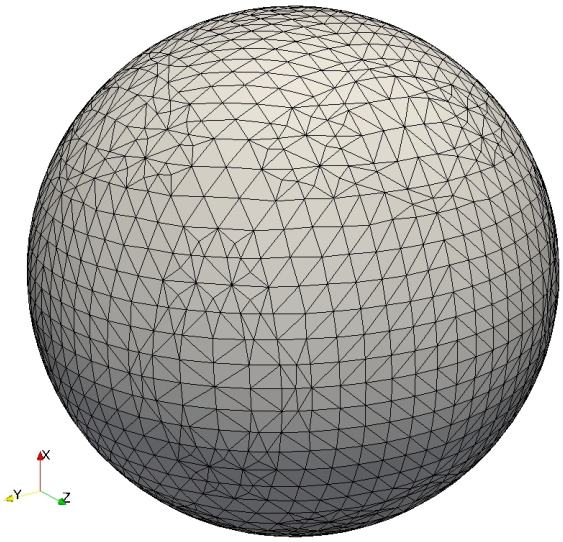

Figure 4.11. The SBFEM mesh of 3D open structure model - the view of outer surface.

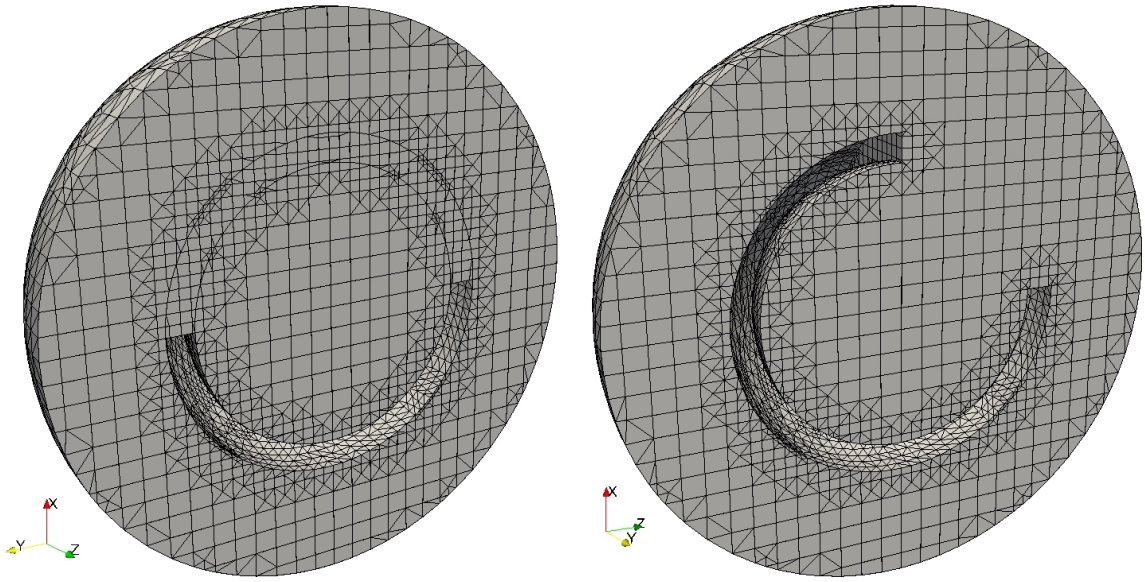

(a) (b)

Figure 4.12. Half of SBFEM mesh of 3D open structure model: (a) view from +z direction and (b) view from +y direction.

example in Section 4.5.1, 3-node triangular and 4-node quadrilateral elements are used as the surface elements for each polyhedral subdomains in the SBFEM mesh. The orders of continued-fraction expansion for cells in bounded domain are all set to be $M = 0$ and the orders of high and low frequency continued-fraction expansions for open boundary is again chosen as $M_H = M_L = 1$.

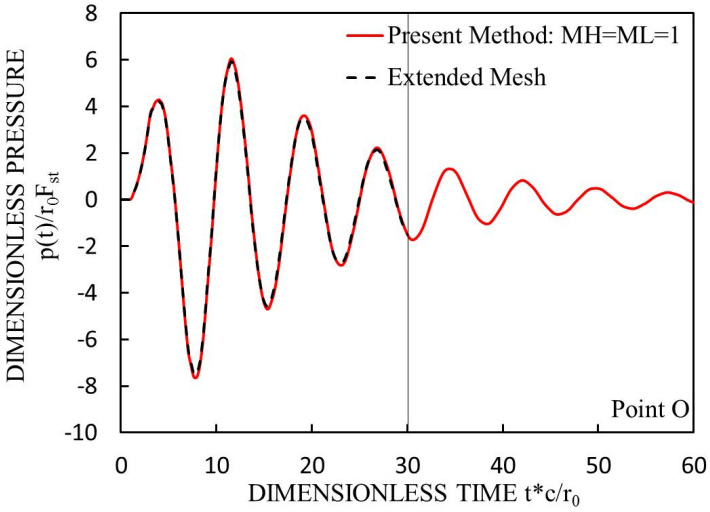

Figure 4.13. Dimensionless pressure response of 3D open structure model at point O.

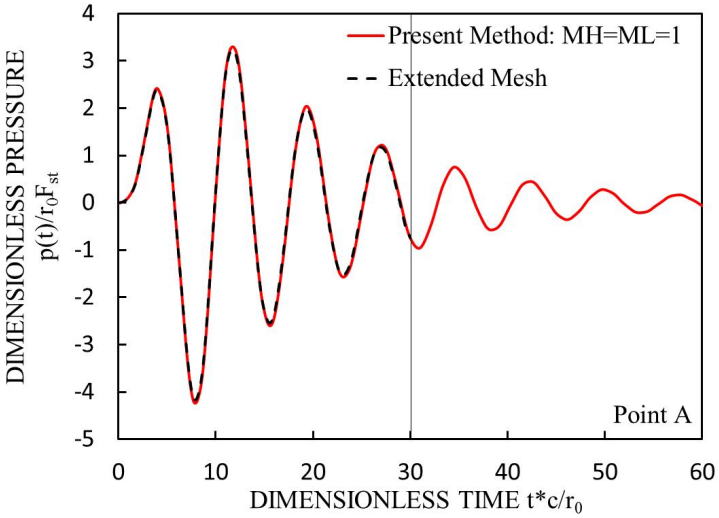

Figure 4.14. Dimensionless pressure response of 3D open structure model at point A.

Newmark's method with a time step of $\Delta t = 0.1r_0/c$ is again applied to Equation (4.45). The transient solutions are obtained during the time between 0 to $60r_0/c$. For verifying the solution obtained using SBFEM, a FEM extended mesh in ANSYS is built for the same problem to calculate the reference solutions. The 4-node tetrahedral element is again used in FEM model with minimum edge length of $0.075r_0$ around cavity and maximum edge length of $0.15r_0$ for accuracy. The truncated spherical boundary of the extended mesh has a radius of $r = 18r_0$. Points $\mathrm{O}(0, 0, 0)$,

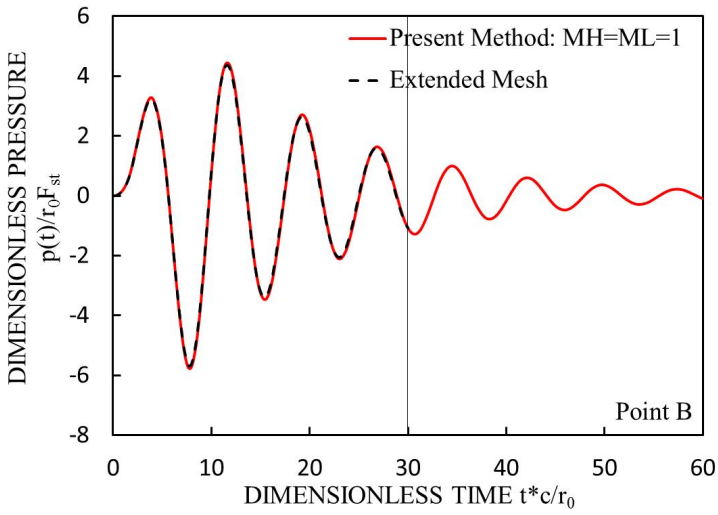

Figure 4.15. Dimensionless pressure response of 3D open structure model at point B.

A$(r_0, 0, 0)$ and B$(0, -r_0, 0)$ are marked in Figure 4.10. Results of the dimensionless pressure $p(t)/r_0F_{st}$ at points O, A and B versus dimensionless time tc/r_0 are plotted as red solid lines in Figures 4.13, 4.14 and 4.15 respectively. The reference solutions from ANSYS are shown by the black dash lines up to the time $30r_0/c$ before the reflected waves reach the observation points. Very good agreements are observed. Additionally, the dimensionless pressure contour plots calculated by SBFEM at times $t\frac{c}{r_0} = 4$, 8, 12, 16 are plotted in Figure 4.16.

4.5.3 Sound propagation around human external ear

The modeling of sound wave propagation around ear is of great significance in various research areas and engineering applications such as sound transmission in the human ear (Volandri et al., 2014)(De Greef et al., 2017), binaural recording (Hammershøi and Møller, 2002)(Paul, 2009) and treatments for hearing loss (Qi et al., 2006). In this example, a human external ear model in infinite air space is subjected to a near field acoustic flux and simulated using the proposed SBFEM. The original STL model of a human right external ear is obtained from Reference (szczehoo, 2014). The STL model is shown in Figure 4.17 with two different views. The sound speed

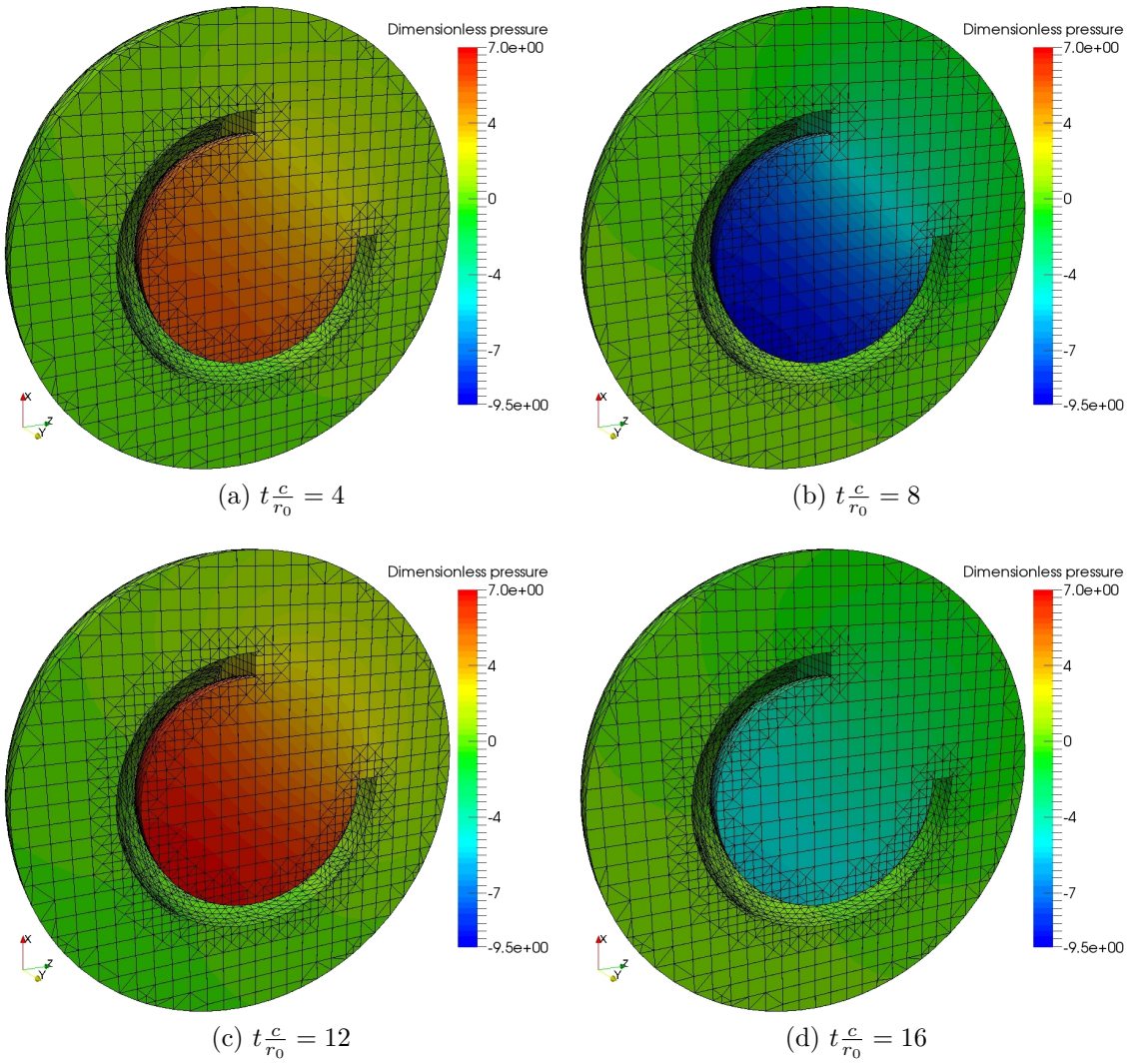

(a) $t\frac{c}{r_0} = 4$ (b) $t\frac{c}{r_0} = 8$

(c) $t\frac{c}{r_0} = 12$ (d) $t\frac{c}{r_0} = 16$

Figure 4.16. 3D open structure. Pressure contour obtained using the proposed SBFEM at: (a) $t\frac{c}{r_0} = 4$, (b) $t\frac{c}{r_0} = 8$, (c) $t\frac{c}{r_0} = 12$ and (d) $t\frac{c}{r_0} = 16$.

in the air is assumed to be $c = 340$m/s.

The system is divided into a bounded domain and an unbounded domains as shown in Figure 4.18. The translucent spherical shell indicates the spherical open boundary with a radius of 6cm, while the model of human external ear is assumed to be rigid and placed inside. It should be noticed that the coordinate axes plotted in the left-bottom of all figures in this example only indicates the orientation of the presented 3D model but not the actual position of the x, y and z axes of Cartesian coordinates. The actual origin of coordinates coincides with the centroid of the translucent spherical shell. The induced flux in the bounded domain is uniformly

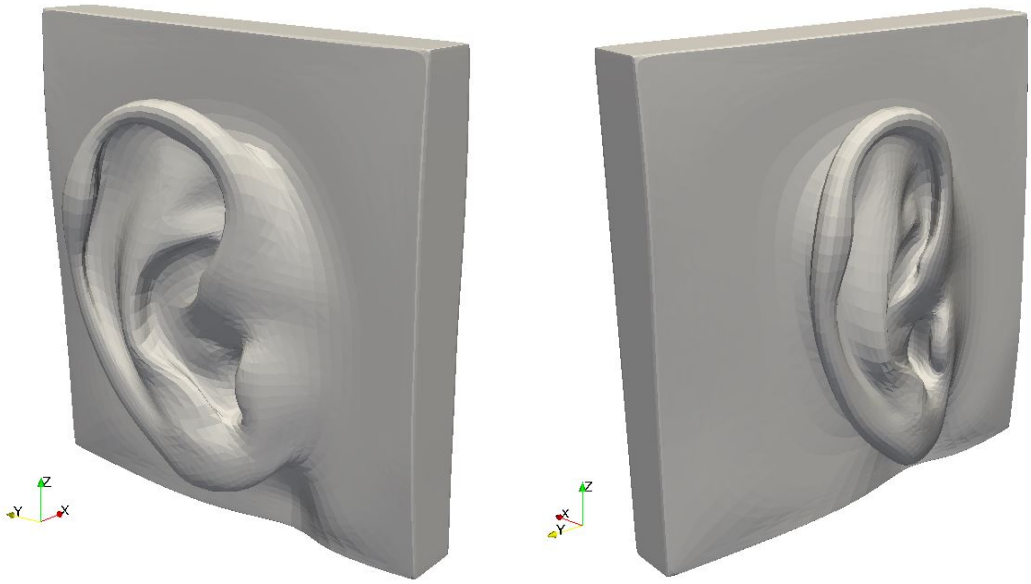

(a) (b)

Figure 4.17. Human external ear STL model: (a) view from the front of ear and (b) view from the back of ear.

applied on a surface indicated by the red squire in Figure 4.18. The red square with the edge length of 2.5cm is parallel to y-z plane and its centroid is located at $(-3.59\text{cm}, 0.16\text{cm}, 0.16\text{cm})$. The time history of the applied transient flux is defined by:

$$f_{ear}(t) = \begin{cases} 10^6 \times (1 - \cos 8\pi t) \left({}^{\text{kg}}/_{(\text{cm}\cdot\text{ms})^2}\right) & \text{when } 0 \leq t \leq 0.25\text{ms}, \\ 0 \qquad\qquad\qquad\qquad \left({}^{\text{kg}}/_{(\text{cm}\cdot\text{ms})^2}\right) & \text{when } 0.25\text{ms} < t. \end{cases} \tag{4.50}$$

$f_{ear}(t)$ is plotted in Figure 4.19(a) with its Fourier transform in Figure 4.19(b). The maximum frequency of interest is estimated at $\omega_{0,max} = 40\text{rad/ms}$. Therefore, the shortest wave length is approximately $\lambda_{min} \approx 5.3\text{cm}$. For generating the octree mesh of the coupled system, the maximum cell size is set to be 0.625cm, which provides about 9 nodes per shortest wave length. 3-node triangular elements or 4-node quadrilateral elements are used on the boundary of each cell. Furthermore, the minimum octree cell size is set to be 0.15625cm ($\frac{1}{4}$ of the maximum cell size) around the ear model to accurately describe the complex geometrical details of the human ear. Then, the meshing process is automatically completed and the final

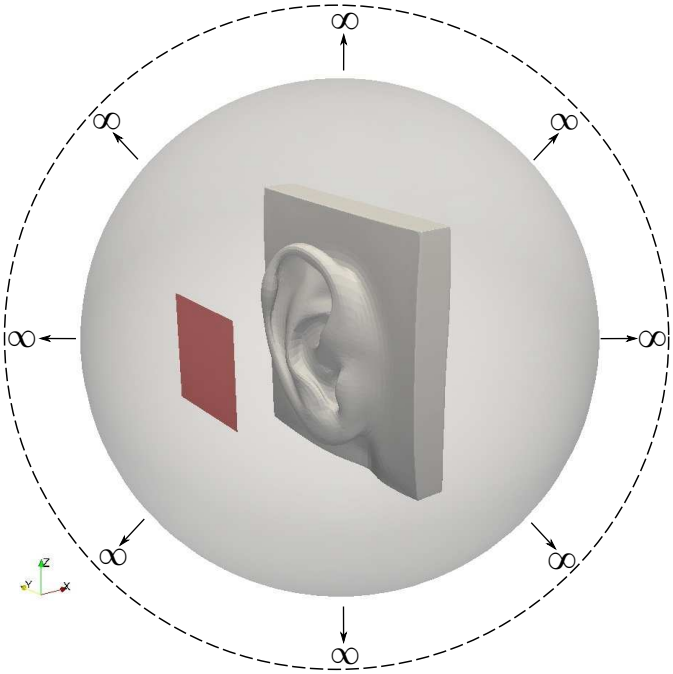

Figure 4.18. The coupled SBFE model for human external ear in infinite space.

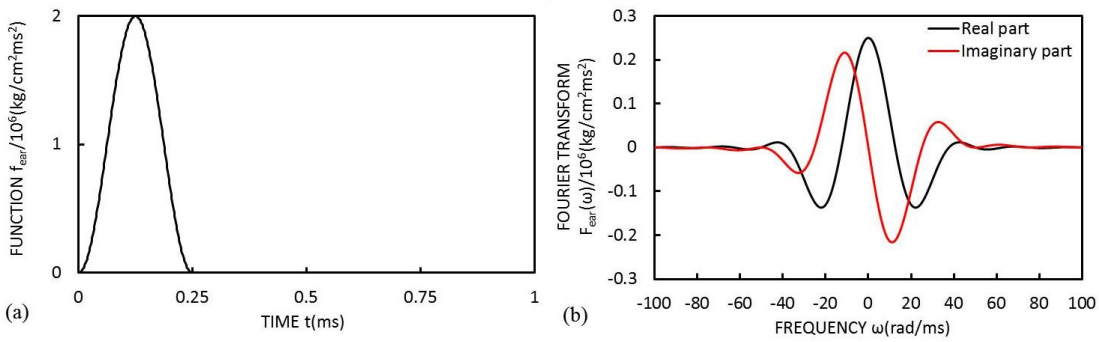

Figure 4.19. Time variation $f_{ear}(t)$ of transient flux applied in the acoustic near field of ear model: (a) time history and (b) Fourier transform.

mesh is shown in Figure 4.20 for the outside view of the sphere. Figure 4.21 also illustrates the inside of the mesh from Figure 4.20 cut in half along the x-z plane. Analogous to Section 4.5.1, the octree cells are sufficiently small and thus the orders of continued-fraction expansion for cells in bounded domain are all set to be $M = 0$. The order of continued-fraction expansion for unbounded domain is $M_H = M_L = 1$.

The time-domain solutions are calculated by Newmark's method with a time step of $\Delta t = 0.01$ms for the first 0.7ms. This selection of Δt yields at least 15 time steps per period at the highest frequency of interest. Contour plots of acoustic

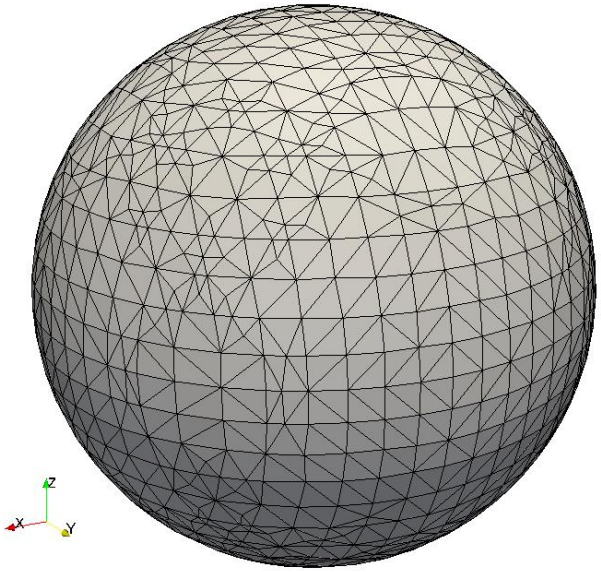

Figure 4.20. The SBFEM mesh of human external ear model - the view of outer surface.

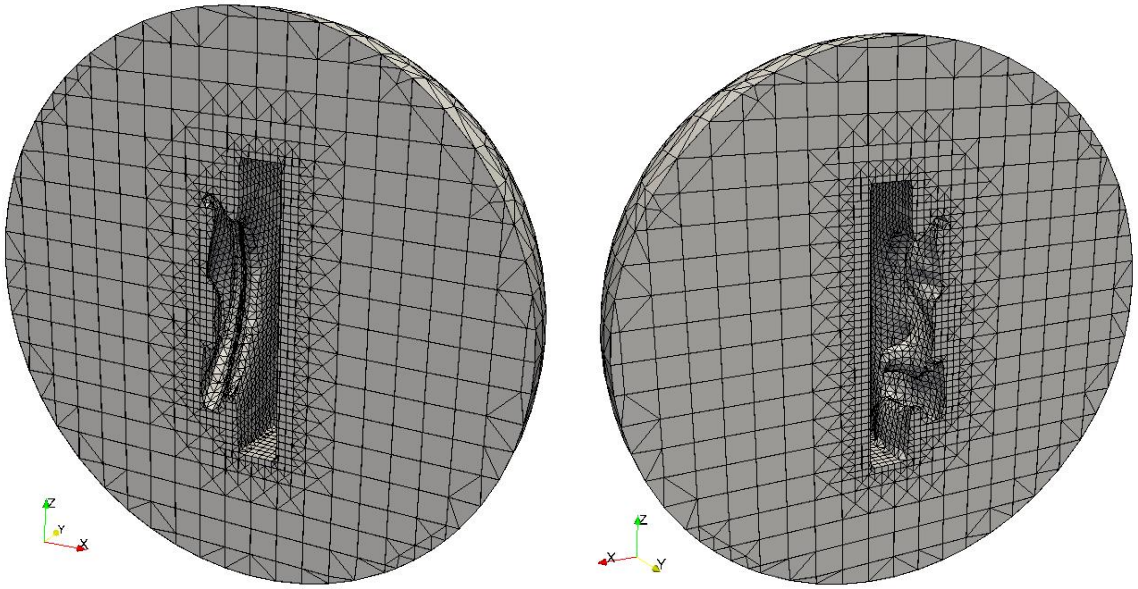

(a) (b)

Figure 4.21. Half of SBFEM mesh of human external ear model: (a) view from -y direction and (b) view from +y direction.

pressures with the unit of Pa at time t = 0.15ms, 0.2ms, 0.25ms and 0.3ms are illustrated in Figure 4.22. It can be seen from these contour plots that part of the sound waves propagate into the ear canal and then reflected back to the infinite air domain at the end.

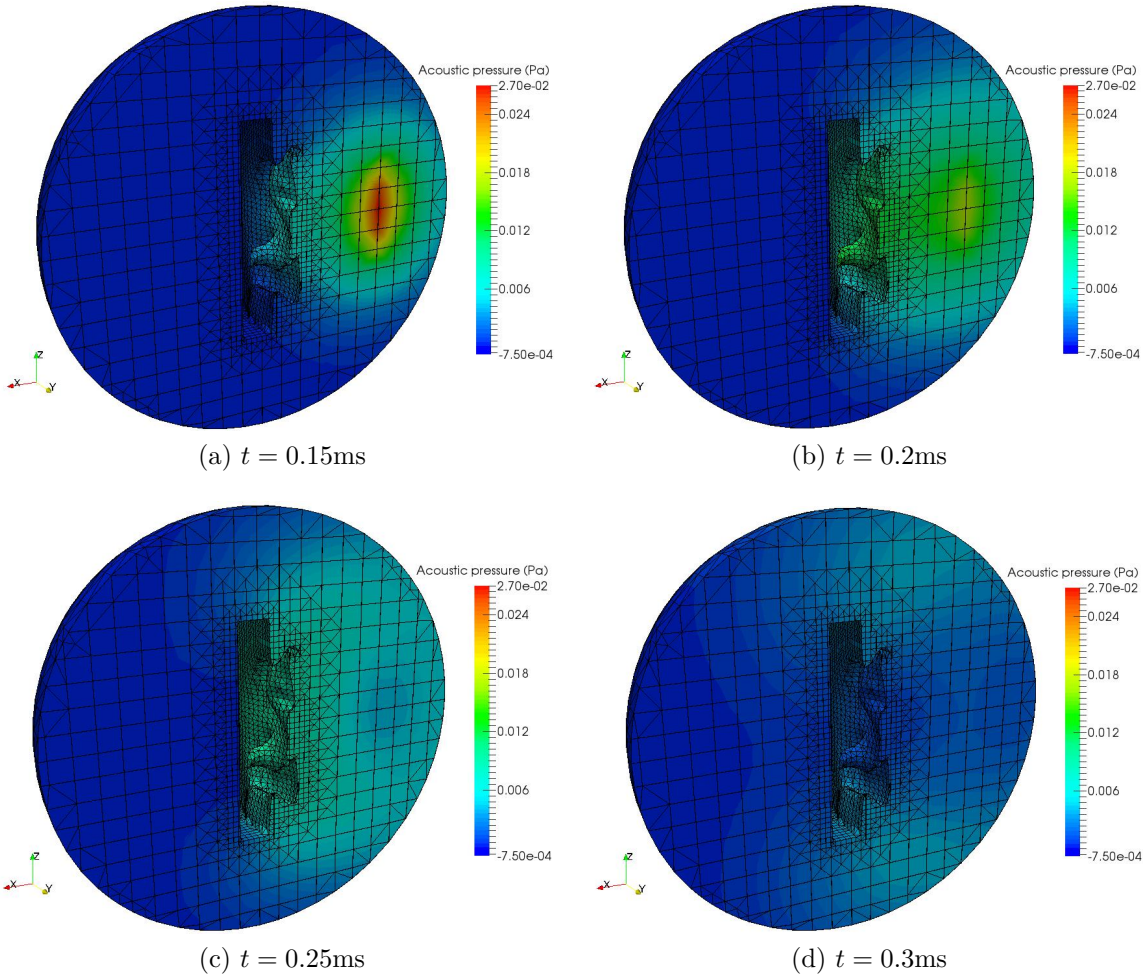

(a) $t = 0.15$ms (b) $t = 0.2$ms

(c) $t = 0.25$ms (d) $t = 0.3$ms

Figure 4.22. Human external ear. Pressure contour obtained using the proposed SBFEM at: (a) $t = 0.15$ms (b) $t = 0.2$ms (c) $t = 0.25$ms (d) $t = 0.3$ms.

4.5.4 Sound radiation from an ancient Chinese bell

One of the most common applications on acoustics is the design of musical instruments. Many cultures in this world have developed their own musical instruments since ancient times and they play an important role in our society, both in the past and present. According to archaeological excavations, the bells began to appear in Chinese civilization around third millennium BC. Later, ancient Chinese musical bells were usually cast in bronze and their early developments can be traced back to 1600-1100 BC. Various literatures, including (Chen, 1996; Pan, 2009; Wu et al., 2013), studied the acoustic properties of ancient Chines bells via modern numerical modelling technology, and the significance of these studies is not only in history and

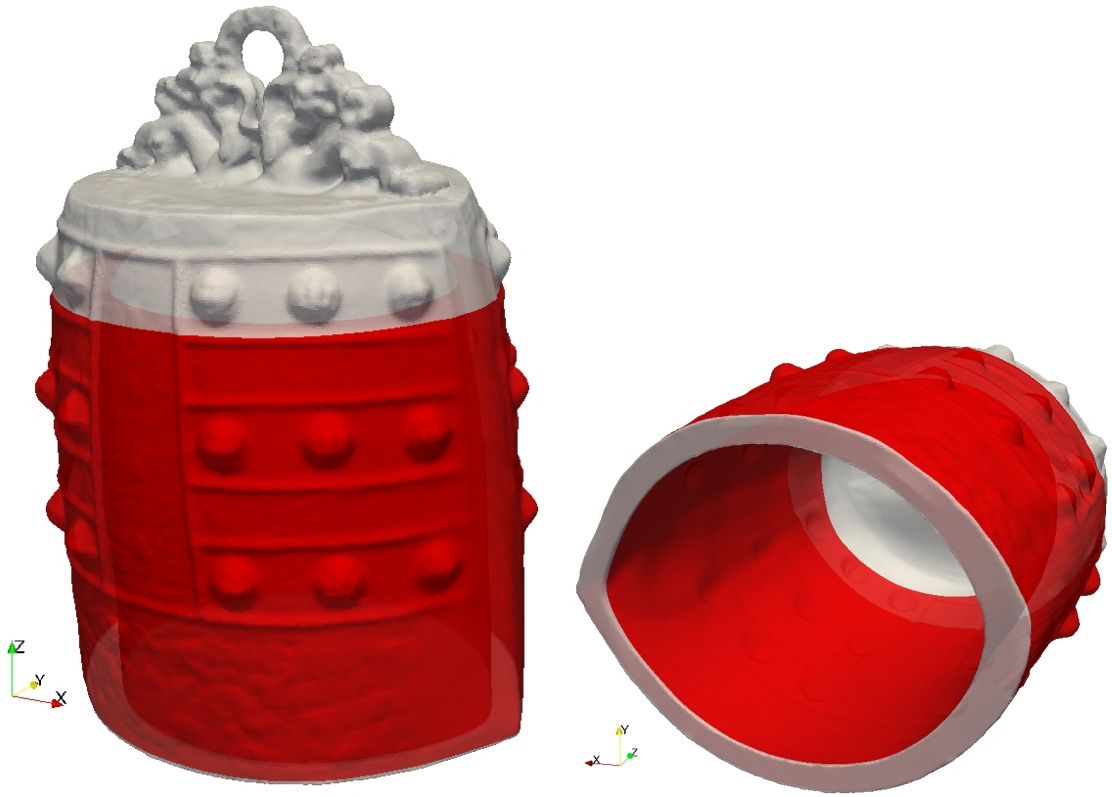

(a) (b)

Figure 4.23. Ancient Chinese bell STL model: (a) view from -y direction and (b) view from -z direction.

culture, but also in the modern acoustic designs.

The acoustic study of an ancient Chinese bell, which is cast about 5th century BC, is performed in this section. This bell is one of the collections in the British Museum and its STL model used in this analysis is downloaded from (ScanTheWorld, 2016) and shown in Figure 4.23 with two different views. The interaction of bell and surrounding acoustic medium is not considered in this example and the bell is thus assumed to be rigid and within the infinite domain as illustrated in Figure 4.24. The translucent spherical shell in Figure 4.24 again represents the spherical open boundary with the radius of 110cm and its centroid coincides with the origin of coordinates. Analogous to Section 4.5.3, the coordinate axes plotted in all figures in this example only indicate the orientation of the displayed model. The red area on part of the surface of bell in Figure 4.23 are subjected to a uniform flux in this

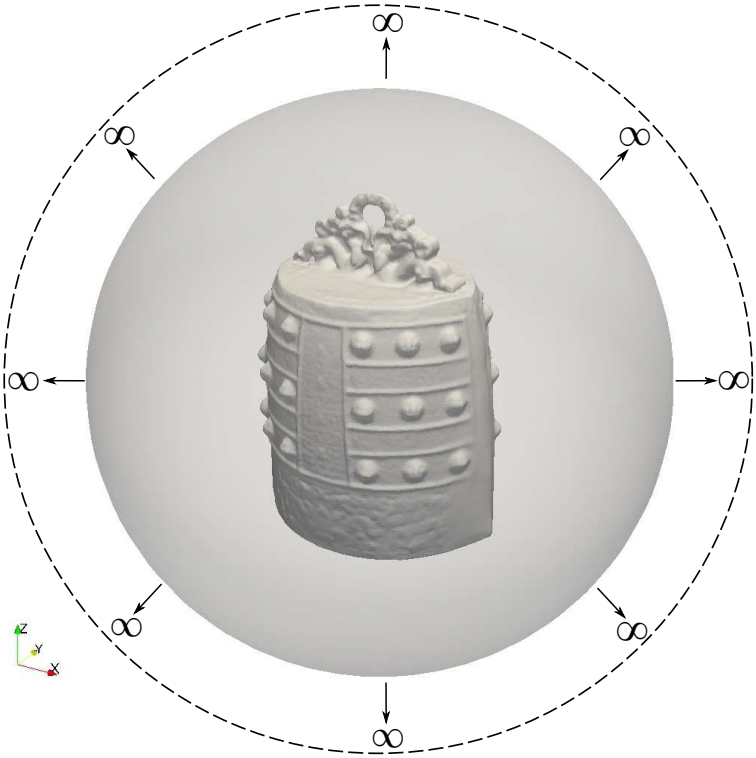

Figure 4.24. The coupled SBFE model for ancient Chinese bell in infinite space.

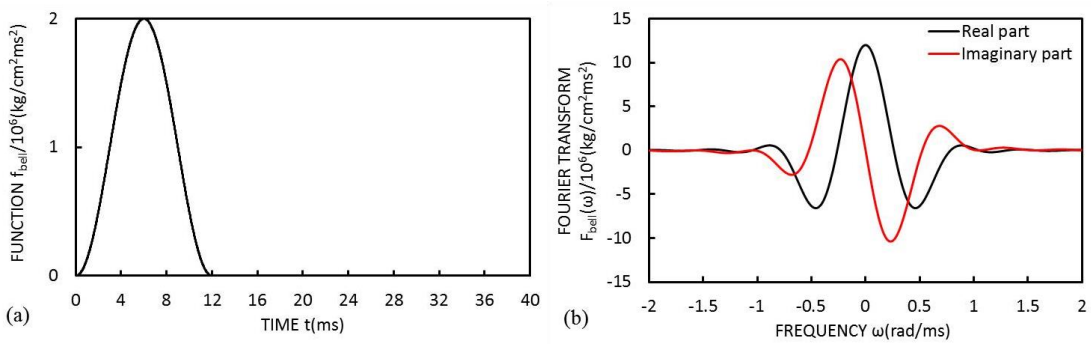

Figure 4.25. Time variation $f_{bell}(t)$ of transient flux applied in the acoustic near field of ancient Chinese bell model: (a) time history and (b) Fourier transform.

example and the applied transient flux $f_{bell}(t)$ is defined by:

$$f_{bell}(t) = \begin{cases} 10^6 \times (1 - \cos\frac{\pi}{6}t) \ (\text{kg}/(\text{cm}\cdot\text{ms})^2) & \text{when } 0 \le t \le 12\text{ms}, \\ 0 \qquad\qquad\qquad\qquad\quad (\text{kg}/(\text{cm}\cdot\text{ms})^2) & \text{when } 12\text{ms} < t. \end{cases} \tag{4.51}$$

The time variation of $f_{bell}(t)$ are also plotted in Figure 4.25(a) with its Fourier transform in Figure 4.25(b). According to Figure 4.25(b), the maximum frequency of interest of the applied flux is estimated at $\omega_{0.max} = 1.5$rad/ms. The acoustic medium

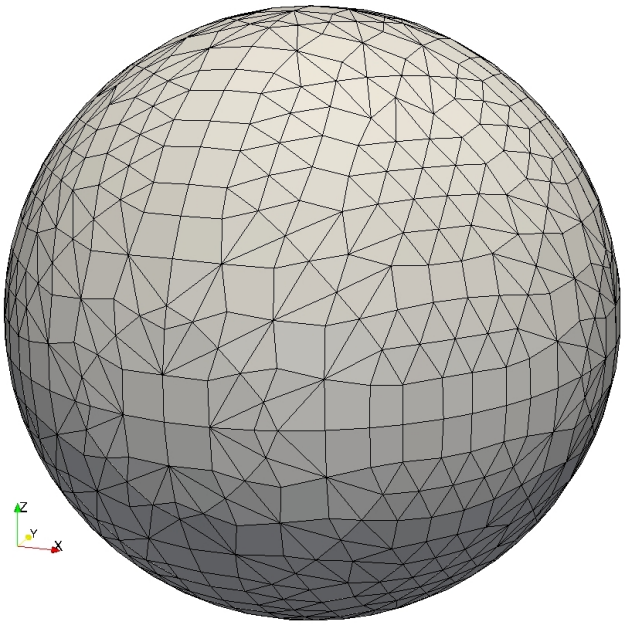

Figure 4.26. The SBFEM mesh of ancient Chinese bell model - the view of outer surface.

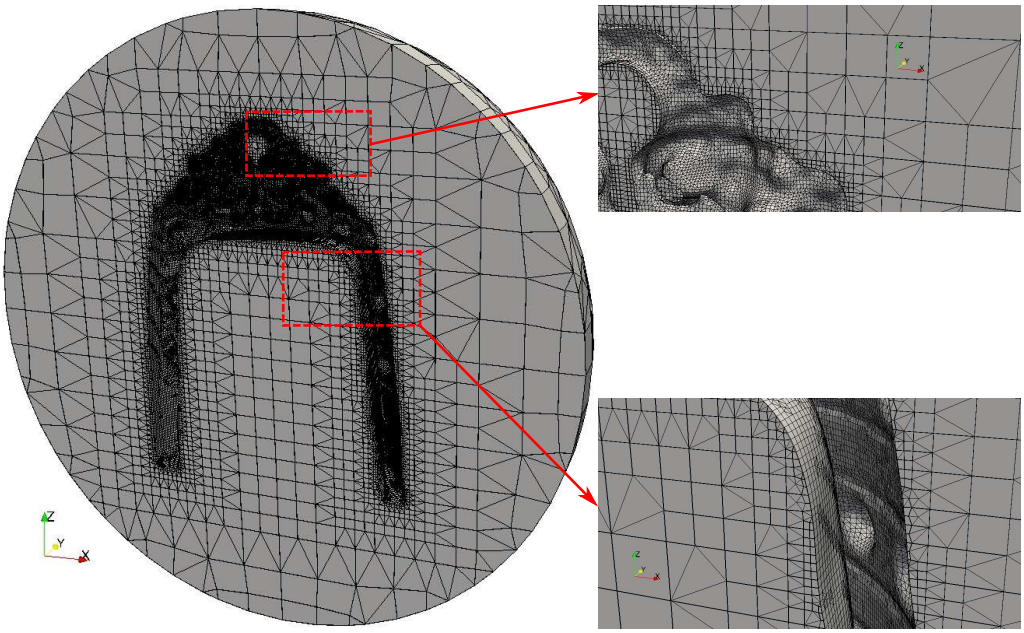

Figure 4.27. Half of SBFEM mesh of ancient Chinese bell model.

in this example is assumed to be air with sound speed of 340m/s. This gives the shortest wavelength of $\lambda_{min} \approx 142.4$cm. Therefore, the maximum cell size of the octree mesh is set to be 15cm. This yields at least 10 nodes per shortest wavelength. For describing the geometrical details of the bell accurately, the minimum cell size is equal to 0.46875cm ($\frac{1}{32}$ of the maximum cell size) around the bell surface. The final

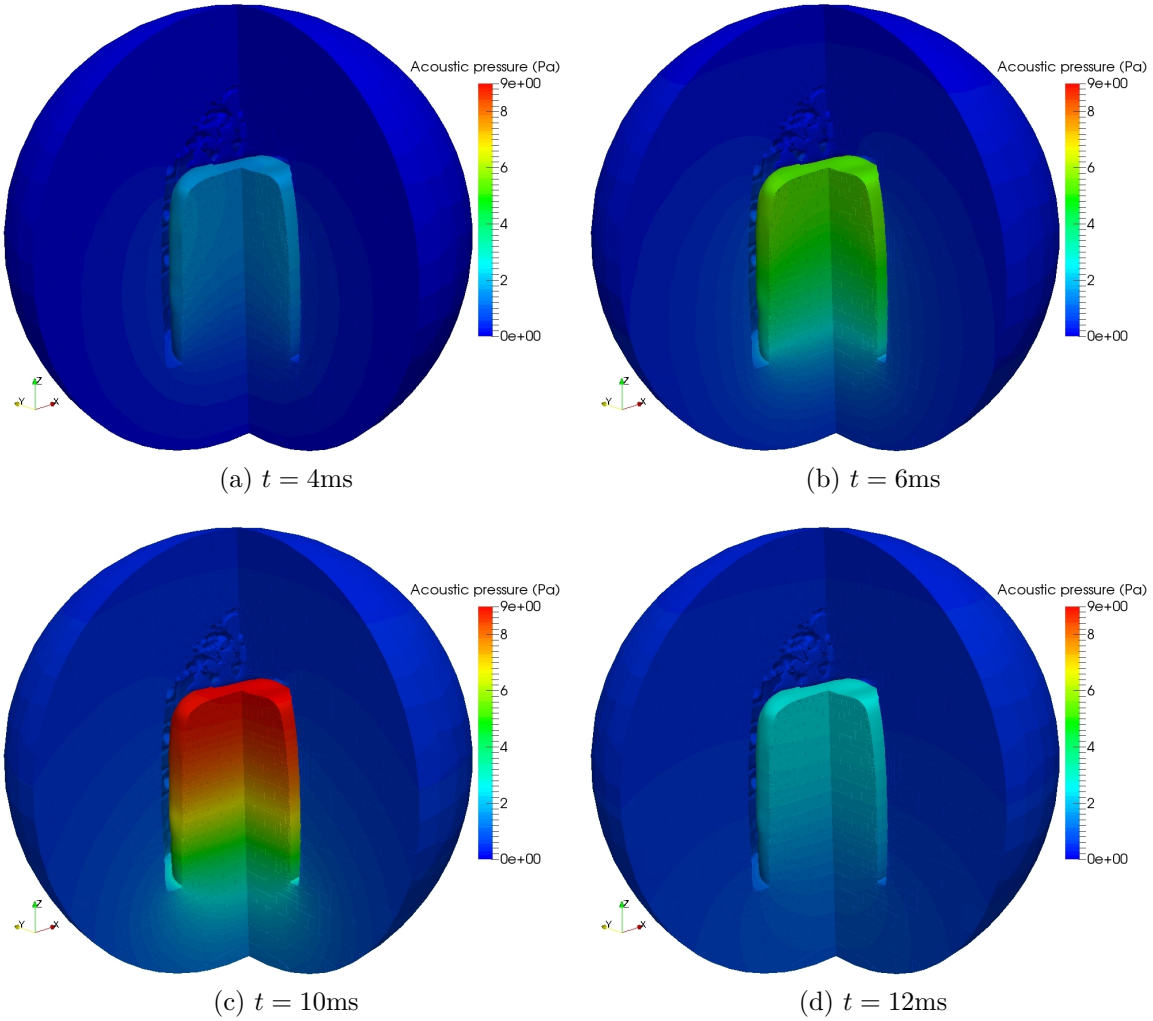

(a) $t = 4$ms (b) $t = 6$ms

(c) $t = 10$ms (d) $t = 12$ms

Figure 4.28. Ancient Chinese bell. Pressure contour obtained using the proposed SBFEM at: (a) $t = 4$ms (b) $t = 6$ms (c) $t = 10$ms (d) $t = 12$ms.

trimmed octree mesh is illustrated in Figure 4.26 and 4.27. Figure 4.26 shows the outside sphere of the mesh, while Figure 4.27 shows the interior of the mesh from Figure 4.26 cut in half along x-z plane. As the cell size in octree mesh is sufficiently small, the orders of continued-fraction expansion for bounded domains are set to be $M = 0$. The order of continued-fraction expansion for doubly-asymptotic open boundary is $M_H = M_L = 1$. Newmark's method is applied to Equation (4.45) to obtain the time-domain solutions of acoustic pressures for the first 50ms with a constant time step of $\Delta t = 0.25$ms. This gives about 16 time steps per period at the highest frequency of interest. The contour plots of acoustic pressures at time

t = 4ms, 6ms, 10ms and 12ms are illustrated in Figure 4.28 with the unit of Pa.

4.6 Conclusions

The SBFEM has been extended to model 3D acoustic problems in this Chapter. In order to solve acoustic problems of arbitrary geometry, the whole region is again divided into a near field (bounded domain) and a far field (unbounded domain). For accurately and efficiently representing the unbounded domain in the acoustic medium, a spherical doubly-asymptotic open boundary is introduced. It is based on the approach presented in Chapter 3 for modeling 2D unbounded acoustics domain. Via introducing the newly defined model impedance and the shifted mode number into the modal impedance equations for spherical unbounded domain, the modal impedance coefficients are determined by utilizing the same doubly-asymptotic continued fractions for 2D doubly-asymptotic open boundary, which has been proved to be efficient, stable and robust in the previous Chapter 3. The time-domain equation is obtained by introducing auxiliary variables. For modeling the 3D bounded domain, the scaled boundary finite element method is applied. The mesh is generated by an octree algorithm with STL models as the inputs. This mesh generation technique automatically captures the geometrical features and handles the mesh transition from fine elements to coarse elements efficiently. The hanging nodes in an octree mesh is easily solved in SBFEM by subdivisions of surface elements. This can greatly reduce the human efforts on the simulations of 3D acoustic problems with complex geometry, which is demonstrated by several numerical examples related to practical applications.

Chapter 5

2D and 3D acoustic-structure interaction analyses using SBFEM

5.1 Introduction

In general, the acoustic-structure interaction analyses consider the dynamic interactions between flexible structures and the acoustic media such as air or water. Due to the ubiquity of the acoustic media in most engineering applications, the structural surfaces are always in contact with the surrounding acoustic media. Examples of engineering applications involving the acoustic-structure interactions includes the dam-reservoir interaction, air-coupled ultrasonic testing, acoustic design of vehicles and earphones to name a few. In all these examples, the acoustic domains have no significant flow. This type of acoustic-structure interaction problems is also termed as vibroacoustic problems and is studied in this chapter. In other examples of structural acoustics, the interaction between structural and acoustic domains may be caused by unsteady fluid flow, which is known as aeroacoustics. The noise generated from propeller, the vibration of vocal cords during speaking and the sounds generated by some music instruments such as flute are all examples of aeroacoustics. The acoustic media investigated in this chapter are assumed to be compressible but

irrotational, isentropic and inviscid with small perturbations.

Due to the increasing complexity of structures involved in acoustic-structure interaction system and the versatility of finite element method (FEM), this numerical tool has been employed to model acoustic-structure interaction problems by many literatures (Belytschko, 1980; Bathe et al., 1995; Mellado and Rodríguez, 2001; Olson and Bathe, 1985; Nitikitpaiboon and Bathe, 1993) based on either displacement-based formulations or potential-based formulations. The displacement-based formulations are attractive as the modeling of acoustics can be achieved by simply setting the shear modulus to be zero. However, spurious or circulation modes may arise in acoustic domain due to the failure of satisfying the irrotational displacement in fluid strictly as reported in (Hamdi et al., 1978). In contrast, the potential-based formulation show no spurious modes in acoustic domain as the scalar functions, which could be velocity potentials or acoustic pressures, are used to describe the behavior of acoustics. Normally, FEM are preferred to model acoustic-structure interaction problems with bounded acoustic domain as any outgoing wave will be reflected back by the boundary of finite element meshes. In order to model the unbounded acoustic domain, the boundary of the finite element model should be far away from the area of interest to avoid the contamination of results by reflected waves. As a result, this will inevitably increase the computational costs for acoustic-structure interaction analyses. Therefore, various open boundaries are developed to represent the unbounded domain by satisfying the radiation condition at infinity. Readers for detailed review of open boundaries are referred to Chapter 2.

One of the well suited numerical tools for modeling unbounded domains is the boundary element method (BEM). The BEM only requires boundary discretization and thus reduces the problem dimension by one. A salient feature of modeling unbounded domain via BEM is that the radiation condition at infinity is naturally satisfied by the fundamental solution (Marburg and Nolte, 2008). No artificial open boundary is required. The coupled acoustic-structure system with infinite acoustic

domain can then be simulated by coupling FEM formulation for structural domain and acoustic near field with BEM formulation for acoustic far field. One of the earliest researches on coupling FEM with BEM was presented by Zienkiewicz et al. (Zienkiewicz et al., 1977) with direct coupling scheme, which enforces equilibrium and compatibility conditions on common interface. The direct FEM-BEM coupling scheme is also applied to fluid-structure interaction analysis in the time domain (Estorff and Antes, 1991) and later extended to fluid-structure interaction problems considering the structural nonlinearity (Czygan and Von Estorff, 2002). The developed FEM-BEM coupling formulations for acoustic-structure interactions are summarized in several literatures (Amini et al., 2012; Brunner et al., 2009). For reducing the computational costs in direct coupling scheme, an alternative option is to couple the FEM and BEM equations through the iterative coupling scheme, which satisfies the equilibrium and compatibility conditions on interface iteratively (Soares Jr et al., 2004; Soares Jr and Mansur, 2005; Soares Jr and Godinho, 2008). Nevertheless, the fundamental solutions in BEM might be complex and difficult to find. In addition, increasing stability of the coupled FEM-BEM formulation and reducing numerical costs for transient analysis may still require extra efforts as reported in some literatures (Rokhlin, 1985; Yu et al., 2002; Soares Jr and Mansur, 2005; Rjasanow and Steinbach, 2007; Soares Jr and Godinho, 2008).

The SBFEM is another promising method for modeling infinite domains as it only requires boundary discretization and provides analytical solutions in the radial direction (Wolf, 2003). Some of its early developments are summarized in (Song and Wolf, 1995; Wolf and Song, 1995; Song and Wolf, 1996, 1997, 1999b,a; Wolf and Song, 2000; Song and Wolf, 2000). High-order elements can be applied into the SBFEM (Vu and Deeks, 2006) for efficiently obtaining accurate solutions under high-frequency excitations, such as the applications of SBFEM in ultrasonic problems (Gravenkamp et al., 2012, 2015). The recently developed automatic meshing techniques based on quadtree or octree mesh can further reduce the human efforts

on mesh generation for complicated models in SBFEM (Saputra et al., 2017a; Liu et al., 2017). Due to the intrinsic advantage of SBFEM in modeling unbounded domains, this method has also been applied to exterior acoustic analysis (Lehmann et al., 2006) and acoustic-structure interaction analysis (Fan et al., 2005; Li, 2006; Fan and Li, 2008) before. Some of the early approaches for modeling unbounded domains are involved, which are less computationally efficient than the high-order doubly-asymptotic open boundaries presented in Chapters 3 and 4 for exterior acoustics as the computationally expensive convolution integral is usually required for transient solutions. Later, the high-order doubly-asymptotic open boundary has been applied to model the infinite layer of reservoir in 2D dam-reservoir interaction problems in (Wang et al., 2011). The dam structure and reservoir near field are still modeled using standard FEM. Therefore, it is demanded to utilize all the advantages in modeling bounded and unbounded domains using SBFEM and extend the SBFEM to model the whole acoustic-structure interaction system for both 2D and 3D cases. Due to the fact that waves travel with different wave lengths in structural and acoustic domains, different mesh sizes are preferred to be used in distinct media. The boundary discretization in SBFEM yields an extra advantage in efficient mesh transition on the acoustic-structure interface for non-matched meshes. In 2D case, the mesh transition can be done by simply dividing line elements on the interface. For 3D scenario, this can be achieved by subdivision of surface elements.

The purpose of this chapter is to develop the coupled 2D and 3D formulations for acoustic-structure interaction analyses based on SBFEM. To this end, the SBFEM formulation for structural dynamics in (Chen et al., 2014) is employed to simulate the wave propagation in elastic structural domain. The acoustic domain is again divided into a near field containing any irregular geometry of structures and a far field representing the infinite acoustic medium of simple geometry. Thus, the formulation for acoustic analyses in Chapters 3 and 4 are directly applied here. The coupling of structural and acoustic formulations is achieved by applying the force

equilibrium and displacement compatibility in the normal direction of the acoustic-structure interface. Different meshes can be used for structures and acoustics in the coupled SBFEM model and the mesh transition on the coupling interface is handled efficiently. The resulting second-order global differential equations of motion for acoustic-structure interaction system is unsymmetrical, which can be transformed into a symmetric one by replacing the variables related to acoustic domain with new variables.

The organization of this chapter is stated as follows: Firstly, Section 5.2 summarizes the SBFEM for structural dynamics based on continued-fraction expansions. Then, the derivations of coupled scaled boundary finite element formulation for both 2D and 3D acoustic-structure interaction analyses are addressed in Section 5.3. Several numerical examples are presented in Section 5.4 for demonstrating the accuracy, efficiency, robustness of the present SBFEM, as well as its ability of solving complex problems in structural acoustics. Finally, conclusions are stated in Section 5.5.

5.2 Scaled boundary finite element solutions for structural dynamics

This section presents the SBFEM formulations for elastic 3D structural dynamics. Corresponding equations for elastic 2D structural dynamics can be found in Appendix A. As the scaled boundary coordinates for a 3D structural domain are the same as those for a bounded acoustic domain summarized in Equations (4.1)-(4.2) in Section 4.2.1, the scaled boundary coordinate transformation will not be reproduced here. The derivation of scaled boundary formulations for structural dynamics starts from the following governing differential equations of motion in frequency domain,

$$\mathbf{L}^T\hat{\boldsymbol{\sigma}} + \hat{\mathbf{F}}_b + \omega^2\rho_s\hat{\mathbf{u}} = 0 \tag{5.1}$$

In Equation (5.1), $\hat{\boldsymbol{\sigma}}$ is the stress amplitude, $\hat{\mathbf{u}}$ is the displacement amplitude and $\hat{\mathbf{F}}_b$ is the amplitude of any body forces. The scalar ρ_s is the density of structure. Differential operator $\mathbf{L}$ denotes the strain-displacement relationship and can be expressed in its 3D form as:

$$\mathbf{L} = \begin{bmatrix} \frac{\partial}{\partial \hat{x}} & 0 & 0 \\ 0 & \frac{\partial}{\partial \hat{y}} & 0 \\ 0 & 0 & \frac{\partial}{\partial \hat{z}} \\ 0 & \frac{\partial}{\partial \hat{z}} & \frac{\partial}{\partial \hat{y}} \\ \frac{\partial}{\partial \hat{z}} & 0 & \frac{\partial}{\partial \hat{x}} \\ \frac{\partial}{\partial \hat{y}} & \frac{\partial}{\partial \hat{x}} & 0 \end{bmatrix} \tag{5.2}$$

In scaled boundary coordinates, the strain-displacement relationship can be described by,

$$\boldsymbol{\epsilon}(\xi, \eta, \zeta) = \mathbf{L}\hat{\mathbf{u}}(\xi, \eta, \zeta) \tag{5.3}$$

The displacement amplitude $\hat{\mathbf{u}}(\xi, \eta, \zeta)$ in Equation (5.3) can be discretized for 3D subdomains using the shape function in Equation (4.1) for geometry interpolation. Every DOF is interpolated independent of the others, yielding

$$\hat{\mathbf{u}}(\xi, \eta, \zeta) = \mathbf{N}_s(\eta, \zeta)\hat{\mathbf{u}}(\xi) \tag{5.4}$$

where $\hat{\mathbf{u}}(\xi)$ is the radial displacement solution. The nodal 2D shape function matrix $\mathbf{N}_s(\eta, \zeta)$ in Equation (5.4) is defined as:

$$\mathbf{N}_s(\eta, \zeta) = [N_1(\eta, \zeta)\mathbf{I},\ N_2(\eta, \zeta)\mathbf{I},\ \cdots,\ N_m(\eta, \zeta)\mathbf{I}] \tag{5.5}$$

for a m-nodes element with the 3×3 identity matrix $\mathbf{I}$.

According to Reference (Song and Wolf, 1997), the differential operator $\mathbf{L}$ in 3D scaled boundary coordinates in Equation (5.3) can be expressed by:

$$\mathbf{L} = \mathbf{b}_1^s(\eta, \zeta)\frac{\partial}{\partial \xi} + \frac{1}{\xi}\left(\mathbf{b}_2^s(\eta, \zeta)\frac{\partial}{\partial \eta} + \mathbf{b}_3^s(\eta, \zeta)\frac{\partial}{\partial \zeta}\right) \tag{5.6}$$

with the $\mathbf{b}_1^s(\eta,\zeta)$, $\mathbf{b}_2^s(\eta,\zeta)$ and $\mathbf{b}_3^s(\eta,\zeta)$ matrices defined as,

$$\mathbf{b}_1^s(\eta,\zeta) = \frac{1}{|\mathbf{J}|}\begin{bmatrix} y_{,\eta}z_{,\zeta} - z_{,\eta}y_{,\zeta} & 0 & 0 \\ 0 & z_{,\eta}x_{,\zeta} - x_{,\eta}z_{,\zeta} & 0 \\ 0 & 0 & x_{,\eta}y_{,\zeta} - y_{,\eta}x_{,\zeta} \\ 0 & x_{,\eta}y_{,\zeta} - y_{,\eta}x_{,\zeta} & z_{,\eta}x_{,\zeta} - x_{,\eta}z_{,\zeta} \\ x_{,\eta}y_{,\zeta} - y_{,\eta}x_{,\zeta} & 0 & y_{,\eta}z_{,\zeta} - z_{,\eta}y_{,\zeta} \\ z_{,\eta}x_{,\zeta} - x_{,\eta}z_{,\zeta} & y_{,\eta}z_{,\zeta} - z_{,\eta}y_{,\zeta} & 0 \end{bmatrix} \tag{5.7a}$$

$$\mathbf{b}_2^s(\eta,\zeta) = \frac{1}{|\mathbf{J}|}\begin{bmatrix} zy_{,\zeta} - yz_{,\zeta} & 0 & 0 \\ 0 & xz_{,\zeta} - zx_{,\zeta} & 0 \\ 0 & 0 & yx_{,\zeta} - xy_{,\zeta} \\ 0 & yx_{,\zeta} - xy_{,\zeta} & xz_{,\zeta} - zx_{,\zeta} \\ yx_{,\zeta} - xy_{,\zeta} & 0 & zy_{,\zeta} - yz_{,\zeta} \\ xz_{,\zeta} - zx_{,\zeta} & zy_{,\zeta} - yz_{,\zeta} & 0 \end{bmatrix} \tag{5.7b}$$

$$\mathbf{b}_3^s(\eta,\zeta) = \frac{1}{|\mathbf{J}|}\begin{bmatrix} yz_{,\eta} - zy_{,\eta} & 0 & 0 \\ 0 & zx_{,\eta} - xz_{,\eta} & 0 \\ 0 & 0 & xy_{,\eta} - yx_{,\eta} \\ 0 & xy_{,\eta} - yx_{,\eta} & zx_{,\eta} - xz_{,\eta} \\ xy_{,\eta} - yx_{,\eta} & 0 & yz_{,\eta} - zy_{,\eta} \\ zx_{,\eta} - xz_{,\eta} & yz_{,\eta} - zy_{,\eta} & 0 \end{bmatrix} \tag{5.7c}$$

In Equation (5.7), $|\mathbf{J}|$ is the determinant of Jacobian matrix defined in Equation (4.4). Substituting Equations (5.6) and (5.4) into (5.3) yields the expression for strain field $\boldsymbol{\epsilon}(\xi,\eta,\zeta)$ in 3D as,

$$\boldsymbol{\epsilon}(\xi,\eta,\zeta) = \mathbf{B}_1^s(\eta,\zeta)\hat{\mathbf{u}}(\xi)_{,\xi} + \frac{1}{\xi}\mathbf{B}_2^s(\eta,\zeta)\hat{\mathbf{u}}(\xi) \tag{5.8}$$

with the $\mathbf{B}_1^s(\eta,\zeta)$ and $\mathbf{B}_2^s(\eta,\zeta)$ matrices defined as:

$$\mathbf{B}_1^s(\eta,\zeta) = \mathbf{b}_1^s(\eta,\zeta)\mathbf{N}_s(\eta,\zeta) \tag{5.9a}$$

$$\mathbf{B}_2^s(\eta,\zeta) = \mathbf{b}_2^s(\eta,\zeta)\mathbf{N}_s(\eta,\zeta)_{,\eta} + \mathbf{b}_3^s(\eta,\zeta)\mathbf{N}_s(\eta,\zeta)_{,\zeta} \tag{5.9b}$$

In order to obtain a general solution for structural dynamics, the method of weighted residuals is applied to the differential equations of motion in Equation (5.1) in circumferential directions (η, ζ) (Song and Wolf, 1997). Assuming that the side-faces in radial direction are traction free and the body forces vanish, a system of ordinary differential equations for radial displacement amplitude $\hat{\mathbf{u}}(\xi)$ in the frequency domain is derived

$$\mathbf{E}_0^s \xi^2 \hat{\mathbf{u}}(\xi)_{,\xi\xi} + \left(2\mathbf{E}_0^s - \mathbf{E}_1^s + [\mathbf{E}_1^s]^T\right) \xi \hat{\mathbf{u}}(\xi)_{,\xi} + \left([\mathbf{E}_1^s]^T - \mathbf{E}_2^s\right) \hat{\mathbf{u}}(\xi) + \omega^2 \mathbf{M}_0^s \xi^2 \hat{\mathbf{u}}(\xi) = 0 \quad (5.10)$$

Equation (5.10) is also known as the scaled boundary finite element equation in displacement formulated in frequency domain. $\mathbf{E}_0^s$, $\mathbf{E}_1^s$, $\mathbf{E}_2^s$ and $\mathbf{M}_0^s$ are coefficient matrices for 3D structures. These coefficient matrices depend on the geometry and materials of the corresponding elements and can be expressed as,

$$\mathbf{E}_0^s = \int_{-1}^{+1}\int_{-1}^{+1} [\mathbf{B}_1^s(\eta,\zeta)]^T \mathbf{D}\mathbf{B}_1^s(\eta,\zeta)\, |\mathbf{J}(\eta,\zeta)|\, d\eta d\zeta \quad (5.11a)$$

$$\mathbf{E}_1^s = \int_{-1}^{+1}\int_{-1}^{+1} [\mathbf{B}_2^s(\eta,\zeta)]^T \mathbf{D}\mathbf{B}_1^s(\eta,\zeta)\, |\mathbf{J}(\eta,\zeta)|\, d\eta d\zeta \quad (5.11b)$$

$$\mathbf{E}_2^s = \int_{-1}^{+1}\int_{-1}^{+1} [\mathbf{B}_2^s(\eta,\zeta)]^T \mathbf{D}\mathbf{B}_2^s(\eta,\zeta)\, |\mathbf{J}(\eta,\zeta)|\, d\eta d\zeta \quad (5.11c)$$

$$\mathbf{M}_0^s = \int_{-1}^{+1}\int_{-1}^{+1} \mathbf{N}_s^T(\eta,\zeta)\rho_s \mathbf{N}_s(\eta,\zeta)\, |\mathbf{J}(\eta,\zeta)|\, d\eta d\zeta \quad (5.11d)$$

where $\mathbf{D}$ is the elasticity matrix for 3D.

The coefficient matrices are calculated on an element-by-element basis and assembled as in finite element method for each subdomain. Equations (5.2) - (5.11) are derived for elastic 3D structural dynamics. Summary of these equations for elastic 2D structural dynamics based on SBFEM are provided in Appendix A. Comparing the scaled boundary finite element equations in displacement in 2D (Equation (A.9)) and in 3D (Equation (5.10)), the unified form of scaled boundary finite element equation in displacement can thus be expressed in Equation (5.12) with the

spatial dimension s,

$$\mathbf{E}_0^s\xi^2\hat{\mathbf{u}}(\xi)_{,\xi\xi} + \left((s-1)\mathbf{E}_0^s - \mathbf{E}_1^s + [\mathbf{E}_1^s]^T\right)\xi\hat{\mathbf{u}}(\xi)_{,\xi} + \left((s-2)\,[\mathbf{E}_1^s]^T - \mathbf{E}_2^s\right)\hat{\mathbf{u}}(\xi) + \omega^2\mathbf{M}_0^s\xi^2\hat{\mathbf{u}}(\xi) = 0 \quad (5.12)$$

In Equation (5.12), the spatial dimension $s = 2$ for 2D problems and $s = 3$ for 3D problems applies.

5.2.1 Solutions for elastostatics

In static analysis, the low-frequency limit $\omega = 0$ is considered in Equation (5.12) and thus this equation can be simplified as,

$$\mathbf{E}_0^s\xi^2\mathbf{u}(\xi)_{,\xi\xi} + \left((s-1)\mathbf{E}_0^s - \mathbf{E}_1^s + [\mathbf{E}_1^s]^T\right)\xi\mathbf{u}(\xi)_{,\xi} + \left([\mathbf{E}_1^s]^T - \mathbf{E}_2^s\right)\mathbf{u}(\xi) = 0 \quad (5.13)$$

For simplifying the notations in static analysis, the hat $\hat{\bullet}$ of $\hat{\mathbf{u}}(\xi)$ in Equation (5.10) is omitted. Introducing the following variable $\boldsymbol{\Theta}(\xi)$,

$$\boldsymbol{\Theta}(\xi) = \begin{Bmatrix} \xi^{0.5(s-2)}\mathbf{u}(\xi) \\ \xi^{-0.5(s-2)}\mathbf{q}(\xi) \end{Bmatrix} \quad (5.14)$$

where $\mathbf{q}(\xi)$ in Equation (5.14) is the internal nodal force. Equation (5.13) can then be transformed to a system of first-order ordinary differential equations (Song, 2004a),

$$\xi\boldsymbol{\Theta}(\xi)_{,\xi} = -\mathbf{Z}\boldsymbol{\Theta}(\xi) \quad (5.15)$$

where $\mathbf{Z}$ is a Hamiltonian matrix and defined as,

$$\mathbf{Z} = \begin{bmatrix} [\mathbf{E}_0^s]^{-1}\,[\mathbf{E}_1^s]^T - 0.5(s-2)\mathbf{I} & -[\mathbf{E}_0^s]^{-1} \\ \mathbf{E}_1^s\,[\mathbf{E}_0^s]^{-1}\,[\mathbf{E}_1^s]^T - \mathbf{E}_2^s & -\mathbf{E}_1^s\,[\mathbf{E}_0^s]^{-1} + 0.5(s-2)\mathbf{I} \end{bmatrix} \quad (5.16)$$

Utilizing the eigenvalue decomposition of $\mathbf{Z}$ leads to,

$$\mathbf{Z}\begin{bmatrix} \boldsymbol{\Psi}_{u_n} & \boldsymbol{\Psi}_{u_p} \\ \boldsymbol{\Psi}_{q_n} & \boldsymbol{\Psi}_{q_p} \end{bmatrix} = \begin{bmatrix} \boldsymbol{\Psi}_{u_n} & \boldsymbol{\Psi}_{u_p} \\ \boldsymbol{\Psi}_{q_n} & \boldsymbol{\Psi}_{q_p} \end{bmatrix}\begin{bmatrix} \mathbf{S}_n & 0 \\ 0 & \mathbf{S}_p \end{bmatrix} \quad (5.17)$$

After sorting the eigenvalues in Equation (5.17) in ascending order of their real parts, the diagonal entries of $\mathbf{S}_n$ include the eigenvalues with negative real parts for a bounded domain. The diagonal entries of $\mathbf{S}_p$ include the eigenvalues with positive real parts for an unbounded domain. The corresponding eigenvectors are also partitioned conformably with submatrices $\mathbf{\Psi}_{u_n}$ and $\mathbf{\Psi}_{q_n}$ indicating modal displacements and forces in bounded domain. The corresponding modal displacements and forces for the unbounded domain are $\mathbf{\Psi}_{u_p}$ and $\mathbf{\Psi}_{q_p}$ respectively. The solutions for displacements and forces in each bounded subdomain can then be expressed in Equations (5.18) and (5.19) respectively

$$\mathbf{u}(\xi) = \mathbf{\Psi}_{u_n} \xi^{-\mathbf{S}_n - 0.5(s-2)\mathbf{I}} \mathbf{c}_n \tag{5.18}$$

$$\mathbf{q}(\xi) = \mathbf{\Psi}_{q_n} \xi^{-\mathbf{S}_n + 0.5(s-2)\mathbf{I}} \mathbf{c}_n \tag{5.19}$$

The elastic stiffness matrix for a subdomain can then be calculated by eliminating the integration constant $\mathbf{c}_n$ in Equations (5.18) and (5.19) as

$$\mathbf{K}_e = \mathbf{\Psi}_{q_n} \mathbf{\Psi}_{u_n}^{-1} \tag{5.20}$$

$\mathbf{c}_n$ can be expressed by using Equation (5.18) and the nodal displacement on the boundary $\mathbf{u}_b = \mathbf{u}(\xi = 1)$ as

$$\mathbf{c}_n = \mathbf{\Psi}_{u_n}^{-1} \mathbf{u}_b \tag{5.21}$$

After computing elastic stiffness matrices $\mathbf{K}_e$ for all subdomains, they can be assembled in the same way as in FEM and give the following global equation for the whole problem domain

$$\left[\sum_{i=1}^{nPol} \mathbf{K}_e \right] \mathbf{U}_b = \mathbf{F}_b \tag{5.22}$$

where $\mathbf{U}_b$ and $\mathbf{F}_b$ are the global nodal displacement and force vectors respectively. $\left[\sum_{i=1}^{nPol} \mathbf{K}_e\right]$ is the assembled global stiffness matrix in elastic analysis. This system of linear equation can be directly solved for $\mathbf{U}_b$ after applying the boundary conditions.

5.2.2 Solutions for elastodynamics

On the boundary of subdomains with the radial coordinate $\xi = 1$, the dynamic-stiffness matrix $\mathbf{S}^s(\omega)$ is introduced for representing the relationship between nodal force amplitude $\hat{\mathbf{F}} = \hat{\mathbf{F}}(\xi = 1)$ and nodal displacement amplitude $\hat{\mathbf{u}} = \hat{\mathbf{u}}(\xi = 1)$ as:

$$\hat{\mathbf{F}} = \mathbf{S}^s(\omega)\hat{\mathbf{u}} \tag{5.23}$$

The nodal force amplitude vector $\hat{\mathbf{F}}$ in Equation (5.23) is defined as:

$$\hat{\mathbf{F}} = \int_{\Gamma_\xi} \mathbf{N}_s^T \hat{\mathbf{T}} d\Gamma \tag{5.24}$$

In Equation (5.24), the integration is over the boundary Γ_ξ with $\xi = 1$ and $d\Gamma$ is an infinitesimal length for 2D or infinitesimal area for 3D. $\hat{\mathbf{T}}$ is the surface traction amplitude applied on the structure. For the bounded domains, the radial force $\hat{\mathbf{F}}(\xi)$ is equal to the internal nodal force $\hat{\mathbf{q}}(\xi)$ on any surface (3D) or line (2D) with constant ξ. The internal nodal force $\hat{\mathbf{q}}(\xi)$ is related to the radial displacement $\hat{\mathbf{u}}(\xi)$ as (Song and Wolf, 1997; Wolf, 2003):

$$\hat{\mathbf{q}}(\xi) = \xi^{(s-2)} \left(\mathbf{E}_0^s \xi \hat{\mathbf{u}}(\xi)_{,\xi} + \left[\mathbf{E}_1^s\right]^T \hat{\mathbf{u}}(\xi) \right) \tag{5.25}$$

Utilizing Equations (5.23), (5.25) and (5.12), the scaled boundary finite element equation in displacement is thus transformed into the following first-order differential equation for the dynamic stiffness $\mathbf{S}^s(\omega)$ on the boundary $\xi = 1$ with independent variable ω,

$$\begin{aligned}\left(\mathbf{S}^s(\omega) - \mathbf{E}_1^s\right)\left[\mathbf{E}_0^s\right]^{-1}\left(\mathbf{S}^s(\omega) - \left[\mathbf{E}_1^s\right]^T\right) - \mathbf{E}_2^s + (s-2)\mathbf{S}^s(\omega) + \omega\mathbf{S}^s(\omega)_{,\omega} \\ + \omega^2 \mathbf{M}_0^s = 0\end{aligned} \tag{5.26}$$

Equation (5.26) is also known as the scaled boundary finite element equation in dynamic stiffness.

In order to obtain mass matrix $\mathbf{M}$ for a subdomain, a low-frequency expansion

of dynamic stiffness matrix (Song and Wolf, 1997),

$$\mathbf{S}^s(\omega) = \mathbf{K}_e - \omega^2 \mathbf{M} \tag{5.27}$$

is considered.

In Equation (5.27), terms of order in ω higher than two are neglected. $\mathbf{K}_e$ in Equation (5.27) is determined in Equation (5.20). Substituting Equation (5.27) into (5.26) results in an equation with constant term independent of ω, a quadratic term in ω^2 and higher-order terms which can be neglected. For satisfying the solution in statics ($\omega = 0$), the constant term is equal to zero. Then, the remaining term in ω^2 is:

$$\left(\left(-\mathbf{K}_e + \mathbf{E}_1^s\right)\left[\mathbf{E}_0^s\right]^{-1} - \frac{s}{2}\mathbf{I}\right)\mathbf{M} + \mathbf{M}\left(\left[\mathbf{E}_0^s\right]^{-1}\left(-\mathbf{K}_e + \left[\mathbf{E}_1^s\right]^T\right) - \frac{s}{2}\mathbf{I}\right) + \mathbf{M}_0^s = 0 \tag{5.28}$$

which is a Lyapunov equation as $\mathbf{K}_e = \mathbf{K}_e^T$ and $\mathbf{E}_0^s = \left(\mathbf{E}_0^s\right)^T$. Equation (5.28) can also be written in the following form

$$\mathbf{A}\mathbf{M} + \mathbf{M}\mathbf{A}^T = \mathbf{C} \tag{5.29}$$

with $\mathbf{A} = \left(\left(-\mathbf{K}_e + \mathbf{E}_1^s\right)\left[\mathbf{E}_0^s\right]^{-1} - \frac{s}{2}\mathbf{I}\right)$, $\mathbf{C} = \left(-\mathbf{M}_0^s\right)$ and $\mathbf{M}$ is the unknown mass matrix.

Equation (5.28) can be solved alternatively via utilizing the intermediate results of eigenvalue decomposition in Equation (5.17). Details of the SBFEM for elasto-dynamics are presented in Reference (Song and Wolf, 1997). Similar to FEM, $\mathbf{K}_e$ and $\mathbf{M}$ for all subdomains can be assembled to form the following global equations of motion in (5.30) with frequency-independent coefficients that represent the whole problem domain

$$\left[\sum_{i=1}^{nPol} \mathbf{K}_e\right]\mathbf{U}_b(t) + \left[\sum_{i=1}^{nPol} \mathbf{M}\right]\ddot{\mathbf{U}}_b(t) = \mathbf{F}_b(t) \tag{5.30}$$

where $\mathbf{U}_b(t)$ and $\mathbf{F}_b(t)$ are the time-dependent global nodal displacement and force vectors due to arbitrary excitations. $\left[\sum_{i=1}^{nPol} \mathbf{M}\right]$ is the assembled global mass matrix. Equation (5.30) can be solved using standard time stepping algorithms,

such as Newmark's method, for elastodynamic analysis. The global mass matrix $\left[\sum_{i=1}^{nPol} \mathbf{M}\right]$ derived here will be directly used later in Section 6.4.2 for dynamic elastoplastic analysis as it remains to be a constant before or after the yielding happens (Chopra, 2001).

Analogous to the solution procedures for impedance matrix in Sections 3.2.1.1 and 3.2.1.2. Equation (5.26) can be solved efficiently by expanding the dynamic-stiffness matrix $\mathbf{S}^s(\omega)$ into continued-fraction expansions as stated in (Song, 2009; Chen et al., 2014). The time-domain transformation is again achieved by introducing auxiliary variables. The final global equations of motion for transient analysis of structure domain is expressed as:

$$\mathbf{M}_G^s \ddot{\mathbf{u}}_G(t) + \mathbf{K}_G^s \mathbf{u}_G(t) = \mathbf{f}_G(t) \tag{5.31}$$

The vector of unknowns for structural dynamics $\mathbf{u}_G(t)$ includes the nodal displacement $\mathbf{U}_b(t)$ and auxiliary variables $\mathbf{u}^{(i)}(t)$:

$$\mathbf{u}_G(t) = \left\{ \mathbf{U}_b(t) \quad \mathbf{u}^{(1)}(t) \quad \mathbf{u}^{(2)}(t) \quad \cdots \quad \mathbf{u}^{(M)}(t) \right\}^T \tag{5.32}$$

The expression in Equation (5.32) is written for M-order continued-fraction solutions with the superscript $i = 1, 2, 3, \cdots, M$ in auxiliary variables $\mathbf{u}^{(i)}(t)$. The right-hand-side vector $\mathbf{f}_G(t)$ in Equation (5.31) contains the transient nodal force vector $\mathbf{F}(t)$ from any external source,

$$\mathbf{f}_G(t) = \left\{ \mathbf{F}_b(t) \quad 0 \quad 0 \quad \cdots \quad 0 \right\}^T \tag{5.33}$$

The global mass $\mathbf{M}_G^s$ and stiffness matrices $\mathbf{K}_G^s$ in Equation (5.31) for structural

dynamics in SBFEM can then be formulated as:

$$\mathbf{M}_G^s = \begin{bmatrix} \mathbf{M}_s & -\mathbf{X}_s^{(1)} & 0 & \cdots & 0 \\ -\left[\mathbf{X}_s^{(1)}\right]^T & \mathbf{S}_{s1}^{(1)} & -\mathbf{X}_s^{(2)} & \cdots & 0 \\ 0 & -\left[\mathbf{X}_s^{(2)}\right]^T & \mathbf{S}_{s1}^{(2)} & \ddots & 0 \\ \vdots & \vdots & \ddots & \ddots & -\mathbf{X}_s^{(M)} \\ 0 & 0 & 0 & -\left[\mathbf{X}_s^{(M)}\right]^T & \mathbf{S}_{s1}^{(M)} \end{bmatrix} \tag{5.34a}$$

$$\mathbf{K}_G^s = \text{diag}\left(\mathbf{K}_s \; \mathbf{S}_{s0}^{(1)} \; \mathbf{S}_{s0}^{(2)} \; \cdots \; \mathbf{S}_{s0}^{(M)}\right) \tag{5.34b}$$

In Equation(5.34), $\mathbf{S}_{s0}^{(i)}$, $\mathbf{S}_{s1}^{(i)}$ and $\mathbf{X}_s^{(i)}$ are those coefficient matrices calculated recursively in the continued-fraction expansion for dynamic-stiffness matrices $\mathbf{S}^s(\omega)$ of all subdomains and assembled using standard finite element techniques. $\mathbf{M}_s$ and $\mathbf{K}_s$ correspond to the low-frequency expansion of $\mathbf{S}^s(\omega)$ of all subdomains. In other words, $\mathbf{M}_s = \left[\sum_{i=1}^{nPol} \mathbf{M}\right]$ and $\mathbf{K}_s = \left[\sum_{i=1}^{nPol} \mathbf{K}_e\right]$ applies. All 's' in superscripts and subscripts indicate the structural domain for the purpose of distinguishing from similar coefficients used in Equation (3.38) for bounded acoustic domain. The global equations for structural domain in Equation (5.31) will be coupled with the global equations for acoustic domain in Equation (3.116) or (4.45) in the next section to perform the acoustic-structure interaction analysis.

5.3 Scaled boundary finite element formulation for acoustic-structure interaction system

A schematic diagram of the general acoustic-structure interaction system modeled by the proposed SBFEM is illustrated in Figure 5.1. In this diagram, the red region represent the structural domain, which is denoted by Ω_s. The surrounding acoustic near field is indicated by the blue area and the acoustic far field is represented by the circular or spherical open boundary Γ for 2D or 3D cases respectively as in Figure 4.1. The whole acoustic domain, which includes both the near field Ω_N and far field

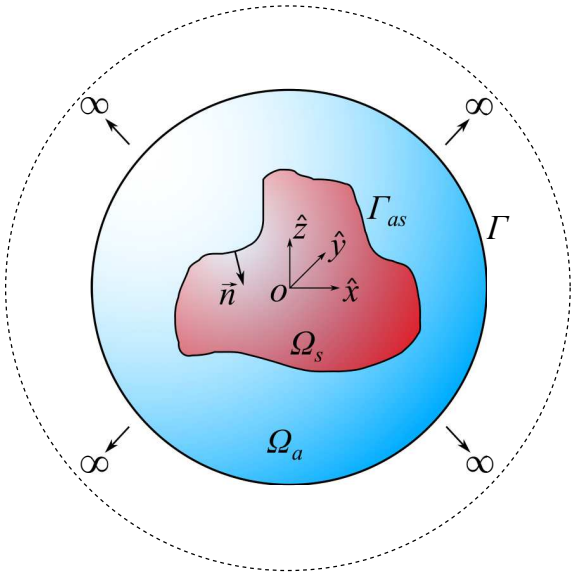

Figure 5.1. A typical acoustic-structure interaction system

Ω_F in Figure 4.1, is denoted by Ω_a here. In Figure 5.1, a predefined unit vector $\vec{\mathbf{n}}$ is normal to the acoustic-structure interface Γ_{as} and pointing from the acoustic domain into the structural domain. The acoustic media in Ω_a is again assumed to be linear, inviscid and isentropic fluid with small perturbations. The structural domain Ω_s is assumed to be linear elastic in this chapter.

For clearer demonstration of the coupling procedures for structural and acoustic formulations in the following Section 5.3.2, the individual equations for structural and acoustic domains in Equations (5.31) and (4.45) are partitioned according to the locations of nodes. To this end, the vector of unknowns $\mathbf{u}_G(t)$ in the global equations for structural dynamics expressed in Equation (5.32) can be divided as:

$$\mathbf{u}_G(t) = \left\{ \begin{array}{ccc|c} \mathbf{u}_o(t) & \mathbf{u}_{as}(t) & & \tilde{\mathbf{u}}(t) \end{array} \right\}^T \tag{5.35}$$

In Equation (5.35), $\mathbf{u}_{as}(t)$ and $\mathbf{u}_o(t)$ are nodal displacements of the structure on the acoustic-structure interface Γ_{as} and other structural region, respectively. $\tilde{\mathbf{u}}(t)$ represents all the auxiliary variables $\mathbf{u}^{(i)}(t)$ in Equation (5.32). For the clarification of notations, the subscript 'as' and 'o' used in all the following equations in this whole chapter denotes nodes on the acoustic-structure interface and other region of structural or acoustic domain. The tilde $\tilde{\bullet}$ is used to indicate any rows and columns

corresponding to the auxiliary variables. Following the same arrangement, the right-hand-side vector $\mathbf{f}_G(t)$ in Equation (5.31) containing the external nodal force can be partitioned as:

$$\mathbf{f}_G(t) = \left\{ \begin{array}{cc|c} \mathbf{F}_o(t) & \mathbf{F}_{as}^{ext}(t) + \mathbf{F}_{as}(t) & 0 \end{array} \right\}^T \tag{5.36}$$

where $\mathbf{F}_{as}^{ext}(t)$ and $\mathbf{F}_o(t)$ are nodal forces applied on acoustic-structure interface and other parts of structural domain from any external source, while $\mathbf{F}_{as}(t)$ represents the force applied on the acoustic-structure interface caused by the excitations from acoustic domain. The global mass and stiffness matrices in Equation (5.34) are then partitioned in the same manner.

$$\mathbf{M}_G^s = \left[\begin{array}{cc|c} \mathbf{M}_o^s & \mathbf{M}_{o\cdot as}^s & \tilde{\mathbf{M}}_2^s \\ [\mathbf{M}_{o\cdot as}^s]^T & \mathbf{M}_{as}^s & \\ \hline \left[\tilde{\mathbf{M}}_2^s\right]^T & & \tilde{\mathbf{M}}_1^s \end{array} \right] \tag{5.37a}$$

$$\mathbf{K}_G^s = \left[\begin{array}{cc|c} \mathbf{K}_o^s & \mathbf{K}_{o\cdot as}^s & 0 \\ [\mathbf{K}_{o\cdot as}^s]^T & \mathbf{K}_{as}^s & \\ \hline 0 & & \tilde{\mathbf{K}}_1^s \end{array} \right] \tag{5.37b}$$

It should be noticed that the $\mathbf{M}_s$ and $\mathbf{K}_s$ in Equation (5.34) related to real nodes in the structural domain, i.e. the upper-left part in Equation (5.37), are divided into four submatrices, respectively. All other coefficient matrices in rows and columns corresponding to auxiliary variables are allocated in $\tilde{\mathbf{M}}_1^s$, $\tilde{\mathbf{M}}_2^s$ and $\tilde{\mathbf{K}}_1^s$. The global equations for structural dynamics in Equation (5.31) can be written as:

$$\left[\begin{array}{cc|c} \mathbf{M}_o^s & \mathbf{M}_{o\cdot as}^s & \tilde{\mathbf{M}}_2^s \\ [\mathbf{M}_{o\cdot as}^s]^T & \mathbf{M}_{as}^s & \\ \hline \left[\tilde{\mathbf{M}}_2^s\right]^T & & \tilde{\mathbf{M}}_1^s \end{array} \right] \left\{ \begin{array}{c} \ddot{\mathbf{u}}_o \\ \ddot{\mathbf{u}}_{as} \\ \hline \ddot{\tilde{\mathbf{u}}} \end{array} \right\} + \left[\begin{array}{cc|c} \mathbf{K}_o^s & \mathbf{K}_{o\cdot as}^s & 0 \\ [\mathbf{K}_{o\cdot as}^s]^T & \mathbf{K}_{as}^s & \\ \hline 0 & & \tilde{\mathbf{K}}_1^s \end{array} \right] \left\{ \begin{array}{c} \mathbf{u}_o \\ \mathbf{u}_{as} \\ \hline \tilde{\mathbf{u}} \end{array} \right\} = \left\{ \begin{array}{c} \mathbf{F}_o \\ \mathbf{F}_{as}^{ext} + \mathbf{F}_{as} \\ \hline 0 \end{array} \right\} \tag{5.38}$$

In Equation (5.38), the argument (t) is omitted from Equations (5.35) and (5.36) for simplifying the presentation of equation. Analogously, the global equations for the whole acoustic domain in Equation (3.116) or (4.45) can be divided into similar partitions as for structural domain. The vector of unknowns $\mathbf{z}_G(t)$ for acoustics is reformulated as:

$$\mathbf{z}_G(t) = \left\{ \begin{array}{cc|c} \mathbf{p}_{as}(t) & \mathbf{p}_o(t) & \tilde{\mathbf{p}}(t) \end{array} \right\}^T \tag{5.39}$$

where $\mathbf{p}_{as}(t)$ and $\mathbf{p}_o(t)$ are nodal acoustic pressure on the acoustic-structure interface and in the other region of acoustic domain, respectively. $\tilde{\mathbf{p}}(t)$ includes all auxiliary variables for both bounded and unbounded acoustic domains $\mathbf{p}^{(i)}(t)$, $\tilde{\mathbf{p}}^{(i_H)}(t)$ and $\tilde{\mathbf{p}}_L^{(i_L)}(t)$ in Equation (3.117). The right-hand-side vector $\mathbf{r}_G(t)$ in Equation (3.116) or (4.45) containing the external flux can then be written as:

$$\mathbf{r}_G(t) = \left\{ \begin{array}{cc|c} \mathbf{R}_{as}^{ext}(t) + \mathbf{R}_{as}(t) & \mathbf{R}_o(t) & 0 \end{array} \right\}^T \tag{5.40}$$

where $\mathbf{R}_{as}^{ext}(t)$ are external nodal fluxes applied on acoustic-structure interface. $\mathbf{R}_o(t)$ are external nodal fluxes applied in other parts of acoustic domain. $\mathbf{R}_{as}(t)$ represents the flux applied on the acoustic-structure interface caused by the excitations of structure. The global mass, damping and stiffness matrices in Equations (3.119)-(3.121), or Equation (4.46) for stiffness matrix in 3D acoustics, are then partitioned as,

$$\mathbf{M}_G^a = \left[\begin{array}{cc|c} \mathbf{M}_{as}^a & \mathbf{M}_{as\cdot o}^a & \tilde{\mathbf{M}}_2^a \\ [\mathbf{M}_{as\cdot o}^a]^T & \mathbf{M}_o^a & \\ \hline \multicolumn{2}{c|}{\left[\tilde{\mathbf{M}}_2^a\right]^T} & \tilde{\mathbf{M}}_1^a \end{array} \right] \tag{5.41a}$$

$$\mathbf{C}_G^a = \left[\begin{array}{cc|c} 0 & 0 & \\ 0 & \mathbf{C}_o^a & 0 \\ \hline \multicolumn{2}{c|}{0} & \tilde{\mathbf{C}}_1^a \end{array} \right] \tag{5.41b}$$

$$\mathbf{K}_G^a = \left[\begin{array}{cc|c} \mathbf{K}_{as}^a & \mathbf{K}_{as\cdot o}^a & \tilde{\mathbf{K}}_2^a \\ [\mathbf{K}_{as\cdot o}^a]^T & \mathbf{K}_o^a & \\ \hline \left[\tilde{\mathbf{K}}_2^a\right]^T & & \tilde{\mathbf{K}}_1^a \end{array}\right] \tag{5.41c}$$

Again, the partitions in Equations (3.119) - (3.121) and (4.46) related to real nodes in the acoustic domain are in the top-left partition in Equation (5.41). All other coefficient matrices in rows and columns corresponding to auxiliary variables are allocated in those coefficient matrices with tilde $\tilde{\bullet}$. In Equation (5.41b), the top-left partition only includes $\mathbf{C}_o^a$ corresponding to nodes in acoustic domain excluding those on the acoustic-structure interface. This is due to the fact that the radiation damping is only contributed by the unbounded acoustic domain, which is just related to those nodes on the doubly-asymptotic open boundary Γ in Figure 5.1. The global equations for acoustics in Equation (4.45) can be written as:

$$\left[\begin{array}{cc|c} \mathbf{M}_{as}^a & \mathbf{M}_{as\cdot o}^a & \tilde{\mathbf{M}}_2^a \\ [\mathbf{M}_{as\cdot o}^a]^T & \mathbf{M}_o^a & \\ \hline \left[\tilde{\mathbf{M}}_2^a\right]^T & & \tilde{\mathbf{M}}_1^a \end{array}\right] \left\{\begin{array}{c} \ddot{\mathbf{p}}_{as} \\ \ddot{\mathbf{p}}_o \\ \hline \ddot{\tilde{\mathbf{p}}} \end{array}\right\} + \left[\begin{array}{cc|c} 0 & 0 & 0 \\ 0 & \mathbf{C}_o^a & \\ \hline 0 & & \tilde{\mathbf{C}}_1^a \end{array}\right] \left\{\begin{array}{c} \dot{\mathbf{p}}_{as} \\ \dot{\mathbf{p}}_o \\ \hline \dot{\tilde{\mathbf{p}}} \end{array}\right\}$$
$$+ \left[\begin{array}{cc|c} \mathbf{K}_{as}^a & \mathbf{K}_{as\cdot o}^a & \tilde{\mathbf{K}}_2^a \\ [\mathbf{K}_{as\cdot o}^a]^T & \mathbf{K}_o^a & \\ \hline \left[\tilde{\mathbf{K}}_2^a\right]^T & & \tilde{\mathbf{K}}_1^a \end{array}\right] \left\{\begin{array}{c} \mathbf{p}_{as} \\ \mathbf{p}_o \\ \hline \tilde{\mathbf{p}} \end{array}\right\} = \left\{\begin{array}{c} \mathbf{R}_{as}^{ext} + \mathbf{R}_{as} \\ \mathbf{R}_o \\ \hline 0 \end{array}\right\} \tag{5.42}$$

The rearranged formulations in Equations (5.38) and (5.42) will be used to derive the coupled formulation for acoustic-structure interaction system in the Section 5.3.2.

5.3.1 Boundary conditions on acoustic-structure interface

When coupling of acoustic and structural domains, two boundary conditions have to be satisfied on the acoustic-structure interface for both 2D and 3D problems. Because the acoustic medium is assumed to be inviscid, no shear force exists in the acoustic domain. Both boundary conditions hold only in the direction normal to the acoustic-structure interface. This normal direction is specified by the unit vector $\vec{\mathbf{n}}$

in Figure 5.1.

For the first boundary condition, the acoustic pressure applied on the acoustic-structure interface should equal to the normal traction applied on the structure side of the interface:

$$\vec{\mathbf{n}} \cdot p_{as} = \mathbf{T}_{as} \tag{5.43}$$

where, $\mathbf{T}_{as}$ is the normal traction applied on the structural side of acoustic-structure interface caused by the acoustic pressure from acoustic side. p_{as} represents the acoustic pressure field on the same interface and can therefore be interpolated by the same shape function $\mathbf{N}$ in Equation (3.8) or (4.7) for interpolating 2D or 3D acoustic fields respectively in SBFEM,

$$p_{as} = \mathbf{N}\mathbf{p}_{as} \tag{5.44}$$

$\mathbf{p}_{as}$ in Equation (5.44) is the nodal acoustic pressure on the acoustic-structure interface as defined in Equation (5.39).

The second boundary condition is about the normal displacement compatibility on the acoustic-structure interface, that is, the normal structural displacement on the acoustic-structure interface should equal to the normal displacement of fluid particles on the same interface in acoustic domain

$$\vec{\mathbf{n}}^T \mathbf{u}_s = \vec{\mathbf{n}}^T \mathbf{u}_a \tag{5.45}$$

where $\mathbf{u}_s$ and $\mathbf{u}_a$ are the displacement fields of structure and fluid particles on the acoustic-structure interface separately. $\mathbf{u}_s$ can also be interpolated by the shape function $\mathbf{N}_s$ in Equation (A.3) or (5.4) for interpolating 2D or 3D structural displacement fields respectively in SBFEM,

$$\mathbf{u}_s = \mathbf{N}_s \mathbf{u}_{as} \tag{5.46}$$

$\mathbf{u}_{as}$ in Equation (5.46) is the nodal displacements of structure on the acoustic-structure interface as defined in Equation (5.35). Applying Equation (5.45) into

Euler equation and neglecting the hydrostatic term, the flux applied on the acoustic-structure interface can be expressed by:

$$\frac{\partial p_{as}}{\partial \vec{\mathbf{n}}} = -\rho_a \vec{\mathbf{n}}^T \ddot{\mathbf{u}}_a = -\rho_a \vec{\mathbf{n}}^T \ddot{\mathbf{u}}_s \tag{5.47}$$

where ρ_a is the density of acoustic medium. $\ddot{\mathbf{u}}_a$ and $\ddot{\mathbf{u}}_s$ are accelerations of fluid particles and structure surface on the acoustic-structure interface.

According to Equation (5.24) for defining the nodal forces, the nodal forces on the acoustic-structure interface can be calculated by:

$$\mathbf{F}_{as} = \int_{\Gamma_{as}} \mathbf{N}_s^T \mathbf{T}_{as} d\Gamma \tag{5.48}$$

Substituting Equation (5.43) and (5.44) into (5.48) yields the expression for nodal force on the acoustic-structure interface:

$$\mathbf{F}_{as} = \int_{\Gamma_{as}} \mathbf{N}_s^T \vec{\mathbf{n}} \mathbf{N} d\Gamma \cdot \mathbf{p}_{as} \tag{5.49}$$

Analogously, the nodal flux on acoustic-structure interface can be defined from Equation (3.15) as:

$$\mathbf{R}_{as} = \int_{\Gamma_{as}} \mathbf{N}^T \frac{\partial p_{as}}{\partial \vec{\mathbf{n}}} d\Gamma \tag{5.50}$$

Substituting Equations (5.47) and (5.46) into (5.50) yields the expression for nodal flux on acoustic-structure interface:

$$\mathbf{R}_{as} = (-\rho_a) \cdot \int_{\Gamma_{as}} \mathbf{N}^T \vec{\mathbf{n}}^T \mathbf{N}_s d\Gamma \cdot \ddot{\mathbf{u}}_{as} \tag{5.51}$$

The nodal force $\mathbf{F}_{as}$ and flux $\mathbf{R}_{as}$ in Equations (5.49) and (5.51) are calculated on an element-by-element basis for all elements on the acoustic-structure interface Γ_{as} and assembled using standard finite element techniques. Corresponding integrations are one-dimensional for 2D problems or two-dimensional for 3D problems. The common terms in Equations (5.49) and (5.51) are defined as the coupling matrix

$\mathbf{H}_{as}$ in acoustic-structure interaction,

$$\mathbf{H}_{as} = \int_{\Gamma_{as}} \mathbf{N}_s^T \vec{\mathbf{n}} \mathbf{N} d\Gamma \tag{5.52}$$

Therefore, the interacting force and flux on the acoustic-structure interface in Equation (5.49) and (5.51) can be written as:

$$\mathbf{F}_{as} = \mathbf{H}_{as} \mathbf{p}_{as} \tag{5.53a}$$

$$\mathbf{R}_{as} = -\rho_a \mathbf{H}_{as}^T \ddot{\mathbf{u}}_{as} \tag{5.53b}$$

5.3.2 Coupling of acoustic and structural domains

In Equation (5.38), the interaction force applied on the structural side of acoustic-structure interface caused by the acoustic pressure $\mathbf{F}_{as}$ is expressed in Equation (5.53a). Substituting Equation (5.53a) into (5.38) yields:

$$\left[\begin{array}{cc|c} \mathbf{M}_o^s & \mathbf{M}_{o\cdot as}^s & \tilde{\mathbf{M}}_2^s \\ \left[\mathbf{M}_{o\cdot as}^s\right]^T & \mathbf{M}_{as}^s & \\ \hline \left[\tilde{\mathbf{M}}_2^s\right]^T & & \tilde{\mathbf{M}}_1^s \end{array}\right] \left\{\begin{array}{c} \ddot{\mathbf{u}}_o \\ \ddot{\mathbf{u}}_{as} \\ \hline \ddot{\tilde{\mathbf{u}}} \end{array}\right\} + \left[\begin{array}{cc|c} \mathbf{K}_o^s & \mathbf{K}_{o\cdot as}^s & 0 \\ \left[\mathbf{K}_{o\cdot as}^s\right]^T & \mathbf{K}_{as}^s & \\ \hline 0 & & \tilde{\mathbf{K}}_1^s \end{array}\right] \left\{\begin{array}{c} \mathbf{u}_o \\ \mathbf{u}_{as} \\ \hline \tilde{\mathbf{u}} \end{array}\right\} = \left\{\begin{array}{c} \mathbf{F}_o \\ \hline \mathbf{F}_{as}^{ext} + \mathbf{H}_{as}\mathbf{p}_{as} \\ \hline 0 \end{array}\right\} \tag{5.54}$$

Since the interaction flux $\mathbf{R}_{as}$ applied on the acoustic side of acoustic-structure interface caused by the structural accelerations is also formulated in Equation (5.53b). Substituting Equation (5.53b) into (5.42) yields:

$$\left[\begin{array}{cc|c} \mathbf{M}_{as}^a & \mathbf{M}_{as\cdot o}^a & \tilde{\mathbf{M}}_2^a \\ \left[\mathbf{M}_{as\cdot o}^a\right]^T & \mathbf{M}_o^a & \\ \hline \left[\tilde{\mathbf{M}}_2^a\right]^T & & \tilde{\mathbf{M}}_1^a \end{array}\right] \left\{\begin{array}{c} \ddot{\mathbf{p}}_{as} \\ \ddot{\mathbf{p}}_o \\ \hline \ddot{\tilde{\mathbf{p}}} \end{array}\right\} + \left[\begin{array}{cc|c} 0 & 0 & 0 \\ 0 & \mathbf{C}_o^a & \\ \hline 0 & & \tilde{\mathbf{C}}_1^a \end{array}\right] \left\{\begin{array}{c} \dot{\mathbf{p}}_{as} \\ \dot{\mathbf{p}}_o \\ \hline \dot{\tilde{\mathbf{p}}} \end{array}\right\}$$

$$+\left[\begin{array}{cc|c} \mathbf{K}_{as}^{a} & \mathbf{K}_{as\cdot o}^{a} & \tilde{\mathbf{K}}_{2}^{a} \\ [\mathbf{K}_{as\cdot o}^{a}]^{T} & \mathbf{K}_{o}^{a} & \\ \hline \left[\tilde{\mathbf{K}}_{2}^{a}\right]^{T} & & \tilde{\mathbf{K}}_{1}^{a} \end{array}\right]\left\{\begin{array}{c} \mathbf{p}_{as} \\ \mathbf{p}_{o} \\ \hline \tilde{\mathbf{p}} \end{array}\right\}=\left\{\begin{array}{c} \mathbf{R}_{as}^{ext}-\rho_{a}\mathbf{H}_{as}^{T}\ddot{\mathbf{u}}_{as} \\ \mathbf{R}_{o} \\ \hline 0 \end{array}\right\} \tag{5.55}$$

Moving the interacting force and flux terms $\mathbf{H}_{as}\mathbf{p}_{as}$ and $\rho_{a}\mathbf{H}_{as}^{T}\ddot{\mathbf{u}}_{as}$ from the right-hand-side of Equations (5.54) and (5.55) to their left-hand-side and rearranging the resulting two equations into one coupled equations. The global equations of motion for coupled acoustic-structure interaction system can thus be formulated as:

$$\mathbf{M}_{G}\ddot{\mathbf{Z}}_{G}(t)+\mathbf{C}_{G}\dot{\mathbf{Z}}_{G}(t)+\mathbf{K}_{G}\mathbf{Z}_{G}(t)=\mathbf{F}_{G}(t) \tag{5.56}$$

with the global vector of unknowns for acoustic-structure interaction system $\mathbf{Z}_{G}(t)$ defined by:

$$\mathbf{Z}_{G}(t)=\left\{\begin{array}{cc|cc|cc} \mathbf{u}_{o}(t) & \mathbf{u}_{as}(t) & \mathbf{p}_{as}(t) & \mathbf{p}_{o}(t) & \tilde{\mathbf{u}}(t) & \tilde{\mathbf{p}}(t) \end{array}\right\}^{T} \tag{5.57}$$

The right-hand-side vector vector for acoustic-structure interaction system $\mathbf{F}_{G}(t)$ in Equation (5.58) contains both the external nodal forces in structural domain and external nodal fluxes in acoustic domain.

$$\mathbf{F}_{G}(t)=\left\{\begin{array}{cc|cc|cc} \mathbf{F}_{o}(t) & \mathbf{F}_{as}^{ext}(t) & \mathbf{R}_{as}^{ext}(t) & \mathbf{R}_{o}(t) & 0 & 0 \end{array}\right\}^{T} \tag{5.58}$$

Following the partitions in Equations (5.57) and (5.58), the global mass, damping and stiffness matrices for acoustic-structure interaction system are given in the following Equation (5.59):

$$\mathbf{M}_{G}=\left[\begin{array}{cc|cc|cc} \mathbf{M}_{o}^{s} & \mathbf{M}_{o\cdot as}^{s} & \multicolumn{2}{c|}{0} & \tilde{\mathbf{M}}_{2}^{s} & 0 \\ [\mathbf{M}_{o\cdot as}^{s}]^{T} & \mathbf{M}_{as}^{s} & & & & \\ \hline 0 & \rho_{a}\mathbf{H}_{as}^{T} & \mathbf{M}_{as}^{a} & \mathbf{M}_{as\cdot o}^{a} & 0 & \tilde{\mathbf{M}}_{2}^{a} \\ 0 & 0 & [\mathbf{M}_{as\cdot o}^{a}]^{T} & \mathbf{M}_{o}^{a} & & \\ \hline \left[\tilde{\mathbf{M}}_{2}^{s}\right]^{T} & & \multicolumn{2}{c|}{0} & \tilde{\mathbf{M}}_{1}^{s} & 0 \\ 0 & & \multicolumn{2}{c|}{\left[\tilde{\mathbf{M}}_{2}^{a}\right]^{T}} & 0 & \tilde{\mathbf{M}}_{1}^{a} \end{array}\right] \tag{5.59a}$$

$$\mathbf{C}_G = \left[\begin{array}{c|cc|cc} 0 & \multicolumn{2}{c|}{0} & \multicolumn{2}{c}{0} \\ \hline 0 & \multicolumn{2}{c|}{\begin{matrix} 0 & 0 \\ 0 & \mathbf{C}_o^a \end{matrix}} & \multicolumn{2}{c}{0} \\ \hline 0 & \multicolumn{2}{c|}{0} & \multicolumn{2}{c}{\begin{matrix} 0 & 0 \\ 0 & \tilde{\mathbf{C}}_1^a \end{matrix}} \end{array}\right] \tag{5.59b}$$

$$\mathbf{K}_G = \left[\begin{array}{cc|cc|cc} \multicolumn{2}{c|}{\begin{matrix} \mathbf{K}_o^s & \mathbf{K}_{o\cdot as}^s \\ [\mathbf{K}_{o\cdot as}^s]^T & \mathbf{K}_{as}^s \end{matrix}} & \multicolumn{2}{c|}{\begin{matrix} 0 & 0 \\ -\mathbf{H}_{as} & 0 \end{matrix}} & \multicolumn{2}{c}{0} \\ \hline \multicolumn{2}{c|}{0} & \multicolumn{2}{c|}{\begin{matrix} \mathbf{K}_{as}^a & \mathbf{K}_{as\cdot o}^a \\ [\mathbf{K}_{as\cdot o}^a]^T & \mathbf{K}_o^a \end{matrix}} & \multicolumn{2}{c}{\begin{matrix} 0 & \tilde{\mathbf{K}}_2^a \end{matrix}} \\ \hline \multicolumn{2}{c|}{0} & \multicolumn{2}{c|}{\begin{matrix} 0 \\ \left[\tilde{\mathbf{K}}_2^a\right]^T \end{matrix}} & \multicolumn{2}{c}{\begin{matrix} \tilde{\mathbf{K}}_1^s & 0 \\ 0 & \tilde{\mathbf{K}}_1^a \end{matrix}} \end{array}\right] \tag{5.59c}$$

In Equation (5.59), the global mass matrix $\mathbf{M}_G$ is a result of structural and acoustic near field. Global damping matrix $\mathbf{C}_G$ is only due to the acoustic far field, while the global stiffness matrix $\mathbf{K}_G$ includes the contributions from both structural and acoustic domains with the near and far fields. Equation (5.56) can then be solved using standard time-stepping schemes, such as Newmark's method. It should be noticed that the global equations of motion for acoustic-structure interaction analysis are not symmetric due to the unsymmetrical terms in the global mass matrix $\mathbf{M}_G$ and stiffness matrix $\mathbf{K}_G$. In the next section, the global equations of motion in Equation (5.56) for acoustic-structure interaction analysis will be transformed into a symmetric formulation by replacing all variables related to acoustic domain in the global vector of unknown $\mathbf{Z}_G(t)$ with newly defined variables.

5.3.3 Symmetric formulation for acoustic-structure interaction system

In Reference (Everstine, 1981), a symmetric formulation is proposed for transient acoustic-structure interaction analysis via merely replacing the acoustic pressure by

velocity potential. Similar approach can be applied to Equation (5.56) to transform this unsymmetrical global system of equation for acoustic-structure interaction analysis in SBFEM to a symmetric formulation. To this end, the following new variables are introduced to the acoustic parts in Equations (5.57) and (5.58)

$$\mathbf{p}_{as}(t) = \dot{\mathbf{q}}_{as}(t),\ \mathbf{p}_o(t) = \dot{\mathbf{q}}_o(t),\ \tilde{\mathbf{p}}(t) = \dot{\tilde{\mathbf{q}}}(t),\ \mathbf{R}_{as}^{ext}(t) = \dot{\mathbf{V}}_{as}^{ext}(t),\ \mathbf{R}_o(t) = \dot{\mathbf{V}}_o(t) \tag{5.60}$$

New variables in Equation (5.60) are substituted into the global vector of unknown $\mathbf{Z}_G(t)$ and global load vector $\mathbf{F}_G(t)$ in the global equation for acoustic-structure interaction system in Equation (5.56). Then, integrating those rows corresponding to newly introduced variables in time and multiplying the resulting rows by $-\frac{1}{\rho_a}$ on both sides yields the symmetric global equations for acoustic-structure interaction system in SBFEM

$$\bar{\mathbf{M}}_G\ddot{\bar{\mathbf{Z}}}_G(t) + \bar{\mathbf{C}}_G\dot{\bar{\mathbf{Z}}}_G(t) + \bar{\mathbf{K}}_G\bar{\mathbf{Z}}_G(t) = \bar{\mathbf{F}}_G(t) \tag{5.61}$$

where the new global vector of unknown $\bar{\mathbf{Z}}_G(t)$ in symmetric formulation is written as:

$$\bar{\mathbf{Z}}_G(t) = \left\{ \begin{array}{cc|cc|cc} \mathbf{u}_o(t) & \mathbf{u}_{as}(t) & \mathbf{q}_{as}(t) & \mathbf{q}_o(t) & \tilde{\mathbf{u}}(t) & \tilde{\mathbf{q}}(t) \end{array} \right\}^T \tag{5.62}$$

Similarly, the global right-hand-side vector in Equation (5.61) is:

$$\bar{\mathbf{F}}_G(t) = \left\{ \begin{array}{cc|cc|cc} \mathbf{F}_o(t) & \mathbf{F}_{as}^{ext}(t) & \mathbf{V}_{as}^{ext}(t) & \mathbf{V}_o(t) & 0 & 0 \end{array} \right\}^T \tag{5.63}$$

For applying any external flux $\mathbf{R}_{as}^{ext}(t)$ or $\mathbf{R}_o(t)$ to the acoustic domain in the symmetric formulation, the relative part $\mathbf{V}_{as}^{ext}(t)$ or $\mathbf{V}_o(t)$ in Equation (5.63) can be obtained by simply integrating the external flux $\mathbf{R}_{as}^{ext}(t)$ or $\mathbf{R}_o(t)$ with respect to time according to Equation (5.60). The symmetric mass, damping and stiffness

matrices in Equation (5.61) are given below:

$$\bar{\mathbf{M}}_G = \left[\begin{array}{cc|cc|cc} \mathbf{M}_o^s & \mathbf{M}_{o\cdot as}^s & & & & \\ [\mathbf{M}_{o\cdot as}^s]^T & \mathbf{M}_{as}^s & & 0 & & 0 \\ \hline 0 & 0 & -\frac{1}{\rho_a}\mathbf{M}_{as}^a & -\frac{1}{\rho_a}\mathbf{M}_{as\cdot o}^a & & \\ 0 & 0 & -\frac{1}{\rho_a}[\mathbf{M}_{as\cdot o}^a]^T & -\frac{1}{\rho_a}\mathbf{M}_o^a & 0 & -\frac{1}{\rho_a}\tilde{\mathbf{M}}_2^a \\ \hline \left[\tilde{\mathbf{M}}_2^s\right]^T & & 0 & & \tilde{\mathbf{M}}_1^s & 0 \\ 0 & & -\frac{1}{\rho_a}\left[\tilde{\mathbf{M}}_2^a\right]^T & & 0 & -\frac{1}{\rho_a}\tilde{\mathbf{M}}_1^a \end{array}\right] \tag{5.64a}$$

$$\bar{\mathbf{C}}_G = \left[\begin{array}{cc|cc|cc} & & 0 & 0 & & \\ 0 & & -\mathbf{H}_{as} & 0 & 0 & \\ \hline 0 & -\mathbf{H}_{as}^T & 0 & 0 & & \\ 0 & 0 & 0 & -\frac{1}{\rho_a}\mathbf{C}_o^a & 0 & \\ \hline & & & & 0 & 0 \\ 0 & & 0 & & 0 & -\frac{1}{\rho_a}\tilde{\mathbf{C}}_1^a \end{array}\right] \tag{5.64b}$$

$$\bar{\mathbf{K}}_G = \left[\begin{array}{cc|cc|cc} \mathbf{K}_o^s & \mathbf{K}_{o\cdot as}^s & & & & \\ [\mathbf{K}_{o\cdot as}^s]^T & \mathbf{K}_{as}^s & & 0 & & 0 \\ \hline & & -\frac{1}{\rho_a}\mathbf{K}_{as}^a & -\frac{1}{\rho_a}\mathbf{K}_{as\cdot o}^a & & \\ 0 & & -\frac{1}{\rho_a}[\mathbf{K}_{as\cdot o}^a]^T & -\frac{1}{\rho_a}\mathbf{K}_o^a & 0 & -\frac{1}{\rho_a}\tilde{\mathbf{K}}_2^a \\ \hline & & 0 & & \tilde{\mathbf{K}}_1^s & 0 \\ 0 & & -\frac{1}{\rho_a}\left[\tilde{\mathbf{K}}_2^a\right]^T & & 0 & -\frac{1}{\rho_a}\tilde{\mathbf{K}}_1^a \end{array}\right] \tag{5.64c}$$

Equation (5.61) can again be solved using standard time-stepping scheme, such as Newmark's method employed in Section 5.4, for transient solutions of structural displacements and acoustic pressures. From a practical point of view, although new variables $\mathbf{q}_{as}(t)$, $\mathbf{q}_o(t)$ and $\tilde{\mathbf{q}}(t)$ in Equation (5.60) are introduced into the symmetric formulation to replace the original acoustic pressures $\mathbf{p}_{as}(t)$, $\mathbf{p}_o(t)$. and $\tilde{\mathbf{p}}(t)$, the acoustic pressures can still be directly calculated as the first-order time derivative of $\mathbf{q}_{as}(t)$, $\mathbf{q}_o(t)$. and $\tilde{\mathbf{q}}(t)$ at each time step without further effort.

5.4 Numerical examples

This section demonstrates the accuracy, efficiency and robustness of the present SBFEM for 2D and 3D acoustic-structure interaction analyses by means of five numerical examples, which include two 2D examples in Sections 5.4.1 and 5.4.2 and three 3D examples in Sections 5.4.3, 5.4.4 and 5.4.5. In all these numerical examples, the structure is assumed to be elastic and the acoustic medium is assumed to be irrotational, isentropic and inviscid with small perturbations. In the first numerical example in Section 5.4.1, an infinitely long tube with elliptical cross-section is submerged in infinite acoustic domain with load applied on the structural inner surface. Then, a example of a simply supported beam subjected to a uniformly distributed load applied on the top surface is studied in Section 5.4.2 to further verify the reliability and accuracy of proposed method for dealing with acoustic-structure interaction systems. Next, a hollow sphere vibrating in the infinite acoustic space due to structural load applied on the internal surface is simulated in Section 5.4.3 to verify the implementation of SBFEM in 3D acoustic-structure interaction. Furthermore, an example of a simply supported plate submerged in infinite acoustic space is investigated in Section 5.4.4. In this example, the hexahedral subdomains are used for modeling structure while octree mesh is employed to model the surrounding acoustic domain to illustrate the versatility of SBFEM in mesh generation for coupled system. Finally, an illustrative example of an ancient Chinese bell submerged in infinite acoustic domain in Section 5.4.5 is simulated using present SBFEM and octree mesh technique for demonstrating the feasibility and advantages of SBFEM in modeling complex acoustic-structure interaction problems. Newmark's method with $\alpha = 0.5$ and $\beta = 0.25$ (average acceleration scheme) is applied to Equation (5.56) or the symmetrical formulation in Equation (5.61) to obtain the transient displacements in structural domain and acoustic pressures in acoustic domain. The first four numerical examples are verified by reference solutions obtained using FEM with extended mesh for acoustic domain in commercial software ANSYS. Again, the

boundaries of extended meshes in FEM models are set to be far away from structures to avoid the spurious reflected waves.

5.4.1 Long elliptical tube submerged in infinite plane water

In this numerical example, a very long tube is submerged in infinite acoustic domain and modeled as a 2D acoustic-structure interaction problem. The tube has elliptical cross-section with the half major and minor axes of the inner surface equal to 9m and 7m respectively, the half major and minor axes of the outer elliptical surface are 10m and 8m. The cross-section of tube is marked by the red area in Figure 5.2. Similar to the modeling of infinite acoustic domain in Chapter 3, the surrounding infinite acoustic medium is again divided into the blue acoustic near field and the far field is represented by the circular open boundary with radius equal to 15m in the same figure. The structure is assumed to have the Young's modulus of $E =$ 210GPa, Poisson ratio of $\nu = 0.3$ and mass density $\rho_s = 7860\text{kg/m}^3$ with plane-strain condition, while the acoustic medium is assumed to be water and has the sound speed of $c = 1482\text{m/s}$ and density $\rho_a = 1000\text{kg/m}^3$.

The entire inner surface of this tube is subjected to a uniformly distributed load F(t) with its time history and Fourier transform plotted in Figure 5.3(a) and 5.3(b) respectively. According to the Fourier transform in Figure5.3(b), the maximum frequency of interest is estimated at $\omega_{max} = 1200\text{rad/s}$ for obtaining accurate solutions. In order to calculate the shortest wavelength in structure domain λ_s, the speed of pressure waves in structure c_p due to the volumetric deformation can be calculated by

$$c_p = \sqrt{\frac{E(1-\nu)}{\rho_s(1+\nu)(1-2\nu)}} \tag{5.65}$$

Substituting required material properties into Equation (5.65), the pressure wave speed in the structure domain $c_p \approx 5997.16\text{m/s}$ is obtained. The speed of shear

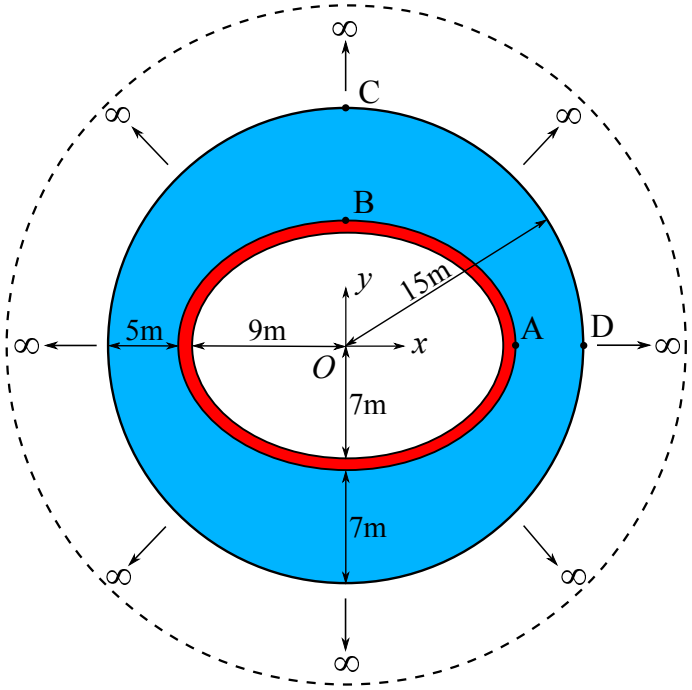

Figure 5.2. The acoustic-structure interaction model of an elliptical tube submerged in infinite acoustic domain.

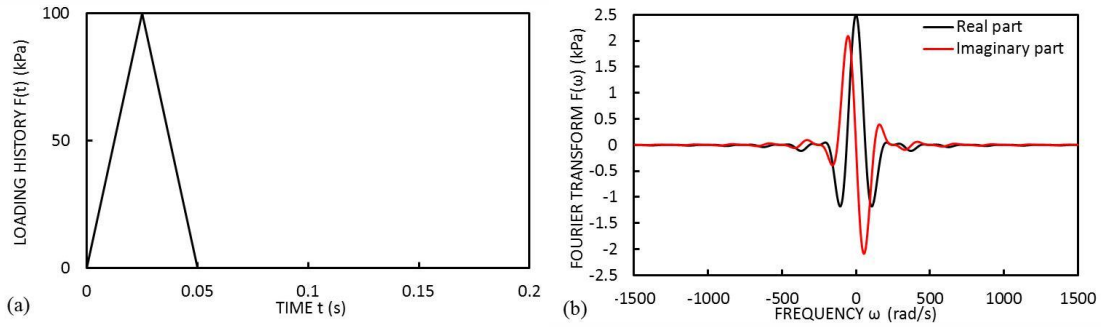

Figure 5.3. Time variation F(t) of transient load applied uniformly on the inner surface of tube: (a) time history and (b) Fourier transform.

waves c_s in structure can be calculated by:

$$c_s = \sqrt{\frac{E}{2\rho_s(1+\nu)}} \tag{5.66}$$

for $\nu < 0.5$, c_p is larger than the shear wave speed c_s. Therefore, c_s is used for calculating the minimum wavelength. By substituting all requires material properties into Equation (5.66) the shear wave speed in structural domain $c_s \approx 3205.62$m/s. Therefore, the shortest wavelength in structure domain can be evaluated as $\lambda_s = \frac{2\pi}{\omega_{max}} c_s \approx 16.78$m. Analogously, the shortest wavelength in the acoustic domain is

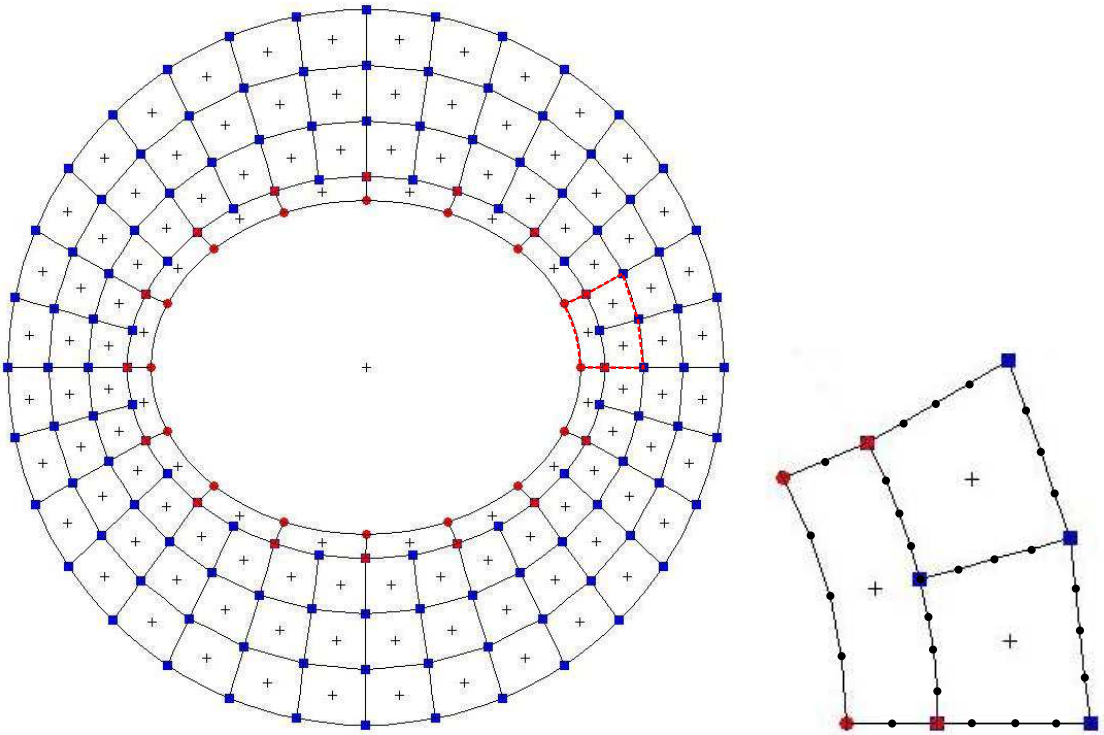

(a) (b)

Figure 5.4. The SBFEM mesh of an elliptical tube submerged in infinite acoustic domain: (a) the mesh of whole coupled system and (b) a detailed view of subdomains around acoustic-structure interface.

approximately $\lambda_a = \frac{2\pi}{\omega_{max}} c \approx 7.76$m.

The scaled boundary finite element mesh of this coupled system is shown in Figure 5.4. In this mesh, different subdomain sizes and number of elements per edge are used in acoustic and structural domains as the result of different shortest wavelengths in two distinct media. From Figure 5.4(a), the acoustic domain has been divided into 32 subdomains in circumferential direction and 3 layers in radial direction with blue dots denoting the keypoints. However, the cross-section of tube is only divided into 16 subdomains in circumferential direction and one layer in radial direction. Red dots are used to specify the keypoints in structural subdomains. The scaling center of each bounded subdomain is marked by cross '+', and the '+' at the center of this whole model is the scaling center of the circular open boundary. It should be noticed that both the blue keypoints from acoustic domain and red keypoints from structural domain exist on the acoustic-structure interface due to

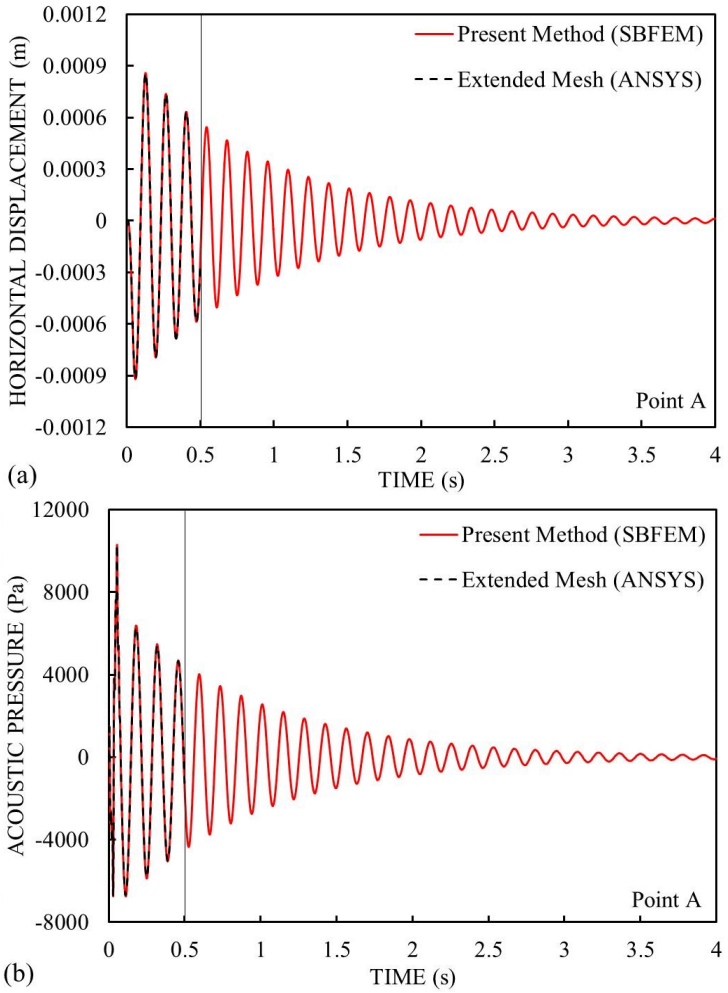

Figure 5.5. Results at point A in the coupled model of an elliptical tube submerged in infinite acoustic domain: (a) horizontal displacement and (b) acoustic pressure.

the non-matched subdomain sizes used in two different domains. Because of the boundary discretization required in SBFEM, the mesh transition on the acoustic-structure interface can be addressed easily and efficiently by simply adding extra nodes on the structure side of the interface to match the mesh on the acoustic side.

A detailed view of subdomains surrounded by red dash-line in Figure 5.4(a) is illustrated in Figure 5.4(b). All the other nodes except keypoints are marked by black dots in the detailed view only for conciseness. For the acoustic domain, two 3-node elements are used on each edge of a subdomain and yields approximately 13 nodes per wavelength. The order of continued fractions for bounded acoustic domain is chosen as 1 according to 3-4 terms per wave length (Song, 2009). The same

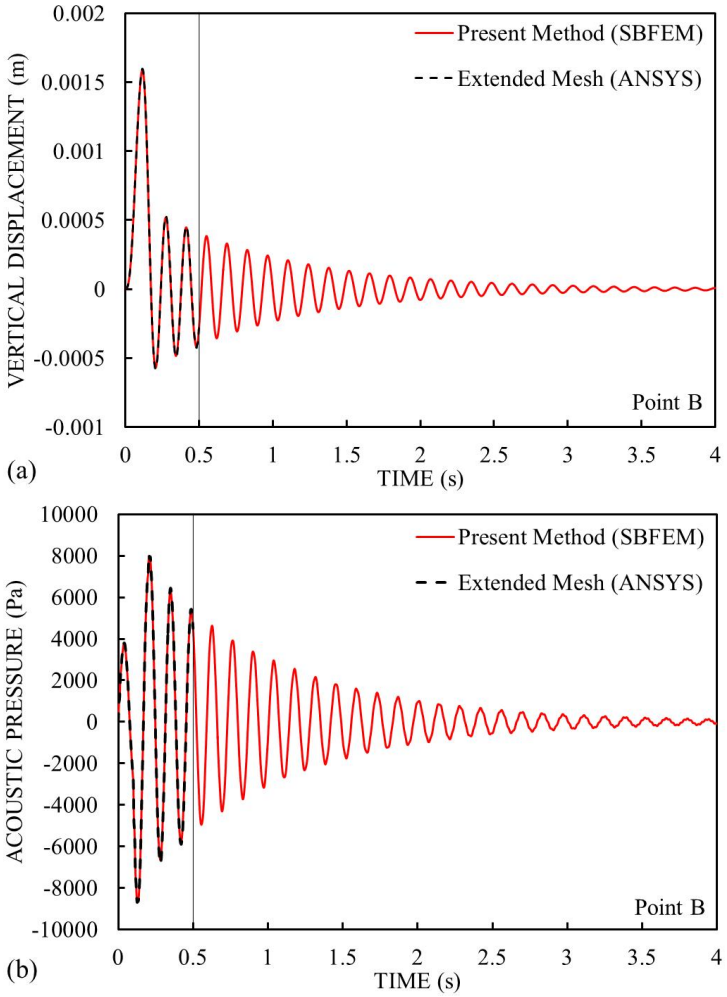

Figure 5.6. Results at point B in the coupled model of an elliptical tube submerged in infinite acoustic domain: (a) vertical displacement and (b) acoustic pressure.

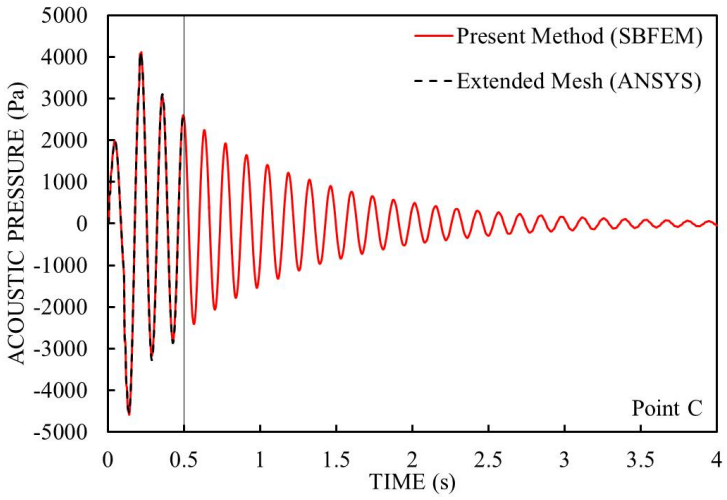

Figure 5.7. Acoustic pressure at point C in the coupled model of an elliptical tube submerged in infinite acoustic domain.

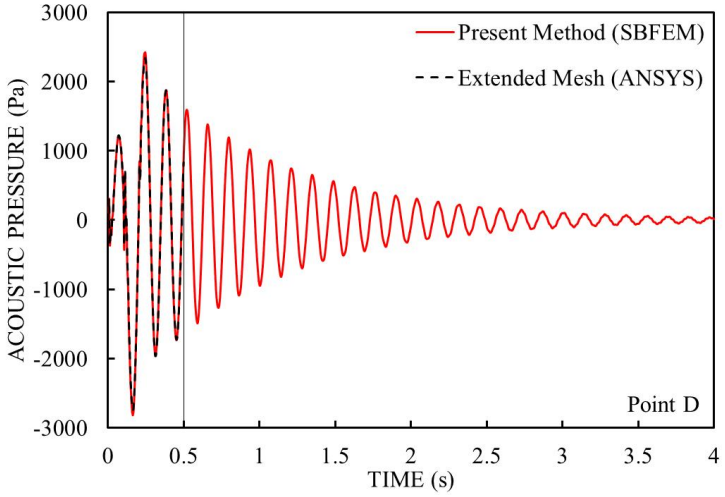

Figure 5.8. Acoustic pressure at point D in the coupled model of an elliptical tube submerged in infinite acoustic domain.

number and arrangements of nodes and elements are used on the acoustic-structure interface for both structure and acoustic domains for matching the meshes. Because the minimum wavelength in structure domain λ_s is about two times larger than the minimum wavelength in the acoustics λ_a, only two 3-node elements are use on each circumferential edge of structural subdomains and one 3-node elements are used on the radial edges to represent the minimum wavelength and bending of structure sufficiently. The terms of continue fractions are set to be zero for all structural subdomains. In addition, the orders of high-frequency and low-frequency continued-fraction expansions of circular open boundary are chosen as $M_H = M_L = 1$.

For the transient analysis of this coupled system, the Newmark's method is applied to Equation (5.56) or (5.61) with the time step $\Delta t = 0.4$ms. The chosen value of Δt give about 13 time steps per period at the highest frequency of interest. Both of the displacement responses and acoustic pressures are calculated for structural and acoustic domains respectively. Results at four points A, B, C and D in Figure 5.2 are summarized and compared with the reference solutions in Figure 5.5 - 5.8. In all these figures, the reference solutions are calculated using extended FEM mesh for acoustic domain in ANSYS for the first 0.5s and plotted with black dash lines. The radius of truncated circular boundary for the acoustic domain in the FEM mo-

del is set to be 390m. During the first 0.5s, the traveling distance of wave front is $1482 \times 0.5 = 741$m. The distance between FEM truncated boundary and the boundary of the domain of interest is $390 - 15 = 375$m, which is more than half of the traveling distance of wave front. Therefore, the reflected wave has not entered the domain of interest yet. Both acoustic and structural domains in FEM model are discretized using 4-node quadrilateral elements with the maximum edge length of 0.5m and 0.25m respectively. Meanwhile, the solutions obtained by present SBFEM are plotted in those corresponding figures with red solid lines during the first 4s.

Among all these selected points for presenting results, points A and B are located on the acoustic-structure interface. Therefore, both the structural displacements and acoustic pressures for points A and B are illustrated in Figures 5.5 and 5.6 separately. As a result of the symmetry of the structure and applied load, only the horizontal displacement plotted in Figure 5.5(a) exist at point A and the acoustic pressure at the same point is plotted in Figure 5.5(b). Consequently, Point B only has vertical displacement and acoustic pressure presented in Figure 5.6(a) and 5.6(b) respectively. Very good agreements between presented SBFEM and reference solutions are obtained for both displacement and acoustic pressure results.

Point C and D are chosen to be just on the truncated circular boundary to test the accuracy of the doubly-asymptotic open boundary employed in the present acoustic-structure interaction model in SBFEM. The acoustic pressures at these two points obtained by present SBFEM agrees well with the reference solutions obtained using extended meshes in FEM as illustrated in Figure 5.7 and 5.8 respectively.

5.4.2 Beam submerged in infinite acoustic water plane

The acoustic-structure interaction problem of a simply supported beam submerged in infinite acoustic media is investigated in this section. The SBFEM model of this system is illustrated in Figure 5.9. The system is simplified as a 2D problem and the beam is represented by the red rectangle in this figure. Similarly, the surrounding

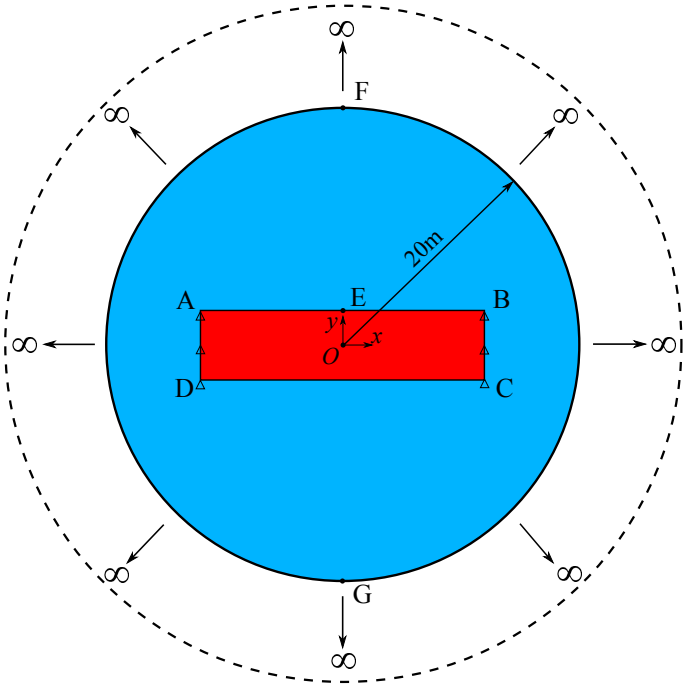

Figure 5.9. The acoustic-structure interaction model of a beam submerged in infinite acoustic domain.

acoustics is divided into a near field, which is denoted by the blue area in Figure 5.9, and a far field by a circular open boundary. The beam has the length of $\overline{DC} = \overline{AB} = 24$m and height of $\overline{AD} = \overline{BC} = 6$m. The radius of the circular open boundary, which represents the acoustic far field, equals to 20m. This beam is fixed in the y-direction along two edges $\overline{AD}$ and $\overline{BC}$ and modeled in plane-stress condition. The material properties of beam are: Young's modulus $E = 100$GPa, mass density $\rho_s = 1500\text{kg/m}^3$ and Poisson ratio $\nu = 0.333$. The acoustic domain is again assumed to be filled with water with the sound speed of $c = 1482$m/s and mass density of $\rho_a = 1000\text{kg/m}^3$.

A uniformly distributed load $F_b(t)$ is applied on the top surface $\overline{AB}$ of this beam. The time-dependent function $F_b(t)$ and its Fourier transform are plotted in Figures 5.10(a) and 5.10(b) separately. The shear wave speed in the structural domain c_s can be calculated by Equation (5.66) and approximately equals to $c_s \approx 5000.63$m/s. From Figure 5.10(b), the maximum relevant frequency is about $\omega_{max} = 1.5\text{rad/ms}$. The shortest wavelength in structural domain are therefore calculated as

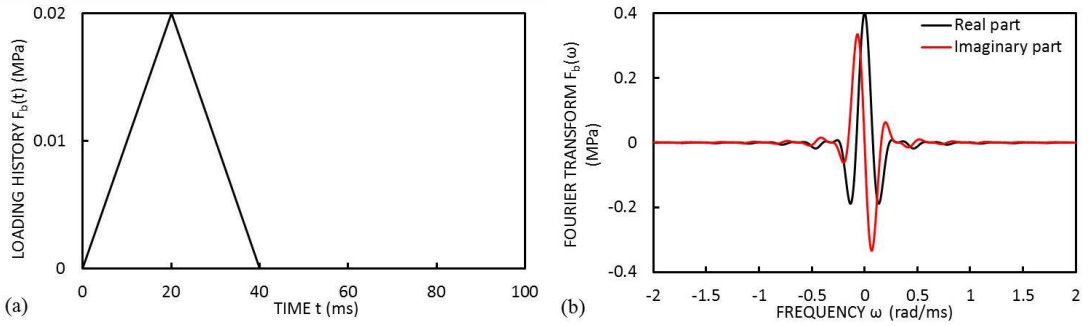

Figure 5.10. Time variation $F_b(t)$ of transient load applied on the top of beam: (a) time history and (b) Fourier transform.

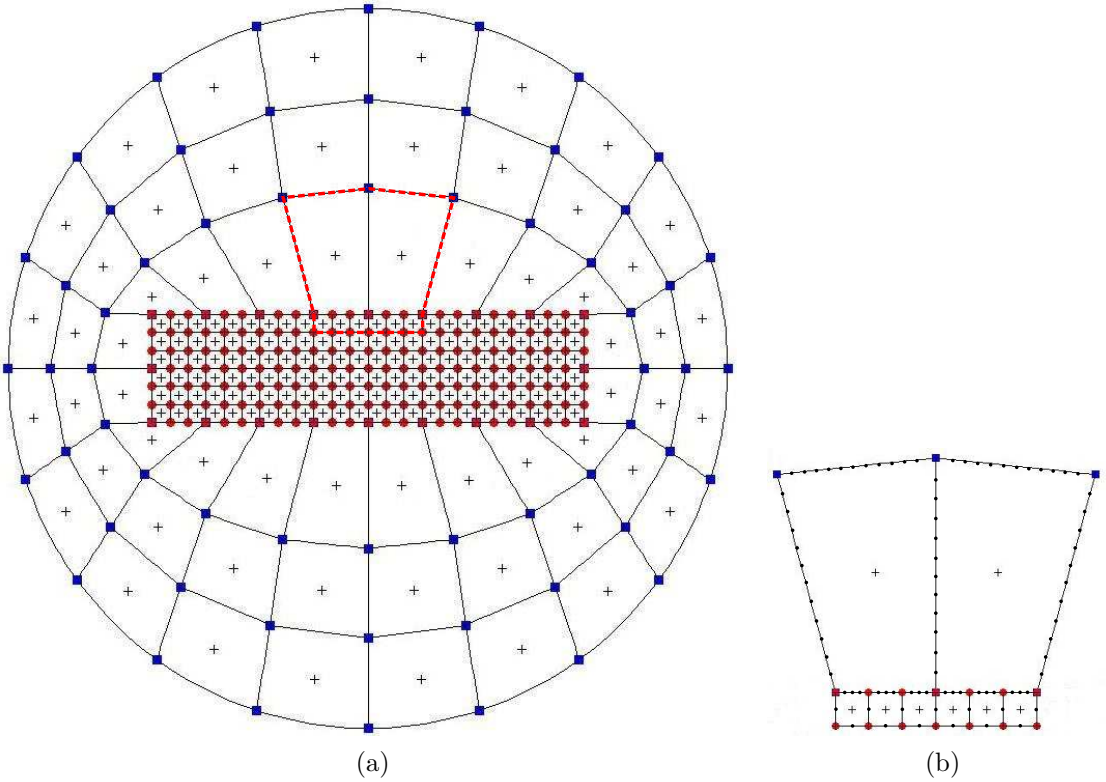

Figure 5.11. The SBFEM mesh of a beam submerged in infinite acoustic domain: (a) the mesh of whole coupled system and (b) a detailed view of subdomains around acoustic-structure interface.

$\lambda_s = \frac{2\pi}{\omega_{max}} c_s \approx 20.95$m. The shortest wavelength in acoustic domain is determined as $\lambda_a = \frac{2\pi}{\omega_{max}} c \approx 6.21$m.

Figure 5.11 shows the scaled boundary finite element mesh of beam and surrounding acoustic domain. In Figure 5.11, the acoustic domain is divided into 20 subdomains in circumferential direction and 3 layers in radial direction and denoted by blue keypoints. In contrast, the rectangular structure domain is divided into 24

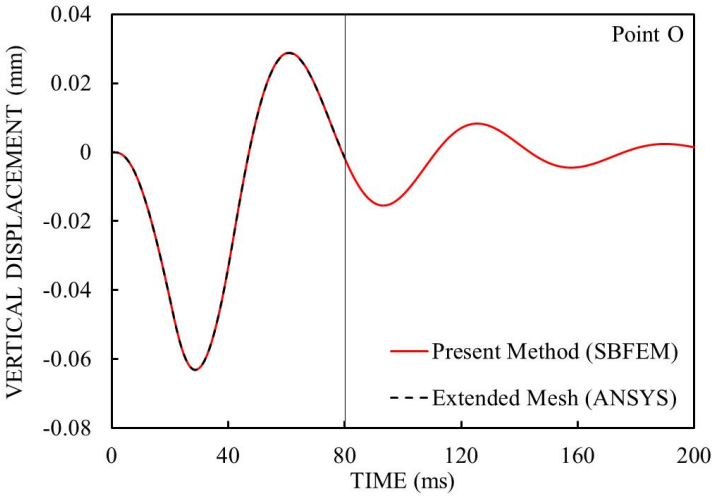

Figure 5.12. Structural displacement at point O in the coupled model of a beam submerged in infinite acoustic domain.

and 6 square subdomains with red keypoints in horizontal and vertical directions respectively for its regular geometry. All scaling centers are marked by the cross '+' and the scaling center of circular unbounded domain is again located at its centroid. The different sizes of structural and acoustic subdomains are matched on the acoustic-structure interface by simply introducing extra nodes on the common edges as in Section 5.4.1. A closer view of subdomains around the acoustic-structure interface within the red dash-line in Figure 5.11(a) is illustrated in Figure5.11(b).

In Figure 5.11(b), all other nodes are marked by black solid dots. For the acoustic subdomains, twelve 2-node elements are used on each edge of subdomains, which yields at least 11 nodes per shortest wavelength. Two terms of continued-fractions are used for the bounded acoustic domain to guarantee the rule of 3-4 terms of continued-fraction expansions per shortest wavelength (Song, 2009). As for the structural subdomains, the edges attached to the acoustic-structure interface use the same number of nodes and type of elements for matching the meshes. On the remaining edges of structural subdomains, only two 2-node elements are applied to each edge for accurately modeling the beam. No continued-fraction terms are assigned to structural subdomains. Orders of high-frequency and low-frequency continued-fraction expansions for circular open boundary are selected as M_H =

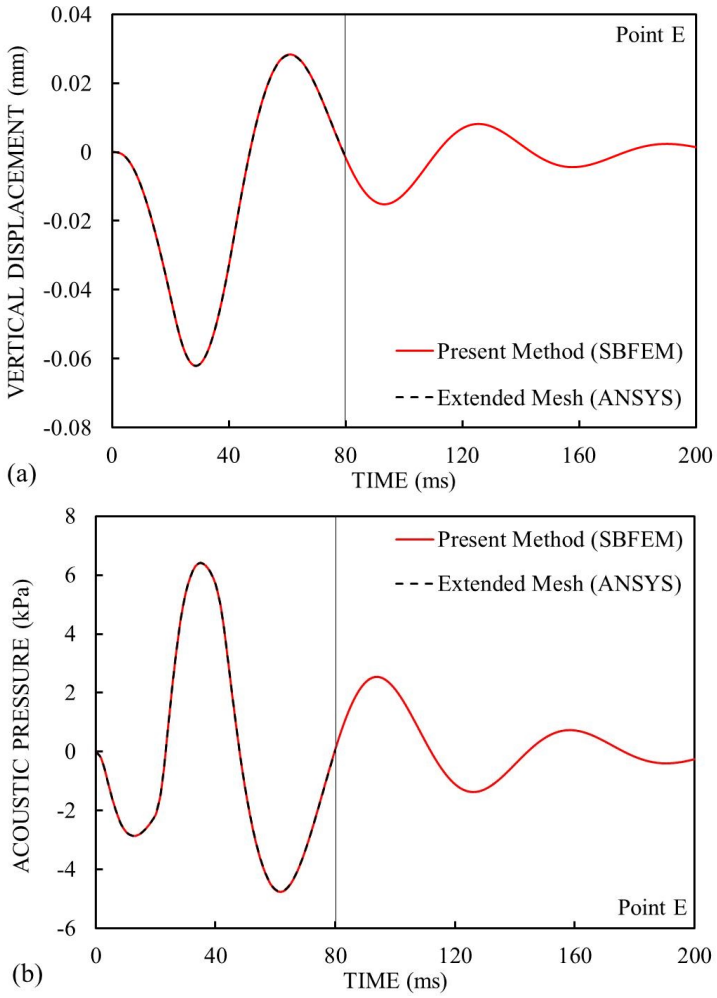

Figure 5.13. Results at point E in the coupled model of a beam submerged in infinite acoustic domain: (a) vertical displacement and (b) acoustic pressure.

$M_L = 1$. In order to obtain the time-domain solutions of this acoustic-structure interaction system, Newmark's method is applied here with the constant time step of $\Delta t = 0.25$ms. This gives at least 16 time steps per period at the highest frequency of interest.

The solutions calculated by present SBFEM at points O(0m, 0m), E(0m, 3m), F(0m, 20m) and G(0m, −20m) are demonstrated in Figures 5.12 - 5.15 with red solid lines for the first 200ms and compared with reference solutions at the same points denoted by black dash lines for the first 80ms. Those reference solutions are calculated using FEM model in ANSYS the bounded acoustic domain modeled by an extended mesh. In this example, the radius of truncated boundary of the

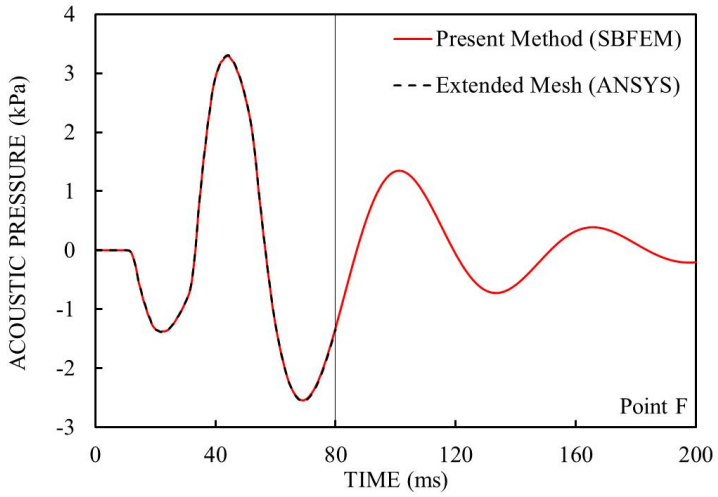

Figure 5.14. Acoustic pressure at point F in the coupled model of a beam submerged in infinite acoustic domain.

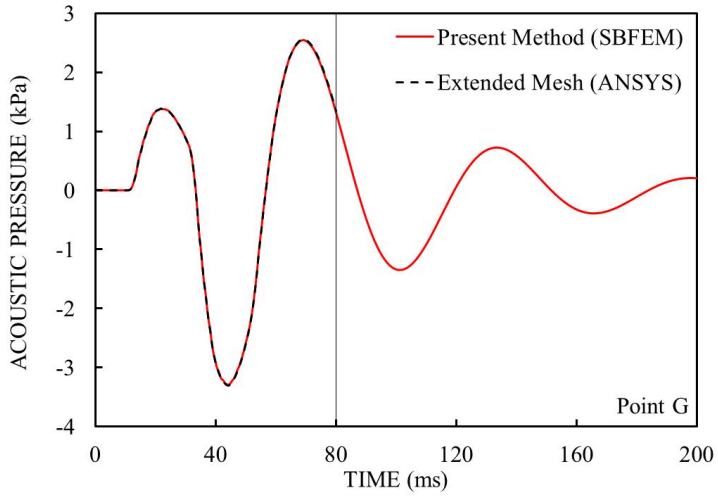

Figure 5.15. Acoustic pressure at point G in the coupled model of a beam submerged in infinite acoustic domain.

extended mesh of finite element is set to be 170m for avoiding reflected waves in the first 80ms. In the FEM mesh, 4-node quadrilateral elements with the edge length of 0.3m are used for the structural domain. 3-node triangular elements with the maximum edge length of 0.6m are used for the acoustic domain to achieve better mesh transition on the acoustic-structure interface.

The structural displacements at points O and E are plotted in Figures 5.12 and 5.13(a) respectively. Due to the symmetry of applied boundary conditions and geometry, only vertical displacements are shown in these two figures. The acoustic

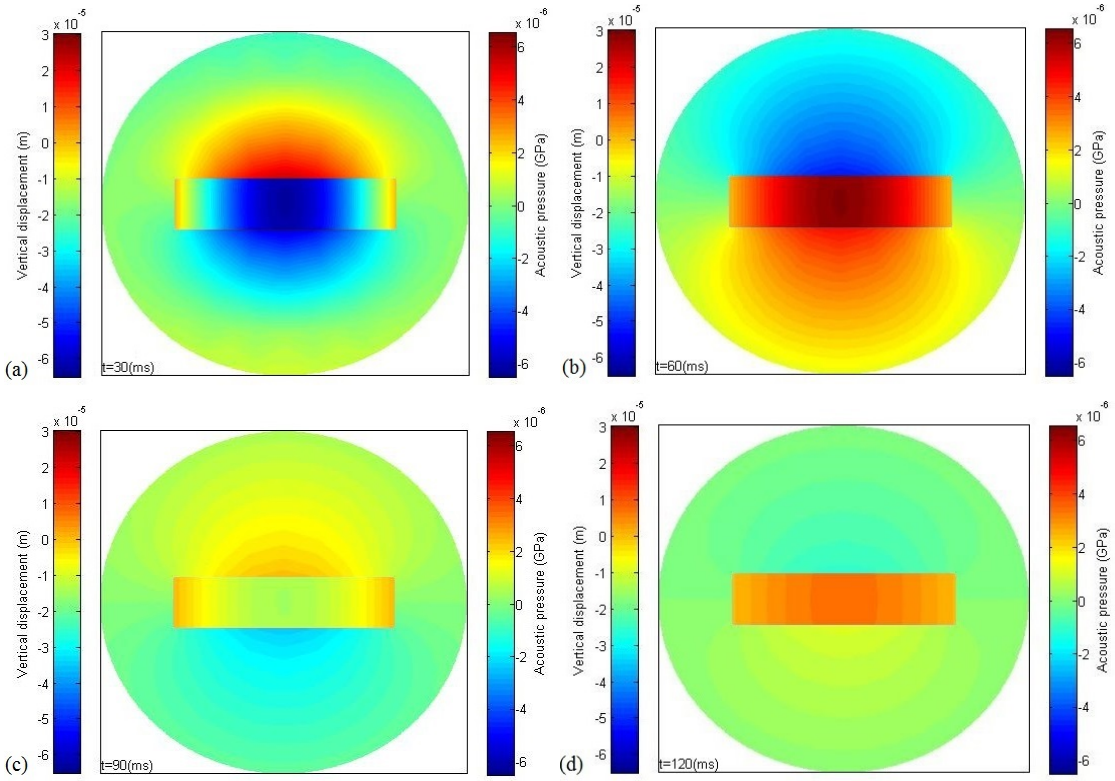

Figure 5.16. Coupled system of beam submerged in infinite acoustic domain. Contour plots of vertical displacements and acoustic pressures at: (a) $t = 30$ms, (b) $t = 60$ms, (c) $t = 90$ms and (d) $t = 120$ms.

pressure at point E is also shown in Figure 5.13(b) as this point is located on acoustic-structure interface. The results of acoustic pressures at other two points F and G on the open boundary are also summarized in Figures 5.14 and 5.15 for demonstrating the accuracy of doubly-asymptotic open boundary. Comparing all solutions obtained by SBFEM and FEM model in ANSYS, very good agreements have been achieved for both structural displacements and acoustic pressures. The contour plots of this coupled system on the mesh in Figure 5.11 are plotted in Figure 5.16 with the solutions obtained by present SBFEM. In all these contour plots, vertical displacements and acoustic pressures are shown for structural and acoustic domains respectively at times $t = 30$ms, $t = 60$ms, $t = 90$ms and $t = 120$ms for illustrating the interactions between acoustic and structural domains in this example.

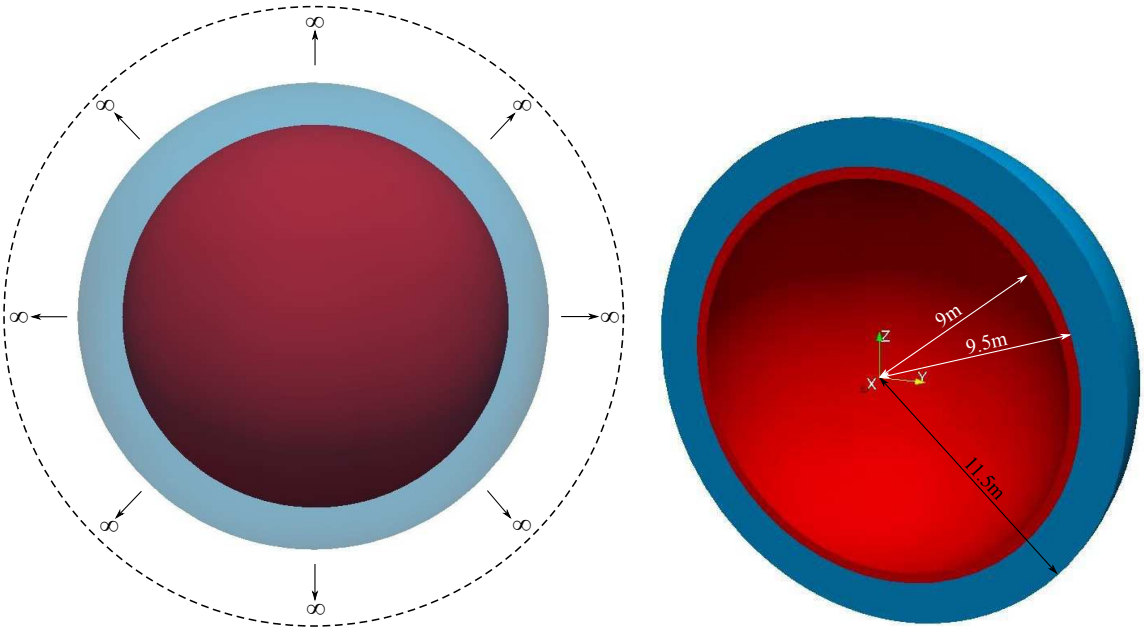

(a) (b)

Figure 5.17. The acoustic-structure interaction model of a hollow sphere submerged in infinite acoustic domain: (a) the whole model and (b) half of the model.

5.4.3 Hollow sphere submerged in infinite acoustic domain

A 3D acoustic-structure interaction problem is studied in this section to verify the implementation of SBFEM in 3D cases. Figure 5.17(a) shows the layout of this system: the red sphere represents the hollow sphere and the translucent region in blue color denotes the surrounding acoustic domain. The red hollow sphere has the inner and outer radii of 9m and 9.5m separately as marked in Figure 5.17(b), and the radius of spherical open boundary is set to be 11.5m to truncate the 3D blue acoustic near field from far field. The same material properties for structural and acoustic domains used in Section 5.4.1 are adopted in this numerical example.

A uniform load is applied on the entire inner surface of the hollow sphere with the time variation $F_s(t)$ defined in Equation (5.67) and plotted in Figure 5.18(a).

$$F_s(t) = \begin{cases} 0.5 \times (1 - \cos 0.2\pi t) \text{ (MPa)} & \text{when } 0 \leq t \leq 10\text{ms}, \\ 0 \text{ (MPa)} & \text{when } 10\text{ms} < t. \end{cases} \tag{5.67}$$

The corresponding Fourier transform of $F_s(t)$ is also given in Figure 5.18(b) with the

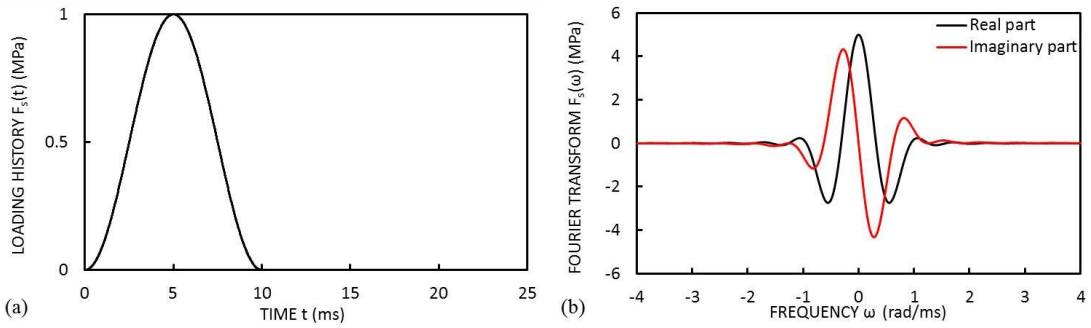

Figure 5.18. Time variation $F_s(t)$ of transient load applied uniformly on the inner surface of hollow sphere: (a) time history and (b) Fourier transform.

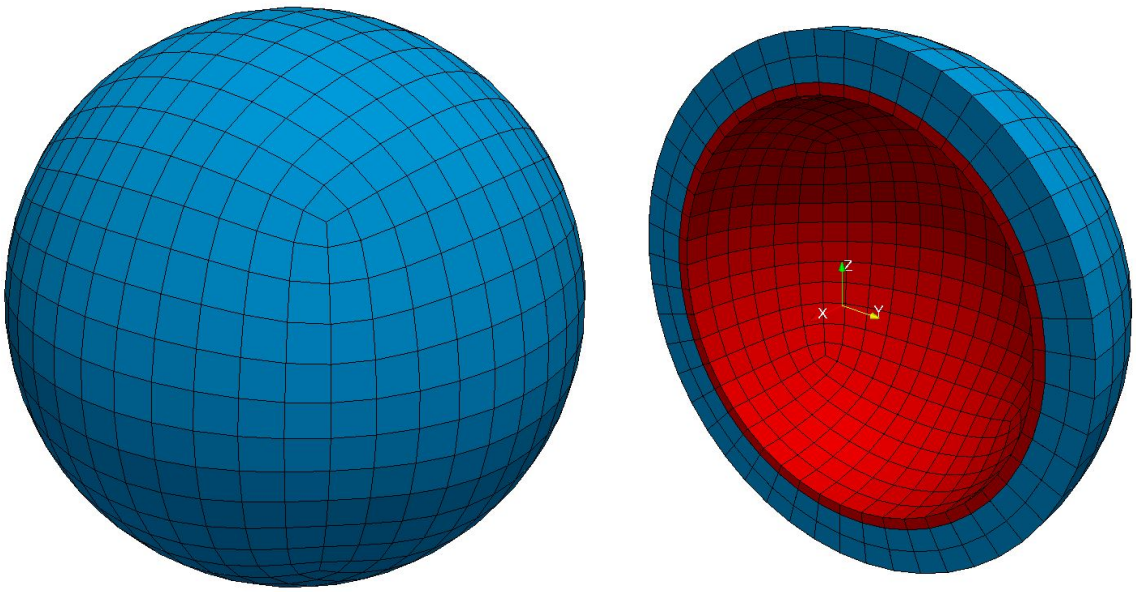

(a) (b)

Figure 5.19. The SBFEM mesh of a hollow sphere submerged in infinite acoustic domain: (a) mesh of the spherical open boundary and (b) half of the mesh showing details of inside.

maximum relevant frequency estimated at $\omega_{max} = 2\text{rad/ms}$. From Section 5.4.1, the speed of shear waves is $c_s \approx 3205.62\text{m/s}$ in structure. Thus, the shortest wavelength in structural domain can be evaluated as $\lambda_s = \frac{2\pi}{\omega_{max}} c_s \approx 10.07\text{m}$. Similarly, the shortest wavelength in the acoustic domain is equal to $\lambda_a = \frac{2\pi}{\omega_{max}} c \approx 4.66\text{m}$. The scaled boundary finite element mesh of this 3D coupled system is illustrated in Figure 5.19 with the blue region denoting the mesh for acoustic domain and the mesh for structure is plotted in red color. For both acoustic and structural domains, they are divided into 48 subdomains in the hoop direction. The structural domain only has

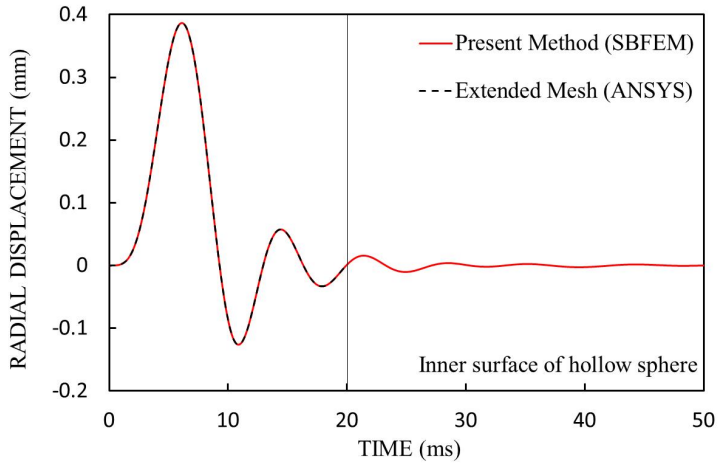

Figure 5.20. Radial displacement on the inner surface of hollow sphere submerged in infinite acoustic domain.

one layer of subdomains in radial direction, while the acoustic domain has two layers of subdomains in radial direction. For all subdomains, the 9-node quadrilateral element is used on each face of them. This can yield about 10 nodes per shortest wavelength in acoustic domain. Because the minimum wavelength in structure is about two times larger than that in acoustics, the 9-node quadrilateral elements in structure can sufficiently represent the wavelength and simulate the geometry accurately. The number of terms of the continued fractions is chosen as 1 for the acoustic subdomains, which satisfies the rule of 3-4 terms per minimum wavelength (Song, 2009). Because of the larger minimum wavelength in structural domain, no continued-fraction expansion is applied to structural subdomains. Orders of high-frequency and low-frequency continued-fraction expansions for spherical open boundary are selected as $M_H = M_L = 1$.

Newmark's method with the constant time step of $\Delta t = 0.2$ms is used to calculate the transient solutions of the structural and acoustic domains of this coupled system during the first 50ms, which yields about 15 time steps per period at highest frequency of interest. For the reason of the symmetry of geometry and applied load, the radial displacements or acoustic pressure on any spherical surface with the same radius should be the same. Hence, the radial displacements on the in-

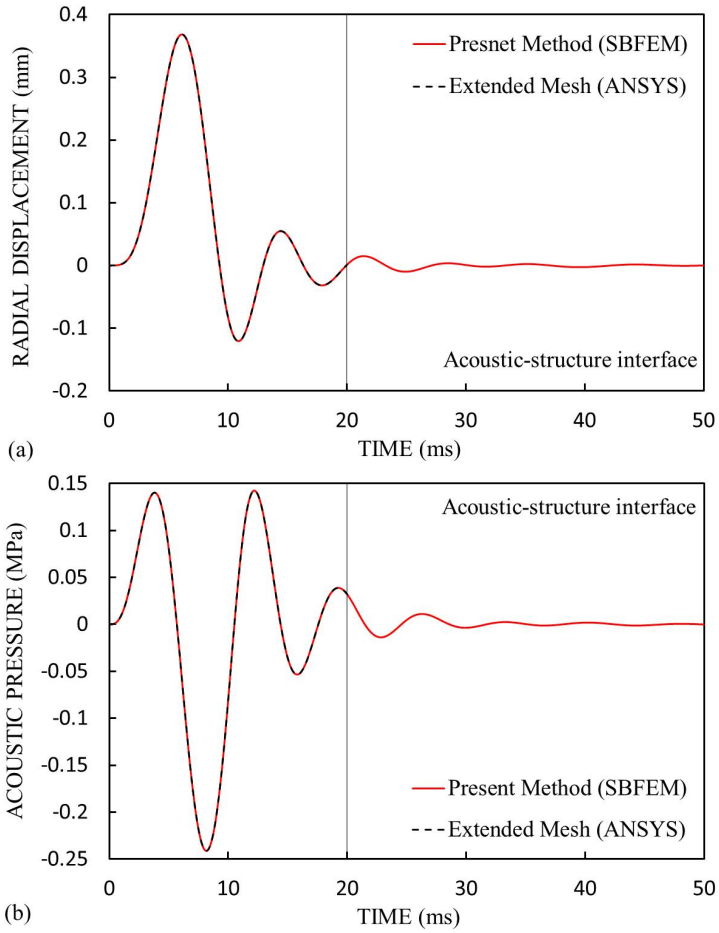

Figure 5.21. Results on the acoustic-structure interface of the coupled model of a hollow sphere submerged in infinite acoustic domain: (a) radial displacement and (b) acoustic pressure.

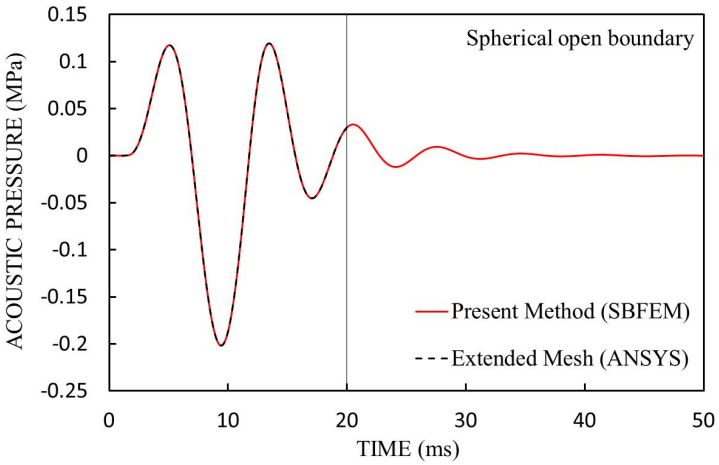

Figure 5.22. Acoustic pressure on the spherical open boundary of the coupled model of a hollow sphere submerged in infinite acoustic domain.

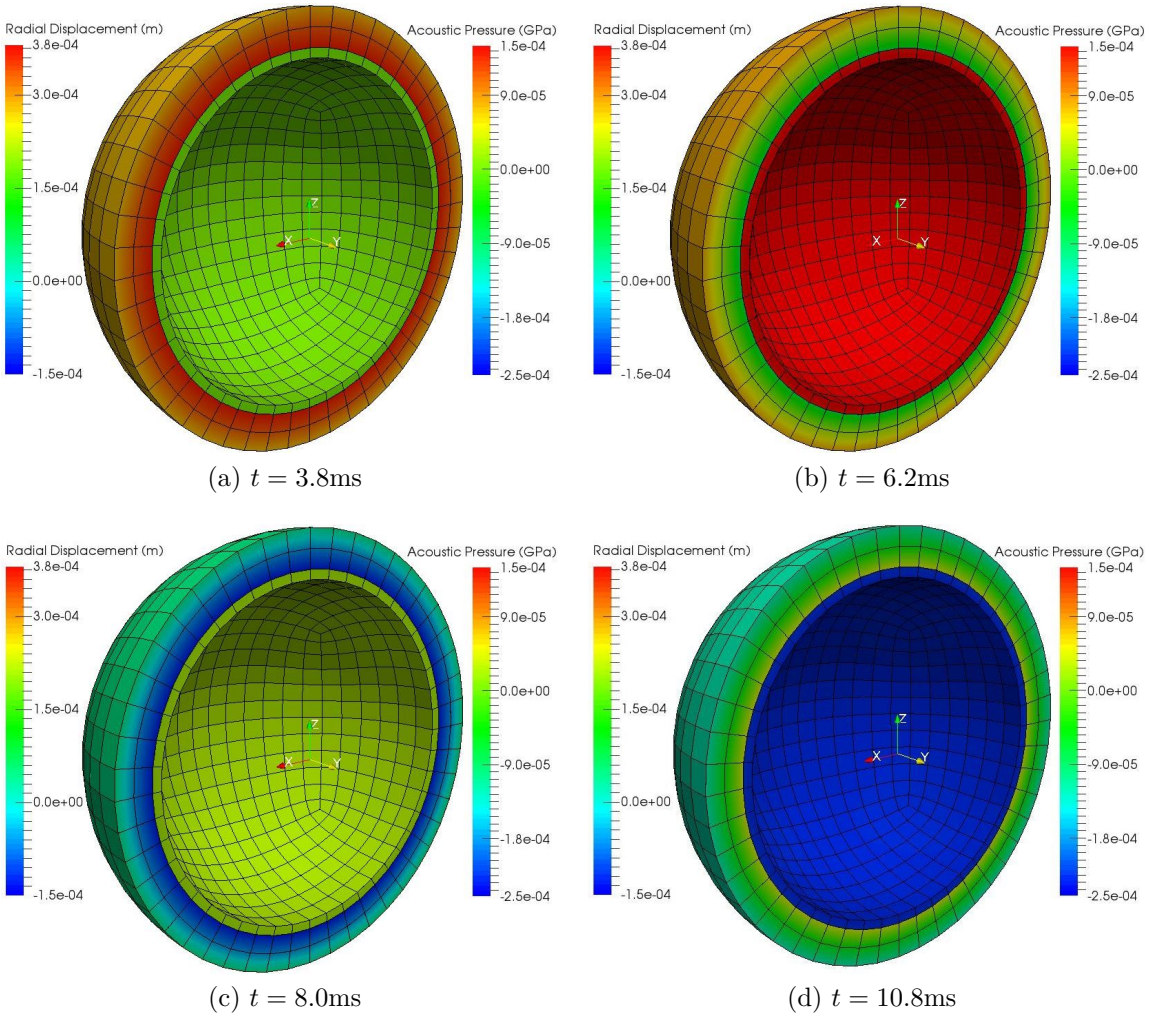

(a) $t = 3.8$ms (b) $t = 6.2$ms

(c) $t = 8.0$ms (d) $t = 10.8$ms

Figure 5.23. Coupled system of hollow sphere submerged in infinite acoustic domain. Contour plots of radial displacement and acoustic pressure at: (a) $t = 3.8$ms, (b) $t = 6.2$ms, (c) $t = 8.0$ms and (d) $t = 10.8$ms.

ner surface of hollow sphere and on the acoustic-structure interface are presented in Figures 5.20 and 5.21(a) separately. Additionally, the acoustic pressures on the acoustic-structure interface and on the spherical open boundary are summarized in Figure 5.21(b) and 5.22 respectively. For verifying the results obtained by SBFEM and demonstrating its accuracy, reference solutions are calculated via using FEM model in ANSYS with extended mesh for representing the infinite acoustic domain. The radius of truncated boundary of extended mesh for acoustic domain is 27m for avoiding the reflected waves during the first 20ms. 20-node hexahedral elements are employed in the FEM model in ANSYS with the discretization pattern shown

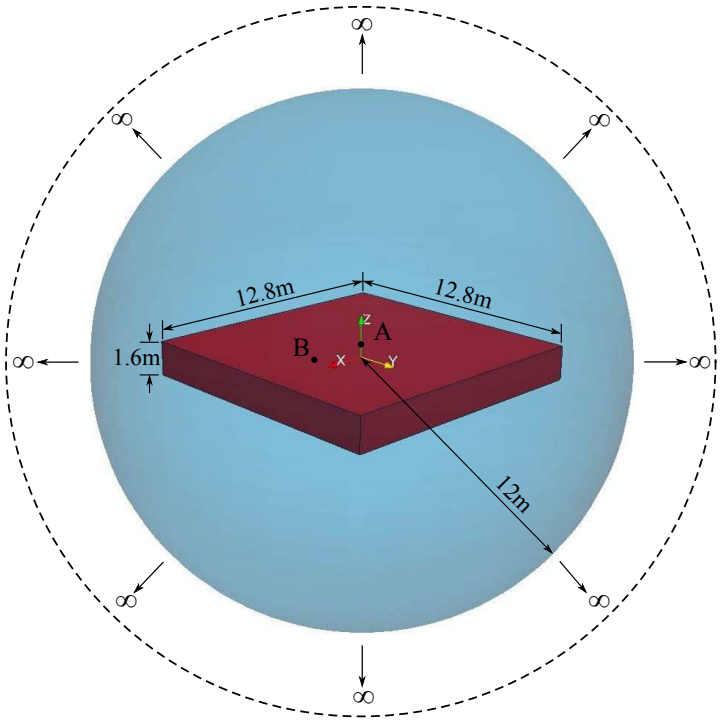

Figure 5.24. The acoustic-structure interaction model of a 3D plate submerged in infinite acoustic domain.

in Figure 5.19. In all Figures 5.20 - 5.22, the results obtained using the proposed SBFEM are shown by red solid lines and the reference solutions from the finite element models in ANSYS are plotted in black dash lines. The results from SBFEM are in good agreements with the reference solutions.

Moreover, the contour plots of the coupled system with the radial displacements from structural domain and acoustic pressures from acoustic domain at times $t =$ 3.8ms, 6.2ms, 8.0ms and 10.8ms are shown in Figures 5.23(a) - (d). All the results shown in contours are calculated from the present SBFEM with the mesh shown in Figure 5.19.

5.4.4 3D plate submerged in infinite acoustic space with octree mesh for acoustic near field

A 3D simply supported plate vibrating in an infinite acoustic domain is investigated in this numerical example. The layout of the coupled acoustic-structure interaction

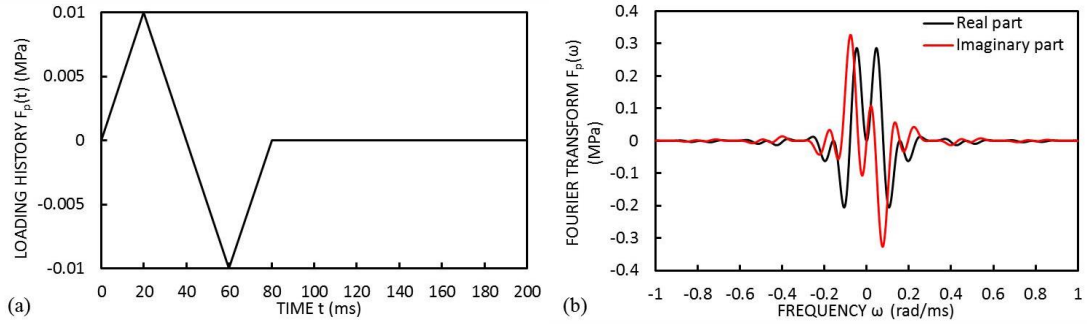

Figure 5.25. Time variation $F_p(t)$ of transient load applied on the top of plate: (a) time history and (b) Fourier transform.

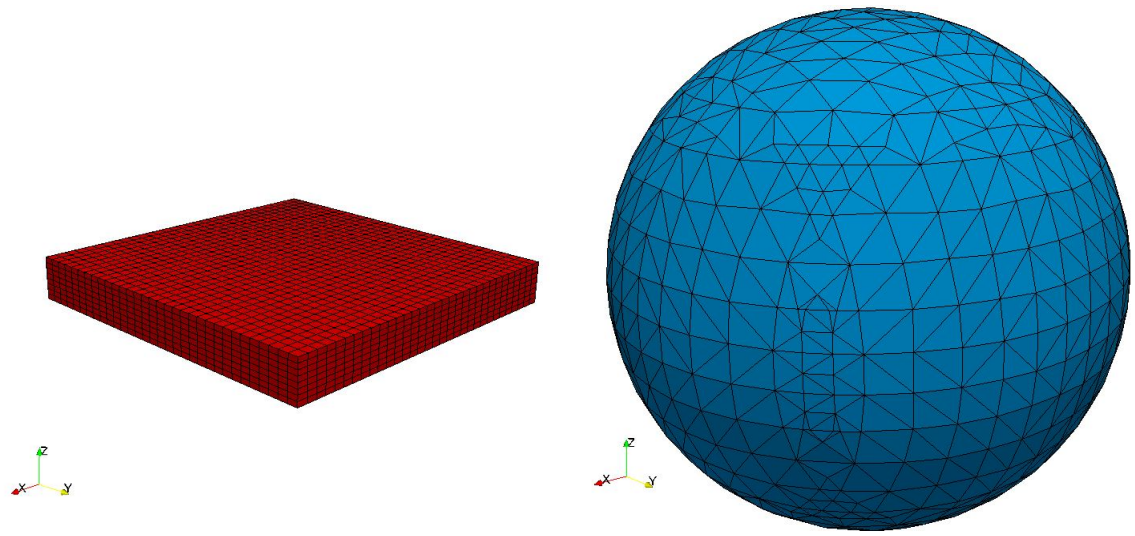

(a) (b)

Figure 5.26. The SBFEM mesh of 3D plate and surrounding acoustics: (a) mesh of plate and (b) octree mesh of acoustic domain.

model is illustrated in Figure 5.24. The red square plate has the edge length of 12.8m and thickness of 1.6m, while the surrounding acoustic domains is represented by the translucent region with blue color. The radius of the spherical open boundary is 12m. The material properties of plate and acoustics in this example are the same as those used in Section 5.4.2. The centroid of the red plate is located at the coordinate origin as shown in Figure 5.24 and coincides with the centroid of the spherical open boundary. The four side faces around the plate are fixed in the z-direction. The entire top surface of this plate is subjected to a uniformly distributed load pointing in -z direction and described by the time-dependent function $F_p(t)$ in Figure 5.25(a)

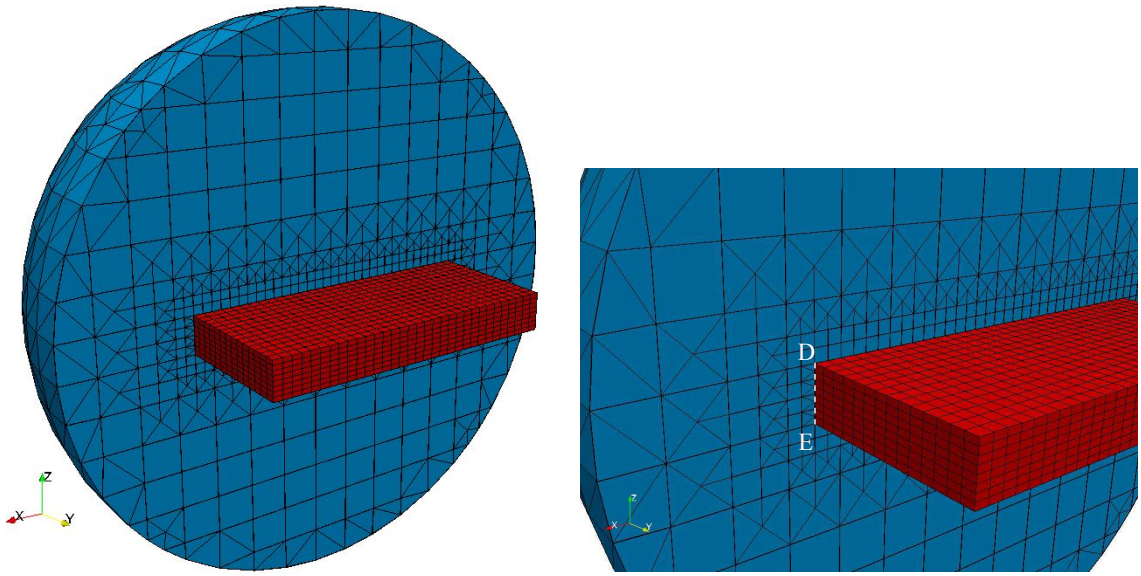

(a) (b)

Figure 5.27. The SBFEM mesh of a 3D plate submerged in infinite acoustic domain: (a) coupled mesh with part of the acoustic mesh showing details of inside and (b) a detailed view of the emsh around acoustic-structure interface.

with its Fourier transform plotted in Figure 5.25(b).

According to the Fourier transform in Figure 5.25(b), the maximum relevant frequency is approximately equal to $\omega_{max} = 0.6$rad/ms. As discussed in Section 5.4.3, the shear wave speed is equal to $c_s \approx 5000.63$m/s. Therefore, the shortest wavelength in 3D plate is $\lambda_s = \frac{2\pi}{\omega_{max}} c_s \approx 52.37$m. The shortest wavelength in acoustic domain λ_a can directly be calculated using the give sound speed as $\lambda_a = \frac{2\pi}{\omega_{max}} c \approx 15.52$m.

The meshes for the structural plate and surrounding acoustic medium are generated separately in the proposed SBFEM. Because the plate has very regular geometry, it is discretized into 32 subdomains in both x and y directions and 8 subdomains in z (thickness) direction as shown in Figure 5.26(a). 4-node quadrilateral elements are used on the boundary of each hexahedral subdomain and represent the shortest wavelength in plate λ_s sufficiently. Due to the dissimilar geometry of the acoustic-structure interface and the spherical open boundary in the acoustic domain, it is difficult to generate structured mesh for the acoustic domain as in Section 5.4.3. For

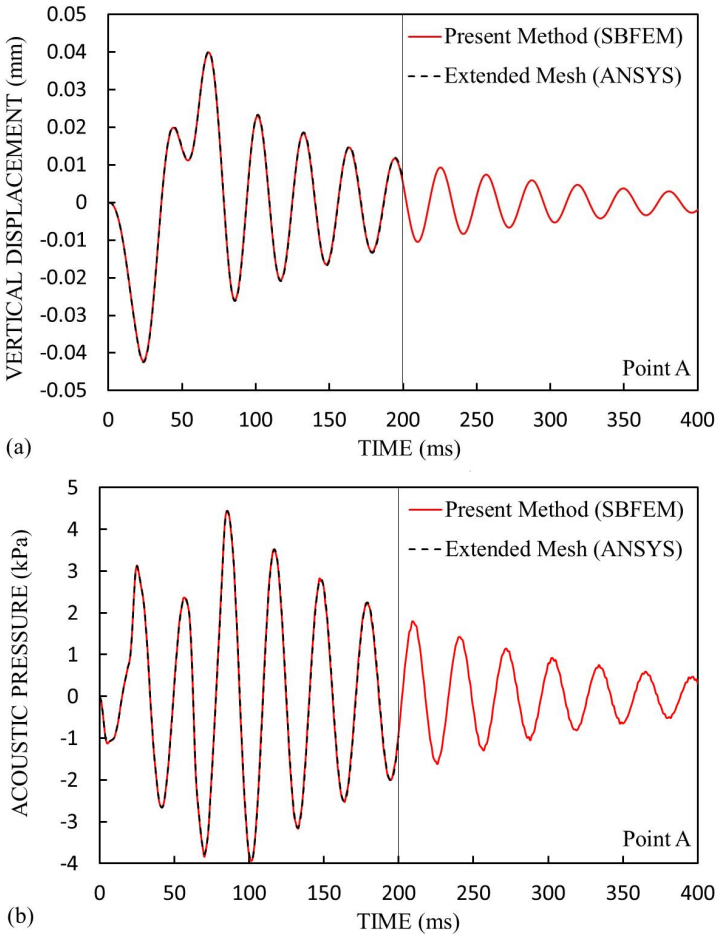

Figure 5.28. Results at point A in the coupled model of a 3D plate submerged in infinite acoustic domain: (a) vertical displacement and (b) acoustic pressure.

reducing the human efforts on mesh generation and making use of the advantage of SBFEM on boundary discretization, octree algorithm once employed in Sections 4.5.1 to 4.5.4 in Chapter 4 is applied here to automatically generate the SBFEM mesh for the acoustic domain. The outer surface of the acoustic domain, which is the spherical open boundary, are illustrated in Figure 5.26(b). The maximum and minimum cell sizes in the octree mesh are set to be 1.6m and 0.4m respectively with smaller cells around the acoustic-structure interface. Both 3-node triangular elements and 4-node quadrilateral elements are used in the octree mesh for acoustic domain, which yields at least 10 nodes per minimum wavelength. As discussed in Section 4.5.1, the terms of continued fractions for all bounded subdomains are set to be zero as these subdomain sizes are small enough to represents the minimum wave-

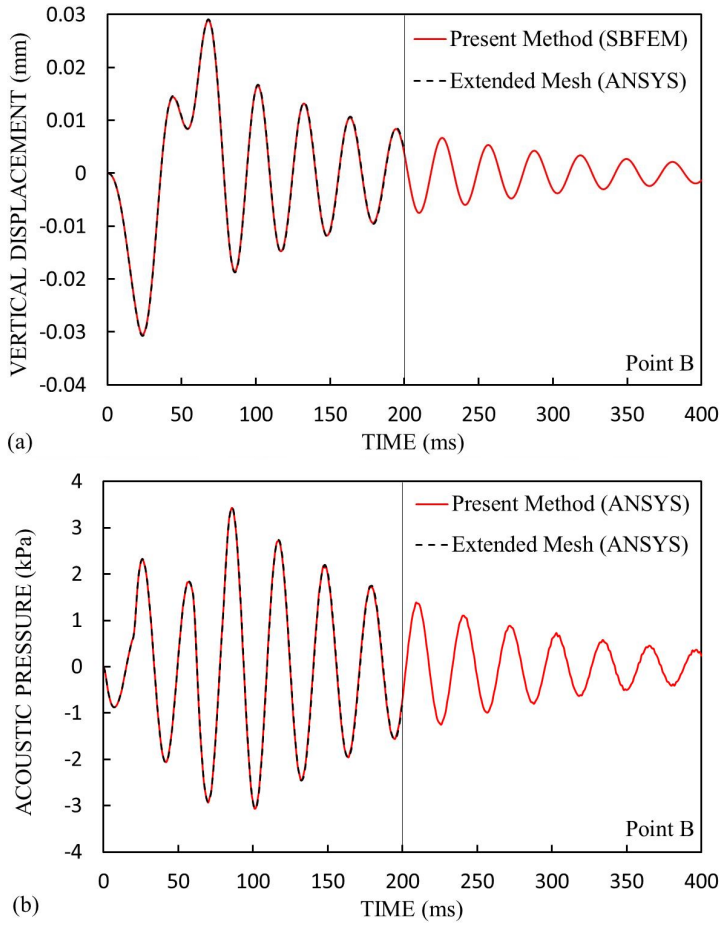

Figure 5.29. Results at point B in the coupled model of a 3D plate submerged in infinite acoustic domain: (a) vertical displacement and (b) acoustic pressure.

lengths in both structural and acoustic domains. The orders of continued fractions for spherical open boundary are again specified as $M_H = M_L = 1$.

Then, the independent meshes for structural and acoustic domains are coupled together along the acoustic-structure interface in Figure5.27(a). In this figure, only part of the acoustic mesh is shown for presenting the inside of the mesh and the coupling between the acoustic and structural domains. In order to address the mismatch of the subdomain sizes from acoustic and structural domains along the side faces of plate, the quadrilateral elements in acoustic domains contacting the structural elements with smaller size are simply subdivided into triangular elements and smaller quadrilateral elements to fulfill the displacement consistency on the acoustic-structure interface. This is clearly shown in Figure 5.27(b) along the edge

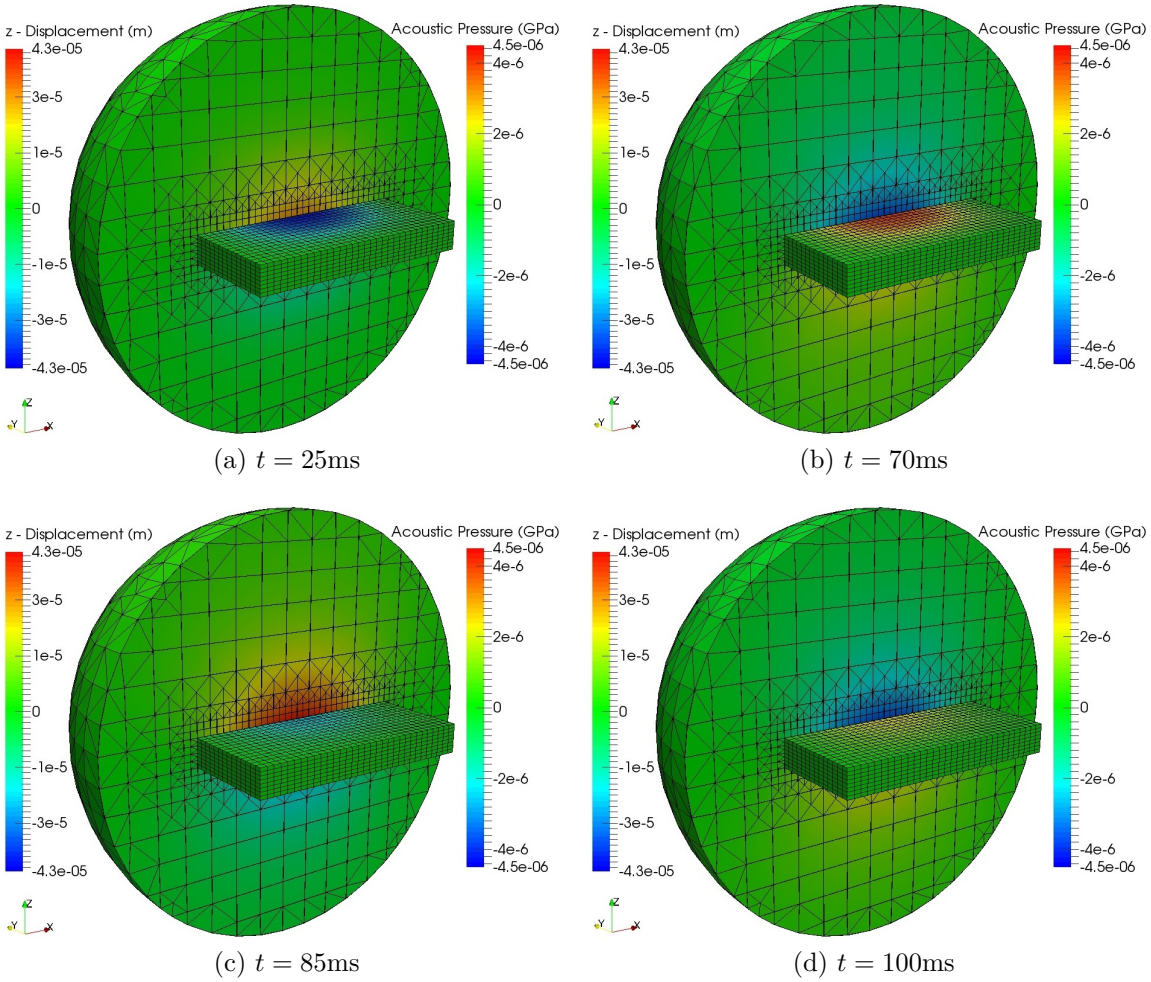

(a) $t = 25$ms (b) $t = 70$ms

(c) $t = 85$ms (d) $t = 100$ms

Figure 5.30. Coupled system of 3D plate submerged in infinite acoustic domain. Contour plots of vertical displacements and acoustic pressures at: (a) $t = 25$ms, (b) $t = 70$ms, (c) $t = 85$ms and (d) $t = 100$ms.

$\overline{DE}$ marked by white dash line. The mesh transition on acoustic-structure interface can still be handled efficiently in SBFEM for 3D problems. The coordinate axes in Figures 5.26 and 5.27 only denote the orientations of the model and are not shown at the coordinate origin.

The Newmark's method with a time step $\Delta t = 0.5$ms are employed to calculate the time-domain solutions of this example. The chosen value of Δt yields about 20 time steps per period at the highest frequency of interest. The results at two points A, B in Figure 5.24 are summarized in Figure 5.28 and 5.29 with the results from present SBFEM plotted in red solid lines and reference solutions in black dash lines.

As usual, the reference solution is obtained via using the FEM model in ANSYS with extended mesh to represent the infinite acoustic domain. Here, the radius of the extended mesh in ANSYS is equal to 165m. During the first 200ms, the traveling distance of wave front is $1.482 \times 200 = 296.4$m. The distance between FEM truncated boundary and the boundary of the domain of interest is $165 - 12 = 153$m, which is more than half of the traveling distance of wave front. The reflected wave has not entered the domain of interest yet. Therefore, the results of reference solution during the first 200ms are used to compare with SBFEM solutions. The plate in the finite element model is still divided into 32 8-node hexahedral elements in x and y directions and 8 divisions in z direction. For discretizing the acoustic domain in FEM, 4-node tetrahedral elements with the maximum edge length of 1.6m are used for the mesh transition on acoustic-structure interface.

Points A and B are both on the top surface of the plate with the coordinates of A$(0\text{m}, 0\text{m}, 0.8\text{m})$ and B$(3.2\text{m}, 0\text{m}, 0.8\text{m})$. As they are located on the acoustic-structure interface, both vertical displacements and acoustic pressures of these two points are given in Figures 5.28 and 5.29 respectively. Very good agreements are obtained by comparing the SBFEM solutions and reference solutions from ANSYS for the first 200ms in both structural and acoustic domains. The contour plots of results calculated from the present SBFEM are also shown in Figure 5.30 for this coupled system at times $t = 25$ms, $t = 70$ms, $t = 85$ms and $t = 100$ms.

5.4.5 Ancient Chinese bell vibrating in infinite air space

In the last numerical example, an acoustic-structure interaction system of an ancient Chinese bell vibrating in air is simulated in this section and used as an illustrative example to demonstrate the advantages of modeling acoustic-structure interaction problems with complex geometries via SBFEM and octree mesh. The STL model of the bell is the same as the one used in Section 4.5.4 Chapter 4, which is only used to model the sound propagation in the surrounding acoustic space but the bell

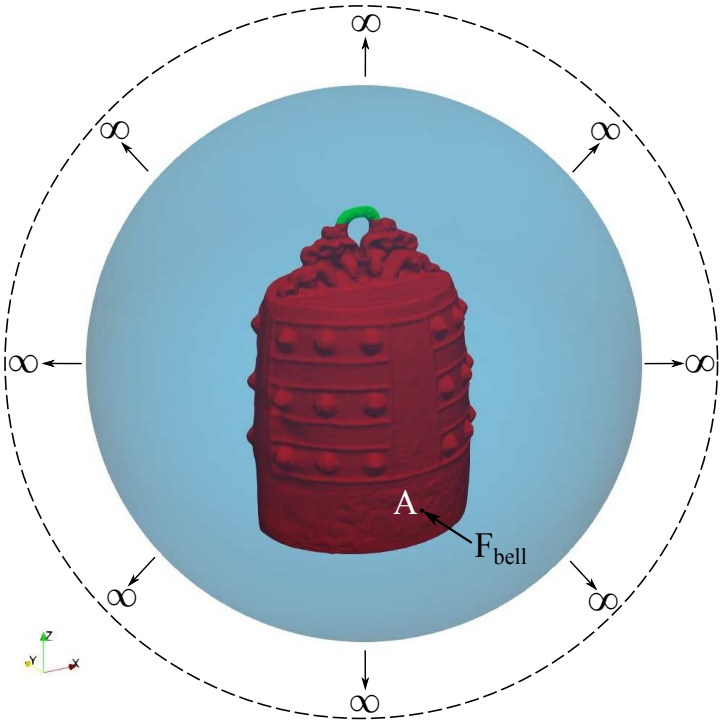

Figure 5.31. The acoustic-structure interaction model of ancient Chinese bell submerged in infinite acoustic domain.

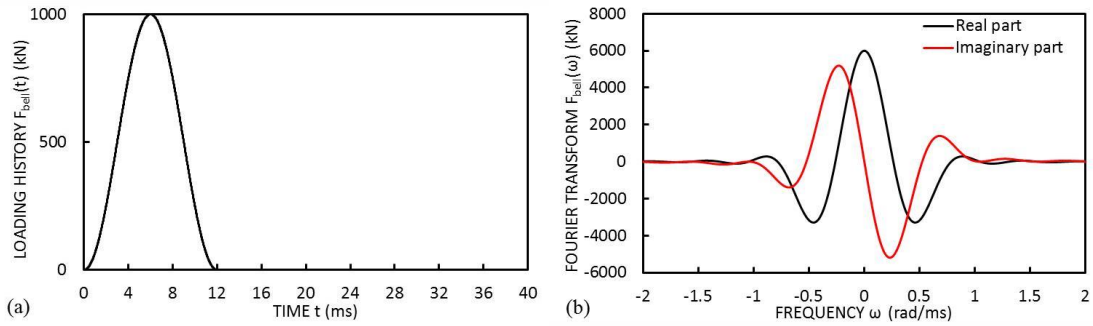

Figure 5.32. Time variation $F_{bell}(t)$ of transient point force applied on ancient Chinese bell: (a) time history and (b) Fourier transform.

itself is assumed to be rigid. In this example, the submerged bell is assumed to be elastic with the material properties of Young's modulus $E = 110$GPa, Poisson ratio $\nu = 0.34$ and mass density $\rho_s = 8000\text{kg/m}^3$. The surrounding air has the sound speed of $c = 340\text{m/s}$ and density $\rho_a = 1.23\text{kg/m}^3$.

Figure 5.31 illustrates the coupled acoustic-structure interaction model of the bell. The bell structure is denoted by the red region and the surrounding acoustic near field is indicated by the translucent blue color. The spherical surface of the

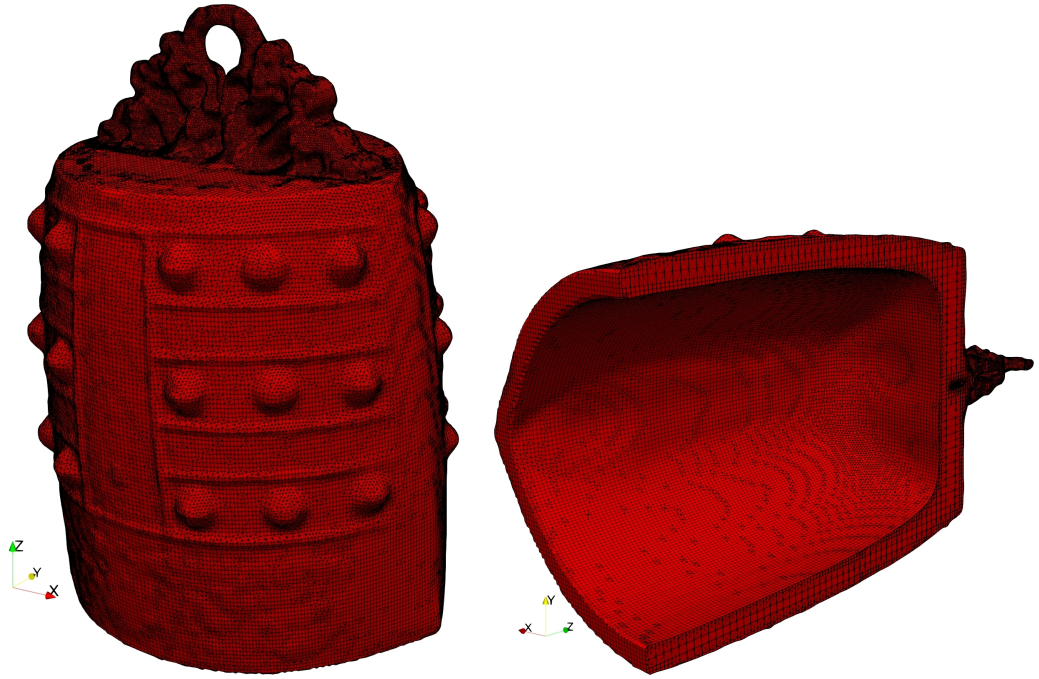

(a) (b)

Figure 5.33. SBFEM mesh of the ancient Chinese bell: (a) view from -y direction and (b) view of half of the mesh from -z direction.

translucent region with blue color is the doubly-asymptotic open boundary for representing the infinite acoustic far field and has the radius of 110cm. The centroid of the open boundary coincides with the coordinates origin and the coordinate axes plotted in all figures in this section only indicate the orientation of the displayed model. All nodes on the part of surface marked by the green area on the handle of the bell in Figure 5.31 are fixed in all DOFs. A transient point force $F_{bell}(t)$ is applied at point A on the surface of bell with the coordinate of $(-0.009\text{m}, -0.4002\text{m}, -0.3844\text{m})$ in +y direction. The point force $F_{bell}(t)$ is given by:

$$F_{bell}(t) = \begin{cases} 500 \times (1 - \cos\frac{\pi}{6}t)\ (\text{kN}) & \text{when } 0 \leq t \leq 12\text{ms}, \\ 0 \qquad\qquad\qquad\qquad\ (\text{kN}) & \text{when } 12\text{ms} < t. \end{cases} \tag{5.68}$$

The time variation of $F_{bell}(t)$ are also plotted in Figure 5.32(a) with its Fourier transform in Figure 5.32(b). According to Figure 5.32(b), the maximum relevant frequency of the applied force is estimated at $\omega_{max} = 1.5\text{rad/ms}$. The acoustic medium in this example is assumed to be air with sound speed of 340m/s. This

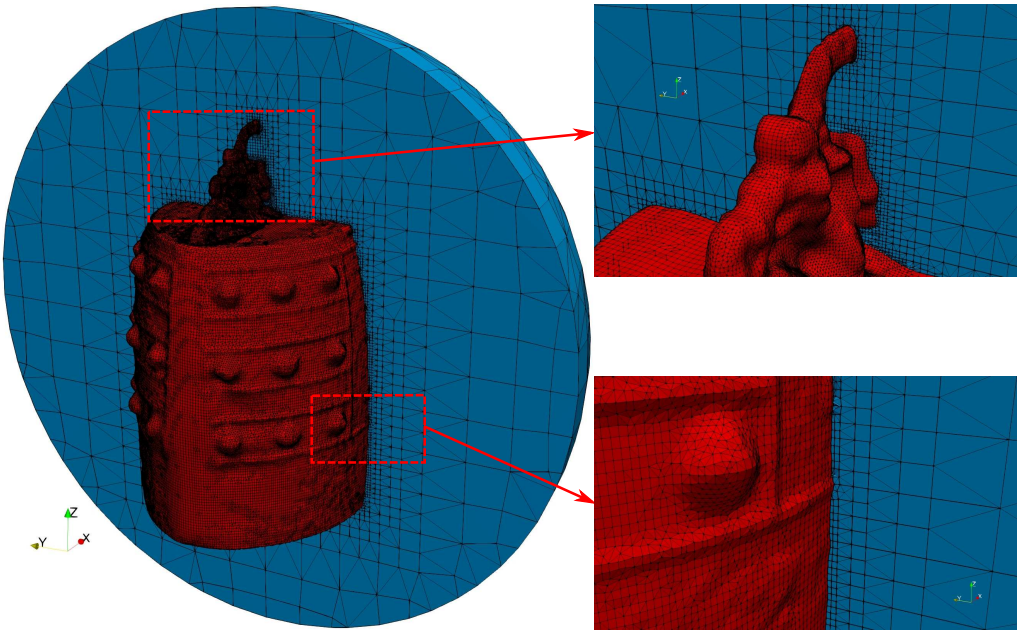

Figure 5.34. The SBFEM mesh of the ancient Chinese bell submerged in infinite acoustic domain.

gives the shortest wavelength in acoustic field of $\lambda_a \approx 142.4$cm, which is equal to the shortest wavelength in acoustic field in Section 4.5.4. Therefore, the octree mesh of the acoustic field in this example is the same as that illustrated in Figures 4.26 and 4.27 with the maximum and minimum cell size of 15cm and 0.46875cm respectively. According to Equation (5.66), the shear wave speed in bell structure is $c_s \approx 2265$m/s. This gives the shortest wavelength in structural domain of $\lambda_s = \frac{2\pi}{\omega_{max}} c_s \approx 9.49$m. However, for better capturing the complex geometrical features on the surface of the bell, the minimum cell size used for generating the octree mesh of the bell structure is set to be 0.46875cm and the maximum cell size of the structural octree mesh is 1.875cm (4 times of the minimum cell size in structural mesh). The octree mesh of the bell structure is also illustrated in Figure 5.33(a) and Figure 5.33(b) with half of the mesh cutting through y-z plane.

The octree meshes of acoustic and structural domain are then coupled together and shown in Figure 5.34. Subdivisions of surface elements are applied to couple these two independent meshes with different element sizes on the same acoustic-structure interface. The meshing process for this acoustic-structure interaction sy-

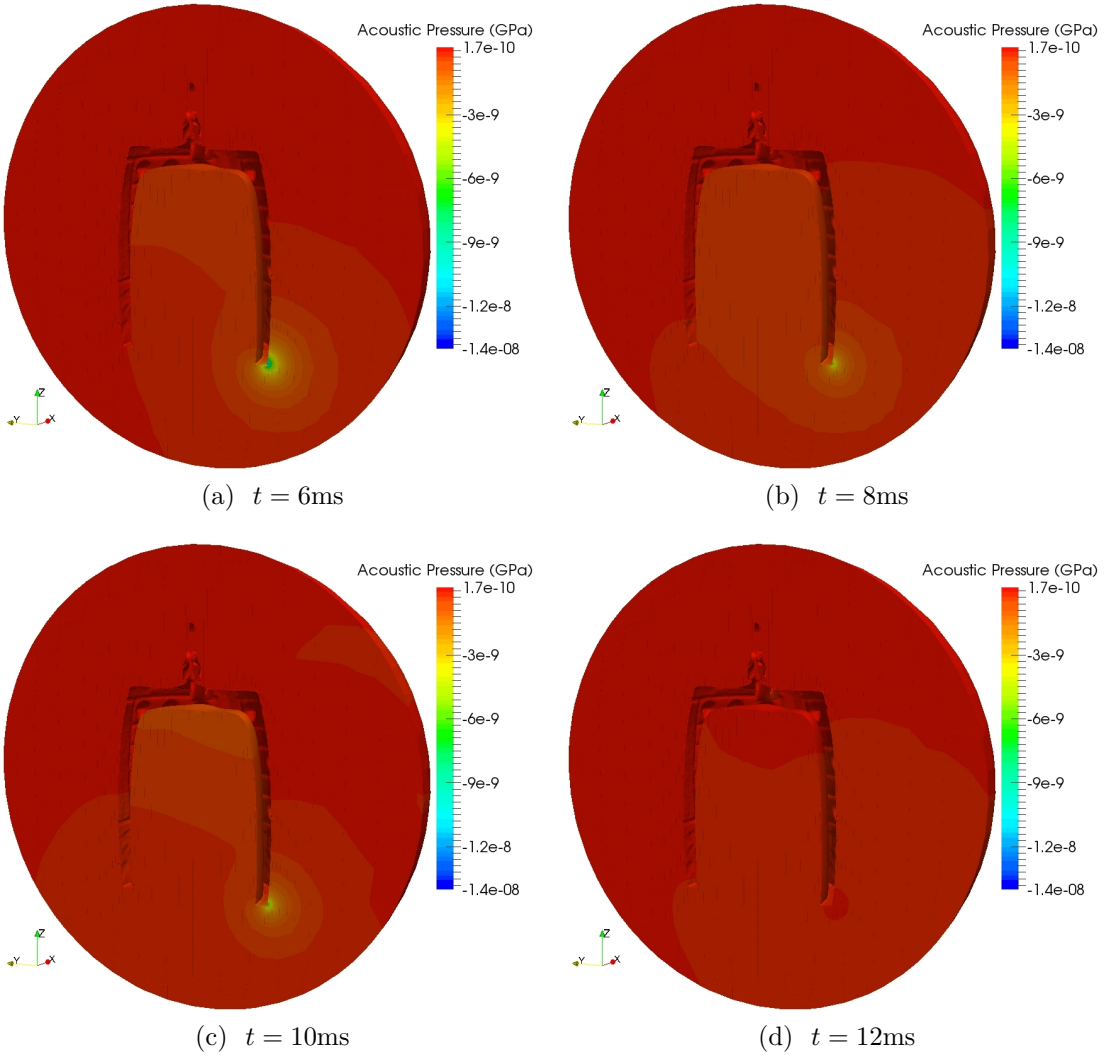

(a) $t = 6$ms (b) $t = 8$ms

(c) $t = 10$ms (d) $t = 12$ms

Figure 5.35. Coupled system of ancient Chinese bell submerged in infinite acoustic domain. Contour plots of acoustic pressures from acoustic domain at: (a) $t = 6$ms, (b) $t = 8$ms, (c) $t = 10$ms and (d) $t = 12$ms.

stem is automatically completed with little human effort. All surface elements in the octree mesh in Figure 5.34 are 3-node triangular or 4-node quadrilateral elements. Because all subdomain sizes are small enough to capture the shortest wavelengths in both acoustic and structural subdomains, the terms of continued-fraction of all bounded subdomains are set to be zero. The orders of continued-fractions for spherical open boundary is set to be $M_H = M_L = 1$. The time-domain solutions of this coupled acoustic-structure interaction system are obtained by applying Newmark's method to Equation (5.56) or (5.61) with the constant time step $\Delta t = 0.2$ms,

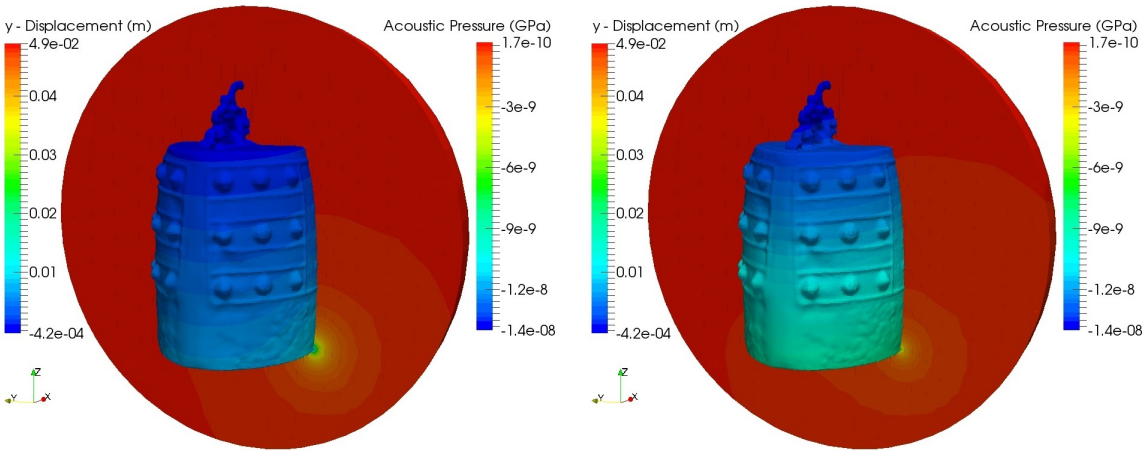

(a) $t = 6$ms (b) $t = 8$ms

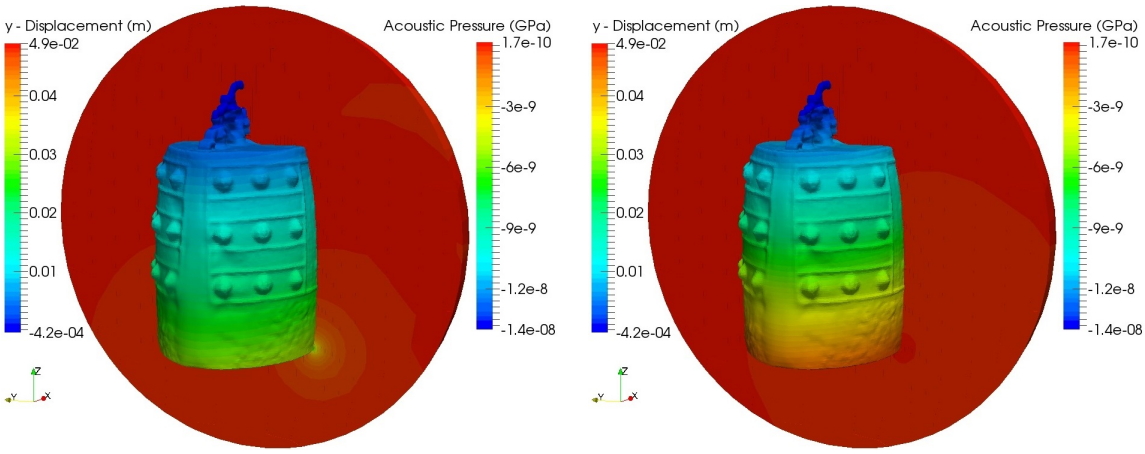

(c) $t = 10$ms (d) $t = 12$ms

Figure 5.36. Coupled system of ancient Chinese bell submerged in infinite acoustic domain. Contour plots of vertical displacements and acoustic pressures at: (a) $t = 6$ms, (b) $t = 8$ms, (c) $t = 10$ms and (d) $t = 12$ms.

which gives about 20 time steps per period at the highest frequency of interest. The contour plots of the pressures in the acoustic domain at time $t = 6$ms, 8ms, 10ms and 12ms are illustrated in Figure 5.35. Additionally, the contour plots of results from both acoustic and structural domains, including both acoustic pressures and structural displacements in y direction, at the same time steps are plotted in Figure 5.36. In both Figures 5.35 and 5.36, the acoustic domains are cut in half along y-z plane for showing more details inside the model.

5.5 Conclusions

In this chapter, the SBFEM has been developed to 2D and 3D acoustic-structure interaction analyses by utilizing the approaches developed in previous Chapters 3 and 4 for simulating infinite acoustic domain. For a general acoustic-structure interaction problem, the infinite acoustic domain is divided into an acoustic near field and an infinite acoustic far field. The acoustic far field is represent by the high-order doubly-asymptotic open boundary in Chapters 3 and 4 for 2D and 3D problems respectively. The dynamic stiffness matrices for bounded subdomains in acoustic near field and structural domain are calculated using continued fractions for accurate and efficient modeling of structural and acoustic wave propagation. With the introduction of auxiliary variables to continued-fraction expansions, the resulting time-domain equations for both structural and acoustic domains can be directly coupled together for transient analysis via satisfying the normal force equilibrium and normal displacement consistency on the acoustic-structure interface. The global equations of motion for the coupled acoustic-structure interaction system can also be transformed to symmetric formulation by replacing the unknowns corresponding to acoustic pressures to newly defined variables. Due to the boundary discretization required in SBFEM, the mesh transition on the acoustic-structure interface can be handled easily and efficiently by adding extra nodes on the interface for 2D problems and subdivisions of surface elements for 3D problems. Two 2D and three 3D examples of acoustic-structure interaction are presented in this chapter to show the accuracy of proposed SBFEM and its efficiency on transition between acoustic and structural meshes. Newmark's method is applied to obtain the transient solutions of all numerical examples. The octree mesh technique is also employed to automatically generate meshes for acoustic-structure interaction problems with complex geometry and reduce the human efforts.

Chapter 6

Automatic 3D elastoplastic analysis using octree mesh and SBFEM with stabilisation

6.1 Introduction

The SBFEM proposed by Song and Wolf (Song and Wolf, 1997) is naturally suitable for applying the quadtree and octree techniques as introduced in Section 4.1 of Chapter 4. SBFEM is a semi-analytical computational method, which only requires the boundary discretization. This reduces the problem dimensions by one and provides more flexibility in the automatic mesh generation. For satisfying the scaling requirement in SBFEM, the problem domain can be divided into multiple subdomains as in FEM but with arbitrary sides (polygonal or polyhedral subdomains in 2D or 3D cases respectively). Both quadtree and octree have been implemented into SBFEM for automatic stress analysis recently (Saputra et al., 2017a; Liu et al., 2017). In quadtree mesh, the hanging-node problem does not exist in SBFEM as each quadtree cell can be treated as a subdomain with arbitrary number of line elements on the edges. Although hanging nodes exist in octree mesh, those faces of an

octree cell with hanging nodes can be simply divided into a combination of standard triangular and quadrilateral elements without additional effort. The recently proposed octree mesh generation technique based on SBFEM in Reference (Liu et al., 2017) presents an efficient way of generating CAD-based mesh automatically. STL format is chosen as the input file format as it is widely supported in CAD industry such as 3D printing and rapid prototyping. The STL format is simple as it only contains unstructured triangular facets for describing the surface of an object. Besides, ill-shaped, overlapping and self-intersecting facets are all allowed to be existed in this file. All these advantages of STL file make the proposed meshing technique universal and simple to use.

In addition to the excels of SBFEM in automatic analysis using quadtree and octree techniques, this method also presents salient advantages in modelling the unbounded domains (Deeks and Augarde, 2007; Wolf, 2003) and stress singularities (Song, 2004a, 2005) as it describes the whole problem domain by scaling the boundary of bounded or unbounded domain using dimensionless radial coordinate and can provide analytical solution for displacements and stresses in the radial direction in terms of matrix power functions (Song and Wolf, 1997). SBFEM has also been applied to elastoplastic and nonlinear analysis in some literatures such as (Ooi et al., 2014; He, 2017; Chen et al., 2017a). In this study, the recently developed octree mesh generation technique from STL model by Liu et al. (Liu et al., 2017), which has only been applied to elastic analysis before, will be introduced to elastoplastic analysis due to its versatility on meshing complex geometry and accuracy of modeling.

For extending the capability of SBFEM to handle material nonlinearity, a novel polygon-based SBFEM formulation is firstly developed by Ooi et al. (Ooi et al., 2014) for elastoplastic analysis. Then, an alternative approach with higher computational efficiency is developed for elastoplastic image-based analysis (He, 2017), which is inspired by the reduced integration method with hourglass control in FEM

(Belytschko and Tsay, 1983; Belytschko and Bachrach, 1986; Liu et al., 1985; Belytschko and Bindeman, 1991; Liu et al., 1994; Korelc and Wriggers, 1997). In elastoplastic analysis, once the stresses exceed the yielding stress of material, a correction procedure should be involved to bring the elastic trial stress back to the yield surface decided by corresponding yielding criteria such as Tresca ,von Mises or Drucker-Prager criteria (Chen and Han, 2007). This correction procedure for updating the stresses in elastoplastic analysis is also known as the return mapping algorithm. The return mapping algorithm needs to be performed on each Gauss points in FEM and is usually computationally expensive as it requires iteration procedures, such as Newton-Raphson method, to return the elastic trial stress back to the yield surface. Compared with normal Gauss quadrature, the reduced integration method in FEM requires the return mapping algorithm to be performed at less Gauss points within each element. This greatly improves the efficiency of elastoplastic analysis and simplifies the implementation, especially for complex nonlinear problems. For overcoming the stability issues in reduced integration method, stabilisation matrix is often required to control those spurious modes, which is also known as hourglass modes in the underintegrated elements. A review of reduced integration methods can be found in Section 2.3.2 of Chapter 2. Analogously, the original polygon-based SBFEM formulation for elastoplasticity needs multiple fitting points in each polygonal subdomain to approximate the varying elastoplastic constitutive matrix and internal stresses via a polynomial function. As a result, return mapping algorithm should be performed at every fitting point in the subdomain with plastic deformation. In the new approach for image-based elastoplastic analysis in SBFEM, the return mapping algorithm should only be performed at one fitting point at the scaling centre of each subdomain experiencing plastic deformation. A stabilisation matrix is also introduced to control the hourglass modes in each underintegrated subdomain. In addition, no fitting operation is required for interpolating the elastoplastic constitutive matrix and internal stresses as they are represented by constant

values in each subdomain. Therefore, smaller subdomain size is suggested to be used in the yield zone as the variations of elastoplastic constitutive matrix and internal stresses should also be small and represented by the constant values. This is consistent with the idea of using automatic meshing techniques for both image-based and CAD-based mesh as smaller mesh size is often preferred to preserve all the geometrical features that can be captured from the input models. Furthermore, the mesh transition from refined plastic region to non-refined elastic region can be handled efficiently by utilizing the quadtree or octree mesh.

The work in this chapter is a natural extension of the improved scaled boundary finite element formulation for elastoplastic analysis with one-point return mapping algorithm in (He, 2017) to three-dimensional static and dynamic elastoplastic analysis. By combining with the automatic mesh generation from STL model with trimmed boundaries, the stress concentration on the jagged boundaries in image-based mesh, reported in literatures (Lian et al., 2013; He, 2017; Saputra et al., 2017a), will not appear in this approach. Similar to 2D analysis, the return mapping algorithm just needs to be performed at the scaling centre of each polyhedral subdomain, which improves the efficiency of SBFEM in 3D elastoplastic analysis. A stabilisation matrix is introduced for controlling the spurious modes of plastic polyhedral subdomains. Newmark's method for nonlinear systems is directly employed in the proposed formulations for performing the dynamic elastoplastic analysis.

The remaining sections in this chapter are organized as follows: the shape function, stress and strain fields of the polyhedral subdomains in SBFEM are firstly summarized in Section 6.2. Then, the derivation of SBFEM formulation with stabilisation for 3D elastoplasticity is illustrated in Section 6.3. Next, the computational procedures for implementing the current approach in both static and dynamic elastoplastic analyses are summarized in Section 6.4. Several numerical examples are presented in Section 6.5 to demonstrate the accuracy, efficiency and practicability of current approach. Finally, conclusions are stated in Section 6.6.

6.2 Polyhedral subdomains in SBFEM

6.2.1 Scaled boundary shape function for polyhedral subdomains

For deriving the formulations for elastoplastic analysis based on SBFEM, the scaled boundary shape function for each polyhedral subdomain is derived at first following a similar procedure as in (Ooi et al., 2014) for polygonal subdomains. Expressing the radial displacement function $\mathbf{u}(\xi)$ in Equation (5.18) by substituting $\mathbf{c}_n$ defined in (5.21) yields

$$\mathbf{u}(\xi) = \mathbf{\Psi}_{u_n} \xi^{-\mathbf{S}_n - 0.5\mathbf{I}} \mathbf{\Psi}_{u_n}^{-1} \mathbf{u}_b \tag{6.1}$$

with $s = 3$ for 3D problems. The displacement field in subdomain $\mathbf{u}(\xi, \eta, \zeta)$ can be expressed by substituting Equation (6.1) into (5.4)

$$\mathbf{u}(\xi, \eta, \zeta) = \mathbf{N}_s(\eta, \zeta) \mathbf{\Psi}_{u_n} \xi^{-\mathbf{S}_n - 0.5\mathbf{I}} \mathbf{\Psi}_{u_n}^{-1} \mathbf{u}_b \tag{6.2}$$

Equation (6.2) can then be written into the following matrix product as in the finite element analysis

$$\mathbf{u}(\xi, \eta, \zeta) = \mathbf{\Phi}(\xi, \eta, \zeta) \mathbf{u}_b \tag{6.3}$$

with the scaled boundary shape function $\mathbf{\Phi}(\xi, \eta, \zeta)$ for polyhedral subdomains defined as

$$\mathbf{\Phi}(\xi, \eta, \zeta) = \mathbf{N}_s(\eta, \zeta) \mathbf{\Psi}_{u_n} \xi^{-\mathbf{S}_n - 0.5\mathbf{I}} \mathbf{\Psi}_{u_n}^{-1} \tag{6.4}$$

This scaled boundary shape function is analytically described in the radial direction ξ and compatible between adjacent polyhedral elements (Ooi et al., 2014). For a crack polyhedral element, it can describe singularities semi-analytically (Chiong et al., 2014). Due to the fact that the rigid body motion modes, constant strain modes and other higher order modes can be identified via their corresponding eigen-

values in $\mathbf{S}_n$, a stabilisation procedure for three-dimensional elastoplastic analysis in SBFEM is developed in this chapter based on the constant stress state of each subdomain.

6.2.2 Scaled boundary stress and strain fields for polyhedral subdomains

The strain field $\boldsymbol{\epsilon}(\xi,\eta,\zeta)$ in Equation (5.8) can be expressed in terms of nodal displacement $\mathbf{u}_b$ by utilizing Equation (6.1). The resulting expression is:

$$\boldsymbol{\epsilon}(\xi,\eta,\zeta) = \left(\mathbf{B}_1^s(\eta,\zeta)\boldsymbol{\Psi}_{u_n}\left[-\mathbf{S}_n - 0.5\mathbf{I}\right] + \mathbf{B}_2^s(\eta,\zeta)\boldsymbol{\Psi}_{u_n}\right)\xi^{-\mathbf{S}_n-1.5\mathbf{I}}\boldsymbol{\Psi}_{u_n}^{-1}\mathbf{u}_b \tag{6.5}$$

Equation (6.5) can be simplified as:

$$\boldsymbol{\epsilon}(\xi,\eta,\zeta) = \mathbf{B}(\xi,\eta,\zeta)\mathbf{u}_b \tag{6.6}$$

with the scaled boundary strain-displacement matrix $\mathbf{B}(\xi,\eta,\zeta)$ for polyhedral subdomain below:

$$\mathbf{B}(\xi,\eta,\zeta) = \boldsymbol{\Psi}_{\epsilon}(\eta,\zeta)\xi^{-\mathbf{S}_n-1.5\mathbf{I}}\boldsymbol{\Psi}_{u_n}^{-1} \tag{6.7}$$

In Equation (6.7), the strain modes $\boldsymbol{\Psi}_{\epsilon}(\eta,\zeta)$ are:

$$\boldsymbol{\Psi}_{\epsilon}(\eta,\zeta) = \mathbf{B}_1^s(\eta,\zeta)\boldsymbol{\Psi}_{u_n}\left[-\mathbf{S}_n - 0.5\mathbf{I}\right] + \mathbf{B}_2^s(\eta,\zeta)\boldsymbol{\Psi}_{u_n} \tag{6.8}$$

The incremental strain field $\Delta\boldsymbol{\epsilon}$ in an elastoplastic analysis can be decomposed into elastic and plastic parts as

$$\Delta\boldsymbol{\epsilon} = \Delta\boldsymbol{\epsilon}_e + \Delta\boldsymbol{\epsilon}_p \tag{6.9}$$

The subscripts 'e' and 'p' in Equation (6.9) denote the incremental elastic and plastic strains, respectively. The incremental plastic strain can be calculated from plastic flow rule. Assuming associative plasticity, it is expressed as

$$\Delta\boldsymbol{\epsilon}_p = \frac{\partial F}{\partial \boldsymbol{\sigma}}\Delta\lambda \tag{6.10}$$

where $F \equiv F(\boldsymbol{\sigma}, \kappa)$ is a yield function depending on the current stress state $\boldsymbol{\sigma}$ and the hardening parameter κ. $\Delta\lambda$ is the plastic multiplier. An example of yield function for isotropic hardening material under von Mises yield criterion is written as

$$F(\boldsymbol{\sigma}, \kappa(\boldsymbol{\epsilon}_p)) = \sqrt{\frac{3}{2}J_2} - \sigma_f(\boldsymbol{\epsilon}_p) = 0 \tag{6.11}$$

with the second deviatoric stress invariant J_2 and instantaneous plastic yield limit $\sigma_f(\boldsymbol{\epsilon}_p)$. According to Hooke's law, the incremental stress field is related to total incremental strain in Equation (6.9) and written as

$$\Delta\boldsymbol{\sigma} = \mathbf{D}_{ep}\Delta\boldsymbol{\epsilon} \tag{6.12}$$

with the elastoplastic constitutive matrix

$$\mathbf{D}_{ep} = \mathbf{D} - \frac{\mathbf{D}\left(\frac{\partial F}{\partial \boldsymbol{\sigma}}\right)\left(\frac{\partial F}{\partial \boldsymbol{\sigma}}\right)^T \mathbf{D}}{H + \left(\frac{\partial F}{\partial \boldsymbol{\sigma}}\right)^T \mathbf{D}\left(\frac{\partial F}{\partial \boldsymbol{\sigma}}\right)} \tag{6.13}$$

and H is the hardening parameter

$$H = -\frac{1}{\Delta\lambda}\frac{\partial F}{\partial \kappa}d\kappa \tag{6.14}$$

In unloading, the state of stress immediately becomes elastic. The corresponding criteria for loading and the start of unloading can be mathematically expressed as (Chen and Han, 2007)

$$F = 0 \,\text{and}\, \left(\frac{\partial F}{\partial \boldsymbol{\sigma}}\right) d\boldsymbol{\sigma} \geq 0 \quad \text{(loading)} \tag{6.15a}$$

$$F = 0 \,\text{and}\, \left(\frac{\partial F}{\partial \boldsymbol{\sigma}}\right) d\boldsymbol{\sigma} < 0 \quad \text{(unloading)} \tag{6.15b}$$

$\left(\frac{\partial F}{\partial \boldsymbol{\sigma}}\right)$ is normal to the yield surface and $d\boldsymbol{\sigma}$ is the additional loading or incremental stress vector. Substituting Equation (6.6) for incremental strain into (6.12) yields the expression for incremental stress field $\Delta\boldsymbol{\sigma}$ as

$$\Delta\boldsymbol{\sigma}(\xi, \eta, \zeta) = \mathbf{D}_{ep}\mathbf{B}(\xi, \eta, \zeta)\Delta\mathbf{u}_b \tag{6.16}$$

with the incremental nodal displacement $\Delta\mathbf{u}_b$.

6.3 Stabilisation procedure for 3D elastoplastic analysis based on scaled boundary finite element formulations

6.3.1 Governing equation of elastoplasticity in SBFEM

Analogous to FEM, the scaled boundary finite element formulation for static elastoplasticity can be derived from the incremental form of the principle of virtual work in the scaled boundary coordinates

$$\int_{\Omega} \delta\Delta\boldsymbol{\epsilon}^T \Delta\boldsymbol{\sigma}(\xi,\eta,\zeta) d\Omega = \int_{\Gamma} \delta\mathbf{u}^T|_{(j+1)} \mathbf{f}_t|_{(j+1)} d\Gamma + \int_{\Omega} \delta\mathbf{u}^T|_{(j+1)} \mathbf{f}_b|_{(j+1)} d\Omega - \int_{\Omega} \delta\boldsymbol{\epsilon}^T|_{(j)} \boldsymbol{\sigma}(\xi,\eta,\zeta)|_{(j)} d\Omega \tag{6.17}$$

where $\Delta\boldsymbol{\sigma}(\xi,\eta,\zeta)$ and $\boldsymbol{\sigma}(\xi,\eta,\zeta)|_{(j)}$ are the incremental stress and current stress field at load step j respectively. $\mathbf{f}_t|_{(j+1)}$ and $\mathbf{f}_b|_{(j+1)}$are the surface traction and body force at load step $j+1$. $\delta\Delta\boldsymbol{\epsilon}$ and $\delta\boldsymbol{\epsilon}|_{(j)}$ are the virtual incremental strain field and virtual strain field at load step j. $\delta\mathbf{u}|_{(j+1)}$ is the virtual displacement field at load step $j+1$. Substituting Equations (6.3), (6.6) and (6.16) into (6.17) yields

$$\left(\int_{\Omega} \mathbf{B}^T(\xi,\eta,\zeta)\mathbf{D}_{ep}\mathbf{B}(\xi,\eta,\zeta) d\Omega\right) \Delta\mathbf{u}_b = \left(\int_{\Gamma} \boldsymbol{\Phi}^T(\xi,\eta,\zeta)\mathbf{f}_t|_{(j+1)} d\Gamma + \int_{\Omega} \boldsymbol{\Phi}^T(\xi,\eta,\zeta)\mathbf{f}_b|_{(j+1)} d\Omega\right) - \int_{\Omega} \mathbf{B}^T(\xi,\eta,\zeta)\boldsymbol{\sigma}(\xi,\eta,\zeta)|_{(j)} d\Omega \tag{6.18}$$

The integration on the left-hand-side of Equation (6.18) represents the elastoplastic stiffness matrix $\mathbf{K}_{ep}$ for the subdomain. The first two terms on the right-hand-side in the parentheses are the external load vector $\mathbf{F}_{ext}|_{(j+1)}$ due to surface traction $\mathbf{f}_t$ and body loads $\mathbf{f}_b$. The internal load vector $\mathbf{F}_{int}|_{(j)}$ is defined by the last term on the right-hand-side. Then, Equation (6.18) can be simplified as

$$\mathbf{K}_{ep}\Delta\mathbf{u}_b = \mathbf{F}_{ext}|_{(j+1)} - \mathbf{F}_{int}|_{(j)} \tag{6.19}$$

Assembling the system of nonlinear equations in (6.19) for all polyhedral subdomains as in FEM yields

$$\left[\sum_{i=1}^{nPol} \mathbf{K}_{ep}\right] \Delta \mathbf{U}_b = \sum_{i=1}^{nPol} \left\{ \mathbf{F}_{ext}|_{(j+1)} - \mathbf{F}_{int}|_{(j)} \right\} \tag{6.20}$$

Equation (6.20) can then be solved using standard nonlinear solution techniques, such as the modified Newton-Raphson iterations employed in this chapter.

6.3.2 Decomposition of SBFEM stress field in polyhedral subdomains

In an elastoplastic analysis, the return mapping algorithm is applied to update the stress field once the trial stress state violates the plastic admissibility. The recently proposed one-point return mapping formulations for polygonal subdomains in 2D elastoplasticity (He, 2017) is extended to 3D elastoplastic analysis in this chapter. Based on the same assumption that each polyhedral subdomain needs to be relatively small, a constant elastoplastic constitutive matrix $\mathbf{D}_{ep}$ is employed to approximate the variation of $\mathbf{D}_{ep}$ within each subdomain. The elastoplastic constitutive matrix $\mathbf{D}_{ep}$ is only required at the scaling centre of each subdomain. Therefore, the computationally expensive return mapping algorithm should just be performed at one point per subdomain for updating the stresses. The constant stresses within each scaled boundary polyhedral subdomain are corresponding to the constant stress modes (Chiong et al., 2014). As a result, once the stresses at the scaling centre reach the yield surface, the whole subdomain is considered to be plastic. Otherwise, this subdomain is still in elastic state.

For decomposing the stress field in Equation (6.16) into a constant stress part and a non-constant (higher-order) stress part, the scaled boundary strain-displacement matrix $\mathbf{B}(\xi, \eta, \zeta)$ should be divided into constant and no-constant parts as well. From the expression for $\mathbf{B}(\xi, \eta, \zeta)$ in Equation (6.7), all three matrices for defining $\mathbf{B}(\xi, \eta, \zeta)$ are decomposed into constant parts with superscript 'c' and non-constant

parts with superscript 'n' respectively in Equations (6.21) - (6.23).

$$\boldsymbol{\Psi}_{\epsilon}(\eta,\zeta) = \begin{bmatrix} \boldsymbol{\Psi}_{\epsilon}^{(n)}(\eta,\zeta) & \boldsymbol{\Psi}_{\epsilon}^{(c)} \end{bmatrix} \tag{6.21}$$

$$\xi^{-\mathbf{S}_n-1.5\mathbf{I}} = \begin{bmatrix} \xi^{-\mathbf{S}_n^{(n)}-1.5\mathbf{I}} & 0 \\ 0 & \xi^{-\mathbf{S}_n^{(c)}-1.5\mathbf{I}} \end{bmatrix} \tag{6.22}$$

$$\boldsymbol{\Psi}_{u_n}^{-1} = \begin{bmatrix} \left(\boldsymbol{\Psi}_{u_n}^{-1}\right)^{(n)} \\ \left(\boldsymbol{\Psi}_{u_n}^{-1}\right)^{(c)} \end{bmatrix} \tag{6.23}$$

The constant part is related to nine constant strain modes for a polyhedral subdomain and can be identified by their corresponding eigenvalues as $\lambda(\mathbf{S}_n^{(c)}) = -1.5$. $\lambda(\mathbf{S}_n^{(n)}) < -1.5$ identifies other non-constant strain modes. By substituting the value of $\lambda(\mathbf{S}_n^{(c)}) = -1.5$ into Equation (6.22), this matrix exponential function is simplified as

$$\xi^{-\mathbf{S}_n-1.5\mathbf{I}} = \begin{bmatrix} \xi^{-\mathbf{S}_n^{(n)}-1.5\mathbf{I}} & \\ & \mathbf{I} \end{bmatrix} \tag{6.24}$$

Substituting Equation (6.21), (6.24) and (6.23) into (6.7), the $\mathbf{B}(\xi,\eta,\zeta)$ matrix can be written into the following form

$$\mathbf{B}(\xi,\eta,\zeta) = \begin{bmatrix} \boldsymbol{\Psi}_{\epsilon}^{(n)}(\eta,\zeta) & \boldsymbol{\Psi}_{\epsilon}^{(c)} \end{bmatrix} \begin{bmatrix} \xi^{-\mathbf{S}_n^{(n)}-1.5\mathbf{I}} & \\ & \mathbf{I} \end{bmatrix} \begin{bmatrix} \left(\boldsymbol{\Psi}_{u_n}^{-1}\right)^{(n)} \\ \left(\boldsymbol{\Psi}_{u_n}^{-1}\right)^{(c)} \end{bmatrix} \tag{6.25}$$

Now, Equation (6.25) can be decomposed as

$$\mathbf{B}(\xi,\eta,\zeta) = \mathbf{B}^{(c)} + \mathbf{B}^{(n)}(\xi,\eta,\zeta) \tag{6.26}$$

with constant and non-constant strain-displacement matrix in Equation (6.27)

$$\mathbf{B}^{(c)} = \boldsymbol{\Psi}_{\epsilon}^{(c)} \left(\boldsymbol{\Psi}_{u_n}^{-1}\right)^{(c)} \tag{6.27a}$$

$$\mathbf{B}^{(n)}(\xi,\eta,\zeta) = \boldsymbol{\Psi}_{\epsilon}^{(n)}(\eta,\zeta)\xi^{-\mathbf{S}_n^{(n)}-1.5\mathbf{I}} \left(\boldsymbol{\Psi}_{u_n}^{-1}\right)^{(n)} \tag{6.27b}$$

Thus, the stress field can be decomposed by substituting Equation (6.26) into (6.16) as

$$\boldsymbol{\sigma}(\xi,\eta,\zeta) = \boldsymbol{\sigma}^{(c)} + \boldsymbol{\sigma}^{(n)}(\xi,\eta,\zeta) \tag{6.28}$$

with constant and non-constant stress parts $\boldsymbol{\sigma}^{(c)}$ and $\boldsymbol{\sigma}^{(n)}(\xi,\eta,\zeta)$ listed below:

$$\boldsymbol{\sigma}^{(c)} = \mathbf{D}_{ep}\mathbf{B}^{(c)}\mathbf{u}_b \tag{6.29a}$$

$$\boldsymbol{\sigma}^{(n)}(\xi,\eta,\zeta) = \mathbf{D}_{ep}\mathbf{B}^{(n)}(\xi,\eta,\zeta)\mathbf{u}_b \tag{6.29b}$$

6.3.3 Decomposition of elastoplastic stiffness matrix for polyhedral subdomains

The total stiffness matrix for elastoplasticity $\mathbf{K}_{ep}$ can also be decomposed corresponding to the decomposition of the stress field in Equation (6.28). Comparing Equation (6.18) and (6.19) gives the expression of elastoplastic stiffness matrix for a polyhedral subdomain

$$\mathbf{K}_{ep} = \int_{\Omega} \mathbf{B}^T(\xi,\eta,\zeta)\mathbf{D}_{ep}\mathbf{B}(\xi,\eta,\zeta)d\Omega \tag{6.30}$$

Replacing the second instance of $\mathbf{B}(\xi,\eta,\zeta)$ with the expression in Equation (6.26) yields

$$\mathbf{K}_{ep} = \int_{\Omega} \left(\mathbf{B}^T(\xi,\eta,\zeta)\mathbf{D}_{ep}\mathbf{B}^{(c)} + \mathbf{B}^T(\xi,\eta,\zeta)\mathbf{D}_{ep}\mathbf{B}^{(n)}(\xi,\eta,\zeta)\right) d\Omega \tag{6.31}$$

where the infinitesimal volume $d\Omega$ is defined as (Song and Wolf, 1997)

$$d\Omega = |\mathbf{J}(\eta,\zeta)|\, \xi^2 d\xi d\eta d\zeta \tag{6.32}$$

with $|\mathbf{J}(\eta,\zeta)|$ the determinant of Jacobian matrix for 3D subdomain defined in Equation (4.4). Substituting Equation (6.7), (6.27), and (6.32) into the expression for $\mathbf{K}_{ep}$ in Equation (6.31) gives

$$\mathbf{K}_{ep} = \boldsymbol{\Psi}_{u_n}^{-T}\mathbf{X}^{(c)}\left(\boldsymbol{\Psi}_{u_n}^{-1}\right)^{(c)} + \boldsymbol{\Psi}_{u_n}^{-T}\mathbf{X}^{(n)}\left(\boldsymbol{\Psi}_{u_n}^{-1}\right)^{(n)} \tag{6.33}$$

with $\mathbf{X}^{(c)}$ and $\mathbf{X}^{(n)}$ expressed as

$$\mathbf{X}^{(c)} = \int_0^1 \xi^{-\mathbf{S}_n^T - 1.5\mathbf{I}} \left[\int_{-1}^{+1} \int_{-1}^{+1} \mathbf{\Psi}_\epsilon^T(\eta,\zeta) \mathbf{D}_{ep} \mathbf{\Psi}_\epsilon^{(c)} \left|\mathbf{J}(\eta,\zeta)\right| d\eta d\zeta \right] \xi^2 d\xi \tag{6.34}$$

$$\mathbf{X}^{(n)} = \int_0^1 \xi^{-\mathbf{S}_n^T - 1.5\mathbf{I}} \cdot \left[\int_{-1}^{+1} \int_{-1}^{+1} \mathbf{\Psi}_\epsilon^T(\eta,\zeta) \mathbf{D}_{ep} \mathbf{\Psi}_\epsilon^{(n)}(\eta,\zeta) \left|\mathbf{J}(\eta,\zeta)\right| d\eta d\zeta \right] \xi^{-\mathbf{S}_n^{(n)} - 1.5\mathbf{I}} \xi^2 d\xi \tag{6.35}$$

Now, the total stiffness matrix for elastoplasticity $\mathbf{K}_{ep}$ has been decomposed into two parts and Equation(6.33) can be written in simplified notations as

$$\mathbf{K}_{ep} = \mathbf{K}_{ep}^{(c)} + \mathbf{K}_{ep}^{(n)} \tag{6.36}$$

with the constant stress part $\mathbf{K}_{ep}^{(c)}$ and non-constant stress part $\mathbf{K}_{ep}^{(n)}$ listed below

$$\mathbf{K}_{ep}^{(c)} = \mathbf{\Psi}_{u_n}^{-T} \mathbf{X}^{(c)} \left(\mathbf{\Psi}_{u_n}^{-1}\right)^{(c)} \tag{6.37a}$$

$$\mathbf{K}_{ep}^{(n)} = \mathbf{\Psi}_{u_n}^{-T} \mathbf{X}^{(n)} \left(\mathbf{\Psi}_{u_n}^{-1}\right)^{(n)} \tag{6.37b}$$

The constant stress part of the elastoplastic stiffness matrix $\mathbf{K}_{ep}^{(c)}$ is an under-integrated matrix and contains spurious modes. In order to overcome the spurious modes and make the whole formulation stable, the elastoplastic stiffness matrix of non-constant stress part $\mathbf{K}_{ep}^{(n)}$ is introduced as a stabilisation matrix here and used later in Section 6.3.4.2 to calculate the internal load vector due to the non-constant stress state part $\mathbf{R}_{int}^{(n)}$. The evaluation of $\mathbf{X}^{(c)}$ and $\mathbf{X}^{(n)}$ are explained in the following Sections 6.3.3.1 and 6.3.3.2 respectively.

6.3.3.1 Evaluate elastoplastic stiffness matrix related to constant stress part

For evaluating $\mathbf{K}_{ep}^{(c)}$ in Equation (6.37a), the calculation of $\mathbf{X}^{(c)}$ term is firstly addressed. Matrix $\mathbf{Y}^{(c)}$ can be used to represent the integration in the surface directions

(η, ζ) of a subdomain in Equation (6.34) as

$$\mathbf{X}^{(c)} = \int_0^1 \xi^{-\mathbf{S}_n^T - 1.5\mathbf{I}} \mathbf{Y}^{(c)} \xi^2 d\xi \tag{6.38}$$

with $\mathbf{Y}^{(c)}$ expressed as

$$\mathbf{Y}^{(c)} = \int_{-1}^{+1} \int_{-1}^{+1} \mathbf{\Psi}_\epsilon^T(\eta, \zeta) \mathbf{D}_{ep} \mathbf{\Psi}_\epsilon^{(c)} \left|\mathbf{J}(\eta, \zeta)\right| d\eta d\zeta \tag{6.39}$$

$\mathbf{Y}^{(c)}$ can also be decomposed into two parts by substituting Equation (6.21) into (6.39)

$$\mathbf{Y}^{(c)} = \begin{bmatrix} \mathbf{Y}_{nc} \\ \mathbf{Y}_{cc} \end{bmatrix} \tag{6.40}$$

with

$$\mathbf{Y}_{nc} = \int_{-1}^{+1} \int_{-1}^{+1} \left(\mathbf{\Psi}_\epsilon^{(n)}(\eta, \zeta)\right)^T \mathbf{D}_{ep} \mathbf{\Psi}_\epsilon^{(c)} \left|\mathbf{J}(\eta, \zeta)\right| d\eta d\zeta \tag{6.41a}$$

$$\mathbf{Y}_{cc} = \int_{-1}^{+1} \int_{-1}^{+1} \left(\mathbf{\Psi}_\epsilon^{(c)}\right)^T \mathbf{D}_{ep} \mathbf{\Psi}_\epsilon^{(c)} \left|\mathbf{J}(\eta, \zeta)\right| d\eta d\zeta \tag{6.41b}$$

Equation (6.41a) and (6.41b) can then be numerically integrated using standard Gauss or Gauss-Lobatto quadrature. Next, substituting Equation (6.24) and (6.40) into (6.38) yields

$$\mathbf{X}^{(c)} = \begin{bmatrix} \mathbf{X}_{nc} \\ \mathbf{X}_{cc} \end{bmatrix} \tag{6.42}$$

with

$$\mathbf{X}_{nc} = \int_0^1 \xi^{-\left(\mathbf{S}_n^{(n)}\right)^T + 0.5\mathbf{I}} d\xi \mathbf{Y}_{nc} \tag{6.43a}$$

$$\mathbf{X}_{cc} = \int_0^1 \xi^2 d\xi \mathbf{Y}_{cc} \tag{6.43b}$$

Integrations in Equation (6.43) can be calculated analytically in ξ direction yielding

$$\mathbf{X}_{nc} = \left(-\left(\mathbf{S}_n^{(n)}\right)^T + 1.5\mathbf{I}\right)^{-1} \mathbf{Y}_{nc} \tag{6.44a}$$

$$\mathbf{X}_{cc} = \frac{\mathbf{Y}_{cc}}{3} \tag{6.44b}$$

Now $\mathbf{K}_{ep}^{(c)}$ can be solved by substituting the results of $\mathbf{X}^{(c)}$ in Equation (6.42) into Equation (6.37a). Notice that the numerical integration is only employed to calculate $\mathbf{Y}^{(c)}$ for evaluating $\mathbf{K}_{ep}^{(c)}$. In other words, $\mathbf{K}_{ep}^{(c)}$ is evaluated semi-analytically for a scaled boundary polyhedral subdomain and requires only a two-dimensional integration along the boundary of subdomain.

6.3.3.2 Evaluate elastoplastic stiffness matrix related to non-constant stress part

Similar to Section 6.3.3.1, $\mathbf{X}^{(n)}$ is calculated at first for evaluating $\mathbf{K}_{ep}^{(n)}$ in Equation (6.37b). The inner part of $\mathbf{X}^{(n)}$ related to the integration on the surface (η, ζ) can be represented by matrix $\mathbf{Y}^{(n)}$. The expression of Equation (6.35) can be simplified as:

$$\mathbf{X}^{(n)} = \int_0^1 \xi^{-\mathbf{S}_n^T - 1.5\mathbf{I}} \mathbf{Y}^{(n)} \xi^{-\mathbf{S}_n^{(n)} - 1.5\mathbf{I}} \xi^2 d\xi \tag{6.45}$$

with $\mathbf{Y}^{(n)}$ expressed as

$$\mathbf{Y}^{(n)} = \int_{-1}^{+1} \int_{-1}^{+1} \mathbf{\Psi}_\epsilon^T(\eta, \zeta) \mathbf{D}_{ep} \mathbf{\Psi}_\epsilon^{(n)}(\eta, \zeta) \left|\mathbf{J}(\eta, \zeta)\right| d\eta d\zeta \tag{6.46}$$

Substitute Equation (6.21) into (6.46) gives

$$\mathbf{Y}^{(n)} = \begin{bmatrix} \mathbf{Y}_{nn} \\ \mathbf{Y}_{cn} \end{bmatrix} \tag{6.47}$$

with $\mathbf{Y}_{nn}$ and $\mathbf{Y}_{cn}$ being expressed as

$$\mathbf{Y}_{nn} = \int_{-1}^{+1} \int_{-1}^{+1} \left(\mathbf{\Psi}_\epsilon^{(n)}(\eta, \zeta)\right)^T \mathbf{D}_{ep} \mathbf{\Psi}_\epsilon^{(n)}(\eta, \zeta) \left|\mathbf{J}(\eta, \zeta)\right| d\eta d\zeta \tag{6.48a}$$

$$\mathbf{Y}_{cn} = \int_{-1}^{+1} \int_{-1}^{+1} \left(\mathbf{\Psi}_\epsilon^{(c)}\right)^T \mathbf{D}_{ep} \mathbf{\Psi}_\epsilon^{(n)}(\eta, \zeta) \left|\mathbf{J}(\eta, \zeta)\right| d\eta d\zeta \tag{6.48b}$$

Equation (6.48a) and (6.48b) can then be numerically integrated using standard Gauss or Gauss-Lobatto quadrature. Next, substituting Equations (6.24) and (6.47)

into (6.45) yields

$$\mathbf{X}^{(n)} = \begin{bmatrix} \mathbf{X}_{nn} \\ \mathbf{X}_{cn} \end{bmatrix} \tag{6.49}$$

with

$$\mathbf{X}_{nn} = \int_0^1 \xi^{-\left(\mathbf{S}_n^{(n)}\right)^T - 1.5\mathbf{I}} \mathbf{Y}_{nn} \xi^{-\mathbf{S}_n^{(n)} + 0.5\mathbf{I}} d\xi \tag{6.50a}$$

$$\mathbf{X}_{cn} = \mathbf{Y}_{cn} \int_0^1 \xi^{-\mathbf{S}_n^{(n)} + 0.5\mathbf{I}} d\xi \tag{6.50b}$$

Equation (6.50) can be solved analytically in radial direction ξ as well. Utilizing the properties of matrix power function and integration by parts as in Reference (Ooi et al., 2014), matrix $\mathbf{X}_{nn}$ expressed in Equation (6.50a) can be solved from the following Lyapunov equation

$$\left(-\mathbf{S}_n^{(n)}\right)^T \mathbf{X}_{nn} + \mathbf{X}_{nn} \left(-\mathbf{S}_n^{(n)}\right) = \mathbf{Y}_{nn} \tag{6.51}$$

Solving the integration in ξ direction analytically in Equation (6.50b) results in

$$\mathbf{X}_{cn} = \mathbf{Y}_{cn} \left(-\mathbf{S}_n^{(n)} + 1.5\mathbf{I}\right)^{-1} \tag{6.52}$$

Now the part of elastoplastic stiffness matrix related to the non-constant stress state part $\mathbf{K}_{ep}^{(n)}$ can be solved by substituting the results for $\mathbf{X}^{(n)}$ from Equation (6.49) into Equation (6.37b). Again, only the two-dimensional integration along the boundary directions (η, ζ) are required to calculate matrix $\mathbf{Y}^{(n)}$ and thus $\mathbf{K}_{ep}^{(n)}$ is evaluated semi-analytically.

6.3.4 Decomposition of internal load vector

To formulate the internal force consistently with the elastoplastic stiffness matrix, the total internal load vector is also decomposed into the internal load vectors related to constant stress part and non-constant stress part respectively. Comparing Equations (6.18) and (6.19) gives the expression of internal load vector for a polyhedral

subdomain

$$\mathbf{F}_{int} = \int_{\Omega} \mathbf{B}^T(\xi,\eta,\zeta)\boldsymbol{\sigma}(\xi,\eta,\zeta)d\Omega \tag{6.53}$$

Substituting the decomposed stress in Equation (6.28) into Equation (6.53) yields

$$\mathbf{F}_{int} = \int_{\Omega} \left(\mathbf{B}^T(\xi,\eta,\zeta)\boldsymbol{\sigma}^{(c)} + \mathbf{B}^T(\xi,\eta,\zeta)\boldsymbol{\sigma}^{(n)}(\xi,\eta,\zeta)\right) d\Omega \tag{6.54}$$

Equation (6.54) can then be written into two parts as

$$\mathbf{F}_{int} = \mathbf{F}_{int}^{(c)} + \mathbf{F}_{int}^{(n)} \tag{6.55}$$

with the internal load vector related to constant and non-constant stress parts $\mathbf{F}_{int}^{(c)}$ and $\mathbf{F}_{int}^{(n)}$ expressed as

$$\mathbf{F}_{int}^{(c)} = \int_{\Omega} \mathbf{B}^T(\xi,\eta,\zeta)\boldsymbol{\sigma}^{(c)}d\Omega \tag{6.56a}$$

$$\mathbf{F}_{int}^{(n)} = \int_{\Omega} \mathbf{B}^T(\xi,\eta,\zeta)\boldsymbol{\sigma}^{(n)}(\xi,\eta,\zeta)d\Omega \tag{6.56b}$$

The evaluations of $\mathbf{F}_{int}^{(c)}$ and $\mathbf{F}_{int}^{(n)}$ will be addressed in the following Sections 6.3.4.1 and 6.3.4.2 separately.

6.3.4.1 Evaluate internal load vector related to constant stress part

The constant stress part of the internal load is calculated based on the constant stress vector $\boldsymbol{\sigma}^{(c)}$ at scaling centre in Equation (6.56a). Return mapping algorithm as used in standard FEM (de Souza Neto et al., 2011; Hinton and Owen, 1986) can be applied here to update $\boldsymbol{\sigma}^{(c)}$ for each plastic polyhedral subdomain and the return mapping algorithm should only be performed at the scaling center. Because the number of locations to perform the return mapping algorithm is reduced to one, this proposed one-point return-mapping formulation is reported to be more computationally efficient than the original scaled boundary finite element formulations for elastoplastic analysis, which requires the return mapping calculation on multiple fitting points within each subdomain (Ooi et al., 2014; He, 2017). As $\boldsymbol{\sigma}^{(c)}$ is

independent of ξ,η and ζ, it can be moved outside from the integral as

$$\mathbf{F}_{int}^{(c)} = \int_{\Omega} \mathbf{B}^T(\xi,\eta,\zeta) d\Omega \boldsymbol{\sigma}^{(c)} \tag{6.57}$$

Substituting the expression for scaled boundary strain-displacement matrix $\mathbf{B}(\xi,\eta,\zeta)$ from Equation (6.7) and expression for $d\Omega$ from Equation (6.32) yields

$$\mathbf{F}_{int}^{(c)} = \boldsymbol{\Psi}_{u_n}^{-T} \int_0^1 \xi^{-\mathbf{S}_n^T - 1.5\mathbf{I}} \mathbf{r}(\eta,\zeta) \xi^2 d\xi \boldsymbol{\sigma}^{(c)} \tag{6.58}$$

with the vector $\mathbf{r}(\eta,\zeta)$ containing integration along surface directions (η,ζ) as:

$$\mathbf{r}(\eta,\zeta) = \int_{-1}^{+1} \int_{-1}^{+1} \boldsymbol{\Psi}_{\epsilon}^T(\eta,\zeta) \left|\mathbf{J}(\eta,\zeta)\right| d\eta d\zeta \tag{6.59}$$

Equation (6.59) can then be numerically integrated using standard Gauss or Gauss-Lobatto quadrature along the boundary. Integration in ξ direction in Equation (6.58) can be calculated analytically and yields

$$\mathbf{F}_{int}^{(c)} = \boldsymbol{\Psi}_{u_n}^{-T} \left(-\mathbf{S}_n^T + 1.5\mathbf{I}\right)^{-1} \mathbf{r}(\eta,\zeta) \boldsymbol{\sigma}^{(c)} \tag{6.60}$$

6.3.4.2 Evaluate internal load vector related to non-constant stress part

Because the subdomains are refined in the yield zone, the contributions of the non-constant stresses $\boldsymbol{\sigma}^{(n)}(\xi,\eta,\zeta)$ is minimized. The reason for evaluating the internal load vector due to non-constant stress part $\mathbf{F}_{int}^{(n)}$ in this section is to use it as the stabilisation term in the internal nodal force vector $\mathbf{F}_{int}$ and control the spurious modes for each subdomain. As a result, $\boldsymbol{\sigma}^{(n)}(\xi,\eta,\zeta)$ is not calculated through the return mapping algorithm. $\mathbf{F}_{int}^{(n)}$ only needs to be calculated once at the beginning of each equilibrium iteration in elastoplastic analysis. Substituting Equations (6.7), (6.29b), (6.27b) and (6.32) into (6.56b) results in

$$\begin{aligned}
&\mathbf{F}_{int}^{(n)} = \boldsymbol{\Psi}_{u_n}^{-T} \int_0^1 \xi^{-\mathbf{S}_n^T - 1.5\mathbf{I}} \cdot \\
&\left[\int_{-1}^{+1} \int_{-1}^{+1} \boldsymbol{\Psi}_{\epsilon}^T(\eta,\zeta) \mathbf{D}_{ep} \boldsymbol{\Psi}_{\epsilon}^{(n)}(\eta,\zeta) \left|\mathbf{J}(\eta,\zeta)\right| d\eta d\zeta\right] \xi^{-\mathbf{S}_n^{(n)} - 1.5\mathbf{I}} \xi^2 d\xi \left(\boldsymbol{\Psi}_{u_n}^{-1}\right)^{(n)} \mathbf{u}_b
\end{aligned} \tag{6.61}$$

In Equation (6.61), the part of right-hand-side before the nodal displacement

vector $\mathbf{u}_b$ is equal to the expression for the elastoplastic stiffness matrix related to non-constant stress $\mathbf{K}_{ep}^{(n)}$ by substituting Equation (6.35) into (6.37b). Therefore, Equation (6.61) can simplified as

$$\mathbf{F}_{int}^{(n)} = \mathbf{K}_{ep}^{(n)} \mathbf{u}_b \tag{6.62}$$

6.3.5 External load vector

Comparing Equations (6.18) and (6.19) gives the expression of external load vector $\mathbf{F}_{ext}$ for a polyhedral subdomain as

$$\mathbf{F}_{ext} = \int_{\Gamma} \mathbf{\Phi}^T(\xi, \eta, \zeta) \mathbf{f}_t d\Gamma + \int_{\Omega} \mathbf{\Phi}^T(\xi, \eta, \zeta) \mathbf{f}_b d\Omega \tag{6.63}$$

The first term on the right-hand-side of Equation (6.63) represents the surface traction applied on the boundary of polyhedral subdomains. As $\xi = 1$ on the boundary, $\mathbf{\Phi}(\xi, \eta, \zeta)$ in Equation (6.4) reduces to $\mathbf{N}_u(\eta, \zeta)$. This term can thus be written as

$$\int_{\Gamma} \mathbf{\Phi}^T(\xi, \eta, \zeta) \mathbf{f}_t d\Gamma = \int_{-1}^{+1} \int_{-1}^{+1} \mathbf{N}_s^T(\eta, \zeta) \left|\mathbf{J}(\eta, \zeta)\right| \mathbf{f}_t d\eta d\zeta \tag{6.64}$$

The second term on the right-hand-side of Equation (6.63) represents the body load vector. For constant body load vector $\mathbf{f}_b$, substituting Equations (6.4) and (6.32) into the second term in Equation (6.63) yields

$$\begin{aligned} &\int_{\Omega} \mathbf{\Phi}^T(\xi, \eta, \zeta) \mathbf{f}_b d\Omega \\ &\qquad = \int_0^1 \int_{-1}^{+1} \int_{-1}^{+1} \left(\mathbf{N}_s(\eta, \zeta) \mathbf{\Psi}_{u_n} \xi^{-\mathbf{S}_n - 0.5\mathbf{I}} \mathbf{\Psi}_{u_n}^{-1}\right)^T \left|\mathbf{J}(\eta, \zeta)\right| \xi^2 d\eta d\zeta d\xi \mathbf{f}_b \end{aligned} \tag{6.65}$$

Then, the Equation (6.65) can be solved analytically in ξ direction and numerically in (η, ζ) directions as

$$\begin{aligned} &\int_{\Omega} \mathbf{\Phi}^T(\xi, \eta, \zeta) \mathbf{f}_b d\Omega \\ &\qquad = \mathbf{\Psi}_{u_n}^{-T} \left(-\mathbf{S}_n^T + 2.5\mathbf{I}\right)^{-1} \mathbf{\Psi}_{u_n}^T \left[\int_{-1}^{+1} \int_{-1}^{+1} \mathbf{N}_s^T(\eta, \zeta) \left|\mathbf{J}(\eta, \zeta)\right| d\eta d\zeta\right] \mathbf{f}_b \end{aligned} \tag{6.66}$$

6.4 Computational procedures

The computational procedures for both static and dynamic elastoplastic analyses are summarized in the following sections 6.4.1 and 6.4.2 separately. In the proposed method for elastoplastic analysis, the strain-displacement matrix $\mathbf{B}(\xi, \eta, \zeta)$ in Equation (6.7) and mass matrix $\mathbf{M}$ in Equation (5.28) do not change in each load step or time step as they are only related to the material and geometry of the problems but irrelevant from the corresponding state of stresses. Therefore, all the matrices for calculating $\mathbf{B}(\xi, \eta, \zeta)$ and $\mathbf{M}$, that include coefficient matrices in Equation (5.11), $\mathbf{\Psi}_{u_n}$, $\mathbf{S}_n$ and $\mathbf{\Psi}_{\epsilon}(\eta, \zeta)$ in Equation (5.17) and (6.8), can be precomputed after the octree mesh generation in SBFEM. Then, they can be stored in the system memory for accessing in the following iterations. In this chapter, the relative norm χ of residual forces is calculated for checking if the solution has converged by satisfying a convergence tolerance value χ_{tol}. Modified Newton-Raphson iteration is applied to the equilibrium iterations for both static and dynamic analysis to minimize the residual forces. The standard Newmark's method for nonlinear systems (Chopra, 2001) with $\gamma = 0.5$ and $\beta = 0.25$ (average acceleration scheme) is employed here for solving the dynamic elastoplastic problems due to its unconditionally stable nature.

6.4.1 Computational procedure for static elastoplastic analysis

The computational procedure for 3D static elastoplastic analysis in SBFEM is summarized in this section as follows:

1. Initial calculations of geometrically similar and trimmed cells and stored the results for later use

   (a) Calculate coefficient matrices from Equations (5.11a) - (5.11c).

   (b) Solve the eigenvalue problem in Equation (5.17) for $\mathbf{\Psi}_{u_n}$, $\mathbf{\Psi}_{q_n}$ and $\mathbf{S}_n$ for

polyhedral subdomains.

(c) Calculate elastic stiffness matrices $\mathbf{K}_e$ and strain modes $\mathbf{\Psi}_\epsilon(\eta, \zeta)$ for these subdomains according to Equations (5.20) and (6.8) respectively.

2. Initializing the total displacement vector as $\mathbf{U}_b|_{(j)} = 0$ at $j = 0$.

3. For load steps $j = 1, 2, 3, \cdots$:

(a) Compute the incremental external load vector $\Delta\mathbf{F}_{ext}|_{(j)}$ for subdomains between load step $j-1$ and j using Equation (6.63).

(b) Compute the elastoplastic constitutive matrix $\mathbf{D}_{ep}|_{(j-1)}$ for subdomains experiencing plastic deformation. If all subdomains are elastic or in unloading step, that is, $\mathbf{D}_{ep}|_{(j-1)} = \mathbf{D}$, then jump to Step (e).

(c) Compute the tangent elastoplastic stiffness matrices related to constant stress state $\mathbf{K}_{ep}^{(c)}|_{(j-1)}$ using Equation (6.37a) for plastic subdomains.

(d) Compute the tangent elastoplastic stiffness matrices related to non-constant stress state $\mathbf{K}_{ep}^{(n)}|_{(j-1)}$ using Equation (6.37b) for plastic subdomains.

(e) Compute the total tangent elastoplastic stiffness matrices $\mathbf{K}_{ep}|_{(j-1)}$ using Equation (6.36) for plastic subdomains. If subdomain is in elastic state, use $\mathbf{K}_{ep}|_{(j-1)} = \mathbf{K}_e$ precomputed before entering the load-step iterations instead.

(f) Assemble the global tangent stiffness matrix $\left[\sum_{i=1}^{nPol} \mathbf{K}_{ep}|_{(j-1)}\right]$ and global incremental load vector for external forces $\left\{\sum_{i=1}^{nPol} \Delta\mathbf{F}_{ext}|_{(j)}\right\}$ as in Equation (6.20) .

(g) Solving initial incremental displacement vector $\Delta\mathbf{U}_b|_{(j)}$:

$$\Delta\mathbf{U}_b|_{(j)} = \left[\sum_{i=1}^{nPol} \mathbf{K}_{ep}|_{(j-1)}\right]^{-1} \left\{\sum_{i=1}^{nPol} \Delta\mathbf{F}_{ext}|_{(j)}\right\} \tag{6.67}$$

(h) At equilibrium iteration $k = 0$, initializing the incremental displacement vector $\Delta\mathbf{U}_b|_{(j)}^k = \Delta\mathbf{U}_b|_{(j)}$ and accumulated total external load vector $\mathbf{F}_{ext}^{tot}|_{(j)} = \sum_{j=1}^{j} \Delta\mathbf{F}_{ext}|_{(j)}$ for each subdomain .

(i) For equilibrium iterations, $k = 1,\ 2,\ 3, \cdots$, the modified Newton-Raphson algorithm is applied to correct the incremental displacement $\Delta\mathbf{U}_b|_{(j)}$:

i. Update the elastoplastic stresses $\boldsymbol{\sigma}^{(c)}|_{(j)}^k$ at scaling centre of polyhedral subdomains using return-mapping algorithm for current iteration step k.

ii. Calculate internal load vector related to constant stress parts $\mathbf{F}_{int}^{(c)}|_{(j)}^k$ for each subdomain using Equation (6.60).

iii. Calculate internal load vector related to non-constant and non-constant stress parts $\mathbf{F}_{int}^{(n)}|_{(j)}^k$ for each subdomain using Equation (6.62).

iv. Calculate total internal load vector $\mathbf{F}_{int}^{tot}|_{(j)}^k$ for each subdomain using Equation (6.55).

v. Assemble the global load vectors for total internal forces in statics $\mathbf{F}_{int}^{static}|_{(j)}^k = \left\{\sum_{i=1}^{nPol} \mathbf{F}_{int}^{tot}|_{(j)}^k\right\}$ and total external forces $\mathbf{F}_{ext}|_{(j)} = \left\{\sum_{i=1}^{nPol} \mathbf{F}_{ext}^{tot}|_{(j)}\right\}$ as in Equation (6.20) .

vi. Calculate global residual force vector in statics $d\mathbf{F}|_{(j)}^k = \mathbf{F}_{ext}|_{(j)} - \mathbf{F}_{int}^{static}|_{(j)}^k$

vii. Calculate incremental displacement $d\mathbf{U}_b|_{(j)}^k$ due to residual force based on Equation (6.20).

$$d\mathbf{U}_b|_{(j)}^k = \left[\sum_{i=1}^{nPol} \mathbf{K}_{ep}|_{(j-1)}\right]^{-1} d\mathbf{F}|_{(j)}^k \tag{6.68}$$

viii. Correct the incremental displacement vector $\Delta\mathbf{U}_b|_{(j)}^k = \Delta\mathbf{U}_b|_{(j)}^{k-1} + d\mathbf{U}_b|_{(j)}^k$.

ix. Calculate norm of residual force vector $\chi = \left\|d\mathbf{F}|_{(j)}^k\right\|$.

x. Check for convergence:

- If $\chi > \chi_{tol}$, set iteration index $k = k + 1$ and return to Step i.
- If $\chi \leq \chi_{tol}$, exit the equilibrium iteration.

(j) Update the total nodal displacement vector $\mathbf{U}_b|_{(j)} = \mathbf{U}_b|_{(j-1)} + \Delta\mathbf{U}_b|^k_{(j)}$ and set the load-step number $j = j + 1$, then returns to Step (a) in load-step loop.

6.4.2 Computational procedure for dynamic elastoplastic analysis

This section describes the Newmark's method used here for dynamic elastoplastic analysis in SBFEM. Based on the procedures described on (Chopra, 2001), the relevant procedures can be summarized as follows without the consideration of damping:

1. Initial calculation of geometrically similar and trimmed cells and stored the results for later use

   (a) Calculate all coefficient matrices in Equation (5.11).

   (b) Solve the eigenvalue problem in Equation (5.17) for $\mathbf{\Psi}_{u_n}$, $\mathbf{\Psi}_{q_n}$ and $\mathbf{S}_n$ for bounded subdomains.

   (c) Calculate elastic stiffness matrices $\mathbf{K}_e$, mass matrices $\mathbf{M}$ and strain modes $\mathbf{\Psi}_\epsilon(\eta, \zeta)$ for these subdomains according to Equations (5.20), (5.28) and (6.8) respectively.

2. Initial calculations for time step $j = 0$ in Newmark's method.

   (a) Assuming structure at rest at the beginning and initialize the total displacement vector $\mathbf{U}_b|_{(j)} = 0$, total velocity vector $\dot{\mathbf{U}}_b|_{(j)} = 0$ and total acceleration vector $\ddot{\mathbf{U}}_b|_{(j)} = 0$ at $j = 0$.

   (b) Select the time-step size Δt.

(c) Calculate the constant matrices used later in Newmark's iterations: $\mathbf{a} = \frac{1}{\beta \Delta t}\mathbf{M}$ and $\mathbf{b} = \frac{1}{2\beta}\mathbf{M}$.

3. For time steps $j = 1, 2, 3, \cdots$:

(a) Compute the incremental external force vector $\Delta \mathbf{F}_{ext}|_{(j)}$ for subdomains between time step $j-1$ and j using Equation (6.63).

(b) Compute effective incremental load vector $\Delta \hat{\mathbf{F}}_{ext}|_{(j)}$.

$$\Delta \hat{\mathbf{F}}_{ext}|_{(j)} = \Delta \mathbf{F}_{ext}|_{(j)} + \mathbf{a}\dot{\mathbf{U}}_b|_{(j-1)} + \mathbf{b}\ddot{\mathbf{U}}_b|_{(j-1)} \tag{6.69}$$

(c) Repeat Steps (b) to (e) in the load-step loop in the procedures for static elastoplastic analysis in Section 6.4.1 to calculate the total tangent elastoplastic stiffness matrices $\mathbf{K}_{ep}|_{(j-1)}$.

(d) Assemble the global tangent stiffness matrix $\left[\sum_{i=1}^{nPol} \mathbf{K}_{ep}|_{(j-1)}\right]$, global mass matrix $\left[\sum_{i=1}^{nPol} \mathbf{M}\right]$ and global effective incremental load vector $\Delta \hat{\mathbf{F}}_{ext}|_{(j)} = \left\{\sum_{i=1}^{nPol} \Delta \hat{\mathbf{F}}_{ext}|_{(j)}\right\}$ for the whole problem domain .

(e) Compute global effective stiffness matrix $\hat{\mathbf{K}}|_{(j-1)}$.

$$\hat{\mathbf{K}}|_{(j-1)} = \left[\sum_{i=1}^{nPol} \mathbf{K}_{ep}|_{(j-1)}\right] + \frac{1}{\beta(\Delta t)^2}\left[\sum_{i=1}^{nPol} \mathbf{M}\right] \tag{6.70}$$

(f) Solving initial incremental displacement vector $\Delta \mathbf{U}_b|_{(j)}$ for each time step.

$$\Delta \mathbf{U}_b|_{(j)} = \left[\hat{\mathbf{K}}|_{(j-1)}\right]^{-1} \Delta \hat{\mathbf{F}}_{ext}|_{(j)} \tag{6.71}$$

(g) At equilibrium iteration $k = 0$, initializing the incremental displacement vector $\Delta \mathbf{U}_b|^k_{(j)} = \Delta \mathbf{U}_b|_{(j)}$, accumulated displacement vector $\mathbf{U}_b|^k_{(j-1)} = \sum_{j=1}^{j-1} \Delta \mathbf{U}_b|_{(j)}$ to last time step $j-1$ ($\mathbf{U}_b|^k_{(j-1)} = 0$ for $j = 1$) and accumulated total effective external load vector $\hat{\mathbf{F}}^{tot}_{ext}|_{(j)} = \sum_{j=1}^{j} \Delta \hat{\mathbf{F}}_{ext}|_{(j)}$ to this time step j for each subdomain.

(h) In dynamic analysis, the modified Newton-Raphson algorithm is again applied to correct the incremental displacement $\Delta\mathbf{U}_b|_{(j)}$ in each time step. The procedures for corresponding equilibrium iterations, $k = 1, 2, 3, \cdots$, are the same as those described in Steps (i) to (ix) for static elastoplastic analysis in Section 6.4.1, except for the calculations of global load vector for total internal forces in statics $\mathbf{F}_{int}^{statics}|_{(j)}^{k}$ in Step (v). In dynamic analysis, these internal force vector should be calculated by considering the effect of inertial and thus the modified Newton-Raphson algorithm in dynamic elastoplastic analysis is changed to:

i. Repeat Steps (i) to (iv) in the equilibrium iterations for static elastoplastic analysis in Section 6.4.1 and assemble the global total internal forces vector in statics $\mathbf{F}_{int}^{static}|_{(j)}^{k} = \left\{\sum_{i=1}^{nPol} \mathbf{F}_{int}^{tot}|_{(j)}^{k}\right\}$

ii. Calculate the effective global vector for total internal forces $\hat{\mathbf{F}}_{int}^{dynamic}|_{(j)}^{k}$,

$$\hat{\mathbf{F}}_{int}^{dynamic}|_{(j)}^{k} = \mathbf{F}_{int}^{static}|_{(j)}^{k} + \frac{1}{\beta(\Delta t)^2}\left[\sum_{i=1}^{nPol}\mathbf{M}\right]\left(\mathbf{U}_b|_{(j-1)}^{k} + \Delta\mathbf{U}_b|_{(j)}^{k}\right) \quad (6.72)$$

and assemble effective external forces $\hat{\mathbf{F}}_{ext}|_{(j)} = \left\{\sum_{i=1}^{nPol} \hat{\mathbf{F}}_{ext}^{tot}|_{(j)}\right\}$

iii. Calculate effective global residual force vector in dynamics $d\hat{\mathbf{F}}|_{(j)}^{k} = \hat{\mathbf{F}}_{ext}|_{(j)} - \hat{\mathbf{F}}_{int}^{dynamic}|_{(j)}^{k}$

iv. Calculate incremental displacement $d\mathbf{U}_b|_{(j)}^{k}$ due to residual force based on Step (f) in time-step iteration.

$$d\mathbf{U}_b|_{(j)}^{k} = \left[\hat{\mathbf{K}}|_{(j-1)}\right]^{-1} d\hat{\mathbf{F}}|_{(j)}^{k} \quad (6.73)$$

v. Repeat Steps (viii) to (x) in the equilibrium iterations for static elastoplastic analysis in Section 6.4.1 to correct the incremental displacement vector $\Delta\mathbf{U}_b|_{(j)}^{k}$ and check $\chi = \left\|d\hat{\mathbf{F}}|_{(j)}^{k}\right\|$ for convergence.

(i) Compute incremental velocity vector $\Delta\dot{\mathbf{U}}_b|_{(j)}^k$,

$$\Delta\dot{\mathbf{U}}_b|_{(j)}^k = \frac{\gamma}{\beta\Delta t}\Delta\mathbf{U}_b|_{(j)}^k - \frac{\gamma}{\beta}\dot{\mathbf{U}}_b|_{(j)} + \Delta t\left(1-\frac{\gamma}{2\beta}\right)\ddot{\mathbf{U}}_b|_{(j)} \tag{6.74}$$

and incremental acceleration vector$\Delta\ddot{\mathbf{U}}_b|_{(j)}^k$

$$\Delta\ddot{\mathbf{U}}_b|_{(j)}^k = \frac{1}{\beta(\Delta t)^2}\Delta\mathbf{U}_b|_{(j)}^k - \frac{1}{\beta\Delta t}\dot{\mathbf{U}}_b|_{(j)} - \frac{1}{2\beta}\ddot{\mathbf{U}}_b|_{(j)} \tag{6.75}$$

(j) Update the total displacement vector

$$\mathbf{U}_b|_{(j)} = \mathbf{U}_b|_{(j-1)} + \Delta\mathbf{U}_b|_{(j)}^k \tag{6.76}$$

total velocity vector

$$\dot{\mathbf{U}}_b|_{(j)} = \dot{\mathbf{U}}_b|_{(j-1)} + \Delta\dot{\mathbf{U}}_b|_{(j)}^k \tag{6.77}$$

total acceleration vector

$$\ddot{\mathbf{U}}_b|_{(j)} = \ddot{\mathbf{U}}_b|_{(j-1)} + \Delta\ddot{\mathbf{U}}_b|_{(j)}^k \tag{6.78}$$

and set the time-step number $j = j + 1$, then returns to Step (a) in time-step loop.

6.5 Numerical examples

In this section, five numerical examples are presented to demonstrate the accuracy, efficiency and robustness of the present SBFEM formulations for 3D elastoplastic analysis. In section 6.5.1 and 6.5.2, a constant stress patch test and hollow sphere subjected to internal pressure with analytical solutions are used to check the accuracy of current method with analytical solutions. Then, a simply supported beam with a cylindrical notch is investigated in Section 6.5.3. A uniformly distributed pressure is applied at the top of the beam. The results for static and dynamic elastoplastic analyses are presented in Sections 6.5.3.1 and 6.5.3.2, respectively. The numerical solutions computed from SBFEM are verified using reference solutions

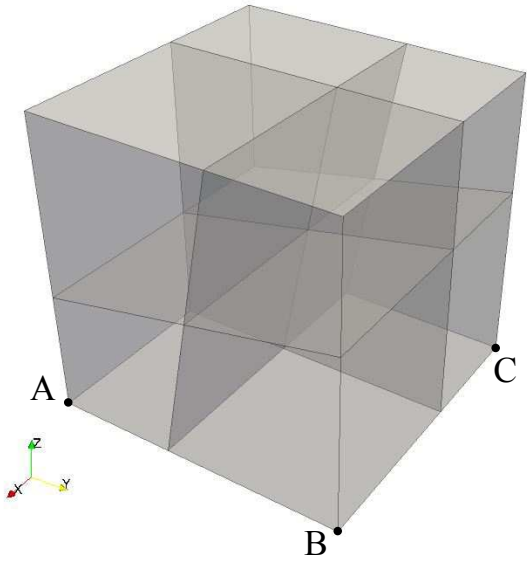

Figure 6.1. SBFEM mesh for constant stress patch test.

obtained from commercial software ANSYS using standard FEM. The efficiency of modeling the same cylindrically notched beam via the present method is also discussed and compared with the model used in ANSYS. Next, a plate with multiple holes is subject to a dynamic excitation and simulated using the present SBFEM in Section 6.5.4. Reference solution obtained from ANSYS is again used for demonstrating the accuracy of SBFEM. In the last example in Section 6.5.5, an attractive example of a 3D humerus-shaped structure is used to demonstrate the ability of the proposed method in analyzing models with complex geometry and shows a possible application of this numerical tool in biomechanics. Newmark's method for nonlinear system described in Section 6.4.2 with computational coefficients ($\gamma = 0.5$ and $\beta = 0.25$, the average acceleration scheme) is applied here for time-domain dynamic analysis in all the following numerical examples.

6.5.1 Elastoplastic constant stress patch test

An uniaxial tension test is performed in this example. A cubic block with the dimensions of 1m×1m×1m is subjected to a uniform pressure of 0.2MPa at the top ($z = 1$m) pointing at positive z-direction. The block is discretized into eight irregular

polyhedral subdomains with 4-node quadrilateral elements on their surfaces. The mesh is shown in Figure 6.1 with the translucent surfaces illustrating the mesh inside the block. The block is fixed in z-direction on the entire bottom surface ($z = 0$m) and with constrains in x-direction along line AB (coordinates for point A (1, 0, 0) and point B (1, 1, 0)) and constrain at y-direction at point C (coordinate for point C (0, 1, 0)) for eliminating all rigid body motions. The material is isotropic with Young's modulus of $E = 200$GPa and Poisson's ratio of $\nu = 0.333$. The von Mises yield criteria is considered in this example with yield stress of $\sigma_y = 0.16$MPa and hardening modulus of $H = 20$GPa. At the end of the loading process, the theoretical values of stress in z-direction are $\sigma_{zz} = 0.2$MPa , while other stresses in each subdomain should be zeros. The results of stresses calculated from the proposed SBFEM at scaling centers of all subdomains are tabulated in Table 6.1. Comparing the results from numerical and analytical solutions, the proposed formulation is able to calculate the stresses of every subdomain accurately and thus passes the elastoplastic constant stress patch test.

6.5.2 Hollow sphere subjected to internal pressure

In this example, a hollow sphere is subjected to a uniform internal pressure on the whole internal cavity. The hollow sphere has an inner radius of $a = 1$m and outer radius of $b = 2$m. Due to its symmetry, only an octant of this sphere is modeled as illustrated in Figure 6.2(a). Normal constrains are applied on all three cutting faces of this octant. The magnitude of the internal pressure is $P = 9.5019$MPa. The material of sphere is assumed to be perfectly plastic with Young's modulus of $E = 100$GPa, Poisson's ratio of $\nu = 0.3$, yield stress of $\sigma_y = 10$MPa. Von Mises yield criteria is also assumed in this example.

Analytical solution is available for this problem (Gao and Davies, 2002). For elastic-perfectly plastic material under von Mises criteria, the analytical solution is derived in spherical coordinates (r, θ, ϕ) with r the radial coordinate and (θ, ϕ)

Table 6.1. Stresses at scaling centres of polyhedral subdomains in constant stress patch test.

Coordinates of scaling centres (m)	Normal stresses (MPa)		
	σ_{xx}	σ_{yy}	σ_{zz}
(0.25, 0.25, 0.25)	6.2787×10^{-9}	5.3204×10^{-9}	2.0000×10^{-1}
(0.75, 0.25, 0.25)	1.9950×10^{-9}	2.1242×10^{-9}	2.0000×10^{-1}
(0.25, 0.75, 0.25)	7.1716×10^{-9}	5.6927×10^{-9}	2.0000×10^{-1}
(0.75, 0.75, 0.25)	3.2813×10^{-9}	2.7854×10^{-9}	2.0000×10^{-1}
(0.25, 0.25, 0.75)	7.0512×10^{-9}	5.3259×10^{-9}	2.0000×10^{-1}
(0.75, 0.25, 0.75)	3.1482×10^{-9}	2.3552×10^{-9}	2.0000×10^{-1}
(0.25, 0.75, 0.75)	6.1311×10^{-9}	5.1017×10^{-9}	2.0000×10^{-1}
(0.75, 0.75, 0.75)	1.8949×10^{-9}	2.1229×10^{-9}	2.0000×10^{-1}
Coordinates of scaling centres (m)	Shear stresses (MPa)		
	τ_{yz}	τ_{xz}	τ_{xy}
(0.25, 0.25, 0.25)	-6.3642×10^{-11}	-6.0494×10^{-11}	-6.5862×10^{-11}
(0.75, 0.25, 0.25)	1.6486×10^{-10}	-4.2895×10^{-10}	3.7842×10^{-10}
(0.25, 0.75, 0.25)	3.3184×10^{-10}	-3.2441×10^{-11}	1.7439×10^{-10}
(0.75, 0.75, 0.25)	6.9339×10^{-10}	2.6614×10^{-10}	-6.9416×10^{-11}
(0.25, 0.25, 0.75)	-1.3021×10^{-10}	1.2233×10^{-10}	-1.1928×10^{-10}
(0.75, 0.25, 0.75)	1.7671×10^{-10}	-3.5742×10^{-10}	-2.5531×10^{-10}
(0.25, 0.75, 0.75)	3.8727×10^{-10}	9.4651×10^{-11}	1.9013×10^{-10}
(0.75, 0.75, 0.75)	8.7902×10^{-10}	2.7184×10^{-10}	-4.9703×10^{-10}

the two angular coordinates in hoop directions. The radial displacements $u_r(r)$ in elastic ($b \geq r > c$) and plastic ($a \leq r \leq c$) zone can be expressed in the following equation as:

$$u_r(r) = \begin{cases} \frac{2}{3E}\frac{c^3}{b^3}\left((1-2\nu)r + (1+\nu)\frac{b^3}{2r^2}\right)\sigma_y & (b \geq r > c) \\ \frac{\sigma_y}{E} r\left((1-\nu)\frac{c^3}{r^3} - \frac{2}{3}(1-2\nu)\left(1 + 3\ln\left(\frac{c}{r}\right) - \frac{c^3}{b^3}\right)\right) & (a \leq r \leq c) \end{cases} \tag{6.79}$$

In Equation (6.79), c is the radial coordinate of the spherical interface between elastic and plastic zones and can be calculated from the following Equation (6.80)

$$P = \frac{2}{3}\sigma_y\left(1 + 3\ln\left(\frac{c}{a}\right) - \frac{c^3}{b^3}\right) \tag{6.80}$$

where P is the applied internal pressure. In this example, $c = 1.25$m, which indicates that the yield zone will propagate from the internal surface to one fourth of the thickness of the hollow sphere.

The stresses in radial direction $\sigma_r(r)$ and hoop directions $\sigma_\theta(r)$ or $\sigma_\phi(r)$ are then

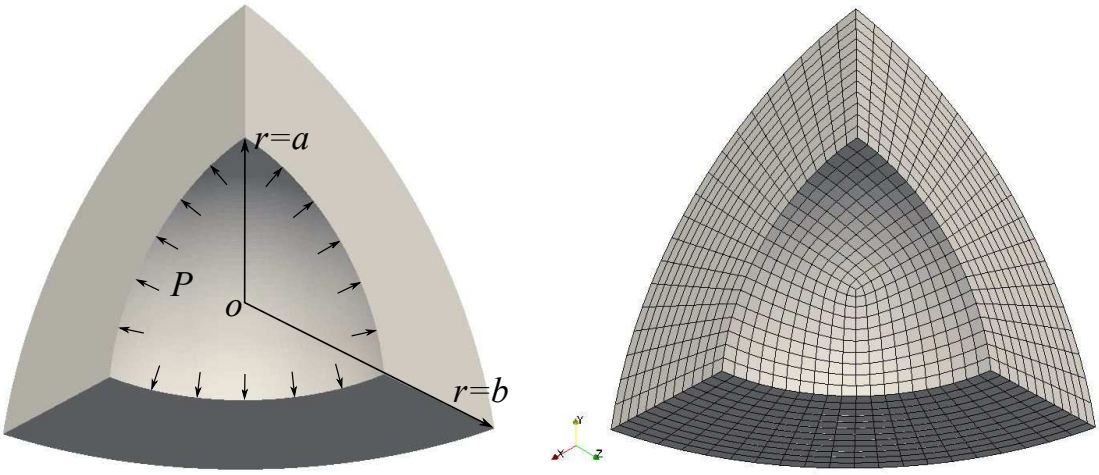

(a) (b)

Figure 6.2. An octant of hollow sphere: (a) geometry and loading and (b) the SBFEM mesh 3.

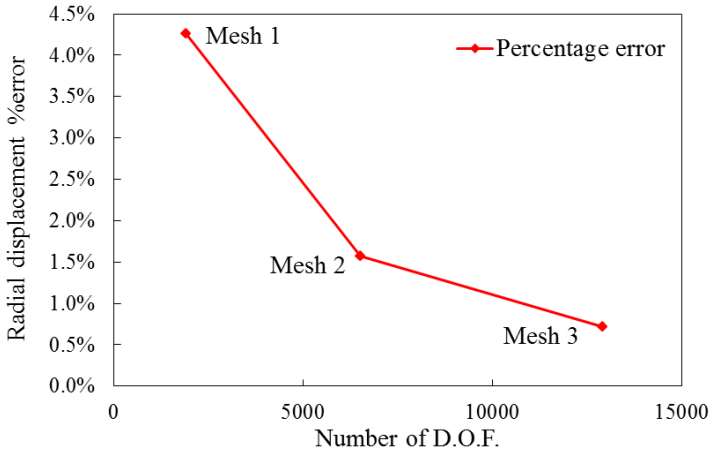

Figure 6.3. Convergence study with three types of meshes.

given in the following two Equations(6.81) and (6.82) respectively

$$\sigma_r(r) = \begin{cases} -\frac{2}{3}\frac{c^3}{b^3}\left(\frac{b^3}{r^3}-1\right)\sigma_y & (b \geq r > c) \\ -\frac{2}{3}\left(1+3\ln\left(\frac{c}{r}\right)-\frac{c^3}{b^3}\right)\sigma_y & (a \leq r \leq c) \end{cases} \tag{6.81}$$

$$\sigma_\theta(r) = \sigma_\phi(r) = \begin{cases} \frac{2}{3}\frac{c^3}{b^3}\left(\frac{b^3}{2r^3}+1\right)\sigma_y & (b \geq r > c) \\ \frac{2}{3}\left(\frac{1}{2}-3\ln\left(\frac{c}{r}\right)+\frac{c^3}{b^3}\right)\sigma_y & (a \leq r \leq c) \end{cases} \tag{6.82}$$

For numerical analysis using SBFEM, three types of meshes are used for convergence study at first. In each of these meshes, the octant is equally discretized into M

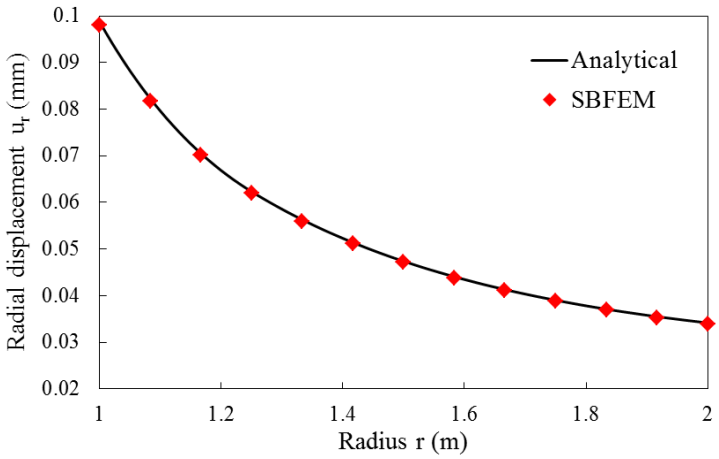

Figure 6.4. Radial displacement u_r in hollow sphere obtained from SBFEM and analytical solution.

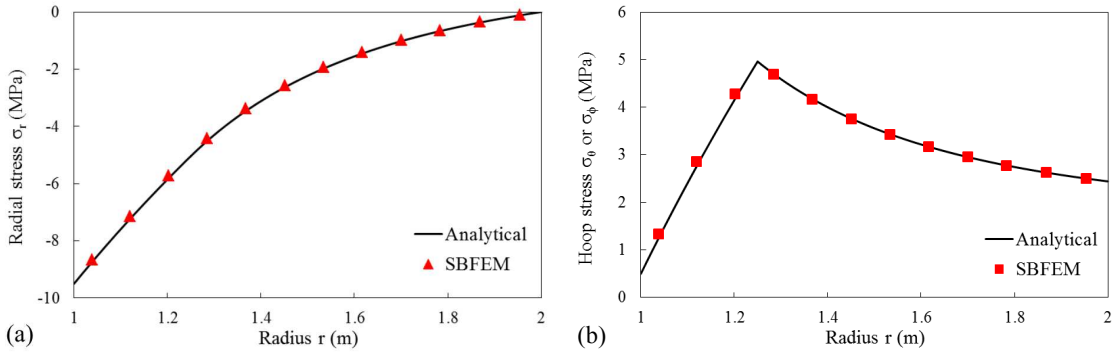

Figure 6.5. Stresses in hollow sphere obtained from SBFEM and analytical solution: (a) Radial stress σ_r and (b) Hoop stresses σ_θ or σ_ϕ.

divisions along the circular edges and N divisions in the thickness direction. 4-node quadrilateral elements are used on the surface of each hexahedral subdomains. All meshes used for convergence study are: mesh 1 with M=10 and N=6, mesh 2 with M=16 and N=9, mesh 3 with M=20 and N=12. Figure 6.2(b) shows an example of mesh 3. The results of convergence study are shown in Figure 6.3. In Figure 6.3, the horizontal and vertical axes represent total number of degree-of-freedom (D.O.F.) in the mesh and percentage error of radial displacement at the outer surface of sphere comparing with analytical solution. In the convergence study, mesh 3 has the percentage error of approximate 0.7% comparing with analytical solution. Therefore, mesh 3 is chosen to present the following results of radial displacements, stresses and contour plots in this example.

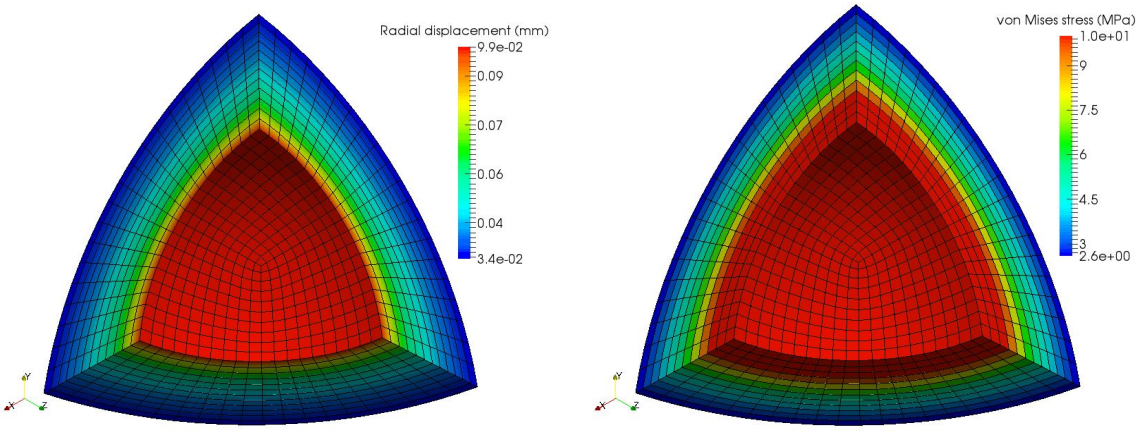

(a) (b)

Figure 6.6. Contour plots for hollow sphere using mesh 3: (a) Radial displacement and (b) von Mises stress.

The radial displacements u_r at each nodes along radial direction computed from proposed SBFEM formulation are shown in Figure 6.4 with red dots. In the proposed method, stresses can only be calculated at scaling centres. Hence, the radial stresses σ_r and hoop stresses, σ_θ or σ_ϕ, at the scaling centres along radial direction are presented in Figure 6.5(a) and (b) respectively. In both Figures 6.4 and 6.5, horizontal axes represent the radial coordinate r and the corresponding analytical solutions are also plotted in these figures with black lines for comparison. The numerical solutions are in very good agreements with the analytical solutions.

Figure 6.6(a) and (b) shows the contour plots of radial displacement and von Mises stress calculated using mesh 3, respectively. Because the present method assumes constant stresses at the scaling centre within each subdomain, the contour color for von Mises stress in Figure 6.6(b) is the same within each hexahedral subdomain. Figure 6.6(b) also shows that the red yield zone only propagates from the inner surface of hollow sphere to one fourth of its thickness, which agrees well with the prediction from analytical solution using Equation (6.80).

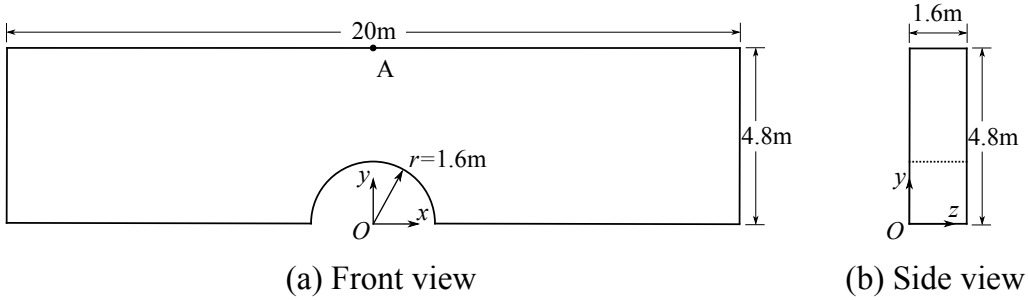

Figure 6.7. Simply supported beam with cylindrical notch: (a) Front view and (b) Side view (from +x direction).

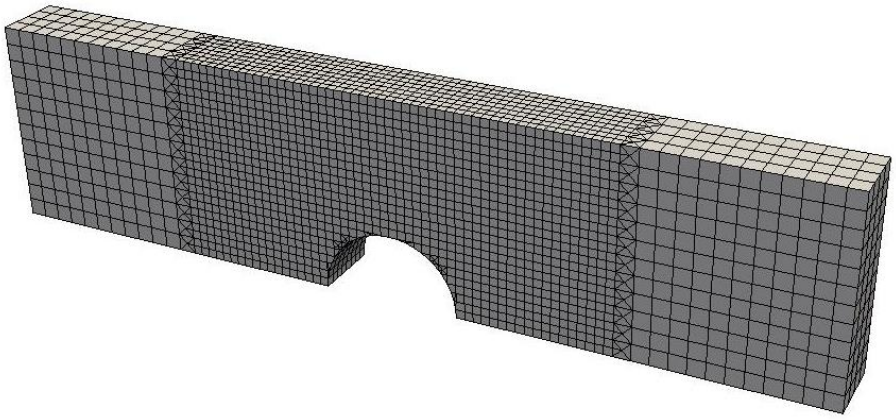

Figure 6.8. The SBFEM mesh for cylindrically notched beam.

6.5.3 Simply supported beam with cylindrical notch

The structure considered in this numerical example is a simply supported beam with a cylindrical notch. The cylindrical notch with a radius of $r = 1.6$m is at the middle of the beam bottom. The dimensions of this beam are illustrated in Figure 6.7. Point A in Figure 6.7 is located at the top-front of the beam with the coordinate of (0, 4.8, 0). The material used for this beam is assumed to be perfectly plastic with Young's modulus of $E = 100$GPa, Poisson's ratio of $\nu = 0.333$, yield stress of $\sigma_y = 0.16$GPa and density of $\rho = 1.5 \times 10^3 \text{kg/m}^3$. Von Mises yield criterion is considered in this example and the self-weight of beam is neglected. Both static and dynamic elastoplastic analyses are performed for this beam in the following Sections 6.5.3.1 and 6.5.3.2, respectively.

The same SBFEM mesh is used for static and dynamic analyses and shown in Figure 6.8. In the SBFEM mesh, only the surface of octree subdomains are

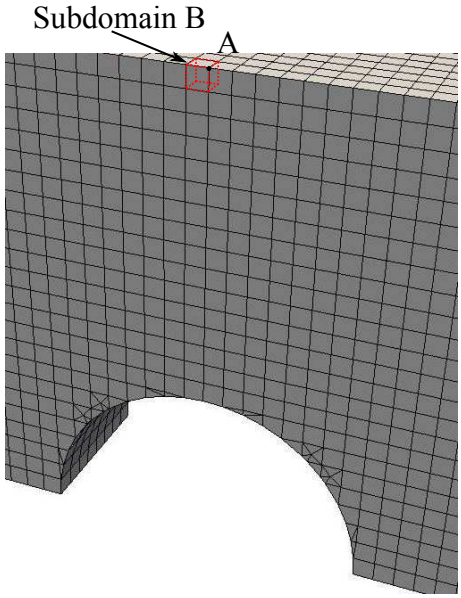

Figure 6.9. A closer look at the trimmed mesh along notched surface in SBFEM mesh.

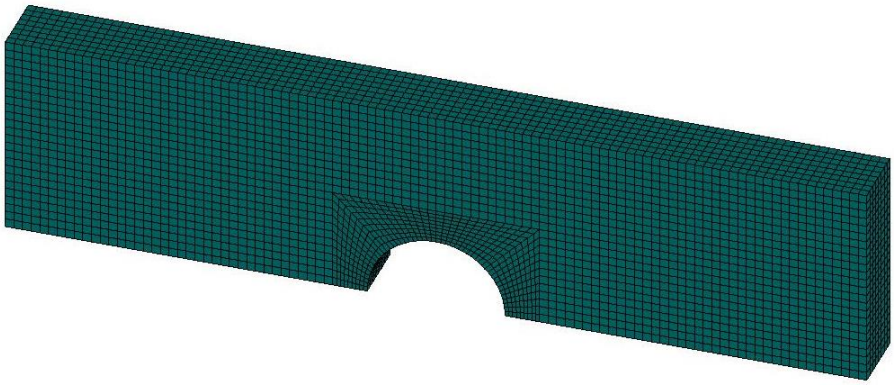

Figure 6.10. The FEM mesh for cylindrically notched beam in ANSYS.

meshed with 4-node quadrilateral and 3-node triangular elements. The size of larger octree cells is 0.4m and the middle part of the beam is refined using smaller octree cells with the size of 0.2m as the internal stresses and elastoplastic constitutive matrices within each polyhedral subdomain in the proposed method are represented by constants. The mesh transition between the smaller and larger quadrilateral elements are handled efficiently using octree mesh. After the generation of octree mesh, the jagged boundary along the cylindrical notch is trimmed by the STL model of this beam to generate a smooth cylindrical boundary, which is clearly shown in Figure 6.9. For verifying the numerical results obtained from the proposed SBFEM

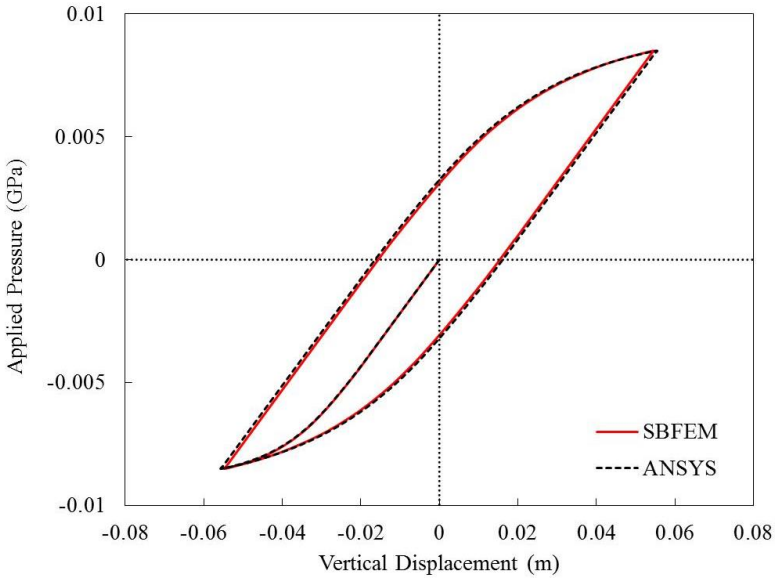

Figure 6.11. Vertical displacement at point A of cylindrically notched beam.

formulation, the same notched beam is modeled in the commercial software ANSYS with the FEM mesh illustrated in Figure 6.10. 8-node hexahedral elements are used in the structured mesh in ANSYS. In order to obtain an accurate reference solution, the maximum element size used in ANSYS mesh is set to be 0.2m. The minimum element edge length in ANSYS mesh is about 0.09m in the refined region around the notch.

6.5.3.1 Static analysis results

In the static elastoplastic analysis, a cyclic pressure P is uniformly applied on the entire top surface ($y = 4.8$m) of the beam. This cyclic pressure P changes from the initial value of $P = -8.5$MPa (downward) to $P = 8.5$MPa (upward), and then decreases and returns back to the initial value of $P = -8.5$MPa (downward). The vertical displacement (in y-direction) at point A in Figure 6.7 during this whole loading-unloading-reloading process is recorded and plotted with the red line in Figure 6.11. The vertical displacement at the same point computed from ANSYS is also illustrated in the same figure with black dash line for comparison.

In Figure 6.11, the result computed from present SBFEM formulation agrees

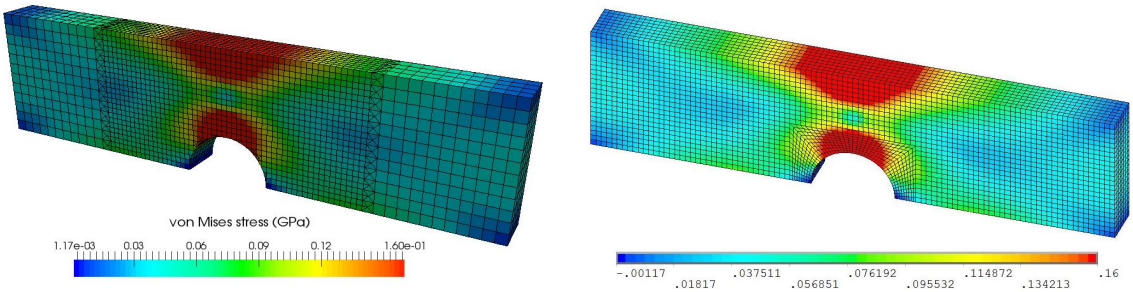

(a) (b)

Figure 6.12. Contour plots of von Mises stress (GPa) for cylindrically notched beam after first loading process: (a) from proposed SBFEM formulations and (b) from ANSYS.

with the reference solution obtained from ANSYS well. After the first loading ($P = -8.5$MPa), the relative difference between the SBFEM and ANSYS solutions for the vertical displacement at point A is approximately 1.6%. There are totally 72630 DOFs used in the FEM analysis in ANSYS. However, the total DOFs used in the present SBFEM formulation is 38859, which is less than 54% of the total DOFs used in the ANSYS model. In addition, the computationally expensive return mapping algorithm only needs to be performed at the scaling centre of each polyhedral subdomain in the proposed method. The contour plots of von Mises stress after the first loading process calculated from the present method and ANSYS are also summarized in Figures 6.12(a) and 6.12(b) separately for illustration.

6.5.3.2 Dynamic analysis results

For performing the dynamic elastoplastic analysis, the top surface ($y = 4.8$m) of the beam is subjected to a suddenly applied (applied during the first time step of Newmark's method) uniform pressure of $\bar{P} = -4.5$MPa (downward). The same mesh used in previous static analysis is again employed here for dynamic analysis. Newmark's method for nonlinear systems are applied to solve the solutions in the time domain for both analyses performed in ANSYS and SBFEM. The dynamic responses during the first 50ms are calculated with the selected time step of $\Delta t = 0.0625$ms for the convergence of nonlinear analysis. Analogously, the vertical displacement at

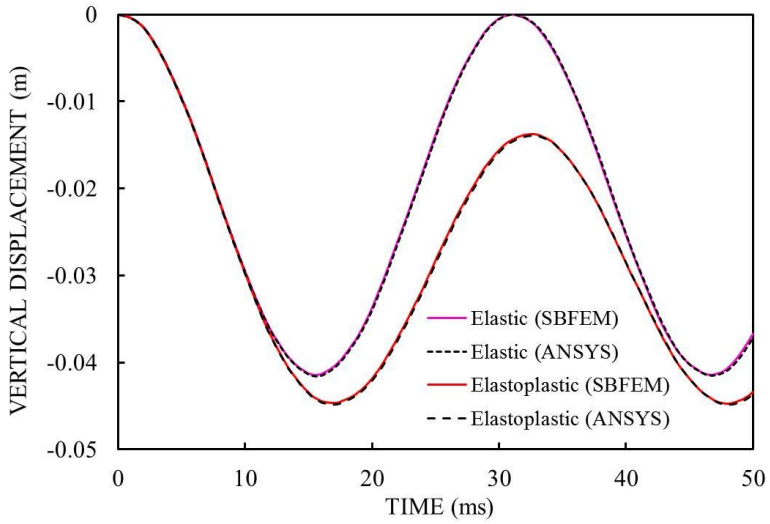

Figure 6.13. The vertical displacements of cylindrically notched beam at point A from both dynamic elastic and elastoplastic analyses.

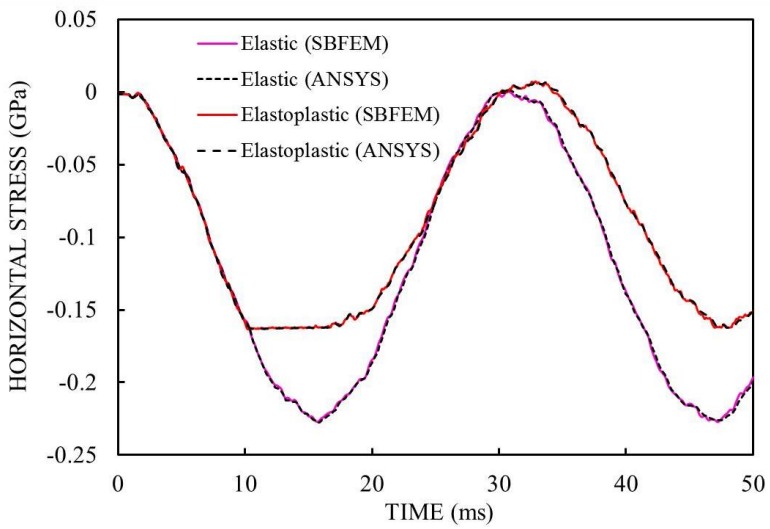

Figure 6.14. The horizontal stresses in subdomain B of cylindrically notched beam from both dynamic elastic and elastoplastic analyses.

point A from present SBFEM is recorded and plotted with red line in Figure 6.13, with the reference solution obtained from ANSYS plotted in black dash line. For comparison, the dynamic elastic analysis of the same simply supported beam with cylindrical notch under the same suddenly applied pressure $\bar{P}$ is performed. The vertical displacement calculated from SBFEM at point A for elastic case is also presented in the Figure 6.13 with purple line. The displacement result from the elastic analysis is still verified using ANSYS and plotted in the same Figure 6.13 with black

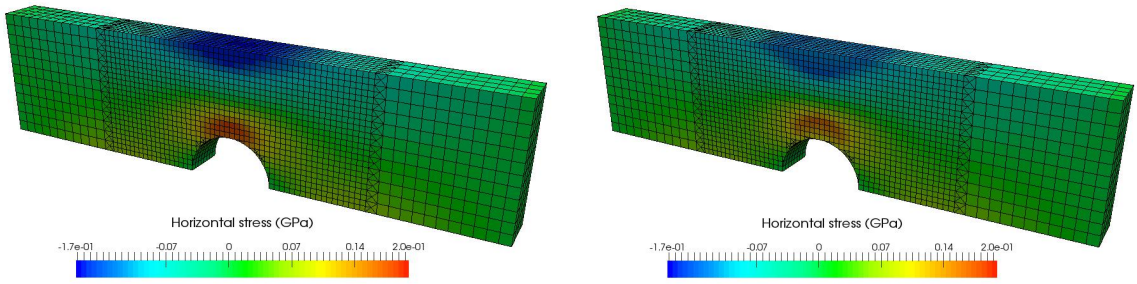

(a) $t = 10$ms (b) $t = 20$ms

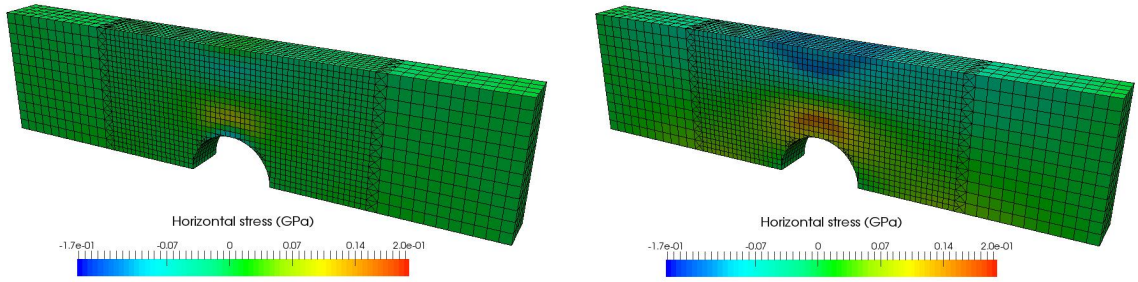

(c) $t = 30$ms (d) $t = 40$ms

Figure 6.15. Contour plots of horizontal stress in cylindrically notched beam using proposed SBFEM at: (a) $t = 10$ms, (b) $t = 20$ms, (c) $t = 30$ms and (d) $t = 40$ms.

dotted line. In the dynamic response of elastoplastic case, the oscillation of vertical displacement will not return back to its initial position as in elastic case due to the permanent plastic deformations in the beam.

The horizontal (x-direction) stress in hexahedral subdomain B shown in Figure 6.9 is also calculated using SBFEM and presented by red and purple lines for dynamic elastoplastic and elastic analyses, as illustrated in Figure 6.14. Here, the elastic analysis in SBFEM is achieved by simply setting the yield stress of structure to be a significantly large value in the proposed approach for elastoplastic analysis and thus avoid the yielding. The average horizontal stresses extracted from the hexahedral element at the same position with the same shape in ANSYS model are plotted in Figure 6.14 for the verification of both elastic and elastoplastic results obtained from SBFEM. Same line styles for presenting different numerical results are used here as in Figure 6.13. According to Figures 6.13 and 6.14, the displacement and stress results from dynamic elastoplastic analyses using both SBFEM and ANSYS

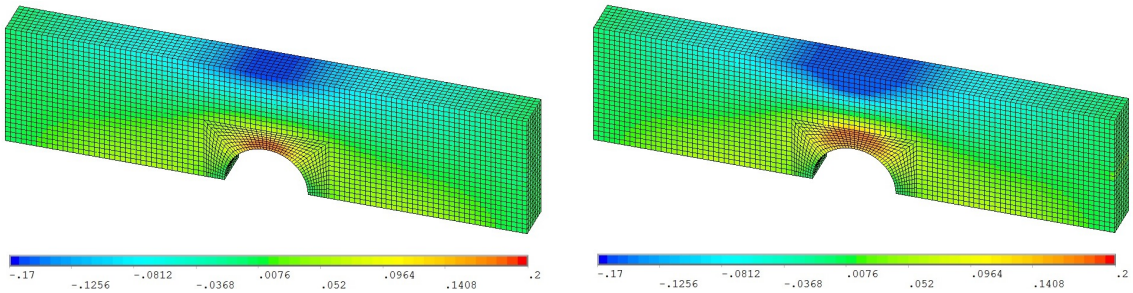

(a) $t = 10$ms (b) $t = 20$ms

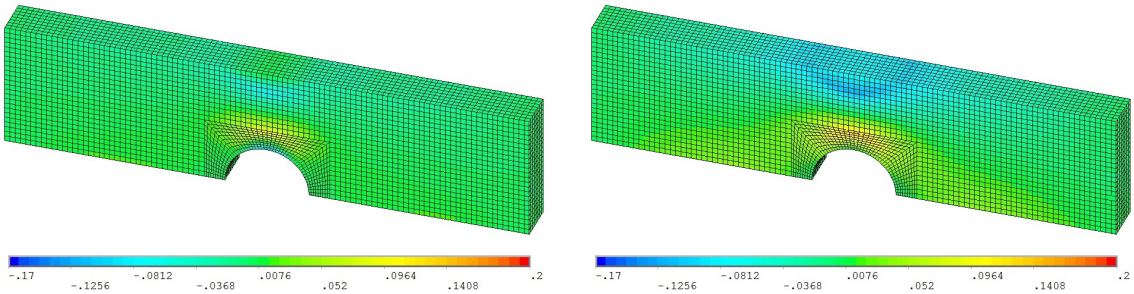

(c) $t = 30$ms (d) $t = 40$ms

Figure 6.16. Contour plots of horizontal stress (GPa) in cylindrically notched beam using ANSYS at: (a) $t = 10$ms, (b) $t = 20$ms, (c) $t = 30$ms and (d) $t = 40$ms.

are in very good agreements. In addition, the contour plots of horizontal stresses from dynamic elastoplastic analyses calculated by the proposed SBFEM and ANSYS at time $t = 10$ms, 20ms, 30ms and 40ms are presented in Figures 6.15 and 6.16 respectively.

6.5.4 3D plate with multiple holes

In this numerical example, a square plate with multiple holes is subjected to a harmonic excitation uniformly on the top. The geometry of this plate is stated in Figure 6.17. Totally five holes are in the square plate which has the dimension of $256\text{mm} \times 256\text{mm} \times 24\text{mm}$. Among those holes, two square holes have the same edge length of 40mm, three circular holes have the same radius of $r = 20$mm with all of their locations marked in Figure 6.17. The whole bottom surface ($y = 0$) is fixed in the vertical direction (y direction) and the uniform harmonic pressure $\bar{P}(t)$ with units of (GPa) and (ms) for time t, given in Equation (6.83), is applied on the top

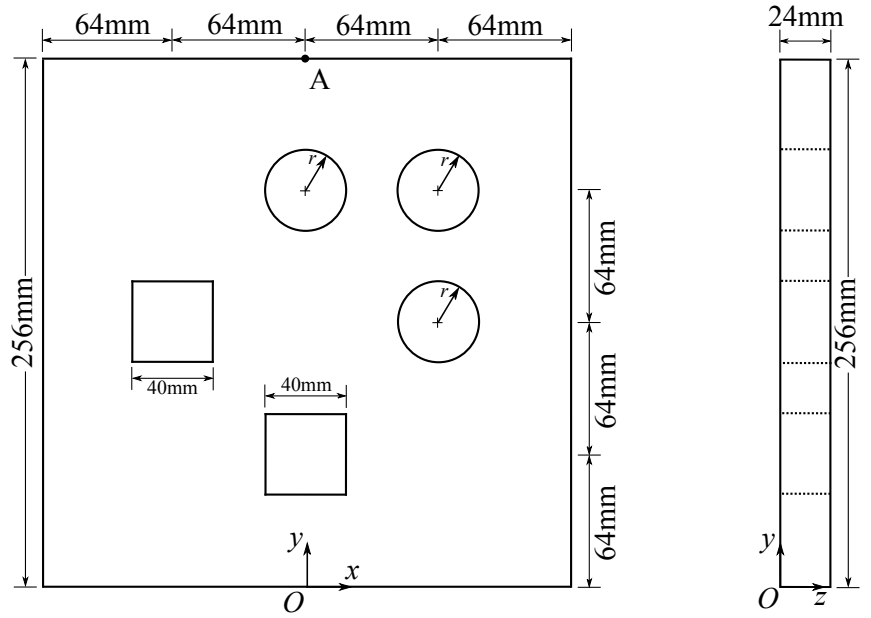

(a) Front view (b) Side view

Figure 6.17. Geometry of plate with multiple holes: (a) Front view and (b) Side view (from +x direction).

of the plate ($y = 256$mm) pointing upward (positive y direction).

$$\bar{P}(t) = 0.082 \times (1 - \cos(20t)) \tag{6.83}$$

The material made of this plate is assumed to be perfectly plastic and follows von Mises yield criterion. It has the Young's modulus of $E = 206.9$GPa, Poisson's ratio of $\nu = 0.3$, yield stress of $\sigma_y = 0.45$GPa and density of $\rho = 7.7 \times 10^3 \text{kg/m}^3$.

In this example, the FEM solution computed from ANSYS is again used as the reference solution for verifying the results obtained using the present SBFEM formulation. The meshes used in ANSYS and SBFEM are illustrated separately in Figure 6.18(a) and (b). In the SBFEM mesh in Figure 6.18a, the octree cells around all the holes are refined for possible plastic deformation occurs within this region. 4-node quadrilateral and triangular elements are used in this octree mesh. The minimum octree cell size is set to be 4mm and the maximum size is 8mm in this SBFEM mesh. The boundaries of holes are also trimmed to make the geometry smooth. In order to make the mesh comparable, the maximum element size in ANSYS mesh is equal

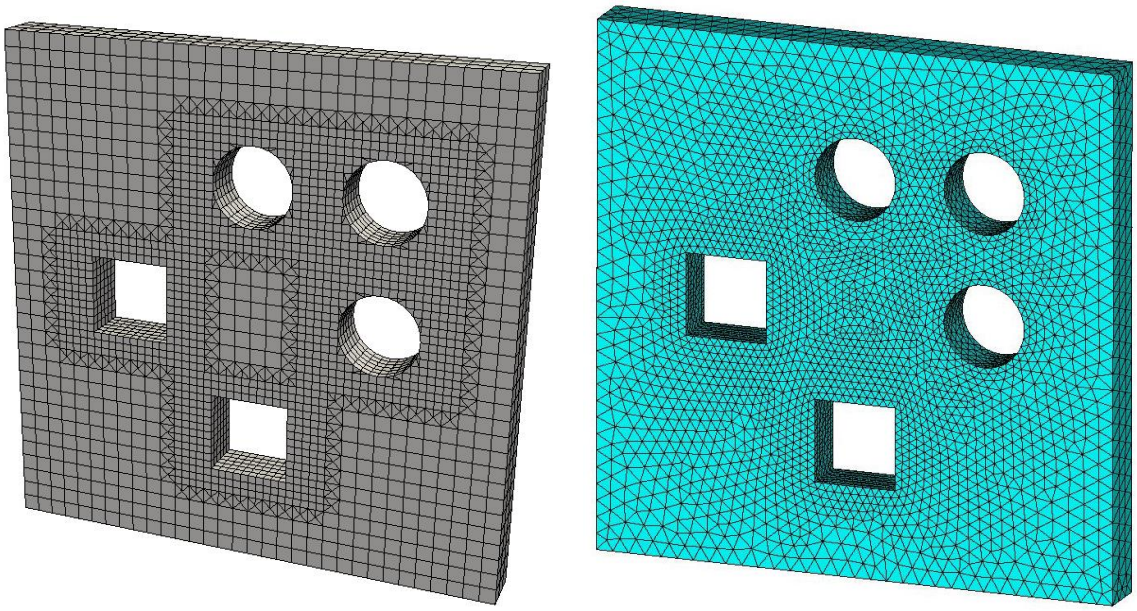

(a) Mesh in SBFEM (b) Mesh in ANSYS

Figure 6.18. Meshes of plate with multiple holes: (a) Mesh in SBFEM and (b) Mesh in ANSYS.

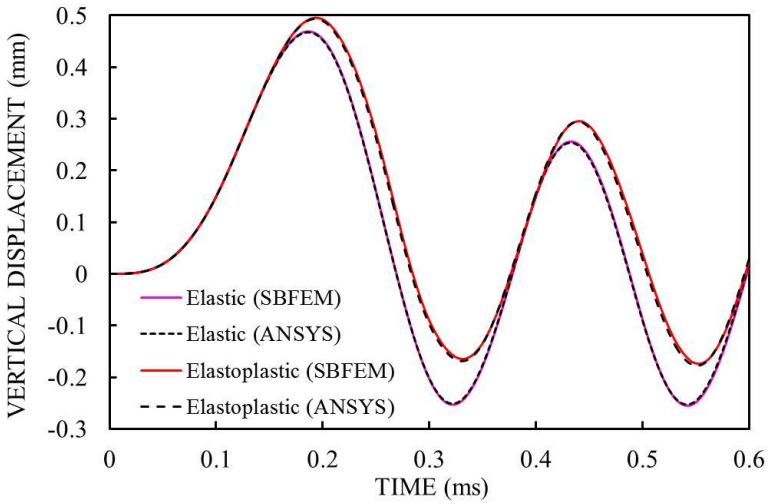

Figure 6.19. The vertical displacements of plate with multiple holes at point A from both dynamic elastic and elastoplastic analyses.

to the maximum cell size in SBFEM mesh around the plate edges. Moreover, the minimum element size in ANSYS mesh is also the same as the minimum cell size in SBFEM mesh around the boundaries of holes. 4-node tetrahedral elements are adopted in the ANSYS model. The total number of DOFs in SBFEM model is about 83% of the total number of DOFs used in ANSYS model. The maximum relevant

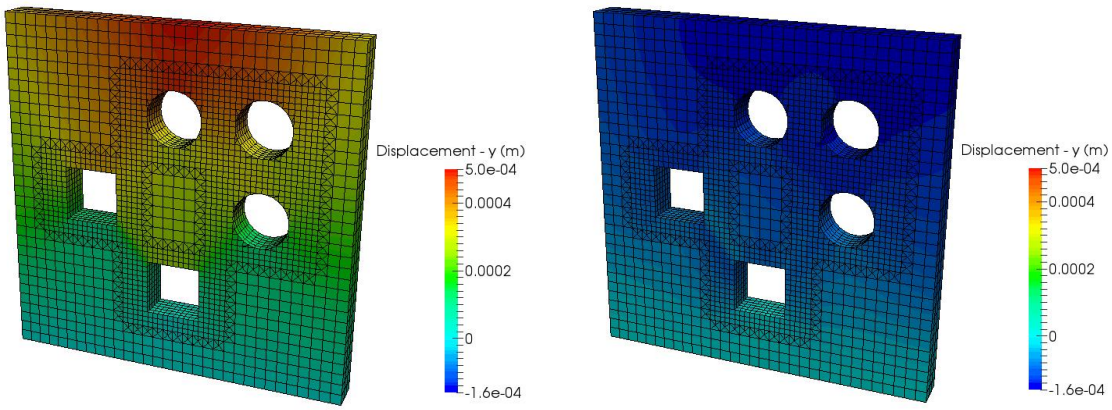

(a) $t = 0.2$ms (b) $t = 0.34$ms

Figure 6.20. Contour plots of vertical displacement (m) in plate with multiple holes using proposed SBFEM at: (a) $t = 0.2$ms and (b) $t = 0.34$ms.

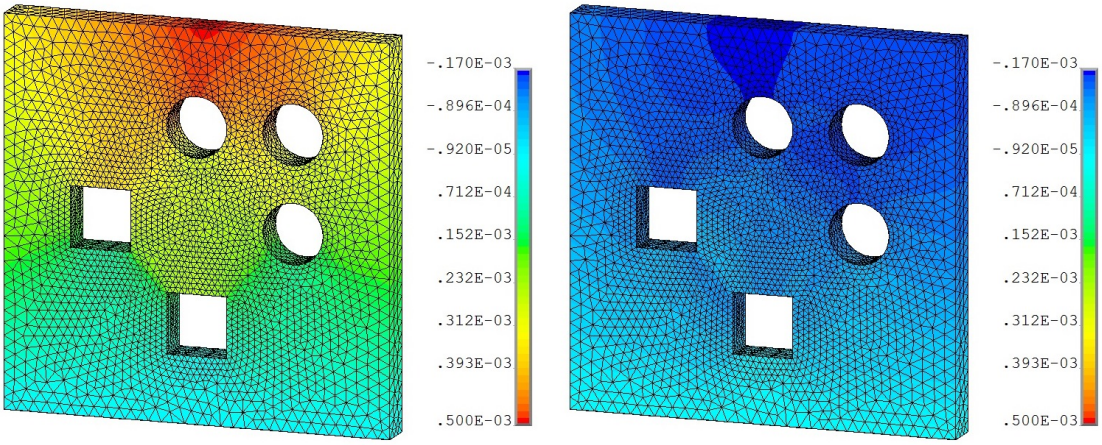

(a) $t = 0.2$ms (b) $t = 0.34$ms

Figure 6.21. Contour plots of vertical displacement (m) in plate with multiple holes using ANSYS at: (a) $t = 0.2$ms and (b) $t = 0.34$ms.

frequency of this excitation is $\omega_{max} = 60$rad/ms. According to Equation (5.66), the speed of shear wave in this plate is $c_s \approx 3214.76$m/s, which gives the shortest wave length $\lambda_{min} = \frac{2\pi}{\omega_{max}} c_s \approx 0.34$m and can be sufficiently represented by the maximum mesh size. Time step for dynamic analyses using Newmark's method is set to be $\Delta t = 2\times10^{-4}$ms for the convergence of nonlinear analysis. The displacement responses from both elastic and elastoplastic analyses at point A(128mm, 256mm, 0mm), shown in Figure 6.17(a), is demonstrated in Figure 6.19. All displacement results are

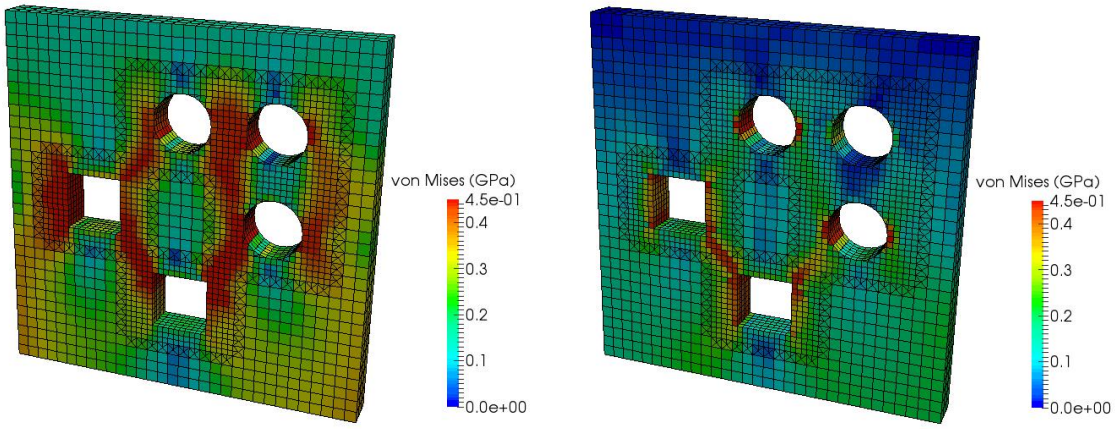

(a) $t = 0.2$ms (b) $t = 0.34$ms

Figure 6.22. Contour plots of von Mises stresses (GPa) in plate with multiple holes using proposed SBFEM at: (a) $t = 0.2ms$ and (b) $t = 0.34ms$.

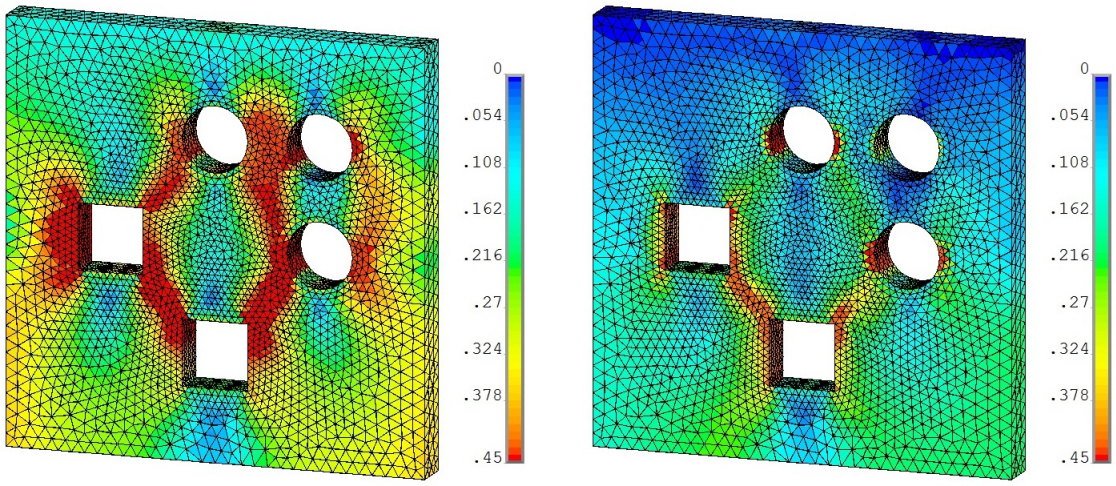

(a) $t = 0.2$ms (b) $t = 0.34$ms

Figure 6.23. Contour plots of von Mises stresses (GPa) in plate with multiple holes using ANSYS at: (a) $t = 0.2ms$ and (b) $t = 0.34ms$.

verified using reference solution from ANSYS, good agreements have been observed in Figure 6.19.

Additionally, the contour plots of vertical displacements and von Mises stresses at time $t = 0.2$ms and 0.34ms are illustrated in Figure 6.20 and 6.22 respectively. For verification purpose, the results of contour plots for vertical displacements and von Mises stresses from ANSYS at the same moments are also shown in Figure 6.21

and 6.23 respectively.

6.5.5 3D humerus-shaped structure

The applications of 3D-printing have been used in producing customized implants and prostheses due to its cost-efficiency, enhanced productivity, democratization and collaboration. The complex geometry of human structures obtained from x-ray, MRI or CT scans can be translated to STL files for 3D printing. This solves a persistent problem in orthopedics that standard implants are often not sufficient for some patients (Ventola, 2014). Therefore, customized implants from 3D printing are increasingly used for individual patients. Examples include customized prosthetic limbs (Fan et al., 2015), skulls in neurosurgery (Banks, 2013) and 3D-printed titanium mandibular prosthesis (Klein et al., 2013). In the last numerical example, the dynamic elastoplastic analysis of a structure with human humeral (upper-limb) shape is performed to demonstrate the capability of proposed SBFEM formulations for addressing problems with complex geometry and extend the practical applications of SBFEM. The STL file of a human right humerus is obtained from the website (profguy, 2014). This prosthesis is assumed to be made of titanium with Young's modulus of $E = 110\text{GPa}$, Poisson's ratio of $\nu = 0.3$, initial yield stress of $\sigma_y = 0.9\text{GPa}$, hardening parameter of $H = 1.25\text{GPa}$ and density of $\rho = 4.5 \times 10^3 \text{kg/m}^3$. Von Mises yield criterion and isotropic hardening rule are considered in this example. The self-weight of prosthesis is neglected. The size of this humeral model is 101mm $\times$ 49.2mm $\times$ 307mm and its geometry with facets in STL file are shown in Figure 6.24(a).

Modeling the real boundary and loading conditions of humerus in human arm can be complicated and involves various muscle forces and numerical joints to simulate the shoulder kinematics accurately (Bolte, 2004; Astier et al., 2008). The discussions on those boundary and loading conditions are out of the scope of this work. Therefore, for the purpose of demonstrating the proposed method for elas-

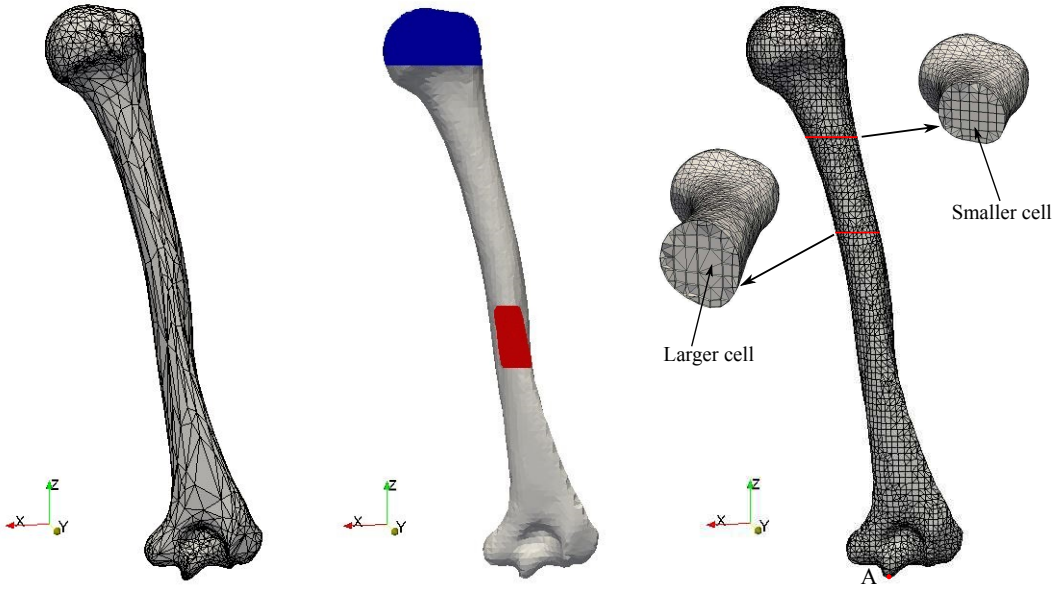

Figure 6.24. The humeral prosthesis: (a) The shape of humerus and STL file (b) Applied boundary conditions and (c) The SBFEM mesh of humerus.

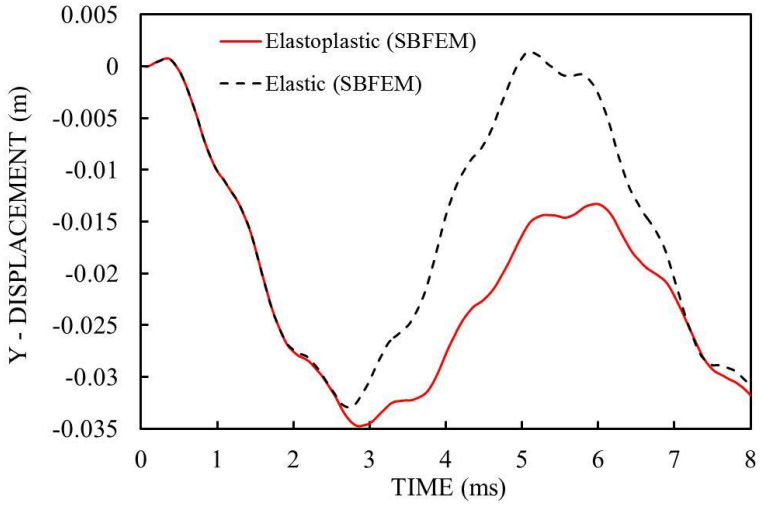

Figure 6.25. The displacements in y direction of humeral prosthesis at point A from both dynamic elastic and elastoplastic analyses.

toplastic analysis, the simplified boundary and loading conditions shown in Figure 6.24(b) is applied in this example. In Figure 6.24(b), all nodes on the surface within the blue area of the humerus is fixed in all DOFs and all elements with nodes within the red region in the deltoid tuberosity are subjected to a suddenly applied (applied during the first time step of Newmark's method) uniform pressure in -y direction

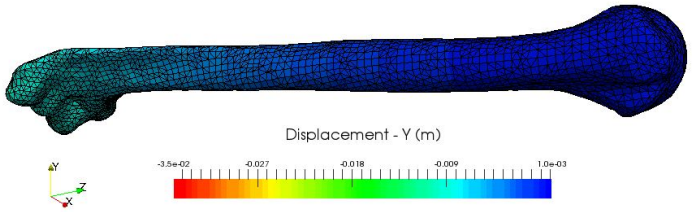

(a) $t = 1$ms

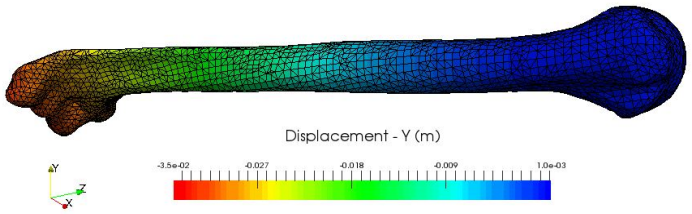

(b) $t = 3$ms

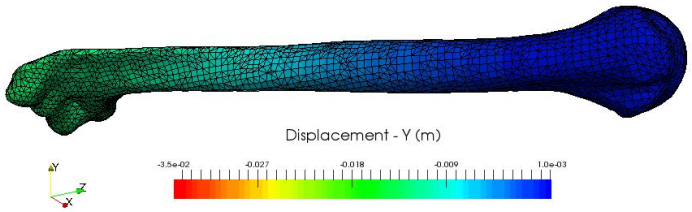

(c) $t = 6$ms

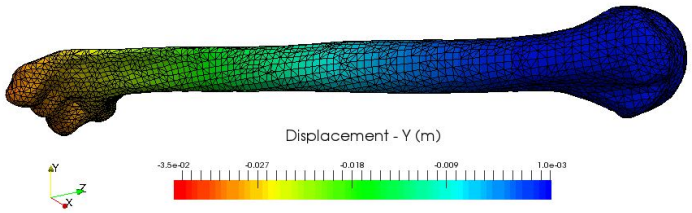

(d) $t = 8$ms

Figure 6.26. Contour plots of displacements (m) in y direction in humeral prosthesis using SBFEM at: (a) $t = 1$ms, (b) $t = 3$ms, (c) $t = 6$ms and (d) $t = 8$ms.

on the surface. The magnitude of the suddenly applied pressure is $\bar{P} = 18$MPa. The minimum and maximum cell size in the octree mesh is set to be 3.24mm and 6.48mm respectively to capture the geometrical features and the final trimmed mesh is shown in Figure 6.24(c). Totally 7567 nodes are used in the presented SBFEM mesh. The mesh inside the humerus around the fixed end is refined using the smaller cell size due to possible plastic deformations that may happen in this region as shown in Figure 6.24(c). Both dynamic elastic and elastoplastic analyses are performed on this example and the displacement results in y direction at point A, which

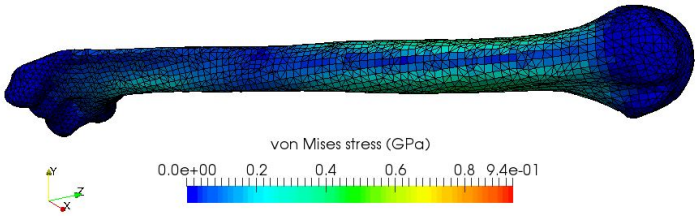

(a) $t = 1$ms

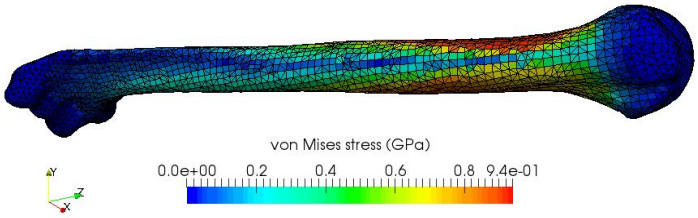

(b) $t = 3$ms

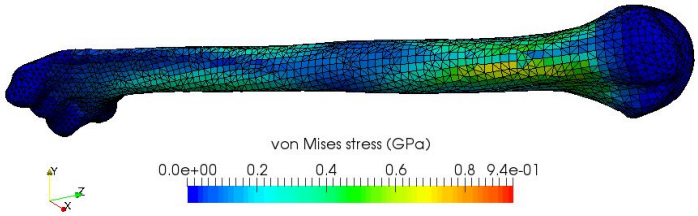

(c) $t = 6$ms

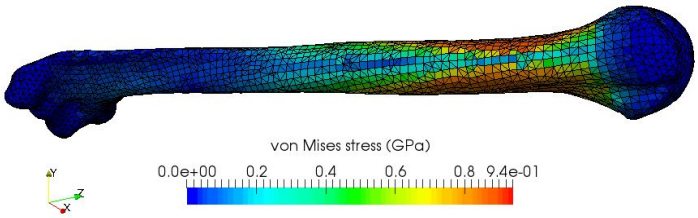

(d) $t = 8$ms

Figure 6.27. Contour plots of von Mises stresses (GPa) in humeral prosthesis using SBFEM at: (a) $t = 1$ms, (b) $t = 3$ms, (c) $t = 6$ms and (d) $t = 8$ms.

is at the bottom with smallest z coordinate marked in Figure 6.24(c) with red dot, are presented in Figure 6.25 with elastic results in black dash line and elastoplastic results in red solid line. The dynamic responses during the first 8ms are calculated with the selected time step of $\Delta t = 0.005$ms in Newmark's method.

The contour plots of the displacements in y direction and von Mises stresses at time $t = 1$ms, 3ms, 6ms and 8ms are presented in Figures 6.26 and 6.27 respectively for illustrating the numerical results from elastoplastic analysis of this humerus-shaped structure using present SBFEM. From results in Figure 6.27 and 6.26, large

displacements in loading (y) direction happen around the free end (capitulum) of this structure and the von Mises stresses tend to concentrate on the head-side (fixed end) of the deltoid tuberosity.

6.6 Conclusions

This chapter presents an automatic way of performing static and dynamic elastoplastic analyses from STL models using SBFEM. The automatic mesh generation from STL model is achieved by utilizing the octree mesh technique and a systematic way of boundary trimming according to STL facets. For guaranteeing the high efficiency and easy of implementation of the automatic elastoplastic analysis in 3D using SBFEM, the proposed method in this chapter is based on the approach in Reference (He, 2017) for 2D image-based elastoplastic analysis and extends it to 3D static and dynamic elastoplasticity. This approach is very efficient in modeling elastoplastic models with quadtree or octree based mesh. Because small cell sizes are preferred to be used in quadtree or octree decomposition for better representing the geometrical features in the input models, the elastoplastic constitutive matrices and internal stresses can be approximated by constant values within each subdomain in SBFEM. As a result, the return mapping algorithm should only be performed at the scaling center of each subdomain with plastic deformation. The internal loads due to the higher order stresses are used as the stabilisation part in the formulation to control the spurious modes in plastic subdomains. The mesh transition between refined yield zone and unrefined elastic zone is also handled efficiently with octree mesh in this chapter. Various numerical examples for 3D elastoplastic analysis are presented in this chapter for verification as well as for demonstrating the accuracy and efficiency of the proposed method. This achieved by comparing the results from SBFEM with available analytical solutions and standard FEM elastoplastic analysis using commercial software ANSYS. Furthermore, a 3D dynamic elastoplastic analy-

sis of a titanium humerus-shaped structure is performed to prove the capability of this proposed SBFEM on handling 3D models with complex geometry and extend the practicability of this numerical tool to possible biomechanical applications.

Chapter 7

2D and 3D acoustic-structure interaction analyses considering structural elastoplasticity using SBFEM

7.1 Introduction

The investigation of interaction between structure and acoustic media, or the acoustic-structure interaction analysis, is a research area of great significance in various civil and mechanical engineering applications. These include the design of dam-reservoir system, marine structures, nuclear rector component, etc. In many cases, the interaction effects between acoustics and structures are not negligible due to the surrounding heavy fluids, for instance water, or the light and flexible structures. For such an acoustic-structure interaction system subjected to severe transient excitations, such as the earthquake response of dam-reservoir system, plastic deformations may occur in part of the structural domain and the elastoplastic behavior of the vibrating structures has to be considered.

In the aforementioned acoustic-structure interaction problems considering structural elastoplasticity, a method to perform direct time-domain analysis is required for considering the nonlinearity of structures in the coupled formulations. In order to model the acoustic-structural interaction system with great flexibility, numerical methods are extensively applied by researches in this research area. Among them, the finite element method (FEM) is possibly the most popular one as it is suitable for modelling structural nonlinearity and the bounded acoustic domain with arbitrary geometry. However, FEM is not suitable for the direct modelling of systems with infinite domains because of the wave reflection from the truncated boundaries of the finite mesh. One of the commonly used method for modelling unbounded domains in acoustic-structure interactions is the boundary element method (BEM) (Marburg and Nolte, 2008) as reviewed in Chapter 5.

As a promising method for performing the numerical analysis in both bounded and unbounded domains, the SBFEM is a semi-analytical computational tool shows advantages from both FEM and BEM. In SBFEM, only the boundary is discretized and the radiation condition at infinity is satisfied exactly (Wolf and Song, 1996) without the requirement of fundamental solution. The original scaled boundary finite element formulation for modelling unbounded domain is global in space and time and thus computationally expensive (Song and Wolf, 1995, 1996). For solving the wave propagation problems in unbounded acoustic domains with higher efficiency, the high-order doubly-asymptotic open boundary (Prempramote et al., 2009; Prempramote, 2011; Birk et al., 2016) is also introduced recently. The dynamic impedance coefficients of an unbounded domain are obtained in the frequency domain by means of continued-fraction expansions. The time-domain formulation is then obtained by introducing auxiliary variables and the resulting global equations of motion for infinite acoustic domain can be solved by standard time-stepping schemes for direct time-domain analysis. For modelling the bounded domain, the SBFEM excels in representing stress singularities as the analytical solutions can be provided in radial

directions (Song, 2004a). For utilizing the advantages of boundary discretization, the SBFEM is combined with quadtree and octree mesh techniques and provides an efficient approach for automatic stress analysis (Saputra et al., 2017a; Liu et al., 2017; He, 2017; Gravenkamp et al., 2017). The SBFEM has also been applied to model structural nonlinearity in (Ooi et al., 2014; Chen et al., 2017a), which requires multiple fitting points within each subdomain for interpolating the nonlinear constitutive matrix and stresses. Later, a more efficient approach is developed for 2D image-based elastoplastic analysis (He, 2017). Comparing with previous methods based on SBFEM for modelling nonlinear structural behavior, this efficient approach for image-based elastoplastic analysis only requires one fitting point within each subdomain and thus reduces the locations for performing the computationally expensive return mapping algorithm.

The SBFEM has been applied to acoustic-structure interaction systems by some researchers (Wolf, 2003; Li, 2006, 2011; Wang et al., 2011; Fan et al., 2005; Fan and Li, 2008; LI et al., 2008; Li, 2012, 2009; Lin et al., 2007, 2012). To the author's knowledge, the scaled boundary finite element formulations published so far for acoustic-structure interaction problems or dam-reservoir interaction problems have only considered the elastic behavior of structures. In this chapter, the SBFEM is further developed to model the 2D and 3D acoustic-structure interaction problems considering the elastoplastic behavior of the finite structural domain. The infinite acoustic domain is modeled by the approaches developed in Chapter 3 and 4 based on SBFEM. The structure is then simulated using the recently developed scaled boundary finite element formulations for 2D (He, 2017) and 3D elastoplasticity in Chapter 6. The Newmark's method is directly applied to the coupled equations of motion for obtaining the transient solutions and the modified Newton-Raphson algorithm is adopted to achieve the force and flux equilibrium states for the coupling equations within each time step.

The remaining parts of this chapter is outlined as follows: Section 7.2 firstly

summarizes the SBFEM formulations for dynamic elastoplastic analysis. Then, the coupling of elastoplastic equations for structures and acoustic formulations are presented in Section 7.3. Next, the computational procedures for performing the acoustic-structure interaction analysis considering the structural elastoplasticity based on SBFEM are summarized in Section 7.4. Some numerical examples are given in Section 7.5 for illustrating the accuracy and robustness of the proposed approach. Finally, conclusions are stated in Section 7.6.

7.2 Scaled boundary finite element method for dynamic elastoplasticity

The 2D and 3D SBFEM formulations for dynamic elastoplastic analysis using only one fitting point in each subdomain are summarized here. Readers are referred to (He, 2017) and Chapter 6 of this thesis for details. Considering the small strain and deformation type of motion for an elastoplastic structure and neglecting the damping, it can be described by the following incremental form of matrix equation at the time step j:

$$\left[\sum_{i=1}^{nPol}\mathbf{M}\right]\Delta\ddot{\mathbf{U}}_b|_{(j)}+\left[\sum_{i=1}^{nPol}\mathbf{K}_{ep}\right]\Delta\mathbf{U}_b|_{(j)}=\Delta\mathbf{F}_{ext}|_{(j)} \tag{7.1}$$

where $\left[\sum_{i=1}^{nPol}\mathbf{M}\right]$ is the assembled global mass matrix and given by Equation (5.29) in SBFEM. $\Delta\mathbf{U}_b|_{(j)}$ and $\Delta\mathbf{F}_{ext}|_{(j)}$ are the global incremental nodal displacement and external force vector respectively due to any applied incremental load during time step j. $\left[\sum_{i=1}^{nPol}\mathbf{K}_{ep}\right]$ is the true global elastoplastic stiffness matrix for time step j. $\left[\sum_{i=1}^{nPol}\mathbf{K}_{ep}\right]$ is normally unknown for the current step as the elastoplastic stiffness matrix for each subdomain $\mathbf{K}_{ep}$ can only be calculated from a given state of stresses. The approach for calculating $\mathbf{K}_{ep}$ is described in Section 6.3.3 for 3D analysis or Appendix B.1 for 2D analysis. Because the elastoplastic stiffness matrix for each subdomain $\mathbf{K}_{ep}$ varies with stress states and thus is a function of struc-

tural displacement vector $\mathbf{u}_b$, it should be recalculated at each time step once the yielding happens. For solving Equation (7.1) for dynamic elastoplastic analysis, time-marching integration schemes are often applied in conjunction with standard iterative scheme for solving nonlinear equations, such as the use of Newmark's method with modified Newton-Raphson iterations for dynamic elastoplastic analysis demonstrated in Section 6.4.2, Chapter 6. The reason for using iterative approach in Newmark's method is that the known elastoplastic stiffness matrix from the last time step $\mathbf{K}_{ep}|_{(j-1)}$ is used to replace the unknown true elastoplastic stiffness matrix $\mathbf{K}_{ep}$ for the current time step. The use of $\mathbf{K}_{ep}|_{(j-1)}$ to predict the deformation under the incremental external force will certainly introduce error in the final incremental nodal displacement $\Delta\mathbf{U}_b|_{(j)}$. Therefore, an additional iterative scheme should be involved to correct $\Delta\mathbf{U}_b|_{(j)}$ and reduce this error. In other words, the following effective static problem at the time step j in Newmark's method is solved iteratively using modified Newton-Raphson iterations as:

$$\hat{\mathbf{K}}|_{(j-1)} d\mathbf{U}_b|_{(j)}^{k} = \hat{\mathbf{F}}_{ext}|_{(j)} - \hat{\mathbf{F}}_{int}^{dynamic}|_{(j)}^{k} \tag{7.2a}$$

$$\Delta\mathbf{U}_b|_{(j)}^{k} = \Delta\mathbf{U}_b|_{(j)}^{k-1} + d\mathbf{U}_b|_{(j)}^{k} \tag{7.2b}$$

In Equation (7.2), $\Delta\mathbf{U}_b|_{(j)}^{k}$ is the incremental displacement vector during time step j at the end of Newton-Raphson iteration step k. $d\mathbf{U}_b|_{(j)}^{k}$ is the incremental displacement vector during the Newton-Raphson iteration step k, which is used to update $\Delta\mathbf{U}_b|_{(j)}^{k}$ within time step j until the effective residual force $\hat{\mathbf{F}}_{ext}|_{(j)} - \hat{\mathbf{F}}_{int}^{dynamic}|_{(j)}^{k}$ is smaller than a predefined tolerance. The evaluation of the residual forces is described by steps (i) to (iii) and Equations (6.69) and (6.72) in Section 6.4.2. In a 3D analysis, the approach for calculating the static internal force vector for $\mathbf{F}_{int}^{static}|_{(j)}^{k}$ in Equation (6.72) is demonstrated in Section 6.3.4. For 2D case, this is summarized in Appendix B.2. $\hat{\mathbf{K}}|_{(j-1)}$ in Equation (7.2a) is the effective stiffness matrix obtained from the last time step $j-1$ via Equation (6.70).

7.3 Coupling of elastoplastic structural domain and acoustic domain

For performing the dynamic acoustic-structure interaction analysis considering the elastoplastic structural behavior, procedures similar to those summarized in Section 7.2 or listed in Section 6.4.2 for dynamic elastoplastic analysis are adopted here. The incremental form of the global equations of motion for the acoustic-structure interaction system considering structural elastoplasticity for any time step j can be formulated as:

$$\mathbf{M}_G^{ep}\Delta\ddot{\mathbf{Z}}_G^{ep}|_{(j)} + \mathbf{C}_G^{ep}\Delta\dot{\mathbf{Z}}_G^{ep}|_{(j)} + \mathbf{K}_G^{ep}\Delta\mathbf{Z}_G^{ep}|_{(j)} = \Delta\mathbf{F}_G^{ep}|_{(j)} \tag{7.3}$$

The global mass, damping and stiffness matrices $\mathbf{M}_G^{ep}$, $\mathbf{C}_G^{ep}$ and $\mathbf{K}_G^{ep}$ in Equation (7.3) can be formulated by coupling the global equations for infinite acoustic domain in Equation (3.116) or (4.45) for 2D or 3D acoustics with the global equations for 2D or 3D dynamic elastoplastic analysis for structural domain in Equation (7.1). Boundary conditions on acoustic-structure interface from Equation (5.53) are satisfied during the coupling of elastoplastic structures and acoustic domains. Following similar coupling procedures and rearrangement of coupled equations in Section 5.3.2, the global vector of unknown $\mathbf{Z}_G^{ep}$ for acoustic-structure interaction system considering the structural elastoplasticity can be defined by:

$$\mathbf{Z}_G^{ep} = \left\{ \begin{array}{cc|cc|c} \mathbf{u}_o(t) & \mathbf{u}_{as}(t) & \mathbf{p}_{as}(t) & \mathbf{p}_o(t) & \tilde{\mathbf{p}}(t) \end{array} \right\}^T \tag{7.4}$$

which contains both the nodal displacement $\mathbf{u}_o$ and $\mathbf{u}_{as}$ of structure, nodal pressure $\mathbf{p}_{as}$ and $\mathbf{p}_o$ from acoustics and auxiliary variables $\tilde{\mathbf{p}}$ used for bounded and unbounded acoustic domain. Subscript 'as' and 'o' denote the DOFs corresponding to acoustic-structure interface and other parts of the system. The corresponding global load vector $\mathbf{F}_G^{ep}$ can therefore be written as

$$\mathbf{F}_G^{ep} = \left\{ \begin{array}{cc|cc|c} \mathbf{F}_o(t) & \mathbf{F}_{as}^{ext}(t) & \mathbf{R}_{as}^{ext}(t) & \mathbf{R}_o(t) & 0 \end{array} \right\}^T \tag{7.5}$$

The global mass, damping and stiffness matrices $\mathbf{M}_G^{ep}$, $\mathbf{C}_G^{ep}$ and $\mathbf{K}_G^{ep}$ are also presented in the following equations:

$$\mathbf{M}_G^{ep} = \left[\begin{array}{cc|cc|c} \mathbf{M}_o^s & \mathbf{M}_{o\cdot as}^s & & & \\ [\mathbf{M}_{o\cdot as}^s]^T & \mathbf{M}_{as}^s & & 0 & 0 \\ \hline 0 & \rho_a \mathbf{H}_{as}^T & \mathbf{M}_{as}^a & \mathbf{M}_{as\cdot o}^a & \\ 0 & 0 & [\mathbf{M}_{as\cdot o}^a]^T & \mathbf{M}_o^a & \tilde{\mathbf{M}}_2^a \\ \hline & 0 & \left[\tilde{\mathbf{M}}_2^a\right]^T & & \tilde{\mathbf{M}}_1^a \end{array}\right] \tag{7.6a}$$

$$\mathbf{C}_G^{ep} = \left[\begin{array}{c|cc|c} 0 & \multicolumn{2}{c|}{0} & 0 \\ \hline 0 & 0 & 0 & \\ & 0 & \mathbf{C}_o^a & 0 \\ \hline 0 & \multicolumn{2}{c|}{0} & \tilde{\mathbf{C}}_1^a \end{array}\right] \tag{7.6b}$$

$$\mathbf{K}_G^{ep} = \left[\begin{array}{cc|cc|c} \mathbf{K}_o^{ep} & \mathbf{K}_{o\cdot as}^{ep} & 0 & 0 & \\ [\mathbf{K}_{o\cdot as}^{ep}]^T & \mathbf{K}_{as}^{ep} & -\mathbf{H}_{as} & 0 & 0 \\ \hline & & \mathbf{K}_{as}^a & \mathbf{K}_{as\cdot o}^a & \\ \multicolumn{2}{c|}{0} & [\mathbf{K}_{as\cdot o}^a]^T & \mathbf{K}_o^a & \tilde{\mathbf{K}}_2^a \\ \hline 0 & & \left[\tilde{\mathbf{K}}_2^a\right]^T & & \tilde{\mathbf{K}}_1^a \end{array}\right] \tag{7.6c}$$

In Equation (7.6c), the top-left partition represents the true global elastoplastic stiffness matrix from structural domain for time step j. Comparing with Equation (7.1) the following relationship is obtained for Equations (7.1) and (7.6):

$$\left[\sum_{i=1}^{nPol} \mathbf{M}\right] = \left[\begin{array}{cc} \mathbf{M}_o^s & \mathbf{M}_{o\cdot as}^s \\ [\mathbf{M}_{o\cdot as}^s]^T & \mathbf{M}_{as}^s \end{array}\right] \tag{7.7a}$$

$$\left[\sum_{i=1}^{nPol} \mathbf{K}_{ep}\right] = \left[\begin{array}{cc} \mathbf{K}_o^{ep} & \mathbf{K}_{o\cdot as}^{ep} \\ [\mathbf{K}_{o\cdot as}^{ep}]^T & \mathbf{K}_{as}^{ep} \end{array}\right] \tag{7.7b}$$

For the elastic case, the elastic stiffness matrix $\left[\sum_{i=1}^{nPol} \mathbf{K}_e\right]$ from Equation (5.22)

is used to replace the top-left partition in Equation (7.6c).

$$\left[\sum_{i=1}^{nPol}\mathbf{K}_e\right] = \begin{bmatrix} \mathbf{K}_o^{ep} & \mathbf{K}_{o\cdot as}^{ep} \\ [\mathbf{K}_{o\cdot as}^{ep}]^T & \mathbf{K}_{as}^{ep} \end{bmatrix} \tag{7.8}$$

Other notations in Equation (7.6) have the same definitions as in Equation (5.59).

The symmetric formulation for acoustic-structure interaction system considering structural elastoplasticity can again be derived using the same strategy presented in Section 5.3.3 or (Everstine, 1981). Therefore, the details of the derivation are omitted here. The incremental form of the symmetric global equations of motion for the acoustic-structure interaction system considering structural elastoplasticity for any time step j can be formulates as:

$$\bar{\mathbf{M}}_G^{ep}\Delta\ddot{\bar{\mathbf{Z}}}_G^{ep}|_{(j)} + \bar{\mathbf{C}}_G^{ep}\Delta\dot{\bar{\mathbf{Z}}}_G^{ep}|_{(j)} + \bar{\mathbf{K}}_G^{ep}\Delta\bar{\mathbf{Z}}_G^{ep}|_{(j)} = \Delta\bar{\mathbf{F}}_G^{ep}|_{(j)} \tag{7.9}$$

The global vector of unknown and load vector for symmetric formulation can be expressed as:

$$\bar{\mathbf{Z}}_G^{ep} = \left\{ \begin{array}{cc|cc|c} \mathbf{u}_o(t) & \mathbf{u}_{as}(t) & \mathbf{q}_{as}(t) & \mathbf{q}_o(t) & \tilde{\mathbf{q}}(t) \end{array} \right\}^T \tag{7.10a}$$

$$\bar{\mathbf{F}}_G^{ep} = \left\{ \begin{array}{cc|cc|c} \mathbf{F}_o(t) & \mathbf{F}_{as}^{ext}(t) & \mathbf{V}_{as}^{ext}(t) & \mathbf{V}_o(t) & 0 \end{array} \right\}^T \tag{7.10b}$$

with the same choices of notations as in Equation (5.62) and (5.63). The symmetric global mass, damping and stiffness matrices $\bar{\mathbf{M}}_G^{ep}$, $\bar{\mathbf{C}}_G^{ep}$ and $\bar{\mathbf{K}}_G^{ep}$ are also given in the following equations:

$$\bar{\mathbf{M}}_G^{ep} = \left[\begin{array}{cc|cc|c} \mathbf{M}_o^s & \mathbf{M}_{o\cdot as}^s & & & \\ [\mathbf{M}_{o\cdot as}^s]^T & \mathbf{M}_{as}^s & \multicolumn{2}{c|}{0} & 0 \\ \hline 0 & 0 & -\frac{1}{\rho_a}\mathbf{M}_{as}^a & -\frac{1}{\rho_a}\mathbf{M}_{as\cdot o}^a & \\ 0 & 0 & -\frac{1}{\rho_a}[\mathbf{M}_{as\cdot o}^a]^T & -\frac{1}{\rho_a}\mathbf{M}_o^a & -\frac{1}{\rho_a}\tilde{\mathbf{M}}_2^a \\ \hline \multicolumn{2}{c|}{0} & \multicolumn{2}{c|}{-\frac{1}{\rho_a}\left[\tilde{\mathbf{M}}_2^a\right]^T} & -\frac{1}{\rho_a}\tilde{\mathbf{M}}_1^a \end{array}\right] \tag{7.11a}$$

$$\bar{\mathbf{C}}_G^{ep} = \left[\begin{array}{cc|cc|c} & & 0 & 0 & \\ & 0 & & & 0 \\ & & -\mathbf{H}_{as} & 0 & \\ \hline 0 & -\mathbf{H}_{as}^T & 0 & 0 & \\ & & & & 0 \\ 0 & 0 & 0 & -\frac{1}{\rho_a}\mathbf{C}_o^a & \\ \hline & 0 & & 0 & -\frac{1}{\rho_a}\tilde{\mathbf{C}}_1^a \end{array}\right] \tag{7.11b}$$

$$\bar{\mathbf{K}}_G^{ep} = \left[\begin{array}{cc|cc|c} \mathbf{K}_o^{ep} & \mathbf{K}_{o\cdot as}^{ep} & & & \\ & & & 0 & 0 \\ [\mathbf{K}_{o\cdot as}^{ep}]^T & \mathbf{K}_{as}^{ep} & & & \\ \hline & & -\frac{1}{\rho_a}\mathbf{K}_{as}^a & -\frac{1}{\rho_a}\mathbf{K}_{as\cdot o}^a & \\ 0 & & & & -\frac{1}{\rho_a}\tilde{\mathbf{K}}_2^a \\ & & -\frac{1}{\rho_a}[\mathbf{K}_{as\cdot o}^a]^T & -\frac{1}{\rho_a}\mathbf{K}_o^a & \\ \hline 0 & & -\frac{1}{\rho_a}\left[\tilde{\mathbf{K}}_2^a\right]^T & & -\frac{1}{\rho_a}\tilde{\mathbf{K}}_1^a \end{array}\right] \tag{7.11c}$$

with other notations in Equation (7.11) have the same definitions as in Equation (5.64).

Equation (7.3) or (7.9) can be solved using the Newmark's scheme for transient analysis. Analogous to the dynamic elastoplastic analysis summarized in Section 7.2, the partitions in Equation (7.7b) relating to the DOFs in structural domain in the global stiffness matrix $\mathbf{K}_G^{ep}$ or $\bar{\mathbf{K}}_G^{ep}$ are the true global elastoplastic stiffness matrix $\left[\sum_{i=1}^{nPol}\mathbf{K}_{ep}\right]$ for current time step j, which is currently unknown. Again, the known elastoplastic stiffness matrix of the structural domain from the last time step $\left[\sum_{i=1}^{nPol}\mathbf{K}_{ep}|_{(j-1)}\right]$ is used to replace the partitions related to the unknown true elastoplastic stiffness matrix $\left[\sum_{i=1}^{nPol}\mathbf{K}_{ep}\right]$ in the global stiffness matrix $\mathbf{K}_G^{ep}$ or $\bar{\mathbf{K}}_G^{ep}$. The structural deformation under the applied external load and interacting force from the acoustic domain can be predicted by using the known elastoplastic stiffness matrix $\left[\sum_{i=1}^{nPol}\mathbf{K}_{ep}|_{(j-1)}\right]$. This estimation will inevitably introduce errors into both structural and acoustic results. Hence, iterative scheme, such as the modified Newton-Raphson method, should again be involved within each time step to minimize the errors. A detailed description of the computational procedures for the dynamic acoustic-structure interaction analysis considering the structural elas-

toplasticity is presented in the following section.

7.4 Computational procedure for acoustic-structure interaction analysis considering structural elastoplasticity

This section demonstrates the computational procedures for the acoustic-structure interaction analysis considering structural elastoplasticity using SBFEM. Before the computation entering the first time step, some coefficient matrices can be precomputed and stored in the system memory for later use as they are irrelevant from the corresponding state of stresses and will remain constants in the following calculations. These precomputed matrices includes the global mass and damping matrices $\mathbf{M}_G^{ep}$, $\mathbf{C}_G^{ep}$ in Equation (7.3), as well as the stiffness matrix $\mathbf{K}_G^{ep}$ in Equation (7.6c) for elastic case using Equation (7.8) (or the symmetric global mass, damping matrices and stiffness matrix in elastic case $\bar{\mathbf{M}}_G^{ep}$, $\bar{\mathbf{C}}_G^{ep}$ and $\bar{\mathbf{K}}_G^{ep}$ from Equation (7.9), if the symmetric formulation is used) before the yielding starts. After the yielding happens, only the partition in the $\mathbf{K}_G^{ep}$ or $\bar{\mathbf{K}}_G^{ep}$ related to the DOFs in the structural domain should be replaced by the elastoplastic stiffness matrix $\left[\sum_{i=1}^{nPol} \mathbf{K}_{ep}\right]$ as described by Equation (7.7b). For calculating the elastoplastic stiffness matrix $\left[\sum_{i=1}^{nPol} \mathbf{K}_{ep}\right]$, the elastoplastic strain-displacement matrix $\mathbf{B}(\xi, \eta, \zeta)$ in Equation (6.7) for 3D or $\mathbf{B}(\xi, \eta)$ in Equation (B.2) for 2D analysis is still unaltered during all time steps, which indicates that $\mathbf{\Psi}_{u_n}$, $\mathbf{S}_n$ and $\mathbf{\Psi}_\epsilon(\eta, \zeta)$ in Equation (5.17) and (6.8) (For 2D analysis, $\mathbf{\Psi}_\epsilon(\eta)$ can be calculated by Equation (B.3)) can be precomputed and stored as described at the beginning of Section 6.4 for elastoplastic analysis. The standard Newmark's method with $\gamma = 0.5$ and $\beta = 0.25$ (average acceleration scheme) is employed here for solving Equation (7.3) or (7.9) in conjunction with the modified Newton-Raphson iteration. The modified Newton-Raphson iteration is applied in each time step after

the start of yielding to minimize the residual load. For acoustic-structure interaction problems, the residual load includes both the residual force from structural domain and residual flux from acoustic domain. The relative norm χ of residual load is calculated and compared with the tolerance value χ_{tol} for checking if the solution has converged. The following computational procedure is directly applicable to the symmetrical formulation in Equation (7.9) as well by simply replacing all the matrices and vectors $\mathbf{M}_G^{ep}$, $\mathbf{C}_G^{ep}$, $\mathbf{K}_G^{ep}$ and $\mathbf{Z}_G^{ep}$, $\mathbf{F}_G^{ep}$ in the following steps with $\bar{\mathbf{M}}_G^{ep}$, $\bar{\mathbf{C}}_G^{ep}$, $\bar{\mathbf{K}}_G^{ep}$ and $\bar{\mathbf{Z}}_G^{ep}$, $\bar{\mathbf{F}}_G^{ep}$ from symmetrical formulation.

1. Initial calculations of geometrically similar and trimmed cells in both acoustic and structural domains and stored the results for later use

   (a) Calculate all global coefficient matrices for acoustic-structure interaction system $\mathbf{M}_G^{ep}$, $\mathbf{C}_G^{ep}$ and $\mathbf{K}_G^{ep}$ with elastic structure in SBFEM. Save $\mathbf{\Psi}_{u_n}$, $\mathbf{\Psi}_{q_n}$ and $\mathbf{S}_n$ in Equation (5.17) when solving each structural subdomain.

   (b) Calculate strain modes $\mathbf{\Psi}_\epsilon(\eta, \zeta)$ for these subdomains according to Equation(6.8) for 3D analysis or $\mathbf{\Psi}_\epsilon(\eta)$ in Equation (B.3) for 2D analysis.

2. Initial calculations for time step $j = 0$ in Newmark's method.

   (a) Assuming structure and acoustics at rest at the beginning and initializing the total vector of unknown $\mathbf{Z}_G^{ep}|_{(j)} = 0$, its first derivative $\dot{\mathbf{Z}}_G^{ep}|_{(j)} = 0$ and second derivative $\ddot{\mathbf{Z}}_G^{ep}|_{(j)} = 0$ at $j = 0$.

   (b) Select the time-step size Δt.

   (c) Calculate the constant matrices used later in Newmark's iterations: $\mathbf{a} = \frac{1}{\beta \Delta t}\mathbf{M}_G^{ep} + \frac{\gamma}{\beta}\mathbf{C}_G^{ep}$ and $\mathbf{b} = \frac{1}{2\beta}\mathbf{M}_G^{ep} + \Delta t \left(\frac{\gamma}{2\beta} - 1\right)\mathbf{C}_G^{ep}$.

3. For time steps $j = 1, 2, 3, \cdots$:

   (a) Compute the incremental external load vector $\Delta\mathbf{F}_G^{ep}|_{(j)}$ between time step $j-1$ and j in Equation (7.3).

(b) Compute effective incremental load vector $\Delta\hat{\mathbf{F}}^{ep}_{G,ext}|_{(j)}$.

$$\Delta\hat{\mathbf{F}}^{ep}_{G,ext}|_{(j)} = \Delta\mathbf{F}^{ep}_{G}|_{(j)} + \mathbf{a}\dot{\mathbf{Z}}^{ep}_{G}|_{(j-1)} + \mathbf{b}\ddot{\mathbf{U}}_{b}|_{(j-1)} \tag{7.12}$$

(c) Repeat Steps 3.(b) to 3.(e) in the load-step loop in the procedures for static elastoplastic analysis in Section 6.4.1 to calculate the total tangent elastoplastic stiffness matrices $\mathbf{K}_{ep}|_{(j-1)}$ for each structural subdomain. If all structural subdomains are elastic, then jump to Step (e).

(d) Assemble the elastoplastic stiffness matrix $\left[\sum_{i=1}^{nPol}\mathbf{K}_{ep}|_{(j-1)}\right]$ for structural domain. Then, replace the partition in the global stiffness matrix for acoustic-structure interaction system $\mathbf{K}^{ep}_{G}|_{(j-1)}$ corresponding to DOFs in structural domain by $\left[\sum_{i=1}^{nPol}\mathbf{K}_{ep}|_{(j-1)}\right]$ according to Equations (7.7b) and (7.6c).

(e) Compute global effective stiffness matrix $\hat{\mathbf{K}}_{ep}|_{(j-1)}$.

$$\hat{\mathbf{K}}_{ep}|_{(j-1)} = \mathbf{K}^{ep}_{G}|_{(j-1)} + \frac{\gamma}{\beta\Delta t}\mathbf{C}^{ep}_{G} + \frac{1}{\beta(\Delta t)^2}\mathbf{M}^{ep}_{G} \tag{7.13}$$

(f) Solving initial incremental vector of unknown $\Delta\mathbf{Z}^{ep}_{G}|_{(j)}$ for each time step.

$$\Delta\mathbf{Z}^{ep}_{G}|_{(j)} = \left[\hat{\mathbf{K}}_{ep}|_{(j-1)}\right]^{-1}\Delta\hat{\mathbf{F}}^{ep}_{G,ext}|_{(j)} \tag{7.14}$$

(g) At equilibrium iteration $k = 0$, initializing the incremental vector of unknown $\Delta\mathbf{Z}^{ep}_{G}|^{k}_{(j)} = \Delta\mathbf{Z}^{ep}_{G}|_{(j)}$, accumulated vector of unknown $\mathbf{Z}^{ep}_{G}|^{k}_{(j-1)} = \sum_{j=1}^{j-1}\Delta\mathbf{Z}^{ep}_{G}|_{(j)}$ to last time step $j-1$ ($\mathbf{Z}^{ep}_{G}|^{k}_{(j-1)} = 0$ for $j = 1$) and accumulated total effective external load vector $\hat{\mathbf{F}}^{ep,tot}_{G,ext}|_{(j)} = \sum_{j=1}^{j}\Delta\hat{\mathbf{F}}^{ep}_{G,ext}|_{(j)}$ to this time step j for each subdomain.

(h) The modified Newton-Raphson algorithm is applied to correct the incremental vector of unknown $\Delta\mathbf{Z}^{ep}_{G}|_{(j)}$ in each time step. For equilibrium iterations $k = 1, 2, 3, \cdots$:

i. Repeat Steps 3.(i).i to 3.(i).iv in the equilibrium iterations for static

elastoplastic analysis in Section 6.4.1 and assemble the global total internal forces vectors in statics $\mathbf{F}_{int}^{static}|_{(j)}^{k} = \left\{ \sum_{i=1}^{nPol} \mathbf{F}_{int}^{tot}|_{(j)}^{k} \right\}$ for the structural domain.

ii. Calculate the static incremental load vector in modified Newton-Raphson iteration for acoustic-structure interaction problem $\mathbf{F}_{G,int}^{ep,static}|_{(j)}^{k}$ defined by:

$$\mathbf{F}_{G,int}^{ep,static}|_{(j)}^{k} = \mathbf{K}_{G}^{ep} \left(\mathbf{Z}_{G}^{ep}|_{(j-1)}^{k} + \Delta \mathbf{Z}_{G}^{ep}|_{(j)}^{k} \right) = \left\{ \begin{array}{c} \mathbf{F}_{int}^{ep,static}|_{(j)}^{k} \\ \mathbf{R}_{int}^{ep,static}|_{(j)}^{k} \end{array} \right\} \quad (7.15)$$

which includes both the static total internal forces vector $\mathbf{F}_{int}^{ep,static}|_{(j)}^{k}$ from structural domain and the static total internal flux vector $\mathbf{R}_{int}^{ep,static}|_{(j)}^{k}$ from acoustic domain. The evaluation of $\mathbf{F}_{G,int}^{ep,static}|_{(j)}^{k}$ is explained in Section 7.4.1. For unsymmetrical formulation in Equation (7.3), it is given by Equations (7.28) and (7.27b). For symmetrical formulation in Equation (7.9), $\mathbf{F}_{G,int}^{ep,static}|_{(j)}^{k}$ is calculated by Equations (7.32).

iii. Calculate the effective global vector for total internal load $\hat{\mathbf{F}}_{G,int}^{ep,dynamic}|_{(j)}^{k}$,

$$\begin{aligned} &\hat{\mathbf{F}}_{G,int}^{ep,dynamic}|_{(j)}^{k} \\ &\quad = \mathbf{F}_{G,int}^{ep,static}|_{(j)}^{k} + \left(\hat{\mathbf{K}}_{ep}|_{(j-1)} - \mathbf{K}_{G}^{ep}|_{(j-1)} \right) \left(\mathbf{Z}_{G}^{ep}|_{(j-1)}^{k} + \Delta \mathbf{Z}_{G}^{ep}|_{(j)}^{k} \right) \end{aligned} \quad (7.16)$$

iv. Calculate effective global residual load vector $d\hat{\mathbf{F}}^{ep}|_{(j)}^{k} = \hat{\mathbf{F}}_{G,ext}^{ep,tot}|_{(j)} - \hat{\mathbf{F}}_{G,int}^{ep,dynamic}|_{(j)}^{k}$

v. Calculate incremental vector of unknown $d\mathbf{Z}_{G}^{ep}|_{(j)}^{k}$ due to residual force based on Step (f) in time-step iteration.

$$d\mathbf{Z}_{G}^{ep}|_{(j)}^{k} = \left[\hat{\mathbf{K}}|_{(j-1)} \right]^{-1} d\hat{\mathbf{F}}^{ep}|_{(j)}^{k} \quad (7.17)$$

vi. Correct the incremental displacement vector $\Delta \mathbf{Z}_{G}^{ep}|_{(j)}^{k} = \Delta \mathbf{Z}_{G}^{ep}|_{(j)}^{k-1} + d\mathbf{Z}_{G}^{ep}|_{(j)}^{k}$.

vii. Calculate norm of effective residual load vector $\chi = \left\| d\hat{\mathbf{F}}^{ep}|_{(j)}^{k} \right\|$.

viii. Check for convergence:

- If $\chi > \chi_{tol}$, set iteration index $k = k + 1$ and return to Step i.
- If $\chi \leq \chi_{tol}$, exit the equilibrium iteration.

(i) Compute incremental velocity vector $\Delta\dot{\mathbf{Z}}_G^{ep}|_{(j)}^{k}$,

$$\Delta\dot{\mathbf{Z}}_G^{ep}|_{(j)}^{k} = \frac{\gamma}{\beta\Delta t}\Delta\mathbf{Z}_G^{ep}|_{(j)}^{k} - \frac{\gamma}{\beta}\dot{\mathbf{Z}}_G^{ep}|_{(j)} + \Delta t\left(1 - \frac{\gamma}{2\beta}\right)\ddot{\mathbf{Z}}_G^{ep}|_{(j)} \tag{7.18}$$

and incremental acceleration vector$\Delta\ddot{\mathbf{U}}_b|_{(j)}^{k}$

$$\Delta\ddot{\mathbf{Z}}_G^{ep}|_{(j)}^{k} = \frac{1}{\beta(\Delta t)^2}\Delta\mathbf{Z}_G^{ep}|_{(j)}^{k} - \frac{1}{\beta\Delta t}\dot{\mathbf{Z}}_G^{ep}|_{(j)} - \frac{1}{2\beta}\ddot{\mathbf{Z}}_G^{ep}|_{(j)} \tag{7.19}$$

(j) Update the total displacement vector

$$\mathbf{Z}_G^{ep}|_{(j)} = \mathbf{Z}_G^{ep}|_{(j-1)} + \Delta\mathbf{Z}_G^{ep}|_{(j)}^{k} \tag{7.20}$$

total velocity vector

$$\dot{\mathbf{Z}}_G^{ep}|_{(j)} = \dot{\mathbf{Z}}_G^{ep}|_{(j-1)} + \Delta\dot{\mathbf{Z}}_G^{ep}|_{(j)}^{k} \tag{7.21}$$

total acceleration vector

$$\ddot{\mathbf{Z}}_G^{ep}|_{(j)} = \ddot{\mathbf{Z}}_G^{ep}|_{(j-1)} + \Delta\ddot{\mathbf{Z}}_G^{ep}|_{(j)}^{k} \tag{7.22}$$

and set the time-step number $j = j + 1$, then returns to Step (a) in time-step loop.

7.4.1 Calculate static incremental load vector in modified Newton-Raphson iteration for acoustic-structure interaction problem

The evaluation of static incremental load vector in Equation (7.15) from the Step 3.(h).ii in the above computational procedure is explained here. First of all, via observing Equations (7.6c), (7.7b) and (5.41c), the global stiffness matrix for the

acoustic-structure interaction system considering structural elastoplasticity $\mathbf{K}_G^{ep}$ based on the unsymmetrical formulation can be subdivided into parts related to structural domain, acoustic domain and coupling part respectively as

$$\mathbf{K}_G^{ep} = \left[\begin{array}{c|c} \left[\sum_{i=1}^{nPol} \mathbf{K}_{ep}\right] & \mathbf{K}_H \\ \hline 0 & \mathbf{K}_G^a \end{array}\right] \tag{7.23}$$

with $\left[\sum_{i=1}^{nPol} \mathbf{K}_{ep}\right]$ the elastoplastic stiffness matrix for structure, $\mathbf{K}_G^a$ the stiffness matrix for acoustic domain and $\mathbf{K}_H$ represents the coupling part in Equation (7.6c) and defined as

$$\mathbf{K}_H = \left[\begin{array}{cc|c} 0 & 0 & \\ -\mathbf{H}_{as} & 0 & 0 \end{array}\right] \tag{7.24}$$

The vector of unknown $\mathbf{Z}_G^{ep}$ from Equation (7.4) can also be partitioned as

$$\mathbf{Z}_G^{ep} = \left\{ \begin{array}{c|c} \mathbf{U}_b & \mathbf{z}_G \end{array} \right\}^T \tag{7.25}$$

with the structural displacement $\mathbf{U}_b = \{ \begin{array}{cc} \mathbf{u}_o(t) & \mathbf{u}_{as}(t) \end{array} \}^T$ from Equation (6.20) and vector of unknowns in acoustics $\mathbf{z}_G = \{ \begin{array}{ccc} \mathbf{p}_{as}(t) & \mathbf{p}_o(t) & \tilde{\mathbf{p}}(t) \end{array} \}^T$ from Equation (5.39). Substitute Equation (7.23) and (7.25) into (7.15) yields

$$\mathbf{F}_{G,int}^{ep,static}|_{(j)}^k = \left[\begin{array}{c|c} \left[\sum_{i=1}^{nPol} \mathbf{K}_{ep}\right] & \mathbf{K}_H \\ \hline 0 & \mathbf{K}_G^a \end{array}\right] \left\{ \begin{array}{c} \mathbf{U}_b|_{(j-1)}^k + \Delta\mathbf{U}_b|_{(j)}^k \\ \hline \mathbf{z}_G|_{(j-1)}^k + \Delta\mathbf{z}_G|_{(j)}^k \end{array} \right\} = \left\{ \begin{array}{c} \mathbf{F}_{int}^{ep,static}|_{(j)}^k \\ \hline \mathbf{R}_{int}^{ep,static}|_{(j)}^k \end{array} \right\} \tag{7.26}$$

Thus, the static total internal forces vector $\mathbf{F}_{int}^{ep,static}|_{(j)}^k$ from structural domain and the static total internal flux vector $\mathbf{R}_{int}^{ep,static}|_{(j)}^k$ from acoustic domain can be obtained from Equation (7.26) for unsymmetrical formulation:

$$\mathbf{F}_{int}^{ep,static}|_{(j)}^k = \left[\sum_{i=1}^{nPol} \mathbf{K}_{ep}\right] \left(\mathbf{U}_b|_{(j-1)}^k + \Delta\mathbf{U}_b|_{(j)}^k\right) + \mathbf{K}_H \left(\mathbf{z}_G|_{(j-1)}^k + \Delta\mathbf{z}_G|_{(j)}^k\right) \tag{7.27a}$$

$$\mathbf{R}_{int}^{ep,static}|_{(j)}^k = \mathbf{K}_G^a \left(\mathbf{z}_G|_{(j-1)}^k + \Delta\mathbf{z}_G|_{(j)}^k\right) \tag{7.27b}$$

In Equation (7.27), $\mathbf{K}_H$ and $\mathbf{K}_G^a$ remain constants in every time step. $\left[\sum_{i=1}^{nPol} \mathbf{K}_{ep}\right]$

is the unknown true elastoplastic stiffness matrix for structure. Thus, the first term on the right-hand-side of Equation (7.27a), which represents the internal nodal forces in statics, can only be evaluated by Equation (6.55) in SBFEM and obtained at Step 3.(h).i as $\mathbf{F}_{int}^{static}|_{(j)}^{k}$ in the computational procedure in Section 7.4 for the kth Newton-Raphson iteration in the time step j. Therefore, the static total internal forces vector $\mathbf{F}_{int}^{ep,static}|_{(j)}^{k}$ can be evaluated by:

$$\mathbf{F}_{int}^{ep,static}|_{(j)}^{k} = \mathbf{F}_{int}^{static}|_{(j)}^{k} + \mathbf{K}_H \left(\mathbf{z}_G|_{(j-1)}^{k} + \Delta \mathbf{z}_G|_{(j)}^{k} \right) \tag{7.28}$$

The second term on the right-hand-side of Equation (7.28) represents the contribution from the acoustic domain in the static total internal forces vector $\mathbf{F}_{int}^{ep,static}|_{(j)}^{k}$.

For the symmetric formulation of acoustic-structure interaction system considering structural elastoplasticity. $\bar{\mathbf{K}}_G^{ep}$ in Equation (7.11c) can be subdivided following the same way in Equation (7.23) as:

$$\bar{\mathbf{K}}_G^{ep} = \left[\begin{array}{c|c} \left[\sum_{i=1}^{nPol} \mathbf{K}_{ep} \right] & 0 \\ \hline 0 & -\frac{1}{\rho_a} \mathbf{K}_G^a \end{array} \right] \tag{7.29}$$

The vector of unknown $\bar{\mathbf{Z}}_G^{ep}$ in Equation (7.10a) can also be partitioned as

$$\bar{\mathbf{Z}}_G^{ep} = \left\{ \begin{array}{c|c} \mathbf{U}_b & \bar{\mathbf{z}}_G \end{array} \right\}^T \tag{7.30}$$

with the vector of unknowns in acoustic domain for symmetric formulation $\bar{\mathbf{z}}_G = \{ \mathbf{q}_{as}(t) \quad \mathbf{q}_o(t) \quad \tilde{\mathbf{q}}(t) \}^T$ with each variable defined by Equation (5.60). Substitute Equation (7.29) and (7.30) into (7.15) yields

$$\mathbf{F}_{G,int}^{ep,static}|_{(j)}^{k} = \left[\begin{array}{c|c} \left[\sum_{i=1}^{nPol} \mathbf{K}_{ep} \right] & 0 \\ \hline 0 & -\frac{1}{\rho_a} \mathbf{K}_G^a \end{array} \right] \left\{ \begin{array}{c} \mathbf{U}_b|_{(j-1)}^{k} + \Delta \mathbf{U}_b|_{(j)}^{k} \\ \hline \bar{\mathbf{z}}_G|_{(j-1)}^{k} + \Delta \bar{\mathbf{z}}_G|_{(j)}^{k} \end{array} \right\} = \left\{ \begin{array}{c} \mathbf{F}_{int}^{ep,static}|_{(j)}^{k} \\ \hline \mathbf{R}_{int}^{ep,static}|_{(j)}^{k} \end{array} \right\} \tag{7.31}$$

Thus, $\mathbf{F}_{int}^{ep,static}|_{(j)}^{k}$ and $\mathbf{R}_{int}^{ep,static}|_{(j)}^{k}$ can be obtained from Equation (7.31) for symme-

tric formulation:

$$\mathbf{F}_{int}^{ep,static}|_{(j)}^{k} = \mathbf{F}_{int}^{static}|_{(j)}^{k} \tag{7.32a}$$

$$\mathbf{R}_{int}^{ep,static}|_{(j)}^{k} = -\frac{1}{\rho_a}\mathbf{K}_G^a\left(\bar{\mathbf{z}}_G|_{(j-1)}^{k} + \Delta\bar{\mathbf{z}}_G|_{(j)}^{k}\right) \tag{7.32b}$$

7.5 Numerical examples

Three numerical examples are presented in this section to validate the proposed approach for both 2D and 3D acoustic-structure interaction analyses considering structural elastoplasticity based on SBFEM. Two 2D examples, which include the same simply supported beam submerged in an infinite acoustic plane and interacted with a semi-infinite acoustic plane, are studied in Section 7.5.1 and 7.5.2 separately. The beam used in Section 7.5.1 and 7.5.2 has the same dimensions as it used in Section 5.4.2 from Chapter 5. In the last example in Section 7.5.3, a 3D elastoplastic plate submerged in infinite acoustic space, which has the same geometry as in Section 5.4.4 from Chapter 5, is simulated. All structures in this section are considered to be elastoplastic with the material properties of: Young's modulus $E = 100$GPa, yield stress $\sigma_y = 0.16$MPa, structural density $\rho_s = 1500\text{kg/m}^3$ and Poisson ratio $\nu = 0.333$. Elastic-perfectly plastic material is also assumed for all structures with von Mises yield criterion. All acoustic media are assumed to be water with the sound speed of $c = 1482$m/s and acoustic density of $\rho_a = 1000\text{kg/m}^3$. Reference solutions are calculated for all three examples using FEM in ANSYS with extended meshes for the 2D and 3D unbounded acoustic domains to verify the feasibility and accuracy of the proposed SBFEM. Newmark's scheme presented in Section 7.4 with the parameters $\alpha = 0.5$ and $\beta = 0.25$ are applied here with modified Newton-Raphson iteration to obtain the solutions for elastoplastic structures and linear acoustic domains.

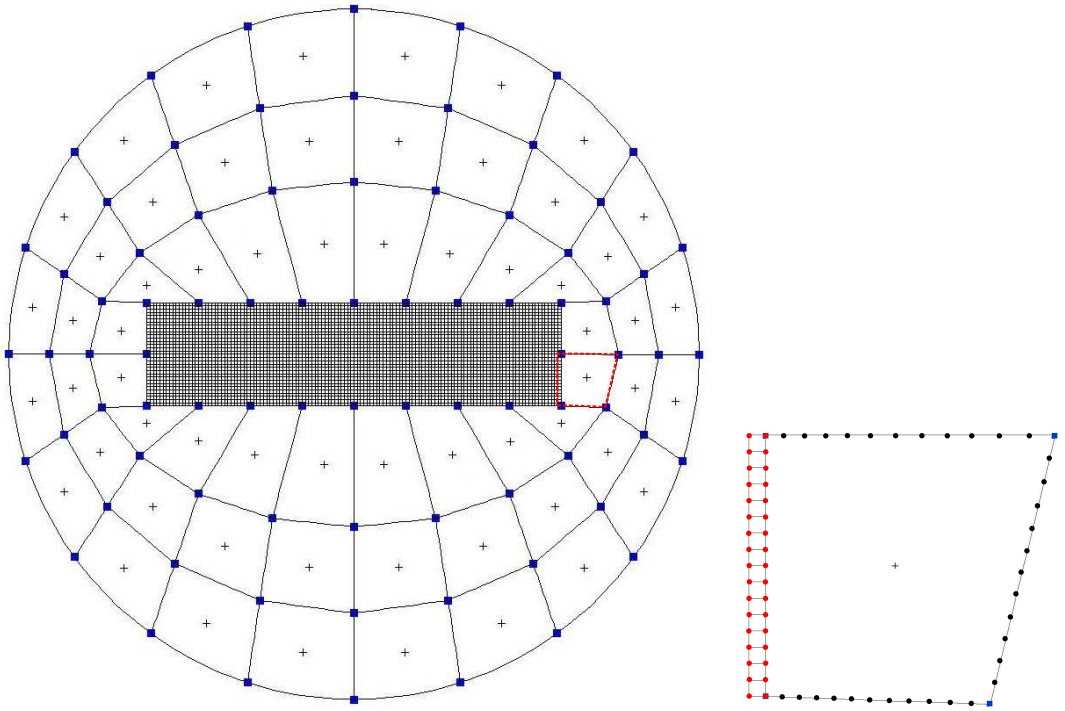

(a) (b)

Figure 7.1. The SBFEM mesh of an elastoplastic beam submerged in infinite acoustic domain: (a) the mesh of whole coupled system and (b) a detailed view of subdomains around acoustic-structure interface.

7.5.1 Elastoplastic beam submerged in infinite acoustic plane

A simply supported elastoplastic beam submerged in infinite acoustic plane is studied in this example. The geometrical layout of the SBFEM model for this problem is the same as the acoustic-structure interaction system demonstrated in Section 5.4.2 and can be referred to Figure 5.9. The red beam in Figure 5.9 is elastic in Section 5.4.2 but is considered to be elastoplastic in this example and subjected to the same uniformly distributed load $F_b(t)$ on the top surface $\overline{AB}$. The time history of $F_b(t)$ and its Fourier transform are presented in Figures 5.10(a) and 5.10(b) respectively.

Because the applied load and acoustic domain are the same as in Section 5.4.2, the shortest wavelength in acoustic domain remains the same. The same SBFEM mesh is used for the acoustic domain. For the structural domain, smaller subdomain size is adopted with 128 subdomains in horizontal direction and 32 subdomains in

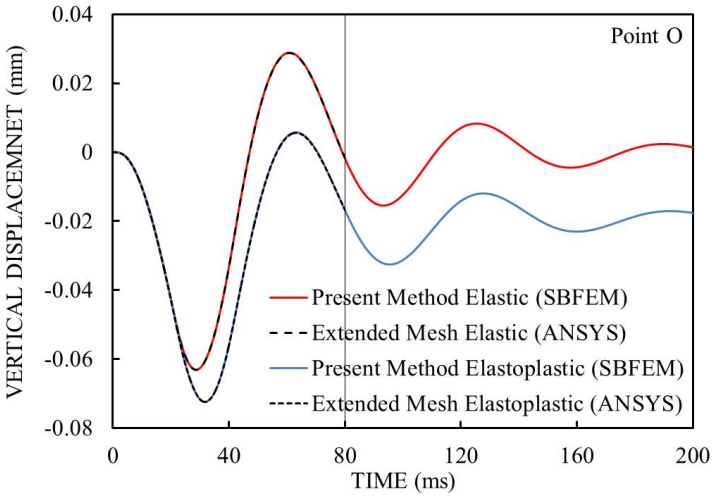

Figure 7.2. Structural displacement at point O in the coupled model of an elastoplastic beam submerged in infinite acoustic domain.

the vertical direction. This is for better predicting the elastoplastic behavior of the beam with constant internal stresses and elastoplastic constitutive matrices in each subdomain. The SBFEM mesh used in this example is shown in Figure 7.1 with a closer view of subdomains surrounded by the red dash line near the acoustic-structure interface. For the clearer presentation of the coupled mesh of acoustic domain and structure, the red keypoints for defining the structural subdomains and the scaling centre are not shown in Figure 7.1(a). Only one 2-node element is used on each edge of the structural subdomain. Analogously, two terms of continued-fractions are used for bounded acoustic domain. Orders of high-frequency and low-frequency continued-fraction expansions for circular open boundary are again selected as $M_H = M_L = 1$. Newmark's method is applied here with the constant time step of $\Delta t = 0.02ms$ to achieve the convergence of modified Newton-Raphson iteration within each time step.

Solutions calculated by the proposed SBFEM at Points O$(0\text{m}, 0\text{m})$, E$(0\text{m}, 3\text{m})$ and F$(0\text{m}, 20\text{m})$ from Figure 5.9 are plotted as blue solid lines in Figures 7.2 - 7.4. These results are also verified by the reference solutions obtained using FEM in ANSYS as black dotted lines in corresponding figures. Those reference solutions from ANSYS are calculated using extended mesh with the radius of 170m for avoiding

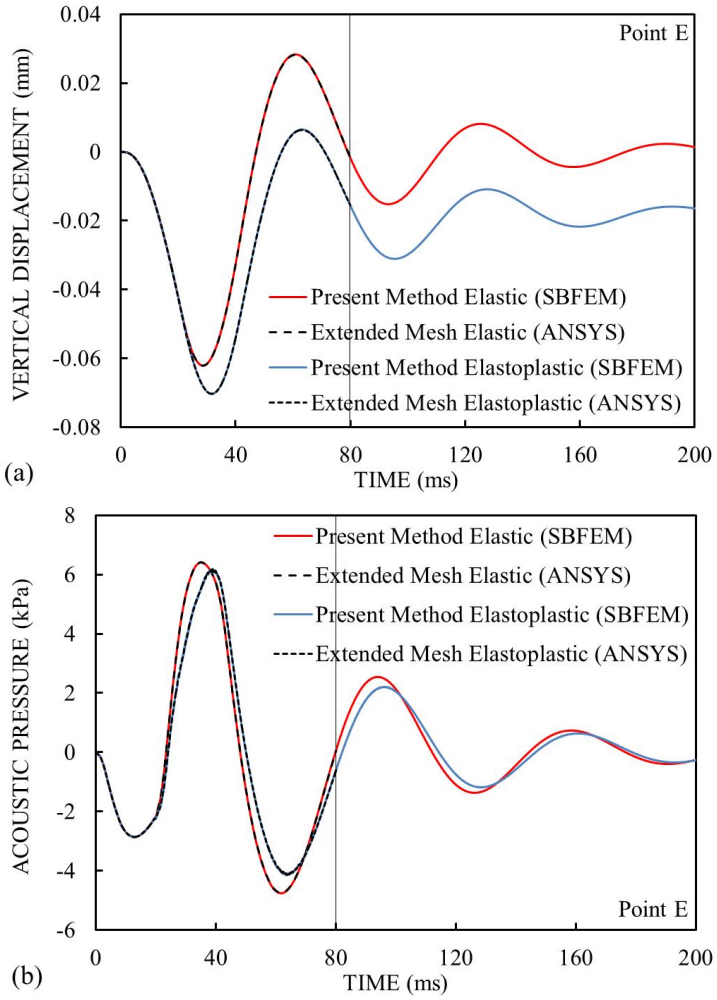

Figure 7.3. Results at point E in the coupled model of an elastoplastic beam submerged in infinite acoustic domain: (a) vertical displacement and (b) acoustic pressure.

reflected waves during the first 80ms for unbounded acoustic domain. The structural domain in FEM mesh is also divided into 128 and 32 elements in horizontal and vertical directions respectively with 4-node quadrilateral elements. 3-node triangular elements with the maximum edge length of 0.6m are again used in ANSYS for the acoustic domain to achieve mesh transition on the acoustic-structure interface.

Point E is located on the acoustic-structure interface, both vertical displacement and acoustic pressure at this point are given in Figure 7.3(a) and (b), respectively. Points O and F are located in the structural and acoustic domains separately, thus the results of vertical displacement and acoustic pressure for these two points are illustrated in Figures 7.2 and 7.4 separately. Very good agreements with the re-

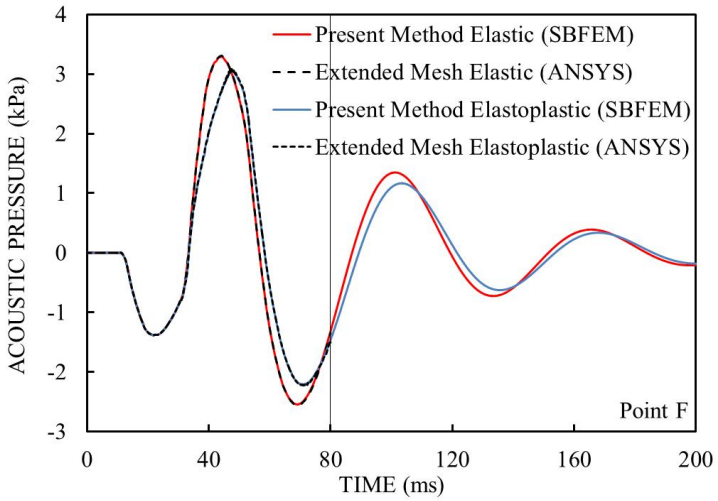

Figure 7.4. Acoustic pressure at point F in the coupled model of an elastoplastic beam submerged in infinite acoustic domain.

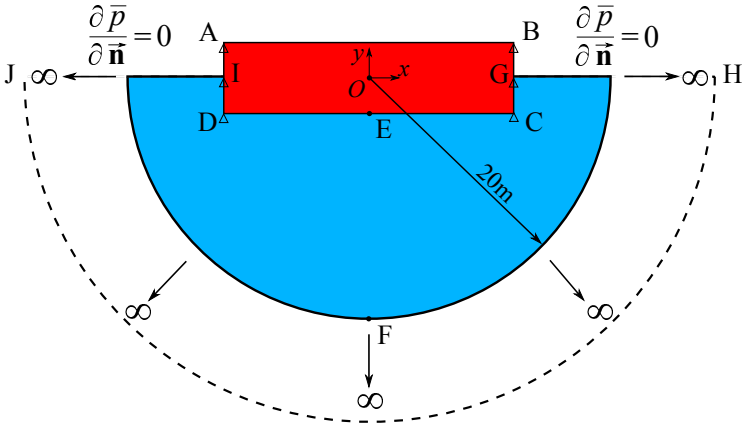

Figure 7.5. The acoustic-structure interaction model of an elastoplastic beam interacting with semi-infinite acoustic domain.

ference solutions are obtained. For all the results given in Figures 7.2 - 7.4, the results obtained in Section 5.4.2 for the case of an elastic beam, are plotted in the corresponding figures for comparisons with solutions obtained by considering the elastoplastic behavior of structure.

7.5.2 Interaction of elastoplastic beam with semi-infinite acoustic plane

For further verifying the proposed SBFEM for acoustic-structure interaction analysis considering the elastoplastic behavior of structure, The simply supported beam used

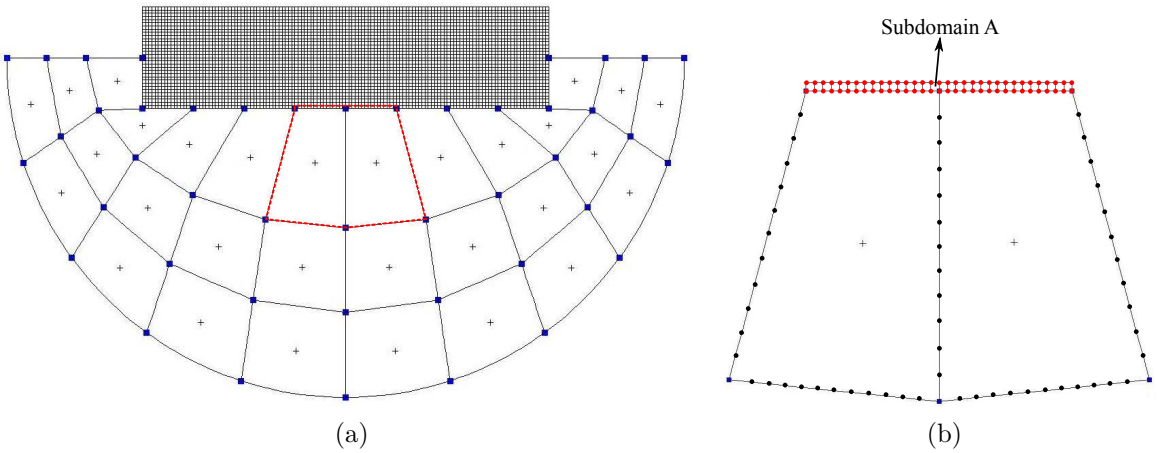

Figure 7.6. The SBFEM mesh of an elastoplastic beam interacting with semi-infinite acoustic domain: (a) the mesh of whole coupled system and (b) a detailed view of subdomains around acoustic-structure interface.

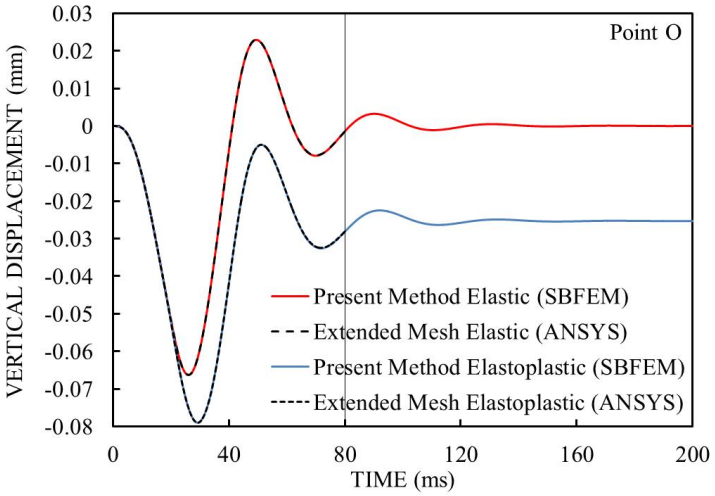

Figure 7.7. Structural displacement at point O in the coupled model of an elastoplastic beam interacting with semi-infinite acoustic domain.

in the last example is again used here and half of it is submerged in the semi-infinite acoustic plane this time. The SBFEM model of this coupled system is described by Figure 7.5. The radius of the open boundary, which is a semicircle this time, is still 20m. The boundary conditions on the top surface of the acoustic domain are assumed to be $\frac{\partial \bar{p}}{\partial \bar{\mathbf{n}}} = 0$ along the semi-infinite lines $\overline{GH}$ and $\overline{IJ}$. The top surface $\overline{AB}$ of this beam is again subjected to the same uniformly distributed load $F_b(t)$ presented in Figures 5.10(a) and 5.10(b) with its Fourier transform.

Because all the material properties, geometry of structure and applied load used

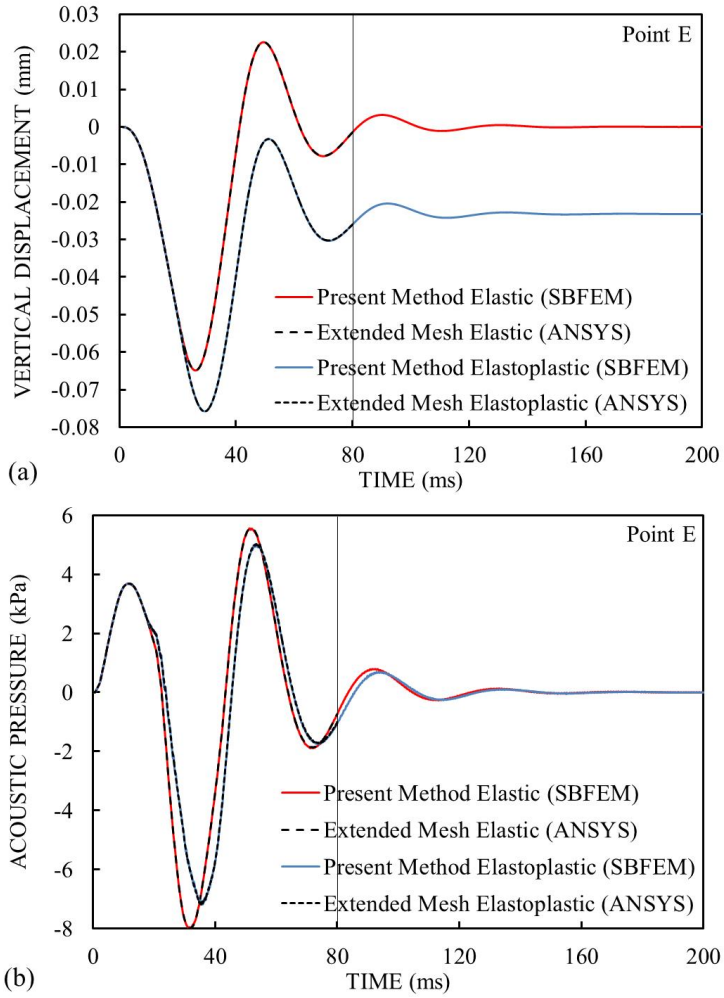

Figure 7.8. Results at point E in the coupled model of an elastoplastic beam interacting with semi-infinite acoustic domain: (a) vertical displacement and (b) acoustic pressure.

in the last example in Section 7.5.1 are directly used in this model except for the geometry of acoustic domain, the subdomain sizes and element type used in the mesh presented in Figure 7.1 are directly adopted here with only half of its mesh for acoustic domain. The final mesh is illustrated in Figure 7.6(a) with a detailed view of subdomains inside the red dash line near the acoustic-structure interface in Figure 7.6(b). Two terms of continued-fractions are used for bounded acoustic subdomains. Orders of high- and low-frequency continued-fraction expansions for the semicircular open boundary are selected as $M_H = M_L = 1$. The structural subdomain A, with the coordinate of its scaling centre $(-9.375\text{cm}, -290.625\text{cm})$, is

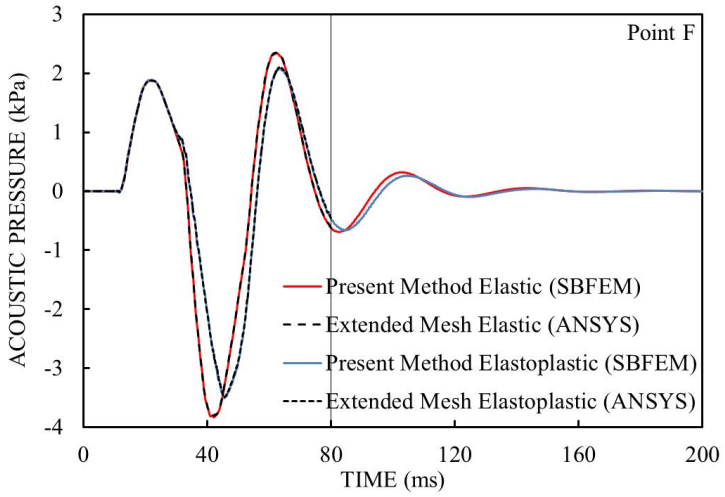

Figure 7.9. Acoustic pressure at point F in the coupled model of an elastoplastic beam interacting with semi-infinite acoustic domain.

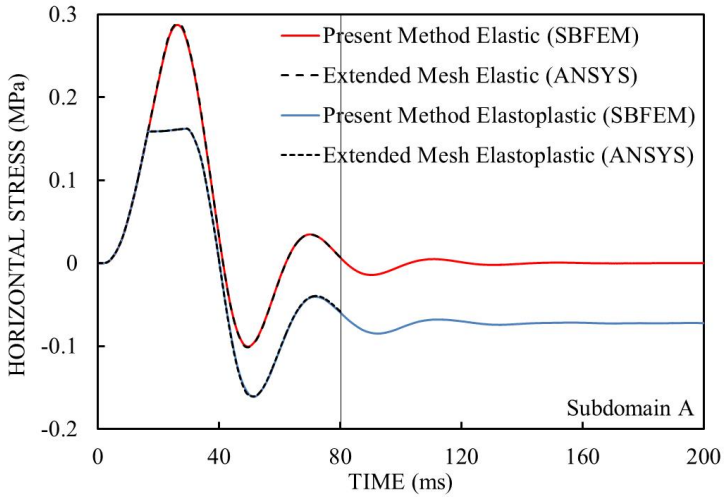

Figure 7.10. Horizontal stress in subdomain A of the coupled model of an elastoplastic beam interacting with semi-infinite acoustic domain.

shown in Figure 7.6(b) and will be used for checking the stress results later. In this example, the constant time step $\Delta t = 0.02$ms is again used in Newmark's method to achieve the convergence of modified Newton-Raphson iteration within each step.

The results obtained by the proposed SBFEM at Points O(0m, 0m), E(0m, −3m) and F(0m, −20m) in Figure 7.5 are plotted as blue solid lines in Figures 7.7 - 7.9. Reference solutions obtained using FEM in ANSYS are plotted in the corresponding figures as black dotted lines to verify the accuracy of present results. Those reference solutions from ANSYS are calculated via the same FEM mesh used in Section 7.5.1

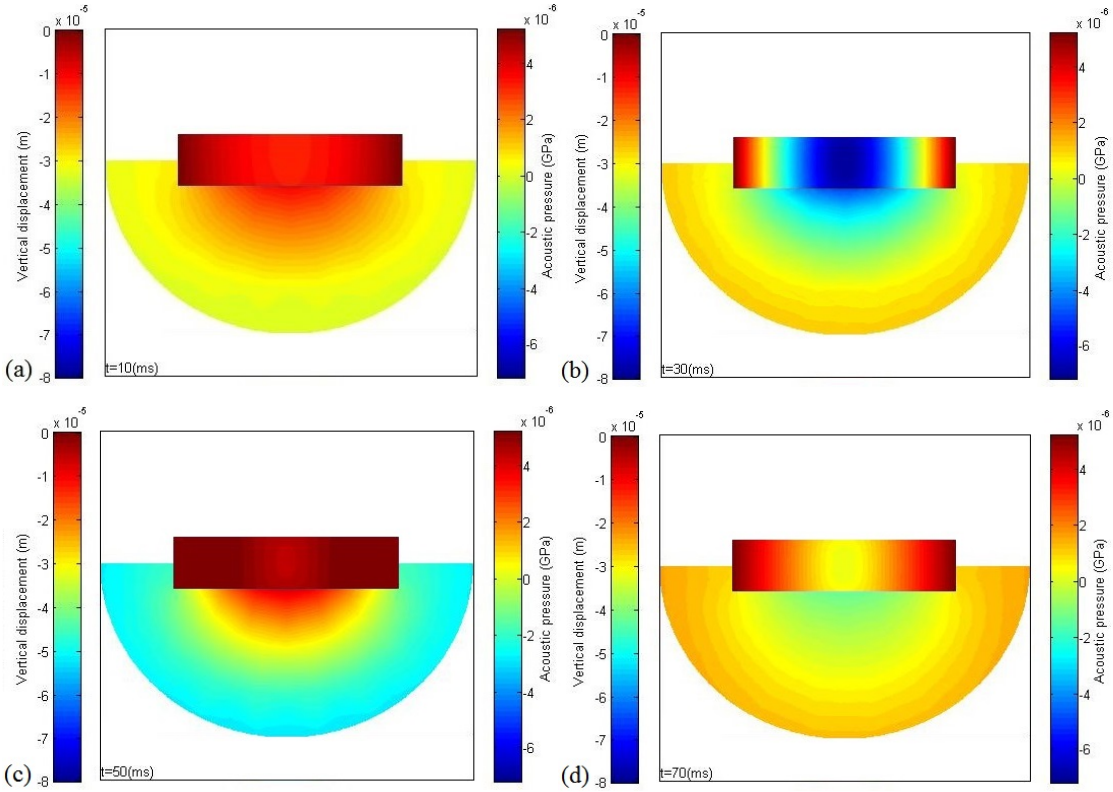

Figure 7.11. Coupled system of elastoplastic beam interacting with semi-infinite acoustic domain. Contour plots of vertical displacements and acoustic pressures at: (a) $t = 10$ms, (b) $t = 30$ms, (c) $t = 50$ms and (d) $t = 70$ms.

except that only lower-half of the acoustic mesh is required this time (the semi-infinite acoustic domain). Vertical displacements are plotted for points O and E in Figures 7.7 and 7.8(a), while the acoustic pressures at point E and F are shown in Figures 7.8(b) and 7.9. They all show very good agreements with the reference solutions from ANSYS. Solutions obtained by assuming elastic behavior of the beam are again plotted in all Figures 7.7 - 7.9 with red solid lines denoting SBFEM results and black dash lines denoting reference solutions from ANSYS for comparisons.

In addition, the horizontal stress of subdomain A is also given in Figure 7.10. In this figure, the blue solid line represents the horizontal stress obtained using SBFEM, which is a constant within this subdomain. The black dotted line represents the horizontal stress calculated using FEM in ANSYS, which is actually the average horizontal stress of the 2D quadrilateral element with the same position and shape

of subdomain A in SBFEM mesh. The average horizontal stresses in subdomain A calculated by SBFEM and ANSYS under the assumption of elastic structure are also shown in red solid line and black dash line respectively. This is achieved by simply setting the yield stress of structure σ_y to a very large value and thus avoid yielding. Contour plots of the results, which include vertical displacement of structure and acoustic pressure of acoustic domain, of this coupled system are illustrated in Figure 7.11 at times $t = 10$ms, $t = 30$ms, $t = 50$ms and $t = 70$ms.

7.5.3 3D elastoplastic plate submerged in infinite acoustic space

The feasibility and accuracy of the proposed approach for 3D acoustic-structure interaction analysis considering structural elastoplasticity are investigated in this numerical example. The 3D square plate and spherical open boundary have the same dimensions as the example shown in Figure 5.24 Section 5.4.4. In contrast to the elastic plate used in the numerical example in Section 5.4.4, the plate here is assumed to be made of elastic-perfectly plastic material with the material properties listed at the beginning of Section 7.5. Again, four side faces around the plate are fixed in the loading (z) direction. The transient load $F_{ep}(t)$ defined by the following Equation (7.33) is applied on the top surface of the plate:

$$F_{ep}(t) = \begin{cases} 4.5 \times (1 - \cos 0.05\pi t) \text{ (kPa)} & \text{when } 0 \leq t \leq 40\text{ms}, \\ 0 \qquad\qquad\qquad\qquad\quad \text{(kPa)} & \text{when } 40\text{ms} < t. \end{cases} \tag{7.33}$$

The time history and Fourier transform of $F_{ep}(t)$ are also plotted in Figure 7.12.

The maximum frequency of interest is approximately equal to $\omega_{max} = 0.6$rad/ms, which is the same as the maximum relevant frequency of the applied load used in Section 5.4.4. Therefore, the same octree mesh for acoustic domain in Section 5.4.4 is again used here with the maximum and minimum cell sizes of 1.6m and 0.4m separately. Since the elastoplastic behavior is considered for the plate, it is uniformly

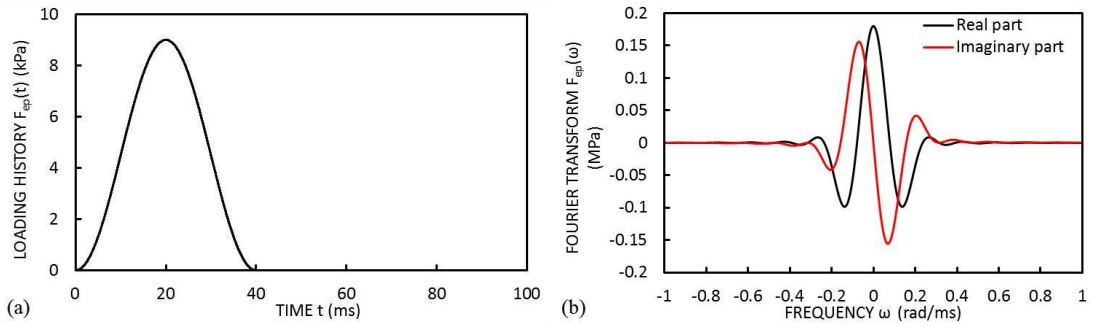

Figure 7.12. Time variation $F_{ep}(t)$ of transient load applied on the top of plate: (a) time history and (b) Fourier transform.

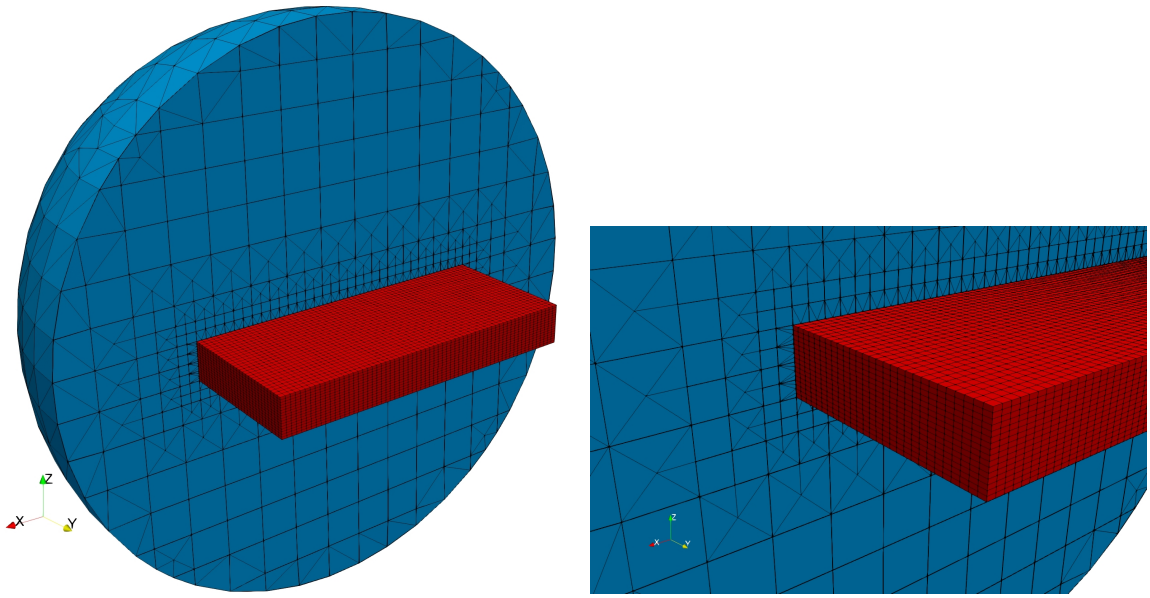

Figure 7.13. The SBFEM mesh of a 3D elastoplastic plate submerged in infinite acoustic domain: (a) coupled mesh with part of the acoustic mesh showing details of inside and (b) a detailed view of the mesh around acoustic-structure interface.

divided into 64 subdomains in the x and y directions and 16 subdomains in the z-direction in this example for accuracy. 4-mode quadrilateral elements are employed in the structural mesh. The coupled mesh for this acoustic-structure interaction system is shown in Figure 7.13 with the red part denoting structural mesh and blue part denoting acoustic mesh. Due to the differences of mesh sizes used in acoustic and structural domain, the two meshes are coupled along the acoustic-structure interface via subdividing the surface elements into matched quadrilateral or triangular elements. Details of the mesh around acoustic-structure interface are

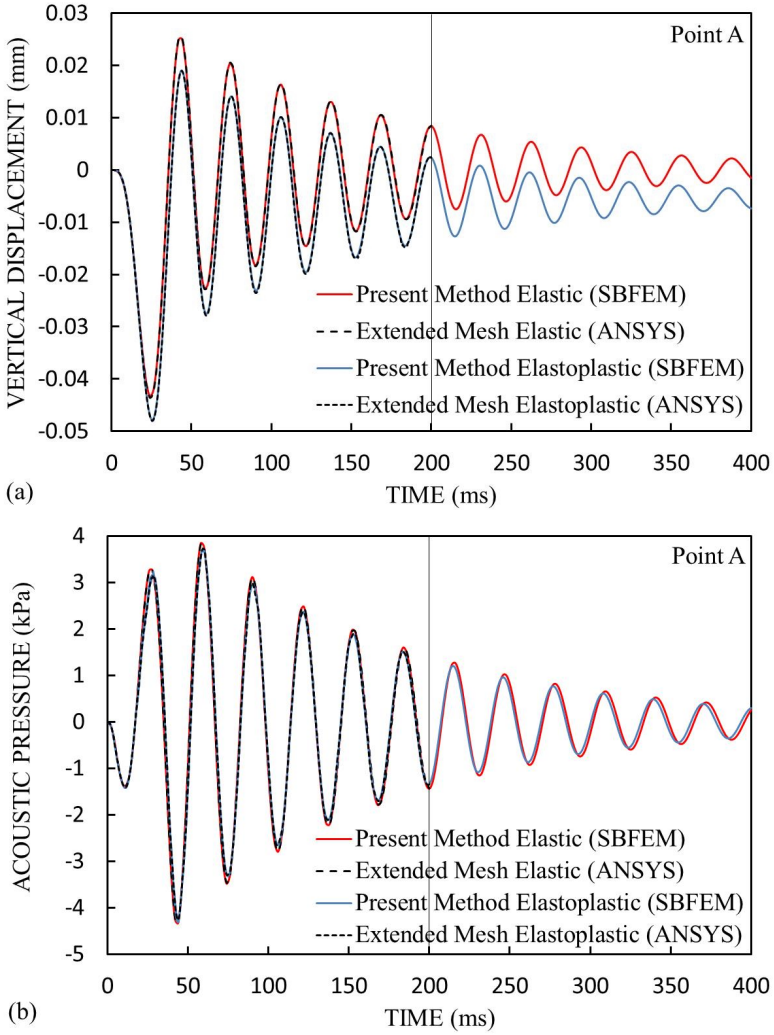

Figure 7.14. Results at point A in the coupled model of a 3D elastoplastic plate submerged in infinite acoustic domain: (a) vertical displacement and (b) acoustic pressure.

also illustrated in Figure 7.13(b) with efficient mesh transition between two media. In this figure, larger elements in acoustic domain contacting smaller elements from structural domain are simply subdivided into smaller triangular or quadrilateral elements that can satisfy the displacement consistency on the interface. Similarly, the coordinate axes in Figure 7.13 only denote the orientations of the coupled model. The orders of continued-fractions for the spherical open boundary are set to be $M_H = M_L = 1$. The results of this coupled system are calculated by applying Newmark's method with the constant time step of $\Delta t = 0.05$ms for the convergence of modified Newton-Raphson iteration within each time step.

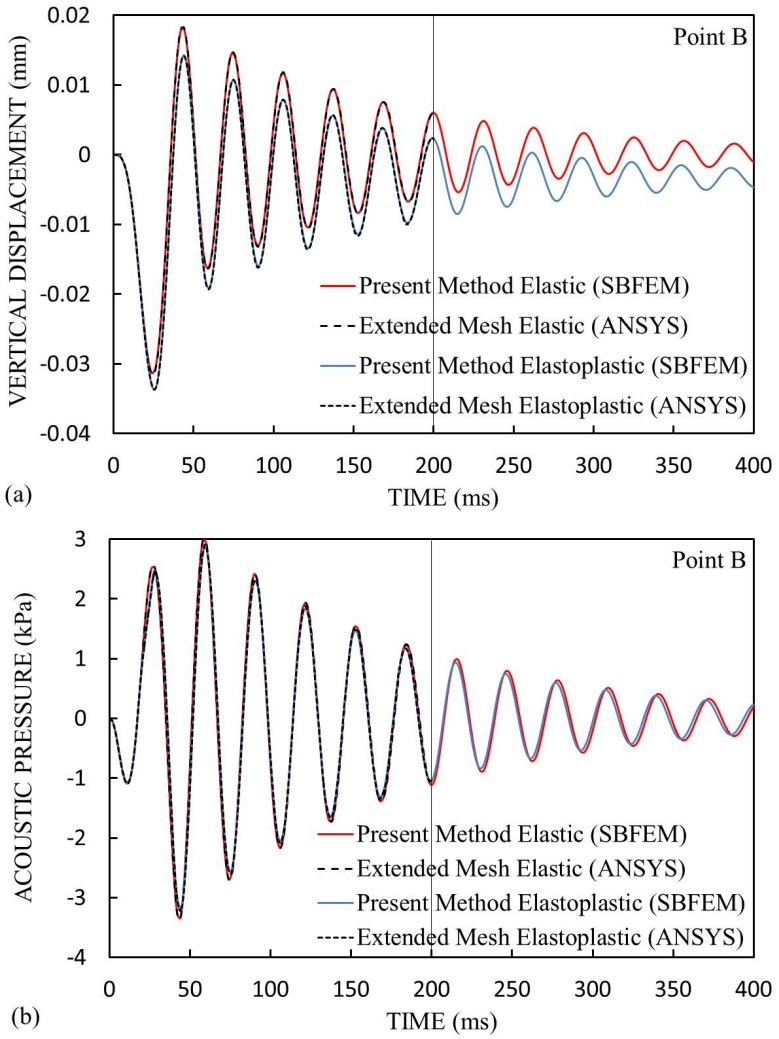

Figure 7.15. Results at point B in the coupled model of a 3D elastoplastic plate submerged in infinite acoustic domain: (a) vertical displacement and (b) acoustic pressure.

The vertical displacements and acoustic pressures at point A(0m, 0m, 0.8m) and B(3.2m, 0m, 0.8m) (see Figure 5.24) during the first 400ms are illustrated in Figures 7.14 and 7.15 respectively as they are located on the acoustic-structural interface. Analogous to previous examples in Sections 7.5.1 and 7.5.2, the displacements and acoustic pressures obtained using the present SBFEM by assuming the elastoplastic behavior of structure are plotted in blue solid lines in Figures 7.14 and 7.15, while the results from the proposed SBFEM obtained by assuming elastic behavior of structure are plotted in red solid lines for comparisons. The accuracy of these SBFEM results are verified by references solutions calculated using FEM in ANSYS, which are

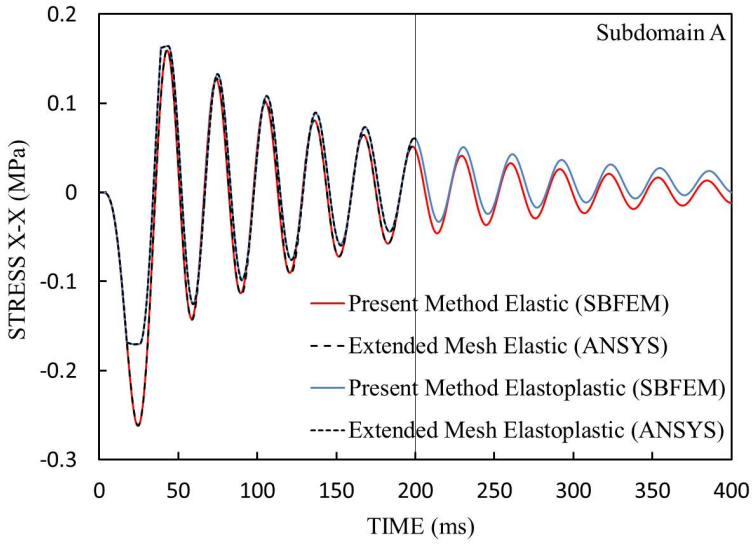

Figure 7.16. X-X stress in subdomain A of the coupled model of a 3D elastoplastic plate submerged in infinite acoustic domain.

plotted in black dash and dotted lines for the cases of elastoplastic and elastic structures separately in corresponding figures. In the FEM model, the structural plate is divided into 64 8-node hexahedral elements in x and y directions and 16 8-node hexahedral elements in z direction. For modelling the unbounded acoustic domain, an extended mesh with the radius of 165m is constructed in the FEM model. During the first 200ms, the traveling distance of wave front is $1482 \times 0.2 = 296.4$m. The distance between the FEM truncated boundary and the boundary of the domain of interest is $165 - 12 = 153$m, which is more than half of the traveling distance of wave front. Therefore, the reflected wave has not entered the domain of interest yet. 4-node tetrahedral elements with the maximum edge length of 1.6m are used for acoustic domain in FEM model. Very good agreements between the results calculated using proposed SBFEM and FEM model in ANSYS are obtained during the first 200ms.

The stress in the x direction of subdomain A, which is adjacent to the centre of the top surface of plate with the coordinate of the scaling centre $(0.1\text{m}, 0.1\text{m}, 0.75\text{m})$, calculated by SBFEM model is also plotted in Figure 7.16 with the blue solid line considering elastoplastic behavior of structure and red solid line considering elastic

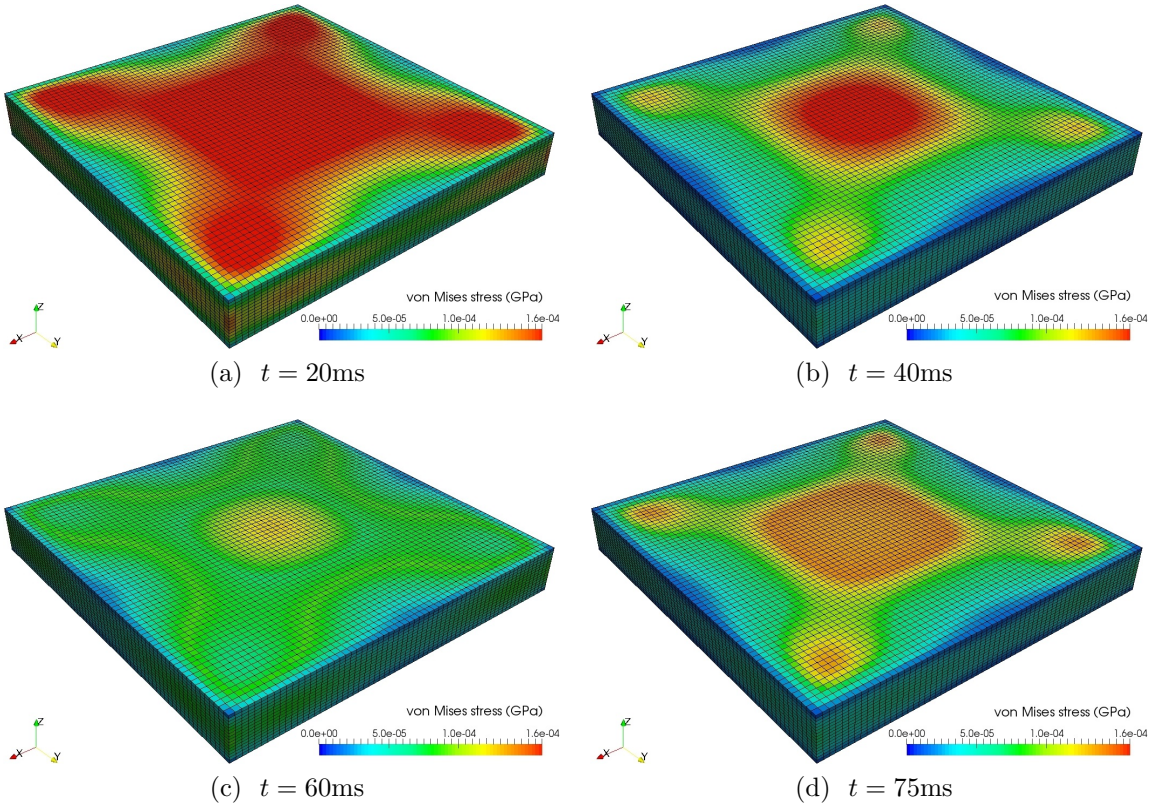

(a) $t = 20$ms (b) $t = 40$ms

(c) $t = 60$ms (d) $t = 75$ms

Figure 7.17. Coupled system of 3D elastoplastic plate submerged in infinite acoustic domain. Contour plots of von Mises stresses in the plate at: (a) $t = 20$ms, (b) $t = 40$ms, (c) $t = 60$ms and (d) $t = 75$ms.

behavior of structure respectively. Because the constant stresses are assumed within each polyhedral subdomain in SBFEM model, the average of the stresses in the x direction of the corresponding hexahedral element in FEM model are used for verifying the stress result and plotted as black dotted and dash lines for elastoplastic and elastic cases separately. This hexahedral element in from FEM model has the same shape and location as the subdomain A in SBFEM mesh. Excellent agreements between stress results obtained from proposed SBFEM and reference solutions are observed. The contour plots of the von Mises stresses and effective plastic strains in the plate at times $t = 20$ms, $t = 40$ms, $t = 60$ms and $t = 75$ms are also illustrated in Figures 7.17 and 7.18, respectively.

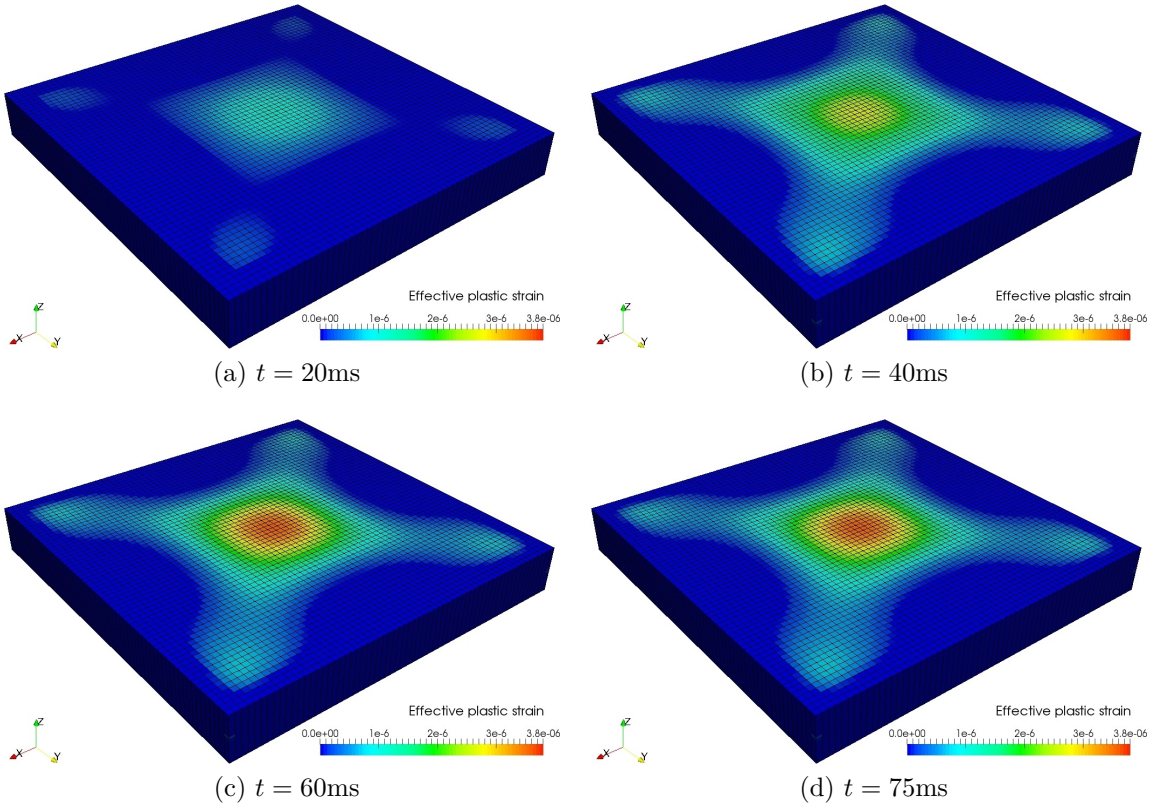

(a) $t = 20$ms (b) $t = 40$ms

(c) $t = 60$ms (d) $t = 75$ms

Figure 7.18. Coupled system of 3D elastoplastic plate submerged in infinite acoustic domain. Contour plots of effective plastic strains in the plate at: (a) $t = 20$ms, (b) $t = 40$ms, (c) $t = 60$ms and (d) $t = 75$ms.

7.6 Conclusions

In this chapter, the SBFEM is firstly developed to model the interactions between elastoplastic structures and infinite acoustic domains in both 2D and 3D cases. To this end, the novel approaches in (He, 2017) and Chapter 6 for elastoplastic analysis are adopted here for modelling the structural domains as these approaches only require the return mapping algorithm to be performed at scaling centre of each 2D or 3D subdomain, which makes them very efficient in elastoplastic analysis. For the representations of unbounded acoustic domains, the high-order doubly-asymptotic open boundaries for 2D and 3D acoustics from Chapters 3 and 4 are also employed here as these open boundaries are robust and accurate at both high- and low-frequency limits. As spatially and temporally local open boundaries, they are also very efficient in modelling the unbounded domains due to the fast conver-

gence rate of continued-fractions and can be directly used for transient analysis. Mesh transitions on the acoustic-structure interface can also be addressed easily and efficiently via subdividing line elements in 2D models or surface elements in 3D models due to the boundary discretization in SBFEM. The mesh generations of 3D models are accomplished by octree mesh technique, which leads to significant reduction on human efforts. For performing the nonlinear dynamic analysis, Newmark's method is applied to obtain all transient solutions with the modified Newton-Raphson iteration within each time step to enforce the equilibrium of the coupled acoustic-structure interaction system. Both 2D and 3D examples are presented in this chapter for the demonstration of the feasibility and accuracy of the proposed approach.

Chapter 8

Conclusions

8.1 Summary

In this thesis, reliable and efficient computational techniques for acoustic analysis, structural elastoplastic analysis and acoustic-structure interaction analysis are developed based on the theoretical framework of scaled boundary finite element method (SBFEM). The proposed techniques are also applicable to both 2D and 3D problems. Furthermore, octree mesh technique is integrated in all 3D analysis in this research for reducing the human efforts on mesh generation and automatic analysis. The SBFEM is a semi-analytical computational method which only requires the boundary discretization but no fundamental solution is needed. This method can also provide analytical solution in the radial direction. Therefore, this unique feature makes the SBFEM naturally suitable to model the unbounded domain as the radiation condition at infinity is satisfied rigorously in the scaled boundary finite element equation. In addition, the arbitrary polygon or hexahedral shape and boundary discretization allows high flexibility in 2D and 3D mesh generations. The mesh transition on acoustic-structure interface and material interface can be easily and efficiently addressed in this method.

In order to model the infinite acoustic domain, the high-order doubly-asymptotic

open boundary with continued-fraction expansion for solving the model impedance is employed on account of its high convergence rate and accuracy in full frequency range. Additional factor coefficients are used to eliminate singularities in continued-fraction expansions. Rules for applying singly-asymptotic continued fraction for low-frequency modes are provided to improve the stability of the doubly-asymptotic open boundary. The resulting model is capable of simulating both 2D and 3D infinite acoustic full space, semi-infinite acoustic half space and wedges with high efficiency and accuracy.

For modelling the 3D elastoplastic structures, the scaled boundary finite element formulation with stabilization for elastoplasticity is developed. Comparing with the original scaled boundary formulation for elastoplasticity in (Ooi et al., 2014), this novel formulation assumes constant elastoplastic constitutive matrix and stresses within each scaled boundary subdomain. As a result, the computationally expensive return mapping algorithm should only be performed at the scaling centre in each subdomain.

The scaled boundary models for structures and acoustics are directly coupled together in 2D and 3D acoustic-structure interaction analyses. Iterative approach is adopted to ensure the equilibrium in each time step when plastic deformation occurs in the structure. The conclusions and features of techniques developed in each chapter are summarized below:

In Chapter 1, this thesis is commenced with an introduction of the research topic. Next, the statement of problem and motivations are presented. These are then followed by the objectives and outline of this thesis.

In Chapter 2, a detailed literature review has been performed on two relevant parts: procedures for modelling the wave propagation in unbounded domain and structural elastoplasticity with reduced integration method to improve the computational efficiency. For the first part on modelling the unbounded domain, the reviewed techniques are categorized into two groups: the global procedures and local

procedures. The global procedures, such as the boundary element method (BEM), DtN finite element method and SBFEM, are spatially and temporally global. They can provide accurate solutions but with relatively higher computational costs than local procedures. The local procedures are usually spatially and temporally local. They are normally computationally efficient but with lower accuracy than global procedures. Reviewed local procedures in this chapter includes different types of artificial boundary conditions (ABCs), the infinite elements and perfectly matched layer (PML). Introductions of these computational approaches, as well as the corresponding advantages and limitations for modelling the unbounded domain, are also presented. In the second part about structural elastoplasticity, the fundamentals of classic plastic theory, including the yield criteria, hardening rules and elastoplastic constitutive relationship, are firstly introduced. These are followed by a summary of the computational procedures for elastoplastic analysis using the finite element scheme. Finally, the developments and discussions on the existing reduced integration methods with hourglass control are stated.

In Chapter 3, the SBFEM is extended to model the 2D acoustic problems. For handling the 2D acoustic domain with arbitrary geometry, the whole infinite domain is divided into the acoustic near field, which contains the complex geometry, and the circular far field of the unbounded acoustic domain. The near field is modeled by SBFEM due to the high efficiency in obtaining the dynamic impedance of each scaled boundary subdomain using continued fractions. As for the unbounded far field, the high-order doubly-asymptotic open boundary from reference (Prempramote, 2011) is employed. Via decoupling the scaled boundary finite element equation in nodal pressure for unbounded domain, the scalar equations for model impedance coefficients for circular unbounded domain are obtained. The model impedance coefficients are then solved using continued-fraction expansions. These continued fractions are doubly asymptotic, which implies that these solutions are exact at both the high-frequency and low-frequency (static) limits. The computatio-

nally expensive numerical integration for forming the stiffness and damping matrices are circumvented as the introduction of auxiliary variables can directly transform the continued-fraction expansions into time-domain equations. The time-domain equations of unbounded domain can be easily coupled with the equations of bounded near field to form the global system of equations for the whole acoustic model for direct transient analysis. Numerical examples demonstrate that the proposed technique shows higher accuracy in acoustic analysis than singly asymptotic open boundary without additional cost and is accurate for representing infinite full space, semi-infinite half space and wedges.

In Chapter 4, the high-order doubly-asymptotic open boundary proposed in Chapter 3 is further developed for 3D unbounded acoustic domains. Analogously, the whole infinite acoustic domain is subdivided into the acoustic near field and far field by defining a spherical boundary. After shifting the mode number and introducing the modal impedance coefficients of spherical unbounded domain, the same doubly-asymptotic continued-fraction expansions from 2D acoustic analysis is directly applied to 3D analysis. The implementation of this open boundary to 3D analysis is thus straightforward. The SBFEM is again used to model the acoustic near field. Due to the advantage of high flexibility of SBFEM in element shapes, an automatic mesh techniques based on octree is implemented for 3D acoustic analysis. The integration of octree mesh greatly reduces the human efforts on solving acoustic problems with complex geometries described by, for example, STL models. The accuracy and practicability of the proposed technique are also illustrated by several numerical examples in this chapter.

Chapter 5 extends the SBFEM to model acoustic-structure interaction problems for both 2D and 3D cases with elastic structural behavior. In this study, the 2D and 3D acoustic domains are considered to be infinite and modeled using the SBFEM proposed in Chapters 3 and 4 respectively. The structural domain is still modeled by SBFEM due to the efficiency of using continued fractions for obtaining dynamic

stiffness in the frequency domain. The continued-fraction expansion for the dynamic stiffness of a structure can be transformed into time-domain equations using auxiliary variables. The equations of motion for acoustic and structural domains are then directly coupled by enforcing the boundary conditions on the acoustic-structure interface to obtain the global equations of motion for the coupled system. A symmetric formulation is also derived for the acoustic-structure interaction system by replacing the unknowns related to acoustic field with new variables. By applying first-order derivative to these new variables, they can yield the original unknowns in the acoustic domain. In SBFEM, the mesh transition on acoustic-structure interface is addressed efficiently by simple subdivisions of boundary elements (line elements for 2D or surface elements in 3D). For automatic mesh generation of 3D acoustic-structure interaction systems, octree mesh is again introduced to generate appropriate meshes. Both 2D and 3D numerical examples, including a practical example with very complex geometry of a Chinese bell, are presented to demonstrate the accuracy, efficiency and robustness of the proposed technique.

In Chapter 6, the scaled boundary finite element formulation with stabilization for 3D static and dynamic elastoplastic analysis is proposed based on the similar formulation for 2D image-based elastoplastic analysis in (He, 2017). In this formulation, the elastoplastic constitutive matrix and stresses within each subdomain in SBFEM are assumed to be represented by constants. Consequently, the computationally expensive return mapping algorithm should only be performed once at the scaling centre of each subdomain to update the stresses. Stabilization matrix is also introduced to control the hourglass modes. Comparing with the original formulation in (Ooi et al., 2014), this new formulation can greatly simplify the implementation and improve the efficiency of elastoplastic analysis based on SBFEM. The assumptions of constant elastoplastic constitutive matrix and stresses in each subdomain are especially useful for the elastoplastic analysis based on automatically generated meshes for structures with complicated geometry as small cells or elements are fre-

quently used to capture the details of geometry. Automatic mesh generation from STL models based on octree technique is applied in this chapter to obtain the meshes for 3D elastoplastic analysis. The stress concentrations along the jagged boundary in image-based mesh are thus avoided. Various numerical examples are presented to highlight the efficiency and accuracy of the proposed technique for both static and dynamic elastoplastic analyses in 3D, as well as its capability to model complex structures.

Chapter 7 proposed the extension of SBFEM to simulate the 2D and 3D acoustic-structure interaction problems with the consideration of elastoplastic structural behavior and infinite acoustic domain. To this end, the acoustic models developed in Chapters 3 and 4 for 2D and 3D cases are coupled with the structural models for 2D and 3D elastoplastic analysis in (He, 2017) and Chapter 6 separately. The same boundary conditions on acoustic-structure interface in Chapter 5 are adopted here again to couple the acoustic models and elastoplastic structural models. Due to the fact that the structure is elastoplastic in this coupled system, the partition of coupled stiffness matrix corresponding to structural domain should be updated in each time step after the initial yielding. Meanwhile, the iterative procedure, such as modified Newton-Raphson method, is applied within each time step to enforce the equilibrium between structures and acoustics in this coupled system. Numerical examples for both 2D and 3D scenarios are studied using the proposed technique to demonstrate its accuracy and robustness in the analysis of acoustic-structure interaction with structural elastoplasticity. The efficient mesh transition on acoustic-structure interface is also illustrated.

8.2 Recommendations for future research

- In Chapter 3 and 4, the high-order doubly-asymptotic open boundary has only been applied to the scalar wave propagation. It is of great interest to

extend this open boundary to model vector wave propagation in unbounded domain. In addition, the geometry of this open boundary is circular for 2D unbounded domain or spherical for 3D unbounded domain. Further research could focus on developing high-order doubly-asymptotic open boundary with arbitrary geometry of unbounded domain.

- The acoustic-structure interaction analyses proposed in Chapter 5 and 7 could be extended to other research areas in practical engineering, such as the dam-reservoir interaction system and air-coupled ultrasonic testing. Acoustic scattering problems could also be studied by incorporating incident waves from the far field.

- In Chapter 6, only the perfectly plastic model and von Mises model of elastoplasticity is considered as the material nonlinearity in this study. For modelling more practical problems, other nonlinear material models can be included in the same framework of proposed technique. Furthermore, other iterative procedures, such as the arc-length method, can be employed to replace the modified Newton-Raphson method to achieve better convergence rate and solve highly nonlinear systems of equations even when the modified Newton-Raphson method fails.

- In many acoustic-structure interaction problems in engineering with liquid as the acoustic medium, the cavitation, which frequently appears when the pressure drops below the vapor pressure, may exist under very strong excitations. The existence of cavitation changes the hydrodynamic force applied on structures and varies the responses of acoustic-structure interaction system. In the future, cavitation can be considered in the acoustic analysis and in acoustic-structure interaction analysis performed in this thesis.

- For all the octree meshes used in this research, only low-order surface elements, including 3-nodes triangular and 4-nodes quadrilateral elements, are adopted.

However, in dynamic analysis with high-frequency excitations, high-order elements are preferred. The next step of research could focus on implementing high-order elements into octree mesh.

- Due to the advantages of implementing automatic mesh generation techniques in SBFEM, as well as its developments on acoustics and structural elastoplasticity in this thesis, the SBFEM can be further used as a powerful computational tool for modelling biomechanical problems. Some preliminary examples have already been studied in Sections 4.5.3 and 6.5.5.

Appendices

Appendix A Scaled boundary finite element equations for 2D structural dynamics

The derivations of scaled boundary finite element equations for elastic 2D structural dynamics are demonstrated in this section. The scaled boundary coordinates in 2D structural dynamics are the same as the one defined by Equations (3.2)-(3.4) in Section 3.2.1, so it won't be repeated in this section. The derivation of scaled boundary formulations for 2D structural dynamics also starts from the governing differential equations of motion in frequency domain given by Equation (5.1) in Section 5.2. In 2D case, the differential operator $\mathbf{L}$ for strain-displacement relationship are expressed as:

$$\mathbf{L} = \begin{bmatrix} \frac{\partial}{\partial \hat{x}} & 0 \\ 0 & \frac{\partial}{\partial \hat{y}} \\ \frac{\partial}{\partial \hat{y}} & \frac{\partial}{\partial \hat{x}} \end{bmatrix} \tag{A.1}$$

Then, the 2D strain-displacement relationship in scaled boundary coordinate can be expressed by,

$$\boldsymbol{\epsilon}(\xi, \eta) = \mathbf{L}\hat{\mathbf{u}}(\xi, \eta) \tag{A.2}$$

The displacement amplitude $\hat{\mathbf{u}}(\xi,\eta)$ in Equation (A.2) can be discretized for 2D subdomains using the 1D shape function $\mathbf{N}_s(\eta)$ as:

$$\hat{\mathbf{u}}(\xi,\eta) = \mathbf{N}_s(\eta)\hat{\mathbf{u}}(\xi) \tag{A.3}$$

with

$$\mathbf{N}_s(\eta) = [N_1(\eta)\mathbf{I},\ N_2(\eta)\mathbf{I},\ \cdots,\ N_m(\eta)\mathbf{I}] \tag{A.4}$$

for a m-node element with $\mathbf{I}$ the 2×2 identity matrix.

In scaled boundary coordinate, the differential operator $\mathbf{L}$ in 2D can be written as: (Wolf and Song, 2000)

$$\mathbf{L} = \mathbf{b}_1^s(\eta)\frac{\partial}{\partial\xi} + \frac{1}{\xi}\mathbf{b}_2^s(\eta)\frac{\partial}{\partial\eta} \tag{A.5}$$

In Equation (A.5), the $\mathbf{b}_1^s(\eta)$ and $\mathbf{b}_2^s(\eta)$ matrices are defined as,

$$\mathbf{b}_1^s(\eta) = \frac{1}{|\mathbf{J}|}\begin{bmatrix} y_{,\eta} & 0 \\ 0 & -x_{,\eta} \\ -x_{,\eta} & y_{,\eta} \end{bmatrix} \tag{A.6a}$$

$$\mathbf{b}_2^s(\eta) = \frac{1}{|\mathbf{J}|}\begin{bmatrix} -y & 0 \\ 0 & x \\ x & -y \end{bmatrix} \tag{A.6b}$$

$\mathbf{J}$ in Equation (A.6) is the Jacobian matrix defined in Equation (3.6). Substituting Equations (A.5) and (A.3) into (A.2) yields the expression for strain field $\boldsymbol{\epsilon}(\xi,\eta)$ in 2D as,

$$\boldsymbol{\epsilon}(\xi,\eta) = \mathbf{B}_1^s(\eta)\hat{\mathbf{u}}(\xi)_{,\xi} + \frac{1}{\xi}\mathbf{B}_2^s(\eta)\hat{\mathbf{u}}(\xi) \tag{A.7}$$

with the $\mathbf{B}_1^s(\eta)$ and $\mathbf{B}_2^s(\eta)$ matrices for 2D structures defined as:

$$\mathbf{B}_1^s(\eta,\zeta) = \mathbf{b}_1^s(\eta)\mathbf{N}_s(\eta) \tag{A.8a}$$

$$\mathbf{B}_2^s(\eta,\zeta) = \mathbf{b}_2^s(\eta)\mathbf{N}_s(\eta)_{,\eta} \tag{A.8b}$$

Applying the method of weighted residuals to the differential equations of motion in Equation (5.1) in circumferential direction (η) (Song and Wolf, 1997), a differential equation for radial displacement amplitude $\mathbf{u}(\xi)$ in the frequency domain is derived for free side-face in radial direction and vanishing of body forces, and its 2D form is written as,

$$\mathbf{E}_0^s \xi^2 \hat{\mathbf{u}}(\xi)_{,\xi\xi} + \left(\mathbf{E}_0^s - \mathbf{E}_1^s + [\mathbf{E}_1^s]^T\right) \xi \hat{\mathbf{u}}(\xi)_{,\xi} - \mathbf{E}_2^s \hat{\mathbf{u}}(\xi) + \omega^2 \mathbf{M}_0^s \xi^2 \hat{\mathbf{u}}(\xi) = 0 \tag{A.9}$$

with the coefficient matrices $\mathbf{E}_0^s$, $\mathbf{E}_0^s$, $\mathbf{E}_0^s$ and $\mathbf{E}_0^s$ for 2D case:

$$\mathbf{E}_0^s = \int_{-1}^{+1} [\mathbf{B}_1^s(\eta)]^T \mathbf{D} \mathbf{B}_1^s(\eta) \, |\mathbf{J}(\eta)| \, d\eta \tag{A.10a}$$

$$\mathbf{E}_1^s = \int_{-1}^{+1} [\mathbf{B}_2^s(\eta)]^T \mathbf{D} \mathbf{B}_1^s(\eta) \, |\mathbf{J}(\eta)| \, d\eta \tag{A.10b}$$

$$\mathbf{E}_2^s = \int_{-1}^{+1} [\mathbf{B}_2^s(\eta)]^T \mathbf{D} \mathbf{B}_2^s(\eta) \, |\mathbf{J}(\eta)| \, d\eta \tag{A.10c}$$

$$\mathbf{M}_0^s = \int_{-1}^{+1} \mathbf{N}_s^T(\eta) \rho_s \mathbf{N}_s(\eta) \, |\mathbf{J}(\eta)| \, d\eta \tag{A.10d}$$

where $\mathbf{D}$ is the elasticity matrix for 2D. All coefficient matrices in Equation (A.10) are calculated in an element-by-element basis and assembled as in finite element method for each 2D polygonal subdomain.

Appendix B 2D elastoplastic stiffness matrix and internal load vector in scaled boundary finite element formulation with stabilization

The details of the derivation of 2D static elastoplastic analysis based on SBFEM with stabilization are well established and documented in reference (He, 2017). Only the derivations for the 2D elastoplastic stiffness matrix $\mathbf{K}_{ep}$ and internal load vector $\mathbf{R}_{int}$ are briefly summarized here for the completeness of this thesis. Similar to Equation

(6.6), the relationship between the strain field in a 2D polygonal subdomain $\boldsymbol{\epsilon}(\xi,\eta)$ and nodal displacement on its boundary $\mathbf{u}_b$ can be written by:

$$\boldsymbol{\epsilon}(\xi,\eta) = \mathbf{B}(\xi,\eta)\mathbf{u}_b \tag{B.1}$$

with the scaled boundary strain-displacement matrix $\mathbf{B}(\xi,\eta)$ for the polygonal subdomain

$$\mathbf{B}(\xi,\eta) = \boldsymbol{\Psi}_\epsilon(\eta)\xi^{-\mathbf{S}_n-\mathbf{I}}\boldsymbol{\Psi}_{u_n}^{-1} \tag{B.2}$$

and strain modes $\boldsymbol{\Psi}_\epsilon(\eta)$ for the polygonal subdomain

$$\boldsymbol{\Psi}_\epsilon(\eta) = \mathbf{B}_1^s(\eta)\boldsymbol{\Psi}_{u_n}\left[-\mathbf{S}_n\right] + \mathbf{B}_2^s(\eta)\boldsymbol{\Psi}_{u_n} \tag{B.3}$$

In Equations (B.2) and (B.3), The $\mathbf{S}_n$ are eigenvalues with negative real parts (which indicate bounded domain as well) calculated from the equivalent eigenvalue problem in Equation (5.17) for 2D analysis and $\boldsymbol{\Psi}_{u_n}$ are the corresponding modal displacements. As discussed in Section 6.3.2, the stress field in a subdomain should be decomposed into a constant-stress part and a non-constant stress part, which can be easily identified by their corresponding eigenvalues. For a 2D polygonal subdomain, there are totally four constant strain modes with the eigenvalues of $\lambda(\mathbf{S}_n^{(c)}) = -1$ and other non-constant strain modes identified by the eigenvalues of $\lambda(\mathbf{S}_n^{(c)}) < -1$. Analogous to Equation (6.26) in 3D, Equation (B.2) can be decomposed into constant and non-constant parts as:

$$\mathbf{B}(\xi,\eta) = \mathbf{B}^{(c)} + \mathbf{B}^{(n)}(\xi,\eta) \tag{B.4}$$

with

$$\mathbf{B}^{(c)} = \boldsymbol{\Psi}_\epsilon^{(c)}\left(\boldsymbol{\Psi}_{u_n}^{-1}\right)^{(c)} \tag{B.5a}$$

$$\mathbf{B}^{(n)}(\xi,\eta) = \boldsymbol{\Psi}_\epsilon^{(n)}(\eta,\zeta)\xi^{-\mathbf{S}_n^{(n)}-\mathbf{I}}\left(\boldsymbol{\Psi}_{u_n}^{-1}\right)^{(n)} \tag{B.5b}$$

The stress field in 2D polygonal subdomain $\boldsymbol{\sigma}(\xi,\eta)$ can be decomposed in the

similar way as:

$$\boldsymbol{\sigma}(\xi,\eta) = \boldsymbol{\sigma}^{(c)} + \boldsymbol{\sigma}^{(n)}(\xi,\eta) \tag{B.6}$$

with constant and non-constant stress parts $\boldsymbol{\sigma}^{(c)}$ and $\boldsymbol{\sigma}^{(n)}(\xi,\eta)$ defined by:

$$\boldsymbol{\sigma}^{(c)} = \mathbf{D}_{ep}\mathbf{B}^{(c)}\mathbf{u}_b \tag{B.7a}$$

$$\boldsymbol{\sigma}^{(n)}(\xi,\eta) = \mathbf{D}_{ep}\mathbf{B}^{(n)}(\xi,\eta)\mathbf{u}_b \tag{B.7b}$$

In Equation (B.7), $\mathbf{D}_{ep}$ is the elastoplastic constitutive matrix for 2D analysis.

Appendix B.1 Decomposition of elastoplastic stiffness matrix for polygonal subdomains

Analogous to Equation (6.30) for 3D analysis, the elastoplastic stiffness matrix $\mathbf{K}_{ep}$ for a 2D polygonal element is,

$$\mathbf{K}_{ep} = \int_{\Omega} \mathbf{B}^T(\xi,\eta)\mathbf{D}_{ep}\mathbf{B}(\xi,\eta)d\Omega \tag{B.8}$$

with the infinitesimal area $d\Omega$ defined as(Song and Wolf, 1997)

$$d\Omega = |\mathbf{J}(\eta)|\,\xi d\xi d\eta \tag{B.9}$$

Replacing the second instance of $\mathbf{B}(\xi,\eta)$ in Equation (B.8) with Equation (B.4) and utilizing Equations (B.2), (B.5) and (B.9), $\mathbf{K}_{ep}$ can be decomposed in the same form as Equations (6.36) and (6.37) but with $\boldsymbol{\Psi}_{u_n}$ calculated from a 2D subdomain and the matrices $\mathbf{X}^{(c)}$ and $\mathbf{X}^{(n)}$ for 2D analysis are defined as:

$$\mathbf{X}^{(c)} = \int_0^1 \xi^{-\mathbf{S}_n^T-\mathbf{I}} \left[\int_{-1}^{+1} \boldsymbol{\Psi}_{\epsilon}^T(\eta)\mathbf{D}_{ep}\boldsymbol{\Psi}_{\epsilon}^{(c)}\,|\mathbf{J}(\eta)|\,d\eta\right] \xi d\xi \tag{B.10a}$$

$$\mathbf{X}^{(n)} = \int_0^1 \xi^{-\mathbf{S}_n^T-\mathbf{I}} \left[\int_{-1}^{+1} \boldsymbol{\Psi}_{\epsilon}^T(\eta)\mathbf{D}_{ep}\boldsymbol{\Psi}_{\epsilon}^{(n)}\,|\mathbf{J}(\eta)|\,d\eta\right] \xi^{-\mathbf{S}_n^{(n)}-\mathbf{I}} d\xi \tag{B.10b}$$

$\mathbf{X}^{(c)}$ and $\mathbf{X}^{(n)}$ can then be calculated via following the same procedures presented in Sections 6.3.3.1 and 6.3.3.2 except for a few differences in the expressions of formulations for 2D analysis. For $\mathbf{X}^{(c)}$ defined in Equation (6.38) in 3D analysis, its

2D expression is,

$$\mathbf{X}^{(c)} = \int_0^1 \xi^{-\mathbf{S}_n^T - \mathbf{I}} \mathbf{Y}^{(c)} \xi d\xi \tag{B.11}$$

which leads to the analytical solutions of $\mathbf{X}_{nc}$ and $\mathbf{X}_{cc}$:

$$\mathbf{X}_{nc} = \left(-\left(\mathbf{S}_n^{(n)}\right)^T + \mathbf{I} \right)^{-1} \mathbf{Y}_{nc} \tag{B.12a}$$

$$\mathbf{X}_{cc} = \frac{\mathbf{Y}_{cc}}{2} \tag{B.12b}$$

For the evaluation of $\mathbf{X}^{(n)}$ given in Equation (6.45) for 3D analysis, its 2D form is:

$$\mathbf{X}^{(n)} = \int_0^1 \xi^{-\mathbf{S}_n^T - \mathbf{I}} \mathbf{Y}^{(n)} \xi^{-\mathbf{S}_n^{(n)} - \mathbf{I}} \xi d\xi \tag{B.13}$$

which again leads to the analytical solutions of $\mathbf{X}_{nn}$ and $\mathbf{X}_{cn}$:

$$\mathbf{Y}_{nn} = \left(-\mathbf{S}_n^{(n)}\right)^T \mathbf{X}_{nn} + \mathbf{X}_{nn} \left(-\mathbf{S}_n^{(n)}\right) \tag{B.14a}$$

$$\mathbf{X}_{cn} = \mathbf{Y}_{cn} \left(-\mathbf{S}_n^{(n)} + \mathbf{I}\right)^{-1} \tag{B.14b}$$

It should be noticed that the Lyapunov equation in Equation (B.14a) for solving $\mathbf{X}_{nn}$ from 2D analysis has the same format as the Lyapunov equation for solving $\mathbf{X}_{nn}$ in 3D analysis in Equation (6.51).

Appendix B.2 Decomposition of internal load vector for 2D elastoplastic analysis

Similar to Equation (6.53) for 3D analysis, the internal load vector for a 2D polygonal subdomain is defined by,

$$\mathbf{F}_{int} = \int_\Omega \mathbf{B}^T(\xi, \eta) \boldsymbol{\sigma}(\xi, \eta) d\Omega \tag{B.15}$$

with the infinitesimal area $d\Omega$ given in Equation (B.9). Substituting Equation (B.6) into Equation (B.15), $\mathbf{F}_{int}$ can be decomposed and evaluated via the similar procedure described in Section 6.3.4. In 2D analysis, the internal load vector related to

constant stress parts $\mathbf{F}_{int}^{(c)}$ is expressed as:

$$\mathbf{F}_{int}^{(c)} = \boldsymbol{\Psi}_{u_n}^{-T} \left(-\mathbf{S}_n^T + \mathbf{I}\right)^{-1} \mathbf{r}(\eta)\boldsymbol{\sigma}^{(c)} \tag{B.16}$$

where $\boldsymbol{\sigma}^{(c)}$ is the constant stress vector at scaling centre of the polygonal subdomain expressed in Equation (B.7a). $\mathbf{r}(\eta)$ can be calculated by evaluating the following integration in η direction,

$$\mathbf{r}(\eta) = \int_{-1}^{+1} \boldsymbol{\Psi}_{\epsilon}^{T}(\eta) \left|\mathbf{J}(\eta)\right| d\eta \tag{B.17}$$

The internal load vector related to non-constant stress parts $\mathbf{F}_{int}^{(n)}$ is expressed as:

$$\mathbf{F}_{int}^{(n)} = \boldsymbol{\Psi}_{u_n}^{-T} \int_0^1 \xi^{-\mathbf{S}_n^T - \mathbf{I}} \left[\int_{-1}^{+1} \boldsymbol{\Psi}_{\epsilon}^{T}(\eta) \mathbf{D}_{ep} \boldsymbol{\Psi}_{\epsilon}^{(n)}(\eta) \left|\mathbf{J}(\eta)\right| d\eta \right] \xi^{-\mathbf{S}_n^{(n)}} d\xi \left(\boldsymbol{\Psi}_{u_n}^{-1}\right)^{(n)} \mathbf{u}_b \tag{B.18}$$

Utilizing Equation (B.10b) and (6.37b), Equations (B.18) can be simplified as:

$$\mathbf{F}_{int}^{(n)} = \mathbf{K}_{ep}^{(n)} \mathbf{u}_b \tag{B.19}$$

with the non-constant stress part of the 2D elastoplastic stiffness matrix $\mathbf{K}_{ep}^{(n)}$.

Bibliography

Abarbanel, S. and Gottlieb, D. (1997). A mathematical analysis of the pml method. *Journal of Computational Physics*, 134(2):357–363.

Abarbanel, S. and Gottlieb, D. (1998). On the construction and analysis of absorbing layers in cem. *Applied Numerical Mathematics*, 27(4):331–340.

Adam, C., Hughes, T. J., Bouabdallah, S., Zarroug, M., and Maitournam, H. (2015). Selective and reduced numerical integrations for nurbs-based isogeometric analysis. *Computer Methods in Applied Mechanics and Engineering*, 284:732–761.

Amini, S., Harris, P. J., and Wilton, D. T. (2012). *Coupled boundary and finite element methods for the solution of the dynamic fluid-structure interaction problem*, volume 77. Springer Science & Business Media.

ANSYS, I. (2002). Ansys/ls-dyna users guide.

Astier, V., Thollon, L., Arnoux, P.-J., Mouret, F., and Brunet, C. (2008). Development of a finite element model of the shoulder: application during a side impact. *International journal of crashworthiness*, 13(3):301–312.

Astley, R. (1983). Wave envelope and infinite elements for acoustical radiation. *International Journal for Numerical Methods in Fluids*, 3(5):507–526.

Astley, R. (1996). Transient wave envelope elements for wave problems. *Journal of Sound and Vibration*, 192(1):245–261.

Astley, R. and Coyette, J.-P. (2001). The performance of spheroidal infinite elements. *International Journal for Numerical Methods in Engineering*, 52(12):1379–1396.

Astley, R. and Hamilton, J. (2006). The stability of infinite element schemes for transient wave problems. *Computer methods in applied mechanics and engineering*, 195(29-32):3553–3571.

Astley, R., Macaulay, G., and Coyette, J. (1994). Mapped wave envelope elements for acoustical radiation and scattering. *Journal of Sound and Vibration*, 170(1):97–118.

Astley, R. J. (2000). Infinite elements for wave problems: a review of current formulations and an assessment of accuracy. *International Journal for Numerical Methods in Engineering*, 49:951–976.

Astley, R. J. and Eversman, W. (1983). Finite element formulations for acoustical radiation. *Journal of Sound and Vibration*, 88(1):47–64.

Ayappa, K., Davis, H., Davis, E., and Gordon, J. (1992). Two-dimensional finite element analysis of microwave heating. *AIChE Journal*, 38(10):1577–1592.

Baker, G. A. and Graves-Morris, P. (1996). *Padé approximants*, volume 59. Cambridge University Press.

Banerjee, P. and Butterfield, R. (1976). Boundary element methods in geomechanics, chapter 16. *Finite Elements in Geomechanics, Gudehus, Ed. Wiley*.

Banks, J. (2013). Adding value in additive manufacturing: Researchers in the united kingdom and europe look to 3d printing for customization. *IEEE pulse*, 4(6):22–26.

Basu, U. and Chopra, A. K. (2003). Perfectly matched layers for time-harmonic elastodynamics of unbounded domains: theory and finite-element implementation. *Computer methods in applied mechanics and engineering*, 192(11-12):1337–1375.

Basu, U. and Chopra, A. K. (2004). Perfectly matched layers for transient elastodynamics of unbounded domains. *International Journal for Numerical Methods in Engineering*, 59(8):1039–1074.

Bathe, K., Nitikitpaiboon, C., and Wang, X. (1995). A mixed displacement-based finite element formulation for acoustic fluid-structure interaction. *Computers & Structures*, 56(2-3):225–237.

Bayliss, A., Goldstein, C. I., and Turkel, E. (1985). The numerical solution of the helmholtz equation for wave propagation problems in underwater acoustics. *Computers & Mathematics with Applications*, 11(7-8):655–665.

Bayliss, A. and Turkel, E. (1980). Radiation boundary conditions for wave-like equations. *Communications on Pure and Applied Mathematics*, 33:707–725.

Bayliss, A. and Turkel, E. (1982). Far field boundary conditions for compressible flows. *Journal of Computational Physics*, 48(2):182–199.

Bazyar, M. H. and Song, C. (2008). A continued-fraction-based high-order transmitting boundary for wave propagation in unbounded domains of arbitrary geometry. *International Journal for Numerical Methods in Engineering*, 74(2):209–237.

Bazyar, M. H. and Song, C. (2017). Analysis of transient wave scattering and its applications to site response analysis using the scaled boundary finite-element method. *Soil Dynamics and Earthquake Engineering*, 98:191–205.

Bécache, E., Dhia, A. B.-B., and Legendre, G. (2004). Perfectly matched layers for the convected helmholtz equation. *SIAM Journal on Numerical Analysis*, 42(1):409–433.

Belytschko, T. (1980). Fluid-structure interaction. *Computers & Structures*, 12(4):459–469.

Belytschko, T. and Bachrach, W. E. (1986). Efficient implementation of quadrilaterals with high coarse-mesh accuracy. *Computer Methods in Applied Mechanics and Engineering*, 54(3):279–301.

Belytschko, T. and Bindeman, L. (1991). Assumed strain stabilization of the 4-node quadrilateral with 1-point quadrature for nonlinear problems. *Computer Methods in Applied Mechanics and Engineering*, 88(3):311–340.

Belytschko, T. and Bindeman, L. P. (1993). Assumed strain stabilization of the eight node hexahedral element. *Computer Methods in Applied Mechanics and Engineering*, 105(2):225–260.

Belytschko, T., Ong, J. S.-J., Liu, W. K., and Kennedy, J. M. (1984). Hourglass control in linear and nonlinear problems. *Computer Methods in Applied Mechanics and Engineering*, 43(3):251–276.

Belytschko, T. and Tsay, C.-S. (1983). A stabilization procedure for the quadrilateral plate element with one-point quadrature. *International Journal for Numerical Methods in Engineering*, 19(3):405–419.

Berenger, J.-P. (1994). A perfectly matched layer for the absorption of electromagnetic waves. *Journal of Computational Physics*, 114:185–200.

Berenger, J.-P. (1996). Three-dimensional perfectly matched layer for the absorption of electromagnetic waves. *Journal of computational physics*, 127(2):363–379.

Bermúdez, A., Hervella-Nieto, L., Prieto, A., Rodrı, R., et al. (2007). An optimal perfectly matched layer with unbounded absorbing function for time-harmonic acoustic scattering problems. *Journal of Computational Physics*, 223(2):469–488.

Bettess, P. (1977). Infinite elements. *International Journal for numerical methods in engineering*, 11(1):53–64.

Bettess, P. (1987). A simple wave envelope element example. *International Journal for Numerical Methods in Biomedical Engineering*, 3(1):77–80.

Bettess, P. and Zienkiewicz, O. (1977). Diffraction and refraction of surface waves using finite and infinite elements. *International Journal for Numerical Methods in Engineering*, 11(8):1271–1290.

Birk, C. and Behnke, R. (2012). A modified scaled boundary finite element method for three-dimensional dynamic soil-structure interaction in layered soil. *International Journal for Numerical Methods in Engineering*, 89(3):371–402.

Birk, C., Liu, L., and Song, C. (2016). Coupled acoustic response of two-dimensional bounded and unbounded domains using doubly-asymptotic open boundaries. *Journal of Computational Physics*, 310:252–284.

Birk, C., Prempramote, S., and Song, C. (2012). An improved continued-fraction-based high-order transmitting boundary for time-domain analyses in unbounded domains. *International Journal for Numerical Methods in Engineering*, 89:269–298.

Birk, C. and Song, C. (2010). A local high-order doubly asymptotic open boundary for diffusion in a semi-infinite layer. *Journal of Computational Physics*, 229(17):6156–6179.

Blacker, T. (2001). Automated conformal hexahedral meshing constraints, challenges and opportunities. *Engineering with Computers*, 17(3):201–210.

Blacker, T. D. and Meyers, R. J. (1993). Seams and wedges in plastering: a 3-d hexahedral mesh generation algorithm. *Engineering with computers*, 9(2):83–93.

Bolte, J. H. (2004). *Injury and impact response of the shoulder due to lateral and oblique loading.* PhD thesis, Ohio State University.

Brebbia, C. and Dominguez, J. (1977). Boundary element methods for potential problems. *Applied Mathematical Modelling*, 1(7):372–378.

Brebbia, C. A. (1978). *The Boundary Element Method for Engineers*. Pentech Press, London.

Brunner, D., Junge, M., and Gaul, L. (2009). A comparison of fe–be coupling schemes for large-scale problems with fluid–structure interaction. *International Journal for Numerical Methods in Engineering*, 77(5):664–688.

Burton, A. and Miller, G. (1971). The application of integral equation methods to the numerical solution of some exterior boundary-value problems. In *Proc. R. Soc. Lond. A*, volume 323, pages 201–210. The Royal Society.

Canuto, C., Hariharan, S., and Lustman, L. (1985). Spectral methods for exterior elliptic problems. *Numerische Mathematik*, 46(4):505–520.

Chen, D., Birk, C., Song, C., and Du, C. (2014). A high-order approach for modelling transient wave propagation problems using the scaled boundary finite element method. *International Journal for Numerical Methods in Engineering*, 97(13):937–959.

Chen, J. C. (1996). *Early Chinese work in natural science: A re-examination of the physics of motion, acoustics, astronomy and scientific thoughts*, volume 1. Hong Kong University Press.

Chen, K., Zou, D., and Kong, X. (2017a). A nonlinear approach for the three-dimensional polyhedron scaled boundary finite element method and its verification using koyna gravity dam. *Soil Dynamics and Earthquake Engineering*, 96:1–12.

Chen, K., Zou, D., Kong, X., Chan, A., and Hu, Z. (2017b). A novel nonlinear solution for the polygon scaled boundary finite element method and its application to geotechnical structures. *Computers and Geotechnics*, 82:201–210.

Chen, K., Zou, D., Kong, X., and Yu, X. (2017c). An efficient nonlinear octree sbfem and its application to complicated geotechnical structures. *Computers and Geotechnics*.

Chen, K., Zou, D., Kong, X., and Yu, X. (2018). An efficient nonlinear octree sbfem and its application to complicated geotechnical structures. *Computers and Geotechnics*, 96:226–245.

Chen, W.-F. and Han, D.-J. (2007). *Plasticity for structural engineers*. J. Ross Publishing.

Cheng, A. H.-D. and Cheng, D. T. (2005). Heritage and early history of the boundary element method. *Engineering Analysis with Boundary Elements*, 29(3):268–302.

Chew, W. and Liu, Q. (1996). Perfectly matched layers for elastodynamics: A new absorbing boundary condition. *Journal of Computational Acoustics*, 4(04):341–359.

Chiong, I., Ooi, E. T., Song, C., and Tin-Loi, F. (2014). Computation of dynamic stress intensity factors in cracked functionally graded materials using scaled boundary polygons. *Engineering Fracture Mechanics*, 131:210–231.

Chopra, A. K. (2001). *Dynamics of structures: theory and applications to earthquake engineering*. Prentice-Hall.

Clayton, R. and Engquist, B. (1977). Absorbing boundary conditions for acoustic and elastic wave equations. *Bulletin of the seismological society of America*, 67(6):1529–1540.

Collino, F. et al. (1993). High order absorbing boundary conditions for wave propagation models. straight line boundary and corner cases. In *Second International Conference on Mathematical and Numerical Aspects of Wave Propagation (Newark, DE, 1993)*, pages 161–171.

Collino, F. and Monk, P. B. (1998). Optimizing the perfectly matched layer. *Computer methods in applied mechanics and engineering*, 164(1-2):157–171.

Crisfield, M. (1983). An arc-length method including line searches and accelerations. *International journal for numerical methods in engineering*, 19(9):1269–1289.

Crisfield, M. (1984). Accelerating and damping the modified newton-raphson method. *Computers & structures*, 18(3):395–407.

Crisfield, M. A., Remmers, J. J., Verhoosel, C. V., et al. (2012). *Nonlinear finite element analysis of solids and structures*. John Wiley & Sons.

Cruse, T. (1968). A direct formulation and numerical solution of the general transient elastodynamic problem. ii. *Journal of Mathematical Analysis and Applications*, 22(2):341–355.

Cruse, T. (1969). Numerical solutions in three dimensional elastostatics. *International journal of solids and structures*, 5(12):1259–1274.

Cruse, T. and Vanburen, W. (1971). Three-dimensional elastic stress analysis of a fracture specimen with an edge crack. *International Journal of Fracture Mechanics*, 7(1):1–15.

Cruse, T. A. (1974). An improved boundary-integral equation method for three dimensional elastic stress analysis. *Computers & Structures*, 4(4):741–754.

Cruse, T. A. and Rizzo, F. J. (1968). A direct formulation and numerical solution of the general transient elastodynamic problem. i. *Journal of Mathematical Analysis and Applications*, 22(1):244–259.

Czygan, O. and Von Estorff, O. (2002). Fluid-structure interaction by coupling bem and nonlinear fem. *Engineering Analysis with Boundary Elements*, 26(9):773–779.

De Greef, D., Pires, F., and Dirckx, J. J. (2017). Effects of model definitions and parameter values in finite element modeling of human middle ear mechanics. *Hearing research*, 344:195–206.

de Souza Neto, E. A., Peric, D., and Owen, D. R. (2011). *Computational methods for plasticity: theory and applications*. John Wiley & Sons.

Deeks, A. J. (2004). Prescribed side-face displacements in the scaled boundary finite-element method. *Computers & structures*, 82(15-16):1153–1165.

Deeks, A. J. and Augarde, C. E. (2007). A hybrid meshless local petrov–galerkin method for unbounded domains. *Computer methods in applied mechanics and engineering*, 196(4):843–852.

Deeks, A. J. and Randolph, M. F. (1994). Axisymmetric time-domain transmitting boundaries. *Journal of Engineering Mechanics*, 120(1):25–42.

Deeks, A. J. and Wolf, J. P. (2002a). Semi-analytical elastostatic analysis of unbounded two-dimensional domains. *International journal for numerical and analytical methods in Geomechanics*, 26(11):1031–1057.

Deeks, A. J. and Wolf, J. P. (2002b). A virtual work derivation of the scaled boundary finite-element method for elastostatics. *Computational Mechanics*, 28(6):489–504.

Ding, J. and Ye, W. (2004). A fast integral approach for drag force calculation due to oscillatory slip stokes flows. *International Journal for Numerical Methods in Engineering*, 60(9):1535–1567.

Ding, J. and Ye, W. (2006). A grid-based integral approach for quasilinear problems. *Computational Mechanics*, 38(2):113–118.

Drucker, D. C. and Prager, W. (1952). Soil mechanics and plastic analysis or limit design. *Quarterly of applied mathematics*, 10(2):157–165.

Du, Q. and Wang, D. (2006). Recent progress in robust and quality delaunay mesh generation. *Journal of Computational and Applied Mathematics*, 195(1):8–23.

Du Buat, M. et al. (1779). Principes d'hydraulique.

Engquist, B. and Majda, A. (1977). Absorbing boundary conditions for numerical simulation of waves. *Proceedings of the National Academy of Sciences*, 74(5):1765–1766.

Engquist, B. and Majda, A. (1979). Radiation boundary conditions for acoustic and elastic wave calculations. *Communications on pure and applied mathematics*, 32(3):313–357.

Estorff, O. v. and Antes, H. (1991). On fem-bem coupling for fluid-structure interaction analyses in the time domain. *International Journal for Numerical Methods in Engineering*, 31(6):1151–1168.

Everstine, G. C. (1981). A symmetric potential formulation for fluid-structure interaction. *Journal of Sound and Vibration*, 79(1):157–160.

Fahrendorf, F., De Lorenzis, L., and Gomez, H. (2018). Reduced integration at superconvergent points in isogeometric analysis. *Computer Methods in Applied Mechanics and Engineering*, 328:390–410.

Fan, H., Fu, J., Li, X., Pei, Y., Li, X., Pei, G., and Guo, Z. (2015). Implantation of customized 3-d printed titanium prosthesis in limb salvage surgery: a case series and review of the literature. *World journal of surgical oncology*, 13(1):308.

Fan, S. and Li, S. (2008). Boundary finite-element method coupling finite-element method for steady-state analyses of dam-reservoir systems. *Journal of engineering mechanics*, 134(2):133–142.

Fan, S., Li, S., and Yu, G. (2005). Dynamic fluid-structure interaction analysis

using boundary finite element method–finite element method. *Journal of Applied Mechanics*, 72(4):591–598.

Fata, S. N. (2008). Fast galerkin bem for 3d-potential theory. *Computational Mechanics*, 42(3):417.

Felippa, C. (1980). A family of early-time approximations for fluid-structure interaction. *Journal of applied mechanics*, 47(4):703–708.

Feng, K. (1983). Finite element method and natural boundary reduction. In *Proceedings of the international congress of mathematicians*, pages 1439–1453.

Feng, K. (1984). Asymptotic radiation conditions for reduced wave equations. *J. Comput. Math*, 2(2):130–138.

Fix, G. J. and Marin, S. P. (1978). Variational methods for underwater acoustic problems. *Journal of Computational Physics*, 28(2):253–270.

Flanagan, D. and Belytschko, T. (1981). A uniform strain hexahedron and quadrilateral with orthogonal hourglass control. *International journal for numerical methods in engineering*, 17(5):679–706.

Fries, T.-P., Byfut, A., Alizada, A., Cheng, K. W., and Schröder, A. (2011). Hanging nodes and xfem. *International Journal for Numerical Methods in Engineering*, 86(4-5):404–430.

Gao, X.-W. and Davies, T. G. (2002). *Boundary element programming in mechanics*, volume 1. Cambridge University Press.

Gedney, S. D. (1998). The perfectly matched layer absorbing medium. *Advances in Computational Electrodynamics: The Finite-Difference Time-Domain Method*, pages 263–344.

Geers, T. (1974). Shock response analysis of submerged structures. *Shock and Vibration Bulletin*, 44(3):17–32.

Geers, T. (1991). A fully consistent formulation of early-time approximations for acoustic media. In *The finite element method in the 1990Šs*, pages 521–528. Springer.

Geers, T. and Toothaker, B. (2000). Third-order doubly asymptotic approximations for computational acoustics. *Journal of Computational Acoustics*, 8(01):101–120.

Geers, T. L. (1971). Residual potential and approximate methods for three-dimensional fluid-structure interaction problems. *The Journal of the Acoustical Society of America*, 49(5B):1505–1510.

Geers, T. L. (1978). Doubly asymptotic approximations for transient motions of submerged structures. *Journal of the Acoustical Society of America*, 64:1500–1508.

Geers, T. L. and Felippa, C. A. (1983). Doubly asymptotic approximations for vibration analysis of submerged structures. *The Journal of the Acoustical Society of America*, 73(4):1152–1159.

Geers, T. L. and Sprague, M. A. (2010). A residual-potential boundary for time-dependent, infinite-domain problems in computational acoustics. *The Journal of the Acoustical Society of America*, 127(2):675–682.

Geers, T. L. and Zhang, P. (1988). Doubly asymptotic approximations for electromagnetic scattering problems. In *Boundary Element Methods in Applied Mechanics: Proceedings of the First Joint Japan/US Symposium on Boundary Element Methods, University of Tokyo, Tokyo, Japan, 3-6 October 1988*, page 357. Pergamon.

Givoli, D. (1990a). A combined analytic-finite element method for elastic shells. *International journal of solids and structures*, 26(2):185–198.

Givoli, D. (1990b). Finite element analysis of long cylindrical shells. *AIAA journal*, 28(7):1331–1333.

Givoli, D. (1991). Non-reflecting boundary conditions. *Journal of computational physics*, 94(1):1–29.

Givoli, D. (1999). Recent advances in the dtn fe method. *Archives of Computational Methods in Engineering*, 6(2):71–116.

Givoli, D. (2004). High-order local non-reflecting boundary conditions: a review. *Wave motion*, 39(4):319–326.

Givoli, D., Hagstrom, T., and Patlashenko, I. (2006). Finite element formulation with high-order absorbing boundary conditions for time-dependent waves. *Computer Methods in Applied Mechanics and Engineering*, 195(29-32):3666–3690.

Givoli, D. and Keller, J. B. (1989). A finite element method for large domains. *Computer Methods in Applied Mechanics and Engineering*, 76(1):41–66.

Givoli, D. and Keller, J. B. (1990). Non-reflecting boundary conditions for elastic waves. *Wave motion*, 12(3):261–279.

Givoli, D. and Neta, B. (2003). High-order non-reflecting boundary scheme for time-dependent waves. *Journal of Computational Physics*, 186(1):24–46.

Givoli, D., Neta, B., and Patlashenko, I. (2003). Finite element analysis of time-dependent semi-infinite wave-guides with high-order boundary treatment. *International Journal for Numerical Methods in Engineering*, 58(13):1955–1983.

Givoli, D. and Vigdergauz, S. (1993). Artificial boundary conditions for 2d problems in geophysics. *Computer methods in applied mechanics and engineering*, 110(1-2):87–101.

Goldstein, C. I. (1982). A finite element method for solving helmholtz type equations in waveguides and other unbounded domains. *Mathematics of Computation*, 39(160):309–324.

Goransson, J. and Davidsson, C. (1987). A three dimensional infinite element for wave propagation. *Journal of sound and vibration*, 115(3):556–559.

Gravenkamp, H., Bause, F., and Song, C. (2014). On the computation of dispersion curves for axisymmetric elastic waveguides using the scaled boundary finite element method. *Computers & Structures*, 131:46–55.

Gravenkamp, H., Birk, C., and Song, C. (2015). Simulation of elastic guided waves interacting with defects in arbitrarily long structures using the scaled boundary finite element method. *Journal of Computational Physics*, 295:438–455.

Gravenkamp, H., Man, H., Song, C., and Prager, J. (2013). The computation of dispersion relations for three-dimensional elastic waveguides using the scaled boundary finite element method. *Journal of Sound and Vibration*, 332(15):3756–3771.

Gravenkamp, H., Prager, J., Saputra, A. A., and Song, C. (2012). The simulation of lamb waves in a cracked plate using the scaled boundary finite element method. *The Journal of the Acoustical Society of America*, 132(3):1358–1367.

Gravenkamp, H., Saputra, A. A., Song, C., and Birk, C. (2017). Efficient wave propagation simulation on quadtree meshes using sbfem with reduced modal basis. *International Journal for Numerical Methods in Engineering*, 110(12):1119–1141.

Greengard, L. and Rokhlin, V. (1987). A fast algorithm for particle simulations. *Journal of computational physics*, 73(2):325–348.

Grote, M. J. and Keller, J. B. (1995). On nonreflecting boundary conditions. *Journal of Computational Physics*, 122(2):231–243.

Hagstrom, T. (1999). Radiation boundary conditions for the numerical simulation of waves. *Acta numerica*, 8:47–106.

Hagstrom, T., De Castro, M. L., Givoli, D., and Tzemach, D. (2007). Local high-order absorbing boundary conditions for time-dependent waves in guides. *Journal of Computational Acoustics*, 15(01):1–22.

Hagstrom, T. and Hariharan, S. (1998). A formulation of asymptotic and exact boundary conditions using local operators. *Applied Numerical Mathematics*, 27(4):403–416.

Hagstrom, T., Mar-Or, A., and Givoli, D. (2008). High-order local absorbing conditions for the wave equation: Extensions and improvements. *Journal of Computational Physics*, 227(6):3322–3357.

Hagstrom, T. and Warburton, T. (2004). A new auxiliary variable formulation of high-order local radiation boundary conditions: corner compatibility conditions and extensions to first-order systems. *Wave motion*, 39(4):327–338.

Hallquist, J. O. (1983). Theoretical manual for dyna3d. Technical report, Lawrence Livermore National Lab., CA (USA).

Hallquist, J. O. (1994). *LS-DYNA3D theoretical manual*. Livermore software technology corporation Livermore, CA.

Hamdan, F. (1999). Near-field fluid–structure interaction using lagrangian fluid finite elements. *Computers & structures*, 71(2):123–141.

Hamdi, M. A., Ousset, Y., and Verchery, G. (1978). A displacement method for the analysis of vibrations of coupled fluid-structure systems. *International Journal for Numerical Methods in Engineering*, 13(1):139–150.

Hammershøi, D. and Møller, H. (2002). Methods for binaural recording and reproduction. *Acta Acustica united with Acustica*, 88(3):303–311.

Harari, I. and Albocher, U. (2006). Studies of fe/pml for exterior problems of time-harmonic elastic waves. *Computer methods in applied mechanics and engineering*, 195(29-32):3854–3879.

Harari, I., Grosh, K., Hughes, T., Malhotra, M., Pinsky, P., Stewart, J., and Thompson, L. (1996). Recent developments in finite element methods for structural acoustics. *Archives of Computational Methods in Engineering*, 3(2-3):131–309.

Harari, I. and Hughes, T. J. (1992). Analysis of continuous formulations underlying the computation of time-harmonic acoustics in exterior domains. *Computer Methods in Applied Mechanics and Engineering*, 97(1):103–124.

Harari, I. and Hughes, T. J. (1994). Studies of domain-based formulations for computing exterior problems of acoustics. *International journal for numerical methods in engineering*, 37(17):2935–2950.

Harari, I., Patlashenko, I., and Givoli, D. (1998). Dirichlet-to-neumann maps for unbounded wave guides. *Journal of Computational Physics*, 143(1):200–223.

Harari, I., Slavutin, M., and Turkel, E. (2000). Analytical and numerical studies of a finite element pml for the helmholtz equation. *Journal of Computational Acoustics*, 8(01):121–137.

He, K. (2017). *Numerical Modelling of Cracking in Embankment Dams*. PhD thesis, School of civil and environmental Engineering, The University of New South Wales, Sydney, Australia.

Hiemstra, R. R., Calabro, F., Schillinger, D., and Hughes, T. J. (2017). Optimal and reduced quadrature rules for tensor product and hierarchically refined splines in isogeometric analysis. *Computer Methods in Applied Mechanics and Engineering*, 316:966–1004.

Higdon, R. L. (1986). Absorbing boundary conditions for difference approximations to the multidimensional wave equation. *Mathematics of Computation*, 47(176):437–459.

Higdon, R. L. (1992). Absorbing boundary conditions for acoustic and elastic waves in stratified media. *Journal of Computational Physics*, 101(2):386–418.

Higdon, R. L. (1994). Radiation boundary conditions for dispersive waves. *SIAM Journal on Numerical Analysis*, 31(1):64–100.

Hill, R. (1998). *The mathematical theory of plasticity*, volume 11. Oxford university press.

Hinton, E. and Owen, D. R. J. (1986). *Finite elements in plasticity: Theory and practice*. Pineridge Press Limited.

Hoskins, L. M. and Jacobsen, L. S. (1934). Water pressure in a tank caused by a simulated earthquake. *Bulletin of the seismological society of America*, 24(1):1–32.

Housner, G. W. (1957). Dynamic pressures on accelerated fluid containers. *Bulletin of the seismological society of America*, 47(1):15–35.

Hu, F. Q. (1996). On absorbing boundary conditions for linearized euler equations by a perfectly matched layer. *Journal of Computational Physics*, 129(1):201–219.

Huang, M. and Li, Y.-m. (2013). X-ray tomography image-based reconstruction of microstructural finite element mesh models for heterogeneous materials. *Computational Materials Science*, 67:63–72.

Hueck, U. and Wriggers, P. (1995). A formulation for the 4-node quadrilateral element. *International journal for numerical methods in engineering*, 38(18):3007–3037.

Hughes, T. J., Cohen, M., and Haroun, M. (1978). Reduced and selective integration techniques in the finite element analysis of plates. *Nuclear Engineering and Design*, 46(1):203–222.

Hull, D. and Bacon, D. J. (2001). *Introduction to dislocations*. Butterworth-Heinemann.

Israeli, M. and Orszag, S. A. (1981). Approximation of radiation boundary conditions. *Journal of computational physics*, 41(1):115–135.

Jacobsen, L. S. (1949). Impulsive hydrodynamics of fluid inside a cylindrical tank and of fluid surrounding a cylindrical pier. *Bulletin of the Seismological Society of America*, 39(3):189–204.

Jacquotte, O.-P. and Oden, J. T. (1984). Analysis of hourglass instabilities and control in underintegrated finite element methods. *Computer methods in applied mechanics and engineering*, 44(3):339–363.

Jaswon, M. (1963). Integral equation methods in potential theory. i. In *Proc. R. Soc. Lond. A*, volume 275, pages 23–32. The Royal Society.

Jaswon, M. and Ponter, A. (1963). An integral equation solution of the torsion problem. In *Proc. R. Soc. Lond. A*, volume 273, pages 237–246. The Royal Society.

Keller, J. B. and Givoli, D. (1989). Exact non-reflecting boundary conditions. *Journal of computational physics*, 82(1):172–192.

Khazaee, A. and Lotfi, V. (2014). Application of perfectly matched layers in the transient analysis of dam–reservoir systems. *Soil Dynamics and Earthquake Engineering*, 60:51–68.

Kim, N.-H. (2014). *Introduction to nonlinear finite element analysis*. Springer Science & Business Media.

Klein, G. T., Lu, Y., and Wang, M. Y. (2013). 3d printing and neurosurgeryŮready for prime time? *World neurosurgery*, 80(3):233–235.

Koh, B. C. and Kikuchi, N. (1987). New improved hourglass control for bilinear and trilinear elements in anisotropic linear elasticity. *Computer Methods in Applied Mechanics and Engineering*, 65(1):1–46.

Korelc, J. and Wriggers, P. (1997). Improved enhanced strain four-node element with taylor expansion of the shape functions. *International Journal for Numerical Methods in Engineering*, 40(3):407–421.

Kosloff, D. and Frazier, G. A. (1978). Treatment of hourglass patterns in low order finite element codes. *International journal for numerical and analytical methods in geomechanics*, 2(1):57–72.

Kress, R. (1985). Minimizing the condition number of boundary integral operators in acoustic and electromagnetic scattering. *The Quarterly Journal of Mechanics and Applied Mathematics*, 38(2):323–341.

Krysl, P., Grinspun, E., and Schröder, P. (2003). Natural hierarchical refinement for finite element methods. *International Journal for Numerical Methods in Engineering*, 56(8):1109–1124.

Kulak, R. (1985). Three-dimensional fluid-structure coupling in transient analysis. *Computers & structures*, 21(3):529–542.

Lachat, J. and Watson, J. (1976). Effective numerical treatment of boundary integral equations: A formulation for three-dimensional elastostatics. *International Journal for Numerical Methods in Engineering*, 10(5):991–1005.

Lahey, R. S., Miller, M. P., and Reymond, M. (1994). Msc/nastran reference manual, version 68. *The MacNeal-Schwendler Corporation*.

Lamb, H. (1932). *Hydrodynamics*. Cambridge university press.

Lee, J. H., Kim, J. K., and Kim, J. H. (2014). Nonlinear analysis of soil–structure interaction using perfectly matched discrete layers. *Computers & Structures*, 142:28–44.

Legrain, G., Allais, R., and Cartraud, P. (2011). On the use of the extended finite element method with quadtree/octree meshes. *International Journal for Numerical Methods in Engineering*, 86(6):717–743.

Lehmann, L. (2005). An effective finite element approach for soil-structure analysis in the time-domain. *Structural Engineering and Mechanics*, 21(4):437–450.

Lehmann, L., Langer, S., and Clasen, D. (2006). Scaled boundary finite element method for acoustics. *Journal of Computational Acoustics*, 14(04):489–506.

Lehmann, L. and Rüberg, T. (2006). Application of hierarchical matrices to the simulation of wave propagation in fluids. *International Journal for Numerical Methods in Biomedical Engineering*, 22(5):489–503.

Leis, R. (2013). *Initial boundary value problems in mathematical physics*. Courier Corporation.

Lenoir, M. and Tounsi, A. (1988). The localized finite element method and its application to the two-dimensional sea-keeping problem. *SIAM Journal on Numerical Analysis*, 25(4):729–752.

Leonetti, L., Liguori, F., Magisano, D., and Garcea, G. (2018). An efficient isogeometric solid-shell formulation for geometrically nonlinear analysis of elastic shells. *Computer Methods in Applied Mechanics and Engineering*, 331:159–183.

Li, C., Man, H., Song, C., and Gao, W. (2013). Fracture analysis of piezoelectric materials using the scaled boundary finite element method. *Engineering Fracture Mechanics*, 97:52–71.

Li, C., Song, C., Man, H., Ooi, E. T., and Gao, W. (2014). 2d dynamic analysis of cracks and interface cracks in piezoelectric composites using the sbfem. *International Journal of Solids and Structures*, 51(11-12):2096–2108.

Li, J., Shi, Z., and Liu, L. (2018). A unified scaled boundary finite element method for transient two-dimensional vibro-acoustic analysis of plate-like structures. *Computers & Structures*, 202:105–128.

Li, S. (2006). *Scaled boundary finite element method for fluid-structure interaction.* PhD thesis, Nanyang Technological University.

Li, S. (2009). Diagonalization procedure for scaled boundary finite element method in modeling semi-infinite reservoir with uniform cross-section. *International journal for numerical methods in engineering*, 80(5):596–608.

Li, S. (2011). Coupled finite element-scaled boundary finite element method for transient analysis of dam-reservoir interaction. *Computational Science and Its Applications-ICCSA 2011*, pages 26–34.

Li, S. (2012). Scaled boundary finite element method for semi-infinite reservoir with uniform cross section. *International Journal of Computational Methods*, 9(01):1240006.

LI, S.-m., LIANG, H., and LI, A.-m. (2008). A semi-analytical solution for characteristics of a dam-reservoir system with absorptive reservoir bottom. *Journal of Hydrodynamics, Ser. B*, 20(6):727–734.

Lian, W.-D., Legrain, G., and Cartraud, P. (2013). Image-based computational homogenization and localization: comparison between x-fem/levelset and voxel-based approaches. *Computational Mechanics*, 51(3):279–293.

Lin, G., Du, J., and Hu, Z. (2007). Dynamic dam-reservoir interaction analysis

including effect of reservoir boundary absorption. *Science in China Series E: Technological Sciences*, 50:1–10.

Lin, G., Wang, Y., and Hu, Z. (2012). An efficient approach for frequency-domain and time-domain hydrodynamic analysis of dam-reservoir systems. *Earthquake Engineering and Structural Dynamics*, 41:1725–1749.

Lindman, E. (1975). Şfree-spaceŤ boundary conditions for the time dependent wave equation. *Journal of computational physics*, 18(1):66–78.

Liu, J. and Lin, G. (2012). A scaled boundary finite element method applied to electrostatic problems. *Engineering Analysis with Boundary Elements*, 36(12):1721–1732.

Liu, W. K. and Belytschko, T. (1984). Efficient linear and nonlinear heat conduction with a quadrilateral element. *International Journal for Numerical Methods in Engineering*, 20(5):931–948.

Liu, W. K. and Chang, H. (1984). Efficient computational procedures for long-time duration fluid-structure interaction problems. *Journal of pressure vessel technology*, 106(4):317–322.

Liu, W. K., Hu, Y.-K., and Belytschko, T. (1994). Multiple quadrature underintegrated finite elements. *International Journal for Numerical Methods in Engineering*, 37(19):3263–3289.

Liu, W. K., Ong, J. S.-J., and Uras, R. A. (1985). Finite element stabilization matrices-a unification approach. *Computer Methods in Applied Mechanics and Engineering*, 53(1):13–46.

Liu, Y. (2009). *Fast multipole boundary element method: theory and applications in engineering*. Cambridge university press.

Liu, Y., Saputra, A. A., Wang, J., Tin-Loi, F., and Song, C. (2017). Automatic polyhedral mesh generation and scaled boundary finite element analysis of stl models. *Computer Methods in Applied Mechanics and Engineering*, 313:106–132.

Lo, S., Wu, D., and Sze, K. (2010). Adaptive meshing and analysis using transitional quadrilateral and hexahedral elements. *Finite Elements in Analysis and Design*, 46(1):2–16.

Löhner, R. and Parikh, P. (1988). Generation of three-dimensional unstructured grids by the advancing-front method. *International Journal for Numerical Methods in Fluids*, 8(10):1135–1149.

Lysmer, J. and Kuhlemeyer, R. L. (1969). Finite dynamic model for infinite media. *Journal of the Engineering Mechanics Division*, 95(4):859–878.

Maccamy, R. C. and Marin, S. (1980). A finite element method for exterior interface problems. *International Journal of Mathematics and Mathematical Sciences*, 3(2):311–350.

Maenchen, G. and Sack, S. (1964). The tensor code. in$\check{\text{T}}$ methods in computational physics$\check{\text{T}}$, vol. 3, fundamental methods in hydrodynamics.

Marburg, S. and Nolte, B. (2008). *Computational acoustics of noise propagation in fluids: finite and boundary element methods*, volume 578. Springer.

Marcal, P. and King, I. P. (1967). Elastic-plastic analysis of two-dimensional stress systems by the finite element method. *International Journal of Mechanical Sciences*, 9(3):143–155.

Marin, S. (1982). Computing scattering amplitudes for arbitrary cylinders under incident plane waves. *IEEE Transactions on antennas and propagation*, 30(6):1045–1049.

Masmoudi, M. (1987). Numerical solution for exterior problems. *Numerische mathematik*, 51(1):87–101.

Masters, N. and Ye, W. (2004). Fast bem solution for coupled 3d electrostatic and linear elastic problems. *Engineering Analysis with Boundary Elements*, 28(9):1175–1186.

Mathews, I. C. and Geers, T. L. (1987). A doubly asymptotic, nonreflecting boundary for ground-shock analysis. *Journal of applied mechanics*, 54(3):489–497.

Matthies, H. and Strang, G. (1979). The solution of nonlinear finite element equations. *International journal for numerical methods in engineering*, 14(11):1613–1626.

Mellado, M. and Rodríguez, R. (2001). Efficient solution of fluid-structure vibration problems. *Applied numerical mathematics*, 36(4):389–400.

Mises, R. v. (1913). Mechanik der festen körper im plastisch-deformablen zustand. *Nachrichten von der Gesellschaft der Wissenschaften zu Göttingen, Mathematisch-Physikalische Klasse*, 1913(4):582–592.

Moës, N., Dolbow, J., and Belytschko, T. (1999). A finite element method for crack growth without remeshing. *International journal for numerical methods in engineering*, 46(1):131–150.

Mohr, O. (1906). *Abhandlungen aus dem gebiete der technischen mechanik...*

Moyer, E. T. (1992). Performance of mapped infinite elements for exterior wave scattering applications. *International Journal for Numerical Methods in Biomedical Engineering*, 8(1):27–39.

Natarajan, S., Ooi, E. T., Saputra, A., and Song, C. (2017). A scaled boundary finite element formulation over arbitrary faceted star convex polyhedra. *Engineering Analysis with Boundary Elements*, 80:218–229.

Natarajan, S., Wang, J., Song, C., and Birk, C. (2015). Isogeometric analysis enhanced by the scaled boundary finite element method. *Computer Methods in Applied Mechanics and Engineering*, 283:733–762.

Nishimura, N. (2002). Fast multipole accelerated boundary integral equation methods. *Applied Mechanics Reviews*, 55(4):299–324.

Nitikitpaiboon, C. and Bathe, K. (1993). An arbitrary lagrangian-eulerian velocity potential formulation for fluid-structure interaction. *Computers & structures*, 47(4-5):871–891.

Olson, L. G. and Bathe, K.-J. (1985). Analysis of fluid-structure interactions. a direct symmetric coupled formulation based on the fluid velocity potential. *Computers & Structures*, 21(1-2):21–32.

Ooi, E., Natarajan, S., Song, C., and Ooi, E. (2017). Crack propagation modelling in concrete using the scaled boundary finite element method with hybrid polygon–quadtree meshes. *International Journal of Fracture*, 203(1-2):135–157.

Ooi, E. and Yang, Z. (2009). Modelling multiple cohesive crack propagation using a finite element–scaled boundary finite element coupled method. *Engineering analysis with boundary elements*, 33(7):915–929.

Ooi, E. and Yang, Z. (2011). Modelling dynamic crack propagation using the scaled boundary finite element method. *International journal for numerical methods in engineering*, 88(4):329–349.

Ooi, E. T., Natarajan, S., Song, C., and Ooi, E. H. (2016). Dynamic fracture simulations using the scaled boundary finite element method on hybrid polygon–quadtree meshes. *International Journal of Impact Engineering*, 90:154–164.

Ooi, E. T., Song, C., and Tin-Loi, F. (2014). A scaled boundary polygon formu-

lation for elasto-plastic analyses. *Computer methods in applied mechanics and engineering*, 268:905–937.

Ooi, E. T., Song, C., Tin-Loi, F., and Yang, Z. (2012). Polygon scaled boundary finite elements for crack propagation modelling. *International Journal for Numerical Methods in Engineering*, 91(3):319–342.

Owen, D. and Hinton, E. (1980). *Finite elements in plasticity*, volume 271. Pineridge press Swansea.

Pan, J. (2009). Acoustical properties of ancient chinese musical bells. *Proceedings of Acoustics 2009*.

Paronesso, A. and Wolf, J. P. (1995). Global lumped-parameter model with physical representation for unbounded medium. *Earthquake engineering & structural dynamics*, 24(5):637–654.

Paronesso, A. and Wolf, J. P. (1998). Recursive evaluation of interaction forces and property matrices from unit-impulse response functions of unbounded medium based on balancing approximation. *Earthquake engineering & structural dynamics*, 27(6):609–618.

Parvizian, J., Düster, A., and Rank, E. (2007). Finite cell method. *Computational Mechanics*, 41(1):121–133.

Patlashenko, I. and Givoli, D. (1997). Non-reflecting finite element schemes for three-dimensional acoustic waves. *Journal of Computational Acoustics*, 5(01):95–115.

Paul, S. (2009). Binaural recording technology: A historical review and possible future developments. *Acta acustica united with Acustica*, 95(5):767–788.

Phillips, J. R. and White, J. K. (1997). A precorrected-fft method for electrostatic

analysis of complicated 3-d structures. *IEEE Transactions on Computer-Aided Design of Integrated Circuits and Systems*, 16(10):1059–1072.

Prempramote, S. (2011). *Development of higher-order doubly asymptotic open boundaries for wave propagation in unbounded domains by extending the scaled boundary finite element method*. PhD thesis, School of civil and environmental Engineering, The University of New South Wales, Sydney, Australia.

Prempramote, S., Song, C., Tin-Loi, F., and Lin, G. (2009). High-order doubly asymptotic open boundaries for scalar wave equation. *International Journal for Numerical Methods in Engineering*, 79(3):340–374.

profguy (2014). Humerus right human skeleton upper arm bone.

Qi, L., Liu, H., Lutfy, J., Funnell, W. R. J., and Daniel, S. J. (2006). A nonlinear finite-element model of the newborn ear canal. *The Journal of the Acoustical Society of America*, 120(6):3789–3798.

Qi, Q. and Geers, T. L. (1997). Doubly asymptotic approximations for transient poroelastodynamics. *The Journal of the Acoustical Society of America*, 102(3):1361–1371.

Qi, Q. and Geers, T. L. (1998). Evaluation of the perfectly matched layer for computational acoustics. *Journal of Computational Physics*, 139(1):166–183.

Rabinovich, D., Givoli, D., and Bécache, E. (2010). Comparison of high-order absorbing boundary conditions and perfectly matched layers in the frequency domain. *International Journal for Numerical Methods in Biomedical Engineering*, 26(10):1351–1369.

Riks, E. (1972). The application of newtonŠs method to the problem of elastic stability. *Journal of Applied Mechanics*, 39(4):1060–1065.

Riks, E. (1979). An incremental approach to the solution of snapping and buckling problems. *International journal of solids and structures*, 15(7):529–551.

Rizzo, F. and Shippy, D. (1968). A formulation and solution procedure for the general non-homogeneous elastic inclusion problem. *International Journal of Solids and Structures*, 4(12):1161–1179.

Rizzo, F. and Shippy, D. (1970a). A method for stress determination in plane anisotropic elastic bodies. *Journal of Composite Materials*, 4(1):36–61.

Rizzo, F. and Shippy, D. (1970b). A method of solution for certain problems of transient heat conduction. *AIAA Journal*, 8(11):2004–2009.

Rizzo, F. and Shippy, D. (1971). An application of the correspondence principle of linear viscoelasticity theory. *SIAM Journal on Applied Mathematics*, 21(2):321–330.

Rizzo, F. and Shippy, D. (1977). An advanced boundary integral equation method for three-dimensional thermoelasticity. *International Journal for Numerical Methods in Engineering*, 11(11):1753–1768.

Rizzo, F. J. (1967). An integral equation approach to boundary value problems of classical elastostatics. *Quarterly of applied mathematics*, 25(1):83–95.

Rjasanow, S. and Steinbach, O. (2007). *The fast solution of boundary integral equations*. Springer Science & Business Media.

Rokhlin, V. (1985). Rapid solution of integral equations of classical potential theory. *Journal of computational physics*, 60(2):187–207.

Saad, Y. and Schultz, M. H. (1986). Gmres: A generalized minimal residual algorithm for solving nonsymmetric linear systems. *SIAM Journal on scientific and statistical computing*, 7(3):856–869.

Saputra, A., Talebi, H., Tran, D., Birk, C., and Song, C. (2017a). Automatic image-based stress analysis by the scaled boundary finite element method. *International Journal for Numerical Methods in Engineering*, 109(5):697–738.

Saputra, A. A., Sladek, V., Sladek, J., and Song, C. (2017b). Micromechanics determination of effective material coefficients of cement-based piezoelectric ceramic composites. *Journal of Intelligent Material Systems and Structures*, page 1045389X17721047.

ScanTheWorld (2016). Bronze bell (bo) at the british museum, london.

Schenck, H. A. (1968). Improved integral formulation for acoustic radiation problems. *The journal of the acoustical society of America*, 44(1):41–58.

Schillinger, D., Hossain, S. J., and Hughes, T. J. (2014). Reduced bézier element quadrature rules for quadratic and cubic splines in isogeometric analysis. *Computer Methods in Applied Mechanics and Engineering*, 277:1–45.

Schulz, J. (1985). Finite element hourglassing control. *International journal for numerical methods in engineering*, 21(6):1039–1048.

Seybert, A., Soenarko, B., Rizzo, F., and Shippy, D. (1985). An advanced computational method for radiation and scattering of acoustic waves in three dimensions. *The journal of the acoustical society of America*, 77(2):362–368.

Simo, J. C. and Taylor, R. L. (1985). Consistent tangent operators for rate-independent elastoplasticity. *Computer methods in applied mechanics and engineering*, 48(1):101–118.

Singer, I. and Turkel, E. (2004). A perfectly matched layer for the helmholtz equation in a semi-infinite strip. *Journal of Computational Physics*, 201(2):439–465.

Soares Jr, D. and Godinho, L. (2008). An optimised fem–bem time-domain iterative

coupling algorithm for dynamic analyses. *Computers & Structures*, 86(19):1839–1844.

Soares Jr, D. and Mansur, W. (2005). An efficient time-domain bem/fem coupling for acoustic-elastodynamic interaction problems. *CMES Comput. Model. Eng. Sci*, 8(2):153–164.

Soares Jr, D., Von Estorff, O., and Mansur, W. (2004). Iterative coupling of bem and fem for nonlinear dynamic analyses. *Computational Mechanics*, 34(1):67–73.

Sommerfeld, A. (1949). *Partial differential equations in physics*, volume 1. Academic press.

Song, C. (2004a). A matrix function solution for the scaled boundary finite-element equation in statics. *Computer Methods in Applied Mechanics and Engineering*, 193(23):2325–2356.

Song, C. (2004b). A super-element for crack analysis in the time domain. *International journal for numerical methods in engineering*, 61(8):1332–1357.

Song, C. (2005). Evaluation of power-logarithmic singularities, t-stresses and higher order terms of in-plane singular stress fields at cracks and multi-material corners. *Engineering Fracture Mechanics*, 72(10):1498–1530.

Song, C. (2006). Dynamic analysis of unbounded domains by a reduced set of base functions. *Computer methods in applied mechanics and engineering*, 195(33-36):4075–4094.

Song, C. (2009). The scaled boundary finite element method in structural dynamics. *International Journal for Numerical Methods in Engineering*, 77(8):1139–1171.

Song, C. and Bazyar, M. H. (2007). A boundary condition in padé series for frequency-domain solution of wave propagation in unbounded domains. *International journal for numerical methods in engineering*, 69(11):2330–2358.

Song, C., Ooi, E. T., and Natarajan, S. (2017). A review of the scaled boundary finite element method for two-dimensional linear elastic fracture mechanics. *Engineering Fracture Mechanics*.

Song, C., Tin-Loi, F., and Gao, W. (2010). Transient dynamic analysis of interface cracks in anisotropic bimaterials by the scaled boundary finite-element method. *International Journal of Solids and Structures*, 47(7-8):978–989.

Song, C. and Vrcelj, Z. (2008). Evaluation of dynamic stress intensity factors and t-stress using the scaled boundary finite-element method. *Engineering fracture mechanics*, 75(8):1960–1980.

Song, C. and Wolf, J. P. (1995). Consistent infinitesimal finite-element-cell method: out-of-plane motion. *Journal of engineering mechanics*, 121(5):613–619.

Song, C. and Wolf, J. P. (1996). Consistent infinitesimal finite-element-cell method: three-dimensional vector wave equation. *International Journal for Numerical Methods in Engineering*, 39(13):2189–2208.

Song, C. and Wolf, J. P. (1997). The scaled boundary finite-element method-alias consistent infinitesimal finite-element cell method-for elastodynamics. *Computer Methods in applied mechanics and engineering*, 147(3-4):329–355.

Song, C. and Wolf, J. P. (1999a). Body loads in scaled boundary finite-element method. *Computer methods in applied mechanics and engineering*, 180(1):117–135.

Song, C. and Wolf, J. P. (1999b). The scaled boundary finite element method-alias consistent infinitesimal finite element cell method-for diffusion. *International Journal for Numerical Methods in Engineering*, 45(10):1403–1431.

Song, C. and Wolf, J. P. (2000). The scaled boundary finite-element method–a primer: solution procedures. *Computers & Structures*, 78(1):211–225.

St Venant, B. d. (1870). Mémoire sur l'etablissement des equations différentielles des mouvements intérieurs opérés dans les corps solids ductiles au delà des limites où l'elasticité pourrait les ramener à leur premier etat. *Comptes Rendus70*, 473.

Staten, M. L., Canann, S. A., and Owen, S. J. (1999). Bmsweep: locating interior nodes during sweeping. *Engineering with Computers*, 15(3):212–218.

Steinbrugge, K. V. (1970). Earthquake damage and structural performance in the united states.

Stelson, T. E. (1955). Virtual mass and acceleration in fluids. In *Proceedings of the American Society of Civil Engineers*, volume 81, pages 1–9. ASCE.

Stippes, M. and Rizzo, F. (1977). A note on the body force integral of classical elastostatics. *Zeitschrift für angewandte Mathematik und Physik ZAMP*, 28(2):339–341.

Sun, Z., Ooi, E. T., and Song, C. (2015). Finite fracture mechanics analysis using the scaled boundary finite element method. *Engineering Fracture Mechanics*, 134:330–353.

Symm, G. (1963). Integral equation methods in potential theory. ii. In *Proc. R. Soc. Lond. A*, volume 275, pages 33–46. The Royal Society.

Systèmes, D. (2007). Abaqus theory manual. *Dessault Systémes, Providence, RI.*

szczehoo (2014). Ear.

Tabarraei, A. and Sukumar, N. (2007). Adaptive computations using material forces and residual-based error estimators on quadtree meshes. *Computer methods in applied mechanics and engineering*, 196(25):2657–2680.

Talebi, H., Saputra, A., and Song, C. (2016). Stress analysis of 3d complex geometries using the scaled boundary polyhedral finite elements. *Computational Mechanics*, 58(4):697–715.

Tautges, T. J., Blacker, T., and Mitchell, S. A. (1996). The whisker weaving algorithm: A connectivity-based method for constructing all-hexahedral finite element meshes. *International Journal for Numerical Methods in Engineering*, 39(19):3327–3349.

Thompson, L. and Pinsky, P. (2004). Acoustics: Encyclopedia of computational mechanics. *Edited by E. Stein, R. de Borst and TJR Hughes. Jonh Wiley & Sons, Ltda.*

Tresca, H. (1864). Sur l'gcoulement des corps solides soumis d de fortes pressions,'. *Comptes Rendus de l'Acaddmie des Sciences (Paris), 59*, 754.

Tsynkov, S. and Turkel, E. (2001). A cartesian perfectly matched layer for the helmholtz equation. artificial boundary conditions with applications to cem. loic tourvete.

Tsynkov, S. V. (1998). Numerical solution of problems on unbounded domains. a review. *Applied Numerical Mathematics*, 27(4):465–532.

Underwood, P. and Geers, T. L. (1981). Doubly asymptotic boundary–element analysis of dynamic soil–structure interaction. *International Journal of Solids and Structures*, 17:687–697.

Vaish, A. K. and Chopra, A. K. (1974). Earthquake finite element analysis of structure-foundation systems. *Journal of the Construction Division*, 100(ASCE 10990).

Ventola, C. L. (2014). Medical applications for 3d printing: current and projected uses. *Pharmacy and Therapeutics*, 39(10):704.

Vermeer, P. A. (1998). Non-associated plasticity for soils, concrete and rock. In *Physics of dry granular media*, pages 163–196. Springer.

Volandri, G., Carmignani, C., Di Puccio, F., and Forte, P. (2014). Finite element formulations applied to outer ear modeling. *Strojniški vestnik-Journal of Mechanical Engineering*, 60(5):363–372.

von Karman, T., Bauman, P., Rowe, R. R., Prandtl, L., Pearce, C. E., Brahtz, J. H., Heilbron, C., Bakhmeteff, B. A., and Mononobe, N. (1933). Discussion of "water pressures on dams during earthquakes by h. m. westergaard". *Transactions of the American Society of Civil Engineers*, 98(2):434–470.

Vu, T. H. and Deeks, A. J. (2006). Use of higher-order shape functions in the scaled boundary finite element method. *International Journal for Numerical Methods in Engineering*, 65(10):1714–1733.

Wang, X., Jin, F., Prempramote, S., and Song, C. (2011). Time-domain analysis of gravity dam–reservoir interaction using high-order doubly asymptotic open boundary. *Computers & structures*, 89(7):668–680.

Wegner, J., Yao, M., and Zhang, X. (2005). Dynamic wave-soil-structure interaction analysis in the time domain. *Computers & structures*, 83(27):2206–2214.

Wempner, G. A. (1971). Discrete approximations related to nonlinear theories of solids. *International Journal of Solids and Structures*, 7(11):1581–1599.

Westergaard, H. M. (1933). Water pressures on dams during earthquakes. *Trans. ASCE*, 98:418–432.

White, W., Lee, I. K., and Valliappan, S. (1977). Unified boundary for finite dynamic models. *Journal of the Engineering Mechanics Division*, 103(5):949–964.

Wilson, R. and Cruse, T. (1978). Efficient implementation of anisotropic three dimensional boundary-integral equation stress analysis. *International Journal for Numerical Methods in Engineering*, 12(9):1383–1397.

Wolf, J. and Hall, W. (1988). *Soil-structure-interaction analysis in time domain*. Number LCH-BOOK-2008-037. A Division of Simon & Schuster.

Wolf, J. P. (2003). *The scaled boundary finite element method*. John Wiley & Sons.

Wolf, J. P. and Song, C. (1995). Consistent infinitesimal finite-element-cell method: in-plane motion. *Computer methods in applied mechanics and engineering*, 123(1-4):355–370.

Wolf, J. P. and Song, C. (1996). *Finite-element modelling of unbounded media*. Wiley Chichester.

Wolf, J. P. and Song, C. (2000). The scaled boundary finite-element method–a primer: derivations. *Computers & Structures*, 78(1):191–210.

Wriggers, P. and Hueck, U. (1996). A formulation of the qs6 element for large elastic deformations. *International journal for numerical methods in engineering*, 39(9):1437–1454.

Wu, C.-W., Huang, C.-F., and Liu, Y.-W. (2013). Sound analysis and synthesis of marquis yi of zeng's chime-bell set. In *Proceedings of Meetings on Acoustics ICA2013*, volume 19, page 035077. ASA.

Xu, H., Zou, D., Kong, X., Hu, Z., and Su, X. (2018). A nonlinear analysis of dynamic interactions of cfrd–compressible reservoir system based on fem–sbfem. *Soil Dynamics and Earthquake Engineering*, 112:24–34.

Yamada, Y., Yoshimura, N., and Sakurai, T. (1968). Plastic stress-strain matrix and its application for the solution of elastic-plastic problems by the finite element method. *International Journal of Mechanical Sciences*, 10(5):343–354.

Yan, Z., Zhang, J., and Ye, W. (2010a). Rapid solution of 3-d oscillatory elastodynamics using the pfft accelerated bem. *Engineering analysis with boundary elements*, 34(11):956–962.

Yan, Z., Zhang, J., Ye, W., and Yu, T. (2010b). Numerical characterization of porous solids and performance evaluation of theoretical models via the precorrected-fft accelerated bem. *Computer Modeling in Engineering and Sciences (CMES)*, 55(1):33.

Yang, Z. (2006). Fully automatic modelling of mixed-mode crack propagation using scaled boundary finite element method. *Engineering Fracture Mechanics*, 73(12):1711–1731.

Yerry, M. A. and Shephard, M. S. (1984). Automatic three-dimensional mesh generation by the modified-octree technique. *International Journal for Numerical Methods in Engineering*, 20(11):1965–1990.

Young, P., Beresford-West, T., Coward, S., Notarberardino, B., Walker, B., and Abdul-Aziz, A. (2008). An efficient approach to converting three-dimensional image data into highly accurate computational models. *Philosophical Transactions of the Royal Society of London A: Mathematical, Physical and Engineering Sciences*, 366(1878):3155–3173.

Yu, G., Lie, S., and Fan, S. (2002). Stable boundary element method/finite element method procedure for dynamic fluid–structure interactions. *Journal of engineering mechanics*, 128(9):909–915.

Zeng, Y., He, J., and Liu, Q. (2001). The application of the perfectly matched layer in numerical modeling of wave propagation in poroelastic media. *Geophysics*, 66(4):1258–1266.

Zhang, X., Wegner, J., and Haddow, J. (1999). Three-dimensional dynamic soil–structure interaction analysis in the time domain. *Earthquake engineering & structural dynamics*, 28(12):1501–1524.

Zhong, H., Li, H., Ooi, E. T., and Song, C. (2018). Hydraulic fracture at the dam-foundation interface using the scaled boundary finite element method coupled

with the cohesive crack model. *Engineering Analysis with Boundary Elements*, 88:41–53.

Zienkiewicz, O. and Bettess, P. (1976). Infinite elements in the study of fluid-structure interaction ppoelems. In *Computing methods in applied sciences*, pages 133–172. Springer.

Zienkiewicz, O., Emson, C., and Bettess, P. (1983). A novel boundary infinite element. *International Journal for Numerical Methods in Engineering*, 19(3):393–404.

Zienkiewicz, O., Kelly, D., and Bettess, P. (1977). The coupling of the finite element method and boundary solution procedures. *International Journal for Numerical Methods in Engineering*, 11(2):355–375.

Zienkiewicz, O., Valliappan, S., and King, I. (1969). Elasto-plastic solutions of engineering problems Śinitial stressŠ, finite element approach. *International Journal for Numerical Methods in Engineering*, 1(1):75–100.

Zou, D., Chen, K., Kong, X., and Liu, J. (2017). An enhanced octree polyhedral scaled boundary finite element method and its applications in structure analysis. *Engineering Analysis with Boundary Elements*, 84:87–107.